IAGA Special Sopron Book Series 3

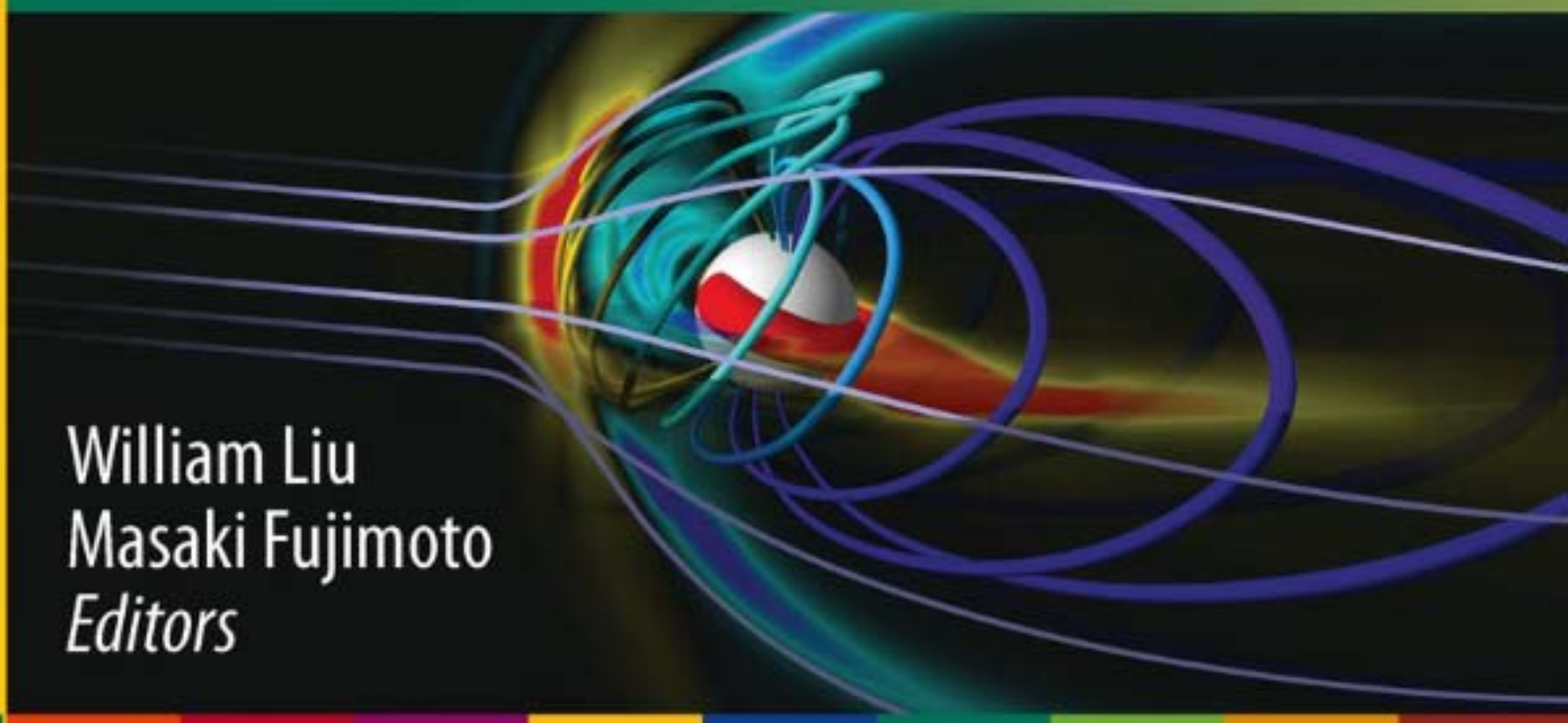

William Liu
Masaki Fujimoto
Editors

The Dynamic Magnetosphere

planetearth® Earth Sciences for Society
IAGA
Springer

IAGA Special Sopron Book Series

Volume 3

Series Editor

Bengt Hultqvist
The Swedish Institute of Space Physics, Kiruna, Sweden

The International Association of Geomagnetism and Aeronomy is one of the eight Associations of the International Union of Geodesy and Geophysics (IUGG).

IAGA's Mission

The overall purpose of IAGA is set out in the first statute of the Association:

- to promote studies of magnetism and aeronomy of the Earth and other bodies of the solar system, and of the interplanetary medium and its interaction with these bodies, where such studies have international interest;
- to encourage research in these subjects by individual countries, institutions or persons and to facilitate its international coordination;
- to provide an opportunity on an international basis for discussion and publication of the results of the researches; and
- to promote appropriate standardizations of observational programs, data acquisition systems, data analysis and publication.

Volumes in this series:

The Earth's Magnetic Interior
Edited by E. Petrovský, E. Herrero-Bervera, T Harinarayana and D. Ivers

Aeronomy of the Earth's Atmosphere and Ionosphere
Edited by M.A. Abdu, D. Pancheva and A. Bhattacharyya

The Dynamic Magnetosphere
Edited by W. Liu and M. Fujimoto

The Sun, the Solar Wind, and the Heliosphere
Edited by M.P. Miralles and J. Sánchez Almeida

Geomagnetic Observations and Models
Edited by M. Mandea and M. Korte

For titles published in this series, go to
http://www.springer.com/series/8636

The Dynamic Magnetosphere

Editors

William Liu
Canadian Space Agency, St. Hubert, QC, Canada

Masaki Fujimoto
Institute of Space and Astronautical Science, Kanagawa, Japan

Springer

planetearth® Earth Sciences for Society

IAGA

Editors
Prof. Dr. William Liu
Canadian Space Agency
Space Science and Technology Branch
6767 route de l'Aéroport
St-Hubert, Québec J3Y 8Y9
Canada
william.liu@asc-csa.gc.ca

Prof. Dr. Masaki Fujimoto
Institute of Space
& Astronautical Science (ISAS)
Yoshinodai 3-1-1
229-8510 Sagamihara
Kanagawa
Japan
fujimoto@stp.isas.jaxa.jp

ISBN 978-94-007-0500-5 e-ISBN 978-94-007-0501-2
DOI 10.1007/978-94-007-0501-2
Springer Dordrecht Heidelberg London New York

Library of Congress Control Number: 2011930414

Cover illustration: In a Space Weather Modeling Framework (SWMF) simulation of the Halloween 2003 space storms, the magnetosphere responds to a CME associated with the X-17.2 flare on October 29. The visualization shows the last closed magnetic field lines, color-coded with pressure. The gray sphere is located at 3 Earth radii, while the red band on that sphere is a 100 nano-Pascals (nPa) pressure isosurface (Image credit: Darren De Zeeuw, Center for Space Environment Modeling, University of Michigan).

Printed on acid-free paper

Springer is part of Springer Science+Business Media (www.springer.com)

Foreword by the Series Editor

The IAGA Executive Committee decided in 2008, at the invitation of Springer, to publish a series of books, which should present the status of the IAGA sciences at the time of the IAGA 2009 Scientific Assembly in Sopron, Hungary, the "IAGA Special Sopron Series". It consists of five books, one for each of the IAGA Divisions, which together cover the IAGA sciences:

Division I – Internal Magnetic Field
Division II – Aeronomic Phenomena
Division III – Magnetospheric Phenomena
Division IV – Solar Wind and Interplanetary Field
Division V – Geomagnetic Observatories, Surveys and Analyses.

The groups of Editors of the books contain members of the IAGA Executive Committee and of the leadership of the respective Division, with, for some of the books, one or a few additional leading scientists in the respective fields.

The IAGA Special Sopron Series of books are the first ever (or at least in many decades) with the ambition to present a full coverage of the present status of all the IAGA fields of the geophysical sciences. In order to achieve this goal each book contains a few "overview papers", which together summarize the knowledge of all parts of the respective field. These major review papers are complemented with invited reviews of special questions presented in Sopron. Finally, in some of the books a few short "contributed" papers of special interest are included. Thus, we hope the books will be of interest to both those who want a relatively concise presentation of the status of the sciences and to those who seek the most recent achievements.

I want to express my thanks to the editors and authors who have prepared the content of the books and to Petra van Steenbergen at Springer for good cooperation.

Kiruna, Sweden
October 2010

Bengt Hultqvist

Preface

On August 23–30, 2009, the 11th Scientific Assembly of International Association of Geomagnetism and Aeronomy (IAGA) took place in Sopron, Hungary. Following the successful conclusion of the Assembly, the IAGA Executive Committee decided that a Book Series was to be published to summarize the important research progress reported during the meeting. A book was dedicated to each of IAGA's five divisions. *The Dynamic Magnetosphere* is a representation of research highlights from IAGA Division III – Magnetospheric Phenomena.

In the decade preceding the Sopron Assembly, the state of the art of magnetospheric research had evolved to a new level, thanks to the variety and sophistication of experimental satellite missions flown. Cluster, IMAGE, THEMIS, to name but a few, were launched in this period, while ISTP stalwarts such as Polar, Geotail, and FAST had their peak periods of scientific performance well into the decade, as well. Not to be overlooked was the flights of the Cassini satellite to Saturn and Kaguya satellite to the moon, missions that have expanded our observational coverage of magnetospheric phenomena. While research results from these missions have been reported extensively in the literature, a book that projects a reasonably broad and insightful cross section of our field has been lacking. This is the void the present volume seeks to fill.

With this goal in mind, working with Division III leaders, we have invited a number of researchers, who participated in the Sopron IAGA Assembly, to write reviews and research articles for the volume. These contributions were reviewed by peer experts and accepted after major scientific issues were resolved. While not an exhaustive report of the state of magnetospheric research today, the volume distinguishes itself as a 'quick' entry point and handy roadmap for the reader to appraise major trends and research problems, particularly in light of the satellite missions mentioned above.

The past decade also saw tremendous progress in our ability to use computer simulations to achieve first-principle understanding of magnetospheric phenomena and novel data analysis techniques to recognize features and patterns that may not be captured by a more traditional approach. This volume contains examples of the latest of our endeavours in these areas.

The 20 chapters making up the volume can be divided into six themes: Solar Wind-Magnetosphere Interaction, Magnetotail Dynamics, Inner Magnetopheric Processes; Waves and Turbulence in Magnetosphere-Ionosphere Coupling; Ionospheric Drivers of the Magnetosphere, and Extraterrestrial Magnetospheres. In each of the themes, some of the latest results are presented. Combined with the extensive references, these chapters serve to give graduate students, as well as working scientists interested in the development of a related area, an overview of some problems of current interest.

Moreover, read as an organic whole, the volume serves to highlight the interconnected nature of the magnetosphere and give the reader an outlook on how our science will likely evolve in the new decade, as new missions and new data enter into the fray.

Many people have made valuable contributions to this book. Bengt Hulqvist, as Series Editor, exercised leadership in ensuring a high standard of publication. Anna Milillo played an instrumental role in identifying potential authors. John Ma helped with the preparation of the volume. Last but not least, more than twenty researchers acted as referees for the articles, and their assistance was an essential factor the success of this endeavour which, we believe, will stand the test of time as an authoritative source of information of magnetospheric research at a crucial juncture in time.

Montréal, Canada — William Liu
Tokyo, Japan — Masaki Fujimoto

Contents

Contributors

Takumi Abe Japan Aerospace Exploration Agency, Institute of Space and Astronautical Science, Sagamihara, Kanagawa, Japan, takumi.abe@isas.jaxa.jp

Anastasios Anastasiadis Institute for Space Applications and Remote Sensing, National Observatory of Athens, Athens, Greece, anastasi@noa.gr

C.R. Anekallu Finnish Meteorological Institute, Helsinki, Finland, Chandrasekhar.anekallu@fmi.fi

V. Angelopoulos Institute of Geophysics and Planetary Physics, University of California, Los Angeles, CA, USA, vassilis@ucla.edu

Elizaveta E. Antonova Skobeltsyn Institute of Nuclear Physics, Moscow State University, Moscow, Russia; Space Research Institute RAS, Moscow, Russia, antonova@orearm.msk.ru

Christopher S. Arridge Mullard Space Science Laboratory, Department of Space and Climate Physics, University College London, Dorking, Surrey, UK; The Centre for Planetary Sciences at UCL/Birkbeck, London, UK, csa@mssl.ucl.ac.uk

Kazushi Asamura Institute of Space and Astronautical Science, Japan Aerospace Exploration Agency, Sagamihara, Kanagawa, Japan, asamura@stp.isas.jaxa.jp

Georgios Balasis Institute for Space Applications and Remote Sensing, National Observatory of Athens, Athens, Greece, gbalasis@space.noa.gr

Joachim Birn Los Alamos National Laboratory, Los Alamos, NM, USA, jbirn@lanl.gov

Christopher C. Chaston Space Sciences Laboratory, University of California, Berkeley, CA, USA, ccc@ssl.berkeley.edu

Ioannis A. Daglis Institute for Space Applications and Remote Sensing, National Observatory of Athens, Athens, Greece, daglis@space.noa.gr

I. Dandouras CESR, Université de Toulouse, Toulouse, France, iannis.dandouras@cesr.fr

Jonathan P. Eastwood The Blackett Laboratory, Imperial College London, London, UK, jonathan.eastwood@imperial.ac.uk

Y. Ebihara Institute for Advanced Research, Nagoya University, Aichi, Japan (Now at Research Institute for Sustainable Humanosphere, Kyoto University, Uji, Japan), ebihara@rish.kyoto-u.ac.jp

Konstantinos Eftaxias Section of Solid State Physics, Department of Physics, University of Athens, Athens, Greece, ceftax@phys.uoa.gr

M.J. Engebretson Augsburg College, Minneapolis, MN, USA, engebret@augsburg.edu

Charles J. Farrugia Department of Physics, University of New Hampshire, Durham, NC, USA; Space Science Center, University of New Hampshire, Durham, NC, USA, charlie.farrugia@unh.edu

E. Fedorov Institute of the Physics of the Earth, Moscow, Russia, ENFedorov1@yandex.ru

Colin Forsyth Mullard Space Science Laboratory, University College London, Dorking, Surrey, UK, cfo@mssl.ucl.ac.uk

Claire Foullon Department of Physics, Centre for Fusion, Space and Astrophysics, University of Warwick, Coventry, UK, claire.foullon@warwick.ac.uk

Shigeru Fujita Meteorological College, Kashiwa, Chiba, Japan, sfujita@mc-jma.go.jp

B. Heilig Eotvos Lorand Geophysical Institute, Tihany, Hungary, heilig@elgi.hu

M. Hirahara Department of Earth and Planetary Science, Graduate School of Science, The University of Tokyo, Tokyo, Japan, hirahara@stelab.nagoya-u.ac.jp

A. Ieda Solar-Terrestrial Environment Laboratory, Nagoya University, Furo-cho, Chikusa-ku, Nagoya, Japan, ieda@stelab.nagoya-u.ac.jp

Vania K. Jordanova Space Science and Applications, Los Alamos National Laboratory, Los Alamos, NM, USA, vania@lanl.gov

Igor P. Kirpichev Space Research Institute RAS, Moscow, Russia; Skobeltsyn Institute of Nuclear Physics, Moscow State University, Moscow, Russia, ikir@iki.rssi.ru

H.E.J. Koskinen Department of Physics, University of Helsinki, Helsinki, Finland; Finnish Meteorological Institute, Helsinki, Finland, hannu.e.koskinen@helsinki.fi

T.V. Laitinen Finnish Meteorological Institute, Helsinki, Finland, tiera.laitinen@fmi.fi

Benoit Lavraud Centre d'Etude Spatiale des Rayonnements, Université de Toulouse (UPS), Toulouse Cedex 4, France; Centre National de la Recherche Scientifique, UMR, Toulouse, France, benoit.lavraud@cesr.fr

E.A. Lucek Department of Physics, Imperial College, London, UK, e.lucek@imperial.ac.uk

H. Luehr German Research Centre for Geosciences, Telegrafenberg, Potsdam, Germany, luehr@gfz-potsdam.de

Anthony T.Y. Lui Applied Physics Laboratory, The Johns Hopkins University, Laurel, MD, USA, tony.lui@jhuapl.edu

L.R. Lyons Department of Atmospheric and Ocean Sciences, University of California, Los Angeles, CA, USA, larry@atmos.ucla.edu

S. Machida Department of Geophysics, Kyoto University, Kitashirakawa-Oiwake-cho, Sakyo-ku, Kyoto, Japan, machida@kugi.kyoto-u.ac.jp

Masaki Matsushima Tokyo Institute of Technology, Tokyo, Japan, mmatsush@geo.titech.ac.jp

S.B. Mende Space Science Laboratory, University of California, Berkeley, CA, USA, mende@ssl.berkeley.edu

Frederick W. Menk School of Mathematical and Physical Sciences, The University of Newcastle, Callaghan, NSW, Australia, fred.menk@newcastle.edu.au

Y. Miyashita Solar-Terrestrial Environment Laboratory, Nagoya University, Furo-cho, Chikusa-ku, Nagoya, Japan, miyasita@stelab.nagoya-u.ac.jp

Y. Miyoshi Solar-Terrestrial Environment Laboratory, Nagoya University, Aichi, Japan, miyoshi@stelab.nagoya-u.ac.jp

Tetsuo Motoba National Institute of Polar Research, Tachikawa, Tokyo, Japan, motoba.tetsuo@nipr.ac.jp

Hans Nilsson Swedish Institute of Space Physics, Kiruna, Sweden, hans.nilsson@irf.se

Y. Nishimura Department of Atmospheric and Ocean Sciences, University of California, Los Angeles, CA, USA; Solar-Terrestrial Environment Laboratory, Nagoya University, Furocho, Chikusa, Nagoya, Japan, toshi@atmos.ucla.edu

Masaki N. Nishino Institute of Space and Astronautical Science, Japan Aerospace Exploration Agency, Sagamihara, Kanagawa, Japan, nishino@stp.isas.jaxa.jp

Ksenia G. Orlova Skobeltsyn Institute of Nuclear Physics, Moscow State University, Moscow, Russia, ks13orl@list.ru

Ilya L. Ovchinnikov Skobeltsyn Institute of Nuclear Physics, Moscow State University, Moscow, Russia, ilya@prao.ru

M. Palmroth Finnish Meteorological Institute, Helsinki, Finland, minna.palmroth@fmi.fi

W.K. Peterson Laboratory of Atmospheric and Space Physics, University of Colorado, Boulder, CO, USA, bill.peterson@lasp.colorado.edu

V. Pilipenko Space Research Institute, Moscow, Russia, pilipenk@augsburg.edu

Maria S. Pulinets Skobeltsyn Institute of Nuclear Physics, Moscow State University, Moscow, Russia, cotopaxy@gmail.com

T.I. Pulkkinen Aalto University, School of Electrical Engineering, Espoo, Finland, tuija.i.pulkkinen@aalto.fi

Yoshifumi Saito Institute of Space and Astronautical Science, Japan Aerospace Exploration Agency, Sagamihara, Kanagawa, Japan, saito@stp.isas.jaxa.jp

T. Sakanoi Graduate School of Science, Planetary Plasma and Atmospheric Research Centre, University of Tohoku, Sendai, Japan, sakanoi@pparc.geophys.tohoku.ac.jp

Ludger Scherliess Center for Atmospheric and Space Sciences, Utah State University, Logan, UT, USA, ludger.scherliess@usu.edu

Robert W. Schunk Center for Atmospheric and Space Sciences, Utah State University, Logan, UT, USA, Robert.Schunk@usu.edu

K. Seki Solar Terrestrial Environment Laboratory, University of Nagoya, Nagoya, Japan, seki@stelab.nagoya-u.ac

Hidetoshi Shibuya Kumamoto University, Kumamoto, Japan, shibuya@sci.kumamoto-u.ac.jp

Hisayoshi Shimizu Earthquake Research Institute, University of Tokyo, Tokyo, Japan, shimizu@eri.u-tokyo.ac.jp

Marina V. Stepanova Physics Department, Universidad de Santiago de Chile, Santiago, Chile, marina.stepanova@usach.cl

P. Sutcliffe Hermanus Magnetic Observatory, Hermanus, South Africa, psutcliffe@hmo.ac.za

Futoshi Takahashi Tokyo Institute of Technology, Tokyo, Japan, futoshi@geo.titech.ac.jp

Takaaki Tanaka Institute of Space and Astronautical Science, Japan Aerospace Exploration Agency, Sagamihara, Kanagawa, Japan, t_tanaka@stp.isas.jaxa.jp

Takashi Tanaka Kyushu University, Fukuoka, Japan, tatanaka09@hotmail.co.jp

Donald C. Thompson Center for Atmospheric and Space Sciences, Utah State University, Logan, UT, USA, Donald.Thompson@kirtland.af.mil

Hideo Tsunakawa Tokyo Institute of Technology, Tokyo, Japan, htsuna@geo.titech.ac.jp

Andrew P. Walsh Mullard Space Science Laboratory, University College London, Dorking, Surrey, UK, apw@mssl.ucl.ac.uk

Tadateru Yamamoto Institute of Space and Astronautical Science, Japan Aerospace Exploration Agency, Sagamihara, Kanagawa, Japan, tadater@eps.s.u-tokyo.ac.jp

Andrew W. Yau Department of Physics and Astronomy, University of Calgary, Calgary, AB, Canada, yau@phys.ucalgary.ca

Shoichiro Yokota Institute of Space and Astronautical Science, Japan Aerospace Exploration Agency, Sagamihara, Kanagawa, Japan, yokota@stp.isas.jaxa.jp

Svetlana S. Znatkova Skobeltsyn Institute of Nuclear Physics, Moscow State University, Moscow, Russia, svetlana.znatkova@mail.ru

S. Zou Department of Atmospheric and Ocean Sciences, University of California, Los Angeles, CA, USA; Department of Atmospheric, Oceanic and Space Sciences, University of Michigan, Ann Arbor, MI, USA, shashaz@umich.edu

Part I
Solar Wind-Magnetosphere Interaction

The Magnetopause, Its Boundary Layers and Pathways to the Magnetotail

1

Benoit Lavraud, Claire Foullon, Charles J. Farrugia, and Jonathan P. Eastwood

Abstract

We review the current understanding of the dynamics of the Earth's magnetopause and boundary layers. We describe basic insights and recent advances concerning the main mechanisms that mediate solar wind energy, momentum and plasma transfer into the magnetosphere: magnetic reconnection, the Kelvin–Helmholtz instability and diffusive processes. We also present more global aspects of magnetopause and boundary layer dynamics, focusing specifically on recent studies of global solar wind–magnetosphere coupling and on solar wind plasma pathways to the magnetotail.

1.1 Introduction

Earth's magnetopause and boundary layers have been widely studied over the last few decades. They have been, and will continue to be, major research targets of many satellite missions such as ISEE, Geotail, Wind, Polar, Interball, Equator-S, Cluster, Double-Star, THEMIS, and in the near future MMS. A number of previous reviews and collections of articles have appeared on the topic, notably those by Song et al. (1995), Treumann and Scholer (1997), Paschmann (1997), Lundin (1997), Sibeck et al. (1999), Farrugia et al. (2001), Newell and Onsager (2003), Phan et al. (2005), De Keyser et al. (2005), Cargill et al. (2005) and Paschmann (2008). For early works and detailed descriptions of the solar wind plasma entry mechanisms that will be addressed here, the reader is referred to these reviews. For the present review, we build on those earlier ones and focus on current efforts that address the role the magnetopause and its boundary layers play in magnetospheric dynamics.

At the interface between two plasma regions, a number of instabilities may mediate plasma transfer and mixing. Of importance for the Earth's magnetopause are magnetic reconnection (e.g., tearing mode instability), the Kelvin–Helmholtz instability (triggered by a velocity shear), and diffusive processes (for example mediated by wave–particle interactions). For the magnetopause, the proof that plasma of solar wind origin does protrude through the boundary comes from frequent in situ observations of mixed magnetospheric and solar wind plasmas just inside and adjacent to the main current sheet: the magnetopause boundary layer. With the advent of multi-spacecraft missions such as Cluster and THEMIS, together with new methods and enhanced instrumental and computer simulation capabilities, many new insights have been

B. Lavraud (✉)
Institut de Recherche en Astrophysique et Planétologie, Université de Toulouse (UPS), 31028 Toulouse Cedex 4, France; Centre National de la Recherche Scientifique, UMR, 5277 Toulouse, France
e-mail: benoit.lavraud@cesr.fr

W. Liu, M. Fujimoto (eds.), *The Dynamic Magnetosphere*, IAGA Special Sopron Book Series 3,
DOI 10.1007/978-94-007-0501-2_1, © Springer Science+Business Media B.V. 2011

gained regarding the aforementioned mechanisms and the role they play in controlling the entry of solar wind plasma into the magnetosphere.

In Section 1.2, we introduce the process of magnetic reconnection in the context of the magnetopause. In particular, we describe how accurate measurements from recent multi-spacecraft missions have permitted a quantification of some properties of magnetic reconnection. In Section 1.3, we review recent work on the Kelvin–Helmholtz (KH) instability and diffusive processes. These are thought to transfer energy and momentum from the solar wind to the magnetosphere and to mediate plasma entry in their non-linear stage during northward interplanetary magnetic field (IMF) conditions, i.e., when magnetic reconnection is not expected to occur at the dayside. Section 1.4 then highlights the importance of magnetic reconnection and the KH instability in the context of global solar wind–magnetosphere coupling, as well as in terms of possible solar wind plasma pathways to the magnetotail.

1.2 Magnetic Reconnection at the Magnetopause

Magnetic reconnection at the magnetopause is believed to play a major role in solar wind–magnetosphere coupling. Accompanying the large-scale magnetic topology changes which occur as a result of magnetic reconnection, mass, energy and momentum of the solar wind are transferred to the magnetosphere. Magnetic reconnection is the primary driver mechanism during enhanced geomagnetic activity. In this section we first describe some basic features of magnetopause reconnection and then present recent results on the topic. We do not address the issue of the initiation process of magnetic reconnection.

1.2.1 Basics of Magnetopause Reconnection

1.2.1.1 Concept of Reconnection

When two different plasma domains are in contact, in the magneto-hydrodynamic (MHD) framework these may be separated by several types of discontinuities (e.g., Chen 1984). In the case of Earth's dayside magnetosphere, the subsonic, shocked solar wind plasma in the magnetosheath was at first believed to be separated from the magnetosphere by an impermeable tangential discontinuity: the magnetopause (Chapman and Ferraro 1931). As first envisaged by Dungey (1961), plasma entry into the magnetosphere may in fact occur by means of the process of magnetic reconnection. The process requires the breakdown of the "frozen-in" condition of MHD ($\mathbf{E} + \mathbf{v} \times \mathbf{B} = 0$) in a localized region called the diffusion region (here $\mathbf{E}$ is the electric field, $\mathbf{v}$ the plasma velocity and $\mathbf{B}$ the magnetic field). Oppositely directed magnetic fields from the two sides of a reconnecting current sheet are convected into the diffusion region where they decouple from the plasma, and then effectively "reconnect" to their counterpart from the opposite side, freezing back into the plasma in the reconnection outflow. The process leads to a dramatic change in the magnetic connectivity, or topology, as sketched in two dimensions in the bottom of Fig. 1.1. In three dimensions, the X-point of Fig. 1.1 translates into a magnetic reconnection X-line (in the out-of-page direction) whose geometry and length at the magnetopause is quite variable, as we shall see later. The topological change that results from magnetic reconnection has a direct consequence: it permits previously separated plasmas to mix thanks to the presence of a finite magnetic field component normal to the boundary ($B_N \neq 0$), which is now akin to a rotational discontinuity (or a standing, large-amplitude Alfvén wave). In other words, magnetic reconnection allows plasma to flow through an originally impermeable boundary.

The amount of magnetic flux that reconnects per unit time and unit length through a magnetic reconnection X-line is called the reconnection rate. It is equal to the reconnection electric field, i.e., the electric field along the X-line. Reconnection rate is often studied in its dimensionless form, where $R = B_N/B_T = V_N/V_A$; with B_N, B_T, V_N, and V_A being the normal magnetic field component, the total magnetic field strength, the normal inflow velocity component and the total Alfvén speed in the inflow region, respectively. In three dimensions, B_T (and correspondingly V_A) should be the magnitude of the magnetic field component perpendicular to the X-line. R in this context is essentially an aspect ratio of the width to the length of the ion diffusion region (e.g., Cassak and Shay 2007). Models predict that the reconnection rate can be either slow (Sweet 1958; Parker 1963) or fast (Petschek 1964), with a number of variants (see, e.g., Biskamp 1986;

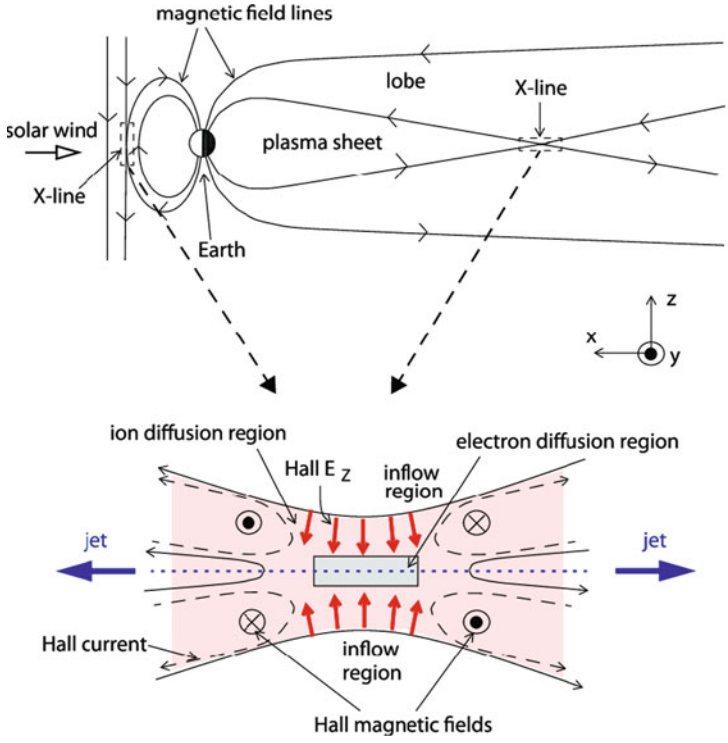

Fig. 1.1 (*top*) Schematic illustration of the magnetospheric magnetic field and preferential locations of magnetic reconnection for southward IMF, i.e., at low-latitudes on the dayside (*left*) and in the mid-tail on the nightside (*right*). (*bottom*) Sketch of the structure of the diffusion region during magnetic reconnection, showing the ion and electron diffusion regions, outflow jets and the Hall electric and magnetic fields. From Paschmann (2008); adapted from Øieroset et al. (2001)

Priest and Forbes 1992; Forbes 1995). The rate of magnetic reconnection in collisionless (proton-electron) plasmas is thought to be controlled by differential ion-electron motion (Hall effects), leading to a characteristic two-scale structure (Fig. 1.1, bottom) and is typically fast (e.g., Birn et al. 2001). Here we do not discuss theories of magnetic reconnection further but only point out that there are observational clues for magnetic reconnection often being fast in astrophysical plasmas, e.g., from the duration of a flare (Priest and Forbes 1992). At the magnetopause a dimensionless reconnection rate of 0.1, corresponding to a theoretical upper limit for fast reconnection (Levy et al. 1964), is often assumed (e.g., Cassak and Shay 2007; Borovsky 2008) (cf. Section 1.4.1 and the discussion of Section 1.2.2.4).

1.2.1.2 Signatures of Magnetic Reconnection

The upper schematic of Fig. 1.1 depicts the basic topology that follows from magnetic reconnection as it occurs in the magnetosphere. It shows where reconnection is expected to initiate for the case of southward IMF (for the northward IMF case, see Section 1.2.4). Because under such conditions the orientations of the IMF and geomagnetic field are anti-parallel on the dayside, magnetic reconnection is favored in the sub-solar region (but see Section 1.2.2.3 for deviation from this idealized anti-parallel scenario). Sub-solar reconnection adds open magnetic flux to the polar regions (expanding the polar cap) and lobes (loading the magnetotail). In order to remove the excess magnetic flux in the magnetotail, magnetic reconnection is also expected to occur at the nightside current sheet, thereby allowing circulation of the magnetic flux in the magnetosphere and, in particular, returning it to the dayside. Here we only deal with magnetic reconnection at the magnetopause. The reader is referred to Birn (Chapter 4, this volume) for magnetotail dynamics.

In the process of magnetic reconnection, magnetic energy is converted into thermal and kinetic energy of the plasma. The magnetic tension on the newly reconnected field lines accelerates plasma inflowing from above and below the current sheet into two outflow jets on each side of the X-line topology. Because the sub-solar magnetopause is an asymmetric boundary, typically with magnetic (plasma) energy dominating on the Earthward (Sunward) side, detection of magnetic reconnection at the magnetopause has largely been based on observation of flow jets of solar wind plasma in the boundary layer inside (Earthward) of the

magnetopause current sheet (Paschmann et al. 1979; Sonnerup et al. 1981). MHD predicts that the outflow jets should be Alfvénic in the deHoffmann-Teller frame (deHoffmann and Teller 1950), a characteristic that may be gauged via the Walén test (Sonnerup et al. 1987). The most commonly used fluid and kinetic signatures of magnetic reconnection are (e.g., Phan et al. 2001): (1) a finite normal magnetic field component across the boundary (Sonnerup and Cahill 1967), (2) Alfvénic flow jets (see above), (3) particle acceleration and heating (e.g., Gosling et al. 1990; Onsager et al. 2001), (4) D-shaped ion distributions with low energy cut-off at the deHoffmann-Teller velocity (Cowley 1982), (5) mixing of the ion and electron populations from each side of the boundary, together with the formation of distinct separatrix layers for ions and electrons owing to time-of-flight effects (Gosling et al. 1990), and (6) ions reflected from the magnetopause (Sonnerup et al. 1981; Fuselier et al. 1991). Numerous recent studies have confirmed the link between such signatures and the occurrence of magnetic reconnection.

Another signature related to magnetic reconnection is that of a Hall electric and magnetic fields structure. In collision-less plasma with low resistivity the ion and electron's different masses (and gyroradii) imply that ions motion decouple from the magnetic field ("demagnetize") in an ion diffusion region that has a substantially larger size than the electron diffusion region, where electrons eventually demagnetize as well. This scale size separation leads to differential ion and electron motions in the ion diffusion region, which sets up a system of Hall currents. In the context of symmetric reconnection, the Hall current system comes with quadrupolar magnetic field and bipolar electric field (Fig. 1.1; Øieroset et al. (2001)) signatures, but the picture differs in the asymmetric case of the magnetopause as we shall see in Section 1.2.2.2.

1.2.2 Quantifying Magnetic Reconnection

1.2.2.1 Bulk Plasma Heating at the Magnetopause

The bulk plasma heating associated with magnetic reconnection has not been studied as much as other signatures such as bulk flow acceleration. Observationally, it was recognized early on that both solar wind ions and electrons are heated at the reconnection site and at the magnetopause rotational discontinuity (e.g., Gosling et al. 1990; Phan et al. 1994). Note, indeed, that from observations plasma is heated all along the magnetopause and not just at the reconnection site (Onsager et al. 2001; Lavraud et al. 2005b).

Early theoretical studies have suggested wave–particle interactions as a means of heating at the magnetopause. Lee et al. (1994), and later Johnson and Cheng (1997, 2001), proposed kinetic Alfvén waves (KAW). Spacecraft observations have been investigated for signatures of KAW heating. A signature supportive of such heating is the regular, combined observation of ion perpendicular temperature anisotropy (relative to magnetic field) and electron parallel temperature anisotropy in the boundary layers, as predicted by KAW theory (e.g., Wing et al. 2006; Nishino et al. 2007a, b, c; and references therein).

Although they have not been investigated in the context of the magnetopause, it is worth mentioning the heating mechanisms of Drake et al. (2006, 2009), respectively for electrons and ions. The former is based on Fermi-type acceleration in coalescing island structures at current sheets (i.e., such as for intermittent reconnection; cf. Section 1.2.3.2), while the latter is based on a pick-up process in the reconnection electric field.

Based on observations made during low solar wind Alfvén Mach number conditions, Lavraud et al. (2009) found that the ion-to-electron temperature ratio in the boundary layers is not prescribed by the plasma entry mechanism (associated with either reconnection or the KH instability). This observation puts constraints on potential magnetopause heating processes which remain to be addressed by theory. Finally, it is noted that in solar wind reconnection exhausts, there is little sign of heating, in particular for electrons (Gosling 2009).

1.2.2.2 Measurement of the Hall Term in the Generalized Ohm's Law

Magnetic reconnection Hall signatures have been observed in the magnetotail (Øieroset et al. 2001; Nagai et al. 2001; Wygant et al. 2005; Eastwood et al. 2007, 2010) and at the magnetopause (e.g., Deng and Matsumoto 2001; Vaivads et al. 2004, 2006; Mozer et al. 2008) (cf. Section 1.2.1.2). Mozer et al. (2008) recently investigated the Hall signatures for

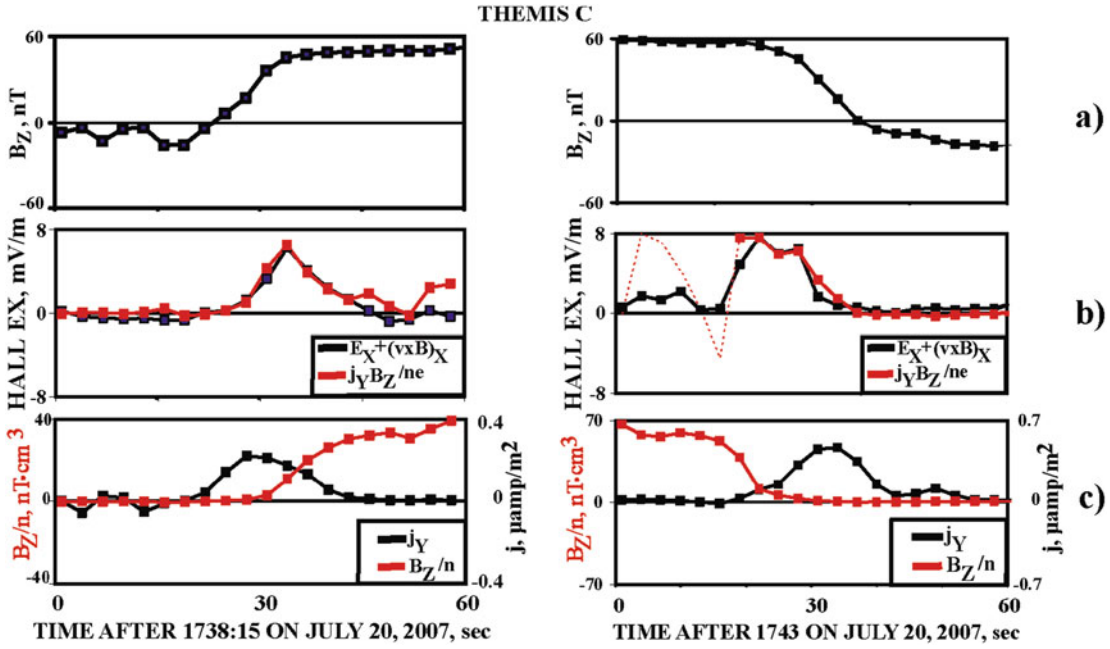

Fig. 1.2 Comparison of $(\mathbf{E} + \mathbf{v} \times \mathbf{B})_X$ and $(\mathbf{j} \times \mathbf{B}/en)_X$ terms for an inbound (outbound) THEMIS magnetopause crossing on the *left* (*right*). The data illustrate the quantitative agreement between the two terms in the Generalized Ohm's law (*red* and *black curves* in panel (**b**)). From Mozer et al. (2008)

asymmetric dayside magnetopause crossings by the THEMIS spacecraft. Using estimates of the magnetopause boundary velocity and normal direction, they were able to assess the normal electric field component that results from the Hall $\mathbf{j} \times \mathbf{B}$ term ($\mathbf{j}$ is the electric current) in the generalized Ohm's law, i.e., $\mathbf{E} + \mathbf{v} \times \mathbf{B} = (1/en)\, \mathbf{j} \times \mathbf{B}$ (other terms were neglected owing to the spacecraft crossing only the ion diffusion region). Only a single peak was observed in this normal electric field (Fig. 1.2). They explained it as the result of the ratio of magnetic field tangential component (B_Z) to the plasma density being too small for the Hall electric field on the magnetosheath side to be important. In this case the effect is thus directly the consequence of magnetopause reconnection being highly asymmetric. This event provides a nice quantitative test for the Hall term at the dayside magnetopause, and for the impact of the boundary asymmetry on the Hall system structure (see Mozer and Pritchett (2009) for further electron physics issues related with asymmetric reconnection). We note that this study particularly emphasizes that in situ plasma sensors currently being flown have reached a high level of accuracy. This allows not only the discovery of new effects but also their precise quantification.

1.2.2.3 Anti-parallel Versus Component Magnetic Reconnection

The bottom sketch of Fig. 1.1 shows the magnetic field configuration resulting from reconnection in two dimensions in the context of purely oppositely directed magnetic fields each side of the boundary. Such a scenario leads to magnetic field annihilation at the neutral point, or X-line, and is called anti-parallel reconnection (e.g., Crooker 1979). However, in three dimensions, reconnection may as well occur without magnetic field annihilation but rather in the presence of a guide field along the direction of the X-line; this model is called component reconnection (Gonzalez and Mozer 1974; Cowley 1976).

For strictly southward IMF the anti-parallel reconnection site is an extended X-line across the equatorial dayside magnetopause. However, Crooker (1979) and Luhmann et al. (1984) showed that when a strong IMF B_Y component exists the pure anti-parallel reconnection line splits. Two distinct reconnection X-lines are expected at higher latitudes in each hemisphere, with a gap at local noon. In contrast, models of component reconnection, which we do not describe in detail here (see, e.g., Cowley and Owen 1989; Moore et al. 2002; Trattner et al. 2007a), predict that with a finite IMF B_Y

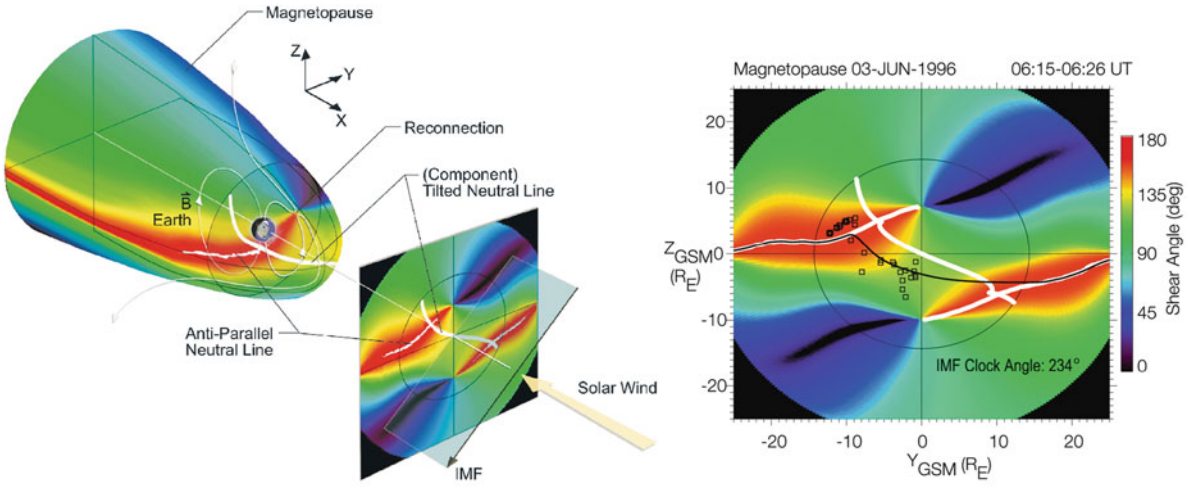

Fig. 1.3 (*left*) Illustration of the variation of the magnetic shear (color-coding with *red* showing highest shear) across the magnetopause based on mapping the IMF on a magnetospheric magnetic field model. *White* lines show the predicted dayside X-line geometries for the anti-parallel and component (or tilted X-line, the one passing through the sub-solar region) reconnection models. (*right*) Results of mapping cusp plasma precipitation observations (*black squares*) back to the magnetopause. The *black thin line* shows the X-line geometry from a component reconnection model based on maximizing the shear angle along the X-line. From Trattner et al. (2007a)

the reconnection line remains continuous and always passes near the sub-solar region for southward IMF (the first point of contact of the solar wind). It extends toward dawn and dusk and towards the poles with a tilt that depends on the IMF B_Y component in particular. This is exemplified in Fig. 1.3 (left).

Results from data analysis by Trattner et al. (2007a), who aimed at differentiating between the two reconnection models mentioned above, are shown in Fig. 1.3 (right). They used cusp ion precipitation data (from low energy cut-offs of incoming and mirrored populations) to estimate the spacecraft distance to the X-line (e.g., Onsager et al. 1991). Mapping that distance back along a magnetic field model then allowed them to compare the X-line location inferred from the data with that of different reconnection models. As can be seen in Fig. 1.3 (right), for a case of southward IMF with a substantial positive IMF B_Y, they found that the data were consistent with component reconnection along a tilted X-line. In a follow-up study Trattner et al. (2007b) confirmed a tendency for preferential component reconnection during southward IMF, but also noted a prevalence of the anti-parallel reconnection model for strong IMF B_X cases. Note that Trattner et al. (2007b) defined a new component reconnection model based on maximizing the magnetic shear angle along the X-line.

Dunlop et al. (2009) recently studied a high-latitude reconnection event during northward IMF. Using a multi-spacecraft method to reconstruct the local magnetic field topology from Cluster data, they found the event to fit the anti-parallel reconnection model. As the IMF changed orientation to include a substantial IMF B_Y, the initiation of component merging at lower latitude was inferred. While anti-parallel reconnection cases have often been found in past studies, and in particular for reconnection under due southward and northward IMF, most recent works (e.g., Pitout et al. 2002; Chandler and Avanov 2003; Lockwood et al. 2003; Pu et al. 2007; Berchem et al. 2008; Trenchi et al. 2008) have pointed towards a predominance of component reconnection in the sub-solar region during periods with a finite transverse IMF B_Y component.

Although the reasons for the predominance of either of these reconnection models still needs to be fully determined, we note that the above results imply that component reconnection is likely to be a regular mode of solar wind–magnetosphere coupling since the heliospheric "Parker" spiral entails a significant transverse IMF component, at least statistically.

1.2.2.4 Estimates of the Magnetic Reconnection Rate

As described in Section 1.2.1.1, the rate at which magnetic reconnection cuts and reconnects inflowing magnetic field lines is related to the geometry of the X-line (i.e., the dimensionless reconnection rate $R = B_N/B_T$). Assessing the reconnection rate from in situ data thus requires an accurate estimate of the local magnetic field topology, i.e., namely of the normal component of the magnetic field across the magnetopause. The boundary normal direction may be estimated by use of either single (e.g., Minimum Variance Analysis, MVA; Sonnerup and Scheible (1998)) or multi-spacecraft methods (e.g., Dunlop et al. 2002). However, estimates of the normal direction to a boundary based on either of these methods yield errors (Haaland et al. 2004) that strongly affect the inferred reconnection rate. In addition, the estimation of the reconnection rate is affected by the orientation and motion of the X-line. In order to properly measure the reconnection electric field in the X-line rest frame and along the X-line direction (cf. Section 1.2.1.1), methods to assess the orientation and/or motion of a two-dimensional reconnection X-line have been developed (Sonnerup and Hasegawa 2005; Shi et al. 2005; Zhou et al. 2006).

Rosenqvist et al. (2008) recently proposed a new method, derived from the Poynting flux theorem, to determine the reconnection rate. Using this, they estimated the reconnection rate for eleven sequential magnetopause crossings by Cluster which all occurred in less than an hour. They found that the reconnection rate varied from nearly 0 to 0.4 over all their cases. Other single and multi-spacecraft methods (e.g., Vaivads et al. 2004; Fuselier et al. 2005; Penz et al. 2008; Wendel and Reiff 2009) have been used to estimate the reconnection rate at the magnetopause. Overall, they concluded that dimensionless reconnection rates (1) are generally significantly lower than 0.1 in the context of component merging, (2) they are quite variable, even during the same event, and (3) are sometimes larger than 0.1, although the reconnection model of Levy et al. (1964) would predict a dimensionless reconnection rate of 0.1 as an upper limit to steady, fast magnetic reconnection.

Assuming the uncertainty in estimating the reconnection rate to primarily arise from the determination of the normal direction, Mozer and Retinò (2007) proposed a method for minimizing errors. It is based on an analysis of the correlation between the normal electric field and the tangential magnetic field, which are both large (unlike the other components). These correlation coefficients are equal to ratios of the small field components and may thus be used to better estimate the normal field components. The method was applied to 22 sub-solar magnetopause crossings, out of which 14 had large and steady reconnection rates. They found that the reconnection electric field decreases with increasing guide field and that the average dimensionless reconnection rate was about 0.06 for their dataset. The disparity of these estimates implies that accurate determination of the reconnection rate from in situ observation remains a key challenge.

That the reconnection rate may fluctuate has gained credence from recent in situ observations. It has also been pointed out on the basis of remote sensing observations of auroral precipitation intensity (Fig. 1.4; from Fuselier et al. (2007)). Such fluctuations in the reconnection rate at the magnetopause are far from unusual and are the subject of the following Section 1.2.3.

1.2.2.5 Determination of the Local Magnetic Topology

The local magnetic structure at the magnetopause depends on the processes that occur there. The magnetic topology will in particular depend upon (1) whether magnetic reconnection is ongoing or not (i.e., tangential versus rotational discontinuity), (2) whether it is continuous or intermittent (varying reconnection rate), (3) which of the KH instability, pressure pulses, or flux transfer events (FTEs) are present

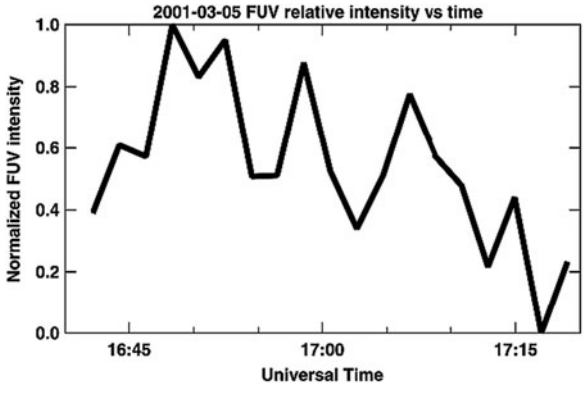

Fig. 1.4 Intensity of the far ultra-violet dayside auroral emissions measured by the IMAGE spacecraft during an event which suggests fluctuations in the reconnection rate at the magnetopause, with a period of a few minutes. From Fuselier et al. (2007)

(cf. next sections), and (4) which FTE formation mechanism prevails (cf. Section 1.2.3.2). Knowing the local magnetic topology is thus of importance to decipher between entry mechanisms and their modes of operation. However, it may not be inferred easily from "point" in situ observations. For that purpose, and apart from obvious extrapolations (e.g., extrapolating the local structure from the normal magnetic field component obtained by minimum variance analysis), several reconstruction technique approaches have been used.

A method for reconstructing local, two-dimensional (2D), time-independent magnetic structures from in situ data, called the Grad-Shafranov reconstruction, has been developed by Sonnerup and Guo (1996) (cf. also Hau and Sonnerup 1999; Hu and Sonnerup 2003; Sonnerup et al. 2006). The technique assumes that structures are magnetohydrostatic, so that the MHD force balance equation reduces to $\nabla \mathbf{p} = \mathbf{j} \times \mathbf{B}$. The equation may be written using the magnetic vector potential into the Grad-Shafranov equation, which can be solved to recover the local magnetic structure from observations. It has been applied to magnetopause crossings suggestive of tangential and rotational discontinuities (e.g., Sonnerup and Guo 1996; Hasegawa et al. 2004a), as well as to flux transfer events (Sonnerup et al. 2004; Hasegawa et al. 2006a; Lui et al. 2008; Zhang et al. 2008; Eriksson et al. 2009) and recently to Kelvin–Helmholtz flow vortices using a variant of this method (Hasegawa et al. 2007).

Empirical 2D reconstruction techniques have also been used (De Keyser et al. 2002; De Keyser and Roth 2003). The method has notably been used in its multi-spacecraft form by De Keyser et al. (2004) to reconstruct wavy structures on the magnetopause. A review by De Keyser (2005) is dedicated to magnetopause reconstruction methods.

1.2.3 Continuous and Intermittent Magnetic Reconnection

Cases of both "continuous" and "intermittent" magnetic reconnection have been reported at the magnetopause. Continuous reconnection refers to a mode where the reconnection rate may vary but does not totally stop. Intermittent reconnection is typically referred to as the mode when magnetic reconnection ceases totally at a given magnetic reconnection X-line. Possibilities exist that combine these two extremes on global and local scales. While we focus on continuous magnetic reconnection, either local or global, in Section 1.2.3.1, we explicit how each mode may be related to the observation of Flux Transfer Events (FTEs) in Section 1.2.3.2.

1.2.3.1 Continuous Magnetic Reconnection

From single spacecraft observations, determining the occurrence of continuous reconnection is difficult to ascertain. Arguably, repetitive encounters with reconnection flow jets in the neighborhood of the magnetopause provided the earliest pieces of evidence for continuous reconnection (e.g., Sonnerup et al. 1981; Gosling et al. 1982). With the advent of multi-spacecraft missions, however, the possibility opened for observing reconnection flow jets simultaneously at several spacecraft, and thus to unambiguously confirm the continuous nature of magnetic reconnection, locally at a given X-line. This is essentially the result obtained by Phan et al. (2004). With the Cluster spacecraft separated by about 600 km, they found that magnetic reconnection at the duskside magnetopause during a predominantly southward IMF period was continuous for about 2 h (cf. also Zheng et al. (2005) for continuous reconnection observations near the cusp), although the reconnection rate may have been variable.

Another result suggesting that magnetic reconnection can occur in a continuous fashion at the magnetopause comes from studies by Frey et al. (2003) and Phan et al. (2003). Combining IMAGE proton aurora observations in the cusp for steady northward IMF and in situ Cluster observations nearby the conjugate high-latitude reconnection site, they could show (1) that magnetic reconnection was ongoing at the expected high-latitude location (upper part of Fig. 1.5), and (2), based on the proton aurora data (lower part of Fig. 1.5), that magnetic reconnection was continuous at the high-latitude magnetopause for ~4 h. The proton auroral spot, and by inference at least one high-latitude reconnection X-line, was active at any given time during the interval, thus allowing a continuous response to IMF B_Y changes by shifting the reconnection location as expected (see inserts showing the clock angle direction in each auroral image of Fig. 1.5).

While the study by Phan et al. (2004) was suggestive of magnetic reconnection being continuous at a given X-line, the works by Frey et al. (2003) and Phan et al. (2003) rather demonstrated that magnetic

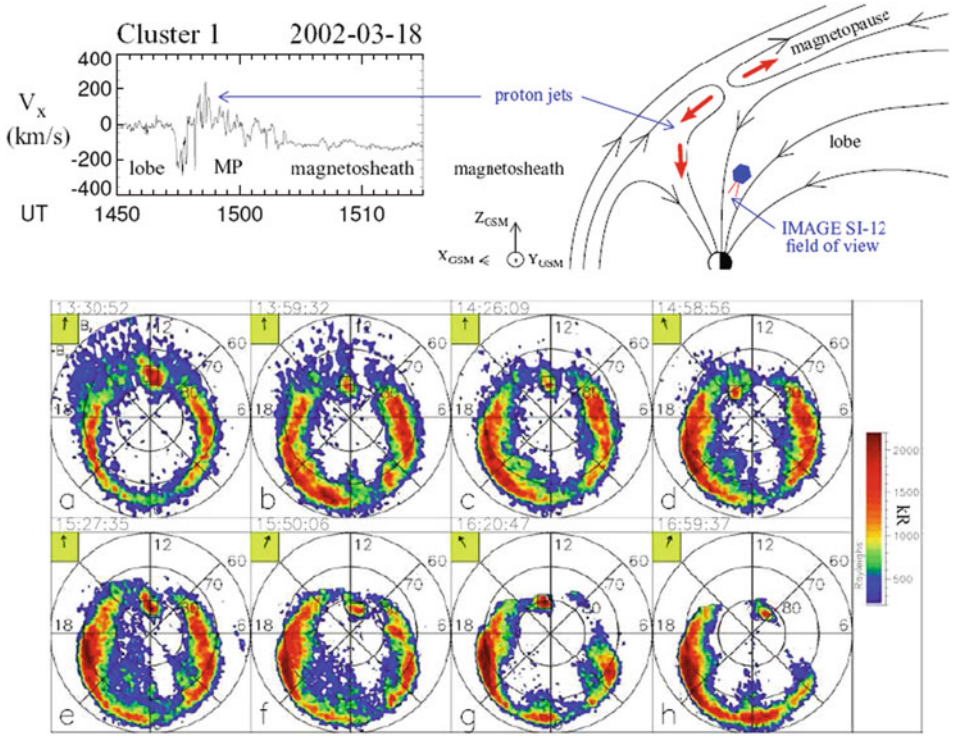

Fig. 1.5 (*Upper left*) Cluster ion V_X component showing passage from anti-sunward to sunward of a high-latitude reconnection site. (*Upper right*) Schematic of the magnetic topology of the northern dayside magnetosphere during the event, with illustration of the plasma flow jets observed by Cluster and the IMAGE position and field-of-view. (*Lower panels*) Eight proton aurora images during the 4 h of high-latitude reconnection. Note the small red spot in the noon area and how it shifts position with IMF clock angle (cf. inserts). From Phan et al. (2005)

reconnection was continuously ongoing at the high-latitude magnetopause in the global sense. Indeed, whether magnetic reconnection over the course of their event consisted of the same X-line being continuously active or whether several X-lines were sequentially activated to follow the IMF changes could not be determined from their case study.

Trattner et al. (2003), using mid-altitude cusp data mapped onto ionospheric convection patterns derived from SuperDARN ground observations, also concluded that reconnection was continuous in the global sense. Although mid-altitude cusp observations of step-like structures (see next section) were observed, results of their mapping method suggest that step-like structures at times stem from the presence of several convection flow channels (cf. also Trattner et al. 1999, 2002). In other words, there can be several distinct reconnection X-lines at the dayside magnetopause (cf. Section 1.2.4) forming several distinct convection flow channels, but reconnection might be continuous at each reconnection site.

1.2.3.2 Intermittent or Unsteady Magnetic Reconnection: Flux Transfer Events

Studies illustrating signatures of continuous reconnection from either spacecraft or ground observations have not been all that numerous. By contrast, the recurrent observation of (1) step-like structures in ion "energy versus latitude" data from mid- and low-altitude spacecraft (e.g., Escoubet et al. 1992; Lockwood and Smith 1992), (2) repeated poleward moving dispersed signatures in ground observations (e.g., Provan and Yeoman 1999; Milan et al. 1999; Lockwood et al. 2001; Wild et al. 2001), (3) correspondence between step-like structures in the cusp and poleward moving auroral forms (Sandholt et al. 1986; Farrugia et al. 1998a) and (4) widespread FTE signatures measured by spacecraft in the vicinity of the magnetopause (e.g., Russell and Elphic 1978; Owen et al. 2001; Wang et al. 2005, 2006; Hasegawa et al. 2006a; Sibeck et al. 2008), have often been interpreted in terms of intermittent reconnection being a common mode of reconnection at the dayside magnetopause. However, continuous reconnection

with time-varying, "unsteady" reconnection rates may also result in the generation of the aforementioned transient signatures. For example, although Phan et al. (2004) observed continuous magnetic reconnection, they also argued for the occurrence of unsteady reconnection rate that led to FTE-type signatures. This issue is the subject of active research. It pertains to the question of the formation mechanism of FTEs (the reader is referred to Scholer (1995) for a review of different models). Below we now review a few recent articles on FTE properties and propagation before coming back to recent works about FTE formation.

Wang et al. (2005, 2006) showed various aspects of FTE characteristics based on a large statistical analysis of 3 years of Cluster data. They showed that FTEs are more frequent for southward than for northward IMF, consistent with earlier studies (Rijnbeek et al. 1984; Berchem and Russell 1984). In addition, thanks to the Cluster orbit, they found a relatively larger number of FTEs that occurred for northward IMF. Sibeck (2009) developed an analytical model of FTE properties as a function of the local magnetic fields each side of the magnetopause. This model predicts that FTE signatures should be fainter as the local magnetic shear decreases, thus favoring observations of FTEs during southward IMF even if the intrinsic FTE occurrence rate were independent of IMF orientation (cf. also Sibeck and Lin 2010).

With the advent of multi-spacecraft missions such as THEMIS and Cluster, which were further flying together with the Double Star spacecraft for some time, it has been possible to find appropriate spatial conjunctions to address issues such as FTE origin and propagation properties. Fear et al. (2009) used such a favorable conjunction, together with SuperDARN ground observations, to infer the locations of FTE initiation as well as to track their propagation along the magnetopause. They found a good agreement with the FTE propagation model of Cooling et al. (2001) (for recent studies of FTEs, see also Daum et al. (2008); Liu et al. (2008); Zhang et al. (2008); Le et al. (2008); Eriksson et al. (2009)). FTEs have also been studied using Grad-Shafranov reconstruction techniques (cf. Section 1.2.2.5), using both single and multi-spacecraft data (Sonnerup et al. 2004; Hasegawa et al. 2006a; Lui et al. 2008). The technique allowed accurate recovery of complex magnetopause structures (e.g., see Lui et al. (2008) for reconstruction, and Sibeck et al. (2008) for simulations, of "crater" FTE cases).

Increasing computer capabilities in the last decade have permitted the context of various physical problems to be addressed more deeply, including for instance the generation mechanism of FTEs. Dorelli and Bhattacharjee (2009) used global MHD simulations of the magnetosphere for such a purpose. In their simulations, an FTE formed without dipole tilt as a result of vortex flow-induced reconnection. This result is in contrast with previous MHD simulations by Raeder (2006), which suggested that FTEs preferentially develop in the winter hemisphere as a result of a double X-line formation process. This seasonal prediction of Raeder (2006) has been suggested in the statistical work of Wang et al. (2005) (although the actual seasonal-dependent results were not published). Further support to a double (or sequential) X-line formation process was recently given by Hasegawa et al. (2010) using THEMIS observation and Grad-Shafranov reconstruction (see Fig. 1.6).

Finally, we note that there exists a whole spectrum of FTE properties (shape, frequency, amplitude, etc.) (Wang et al. 2005, 2006). This makes statistical analysis of their characteristics dependent upon the observer's criteria and capacity to survey large amounts of data. A new tool, based on data mining techniques widely used in other fields (e.g., medical), has recently shown great capability for the automatic detection of FTEs (Karimabadi et al. 2009).

1.2.4 Magnetic Reconnection for Northward IMF

In the previous sections we have discussed the properties of magnetic reconnection mostly in the context of southward IMF. For northward IMF, magnetic reconnection was originally believed to have little influence on magnetospheric dynamics because the IMF and geomagnetic field are parallel in the sub-solar region. However, under such conditions a large magnetic shear does exist at the magnetopause at high latitudes, tailward of the cusps. The first observations of magnetic reconnection at high latitudes were obtained only relatively recently from spacecraft with polar orbits (e.g., Gosling et al. 1991; Kessel et al. 1996; Safrankova et al. 1998).

Magnetosheath flows increase in strength with latitude and longitude away from the sub-solar region (Spreiter et al. 1966). If the flow becomes

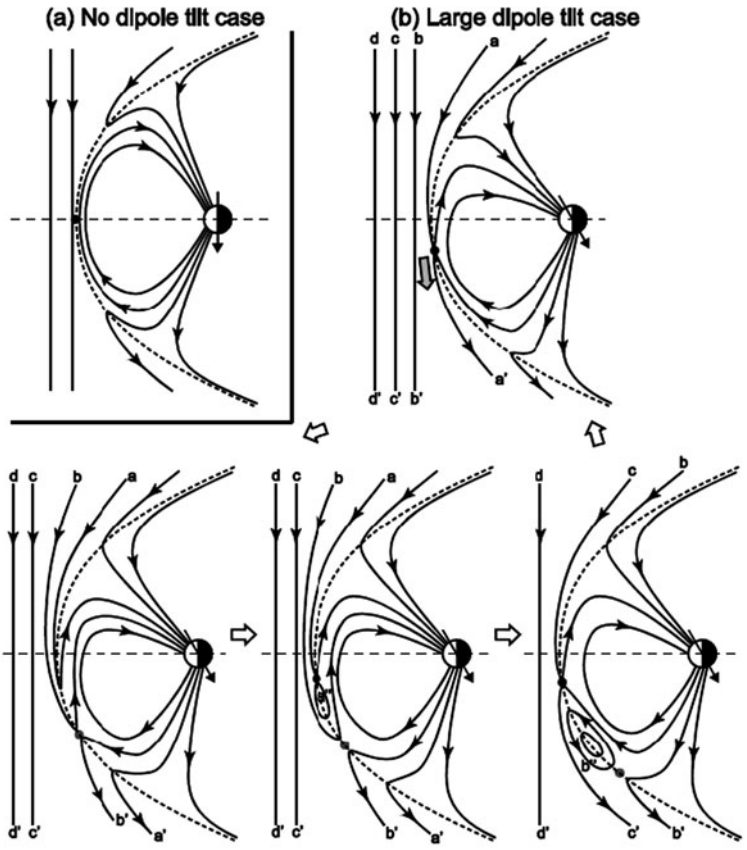

Fig. 1.6 Two-dimensional views, from the duskside, of the dayside magnetic field line evolution (**a**) for no geomagnetic dipole tilt and (**b**) for large dipole tilt. With no dipole tilt, the subsolar X-line can stand still in the subsolar region. If reconnection is continuous, open magnetic flux can be continuously, and thus efficiently, transported into the magnetotail. With a large dipole tilt, on the other hand, an X-line in the subsolar region tends to move into the winter hemisphere with the magnetosheath flow and eventually become inactive or less active. A new X-line can then form near the location of the old X-line in the subsolar region, the result being the generation of a flux rope between the two X-lines: a Flux Transfer Event. From Hasegawa et al. (2010)

super-Alfvénic at latitudes lower than that of the reconnection region then the high-latitude reconnection site would be swept downtail. To reconcile this with observations of apparently steady reconnection from cusp observation under northward IMF, Fuselier et al. (2000) proposed that the formation of a plasma depletion layer (PDL) (Zwan and Wolf 1976) may allow a lower Alfvén Mach number near the magnetopause, and up to tailward-of-the-cusp reconnection sites. Indeed, a PDL is essentially always observed on approach to the magnetopause under northward IMF (Crooker et al. 1979; Phan et al. 1994), with a gradual increase in magnetic field and decrease in density both conspiring to increase the Alfvén speed near the magnetopause. The prediction of sub-Alfvénic flows near the high-latitude reconnection regions for northward IMF was later confirmed based on both case studies (Avanov et al. 2001; Lavraud et al. 2004) and statistical analyses (Lavraud et al. 2005a).

For due northward IMF, a magnetic field line that reconnects poleward of the cusp in one hemisphere may in principle also reconnect in the other hemisphere. Such a double high-latitude reconnection mechanism was proposed by Song and Russell (1992) to allow solar wind plasma entry into the magnetosphere during northward IMF (Fig. 1.7). This prediction was later given substantial support from satellite observations (Le et al. 1996; Sandholt et al. 1999; Onsager et al. 2001; Lavraud et al. 2005b, 2006; Bavassano Cattaneo et al. 2006; Øieroset et al. 2008; Hasegawa et al. 2009) and global MHD simulations (Ogino et al. 1994; Fedder and Lyon 1995; Raeder et al. 1997; Li et al. 2008, 2009).

Figure 1.7a, b show the dayside magnetic topologies under northward IMF from both sideways and front view angles. Figure 1.7c shows statistical results from Cluster observations at the high-latitude magnetopause by Lavraud et al. (2006). This study used the fact that heated electrons, which are very fast compared to thermal ions, can be used as tracers of the global topology at the dayside magnetopause, as first suggested by Onsager et al. (2001). By surveying 3 years of

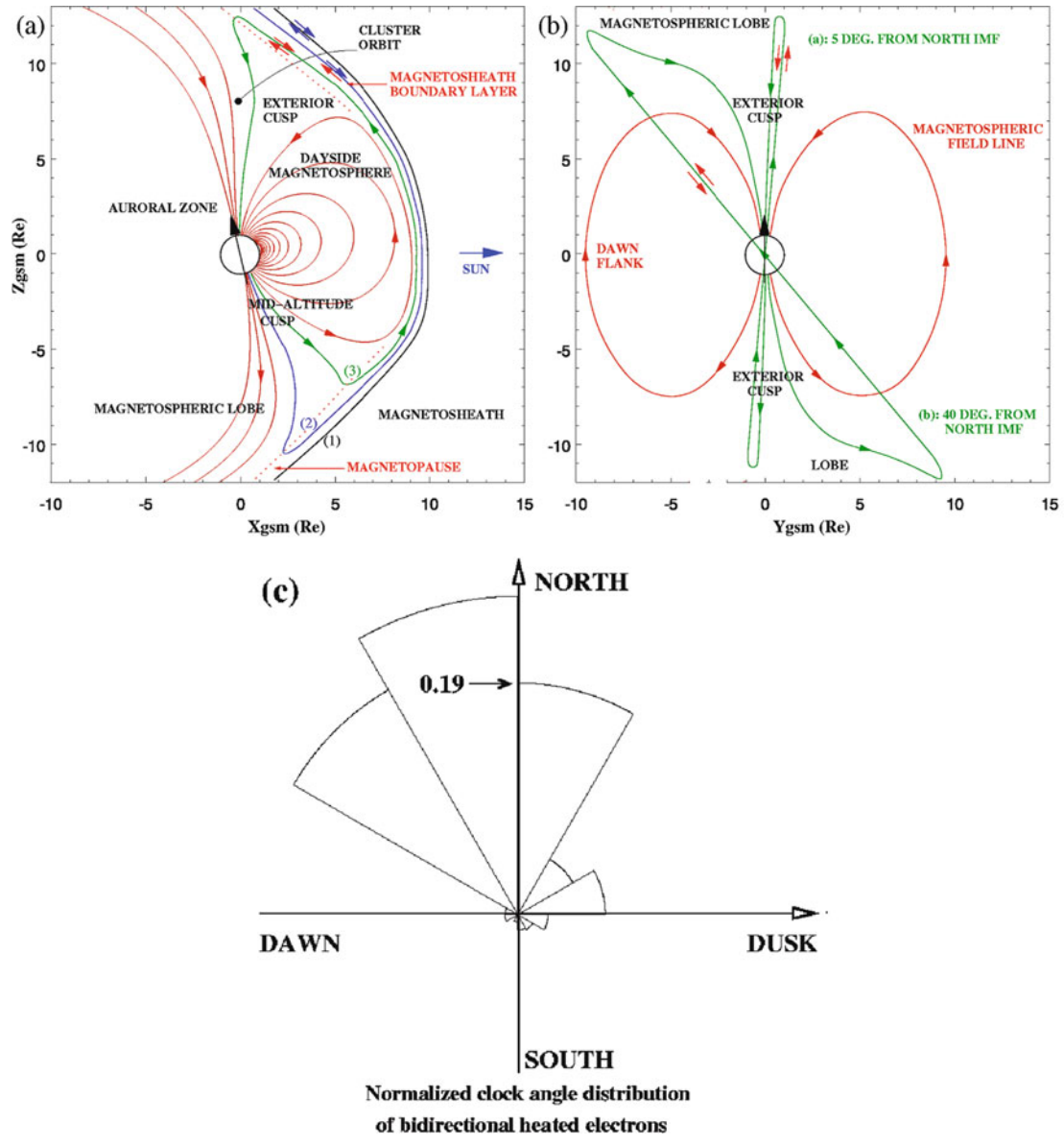

Fig. 1.7 (**a**) Schematic of the dayside magnetic topology for northward IMF and sequential magnetic reconnection of the same magnetosheath field line first in the southern hemisphere and next in the northern hemisphere. The *blue* (*red*) color of the small field-aligned *arrows* next to the field lines in the upper part of the figure indicates the cold (hot) temperature of electrons in the given directions. (**b**) Schematic of the magnetic field topology viewed from the Sun, and illustrating the impact of the presence of a finite IMF B_Y component. (**c**) Results of a statistical survey of bidirectional heated electrons outside the magnetopause, which are believed to indicate newly closed field lines, as a function of IMF clock angle. Adapted from Lavraud et al. (2006)

high-latitude magnetopause crossings, Lavraud et al. (2006) showed that the expected signature of newly closed field lines was observed primarily for northward IMF, both with and without a significant IMF B_Y component. Consistent with this result, Li et al. (2008) analyzed global MHD simulations and found that such solar wind plasma capture mechanism may occur for absolute IMF clock angles of up to 60° (cf. also Li et al. 2008; Øieroset et al. 2008).

1.3 Kelvin–Helmholtz Instability and Diffusive Processes

In this section we discuss the roles of the KH instability and diffusion mechanisms in the dynamics of the magnetopause and boundary layers. We first introduce signatures of the KH instability. We then discuss it in relation to "so-called" secondary plasma entry processes (since the KH instability is not a plasma entry process per se) for which KH may be viewed as a mediating process. Some recent studies on diffusive processes are then presented.

1.3.1 Location and Signatures of the Kelvin–Helmholtz Instability

As Dungey (1954) first pointed out, the velocity shear which exists at the magnetopause as the solar wind flows around the magnetosphere, gathering speed along its flanks, may render the magnetopause KH unstable and provide an energy source for some geomagnetic pulsations. Since then, the KH instability has been widely addressed in theoretical, simulation and data analysis works (e.g., Southwood 1968, 1979; Miura 1984, 1995a, b; Fitzenreiter and Ogilvie 1995; Kivelson and Chen 1995; Belmont and Chanteur 1989; Farrugia et al. 2001). Although there have been suggestions for KH activity at the flanks of the magnetosphere for southward IMF (Pu et al. 1990; Kawano et al. 1994; Mozer et al. 1994; Miura 1995b), KH waves and vortices at the flanks are rather expected to occur under northward IMF conditions (e.g., Fairfield et al. 2000; Farrugia et al. 2001). KH waves are typically characterized by large plasma (density, temperature, velocity) and magnetic field fluctuations with periods on the order of a few minutes.

An important advance in global numerical KH studies has been the incorporation of realistic magnetic fields and flows that arise in the magnetosheath under northward IMF owing to the formation of a PDL. Changes in plasma flow that stem from the PDL are of the stagnation line-type (Sonnerup 1974), i.e., enhanced magnetic forces accelerate plasma tangential to the magnetopause and perpendicular to the local magnetic field. Inclusion of the PDL properties in KH instability studies was first made by Farrugia et al. (1998b). They studied two orientations of the IMF (due north and 30° away from north). They considered both "thin" (sharp) and "thick" (magnetopause with an attached boundary layer) transitions. When maps of the distribution of the magnetic shear across the magnetopause were drawn, they found that bands of low magnetic shear (in the sense of permitting KH instability growth) appear in each hemisphere (Fig. 1.8). For an IMF tilted 30° west of north the lowest shear bands fan out from below the cusp to cover midlatitudes at the dusk flank in the northern hemisphere and the dawn flank in the southern hemisphere. From there, short wavelength perturbations are generated which propagate as surface ripples on the high-latitude magnetopause. This noteworthy dawn-dusk asymmetry was given preliminary confirmation from ground response observations by Farrugia et al. (2003).

Global, 3D, ideal MHD simulations have recently shown success in generating KH surface waves and large vortical structures (e.g., Fairfield et al. 2007; Collado-Vega et al. 2007; Claudepierre et al. 2008). Interestingly, KH-type waves were also seen at the inner edge of the magnetopause boundary layer. Indeed, it is worth keeping in mind that the magnetopause and its boundary layer generally form a spatially broad transition. Therefore, the much-used

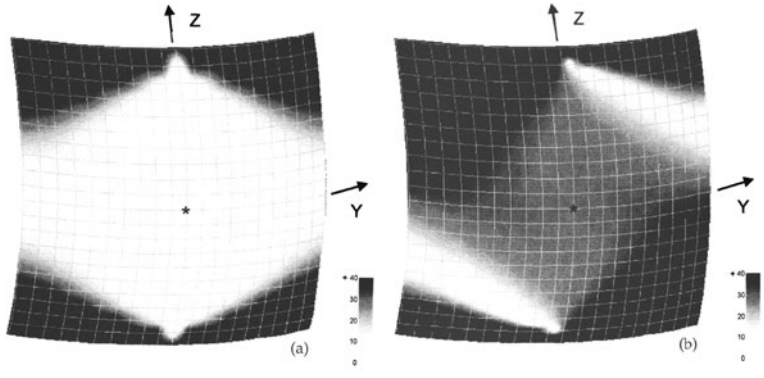

Fig. 1.8 Distribution of magnetic shear across the magnetopause, obtained from modeled dipole and magnetosheath magnetic fields, for (**a**) an IMF pointing due northward and (**b**) an IMF inclined at 30° west of north. Adapted from Farrugia et al. (1998b)

KH instability criterion based on a tangential discontinuity approximation (i.e., zero-thickness boundary) is of limited use. Gratton et al. (2004) gave examples of magnetopause transitions of finite thickness which were stable when the tangential discontinuity model was utilized to model the magnetopause, but which were found to be KH-unstable when continuous functions were used instead (see also Gratton et al. 2003). We also note that oscillations of the magnetopause can have other causes besides intrinsic KH instability. Along these lines, studies of magnetopause wave motions which involve both the KH instability and dynamic pressure changes were undertaken by Farrugia et al. (2000) and Fairfield et al. (2003).

Numerous observational reports of KH waves at the magnetopause have been made (e.g., see also Hasegawa et al. 2004b; Owen et al. 2004; Foullon et al. 2008; Taylor et al. 2008), with the recent results of four-spacecraft analysis with Cluster giving accurate, albeit spatially limited, determination of surface wave characteristics (Foullon et al. 2010). Most of the studies mentioned so far have addressed the linear regime of the KH instability. A result of particular interest in recent years is the demonstration of the non-linear, rolled-up nature of KH vortices at the magnetopause by Hasegawa et al. (2004b). Their interpretation of multi-spacecraft data from Cluster showed the non-linear rolling-up of KH waves on the scale of the spacecraft separation (∼ few thousand km, cf. Fig. 1.9). As shown in Fig. 1.9, density tongues (panels (c) and (d)), with corresponding temperature (panel (b)) and magnetic field (not shown here) fluctuations, were observed to roll-up. Such definitive observations were only made possible thanks to the four-point measurements of the Cluster mission. Note also the work by Hasegawa et al. (2007) who could recover KH flow vortex streamlines using a variant of the Grad-Shafranov reconstruction technique (Sonnerup and Guo 1996).

Based on local MHD simulations, Hasegawa et al. (2006b) highlighted that the rolling-up of plasma around vortices should lead low density plasma parcels (from the magnetospheric side of the boundary) to attain anti-sunward speeds larger than that of the magnetosheath itself. They confirmed this signature from analyses of numerous KH wave cases from the Geotail spacecraft dataset (see also Taylor et al. (2008)). Another signature possibly related to the occurrence of the KH instability was suggested by Taylor and Lavraud (2008). After passage through rolled-up vortices (according to the signature of Hasegawa et al. (2006b)) at the magnetopause, Taylor and Lavraud (2008) noted the presence of two distinct low energy (i.e., of solar wind origin) boundary layer ion populations with different temperature anisotropies (from Double Star three-dimensional ion distribution functions). They suggested that one of the populations might be the result of local plasma entry through the KH instability, while the other might for instance result from prior double high-latitude reconnection on the dayside. However, this single event did not permit to obtain a definite interpretation.

Finally, global signatures of the KH instability have been obtained from multi-spacecraft Cluster data (Foullon et al. 2008). In this work, the inverse

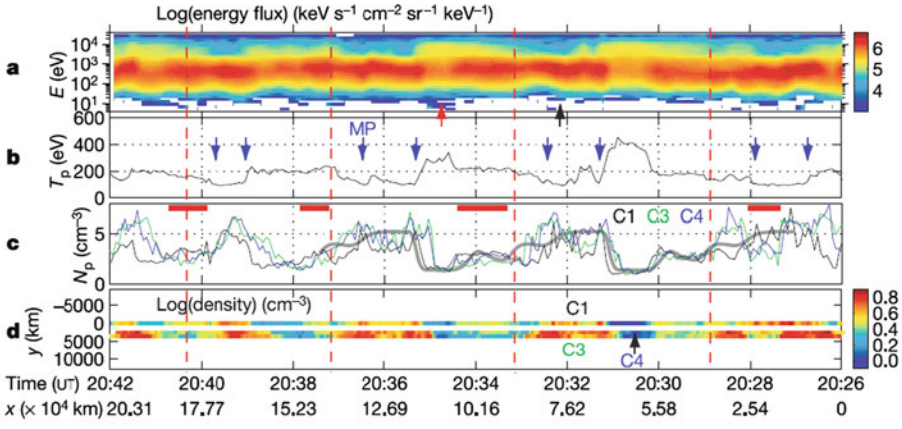

Fig. 1.9 Multi-spacecraft Cluster observations of rolled-up KH vortices. (**a**) Ion energy-time spectrogram, (**b**) ion temperature, (**c**) ion density, and (**d**) color-coded ion densities along the spacecraft paths in the plane of the vortices. Adapted from Hasegawa et al. (2004b)

dependence found between the IMF clock angle and the wavelength at the flanks was interpreted as a clear manifestation that KH unstable domains (cf. Fig. 1.8) are the remote sources for these waves. In addition, the temporal evolution of the magnetopause boundary layer could be estimated via a novel technique, extending the transition parameter (TP) technique (Hapgood and Bryant 1992) based on the relationship between the electron density and temperature across the magnetopause transition. The results gave credence to the contribution of the KH mechanism to the widening of the LLBL.

1.3.2 Kelvin–Helmholtz and Secondary Processes

Unlike magnetic reconnection or diffusive processes, the Kelvin–Helmholtz instability is not a plasma entry process per se. Its occurrence is rather believed to be of importance for plasma entry at the flank magnetopause because it may entrain local plasma transport by favoring the development of secondary processes such as diffusion and magnetic reconnection.

1.3.2.1 Kelvin–Helmholtz and Secondary Diffusive Processes

Early local numerical simulations of the KH instability have indicated that fast anomalous diffusion was possible for sufficiently thin boundaries within the vortices (Thomas and Winske 1993; Fujimoto and Terasawa 1994).

More recently, but on the basis of earlier work by Sharp (1984), the non-linear growth of the KH instability was recognised to lead to the further development of secondary KH and Rayleigh-Taylor (RT) instabilities (Matsumoto and Hoshino 2006; Matsumoto and Seki 2007). Figure 1.10 shows cuts of the plasma density at four different stages during the simulation of Matsumoto and Hoshino (2006) which highlight the generation of secondary KH and RT instabilities. These secondary growing instabilities entrain a turbulent decay of the vortices, vortex coalescence and particle super-diffusion, as recently emphasized by Cowee et al. (2009) with hybrid simulations.

A more peculiar but interesting secondary process related to the KH instability was studied by Smets et al. (2007). Using hybrid simulations with anti-parallel magnetic fields as boundary conditions, they observed the growth of the KH instability and subsequent diffusion, or mixing, of plasmas across the boundary thanks to finite gyro-radius effects. The boundary conditions they used may appear unrealistic for such study because the onset of reconnection for anti-parallel magnetic fields generally precludes the growth of the KH instability. It is worth mentioning, however, that Kawano et al. (1994) and Mozer

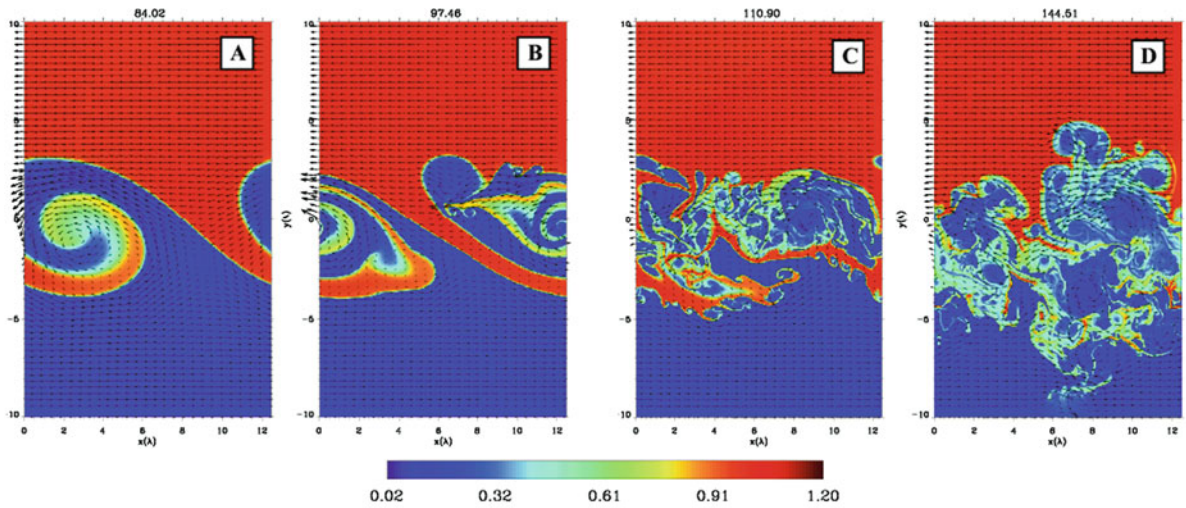

Fig. 1.10 Cuts of the plasma density (color-coded) for four different times during an MHD simulation of the KH instability. Note that similar results were obtained with full particle simulations. Adapted from Matsumoto and Hoshino (2006)

et al. (1994) have reported KH waves under southward IMF conditions.

1.3.2.2 Kelvin–Helmholtz and Localized Magnetic Reconnection

An alternate secondary transport process that may develop in conjunction with the KH instability is magnetic reconnection. This possibility was first identified from MHD simulations by Belmont and Chanteur (1989). It was later confirmed and quantified by use of other simulations (e.g., Min et al. 1997; Otto and Fairfield 2000; Nykyri and Otto 2001; Nakamura and Fujimoto 2005). Figure 1.11 (left) shows the magnetic topology that results from such localized reconnection within KH vortices, as deduced from MHD simulations performed by Nykyri and Otto (2001).

Identification of the observational signatures of reconnection as a secondary process to the KH instability has recently been attempted. Nykyri et al. (2006) studied a magnetopause crossing at the flanks by Cluster. They looked both for signatures of the KH instability (cf. Section 1.3.1) and magnetic reconnection (e.g., via the Walén test; cf. Section 1.2.1.2). During a period showing KH wave activity, they found intervals consistent with the occurrence of magnetic reconnection. In particular, the observation of multiple populations in the ion distribution functions (Fig. 1.11, right) was pointed as evidence for the local entry of solar wind plasma through magnetic reconnection. Recent Geotail observations of heated bidirectional electrons in the vicinity of KH vortices were also proposed in support of magnetic reconnection as a secondary process (Nishino et al. 2007a).

1.3.3 Other Diffusive Processes

Diffusive processes have been investigated for the magnetopause (e.g., Treumann 1997; Terasawa et al. 1997; Lee et al. 1994; Johnson and Cheng 1997, 2001; Bauer et al. 2001; Wing et al. 2006; Zhou et al. 2007). However, their efficiency has often been questioned, primarily on the basis of the lack of observational evidence, i.e., a lack of conclusive signatures.

It has long been thought, for instance, that the presence of a thick boundary layer at the dayside magnetopause under northward IMF, and thus in the absence of both sub-solar reconnection and significant velocity shear (i.e., precluding the KH instability), was the signature of ongoing diffusion. It is now rather believed that double high-latitude reconnection (Section 1.2.4) may be the main mechanism contributing to the formation of boundary layers on the dayside under northward IMF. For theories and past attempts to identify diffusive processes, the reader is referred to the review by Scholer and Treumann (1997). Below we only note a few recent studies.

The possibility of plasma protrusion through the magnetopause without invoking magnetic reconnection has also been raised (Lemaire and Roth, 1978) (see also Roth (1992) and Lui (2001) for reviews). Lundin et al. (2003) studied plasma transfer event (PTEs) signatures using multi-spacecraft Cluster data. They note that PTE and FTE signatures have commonalities during southward IMF, but highlight the fact that PTEs occurrence is largely independent of IMF orientation, thus making them unlikely the result of reconnection.

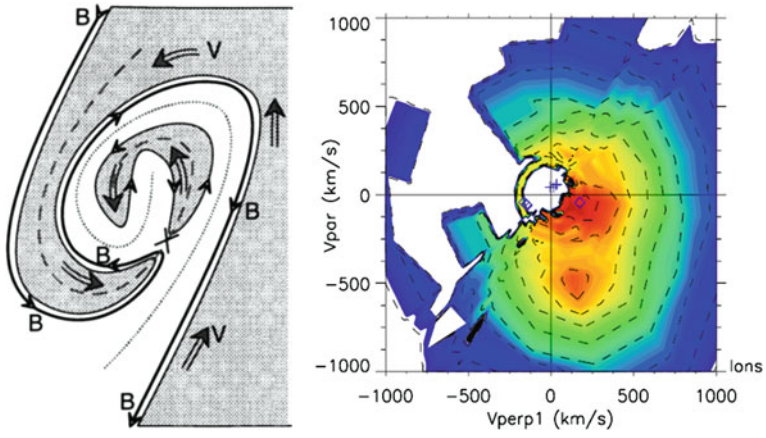

Fig. 1.11 (*left*) Magnetic topology from MHD simulation of a vortex structure showing secondary reconnection at a thin current sheet. Adapted from Nykyri and Otto (2001). (*right*) V_{PAR}, V_{PERP} plane cut of a Cluster ion distribution function showing the presence of two populations as a result of localized magnetic reconnection in the vicinity of a vortex. Adapted from Nykyri et al. (2006)

In a series of articles, Chaston et al. (2007, 2008, 2009) focused on Kinetic Alfvén wave (KAW) signatures at the magnetopause. They found that the location and power of KAWs may produce significant plasma transport within KH vortices and reconnection ion diffusion region, but also away or in the absence of those processes (cf. also Lee et al. 1994; Johnson and Cheng 1997, 2001).

Finally, we note that because the dynamic pressure of the solar wind varies considerably, the magnetopause and its environs are almost constantly in motion. When a sharp pressure drop accelerates the magnetopause sunward the situation becomes akin to dense over tenuous plasma in a gravitational field. This may render the magnetopause prone to the Rayleigh-Taylor (RT) instability, provided the accelerations are strong enough (>1 km/s^2), last long enough (1–2 min or longer), and that the magnetic shear is small (Mishin 1993; Gratton et al. 1996). In their analysis, Mishin (1993) showed that magnetopause accelerations also influence KH instability growth rates.

1.4 Global Coupling and Pathways for Solar Wind Plasma

We now discuss some global aspects that pertain to the magnetopause and boundary layers. We first illustrate how recent works on magnetic reconnection may be applied to assess and predict some aspects of global solar wind–magnetosphere coupling. We then present some possible paths that may be followed by solar wind plasma across the dayside and flank boundaries, and towards the magnetotail.

1.4.1 Global Coupling and Magnetic Reconnection

Magnetic reconnection at the dayside magnetopause has long been viewed as the main driver of geomagnetic activity, i.e., as the regulator of the transfer of energy between the solar wind and magnetosphere. When theories of this coupling are constructed the solar wind electric field is generally taken as the main ingredient that drives the dayside reconnection rate (Gonzalez and Mozer 1974; Siscoe and Crooker 1974; Burton et al. 1975; Perreault and Akasofu 1978).

Although it is still unclear as to whether magnetic reconnection at the magnetopause always occurs in a fast regime (i.e., with a dimensionless reconnection rate of 0.1; cf. Sections 1.2.1.1 and 1.4.1), Cassak and Shay (2007) recently theorized that in the fast, asymmetric reconnection regime the reconnection electric field (amount of magnetic flux being reconnected per unit time and length) directly scales with the mesoscale density and magnetic field each side of the boundary (cf. also Swisdak and Drake 2007; Borovsky and Hesse 2007).

Based on this scaling law, first principles and parameterization of global MHD simulations, Borovsky (2008) derived an analytic formula for the reconnection rate at the dayside magnetopause. This coupling function turned out to be essentially as good as that of Newell et al. (2007), who also reported a solar wind–magnetosphere coupling function in an empirical manner, when tested statistically against geomagnetic indices (cf. also Newell et al. 2008).

Performing a parametric study of the coupling function of Borovsky (2008), Lavraud and Borovsky (2008) highlighted the Mach number dependence of the dayside reconnection rate, and in particular when the Mach number changes come from varying the solar wind density (cf. also Scurry and Russell 1991; Lopez et al. 2004; Grocott et al. 2009). In their study, Lavraud and Borovksy (2008) also highlighted other Mach number effects on the magnetopause, such as changes in reconnection rate (with a plasmasphere effect; see next), magnetopause shape, current systems, and magnetosheath flows which influence the velocity shear at the magnetopause.

The plasmasphere, a cold and dense plasma population of ionospheric origin, builds up in the equatorial region of the magnetosphere primarily during quiet times. When convection is enhanced as a result of magnetic reconnection at the dayside magnetopause, part of the plasmasphere is drained towards the magnetopause in the form of a plume which will eventually get sucked into the reconnection region (being cold, it has to convect into the dayside reconnection line). Observations of such cold plasma close to the magnetopause, or even participating into the reconnection process, have been frequently reported (e.g., Su et al. 2000; Sauvaud et al. 2001; McFadden et al. 2008). Adding such dense plasma into the reconnection site may impact the reconnection rate. This was found

parametrically using a solar wind–magnetosphere coupling function (Lavraud and Borovsky 2008), and further demonstrated from statistical analysis of geomagnetic data by Borovsky and Denton (2006).

1.4.2 Pathways to the Magnetotail

Under southward IMF, magnetic reconnection at the dayside magnetopause as the basic driver of magnetospheric dynamics has attained the level of a paradigm. However, it still remains unclear whether solar wind plasma constitutes the main contributor to the nightside plasma sheet. Observations of the polar cap and lobes, being devoid of solar wind plasma in the near-Earth regions, suggest that if solar wind plasma circulates over the poles before reaching the plasma sheet, it likely may only manage to populate the central tail at some distances downtail (cf. Fig. 1.1). Recent simulations have on the other hand suggested that, during active times, both polar cap outflows and plasmasphere re-circulation may allow the entire plasma sheet to fill with populations of ionospheric origin (e.g., Moore et al. 2005, 2007, 2008, and references therein). The composition of these source populations (e.g., dominance of O^+) is compatible with the observed composition of the plasma sheet during active times. It is also unclear whether solar wind plasma may enter into the magnetosphere from the flanks under southward IMF.

Under northward IMF, solar wind plasma may not circulate over the poles. The fact that solar wind enters through the flanks under such conditions has been well documented. It remains unknown, however, which of the double high-latitude reconnection or KH instability (and its secondary processes) mechanisms dominates in terms of plasma entry efficiency (cf. Fig. 1.12) (e.g., Fujimoto et al. 1998; Li et al. 2005; Øieroset et al. 2005, 2008; Safrankova et al. 2007; Nishino et al. 2007a, b, c; Foullon et al. 2008; Taylor et al. 2008). Some quantitative comparisons using, e.g., global MHD simulations and actual in situ data, have been attempted for the double high-latitude reconnection mechanism (e.g., Li et al. 2005; Øieroset et al. 2005; Wing et al. 2006). However, because the KH instability does not naturally occur in simulations (generally owing to too coarse grid sizes), it is not possible to tell whether the inferred agreement was observed for the right reason. On the other hand, although diffusive processes do occur in simulations of the KH instability,

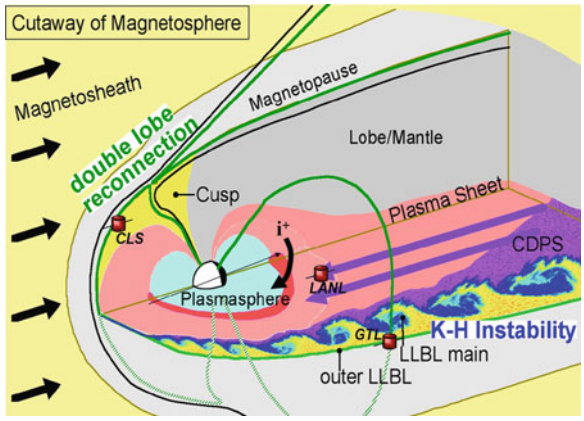

Fig. 1.12 Schematic of the magnetosphere under northward IMF with representations of both (1) double-high latitude reconnection, and (2) the KH instability at the flanks. Each process has been most studied respectively by use of Cluster at high latitude and Geotail (or THEMIS and Cluster) at the low-latitude flanks. The formation of a cold-dense plasma sheet as a result of these processes is of importance for inner magnetosphere dynamics, which may be monitored for instance by use of geosynchronous spacecraft (e.g., LANL), as shown (Figure courtesy of Kanako Seki)

most studies agree with the fact that the amount of plasma transport mediated by the KH instability is hard to estimate. Observationally, it also remains unclear primarily because definite signatures of plasma entry through KH and its secondary processes, and diffusion in particular, have not been unambiguously identified. Furthermore, the relative efficiency of each mechanism may vary in non-trivial manners with conditions such as the solar wind Mach number, plasma beta, IMF clock angle, preconditioning by plasmasphere, etc.

Conclusions

In the present review, we have summarized some basic properties of the prime solar wind entry mechanisms that occur at the Earth's magnetopause: namely magnetic reconnection, the KH instability and diffusive processes. A dichotomy is observed between times dominated by southward (active times) and northward IMF (quiet times). Recent works have confirmed the establishment of a paradigm: the predominance of dayside magnetic reconnection in the control of solar wind–magnetosphere interaction under southward IMF. Under northward IMF, however, the picture is not as clear. Although high-latitude magnetic reconnection likely plays a significant role, the KH and its

secondary instabilities possibly play as significant a role for the dynamics of the magnetosphere. In each IMF case, we note that there remain uncertainties as to the actual pathway for solar wind plasma towards the magnetotail and inner magnetosphere. Besides, there is some uncertainty as to whether plasma of ionospheric origin may dominate in the near-Earth magnetotail during active times.

A summary of some current issues that relate to the magnetopause and boundary layers may be drawn as follows:

- Although not addressed here, the actual initiation process of magnetic reconnection – that which breaks the frozen-in condition – is still to be determined.
- The mechanisms that lead to particle acceleration and heating (and their amount) during and after reconnection are still debated.
- Although increased measurement accuracy and multi-spacecraft methods have allowed us to investigate fundamental processes in an unprecedented quantitative manner, accurate estimation of key quantities such as the reconnection rate from in situ observation remains a challenge.
- Both anti-parallel and component reconnections are observed to occur. Component reconnection is regularly observed at the magnetopause thanks to the "Parker" spiral configuration of the IMF, but it is not known whether magnetic reconnection may have an intrinsic preference for one or the other.
- Intermittent reconnection often occurs and may be a dominant mode of interaction at the magnetopause. Yet, we note that solar wind observations of steady reconnection at extended X-lines (Phan et al. 2006; Gosling et al. 2007) have proved that reconnection need not be intermittent by nature. Furthermore, truly intermittent reconnection and unsteady, continuous reconnection appear to produce several similar signatures.
- In part for that reason the formation process of FTEs is still the subject of active research.
- Although reconnection dominates under southward IMF, both recent observations and global MHD simulations suggest the KH instability may occur as well.
- Both diffusive processes and reconnection are envisaged as secondary processes to the KH instability. Which is most common and efficient for plasma transfer remains to be studied in detail.
- A current debate concerns the relative contributions of the KH and its secondary instabilities and the double high-latitude reconnection mechanism in filling the plasma sheet with solar wind plasma under northward IMF.
- Concerning diffusion in general, an important issue is as follows: can testable theoretical signatures of diffusive processes be unambiguously identified?

Acknowledgments The authors are grateful to the reviewer for his/her constructive comments. CF acknowledges financial support from the UK STFC on the CFSA Rolling Grant. CJF acknowledges support from NASA grant NNX08AD11G. JPE holds an STFC Advanced Fellowship at ICL.

References

Avanov LA, Smirnov VN, Waite JH Jr, Fuselier SA, Vaisberg OL (2001) High-latitude magnetic reconnection in sub-Alfvénic flow: interball tail observations on May 29, 1996. J Geophys Res 106:29491

Bauer TM, Treumann RA, Baumjohann W (2001) Investigation of the outer and inner low-latitude boundary layers. Ann Geophys 19:1065–1088

Bavassano Cattaneo MB et al (2006) Kinetic signatures during a quasi-continuous lobe reconnection event: cluster ion spectrometer (CIS) observations. J Geophys Res 111:A09212. doi:10.1029/2006JA011623

Belmont G, Chanteur G (1989) Advances in magnetopause Kelvin-Helmholtz instability studies. Phys Scr 40:124–128

Berchem J, Russell CT (1984) Flux transfer events on the magnetopause: spatial distribution and controlling factors. J Geophys Res 89(A8):6689–6703

Berchem J et al (2008) Reconnection at the dayside magnetopause: comparisons of global MHD simulation results with Cluster and Double Star observations. J Geophys Res 113:A07S12. doi:10.1029/2007JA012743

Birn J et al (2001) Geospace Environmental Modeling (GEM) Magnetic Reconnection Challenge. J Geophys Res 106(A3):3715–3719

Biskamp D (1986) Magnetic reconnection via current sheets. Phys Fluids 29:1520

Borovsky JE (2008) The rudiments of a theory of solar wind/magnetosphere coupling derived from first principles. J Geophys Res 113:A08228. doi:10.1029/2007JA012646

Borovsky JE, Denton MH (2006) Effect of plasmaspheric drainage plumes on solar-wind/magnetosphere coupling. Geophys Res Lett 33:L20101. doi:10.1029/2006GL026519

Borovsky JE, Hesse M (2007) The reconnection of magnetic fields between plasmas with different densities: scaling relations. Phys Plasmas 14:102309

Burton RK, McPherron RL, Russell CT (1975) An empirical relationship between interplanetary conditions and Dst. J Geophys Res 80(31):4204–4214

Cargill PJ, Lavraud B, Owen CJ, Grison B, Dunlop MW, Cornilleau-Wehrlin N, Escoubet CP, Paschmann G, Phan TD, Rezeau L, Bogdanova Y, Nykyri K (2005) Cluster at the magnetospheric cusps. Space Sci Rev 118(1–4):321–366. doi:10.1007/s11214-005-3835-0

Cassak PA, Shay MA (2007) Scaling of asymmetric magnetic reconnection: general theory and collisional simulations. Phys Plasmas 14:102114. doi:10.1063/1.2795630

Chandler MO, Avanov LA (2003) Observations at low latitudes of magnetic merging signatures within a flux transfer event during a northward interplanetary magnetic field. J Geophys Res 108(A10):1358. doi:10.1029/2003JA009852

Chapman S, Ferraro VC (1931) A new theory of magnetic storms. Terr Magn Atmos Elec 36:171

Chaston CC, Johnson JR, Wilber M, Acuna M, Goldstein ML, Rème H (2009) Kinetic Alfvén wave turbulence and transport through a reconnection diffusion region. Phys Rev Lett 102:015001.1–015001.4. doi:10.1103/PhysRevLett.102.015001

Chaston CC, Wilber M, Mozer FS, Fujimoto M, Goldstein ML, Acuna M, Rème H, Fazakerley A (2007) Mode conversion and anomalous transport in Kelvin-Helmholtz vortices and kinetic Alfven waves at the Earth's magnetopause. Phys Rev Lett 99:175004.1–175004.4. doi:10.1103/PhysRevLett.99.175004

Chaston C et al (2008) Turbulent heating and cross-field transport near the magnetopause from THEMIS. Geophys Res Lett 35:L17S08. doi:10.1029/2008GL033601

Chen FF (1984) Introduction to plasma physics and controlled fusion. Kluwer, Dordrecht

Claudepierre SG, Elkington SR, Wiltberger M (2008) Solar wind driving of magneto-spheric ULF waves: pulsations driven by velocity shear at the magnetopause. J Geophys Res 113:A05218. doi:10.1029/2007JA012890

Collado-Vega YM, Kessel RL, Shao X, Boller RA (2007) MHD flow visualization of magnetopause boundary region vortices observed during high-speed streams. J Geophys Res 112:A06213. doi:10.1029/2006JA012104

Cooling BMA, Owen CJ, Schwartz SJ (2001) Role of the magnetosheath flow in determining the motion of open flux tubes. J Geophys Res 106(A9):18763–18776

Cowee MM, Winske D, Gary SP (2009) Two-dimensional hybrid simulations of superdiffusion at the magnetopause driven by Kelvin-Helmholtz instability. J Geophys Res 114:A10209. doi:10.1029/2009JA014222

Cowley SWH (1976) Comments on the merging of non antiparallel field. J Geophys Res 81:3455–3458

Cowley SWH (1982) The causes of convection in the Earth's magnetosphere: A review of developments during the IMS. Rev Geophys 20(3):531–565

Cowley SWH, Owen CJ (1989) A simple illustrative model of open flux tube motion over the dayside magnetopause. Planet Space Sci 37:1461–1475

Crooker NU (1979) Dayside merging and cusp geometry. J Geophys Res 84:951–959

Crooker NU, Eastman TE, Satiles GS (1979) Observations of plasma depletion in the magnetosheath at the dayside magnetopause. J Geophys Res 84:869

Daum P, Wild JA, Penz T, Woodfield EE, Rème H, Fazakerley AN, Daly PW, Lester M (2008) Global MHD simulation of flux transfer events at the high-latitude magnetopause observed by the Cluster spacecraft and the SuperDARN radar system. J Geophys Res 113:A07S22. doi:10.1029/2007JA012749

deHoffmann F, Teller E (1950) Magnetohydrodynamics shocks. Phys Rev 80:692

De Keyser J (2005) The Earth's magnetopause: reconstruction of motion and structure. Space Sci Rev 121(1–4):225–235

De Keyser J, Roth M (2003) Structural analysis of periodic surface waves on the magnetospheric boundary. Planet Space Sci 51:757–768

De Keyser J, Darrouzet F, Roth M (2002) Trying to bring the magnetopause to a standstill. Geophys Res Lett 29:93. doi:10.1029/2002GL015001

De Keyser J, Dunlop MW, Owen CJ, Sonnerup BUÖ, Haaland S, Vaivads A, Lundin R, Rezeau L, Paschmann G (2005) Magnetopause and boundary layer. Space Sci Rev 118 (1–4):231–320

De Keyser J, Gustafsson G, Roth M et al (2004) Reconstruction of the magnetopause and low-latitude boundary layer topology using Cluster multi-point measurements. Ann Geophys 22(7):2381–2389

Deng XH, Matsumoto H (2001) Rapid magnetic reconnection in the Earth's magnetosphere mediated by whistler waves. Nature 410:557–560

Dorelli JC, Bhattacharjee A (2009) On the generation and topology of flux transfer events. J Geophys Res 114:A06213. doi:10.1029/2008JA013410

Drake JF, Swisdak M, Phan TD, Cassak PA, Shay MA, Lepri ST, Lin RP, Quataert E, Zurbuchen TH (2009) Ion heating resulting from pickup in magnetic reconnection exhausts. J Geophys Res 114:A05111. doi:10.1029/2008JA013701

Drake JF et al (2006) Electron acceleration from contracting magnetic islands during reconnection. Nature 443(7111):553–556

Dungey JW (1954) Electrodynamics of the outer atmospheres. Penn State Ionos Res Lab Sci Rep 69

Dungey JW (1961) Interplanetary magnetic field and the auroral zones. Phys Rev Lett 6:47

Dunlop MW, Balogh A, Glassmeier K-H (2002) Four-point Cluster application of magnetic field analysis tools: the discontinuity analyzer. J Geophys Res 107(A11):1385. doi:10.1029/2001JA005089

Dunlop MW, Zhang QH, Xiao CJ et al (2009) Reconnection at high latitudes: antiparallel merging. Phys Rev Lett 102(7):075005

Eastwood JP, Phan T-D, Mozer FS, Shay MA, Fujimoto M, Retinò A, Hesse M, Balogh A, Lucek EA, Dandouras I (2007) Multi-point observations of the Hall electromagnetic field and secondary island formation during magnetic reconnection. J Geophys Res 112:A06235. doi:10.1029/2006JA012158

Eastwood JP, Phan TD, Øieroset M, Shay MA (2010) Average properties of the magnetic reconnection ion diffusion region in the Earth's magnetotail: The 2001–2005 cluster observations and comparisons with simulations. J Geophys Res 115:A08215. doi:10.1029/2009JA014962

Eriksson S et al (2009) Magnetic island formation between large-scale flow vortices at an undulating postnoon

magnetopause for northward interplanetary magnetic field. J Geophys Res 114:A00C17. doi:10.1029/2008JA013505

Escoubet CP, Smith MF, Fung SF, Anderson PC, Hoffman RA, Basinska EM, Bosqued J-M (1992) Staircase ion signature in the polar cusp – A case study. Geophys Res Lett 19:1735

Fairfield DH, Farrugia CJ, Mukai T, Nagai T, Fedorov A (2003) Motion of the dusk flank boundary layer caused by solar wind pressure changes and the Kelvin-Helmholtz instability: 10–11 January 1997. J Geophys Res 108(A12):1460. doi:10.1029/2003JA010134

Fairfield DH, Kuznetsova MM, Mukai T, Nagai T, Gombosi TI, Ridley AJ (2007) Waves on the dusk flank boundary layer during very northward interplanetary magnetic field conditions: observations and simulation. J Geophys Res 112:A8. doi:10.1029/2006JA012052

Fairfield DH, Otto A, Mukai T, Kokubun S, Lepping RP, Steinberg JT, Lazarus AJ, Yamamoto T (2000) Geotail observations of the Kelvin-Helmholtz instability at the equatorial magnetotail boundary for parallel northward fields. J Geophys Res 105(A9):21159–21173

Farrugia CJ, Gratton FT, Torbert RB (2001) Viscous-type processes in the solar wind-magnetosphere interaction. Space Sci Rev 95:443–456

Farrugia CJ, Gratton FT, Torbert RB, Bender L, Gnavi G, Ogilvie KW, Lepping RP, Stauning P (2003) On the dependence of dayside Kelvin-Helmholtz activity on IMF orientation. Adv Space Res 31(4):1105

Farrugia C, Gratton F, Bender L, Biernat H, Erkaev N, Quinn J, Torbert R, Dennisenko V (1998b) Charts of joint Kelvin–Helmholtz and Rayleigh–Taylor instabilites at the dayside magnetopause for strongly northward interplanetary magnetic field. J Geophys Res 103(A4):6703–6727

Farrugia CJ, Sandholt PE, Denig WF, Torbert RB (1998a) Observation of a correspondence between poleward moving auroral forms and stepped cusp ion precipitation. J Geophys Res 103(A5):9309–9315

Farrugia CJ et al (2000) Coordinated wind, interball/tail, and ground observations of Kelvin-Helmholtz waves at the near-tail, equatorial magnetopause at dusk: January 11, 1997. J Geophys Res 105:7639–7667

Fear RC, Milan SE, Fazakerley AN, Fornaçon K-H, Carr CM, Dandouras I (2009) Simultaneous observations of flux transfer events by THEMIS, Cluster, Double Star, and SuperDARN: acceleration of FTEs. J Geophys Res 114:A10213. doi:10.1029/2009JA014310

Fedder JA, Lyon JG (1995) The Earth's magnetosphere is 165 R_E long: self-consistent currents, convection, magnetospheric structure, and processes for northward interplanetary magnetic field. J Geophys Res 100(A3):3623–3635

Fitzenreiter RJ, Ogilvie KW (1995) Kelvin-Helmholtz instability at the magnetopause: observations. In: Song P, Sonnerup BUÖ, Thomsen MF (eds) Physics of the magnetopause. Geophysical monograph, vol 90. American Geophysical Union, Washington, DC, p 277

Forbes TG (1995) How does fast reconnection work? In: Meneguzzi M, Pouquet A, Sulem PL (eds) Small scale structures in three-dimensional hydro and magnetohydrodynamic turbulence. Lecture notes in physics, vol 462. Springer, Paris, pp 319–324

Foullon C, Farrugia CJ, Fazakerley AN, Owen CJ, Gratton FT, Torbert RB (2008) Evolution of Kelvin-Helmholtz activity on the dusk flank magnetopause. J Geophys Res 113:A11203. doi:10.1029/2008JA013175

Foullon C, Farrugia CJ, Fazakerley AN, Owen CJ, Gratton FT, Torbert RB (2010) On the multi-spacecraft determination of periodic surface wave phase speeds and wavelengths. J Geophys Res. doi: 10.1029/2009JA015189 (in press)

Frey HU, Phan TD, Fuselier SA, Mende SB (2003) Continuous magnetic reconnection at Earth's magnetopause. Nature 426:533–537

Fujimoto M, Terasawa T (1994) Anomalous ion mixing within an MHD scale Kelvin-Helmholtz vortex. J Geophys Res 99:8601

Fujimoto M, Terasawa T, Mukai T, Saito Y, Yamamoto T, Kokubun S (1998) Plasma entry from the flanks of the near-Earth magnetotail: geotail observations. J Geophys Res 103:4391

Fuselier SA, Klumpar DM, Shelley EG (1991) Ion reflection and transmission during reconnection at the Earth's subsolar magnetopause. Geophys Res Lett 18:139

Fuselier SA, Petrinec SM, Trattner KJ (2000) Stability of the high-Latitude reconnection site for steady northward IMF. Geophys Res Lett 27:473

Fuselier SA, Petrinec SM, Trattner KJ, Fujimoto M, Hasegawa H (2007) Simultaneous observations of fluctuating cusp aurora and low-latitude magnetopause reconnection. J Geophys Res 112:A11207. doi:10.1029/2007JA012252

Fuselier SA, Trattner KJ, Petrinec SM, Owen CJ, Rème H (2005) Computing the reconnection rate at the Earth's magnetopause using two spacecraft observations. J Geophys Res 110:A06212. doi:10.1029/2004JA010805

Gonzalez WD, Mozer FS (1974) A quantitative model for the potential resulting from reconnection with an arbitrary interplanetary magnetic field. J Geophys Res 79(28):4186–4194

Gosling JT (2009) Magnetic reconnection in the heliosphere: new insights from observations in the solar wind. In: Gopalswamy N, Webb DF (eds) Universal heliophysical processes. Proceedings of the International Astronomical Union, IAU Symposium 257(4), Cambridge University Press, Cambridge, pp 367–377. doi:10.1017/S1743921309029597

Gosling JT, Asbridge JR, Bame SJ, Feldman WC, Paschmann G, Sckopke N, Russell CT (1982) Evidence for quasi-stationary reconnection at the dayside magnetopause. J Geophys Res 87(16):2147–2158

Gosling JT, Thomsen MF, Bame SJ, Onsager TG, Russell CT (1990) The electron edge of the low-latitude boundary layer during accelerated flow events. Geophys Res Lett 17:1933

Gosling J, Thomsen M, Bame S, Elphic R, Russell C (1991) Observations of reconnection of interplanetary and lobe magnetic field lines at the high-latitude magnetopause. J Geophys Res 96(A8):14097–14106

Gosling JT, Eriksson S, Blush LM, Phan TD, Luhmann JG, McComas DJ, Skoug RM, Acuna MH, Russell CT, Simunac KD (2007) Five spacecraft observations of oppositely directed exhaust jets from a magnetic reconnection X-line extending > 4.26 × 106 km in the solar wind at 1 AU. Geophys Res Lett 34:L20108. doi:10.1029/2007GL031492

Gratton FT, Farrugia CJ, Cowley SWH (1996) Is the dayside magnetopause Rayleigh-Taylor unstable sometimes? J Geophys Res 101:4929

Gratton FT, Gnavi G, Farrugia CJ, Bender L (2003) The stability of the pristine magnetopause. Planet Space Sci 51:769

Gratton FT, Bender L, Farrugia CJ, Gnavi G (2004) Concerning a problem related to the Kelvin-Helmholtz stability of the thin magnetopause. J Geophys Res 109(A4):A04211. doi:10.1029/2003JA010146

Grocott A, Badman SV, Cowley SWH, Milan SE, Nichols JD, Yeoman TK (2009) Magnetosonic Mach number dependence of the efficiency of reconnection between planetary and interplanetary magnetic fields. J Geophys Res 114:A07219. doi:10.1029/2009JA014330

Haaland S et al (2004) Four-spacecraft determination of magnetopause orientation, motion and thickness: comparison with results from single-spacecraft methods. Ann Geophys 22:1347

Hapgood MA, Bryant DA (1992) Exploring the magnetospheric boundary layer. Planet Space Sci 40(10):1431–1459

Hasegawa H, Sonnerup BUÖ, Dunlop MW, Balogh A, Haaland SE, Klecker B, Paschmann G, Lavraud B, Dandouras I, Rème H (2004a) Reconstruction of two-dimensional magnetopause structures from Cluster observations: verification of method. Ann Geophys 22:1251–1266

Hasegawa H, Fujimoto M, Phan TD et al (2004b) Rolled-up Kelvin-Helmholtz vortices and associated solar wind entry at Earth's magnetopause. Nature 430:755–758

Hasegawa H, Sonnerup BUÖ, Owen CJ, Klecker B, Paschmann G, Balogh A, Rème H (2006a) The structure of flux transfer events recovered from Cluster data. Ann Geophys 24:603–618

Hasegawa H, Fujimoto M, Takagi K, Saito Y, Mukai T, Rème H (2006b) Single-spacecraft detection of rolled-up Kelvin-Helmholtz vortices at the flank magnetopause. J Geophys Res 111:A09203. doi:10.1029/2006JA011728

Hasegawa H, Sonnerup BUÖ, Fujimoto M, Saito Y, Mukai T (2007) Recovery of streamlines in the flank low-latitude boundary layer. J Geophys Res 112:A04213. doi:10.1029/2006JA012101

Hasegawa H et al (2009) Boundary layer plasma flows from high-latitude reconnection in the summer hemisphere for northward IMF: THEMIS multi-point observations. Geophys Res Lett 36:L15107. doi:10.1029/2009GL039410

Hasegawa H, Wang J, Dunlop MW, Pu ZY, Zhang QH, Lavraud B, Taylor MG, Constantinescu DO, Berchem J, Angelopoulos V, McFadden JP, Frey HU, Panov EV, Volwerk M, Bogdanova YV (2010) Evidence for a flux transfer event generated by multiple X-line reconnection at the magnetopause. Geophys Res Lett 37:L16101. doi:10.1029/2010GL044219

Hau L-N, Sonnerup BUÖ (1999) Two-dimensional coherent structures in the magnetopause: recovery of static equilibria from single-spacecraft data. J Geophys Res 104:6899–6917

Hu Q, Sonnerup BUÖ (2003) Reconstruction of two-dimensional structures in the magnetopause: method improvements. J Geophys Res 108(A1):1011. doi:10.1029/2002JA009323

Johnson JR, Cheng CZ (1997) Kinetic Alfvén waves and plasma transport at the magnetopause. Geophys Res Lett 24(11):1423–1426

Johnson JR, Cheng CZ (2001) Stochastic ion heating at the magnetopause due to kinetic Alfvén waves. Geophys Res Lett 28(23):4421–4424

Karimabadi H, Sipes TB, Wang Y, Lavraud B, Roberts A (2009) A new multivariate time series data analysis technique: automated detection of flux transfer events using cluster data. J Geophys Res 114:A06216. doi:10.1029/2009JA014202

Kawano H, Kokubun S, Yamamoto T, Tsuruda K, Hayakawa H, Nakamura M, Okada T, Matsuoka A, Nishida A (1994) Magnetopause characteristics during a four-hour interval of multiple crossings observed with GEOTAIL. Geophys Res Lett 21(25):2895–2898

Kessel RL, Chen S-H, Green JL et al (1996) Evidence of high-latitude reconnection during northward IMF: Hawkeye observations. Geophys Res Lett 23(5):583–586

Kivelson MG, Chen S-H (1995) The magnetopause: surface waves and instabilities and their possible dynamical consequences. In: Song P, Sonnerup BUÖ, Thomsen MF (eds) Physics of the magnetopause. Geophysical monograph, vol 90. American Geophysical Union, Washington, DC, p 257

Lavraud B, Borovsky JE (2008) Altered solar wind-magnetosphere interaction at low Mach numbers: coronal mass ejections. J Geophys Res 113:A00B08. doi:10.1029/2008JA013192

Lavraud B, Phan TD, Dunlop MW, Taylor MGGT, Cargill PJ, Bosqued J-M, Dandouras I, Rème H, Sauvaud J-A, Escoubet CP, Balogh A, Fazakerley A (2004) The exterior cusp and its boundary with the magnetosheath under northward IMF: cluster multi-event analysis. Ann Geophys 22(8):3039–3054

Lavraud B, Fedorov A, Budnik E, Thomsen MF, Grigoriev A, Cargill PJ, Dunlop MW, Rème H, Dandouras I, Balogh A (2005a) High-altitude cusp flows dependence on IMF orientation: a three-year cluster statistical study. J Geophys Res 110:A02209. doi:10.1029/2004JA010804

Lavraud B, Thomsen MF, Taylor MGGT, Wang YL, Phan TD, Schwartz SJ, Elphic RC, Fazakerley A, Rème H, Balogh A (2005b) Characteristics of the magnetosheath electron boundary layer under northward interplanetary magnetic field: implications for high-latitude reconnection. J Geophys Res 110:A06209. doi:10.1029/2004JA010808

Lavraud B, Thomsen MF, Lefebvre B, Schwartz SJ, Seki K, Phan TD, Wang YL, Fazakerley A, Rème H, Balogh A (2006) Evidence for newly closed magnetosheath field lines at the dayside magnetopause under northward IMF. J Geophys Res 111:A05211. doi:10.1029/2005JA011266

Lavraud B et al (2009) Tracing solar wind plasma entry into the magnetosphere using ion-to-electron temperature ratio. Geophys Res Lett 36:L18109. doi:10.1029/2009GL039442

Le G, Russell CT, Gosling JT, Thomsen MF (1996) ISEE observations of low-latitude boundary layer for northward interplanetary magnetic field: Implications for cusp reconnection. J Geophys Res 101(A12):27239–27249

Le G et al (2008) Flux transfer events simultaneously observed by Polar and Cluster: flux rope in the subsolar region and flux tube addition to the polar cusp. J Geophys Res 113:A01205. doi:10.1029/2007JA012377

Lee LC, Johnson JR, Ma ZW (1994) Kinetic Alfvén waves as a source of plasma transport at the dayside magnetopause. J Geophys Res 99(A9):17405–17411

Lemaire J, Roth M (1978) Penetration of solar wind plasma elements into the magnetosphere. J Atmos Sol Terr Phys 40:331

Levy RH, Petschek HE, Siscoe GL (1964) Aerodynamic aspects of the magnetospheric flow. AIAA J 2:2065

Li WH, Raeder J, Dorelli J et al (2005) Plasma sheet formation during long period of northward IMF, Geophys Res Lett 32(12):L12S08, doi:10.1029/2004GL021524

Li W, Raeder J, Thomsen MF, Lavraud B (2008) Solar wind plasma entry into the magnetosphere under northward IMF conditions. J Geophys Res 113:A04204. doi:10.1029/2007JA012604

Li W, Raeder J, Øieroset M, Phan TD (2009) Cold dense magnetopause boundary layer under northward IMF: results from THEMIS and MHD simulations. J Geophys Res 114:A00C15. doi:10.1029/2008JA013497

Liu J, Angelopoulos V, Sibeck D, Phan T, Pu ZY, McFadden J, Glassmeier KH, Auster HU (2008) THEMIS observations of the dayside traveling compression region and flows surrounding flux transfer events. Geophys Res Lett 35:L17S07. doi:10.1029/2008GL033673

Lockwood M, Smith MF (1992) The variation of reconnection rate at the dayside magnetopause and cusp ion precipitation, J Geophys Res 97:14841

Lockwood M et al (2001) Coordinated Cluster and ground-based instrument observations of transient changes in the magnetopause boundary layer during an interval of predominantly northward IMF: relation to reconnection pulses and FTE signatures. Ann Geophys 19:1613–1640

Lockwood M, Lanchester BS, Frey HU, Throp K, Morley SK, Milan SE, Lester M (2003) IMF control of cusp proton emission intensity and dayside convection: implications for component and anti-parallel reconnection. Ann Geophys 21:955–982

Lopez RE, Wiltberger M, Hernandez S, Lyon JG (2004) Solar wind density control of energy transfer to the magnetosphere. Geophys Res Lett 31:L08804. doi:10.1029/2003GL018780

Luhmann JR, Walker RJ, Russell CT, Crooker NU, Speiter JR, Stahara SS (1984) Patterns of potential magnetic field merging sites on the dayside magnetopause. J Geophys Res 89:1739–1742

Lui ATY (2001) Current controversies in magnetospheric physics. Rev Geophys 39:535

Lui ATY et al (2008) Reconstruction of a magnetic flux rope from THEMIS observations. Geophys Res Lett 35:L17S05. doi:10.1029/2007GL032933

Lundin R (1997) Observational and theoretical aspects of processes other than merging and diffusion governing plasma transport across the magnetopause. Space Sci Rev 80 (1–2):269–304

Lundin R, Sauvaud J-A, Rème H, Balogh A, Dandouras I, Bosqued JM, Carlson C, Parks GK, Moebius E, Kistler LM, Klecker B, Amata E, Formisano V, Dunlop MW, Eliasson L, Korth A, Lavraud B, McCarthy M (2003) Evidence for impulsive solar wind plasma penetration through the dayside magnetopause. Ann Geophys 21(2):457–472

Matsumoto Y, Hoshino M (2006) Turbulent mixing and transport of collsionless plasmas across a stratified velocity shear layer. J Geophys Res 111:A05213. doi:10.1029/2004JA010988

Matsumoto Y, Seki K (2007) The secondary instability initiated by the three-dimensional nonlinear evolution of the Kelvin-Helmholtz instability. J Geophys Res 112:A06223. doi:10.1029/2006JA012114

McFadden JP, Carlson CW, Larson D, Bonnell J, Mozer FS, Angelopoulos V, Glassmeier K-H, Auster U (2008) Structure of plasmaspheric plumes and their participation in magnetopause reconnection: first results from THEMIS. Geophys Res Lett 35:L17S10. doi:10.1029/2008GL033677

Milan SE, Lester M, Greenwald RA, Sofko G (1999) The ionospheric signature of transient dayside reconnection and the associated pulsed convection return flow. Ann Geophys 17:1166–1171

Min KW, Kim T, Lee H (1997) Effects of magnetic reconnection in the Kelvin-Helmholtz instability at the magnetospheric boundary. Planet Space Sci 45(4):495–510

Mishin VV (1993) Accelerated motions of the magnetopause as a trigger of the Kelvin-Helmholtz instability. J Geophys Res 98(A12):21365–21371

Miura A (1984) Anomalous transport by magnetohydrodynamic Kelvin-Helmholtz instabilities in the solar wind-magnetosphere interaction. J Geophys Res 89:818

Miura A (1995a) Kelvin-Helmholtz instability at the magnetopause: computer simulations. In: Song P, Sonnerup BUÖ, Thomsen MF (eds) Physics of the magnetopause. Geophysical monograph, vol 90. American Geophysical Union, Washington, DC, p 285

Miura A (1995b) Dependence of the magnetopause Kelvin-Helmholtz instability on the orientation of the magnetosheath magnetic field. Geophys Res Lett 22(21):2993–2996

Moore TE, Fok M-C, Chandler MO (2002) The dayside reconnection X line. J Geophys Res 107(A10):1332. doi:10.1029/2002JA009381

Moore TE et al (2005) Plasma sheet and ring current formation from solar and polar wind sources. J Geophys Res 110:A02210. doi:10.1029/2004JA010563

Moore TE, Fok M-C, Delcourt DC, Slinker SP, Fedder JA (2007) Global aspects of solar wind–ionosphere interactions. J Atmos Sol Terr Phys 69:265. doi:10.1016/j.jastp.2006.08.009

Moore TE, Fok M-C, Delcourt DC, Slinker SP, Fedder JA (2008) Plasma plume circulation and impact in an MHD substorm. J Geophys Res 113:A06219. doi:10.1029/2008JA013050

Mozer FS, Retinò A (2007) Quantitative estimates of magnetic field reconnection properties from electric and magnetic field measurements. J Geophys Res 112:A10206. doi:10.1029/2007JA012406

Mozer FS, Pritchett PL (2009) Regions associated with electron physics in asymmetric magnetic field reconnection. Geophys Res Lett 36:L07102. doi:10.1029/2009GL037463

Mozer FS, Hayakawa H, Kokubun S, Nakamura M, Okada T, Yamamoto T, Tsuruda K (1994) The morningside low-latitude boundary layer as determined from electric and magnetic field measurements on Geotail. Geophys Res Lett 21(25):2983–2986

Mozer FS, Angelopoulos V, Bonnell J, Glassmeier KH, McFadden JP (2008) THEMIS observations of modified Hall fields in asymmetric magnetic field reconnection. Geophys Res Lett 35:L17S04. doi:10.1029/2007GL033033

Nagai T, Shinohara I, Fujimoto M, Hoshino M, Saito Y, Machida S, Mukai T (2001) Geotail observations of the Hall current system: evidence of magnetic reconnection in the magnetotail. J Geophys Res 106(A11):25929–25949

Nakamura T, Fujimoto M (2005) Magnetic reconnection within rolled-up MHD-scale Kelvin-Helmholtz vortices: two-fluid simulations including finite electron inertial effects. Geophys Res Lett 32:L21102. doi:10.1029/2005GL023362

Newell PT, Onsager TG (2003) Earth's low-latitude boundary layer. Geophysical monograph series, vol 133

Newell PT, Sotirelis T, Liou K, Meng C-I, Rich FJ (2007) A nearly universal solar wind-magnetosphere coupling function inferred from 10 magnetospheric state variables. J Geophys Res 112:A01206. doi:10.1029/2006JA012015

Newell PT, Sotirelis T, Liou K, Rich FJ (2008) Pairs of solar wind-magnetosphere coupling functions: combining a merging term with a viscous term works best. J Geophys Res 113:A04218. doi:10.1029/2007JA012825

Nishino MN, Fujimoto M, Terasawa T, Ueno G, Mukai T, Saito Y (2007a) Origin of temperature anisotropies in the cold plasma sheet: geotail observations around the Kelvin-Helmholtz votices. Ann Geophys 25:2069–2086

Nishino MN, Fujimoto M, Terasawa T, Ueno G, Maezawa K, Mukai T, Saito Y (2007b) Geotail observations of temperature anisotropy of the two-component protons in the dusk plasma sheet. Ann Geophys 25:769–777

Nishino MN, Fujimoto M, Terasawa T, Ueno G, Maezawa K, Mukai T, Saito Y (2007c) Temperature anisotropies of electrons and two-component protons in the dusk plasma sheet. Ann Geophys 25:71417–71432

Nykyri K, Otto A (2001) Plasma transport at the magnetospheric boundary due to reconnection in Kelvin-Helmholtz vortices. Geophys Res Lett 28(18):3565–3568

Nykyri K, Otto A, Lavraud B, Mouikis C, Kistler LM, Balogh A, Rème H (2006) Cluster observations of reconnection due to the Kelvin-Helmholtz instability at the dawnside magnetospheric flank. Ann Geophys 24(10):2619–2643

Ogino T, Walker RJ, Ashour-abdalla M (1994) A global magnetohydrodynamic simulation of the response of the magnetosphere to a northward turning of the interplanetary magnetic field. J Geophys Res 99(A6):11027–11042

Øieroset M, Phan TD, Fujimoto M, Lin RP, Lepping RP (2001) In situ detection of collisionless reconnection in Earth's magnetotail. Nature 412:414–417

Øieroset M, Raeder J, Phan TD et al (2005) Global cooling and densification of the plasma sheet during an extended period of purely northward IMF on October 22–24, 2003. Geophys Res Lett 32(12):L12S07. doi:10.1029/2004GL021523

Øieroset M, Phan TD, Angelopoulos V, Eastwood JP, McFadden J, Larson D, Carlson CW, Glassmeier K-H, Fujimoto M, Raeder J (2008) THEMIS multi-spacecraft observations of magnetosheath plasma penetration deep into the dayside low-latitude magnetosphere for northward and strong by IMF. Geophys Res Lett 35:L17S11. doi:10.1029/2008GL033661

Onsager TG et al (1991) Model of electron and ion distributions in the plasma sheet boundary layer. J Geophys Res 96:20999

Onsager TG, Scudder JD, Lockwood M, Russell CT (2001) Reconnection at the high latitude magnetopause during northward interplanetary magnetic field conditions. J Geophys Res 106(A11):25,467– 25,488

Otto A, Fairfield DH (2000) Kelvin-Helmholtz instability at the magnetotail boundary: MHD simulation and comparison with Geotail observations. J Geophys Res 105(A9):21175–21190

Owen CJ, Fazakerley AN, Carter PJ, Coates AJ, Krauklis IC, Szita S, Taylor MGGT, Travnicek P, Watson G, Wilson RJ, Balogh A, Dunlop MW (2001) CLUSTER PEACE observations of electrons during magnetosheric flux transfer events. Ann Geophys 19:1509–1522

Owen CJ, Taylor MGGT, Krauklis IC, Fazakerley AN, Dunlop MW, Bosqued JM (2004) Cluster observations of surface waves on the dawn flank magnetopause. Ann Geophys 22:971–983

Parker EN (1963) The solar flare phenomenon and the theory of reconnection and annihilation of magnetic fields. Astrophys J Suppl Ser 8:177

Paschmann G (1997) Observational evidence for transfer of plasma across the magnetopause. Space Sci Rev 80 (1–2):217–234

Paschmann G (2008) Recent in-situ observations of magnetic reconnection in near-Earth space. Geophys Res Lett 35:L19109. doi:10.1029/2008GL035297

Paschmann G, Sonnerup BUÖ, Papamastorakis I, Sckopke N, Haerendel G, Bame SJ, Asbridge JR, Gosling JT, Russell CT, Elphic RC (1979) Plasma acceleration at the Earth's magnetopause: evidence for magnetic reconnection. Nature 282:243

Penz T, Farrugia CJ, Ivanov VV, Ivanova VV, Semenov VS, Semenov VS, Biernat HK, Torbert R (2008) Two-spacecraft observations of reconnection at the magnetopause: model results and data comparison. Adv Space Res 41(10): 1551–1555

Perreault P, Akasofu S-I (1978) A study of geomagnetic storms. Geophys JR Astron Soc 54:547–573

Petschek HE (1964) Magnetic field annihilation. In: Proceedings of AAS-NASA Symposium on Physics of Solar Flares, NASA Special Publication, SP-50, p 425

Phan T-D, Paschmann G, Baumjohann W, Sckopke N, Lühr H (1994) The magnetosheath region adjacent to the dayside magnetopause: AMPTE/IRM observations. J Geophys Res 99(A1):121–141

Phan TD, Sonnerup BUÖ, Lin RP (2001) Fluid and kinetics signatures of reconnection at the dawn tail magnetopause: wind observations. J Geophys Res 106:25489

Phan T, Frey HU, Frey S, Peticolas L, Fuselier S, Carlson C, Rème H, Bosqued J-M, Balogh A, Dunlop M, Kistler L, Mouikis C, Dandouras I, Sauvaud J-A, Mende S, J McFadden, Parks G, Moebius E, Klecker B, Paschmann G, Fujimoto M, Petrinec S, Marcucci MF, Korth A, Lundin R (2003) Simultaneous cluster and IMAGE observations of cusp reconnection and auroral proton spot for northward IMF. Geophys Res Lett 30:1509. doi:10.1029/2003GL016885

Phan TD, Dunlop MW, Paschmann G, Klecker B, Bosqued JM, Rème H, Balogh A, Twitty C, Mozer FS, Carlson CW, Mouikis C, Kistler LM (2004) Cluster observations of continuous reconnection at the magnetopause under steady interplanetary magnetic field conditions. Ann Geophys 22:2355–2367

Phan TD, Escoubet CP, Rezeau L, Treumann RA, Vaivads A, Paschmann G, Fuselier SA, Attié D, Rogers B, Sonnerup BUÖ (2005) Magnetopause processes. Space Sci Rev 118(1–4):367–424

Phan TD et al (2006) A magnetic x-line extending more than 390 Earth radii in the solar wind. Nature 439:175

Pitout F, Newell PT, Buchert SC (2002) Simultaneous high- and low-latitude reconnection: ESR and DMSP observations. Ann Geophys 20(9):1311–1320

Priest ER, Forbes TG (1992) Does fast magnetic reconnection exist? J Geophys Res 97:16757–16772

Provan G, Yeoman TK (1999) Statistical observations of the MLT, latitude and size of pulsed ionospheric flows with the CUTLASS Finland radar. Ann Geophys 17:855–867

Pu Z, Yei M, Liu Z (1990) Generation of vortex-induced tearing mode instability at the magnetopause. J Geophys Res 95(A7):10559–10566

Pu ZY et al (2007) Global view of dayside magnetic reconnection with the dusk-dawn IMF orientation: a statistical study for Double Star and Cluster data. Geophys Res Lett 34:L20101. doi:10.1029/2007GL030336

Raeder J (2006) Flux transfer events: 1. Generation mechanism for strong southward IMF. Ann Geophys 24:381–392

Raeder J, Berchem J, Ashour-Abdalla M et al (1997) Boundary layer formation in the magnetotail: geotail observations and comparisons with a global MHD simulation. Geophys Res Lett 24(8):951–954

Rijnbeek RP, Cowley SWH, Southwood DJ, Russell CT (1984) A survey of dayside flux transfer events observed by Isee 1 and 2 magnetometers. J Geophys Res 89(A2): 786–800

Rosenqvist L, Vaivads A, Retino A, Phan T, Opgenoorth HJ, Dandouras I, Buchert S (2008) Modulated reconnection rate and energy conversion at the magnetopause under steady IMF conditions. Geophys Res Lett 35:L08104. doi:10.1029/2007GL032868

Roth M (1992) On impulsive penetration of solar wind plasmoids into the geomagnetic field. Planet Space Sci 40:193

Russell CT, Elphic RC (1978) Initial ISEE magnetometer results: magnetopause observations. Space Sci Rev 22:681–715

Safrankova J, Nemecek Z, Sibeck DG, Prech L, Merka J, Santolik O (1998) Two-point observation of high-latitude reconnection. Geophys Res Lett 25:4301–4304

Safrankova J, Nemecek Z, Prech L, Simunek J, Sibeck D, Sauvaud J-A (2007) Variations of the flank LLBL thickness as response to the solar wind dynamic pressure and IMF orientation. J Geophys Res 112:A07201. doi:10.1029/2006JA011889

Sandholt PE, Deehr CS, Egeland A et al (1986) Signatures in the dayside aurora of plasma transfer from the magnetosheath. J Geophys Res 91:10063

Sandholt PE, Farrugia CJ, Cowley SWH, Denig WF (1999) Capture of magnetosheath plasma by the magnetosphere during northward IMF. Geophys Res Lett 26:2833

Sauvaud J-A et al (2001) Intermittent thermal plasma acceleration linked to sporadic motions of the magnetopause, first Cluster results. Ann Geophys 19:1523

Scholer M (1995) Models of flux transfer events. In: Song P, Sonnerup BUÖ, Thomsen MF (eds) Physics of the magnetopause. Geophysical monograph series, vol 90. AGU, Washington, DC, pp 235–245

Scholer M, Treumann RA (1997) The low latitude boundary layer at the flanks of the magnetopause. Space Sci Rev 80(1–2):341–367

Scurry L, Russell CT (1991) Proxy studies of energy transfer to the magnetosphere. J Geophys Res 96(A6):9541–9548

Sharp DH (1984) An overview of Rayleigh-Taylor instability. Physica D 12(1–3):3–18

Shi QQ, Shen C, Pu ZY, Dunlop MW, Zong Q-G, Zhang H, Xiao CJ, Liu ZX, Balogh A (2005) Dimensional analysis of observed structures using multipoint magnetic field measurements: application to Cluster. Geophys Res Lett 32:L12105. doi:10.1029/2005GL022454

Sibeck DG (2009) Concerning the occurrence pattern of flux transfer events on the dayside magnetopause. Ann Geophys 27(2):895–903

Sibeck DG, Lin RQ (2010) Concerning the motion of flux transfer events generated by component reconnection across the dayside magnetopause. J Geophys Res 115:A04209. doi:10.1029/2009JA014677

Sibeck DG et al (1999) Chapter 5: plasma transfer processes at the magnetopause. Space Sci Rev 88(1–2):207–283

Sibeck DG et al (2008) Crater FTEs: simulation results and THEMIS observations. Geophys Res Lett 35:L17S06. doi:10.1029/2008GL033568

Siscoe G, Crooker N (1974) A theoretical relation between Dst and the solar wind merging electric field. Geophys Res Lett 1(1):17–19

Smets R, Belmont G, Delcourt D, Rezeau L (2007) Diffusion at the Earth magnetopause: enhancement by Kelvin-Helmholtz instability. Ann Geophys 25:271–282

Song P, Russell CT (1992) Model of the formation of the low-latitude boundary layer for strongly northward interplanetary magnetic field. J Geophys Res 97(A2):1411–1420

Song P, Sonnerup BUÖ, Thomsen MF (1995) Physics of the magnetopause. Geophysical monograph series, vol 90

Sonnerup BUÖ (1974) The reconnecting magnetopause. In: McCormac BM, Reidel D (eds) Magnetospheric physics. Norwell, MA, p 23

Sonnerup BUÖ, Cahill LJ (1967) Magnetopause structure and attitude from Explorer 12 observations. J Geophys Res 72:171

Sonnerup BUÖ, Guo M (1996) Magnetopause transects. Geophys Res Lett 23:3679–3682

Sonnerup BUÖ, Scheible M (1998) Minimum and maximum variance analysis. In: Multi-spacecraft analysis methods, Int. Space Sci. Inst. Scientific Report Book, p 185

Sonnerup BUÖ, Hasegawa H (2005) Orientation and motion of two-dimensional structures in a space plasma. J Geophys Res 110:A06208. doi:10.1029/2004JA010853

Sonnerup BUÖ, Paschmann G, Papamastorakis I, Sckopke N, Haerendel G, Bame SJ, Asbridge JR, Gosling JT, Russell CT (1981) Evidence for magnetic field reconnection at the Earth's magnetopause. J Geophys Res 86(15):10049–10067

Sonnerup BUÖ, Papamastorakis I, Paschmann G, Luehr H (1987) Magnetopause properties from AMPTE/IRM observations of the convection electric field – method development. J Geophys Res 92:12137

Sonnerup BUÖ, Paschmann G, Phan T-D (1995) Fluid aspects of reconnection at the magnetopause: in situ observations. In: Song P, Sonnerup BUÖ, Thomsen MF (eds) Physics of the magnetopause. Geophysical monograph series, vol 90. AGU, Washington, DC, pp 167–180

Sonnerup BUÖ, Hasegawa H, Paschmann G (2004) Anatomy of a flux transfer event seen by Cluster. Geophys Res Lett 31:L11803. doi:10.1029/2004GL020134

Sonnerup BUÖ, Hasegawa H, Teh W-L, Hau L-N (2006) Grad-Shafranov reconstruction: an overview. J Geophys Res 111:A09204. doi:10.1029/2006JA011717

Southwood DJ (1968) The hydrodynamic stability of the magnetospheric boundary. Planet Space Sci 16:587

Southwood DJ (1979) Magnetopause Kelvin-Helmholtz instability. In: Proceedings of magnetospheric boundary layers conference, ESA SP-148, pp 357–364

Spreiter JR, Summers AL, Alksne AY (1966) Hydromagnetic flow around the magnetosphere. Planet Space Sci 14(3):223–253

Su YJ, Borovsky JE, Thomsen MF, Elphic RC, McComas DJ (2000) Plasmaspheric material at the reconnecting magnetopause. J Geophys Res 105:7591

Sweet PA (1958) The neutral point theory of solar flares. IAU Symp 6:123

Swisdak M, Drake JF (2007) Orientation of the reconnection X-line. Geophys Res Lett 34:L11106. doi:10.1029/2007GL029815

Taylor MGGT, Lavraud B (2008) Observation of three distinct ion populations at the Kelvin-Helmholtz-unstable magnetopause. Ann Geophys 26(6):1559–1566

Taylor MGGT et al (2008) The plasma sheet and boundary layers under northward IMF: a multi-point and multi-instrument perspective. Adv Space Res 41(10):1619–1629

Terasawa T, Fujimoto M, Mukai T, Shinohara I, Saito Y, Yamamoto T, Machida S, Kokubun S, Lazarus AJ, Steinberg JT, Lepping RP (1997) Solar wind control of density and temperature in the near-Earth plasma sheet: WIND/GEOTAIL collaboration. Geophys Res Lett 24:935

Thomas VA, Winske D (1993) Kinetic simulations of the Kelvin-Helmholtz instability at the magnetopause. J Geophys Res 98:11425

Trattner KJ, Fuselier SA, Peterson WK, Sauvaud JA, Stenuit H, Dubouloz N, Kovrazhkin RA (1999) On spatial and temporal structures in the cusp. J Geophys Res 104:28411

Trattner KJ, Fuselier SA, Peterson WK, Boehm M, Klumpar D, Carlson CW, Yeoman TK (2002) Temporal versus spatial interpretation of cusp ion structures observed by two spacecraft. J Geophys Res 107(A10):1287. doi:10.1029/2001JA000181

Trattner KJ, Fuselier SA, Yeoman TK, Korth A, Fraenz M, Mouikis C, Kucharek H, Kistler LM, Escoubet CP, Rème H, Dandouras I, Sauvaud JA, Bosqued JM, Klecker B, Carlson C, Phan T, McFadden JP, Amata E, Eliasson L (2003) Cusp structures: combining multi-spacecraft observations with ground-based observations. Ann Geophys 21: 2031–2041

Trattner KJ, Mulcock JS, Petrinec SM, Fuselier SA (2007a) Location of the reconnection line at the magnetopause during southward IMF conditions. Geophys Res Lett 34:L03108. doi:10.1029/2006GL028397

Trattner KJ, Mulcock JS, Petrinec SM, Fuselier SA (2007b) Probing the boundary between antiparallel and component reconnection during southward interplanetary magnetic field conditions. J Geophys Res 112:A08210. doi:10.1029/2007JA012270

Trenchi L, Marcucci MF, Pallocchia G, Consolini G, Bavassano Cattaneo MB, Di Lellis AM, Rème H, Kistler L, Carr CM, Cao JB (2008) Occurrence of reconnection jets at the dayside magnetopause: double Star observations. J Geophys Res 113:A07S10. doi:10.1029/2007JA012774

Treumann RA (1997) Theory of super-diffusion for the magnetopause. Geophys Res Lett 24:727

Vaivads A et al (2004) Structure of the magnetic reconnection diffusion region from four-spacecraft observations. Phys Rev Lett 93:105001. doi:10.1103/PhysRevLett.93.105001

Vaivads A, Retinò A, André M (2006) Microphysics of magnetic reconnection. Space Sci Rev 122:19–27. doi:10.1007/s11214-006-7019-3

Wang YL, Elphic RC, Lavraud B, Taylor MGGT, Birn J, Raeder J, Russell CT, Kawano H, Zong Q-G, Zhang H, Zhang XX, Friedel RH (2005) Initial results of high-latitude magnetopause and low-latitude flank flux transfer events from three years of Cluster observations. J Geophys Res 110(A11):A11221. doi:10.1029/2005JA011150

Wang YL, Elphic RC, Lavraud B, Taylor MGGT, Birn J, Russell CT, Raeder J, Kawano H, Zhang XX (2006) The dependence of flux transfer events on solar wind conditions from three years of Cluster observations. J Geophys Res 111(A4):A04224. doi:10.1029/2005JA011342

Wendel DE, Reiff PH (2009) Magnetopause reconnection impact parameters from multiple spacecraft magnetic field measurements. Geophys Res Lett 36:L20108. doi:10.1029/2009GL040228

Wild JA et al (2001) First simultaneous observations of flux transfer events at the high-latitude magnetopause by the Cluster spacecraft and pulsed radar signatures in the conjugate ionosphere by the CUTLASS and EISCAT radars. Ann Geophys 19:1491

Wing S, Johnson JR, Fujimoto M (2006) Timescale for the formation of the cold-dense plasma sheet: a case study. Geophys Res Lett 33(23):L23106

Wygant JR et al (2005) Cluster observations of an intense normal component of the electric field at a thin reconnecting current sheet in the tail and its role in the shock-like acceleration of the ion fluid into the separatrix region. J Geophys Res 110:A09206. doi:10.1029/2004JA010708

Zhang H, Khurana KK, Kivelson MG, Angelopoulos V, Pu ZY, Zong Q-G, Liu J, Zhou X-Z (2008) Modeling a force-free flux transfer event probed by multiple Time History of Events and Macroscale Interactions during Substorms (THEMIS) spacecraft. J Geophys Res 113:A00C05. doi:10.1029/2008JA013451

Zheng Y, Le G, Slavin JA, Goldstein ML, Cattell C, Balogh A, Lucek EA, Rème H, Eastwood JP, Wilber M, Parks G, Retino A, Fazakerley A (2005) Cluster observation of continuous reconnection at dayside magnetopause in the vicinity of cusp. Ann Geophys 23:2199–2215

Zhou X-Z, Zong Q-G, Pu ZY, Fritz TA, Dunlop MW, Shi QQ, Wang J, Wei Y (2006) Multiple Triangulation Analysis: another approach to determine the orientation of magnetic flux ropes. Ann Geophys 24:1759–1765

Zhou X-Z, Pu ZY, Zong Q-G, Xie L (2007) Energy filter effect for solar wind particle entry to the plasma sheet via flank regions during southward interplanetary magnetic field. J Geophys Res 112:A06233. doi:10.1029/2006JA012180

Zwan BJ, Wolf RA (1976) Depletion of solar wind plasma near a planetary boundary. J Geophys Res 81(10):1636–1648

Quantifying Energy Transfer at the Magnetopause

2

M. Palmroth, H.E.J. Koskinen, T.I. Pulkkinen, C.R. Anekallu, T.V. Laitinen, E.A. Lucek, and I. Dandouras

Abstract

We review recently developed methods to investigate energy circulation in the near-Earth space using a global magnetohydrodynamic (MHD) simulation GUMICS-4. We describe methods to evaluate the magnetopause energy transfer and ways to quantify effects of the reconnection dynamics. We also present evidence, supported by Cluster spacecraft observations, showing that the interplanetary magnetic field (IMF) *y* component controls the spatial variation of the magnetopause energy transfer. The simulation results also suggests that the energy transfer exhibits a "hysteresis" effect where the energy transfer does not decrease immediately after the driving conditions start to become weaker. We investigate the hysteresis effect in the simulation and conclude that the previous driving conditions as well as the present state of the global magnetosphere may influence the processes at the magnetopause, and thus regulate the energy input to the system.

2.1 Introduction

The magnetospheric activity and dynamics require power that is extracted in the interaction between the magnetosphere and the solar wind. The dominant energy transfer depends on reconnection determined by the interplanetary magnetic field (IMF) (Dungey 1961). The energy circulation from the solar wind, through the magnetosphere, and into the ionosphere is one of the most fundamental questions in space physics, and it has been targeted by international research frameworks such as ISTP (International Solar Terrestrial Physics Program), and more recently ILWS (International Living With a Star). Large computer simulation programs have been set up to resolve the chain of events from the Sun to the ionosphere (e.g., CISM: Center for Integrated Space Weather Modeling http://www.bu.edu/cism, or CSEM: Center for Space Environment Modeling http://csem.engin.umich.edu). In addition, there are several groups running global magnetohydrodynamic (MHD) simulations of the terrestrial space environment.

Global energy transfer has been assessed by correlation analyses of solar wind parameters and magnetic activity indices (Akasofu 1981; Koskinen 2002; Newell et al. 2007) as well as dimensional analyses (Vasyliunas et al. 1982). The energy transfer proxies typically include the solar wind speed, IMF magnitude, IMF clock angle orientation with respect to the north (θ), and sometimes the solar wind density (Newell et al. 2007). Perhaps the most widely known

M. Palmroth (✉)
Finnish Meteorological Institute, Helsinki, Finland
e-mail: minna.palmroth@fmi.fi

W. Liu, M. Fujimoto (eds.), *The Dynamic Magnetosphere*, IAGA Special Sopron Book Series 3,
DOI 10.1007/978-94-007-0501-2_2,

proxy for energy transfer is the ε parameter (Akasofu 1981), resembling electromagnetic energy flux incident at an area upstream of the Earth. As the solar wind kinetic energy flux density exceeds the electromagnetic energy flux density by an order of magnitude, a generator mechanism has been presented (Lundin and Evans 1985) to convert the solar wind flow energy to empower the magnetospheric dynamics during southward IMF: After a field line has been reconnected near the subsolar point, it evolves across the magnetopause and energy is transferred from the magnetic field to the plasma, or vice versa. Sunward of the cusp, the energy is transferred to the plasma by magnetic reconnection (a load in the system). Tailward of the cusp energy is extracted from the motion of the magnetosheath plasma and converted to magnetic energy. The tail magnetopause is hence a dynamo.

While the proxies characterizing the energy input to the magnetosphere depend on solar wind and IMF without a delay, some magnetospheric magnetic field models driven by the solar wind input take into account the time history of the solar wind (Tsyganenko 2002a, b). Bargatze et al. (1985) established using impulse response functions that the ionospheric response exhibits at least a 20-min delay with respect to the driver. The development of the field-aligned current system coupling the magnetosphere and ionosphere takes at least 15 min (Vennerstrøm et al. 2002). Global MHD simulations have shown that the ionospheric reconfiguration time after a sudden change in the IMF depends on the strength of the IMF and the solar wind speed (Kabin et al. 2003). The dense inertial ionosphere can even maintain the magnetospheric convection by a "fly-wheel" effect (Lyons et al. 1985). The plasma sheet and the ring current are large contributors to delays in the magnetospheric system: The plasma sheet mass loading during northward IMF (leading to cold and dense plasma sheet) and the ring current build-up and decay can take days.

Global MHD simulations have proved to be a useful tool in investigations of energy circulation in the near-Earth space. The energy transfer between the solar wind and the magnetosphere, and the energy conversion processes within the magnetopause current layer and the tail reconnection region have been quantified from the simulation output (Palmroth et al. 2003; Laitinen et al. 2006, 2009). The energy dissipation to the ionosphere has also been investigated, and the simulations are in agreement with several observation-based assessments, especially with regard to temporal evolution (Slinker et al. 1999; Palmroth et al. 2005, 2006a). Recently, Cluster observations were used to evaluate the magnetopause dynamo power (Rosenqvist et al. 2006, 2008), and the results were found to agree with a global MHD simulation. Hence, there is ample evidence that the MHD simulations can be used to quantify energy circulation in space plasmas.

In this chapter we review the recent techniques developed to investigate the global energy circulation. We also present new results utilizing the observation-based technique presented in (Rosenqvist et al. 2006), and discuss the results in light of global picture from the MHD simulations. Finally, we concentrate on a "hysteresis" effect, where the energy input at the magnetopause stays enhanced after strong driving, even though the driving conditions start to decrease. While the effect is found from an MHD simulation, we discuss its possible reality within the space physics framework. The chapter is organized as follows: First, we present our global MHD simulation after which we review the developed methods and the new results. Finally, we end the chapter with discussion and conclusions.

2.2 Methodology

2.2.1 GUMICS-4 Simulation

GUMICS-4 (Grand Unified Magnetosphere Ionosphere Coupling Simulation) is the latest revision in a sequence of global MHD simulations developed at the Finnish Meteorological Institute (Janhunen 1996; Palmroth et al. 2001). The code consists of two computational domains: The MHD domain includes the solar wind and the magnetosphere and the electrostatic domain includes the ionosphere. The conservative MHD equations are solved in a simulation box extending from 32 R_E to –224 R_E in the x_{GSE} direction and ±64 R_E in y_{GSE} and z_{GSE}. Near the Earth the MHD simulation box reaches a spherical shell with a radius of 3.7 R_E, which maps along the dipole field to approximately 60° in magnetic latitude. The grid in the MHD domain is a Cartesian cell-by-cell adaptive octogrid. Solar wind density, temperature, velocity and magnetic field are treated as boundary conditions along the sunward wall of the

simulation box; outflow conditions are applied on the other walls of the simulation box. The primary magnetospheric output parameters are plasma density, pressure, velocity, temperature, and magnetic field in space and time. The magnetosphere provides the ionosphere with field-aligned currents and electron precipitation, which are used to solve the ionospheric potential, which then is mapped back to the magnetosphere and used there as a boundary condition. The ionospheric output parameters include the electric field, height-integrated Pedersen and Hall conductivities, ionospheric electric potential, particle precipitation power, Joule heating rate and field-aligned current density in space and time.

2.2.2 Magnetopause Energy Transfer

Palmroth et al. (2003) evaluated the energy transfer rate from the solar wind into the magnetosphere using the GUMICS-4 simulation. First, the magnetopause boundary was identified from each file generated by GUMICS-4 by finding the cavity encompassed by the solar wind streamlines. The streamline surface was found to coincide with the spatial gradients existing at the magnetopause; however, it is smoother than a surface based on plasma or current density characteristics. The total energy perpendicular to the magnetopause boundary was defined as the portion of energy entering the magnetopause.

Figure 2.1a shows the total energy transfer across the magnetopause and scaled $\sin^2(\theta/2)$ function in a simulation run where the IMF magnitude and other solar wind parameters were kept constant but the clock angle θ was rotated from 0° to 360° in 6 h. The run is one of four runs originally presented in (Palmroth et al. 2006b). Figure 2.1b–d present the instantaneous distributions of energy transfer, integrated from the nose of the magnetopause to –30 R_E in the tail. Each sector shows the sum of transferred energy taking place in the angular direction shown in the outer circle, viewing from the Sun looking tailward. The size of the sector is normalized to the outer circle (800 GW). The IMF clock angle direction is indicated by the red arrow. Blue color indicates net energy flow towards the magnetopause, while the black circles plotted over the sectors show the reconnection line, defined with a method reviewed in Section 2.2.3.

Figure 2.1a indicates that in the global MHD simulation the temporal variation of the energy transfer exhibits a $\sin^2(\theta/2)$ behavior, rather than the $\sin^4(\theta/2)$ dependence suggested earlier (Akasofu 1981). The total energy transfer also exhibits a hysteresis effect, where more energy is transferred after large input. This effect was originally presented in (Palmroth et al. 2006b, Pulkkinen et al. 2006), and it was found that the length of the hysteresis time delay can be as long as 40 min. The spatial variation of the energy transfer can be understood in terms of open magnetic field line advection sketched in the top right corner

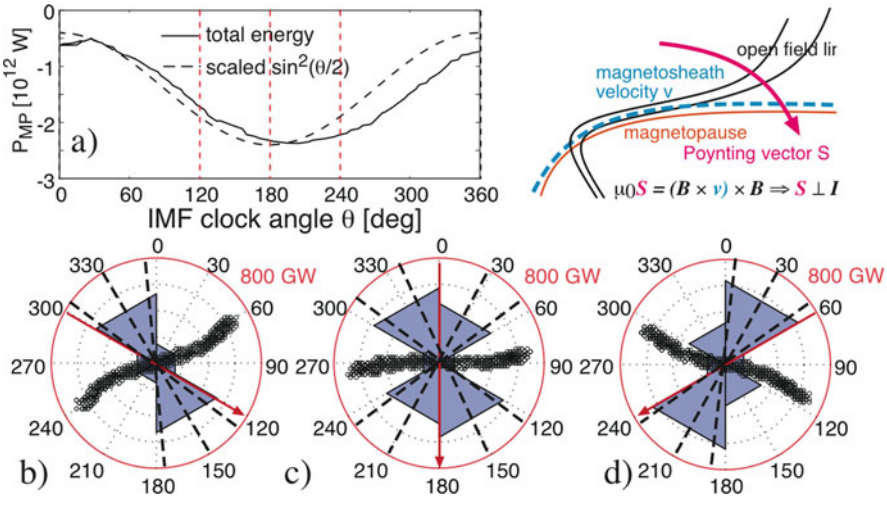

Fig. 2.1 (**a**) Total energy transfer (*solid*) and scaled $\sin^2(\theta/2)$ function (*dashed*) against the IMF clock angle and time in an IMF rotation run. (**b–d**) Spatial distribution of energy transfer during three instants shown as vertical lines in panel (**a**). The schematic drawing in the top right corner explains the spatial energy transfer variation; see text for details

of Fig. 2.1: The dayside reconnection opens the field lines at the reconnection line, and they advect tailwards with an angle with respect to the velocity field in the magnetosheath indicating that electromagnetic (Poynting) energy flux has a component towards the magnetopause. The Poynting flux focusses towards the magnetopause in those locations, where the field lines are primarily advecting tailwards, marked with dashed black lines in Figure 2.1b–d.

2.2.3 Dayside Reconnection Line

Any reconnection setting contains four separate segments of field lines: closed, open, semi-open towards and semi-open away from the Earth (Lau and Finn 1991, Watanabe et al. 2005). Based on this property, a method was introduced to locate the separator line in a three-dimensional grid (Laitinen et al. 2006). This "four-field junction" (FFJ) method searches for locations where the four types of field lines meet in a spatially limited region. The FFJ condition alone is not sufficient for tracking the reconnection sites, but may be used as a reconnection characterization if electromagnetic energy is converted into kinetic energy at the FFJ location. In GUMICS-4, this occurs at the dayside magnetopause approximately for clock angles between $60° < \theta < 300°$, and behind the cusps otherwise, as will be shown in Section 2.2.4.

2.2.4 Magnetopause Reconnection and Dynamo

Laitinen et al. (2007) introduced a method to evaluate the magnetopause dynamo and reconnection powers from the GUMICS-4 simulation. They computed the "energy conversion surface density", which is the divergence of the Poynting vector integrated on a line through the streamline magnetopause. Figure 2.2b–d shows the instantaneous values of this quantity while Fig. 2.2a shows the total reconnection power (blue), and dynamo power (red) computed by integrating all positive (blue) and negative (red) values in Fig. 2.2b–d, respectively. Note that the run is not the same as in Fig. 2.1; a similar rotation was performed in this run but with different plasma and IMF conditions. Blue colors indicate that the electromagnetic energy is converted into kinetic energy, while red depicts the lobe dynamo where electromagnetic energy increases at the expense of kinetic energy. The thick black line is the FFJ reconnection line, while the green lines indicate the areas, where the magnetospheric and magnetosheath magnetic fields are almost antiparallel. Filled black dots refer to Fig. 2.3.

The two quantities, the energy transfer (Section 2.2.2) and the energy conversion discussed here represent two complementary viewpoints in the magnetopause energetics. Figures 2.1 and 2.2 illustrate that both exhibit the same spatial dependence on the IMF y component. The reconnection power (blue colors in Fig. 2.2) is shown as weak energy outflow in the energy transfer process, while the red color (the dynamo in Fig. 2.2) is shown as strong energy transfer towards the magnetopause. As the energy transfer towards the magnetopause occurs on a much larger portion of the magnetopause and is locally stronger than the energy outflow in the reconnection region, the net energy transfer is towards the magnetopause, as also depicted by negative (inward) values of the total energy transfer in Fig. 2.1a.

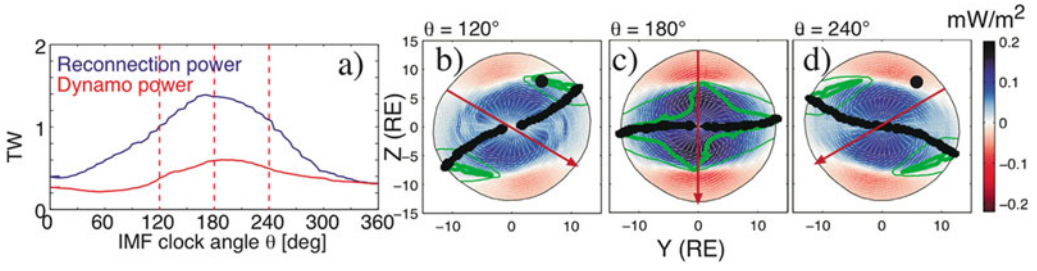

Fig. 2.2 (**a**) Total reconnection (*blue*) and dynamo (*red*) power in an IMF rotation run. (**b–d**) Spatial distribution of the reconnection and dynamo powers (*blue* and *red*, respectively) at three time instants. *Black circles* are the reconnection line and the *green* contours give the area within which the magnetospheric and magnetosheath magnetic fields are almost antiparallel. The *filled black dots* refer to Fig. 2.3

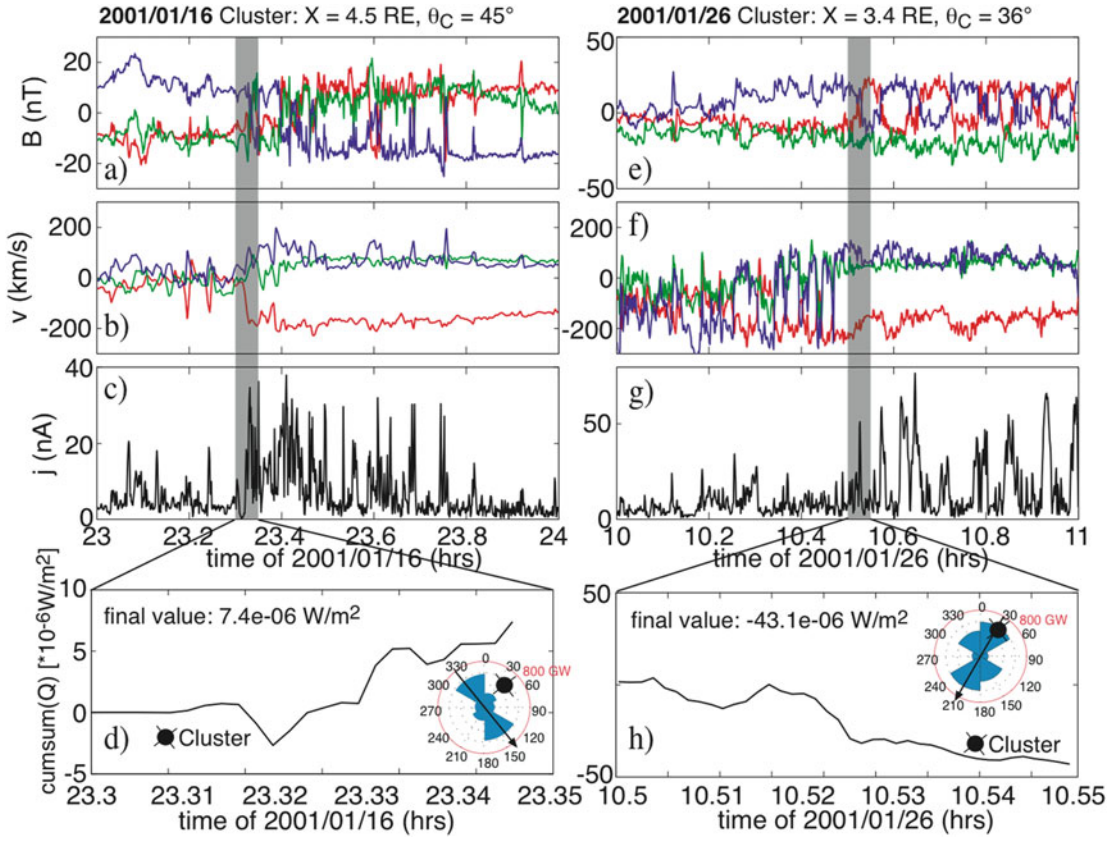

Fig. 2.3 Cluster 1 magnetopause crossing on Jan 16, 2001 (*left*); and on Jan 26, 2001 (*right*). (**a**) and (**e**) Magnetic field x (*red*), y (*green*), and z (*blue*) components; (**b**) and (**f**) plasma velocity x, y, and z components, and (**c**) and (**g**) total current density computed with the curlometer technique. Panels (**d**) and (**h**) are blow-ups of the actual crossing, and depict energy conversion Q

Using the Cluster spacecraft, energy conversion Q in the magnetopause current layer was recently evaluated from

$$Q = \int \mathbf{E} \cdot \mathbf{J} dr = \int (\mathbf{J} \times \mathbf{B}) \cdot \mathbf{v}\, v_{\mathrm{mp}} dt \qquad (2.1)$$

where $\mathbf{E}$ is electric field, $\mathbf{J}$ the current density, $\mathbf{B}$ the magnetic field, $\mathbf{v}$ the plasma velocity, and the integration over a distance dr has been changed to integration over time dt using the magnetopause velocity v_{mp} (Rosenqvist et al. 2006, 2008). Q is given in units of Watts per square meter. We apply the same method to two events in Fig. 2.3 showing Cluster s/c 1 observations on two magnetopause crossings during January 16, 2001 (panels a–d), and January 26, 2001 (panels e–h). Both events occurred during steady solar wind conditions, with similar magnitudes in solar wind speed, density, and IMF strength (not shown). During the Jan 16 event, the IMF clock angle was 143°, while for Jan 26 it was 210°; but in both cases Cluster crossed the magnetopause in the northern dayside afternoon in the same angular direction in the yz plane (45° and 36°, respectively, following the IMF clock angle definition). Depicted are the Cluster s/c 1 FGM observations of magnetic field (Balogh et al. 1997), CIS measurements of plasma density (Rème et al. 1997) and total current density computed with the curlometer technique (Dunlop et al. 2002). The Jan 26, 2001, event is widely studied, and the magnetopause velocity has been reported to be about 40 km/s (Bosqued et al. 2001). For the Jan 16 event, we estimate the magnetopause velocity to about 20 km/s using the generic residue techniques (Sonnerup et al. 2006) that all give a result in agreement with each other (not shown).

The lowest panels of Fig. 2.3 show the energy conversion rate Q such that for each time instant the

cumulative sum (integral) of energy conversion until that time is given. Figure 2.3d and h also show the simulation result of the energy transfer azimuthal distribution and the clock angle orientation from two time instants during the IMF rotation run, where the upstream parameters are similar to those during the two events. The diagrams show the reason why we chose these events: for the Jan 16 event we expect, based on the clock angle and the previous simulation results, that Cluster would have crossed the magnetopause in a region of relatively small energy transfer. For the Jan 26 case we expect that Cluster would have observed significant energy transfer, as it crossed the magnetopause in a sector, where the simulations indicate energy transfer under the upstream conditions of the event. During the Jan 16 event the energy transfer rates (Fig. 2.3d) were an order of magnitude smaller than during the Jan 26 case (Fig. 2.3 h), and they were first negative and then become positive towards the end of the period. We interpret that the Cluster spacecraft crossed the magnetopause in a location marked with a black dot in Fig. 2.2b, within the edge of the load and dynamo regions. On the other hand, as the energy transfer was larger and negative during the Jan 26 event, we interpret that the crossing took place within the strong load area depicted as a black dot in Fig. 2.2d.

2.3 Hysteresis in Energy Transfer

Figure 2.1 showed a hysteresis effect where the energy input remains large although the IMF starts to rotate away from due south. The azimuthal distribution in Fig. 2.1b and d indicate that the extra energy during the return rotation comes from northern morning and southern evening sectors, where the clock angle resided before it reached the due south orientation. As the energy transfer depends on the magnetic field at the magnetopause, in Fig. 2.4a, b we show the magnetopause magnetic field y and z components as vectors in the yz plane at $x = 0\ R_E$ and $x = -5\ R_E$. The blue vectors show the magnetic field at 03:30, and the red vectors from 04:50, when the IMF was $\pm 45°$ from due south direction. The magnetic field at 04:50 has been mirrored with respect to xz plane so that the IMF y component has the same sign in the figure.

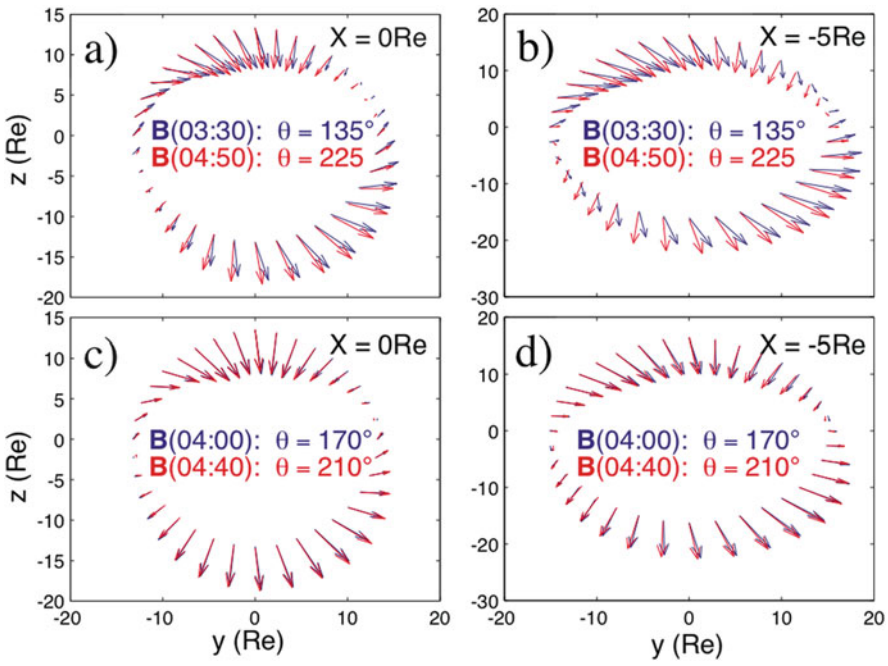

Fig. 2.4 Magnetic field at the magnetopause in the yz plane at (**a**) $x = 0\ R_E$ and (**b**) $x = -5\ R_E$ during 03:30 (*blue*) and 04:50 (*red*). The magnetic field at 04:50 has been mirrored with respect to the xz plane to cancel the effect of different sign in the IMF y component. The times are chosen to be symmetric with respect to due south IMF z. Similar plots of magnetic field in the yz plane at (**c**) $x = 0\ R_E$ and (**d**) $x = -5\ R_E$ during 04:00 (*blue*) and 04:40 (*red*, mirrored). The times are chosen such that the cusp resides 10° from noon (see text for details)

IMF y component tilts the cusps away from noon, and hence without the mirroring the effect from this configurational change would also be visible. Even if the mirroring is carried out, the magnetic field direction at the magnetopause is different during these symmetric times with respect to due south field. The magnetic field after the due south IMF orientation (red arrows) are more perpendicular to the magnetopause surface, indicating that also the circumstances for Poynting flux focussing are different.

Figure 2.5 shows the northern cusp longitude and latitude as determined from the minimum of the magnetic field at the magnetopause. When the positive (negative) IMF y component increases, the northern cusp wanders towards the afternoon (morning); this is due to the penetration of the IMF y component within the magnetosphere (Cowley et al. 1991). When the IMF z becomes negative, reconnection eats away the dayside field faster than the convection feeds closed magnetic flux from the nightside, which displaces the cusp towards the equator. Both displacements driven by the IMF are well-documented and supported by extensive statistical surveys (Newell et al. 1989).

Figure 2.5 indicates that as the IMF changes, the cusp moves in the simulation. However, the cusp is still slightly tilted towards the afternoon when the IMF is due south. The most equatorward position and the noon meridian is reached 15° later in clock angle, at $\theta = 195°$. In Figs. 2.4c and d we now choose two time instants during which the cusp is at $\pm 10°$ from the noon and plot the magnetic field vectors at the magnetopause similarly as in Figs. 2.4a and b. The times

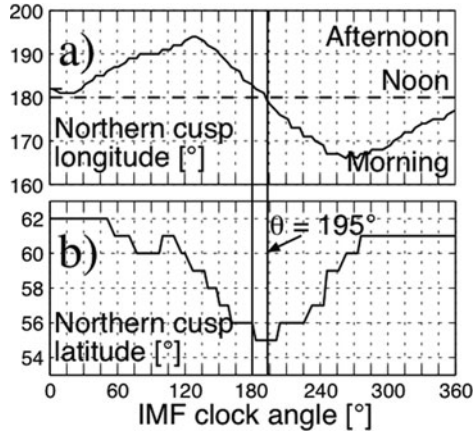

Fig. 2.5 Northern cusp (**a**) longitude and (**b**) latitude as function of the IMF clock angle

are now 04:00 and 04:40, during which the IMF conditions are not symmetric with respect to due south: the IMF clock angle is $\theta = 170°$ and $\theta = 210°$, respectively. Clearly, the magnetic field morphology at the magnetopause is now similar, as the mirrored field is almost identical with the non-mirrored field. The energy transfer, being dependent on the magnetic field at the magnetopause, shows also a symmetric distribution during these times and clock angle directions (not shown here).

2.4 Discussion and Conclusions

In this chapter we have briefly reviewed the techniques and methods developed in order to investigate the global energy circulation in the GUMICS-4 global MHD simulation. Our focus has been in the magnetopause energy transfer and we have not considered the subsequent energy circulation after the energy has entered the magnetosphere. Our results are in qualitative agreement with two representative events observed by the Cluster spacecraft. As similar results are also reported in the recent literature (Rosenqvist et al. 2008), we conclude that the simulation characterization of the magnetopause energy transfer process is at least qualitatively correct.

The two presented events are chosen such that the upstream driving parameters are otherwise similar, but the sign of IMF y component is different. Clearly there is a spatial variation of energy transfer at the magnetopause as the observations show a magnitude difference in the energy conversion estimate, even though the location of crossing and the driving parameters are essentially the same (except for the IMF y). The magnitude of the energy conversion estimate using the Cluster spacecraft seems lower than suggested by GUMICS-4 in Fig. 2.2, but the general picture from GUMICS-4 is in agreement with the interpretation from the observations. In conclusion, IMF y component controls the spatial energy transfer at the magnetopause both in the simulations and in the two events discussed here.

We also investigated a hysteresis effect (Palmroth et al. 2006b), where energy transfer continues strong after strong driving even though the driving starts to become weaker. While the delays observed here are larger than those in (Kabin et al. 2003), the length of the hysteresis time delay depends also on the strength

of the IMF and the solar wind parameters (Palmroth et al. 2006b). Here we have particularly concentrated on the properties of the magnetopause magnetic field, which has a large influence on the energy transfer as the Poynting flux focussing is dependent on the (normal component of) the magnetic field at the magnetopause. We find that as the IMF rotates, the magnetopause magnetic field is not symmetric with respect to due south IMF, but with respect to the cusp position. The cusp position in the simulation has been studied extensively (Palmroth et al. 2001), and the simulated position has been found to correspond to large observational statistical data sets (Newell et al. 1989) particularly during southward IMF.

The azimuthal energy transfer pattern is related to the advection of open field lines from the dayside to the nightside, as in the areas of advection the Poynting flux focusses through the open magnetopause. The advection pattern, on the other hand, is related to the IMF y component: The opening and the advection of the field line start at the cusp area, and the subsequent flows are directed towards the dawn or dusk terminators through the polar cap depending on the sign of the IMF y component (Cowley et al. 1991). These flows continue towards the tail reconnection region with the direction determined by the driving conditions during which they were initiated. The cusp is slow to respond to the driver as it is magnetically tied to the highly conducting ionosphere, and the reconfiguration of the flow pattern and the field-aligned current system takes time (Vennerstrøm et al. 2002). Furthermore, the different conditions in the dayside plasma sheet influence the reconnection between the IMF and the dayside terrestrial magnetic field (Cassak and Shay 2007). This applies to our results as the conditions in the dayside are different if the IMF rotates from the north to the south (after the build-up of the cold and dense plasma sheet) or from the south to the north (during hot and tenuous plasma sheet). Hence, it should not come as a surprise that also the energy transfer at the magnetopause exhibits a memory.

We conclude that previous driving conditions as well as the state of the magnetosphere may influence the processes at the magnetopause, and regulate the energy input to the system. While the presented evidence supporting the conclusion come from a global MHD simulation, we note that the key features in the simulation (the magnetopause position, the advective flows, and the cusp position) are consistent with observations.

Acknowledgments The research leading to these results has received funding from the European Research Council under the European Community's Seventh Framework Programme (FP7/2007-2013)/ERC Starting Grant agreement number 200141-QuESpace. The work of MP and TL is supported by the Academy of Finland.

References

Akasofu S-I (1981) Energy coupling between the solar wind and the magnetosphere. Space Sci Rev 28:121–190

Balogh A, Dunlop MW, Cowley SW et al (1997) The Cluster magnetic field investigation. Space Sci Rev 79:65–91

Bargatze LF, Baker DN, McPherron RL, Hones EW (1985) Magnetospheric impulse response for many levels of geomagnetic activity. J Geophys Res 90:6387–6394

Bosqued JM, Phan TD, Dandouras I, Escoubet CP, Rème H, Balogh A, Dunlop MW, Alcaydé D, Amata E, Bavassano-Cattaneo M-B, Bruno R, Carlson C, Dilellis AM, Eliasson L, Formisano V, Kistler LM, Klecker B, Korth A, Kucharek H, Lundin R, McCarthy M, McFadden JP, Möbius E, Parks GK, Sauvaud J-A (2001) Cluster observations of the high-latitude magnetopause and cusp: initial results from the CIS ion instruments. Ann Geophys 19:1545–1566

Cassak PA, Shay MA (2007) Scaling of asymmetric magnetic reconnection: general theory and collisional simulations. Phys Plasmas 14. doi:10.1063/1.2795630

Cowley SWH, Morelli JP, Lockwood M (1991) Dependence of convective flows and particle precipitation in the high-latitude dayside ionosphere on the X and Y components of the interplanetary magnetic field. J Geophys Res 96:5557–5564

Dungey JW (1961) Interplanetary field and the auroral zones. Phys Res Lett 6:47–48

Dunlop MW, Balogh A, Glassmeier K-H, Robert P (2002) Four-point Cluster application of magnetic field analysis tools: the Curlometer. J Geophys Res 107(A11):1384. doi:10.1029/2001JA005088

Janhunen P (1996) GUMICS-3: a global ionosphere-magnetosphere coupling simulation with high ionospheric resolution. In: Proceedings of environmental modelling for space-based applications, 18–20 Sept 1996, European Space Agency**,** Special Publication, ESA SP-392

Kabin K, Rankin R, Marchand R, Gombosi TI, Clauer CR, Ridley AJ, Papitasvili VO, DeZeeuw DL (2003) Dynamic response of Earth's magnetosphere to by reversals. J Geophys Res 108(A3):1132. doi:10.1029/2002JA009480

Koskinen HEJ, Tanskanen E (2002) Magnetospheric energy budget and the epsilon parameter. J Geophys Res 107(A11):1415. doi:10.1029/2002JA009283

Laitinen TV, Janhunen P, Pulkkinen TI, Palmroth M, Koskinen HEJ (2006) On the characterization of magnetic reconnection in global MHD simulations. Ann Geophys 24:3059–3069

Laitinen TV, Palmroth M, Pulkkinen TI, Janhunen P, Koskinen HEJ (2007) Continuous reconnection line and pressure-dependent energy conversion on the magnetopause in a global MHD model. J Geophys Res 112:A11201. doi:10.1029/2007JA012352

Lau Y-T, Finn JM (1991) Three-dimensional kinematic reconnection in the presence of field nulls and closed field lines. Astrophys J 350:672–691

Lundin R, Evans DS (1985) Boundary layer plasmas as a source for high-latitude, early afternoon, auroral arcs. Planet Space Sci 33:1389–1406

Lyons LR, Killeen TL, Walterscheid RL (1985) The neutral wind flywheel as a source of quiet-time, polar cap currents. Geophys Res Lett 12(2):101104. doi:10.1029/GL012i002p00101

Newell PT, Meng C-I, Sibeck DG, Lepping R (1989) Some low-altitude cusp dependencies on the interplanetary magnetic field. J Geophys Res 94:8921–8927

Newell PT, Sotirelis T, Liou K, Meng C-I, Rich FJ (2007) A nearly universal solar wind-magnetosphere coupling function inferred from 10 magnetospheric state variables. J Geophys Res 112:A01206. doi:10.1029/2006JA012015

Palmroth M, Janhunen P, Pulkkinen TI, Peterson WK (2001) Cusp and magnetopause locations in global MHD simulation. J Geophys Res 106:29435–29450

Palmroth M, Pulkkinen TI, Janhunen P, Wu C-C (2003) Stormtime energy transfer in global MHD simulation. J Geophys Res 108(A1):1048. doi:101029/2002JA009446

Palmroth M, Janhunen P, Pulkkinen TI, Aksnes A, Lu G, Østgaard N, Watermann J, Reeves GD, Germany GA (2005) Assessment of ionospheric Joule heating by GUMICS-4 MHD simulation, AMIE, and satellite-based statistics: towards a synthesis. Ann Geophys 23:2051–2068

Palmroth M, Janhunen P, Germany GA, Lummerzheim D, Liou K, Baker DN, Barth C, Weatherwax AT, Watermann J (2006a) Precipitation and total power consumption in the ionosphere: global MHD simulation results compared with Polar and SNOE observations. Ann Geophys 24: 861–872

Palmroth M, Janhunen P, Pulkkinen TI (2006b) Hysteresis in solar wind power input to the magnetosphere. Geophys Res Lett 33:L03107. doi:10.1029/2005GL025188

Pulkkinen TI, Palmroth M, Tanskanen EI, Janhunen P, Koskinen HEJ, Laitinen TV (2006) New interpretation of magnetospheric energy circulation. Geophys Res Lett 33:L07101. doi:10.1029/2005GL025457

Rème H, Bosqued JM, Sauvaud JA et al (1997) The cluster ion spectrometry (CIS) experiment. Space Sci Rev 79:303–350

Rosenqvist L, Buchert S, Opgenoorth H, Vaivads A, Lu G (2006) Magnetospheric energy budget during huge geomagnetic activity using Cluster and ground-based data. J Geophys Res 111:A10211. doi:10.1029/2006JA011608

Rosenqvist L, Opgenoorth HJ, Rastaetter L, Vaivads A, Dandouras I, Buchert S (2008) Comparison of local energy conversion estimates from cluster with global MHD simulations. Geophys Res Lett 35:L21104. doi:10.1029/2008GL035854

Slinker SP, Fedder JA, Emery BA, Baker KB, Lummerzheim D, Lyon JG, Rich FJ (1999) Comparison of global MHD simulations with AMIE simulations for the events of May 19–20, 1996. J Geophys Res 104:28379–28395

Sonnerup BU, Haaland S, Paschmann G, Dunlop MW, Rème H, Balogh A (2006) Orientation and motion of a plasma discontinuity from single-spacecraft measurements: generic residue analysis of Cluster data. J Geophys Res 111:A05203. doi:10.1029/2005JA011538

Tsyganenko NA (2002a) A model of the near magnetosphere with a dawn-dusk asymmetry 1. Mathematical structure. J Geophys Res 107(A8):1179. doi:10.1029/2001JA000219

Tsyganenko NA (2002b) A model of the near magnetosphere with a dawn-dusk asymmetry 2. Parameterization and fitting to observations. J Geophys Res 107(A8):1176. doi:10.1029/2001JA000220

Vasyliunas VM, Kan JR, Siscoe GL, Akasofu S-I (1982) Scaling relations governing magnetospheric energy transfer. Planet Space Sci 30:359–365

Vennerstrøm S, Moretto T, Olsen N, Friis-Christensen E, Stampe AM, Watermann JF (2002) Field-aligned currents in the day-side cusp and polar cap region during northward IMF. J Geophys Res 107(A8):1188. doi:10.1029/2001JA009162

Watanabe M, Kabin K, Sofko GJ, Rankin R, Gombosi TI, Ridley AJ, Clauer CR (2005) Internal reconnection for northward interplanetary magnetic field. J Geophys Res 110:A06210. doi:10.1029/2004JA010832

Long-Period ULF Waves Driven by Periodic Solar Wind Disturbances

3

Shigeru Fujita, Takashi Tanaka, and Tetsuo Motoba

Abstract

The fundamental nature of ULF waves in the Pc5 range driven by periodic variation of solar-wind dynamic pressure is studied by using a global MHD simulation. It is shown that a spectrum of the magnetospheric ULF wave induced from the periodic variation has a harmonic structure due to nonlinear behavior of magnetospheric response to the solar wind variation. Our simulation also reveals that magnetopause motion is static for the periodic solar wind variation with a period of 10 min, which is consistent with the THEMIS observation of the magnetopause. For a ULF wave with a period of 10 min, the inertia current is significant in the magnetosphere when magnetospheric pressure is depressed under the northward IMF condition, whereas the diamagnetic current is dominant when the pressure is enhanced under the southward IMF condition.

3.1 Introduction

ULF waves in the Pc5 range play an important role in acceleration of high-energy particles in the radiation belt (Elkingston and Hudson 1999). Thus, the Pc5 waves are recently investigated intensively based on in-situ observations with satellites (Takahashi and Ukhorskiy 2007).

Most of all Pc 5 pulsations are regarded to be generated through solar wind sources; one is a solar-wind dynamic pressure variation (Takahashi and Ukhorskiy 2007) and another is the Kelvin–Helmholtz instability in the magnetopause (Fujita et al. 1996). The former mechanism invokes two kinds of the Pc5 pulsations; direct penetration of the solar wind variation into the magnetosphere (Kepko and Spence 2003) and eigenmode oscillations in the magnetosphere excited by the solar wind disturbance (Kivelson et al. 1984).

It should be noted here that the Pc5 pulsation at the higher latitudes has prominent frequencies found by Samson et al. (1992). These frequencies are called as the magic frequencies (1.3–3 mHz) (Kivelson 2006). Finding of the magic frequencies gave rise to a long debate about their source mechanism. Harrold and Samson (1992) assumed that the frequency belongs to eigenfrequencies of an oscillation trapped in a waveguide formed in the region between the Bow shock and a turning point in the inner magnetosphere. On the other hand, Kepko and Spence (2003) insisted that solar-wind variations with the magic frequencies are directly penetrated into the magnetosphere. Later Viall et al. (2009) actually detected the solar-wind variations that are consistent with magnetospheric variations with the

S. Fujita (✉)
Meteorological College, Kashiwa, Chiba, Japan
e-mail: sfujita@mc-jma.go.jp

W. Liu, M. Fujimoto (eds.), *The Dynamic Magnetosphere*, IAGA Special Sopron Book Series 3,
DOI 10.1007/978-94-007-0501-2_3, © Springer Science+Business Media B.V. 2011

magic frequencies. Recently, by using the THEMIS satellites, Plaschke et al. (2009b) detected interesting ULF waves whose frequencies are close to the magic frequencies. From plasma data obtained by the satellites, they concluded that these ULF waves are standing Alfven waves on the magnetopause. Both the direct penetration and the standing Alfven wave on the magnetopause are possible candidates of the source mechanisms for the ULF waves with the magic frequencies. Bearing in mind that the standing Alfven is an evanescent wave with decreasing amplitudes toward the inner magnetosphere, the ULF waves associated with it tends to be confined in the high-latitude region. Whereas, if the ULF waves with the magic frequencies spread in the deep magnetosphere, the direct penetration is a favorable mechanism.

As stated above, direct penetration of the solar wind disturbance is one of probable source mechanisms of the ULF waves in the magnetosphere. In addition, Takahashi and Ukhorskiy (2007) carried out the statistical analysis indicating that the Pc5 pulsations at the geosynchronous altitudes are regarded to be driven by the variation of the Chapman-Ferraro current in the magnetopause. Therefore, it is meaningful to investigate the fundamental nature of ULF waves driven by a periodic variation of the solar-wind dynamic pressure. We have now a powerful tool of a global MHD simulation for investigation of magnetospheric global phenomena such as long-period ULF waves. The simulation technique has been applied already for study of the Pc5 pulsations (Motoba et al. 2007). Although Motoba et al. (2007) discussed mainly the field-aligned current (FAC) generated by periodic compression of the dayside magnetosphere due to the solar wind, fundamental features of ULF waves driven by a periodic variation in the solar-wind dynamic pressure are not investigated so far. Thus, the target of the present chapter is to show the fundamental nature of a ULF waves based on a global MHD simulation.

3.2 Numerical Results

3.2.1 The Numerical Model

Let us first explain in brief the numerical model used in this study. The model is a finite-volume TVD scheme code developed by Tanaka (2002). This model has the anisotropic conducting ionosphere as the inner boundary. The outer boundary is a free boundary where the solar wind is escaping from the model (the downstream side) and continuously connected to the uniform solar wind (the upstream side). A periodic variation of the solar-wind dynamic pressure is given at $X = 20$Re of the upstream side from the Earth.

In the present chapter, the variation of the solar-wind dynamic pressure is given by the density variation. The solar-wind density (n in 1/cc) at $X = 20$Re of the upstream side is given in the following form;

$$n(t) = 10x\{1 + \alpha \sin(2\pi t/T_0)\}, \qquad (3.1)$$

where the intensity parameter α and the period, T_0 as well as the interplanetary magnetic field (IMF) Bz is selected as listed in the Table 3.1. Note that IMFBy is 2.5 nT for all cases.

3.2.2 Waveforms of the Plasma Pressure in the Magnetosphere

Figure 3.1 illustrates waveforms of pressure variations at $L = 9$Re at noon in the magnetospheric equatorial plane. From this figure, we notice that the waveform becomes close to a simple sinusoidal form when the period becomes shorter. On the other hand, for longer-period variations, pressure changes rapidly when the magnetosphere is compressed and slowly when the magnetosphere is expanded. Thus, it is concluded that the magnetosphere behaves as a nonlinear spring for a

Table 3.1 Solar wind parameters used for the simulation

Case#	T_0 (min)	α	Number density (n)	IMFBz (nT)
#1	10	2/3	16.7/cc–3.3/cc	+4.33
#2	10	1/2	15.0/cc–5.0/cc	+4.33
#3	02	2/3	16.7/cc–3.3/cc	+4.33
#4	20	2/3	16.7/cc–3.3/cc	+4.33
#5	10	2/3	16.7/cc–3.3/cc	–4.33

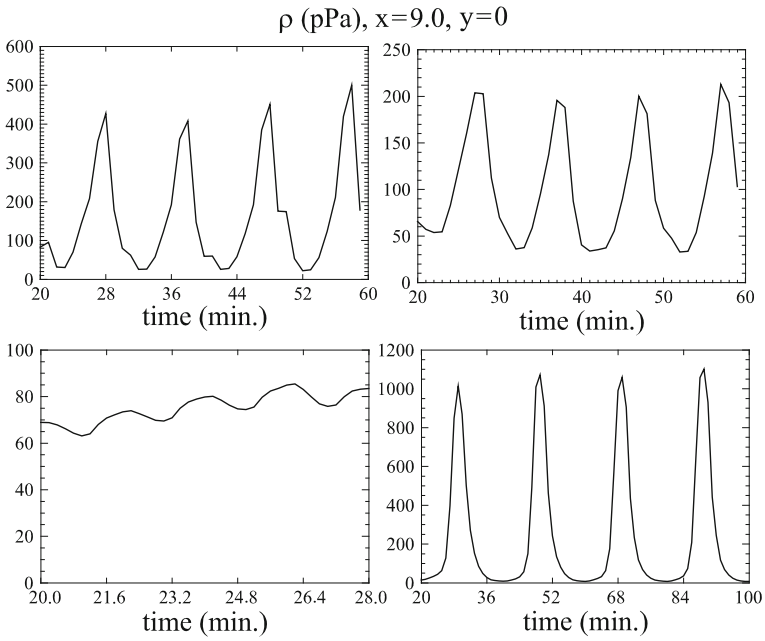

Fig. 3.1 Waveforms of pressure variations at $L = 9$Re at noon in the magnetospheric equatorial plane. (*top-left*) #1, (*top-right*) #2, (*bottom-left*) #3, and (*bottom-right*) #4. See Table 3.1 for the solar wind parameters used for the simulation

periodic variation of the solar-wind dynamic pressure if the period becomes longer.

It is noteworthy that the nonlinear character of the magnetosphere invokes a spectral structure of the ULF wave detected in the magnetosphere somewhat different from that of the original disturbance in the solar wind. We show in Fig. 3.2 the FFT spectra of the pressure variations. When a frequency is shorter (bottom-left panel), there appears a clear spectral peak at the frequency of the original solar-wind dynamic pressure variation. On the other hand, for a longer period variation shown in the bottom-right panel of Fig. 3.2, there appear many higher harmonic spectra. In addition, we notice, from two panels in the top of Fig. 3.2, spectral amplitude of the higher harmonic component becomes smaller when amplitude of the solar-wind dynamic pressure variation becomes smaller. It should be noted here that a higher harmonic spectral structure is not regarded to be derived from the eigenoscillation trapped in the magnetosphere because the frequency is controlled by the frequency of the solar wind variation. If an eigenoscillation in the magnetosphere determines the frequency, there should appear common frequencies among all cases shown in Fig. 3.2.

Let us return to Fig. 3.1. We notice that a pressure variation has smaller amplitude for a higher frequency wave (bottom-left panel) and larger for a lower one (bottom-right panel). Note that each wave has common amplitude at $X = 20$Re. Therefore, this feature is mainly attributed to the fact that the magnetosheath plays a role of a bumper to a periodic variation of the solar-wind dynamic pressure. Namely, solar wind disturbances with higher frequencies are almost attenuated in the magnetosheath and hardly penetrated into the magnetosphere.

3.2.3 Force Balance in the Dayside Magnetopause

Glassmeier et al. (2008) discussed that the magnetopause variation with a time scale of about 10 min observed by THEMIS holds static balance between the solar-wind dynamic pressure and the magnetic pressure in the magnetosphere. Their analysis is quite unique, but it is not easy to conclude definitely only from the observational data that the magnetopause behaves in a static manner during periodic variation of the magnetopause.

As for the numerical simulation, we can check whether a periodic plasma disturbance is static nor not. To investigate this feature, we should evaluate three terms in the momentum equation shown in Eq. (3.2),

$$\rho \, \mathrm{d}\mathbf{u}/\mathrm{d}t = \mathbf{J} \times \mathbf{B}\text{-grad}\, p, \tag{3.2}$$

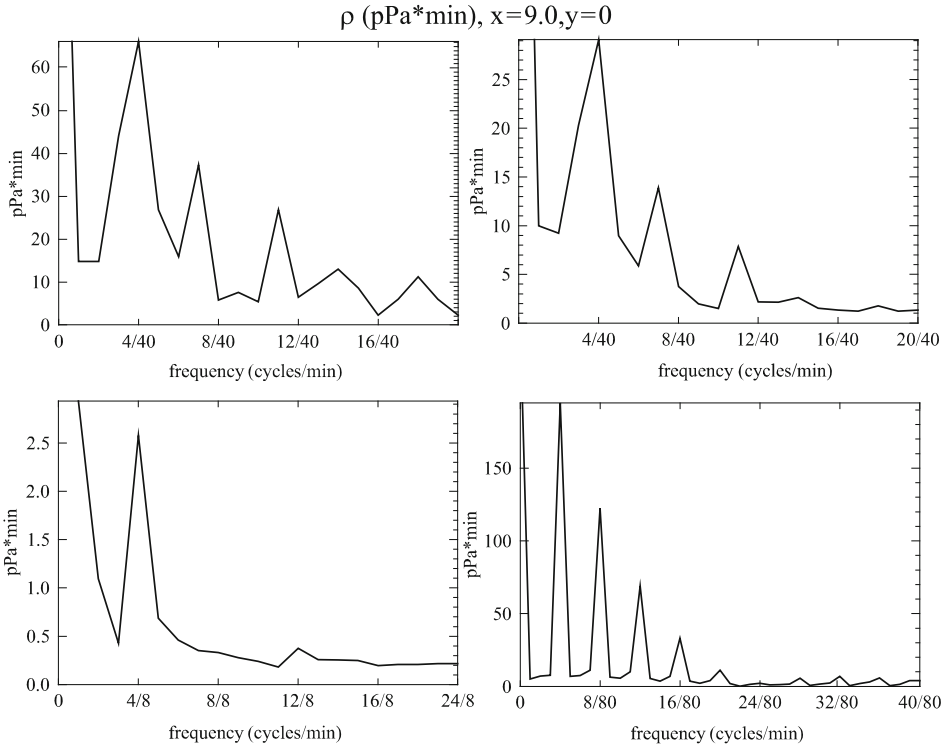

Fig. 3.2 FFT spectra of pressure variations shown in Fig. 3.1. (*top-left*) #1, (*top-right*) #2, (*bottom-left*) #3, and (*bottom-right*) #4. See Table 3.1 for the solar wind parameters used for the simulation

where **u**, **J**, and p are, respectively, a plasma flow vector, a current vector, and pressure. As *Glassmeier* et al. (2008) analyzed the THEMIS data obtained near noon in the magnetopause, we evaluate the x component of three terms in Eq. (3.2) along the noon meridian in the equatorial plane. The result is shown in Fig. 3.3 in which solar wind parameters of the case #1 (Table 3.1) are used. To identify position of the magnetopause, we show time change of pressure profiles along the noon meridian in the top-left panel. From this figure, we notice that the Lorentz force term ($\mathbf{J}\times\mathbf{B}$) is comparable to the pressure gradient term when the magnetopause shifts Earthward. At the same time, the acceleration term is not so significant there. Therefore, the pressure gradient is almost balanced with the Lorentz force in the magnetopause region. Namely, the magnetopause behavior is almost static; this result supports the observation (Glassmeier et al. 2008). On the other hand, the acceleration term becomes dominant over the Lorentz force term in the Bow shock region. Note that, as shown later, static behavior of the magnetopause appears also for the southward IMF case (Fig. 3.4).

3.2.4 Nature of the Magnetospheric Current

As a global MHD simulation presents numerical results in the entire region of the magnetosphere, we can also comprehend plasma behavior in the entire magnetosphere. Here, we investigate which component of the current is dominant in the magnetosphere, the inertia current or the diamagnetic current. If the former is dominant, the plasma behavior essentially has a wave-like character because the inertia force acts as a restitution force against the Lorentz force. On the other hand, when the current is mainly the diamagnetic current, the magnetosphere structure is changing in a quasi-stationary manner according to a variation of the solar-wind dynamic pressure.

When we consider this problem, it is easily understood that the inertia current becomes dominant when a period of the solar-wind dynamic pressure variation becomes shorter. In the present chapter, instead, we investigate the current in two conditions where IMFBz is negative and positive.

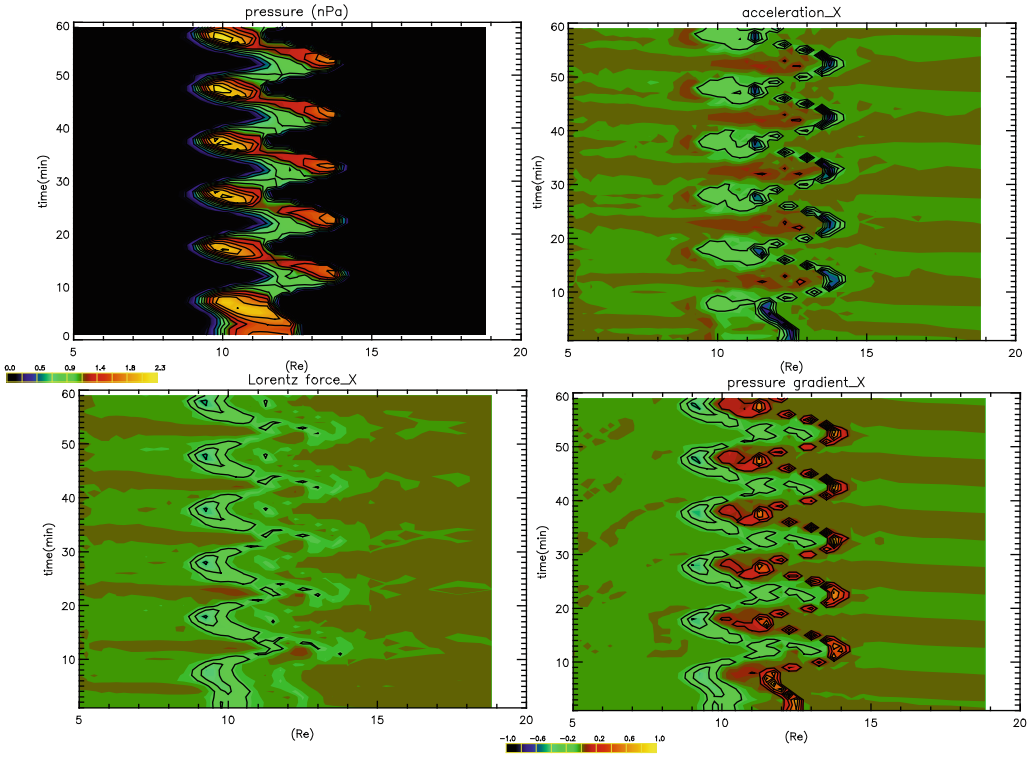

Fig. 3.3 Temporal changes of profiles of four values along noon meridian in the equatorial plane for the case #1. Earth is located to the left of each panel. (*top-left*) pressure, (*top-right*) $\rho du_x/dt$, (*bottom-left*) $\mathbf{J}\times\mathbf{B}_x$, (*bottom-right*) $\text{grad}_x p$. The color contour scale for pressure is shown just below the *top-left* panel and that for other three panels is common as shown in the bottom part of the figure

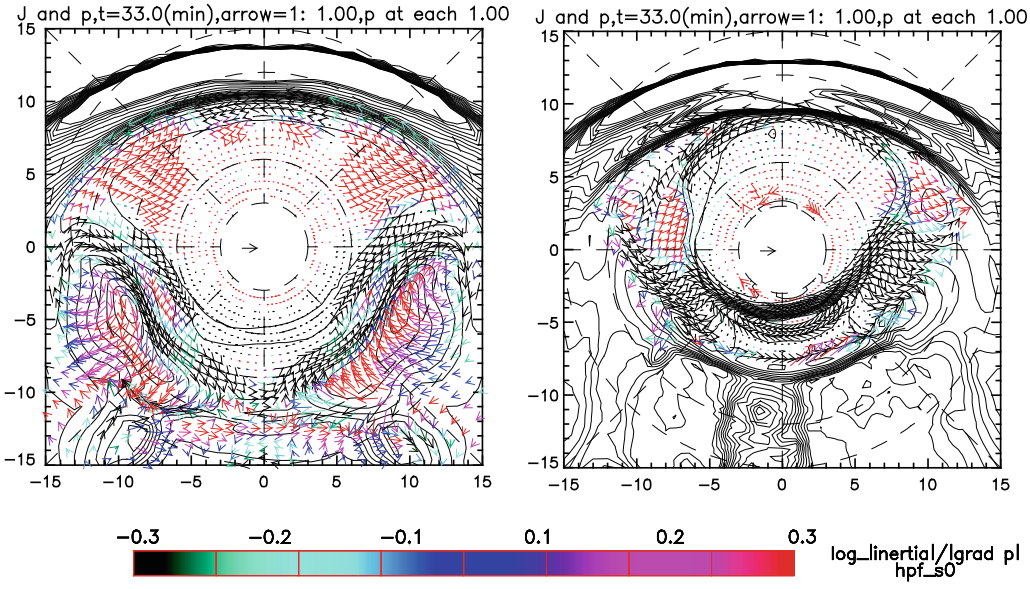

Fig. 3.4 The current pattern and pressure contours in the equatorial plane (*left*) for the case #1 and (*right*) for the case #5. The *red* and *blue arrows* indicate the inertia current and diamagnetic current, respectively

Figure 3.4 shows current arrows and pressure contours in the equatorial plane for the northward IMF case (case #1 in Table 3.1) and for the southward IMF case (case #5 in Table 3.1). In our simulation, the plasma pressure is enhanced in the southward IMF condition (maximum pressure at $L = 9$Re at noon of the equatorial plane is about 3000 pPa) compared with that for the northward IMF condition (maximum pressure at $L = 9$Re at noon is about 400 pPa). From the left panel of Fig. 3.4, in the northward IMF case, it is evident that the inertia current (shown in red arrows) becomes prominent in the dayside magnetosphere except for the magnetopause. The diamagnetic current appears in the dayside magnetopause and in the vicinity of the enhanced pressure in the dawn/dusk regions. On the other hand, the diamagnetic current becomes dominant for the southward IMF case. When pressure is enhanced, a magnetic field line easily bends against pressure force. Namely, the magnetosphere becomes "soft". Thus, the magnetosphere deforms easily to an external force and static balance between the pressure gradient and the Lorentz force holds. On the other hand, when the pressure is depressed, the magnetosphere becomes "hard". In this case, an elastic wave tends to be excited by periodic compression by the solar wind.

3.3 Discussion and Summary

Let us consider the Alfven eigenmode of the magnetopause (Plaschke et al. 2009b). (It should be noted here that the global MHD simulation does not reproduce correctly the Alfven wave because the mesh system does not refer to the magnetic field line. Thus, the Alfven eigenmode is not detected in the simulation.) The idea of the Alfven eigenmode conflicts somewhat with the THEMIS observation (Glassmeier et al. 2008) and the present simulation results because the observation and the simulation insist that the magnetopause motion is static. Bearing in mind that both the observation (Glassmeier et al. 2008) and the simulation (Fig. 3.3) investigate plasma behavior at noon, we should check plasma behavior near the magnetopause at other local time. Then, we notice that there appears the inertia current in the dawn/dusk regions (Fig. 3.4). In particular, the inertia current in the magnetopause is more evident in the northward IMF condition. This result is consistent with the statistical result (Plaschke et al. 2009a) that the Alfven eigenmode appears mainly in the northward IMF condition. Therefore, we conclude no conflict between the Alfven eigenmode (Plaschke et al. 2009b) and the static motion of the magnetopause (Glassmeier et al. 2008), if the eigenmode has spatial distribution of the current along the magnetopause as shown in the Fig. 3.4.

As a summary, fundamental nature of long-period ULF waves driven by a periodic variation of the solar-wind dynamic pressure is discussed. Based on a global MHD simulation, we investigate waveforms of ULF waves induced in the magnetosphere and behavior of the plasmas which is hardly investigated from the satellite observations. The main results are summarized as follows;

1. The magnetosphere behaves as a nonlinear spring against a solar-wind dynamic pressure variation. Accordingly, the induced wave has a higher harmonic spectral structure.
2. We confirm that the dayside magnetopause behaves in a static manner for slowly varying solar-wind dynamic pressure. This result supports the THEMIS result (Glassmeier et al. 2008).
3. The magnetospheric current associated with long-period ULF waves driven by a solar-wind dynamic pressure variation is rather static when pressure in the magnetosphere is enhanced in the southward IMF case. When IMF is northward, the inertia current becomes prominent for a 10-min period variation.

The present chapter did not treat the ULF waves driven by the Kelvin–Helmholtz instability in the magnetopause. It is well-known that activity of Pc5 pulsations observed at high-latitude ground is highly correlated with the solar wind speed (Mathie and Mann 2001). On the other hand, local-time dependence of the magnetospheric ULF waves (Takahashi and Ukhorskiy 2007) is not consistent with hypothesis that magnetospheric ULF waves are generated by the Kelvin–Helmholtz instability in the magnetopause. This topic should be considered elsewhere.

Acknowledgments This work has been done with the OneSpaceNet of National Institute of Information and Communication Technologies, LHD system of National Institute of Fusion Research, and computers installed in Nagoya University.

References

Elkingston SR, Hudson MK (1999) Acceleration of relativistic electrons via drift-resonant interaction with toroidal-mode Pc-5 ULF pulsations. Geophys Res Lett 26:3237–3276

Fujita S, Glassmeier K-H, Kamide K (1996) MHD waves generated by the Kelvin-Helmholtz instability in a nonuniform magnetosphere. J Geophys Res 101:27317–27325

Glassmeier K-H, Auster H-U, Constantinescu D, Fornaccon K-H, Narita Y, Plaschke F, Angelopoulos V, Georgescu E, Baumjohann W, Magnes W, Nakamura R, Carlson CW, Frey S, McFadden JP, Phan T, Mann I, Rae IJ, Vogt J (2008) Magnetospheric quasi-static response to the dynamic magnetosheath: A THEMIS case study. Geophys Res Lett 35:L17S01. doi:10.1029/2008GL033469

Harrold BG, Samson JC (1992) Standing ULF modes of the magnetosphere: A theory. Geophys Res Lett 19:1811–1814

Kepko L, Spence HE (2003) Observations of discrete, global magnetospheric oscillations directly driven by solar wind density variations. J Geophys Res 108(A6):1257. doi:10.1029/2002JA009676

Kivelson MG (2006) ULF waves from the ionosphere to the outer planets. In: Takahashi K et al (eds) Magnetospheric ULF Waves: synthesis and new directions, American Geophysical Union, pp 11–30.

Kivelson MG, Etcheto J, Trotignon JG (1984) Global compressional oscillations of the terrestrial magnetosphere: The evidence and a model. J Geophys Res 89:9851–9856

Mathie RA, Mann IR (2001) On the solar wind control of Pc5 ULF pulsation power at mid-latitudes: Implications for MeV electron acceleration in the outer radiation belt. J Geophys Res 106(A12):29783–29796

Motoba T, Fujita S, Kikuchi T, Tanaka T (2007) Solar wind dynamic pressure forced oscillation of the magnetosphere-ionosphere coupling system: A numerical simulation of directly pressure-forced geomagnetic pulsations. J Geophys Res 112:A11204. doi:10.1029/2006JA012193

Plaschke F, Glassmeier K-H, Auster HU, Angelopoulos V, Constantinescu OD, Fornaccon K-H, Georgescu E, Magnes W, McFadden JP, Nakamura R (2009a) Standing Alfven waves at the magnetopause. J Geophys Res 114:A00C10. doi:10.1029/2008JA013423

Plaschke F, Glassmeier K-H, Auster HU, Constantinescu OD, Magnes W, Angelopoulos V, Sibeck DG, McFadden JP (2009b) Statistical study of the magnetopause motion: First results from THEMIS. Geophys Res Lett 36:L02104. doi:10.1029/2008GL036411

Samson JC, Harrold BG, Ruohoniemi JM, Greenwald RA, Walker ADM (1992) Field line resonances associated with MHD waveguides in the magnetosphere. Geophys Res Lett 19:441–444

Takahashi K, Ukhorskiy AY (2007) Solar wind control of Pc5 pulsation power at geosynchronous orbit. J Geophys Res 112:A11205. doi:10.1029/2007JA012483

Tanaka T (2002) Finite volume TVD scheme on unstructured grids for space MHD simulations and space weather. In: Proceeding of simulation school at Nagoya, Nagoya, 2002

Viall NM, Kepko L, Spence HE (2009) Relative occurrence rates and connection of discrete frequency oscillations in the solar wind density and dayside magnetosphere. J Geophys Res 114:A01201. doi:10.1029/2008JA013334

Part II
Magnetotail Dynamics

Magnetotail Dynamics: Survey of Recent Progress

4

Joachim Birn

Abstract

This survey focuses on three topics of magnetotail dynamics which constitute the vast majority of publications on tail dynamics in the period of this survey, from about mid 2007 to mid 2009: (1) the formation and properties of thin current sheets, (2) the timing of characteristic features around substorm onset, and (3) the properties of fast plasma flows, commonly denoted "bursty bulk flows" (BBFs), and associated dipolarization events. It is concluded that current sheet thinning from external deformation, accompanied by a reduction of B_z provides a viable mechanism for the onset of current sheet activity. After the first THEMIS results, the substorm onset timing remains controversial. However, it can be concluded that the onset arc brightening cannot be the consequence of dipolarization (current disruption) or reconnection and that there is a strong connection between earthward flow bursts and dipolarization events.

4.1 Introduction

The Earth's magnetic tail plays a crucial role in the evolution and dynamics of the magnetosphere, as the site of storage and release of excess energy, and in feeding and instigating inner magnetospheric, ionospheric, and atmospheric phenomena. This survey focuses on three topics of magnetotail dynamics which constitute the vast majority of publications on tail dynamics in the review period from mid 2007 to mid 2009: (1) the formation and properties of thin current sheets, (2) the timing of characteristic features around substorm onset, and (3) the properties of fast plasma flows, which occur typically in short bursts of 1–10 min duration and are commonly denoted "bursty bulk flows" (BBFs) (Baumjohann et al. 1990; Angelopoulos et al. 1992). They are covered in Sections 4.2, 4.3, and 4.4. Topics (1) and (3) can be understood as being related to conditions that lead to substorm onset and consequences of substorm onset, respectively. However, the formation and presence of thin current sheets as well as those of BBFs are not necessarily tied to the occurrence, or particular phases, of substorms (Angelopoulos et al. 1994).

The review period of this survey covers the first major results of the THEMIS mission (Angelopoulos 2008). This mission consists of five satellites with planned line-ups in the tail, combined with extensive ground observations. It is devoted particularly to topic (2), and specifically, the relative timing of ground auroral onset, near tail "current disruption" in the region of

J. Birn (✉)
Los Alamos National Laboratory, Los Alamos, NM 87545, USA
e-mail: jbirn@lanl.gov

W. Liu, M. Fujimoto (eds.), *The Dynamic Magnetosphere*, IAGA Special Sopron Book Series 3,
DOI 10.1007/978-94-007-0501-2_4, © Springer Science+Business Media B.V. 2011

8–10R_E, and the onset of magnetic reconnection further tailward. It seems therefore appropriate to devote one section to this topic.

In addition, the observational results are based heavily on the Cluster mission (Escoubet et al. 2001), which consists of four satellites in a tetrahedron configuration, devoted particularly to separate spatial and temporal variations and to provide spatial gradients, such as current density from the curl of the magnetic field, which is essential for topic (1), and the characteristics of flow patterns, topic (3).

4.2 Thin Current Sheets

The formation, breakup, and activity of thin current sheets are essential elements of the dynamics of the magnetotail. Here we understand as "thin" current sheets those that have a thickness of the order of a typical ion scale (ion gyro radius or ion inertia length) or less. Thin current sheets may occur in various forms, most commonly as single compressed sheets, as single thin sheets embedded in a wider current sheet, or as double sheets at the edges of a wider sheet. The latter are commonly referred to as "bifurcated current sheets." Even more complicated forms are also possible.

Figure 4.1, modified from Figs. 4 and 5 of Baumjohann et al. (2007), illustrates three Cluster encounters with single thin current sheets with quite different characteristics. The current sheet encounters are visible primarily by large differences between the x components of the magnetic field between the satellites (top panels), here particularly between Cluster 3 (green lines) and the other three spacecraft, which are located approximately in a plane, above (i.e. north of) Cluster 3. This indicates that the current sheet thickness is comparable to, or smaller than, the maximum separation of the satellites in the north-south (z) direction, which is of the order of 2000 km for these events. The first encounter occurred on Sept. 9, 2001 from $\sim$21:00 to $\sim$21:15 UT (left panel) at $x \approx -19R_E$. It is very calm without any significant wave activity. The current sheet half-thickness, estimated from the magnetic field differences and the satellite separation, was $H \approx 2000$ km $\approx 2\rho_i$, where ρ_i is the ion gyroradius, comparable to the ion inertia length. A slightly thinner current sheet ($H \approx 1000-2000$ km $\approx 1-2\rho_i$), was crossed about 30 min later. It is found to be active, with fast earthward ion flow bursts (300–600 km/s), possibly from a reconnection site tailward of Cluster, and simultaneous large amplitude fluctuations ($\delta B/B \sim 1$).

A second event, from $\sim$09:40 to $\sim$09:50 UT on Oct. 1, 2001 (right-hand panels) at $x \approx -16R_E$, shows

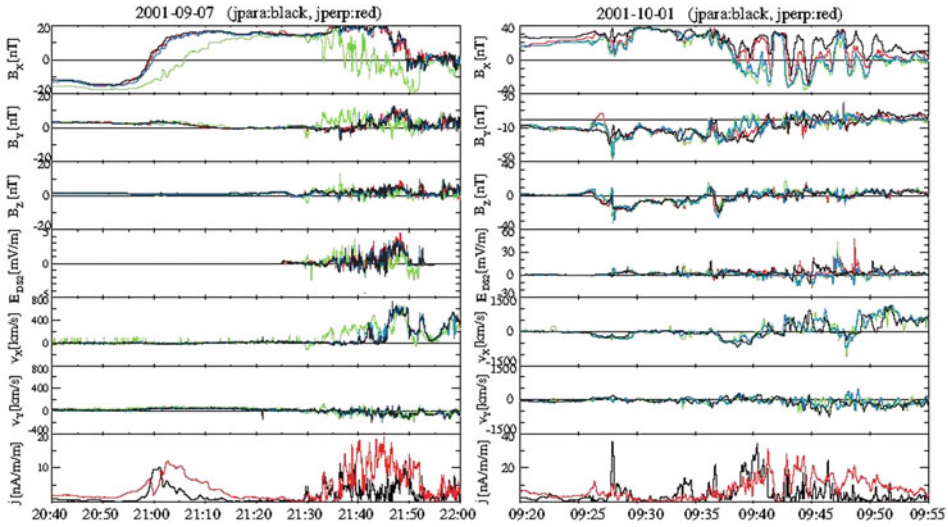

Fig. 4.1 Cluster data of thin current sheet encounters, modified after Figs. 8 and 9 of Baumjohann et al. (2007): (**a**, **b**, **c**) spin resolution data from GSM components of the magnetic field, (**d**) DS2 component of the electric field, (**e**, **f**) GSM X,Y components of the proton bulk velocity, (**g**) current density determined from the magnetic field. For the particle and field plots, profiles for Cluster 1, 2, 3, 4 are plotted with *black*, *red*, *green*, and *blue* lines, respectively. *Black* and *red* lines in the current density plots correspond to X and Y components, respectively

a much more active current sheet crossing than the first one. Large amplitude waves indicate flapping of the current sheet identified as an azimuthally propagating wave. A reversal in the proton flow velocity, from approximately –1000 to +1000 km/s, and the associated change in the sign of B_z suggest tail-ward motion of an X-line with respect to the spacecraft. In addition, rapid variations of fields and flows were interpreted as filamentary field-aligned current structures moving eastward at 200 km/s.

After this brief overview we discuss results on the formation and structure of thin current sheets in Section 4.2.1. Stability properties are discussed in Section 4.2.2 and activity modes in Section 4.2.3, with particular emphasis on the flapping.

4.2.1 Formation and Structure

The most plausible scenario for the formation of embedded and bifurcated thin current sheets is a compression of the magnetotail, for instance, from the addition of magnetic flux to the tail lobes during the substorm growth phase. As demonstrated by Birn and Schindler (2002) and Birn et al. (2009), adiabatic deformation of the tail under conservation of mass and entropy on closed magnetic flux tubes may lead to a critical state, such that neighboring equilibrium solutions cease to exist if the boundary deformation exceeds a certain threshold. The critical state is characterized by the formation of a thin intense current sheet embedded in the wider plasma/current sheet, as illustrated by Fig. 4.2.

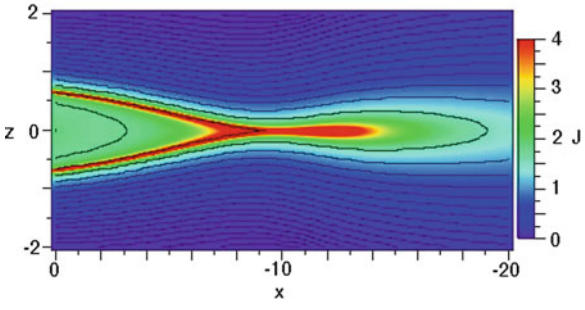

Fig. 4.2 Formation of a thin embedded current sheet (color) resulting from nonuniform adiabatic magnetotail deformation near a critical limit of deformation. As a consequence of the 2D structure, the thin current sheet bifurcates toward the Earth (to the *left*). After Birn et al. (2009)

In two-dimensional (or three-dimensional) tail configurations the embedded current sheet bifurcates into two sheets further earthward (to the left). Similar thinning and current intensification may also result from plasma convection from the inner tail to the dayside (Otto and Hall; IAGA symposium 2009), which is another expected consequence of dayside reconnection driving the substorm growth phase.

These results were obtained by MHD simulations and theory, assuming isotropic plasma pressure. However, the small scale of thin current sheets implies that kinetic effects, anisotropies or nongyrotropies should become relevant when the current sheet thickness becomes smaller than ion kinetic lengths. Using one-dimensional particle-in-cell (PIC) simulations, Schindler and Hesse (2008) demonstrated that bifurcated current structures resulted from slow compression even in the absence of 2D effects. Similar results were obtained by 2D PIC simulations of the compression of an initially 1D current sheet (Lapenta and King 2007).

To incorporate the kinetic effects, several quasi-equilibrium models of thin current sheets have been developed that include anisotropic or nongyrotropic distribution functions and/or multiple (e.g., trapped and nontrapped) ion populations (Zelenyi et al. 2000; Schindler 2002; Sitnov et al. 2003; Steinhauer et al. 2008). These properties have proven useful, or even necessary, in making better comparisons with observed particle distributions (Artemyev et al. 2008; Cai et al. 2008; Israelevich and Ershkovich 2008; Zhou et al. 2009), although no clear favorite has emerged. Detailed analyses primarily from Cluster observations further confirmed that the current in sufficiently thin embedded or bifurcated current sheets is carried by electrons (Baumjohann et al. 2007; Israelevich et al. 2008) (as measured in the satellite frame, which is essentially equivalent to a frame in which the electric field vanishes outside of the current sheet).

4.2.2 Stability

As discussed in Section 4.2.1 in the context of Fig. 4.1, sufficiently thin current sheets may become subject to a variety of unstable modes. Current sheet instabilities and waves are of interest as a means to directly initiate reconnection via a tearing mode (Schindler 1974), as a way to lead into current disruption (Lui et al. 1990),

and as source mechanism for auroral arc brightening (see also Section 4.3). In this section we first focus on waves detected in observations prior to the dipolarization in the current disruption region around 10 R_E distance. Then we present theoretical results, focusing on tearing and ballooning/interchange instabilities.

4.2.2.1 Observations

Wave identifications around dipolarization events in the near tail were done primarily by wavelet analyses of magnetic fluctuations. They typically revealed waves with low frequencies of ~0.1–0.01 Hz below the ion cyclotron frequency. This is illustrated by Fig. 4.3, taken from Saito et al. (2008b). The earliest wave signal is shown primarily in B_x at ~04:01 UT with a frequency of ~0.01–0.02 Hz. This wave was interpreted by Saito et al. (2008b) as a ballooning mode. Similar results were found in four of six dipolarization events studied, which were characterized by large plasma beta. Ballooning modes prior to dipolarization were also identified by Saito et al. (2008a), Liu et al. (2008) and Liu and Liang (2009). In addition, Saito et al. (2008a) identified slow and fast magnetosonic modes preceding dipolarization by

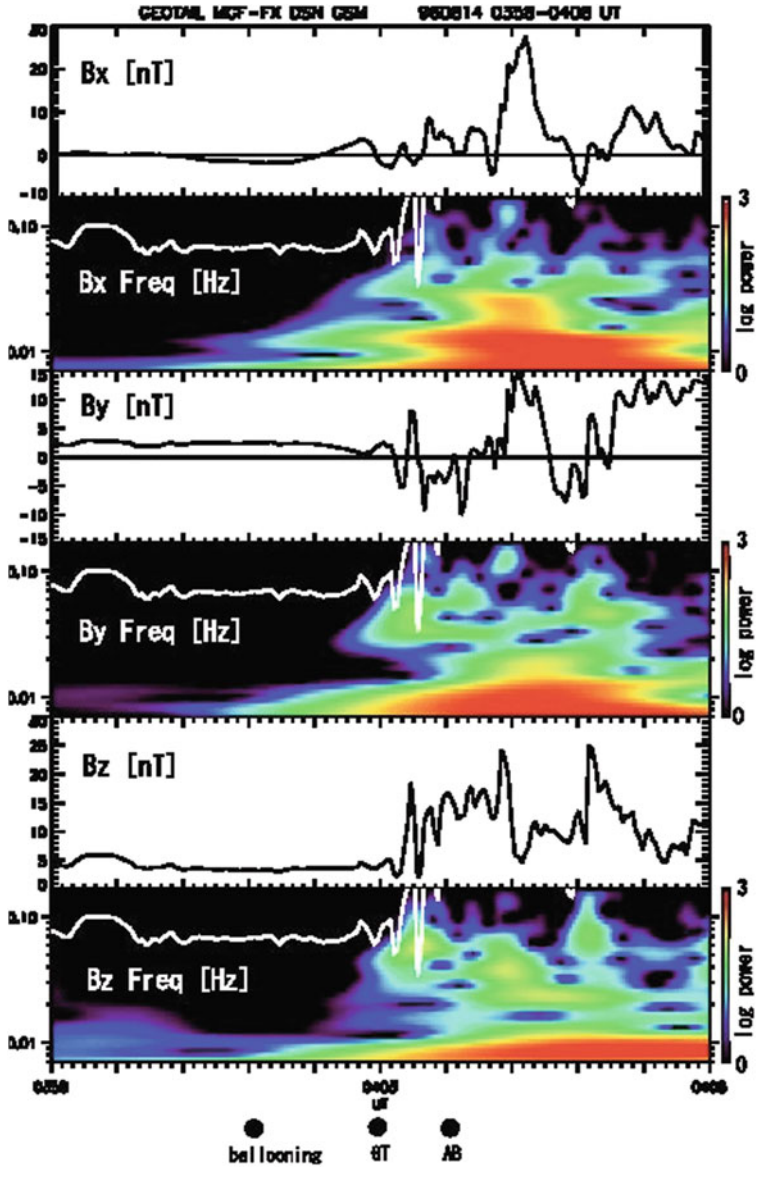

Fig. 4.3 Wavelet scalograms and the corresponding time-series data of the magnetic field on 14 August 1996 obtained by Geotail near $x = -10R_E$. The *white* line indicates the ion cyclotron frequency. The *filled circles* at the *bottom* indicate onset of the ballooning mode, dipolarization onset at Geotail (GT), and auroral breakup (AB), determined by UV images from Polar. After Saito et al. (2008b)

3 and 1.5 min, respectively. In contrast to ballooning modes, which have wave vectors perpendicular to the magnetic field, these waves propagated parallel to the field, earthward (slow mode) and tailward (fast mode). Lui et al. (2008c) and Yoon et al. (2009) also used wavelet analysis to investigate waves associated with a dipolarization event. They identified waves at the onset of dipolarization as Alfvén ion cyclotron waves (propagating perpendicular to the field rather than parallel propagating electromagnetic ion cyclotron waves). They also found an inverse cascade to lower frequency for the B_z component in this event.

4.2.2.2 Theory: Ballooning and Interchange

Here we focus on recent results on ideal ballooning modes. Important results on 2D equilibria with $B_y = 0$ are summarized in Schindler (2007): For typical magnetotail configurations without neutral lines, the general MHD stability problem can be reduced to the problem of stability with respect to the ballooning mode alone. The ballooning criterion can be related to the well-known entropy criterion for interchange modes. That criterion predicts stability (instability) for tailward increase (decrease) of entropy $S = \ln(pV^{\gamma})$, where V denotes the flux tube volume per unit magnetic flux, $V = ds/B$, integrated along field lines. Realistic magnetotail equilibria appropriate for quiet or average conditions were found to be stable.

This result also puts constraints on the development of ballooning instability from initially stable tail configurations. If the tail is deformed adiabatically (i.e., isentropically), the entropy on closed flux tubes is conserved and stability properties are not altered, even if a local embedded current sheet is formed (Fig. 4.2) (Schindler 2007; Birn et al. 2009).

However, these results were based on 2D equilibria with $B_y = 0$. The full analysis of 3D equilibria has not been done. Xing and Wolf (2007) derived a criterion for interchange instability in low-beta 3D configurations with shear flow. This criterion requires $\alpha > \pi/2$, where α is the angle between ∇S and ∇V. For typical 2D tail configurations, V increases downtail, while p decreases. This criterion thus becomes equivalent to the 2D criterion discussed by Schindler (2007). A destabilization of an initially stable configuration hence requires either significant interchange motions (which appears trivial) or nonadiabatic processes, Such processes are discussed in Section 4.4 as processes leading to the formation of underpopulated flux tubes, which are likely related to BBFs. A change in interchange stability may also result from a change in ionospheric boundary conditions (Miura 2007, 2009).

4.2.2.3 Theory: Tearing

An obvious way of initiating reconnection in the magnetotail is via a tearing instability (Coppi et al. 1966; Schindler 1974; Galeev and Zelenyi 1976). A major theoretical concern about the onset of tearing in the magnetotail is the fact that the mode is stabilized in current sheets with relatively modest normal magnetic field component B_z (Pellat et al. 1991). The result that adiabatic deformation of the tail may lead to configurations with an embedded thin current sheet (Section 4.2.1), where locally both B_z and the current sheet thickness are reduced, alleviates this concern. However, a stability analysis of such 2D configurations has not been performed yet. Recent stability analyses (Matsui and Daughton 2008; Haijima et al. 2008) still considered only 1D initial current sheets, even if a normal magnetic field component is included (Zelenyi et al. 2008).

Zelenyi et al. (2008) performed stability analysis, based on an energy principle, of a 1D current sheet model with finite B_z (Zelenyi et al. 2004), which requires pressure anisotropy, and concluded that an unstable regime with $B_z \approx 0.1$ (in units of the reconnecting magnetic field) exists. Using both standard analytic techniques and a formally exact treatment involving a numerical evaluation of full orbit integrals, Matsui and Daughton (2008) concluded that one-dimensional bifurcated thin current sheets are more stable to tearing than single-peaked sheets, however, development of electron anisotropy Te$\perp$ > Tel would be destabilizing. Haijima et al. (2008), using 2D PIC simulations, confirmed the enhancement of the linear growth rate but found no effect on the nonlinear phase nor on the onset threshold.

4.2.3 Active Modes: Flapping

As illustrated in Fig. 4.1, activity in thin current sheets may consist of a variety of modes. Of these modes, the so-called flapping motions (Fig. 4.1b) have drawn particular attention. Figure 4.4a, b, taken from Malova

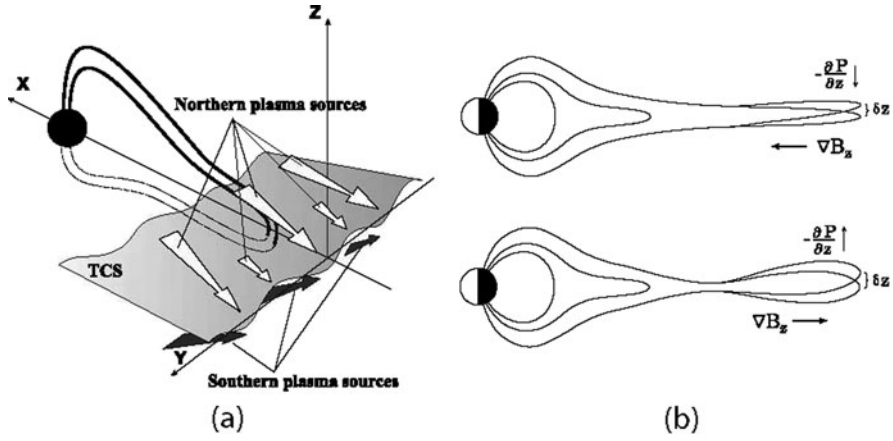

Fig. 4.4 (**a**) Schematic of waves associated with current sheet flapping; after Malova et al. (2007). In this view the waves are caused by asymmetries between the two tail lobes. However, other potential source mechanisms include flow bursts (Gabrielse et al. 2008) and (**b**) MHD instability, illustrating (*top*) a stable, (*bottom*) an unstable situation; after Erkaev et al. (2009a, b)

et al. (2001) and Erkaev et al. (2009b), illustrate the wave perturbations associated with flapping. They consist of an up and down shift of flux tubes, or portions of flux tubes, as indicated in Fig. 4.4b, rather than a bending of the current sheet (Petrukovich et al. 2008; Shen et al. 2008). They have long periods ($\sim$1 min up to several min), large amplitudes (1–3R_E), and propagate typically from the center of the tail toward the flanks (Sergeev et al. 2006; Gabrielse et al. 2008; Runov et al. 2009a) with wave speeds of a few tens of km/s. The inferred wavelengths in the cross-tail direction are also a few R_E. THEMIS observations (Runov et al. 2009a) confirmed that the flapping waves are coherent over long distances in x, larger than the maximum separation of the THEMIS satellites of 7R_E in this event.

The source mechanism is not quite clear yet. Statistical analyses (Sergeev et al. 2006) have shown that flapping events have similar occurrence statistics as bursty bulk flows, although a one-to-one relationship could not be established. Gabrielse et al. (2008) established such a relationship for a particular event, although in other events no such relationship was found (Runov et al. 2009a). The fact that they may occur both before and after substorm onset (Takada et al. 2008) indicates that there is no direct causal relationship one way or the other. Malova et al. (2007) (Fig. 4.4a) suggest that the oscillations are caused by asymmetric loading of the two tail lobes. The role of MHD stability was investigated by Erkaev et al. (2009a, b, c). They concluded that MHD instability could result from local compression, when the gradient of B_z along the tail axis would become locally reversed, as illustrated in Fig. 4.4b. Such a configuration might be associated with the formation of a plasmoid but could also arise even prior to the onset of reconnection (see Fig. 4.2).

4.2.4 Conclusions

Strong thinning may occur as a nonlinear consequence of external forcing, as expected for the substorm growth phase, but is not restricted to growth phase. It is possibly further supported by extraction to the frontside supplying plasma to the dayside reconnection site. The relation between external deformations and local strong thinning supports the possibility of an external trigger but the exact relation remains unclear.

Thinning below ion inertia length, combined with B_z reduction, can ignite many modes almost simultaneously: tearing, etc.; ballooning does not require ion scales but may become destabilized through entropy diffusion when ions become decoupled from the field. There is no strong evidence for one mode driving another.

It is not clear whether flapping is an unstable mode or a stable wave activated by a strong perturbation, such as fast localized flow.

4.3 Onset Timing

This section is devoted particularly to the first results of the THEMIS mission on the timing of signatures surrounding substorm onset. The major goal of this mission is solving a controversy between two substorm onset paradigms depicted in Fig. 4.5, combined from two figures of Angelopoulos (2008). In the "Current Disruption Model" (Lui et al. 1990) (Fig. 4.5a) substorm onset is assumed as being initiated by a current-driven instability in the tail region of about 8–10R_E, causing a current reduction or disruption in this tail region with a diversion of current ("substorm current wedge", McPherron et al. 1973) to the Earth and through the ionosphere, associated with auroral breakup and intensification. A tail portion and indication of the current wedge is the "dipolarization" of the magnetic field. This means a returning from a stretched to a more dipole-like configuration, typically associated with an increase of B_z and a reduction of $|B_x|$. This dipolarization is often accompanied by magnetic fluctuations. In this paradigm, magnetic reconnection is considered a consequence of the current disruption, presumably initiated by a tailward propagating rarefaction wave.

In contrast, in the "Near-Earth Neutral Line Model" (Baker et al. 1996) (Fig. 4.5b) a substorm is initiated by the onset of reconnection in the tail, generating earthward plasma flow. The braking of this flow causes magnetic flux pileup, i.e. dipolarization (Hesse and Birn 1991), and the diversion or shear of the flow causes twist or shear of the magnetic field and thereby generates the field-aligned currents of the substorm current wedge (Birn and Hesse 1991; Keiling et al. 2009). The sequence depicted in (Fig. 4.5b) again assumes that aurora breakup is the consequence of current disruption and distortion in the tail. Considering the relation between the events in the tail, the two scenarios are often distinguished as "inside-out" versus "outside-in."

Rather than discussing individual events or papers, we here provide a summary of the observations. The conclusions from the early THEMIS observations (and a few other cases) are controversial. Whereas Angelopoulos et al. (2008, 2009), Gabrielse et al. (2008), Liu et al. (2008), Sergeev et al. (2008) and, to some extent, Mende et al. (2009) conclude consistency with the outside-in model, Liang et al. (2008), Donovan et al. (2009), Lui et al. (2008a, b), Rae et al. (2009a, b), Henderson (2009) infer consistency with the inside-out model. One might argue that the authors investigated different events, which may have had different signatures. However, other differences are more striking.

Conclusions from Liang et al. (2008), Rae et al. (2009a, b), Henderson (2009) are based entirely on ground observations, which consistently indicate auroral arc brightening as the earliest onset signature, followed by signatures at higher latitude. One must be careful, however, in interpreting poleward motion on the ground with tailward motion in the tail. For instance, when reconnection in the near tail proceeds from the central plasma sheet toward lobe field lines, the separatrix surface connected to the X-line would propagate poleward even when the X-line remains stagnant. This is a plausible interpretation for the poleward expansion of the auroral bulge, and perhaps for energetic particle injection signatures, which are also

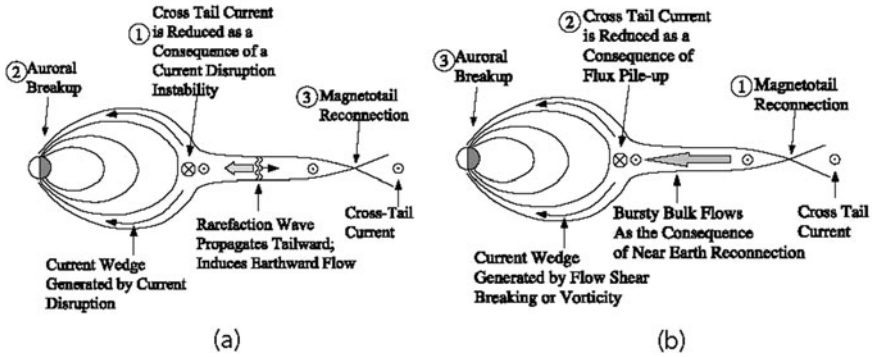

Fig. 4.5 Time sequence of events in two contrasting paradigms of substorm onset, (**a**) the current disruption model, (**b**) the near-Earth neutral line model. After Figs. 4 and 5 of Angelopoulos (2008)

found to propagate poleward (Spanswick et al. 2009). However, a magnetic connection between the early arc brightening and the reconnection site has not been established, and appears to be inconsistent with both the timing and the field line mapping. Ground observation also show that the onset arc commonly exhibits azimuthal structures (Liang et al. 2008; Rae et al. (2009a, b); Henderson 2009), which are most commonly interpreted as signatures of ballooning modes. It is not clear, however, whether these modes indicate the source mechanism of the arc or just provide additional structure.

Tail observations in Lui et al. (2008b) and Donovan et al. (2009) were made inside of $r \approx 10R_E$, where earlier observations already indicated tailward (and longitudinal) expansion of dipolarization signatures. In contrast, observations by Sergeev et al. (2008), made at a similar location, led to a different conclusion. We will return to a possible interpretation of this feature in Section 4.4.

That leaves Angelopoulos et al. (2008, 2009), Gabrielse et al. (2008), Liu et al. (2008), Mende et al. (2009) and Lui et al. (2008a) with observations in the tail beyond $\sim 15R_E$. The majority of these papers inferred consistency with the outside-in model. However, this result is also somewhat controversial (Lui 2009), mainly because the signatures taken as onset of reconnection are more subtle than, say, the onset of fast flow. This is related to the fact that, near substorm onset, typically the outermost THEMIS satellite(s) were located not in the central plasma sheet but closer to the boundary or even outside. The reconnection onset features considered include onset of energetic particle streams away from the inferred reconnection site and onset of magnetic flux transport toward the neutral sheet. Mende et al. (2009) infer an onset location of $11–17R_E$ distance, but do not identify this with the onset of reconnection.

Overall, the tail observations appear not consistent with the onset arc brightening being the consequence of current disruption (dipolarization) in the inner tail, as suggested by both, Fig. 4.5a, b. The arc brightening typically precedes the dipolarization, whether caused by current instability or flow braking. Furthermore, even though Angelopoulos et al. (2008), Gabrielse et al. (2008), Liu et al. (2008) infer reconnection onset times earlier than the onset arc brightening, the time difference appears too short for wave interaction between the reconnection site and the onset arc. Hence it is more likely that auroral breakup is the consequence of prior tail activity, such as waves generated in a thinning current sheet, kinetic properties of a thinning current sheet itself, or increased flow shear in the source region of the Harang discontinuity (Zou et al. 2009), which is presumably associated with the inner edge of the electron plasma sheet. Alternatively, or additionally, the breakup is related to instability onset in the auroral acceleration region under more gradually varying tail conditions.

If one accepts the signals identified as onset of reconnection in the tail, then dipolarization and the formation of the substorm current wedge may indeed be the consequence of reconnection as postulated in the outside-in model. This is supported by the fact that many of the dipolarization events observed in the near tail are associated with fast earthward flow (see also Section 4.4). However, this conclusion is still controversial because of the frequent occurrence of multiple activations, unknown relation to ground signatures, and the fact that the distant THEMIS satellites typically are outside of the central plasma sheet at substorm onset.

4.4 Bursty Bulk Flows and Dipolarization

In Section 4.3 we already discussed dipolarization in the near magnetotail as a signature associated with substorm onset. This signature is frequently, but not always, accompanied by earthward convective flows or BBFs. In this section we further review results on flow bursts (BBFs) and dipolarization.

4.4.1 Observations

Several papers demonstrated characteristic temporal and spatial differences between both, flows and dipolarization events, in the near tail at, say, $8–10R_E$, and further out. On the basis of two years of Geotail statistics, Shue et al. (2008) found that fast earthward convective flows (i.e. flows with a significant velocity component perpendicular to the magnetic field) can be classified into two classes. Class I, typically observed near $x = -10R_E$, was characterized by high auroral power rates and significant global auroral substorm development. Class II flows, found at $x < -15R_E$,

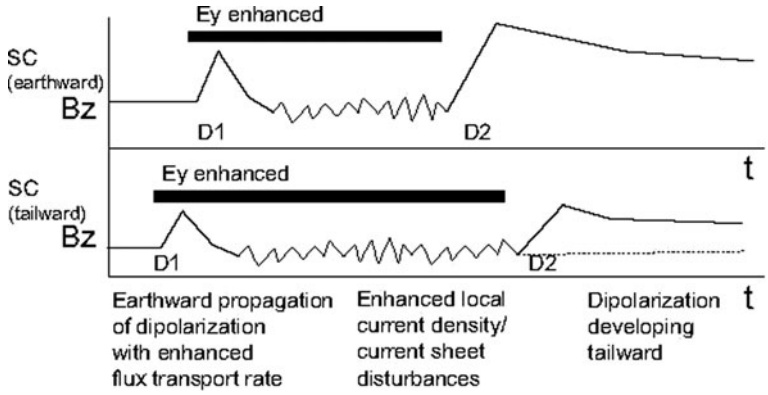

Fig. 4.6 Schematic representation of virtual spacecraft observations separated in x (fast flow direction) describing the two different types of dipolarization. After Nakamura et al. (2009)

were typically associated with low auroral power rates and moderate auroral features such as poleward boundary intensifications (PBIs) and pseudobreakups. Some of the earthward fast flows in this class, however, were able to propagate farther earthward and provide a favorable condition for substorm onset, leading to an auroral bulge development on the nightside. Zhang et al. (2009) found a minimum of occurrence frequency of earthward convective flow bursts near $x = -11.5R_E$ and suggested two different source mechanisms for earthward bursts inside and outside of that location.

Nakamura et al. (2009), using Cluster observations, found that dipolarization events tend to consist of two types or two phases, illustrated in Fig. 4.6: (1) an earthward moving dipolarization pulse, accompanied by rapid earthward flux transport, followed by current sheet disturbances with a decrease in B_z and enhanced local current density, and (2) subsequent increase in B_z toward a more stable level. The latter is more prominent closer to Earth and evolves tailward. A nice example of an earthward propagating dipolarization pulse or front observed by all five THEMIS satellites is shown in Fig. 4.7, modified from Fig. 1 of Runov et al. (2009b). In this event the dipolarization front was observed near the rise of fast earthward flow at all satellites.

Earthward moving fast flow bursts or BBFs are commonly interpreted as "bubbles," that is, magnetic flux tubes or ropes of reduced entropy content in comparison to the surrounding field (Pontius and Wolf 1990; Chen and Wolf 1993). The relationship between BBFs and dipolarization fronts is illustrated in Fig. 4.8, taken from Walsh et al. (2009). Magnetic flux in front of the bubble (gray) is piled up (yellow region) causing an increase in B_z. As the bubble moves earthward this

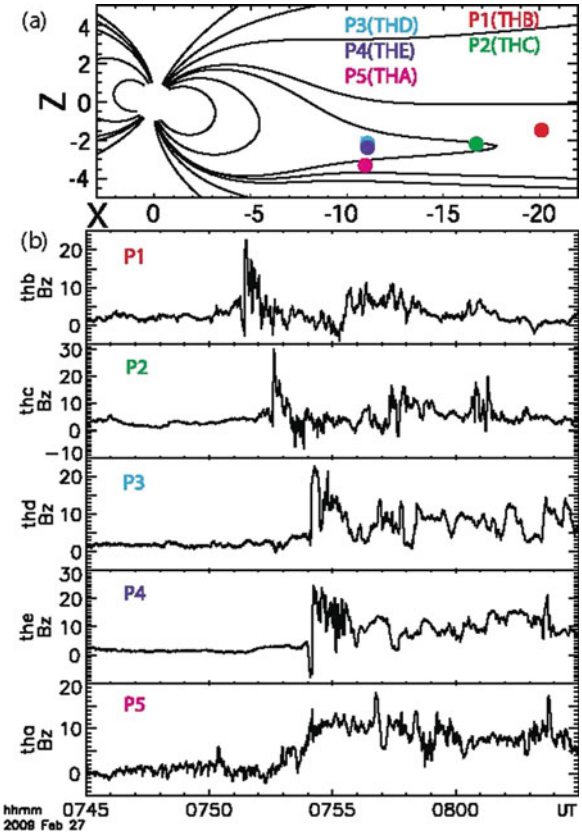

Fig. 4.7 Earthward propagating dipolarization front: (**a**) THEMIS SC positions in the x, z plane with the T96-model magnetic field (Tsyganenko 1995); (**b**) time series of B_z (GSM) at all five probes (P1–P5). Modified after Runov et al. (2009b)

front moves with it. Eventually the earthward flow is stopped and a different type of pile-up takes place with a tailward expansion, as illustrated in Fig. 4.6. Vorticity on the outside of the fast earthward flow may cause magnetic field shear or twist, creating a field-aligned

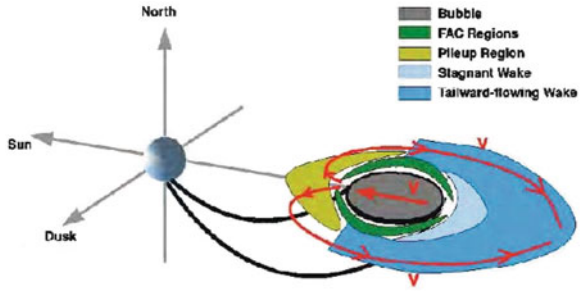

Fig. 4.8 Equatorial cut of the morphology of a plasma bubble; after Walsh et al. (2009). The region of flux and plasma pileup in front of the bubble is in *yellow*, the bubble itself is *gray*, the stagnant and tailward flowing wakes lighter and darker blues, respectively, and the field-aligned current regions green. Flow velocity is marked by the *red arrows*

current system similar to the substorm current wedge (Birn et al. 2004) (green), and may lead to large v_y near the front of the bubble as well as tailward flows on the outside (Dmitrieva 2008; Sharma et al. 2008; Walsh et al. 2009). In addition, tailward and azimuthal flow may also result from a rebound of the earthward flow (Ohtani et al. 2009). Flow characteristics during different phases of substorms do not differ strongly, although the flows tend to be slower, carrying more tenuous plasma, during the recovery phase (Ma et al. 2009).

Earthward moving dipolarization pulses are often preceded by a brief dip in B_z, sometimes even turning negative (Ohtani et al. 2004; Sharma et al. 2008; Sitnov et al. 2009). Such dips are shown, for instance, by P1 and P4 in Fig. 4.7. The mechanism for creating these dips is not clear. Negative B_z could possibly be created by small islands earthward of the X-line (Schindler 1974) or a bulge in the field ejected earthward from the X-line (Sergeev et al. 1992). Earthward moving flux ropes (with south-north structure of B_z) have indeed been found in several investigations (Hasegawa et al. 2007; Zhang et al. 2007; Walsh et al. 2007; Juusola et al. 2008), indicative of multiple X-line reconnection often with strong core fields in the y direction.

4.4.2 Source Mechanism

The most commonly considered mechanism for the generation of a depleted flux tube or bubble is magnetic reconnection in the tail, as illustrated by Fig. 4.9, after Forsyth et al. (2008). The reduction of the flux tube content simply results from the severance of a plasmoid (Birn et al. 2009; Wing and Johnson 2009). Further reduction, however, might occur when lobe field lines with lower plasma content and pressure reconnect. Such uneven filling might also occur at a distant reconnection site (Zesta et al. 2006). As

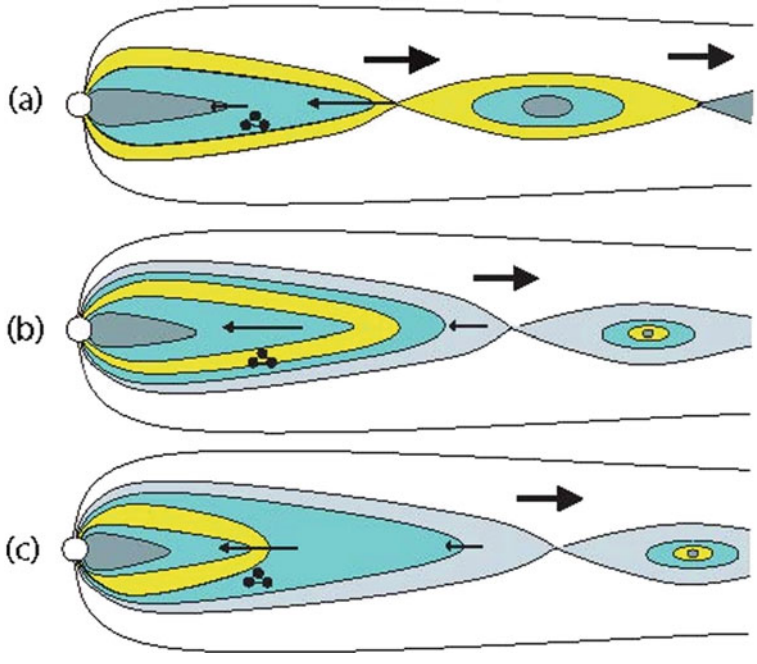

Fig. 4.9 A series of diagrams depicting the generation of a BBF by open field line reconnection as inferred from Cluster observations; modified after Forsyth et al. (2008). The colors represent different ion densities, and the three-dot symbol indicates the location of the Cluster satellites for the event investigated. Panels (**a**–**c**) correspond to panels (**e**–**g**) of the original figure. They illustrate the earthward collapse of an underpopulated flux tube or BBF (*yellow*) together with the tailward retreat of a plasmoid

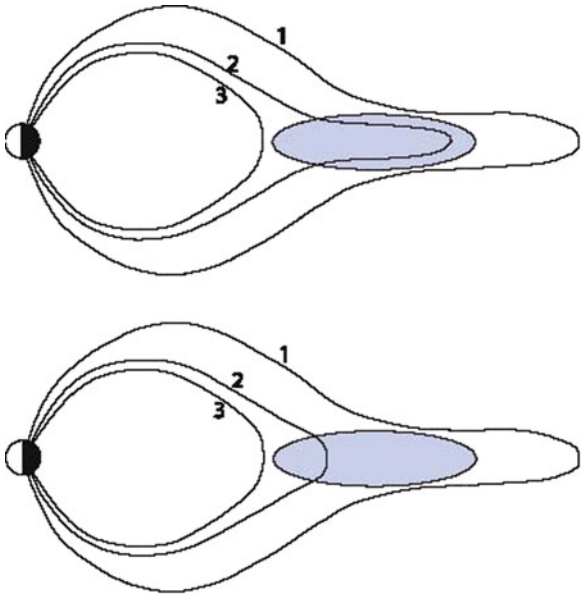

Fig. 4.10 Schematic illustrating creation of an underpopulated flux tube or BBF from *field* line slippage. After Wolf et al. (2009)

pointed out by Wolf et al. (2009), a slippage of field lines, resulting from a local breakdown of the frozen-in approximation of ideal MHD, would also result in a bubble of reduced plasma and entropy content. This is illustrated in Fig. 4.10 taken from Wolf et al. (2009).

MHD simulations have confirmed that the reduction of the entropy content is a crucial element in permitting the earthward motion of a bubble, and the amount of depletion determines how close to Earth a bubble can penetrate (Chen and Wolf 1999; Birn et al. 2009; Wolf et al. 2009). In addition, the entropy reduction also affects the stability (Section 4.2.2): A wider bubble might break up into parts from ballooning instability (Birn et al. 2009), which affects cross-tail structure and possibly also the fate of bubbles.

In a mechanism akin to the substorm current wedge (Birn and Hesse 1991; Keiling et al. 2009), flow shear or vorticity on the outside of the bubble also creates a shear or twist of the magnetic field associated with field-aligned currents (green areas in Fig. 4.8). In a quasi-steady picture the same kind of current system can be inferred from current continuity combined with a reduction of cross-tail current inside the bubble (Chen and Wolf 1993; Wolf et al. 2009). These currents, which have the same direction as those associated with the substorm current wedge, provide the connection with the ionosphere and are presumably the source of auroral streamers or PBIs (Birn et al. 2004, 2009; Sharma et al. 2008; Wolf et al. 2009).

4.4.3 Conclusions

Cluster and THEMIS observations have demonstrated a close association between earthward flow bursts and dipolarization events, apparently characterized by two stages:

Further out they consist of earthward moving "dipolarization fronts" driven by earthward flow. The increase of B_z may be understood as a "snow plow" effect at the front of these flows.

A different kind of magnetic flux "pile-up" occurs in the braking region near $10R_E$. In contrast to the earthward propagating fronts farther out, this dipolarization is more permanent and may expand tailward. This braking may also involve rebounce with tailward and azimuthal flows.

In the interpretation given above the two types are different stages of the same kind of event. In contrast, in the current disruption paradigm, the second kind of event may be considered as a different type, resulting from local current-driven instability, rather than flow braking.

Bubbles of BBFs are associated with a diversion of currents similar to the sub-storm current wedge, providing a connection to the ionosphere via field-aligned currents, presumably causing PBIs or auroral streamers. The generation mechanisms can be understood, in time dependent view, as a twisting of magnetic flux tubes by velocity shear on the outside of a bubble. In a quasi-steady picture the same kind of current system can be attributed to current continuity combined with a reduction of cross-tail current inside the bubble.

4.5 Summary and Conclusions

In this review we have discussed three topics which are crucial elements of magnetotail activity: the formation and stability of thin current sheets, the timing of events at substorm onset, and the properties of bursty bulk flows and dipolarization events. Based on a survey of two years of publications (complemented by some earlier results), we have come to the following conclusions.

4.5.1 Formation and Stability of Thin Current Sheets

Forced current sheet thinning is a plausible mechanism for the onset of current sheet activity. Thinning from compression is possibly accompanied by plasma extraction to the dayside, providing inflow to dayside reconnection. A close relation to external perturbations has been shown but the viability of triggering by a sudden northward turning of the IMF has not been demonstrated.

The reduction of B_z, which accompanies the increase of j_y and the reduction of current sheet thickness, eases the onset of tearing instability and reconnection. However, several other instabilities can be ignited nearly simultaneously. There is no clear evidence for one driving another. Ballooning instability can, in principle, be initiated before ion scales are approached. However, changing ballooning stability by adiabatic processes appears difficult.

4.5.2 Substorm Onset Timing

The timing of the onset of reconnection in relation to dipolarization and initial auroral arc brightening is still a matter of debate. Main reasons are the frequent occurrence of multiple activations and the fact that the signatures taken as indicating initial reconnection onset are more subtle than commonly expected. However, several other conclusions can be drawn from the THEMIS studies:

Initial auroral breakup cannot be the consequence of dipolarization (current disruption) and the formation of the substorm current wedge in the near tail. The timing of events also makes it unlikely that the arc brightening is related to the onset of reconnection. One therefore has to look for tail features preceding reconnection and dipolarization.

Possible tail mechanisms related to the arc brightening include prior wave activity and/or other properties associated with the formation of a thin current sheet in the late substorm growth phase, particularly, the generation of potential differences across field lines and the increase of field-aligned currents. Since these features apparently do not exhibit sudden onsets in the tail, the rapid brightening may be more closely related to a sudden increase of dissipation in the auroral acceleration region associated with the build-up of the parallel electric field.

4.5.3 BBFs and Dipolarization

New observations have established a strong relationship between earthward flows and dipolarization signals with a characteristic spatial and temporal change from earthward propagation further tailward to rebounce and tailward expansion in the stopping region closer to Earth. This supports the view that reconnection in the tail causes earthward flows, dipolarization, and the substorm current wedge, but not the opposite.

Many earthward flow bursts do not penetrate close enough to Earth to cause substorm features, but they generate pseudo breakups and PBIs. Apparently, the penetration depends on the amount of depletion of bubbles. In the reconnection scenario this depends on whether reconnection proceeds to the lobes, which should result in stronger depletion. But it is unclear what governs how far reconnection proceeds.

Acknowledgements This work was performed under the auspices of the U.S. Department of Energy, supported by grants from NASA's MMS/SMART, Heliophysics Theory, and SR&T Programs.

References

Angelopoulos V (2008) The THEMIS mission. Space Sci Rev 141:5

Angelopoulos V, Baumjohann W, Kennel CF, Coroniti FV, Kivelson MG, Pellat R, Walker RJ, Lühr H, Paschmann G (1992) Bursty bulk flows in the inner central plasma sheet. J Geophys Res 97:4027

Angelopoulos V, Kennel CF, Coroniti FV, Pellat R, Kivelson MG, Walker RJ, Russell CT, Baumjohann W, Feldman WC, Gosling JT (1994) Statistical characteristics of bursty bulk flow events. J Geophys Res 99:21257

Angelopoulos V, McFadden JP, Larson D, Carlson CW, Mende SB, Frey H, Phan T, Sibeck DG, Glassmeier KH, Auster U, Donovan E, Mann IR, Rae IJ, Russell CT, Runov A, Zhou XZ, Kepko L (2008) Tail reconnection triggering substorm onset. Science 321:931

Angelopoulos V, McFadden JP, Larson D, Carlson CW, Mende SB, Frey H, Phan T, Sibeck DG, Glassmeier KH, Auster U, Donovan E, Mann IR, Rae IJ, Russell CT, Runov A, Zhou XZ, Kepko L (2009) Response to comment on "tail reconnection triggering substorm onset". Science 324:1391

Artemyev AV, Petrukovich AA, Zelenyi LM, Malova HV, Popov VY, Nakamura R, Runov A, Apatenkov S (2008) Comparison of multi-point measurements of current sheet

structure and analytical models. Ann Geophys 26(9):2749. http://www.anngeophys.net/26/2749/2008/
Baker DN, Pulkkinen TI, Angelopoulos V, Baumjohann W, McPherron RL (1996) Neutral line model of substorms: past results and present view. J Geophys Res 101:12975
Baumjohann W, Paschmann G, Lühr H (1990) Characteristics of high-speed ion flows in the plasma sheet. J Geophys Res 95:3801
Baumjohann W, Roux A, Le Contel O, Nakamura R, Birn J, Hoshino M, Lui ATY, Owen CJ, Sauvaud JA, Vaivads A, Fontaine D, Runov A (2007) Dynamics of thin current sheets: Cluster observations. Ann Geophys 25(6):1365. http://www.ann-geophys.net/25/1365/2007/
Birn J, Hesse M (1991) The substorm current wedge and field-aligned currents in MHD simulations of magnetotail reconnection. J Geophys Res 96:1611
Birn J, Schindler K (2002) Thin current sheets in the magnetotail and the loss of equilibrium. J Geophys Res 107:SMP18. doi:10.1029/2001JA0291
Birn J, Raeder J, Wang YL, Wolf RA, Hesse M (2004) On the propagation of bubbles in the geomagnetic tail. Ann Geophys 22:1773
Birn J, Hesse M, Schindler K, Zaharia S (2009) Role of entropy in magnetotail dynamics. J Geophys Res 114:A00D03. doi:10.1029/2008JA014015
Cai CL, Dandouras I, Rème H, Cao JB, Zhou GC, Parks GK (2008) Cluster observations on the thin current sheet in the magnetotail. Ann Geophys 26(4):929. http://www.ann-geophys.net/26/929/2008/
Chen CX, Wolf RA (1993) Interpretation of high-speed flows in the plasma sheet. J Geophys Res 98:21409
Chen CX, Wolf RA (1999) Theory of thin-fllament motion in earth's magnetotail and its application to bursty bulk flows. J Geophys Res 104:14613
Coppi B, Laval G, Pellat R (1966) Dynamics of the geomagnetic tail. Phys Rev Lett 16:1207
Dmitrieva NP (2008) Cross-tail velocity component in the plasma sheet fast flows. Ann Geophys 26(6):1597. http://www.anngeophys.net/26/1597/2008/
Donovan E, Liu W, Liang J, Spanswick E, Voronkov I, Connors M, Syrjäsuo M, Baker G, Jackel B, Trondsen T, Greffen M, Angelopoulos V, Russell CT, Mende SB, Frey HU, Keiling A, Carlson CW, McFadden JP, Glassmeier KH, Auster U, Hayashi K, Sakaguchi K, Shiokawa K, Wild JA, Rae IJ (2009) Simultaneous THEMIS in situ and auroral observations of a small substorm. Geophys Res Lett 35:L17S18. doi:10.1029/2008GL033794
Erkaev NV, Semenov VS, Biernat K (2009a) Magnetic double gradient mechanism for flapping oscillations of a current sheet. Geophys Res Lett 35:L02111. doi:10.1029/2007GL032277
Erkaev NV, Semenov VS, Kubyshkin IV, Kubyshkina MV, Biernat HK (2009b) MHD model of the flapping motions in the magnetotail current sheet. J Geophys Res 114:A03206. doi:10.1029/2008JA013728
Erkaev NV, Semenov VS, Kubyshkin IV, Kubyshkina MV, Biernat HK (2009c) MHD aspect of current sheet oscillations related to magnetic field gradients. Ann Geophys 27(1):417. http://www.ann-geophys.net/27/417/2009/
Escoubet CP, Fehringer M, Goldstein M (2001) The cluster mission. Ann Geophys 19(10/12), 1197–1200. doi:10.5194/angeo-19-1197-2001. http://www.ann-geophys.net/19/1197/2001/
Forsyth C, Lester M, Cowley SWH, Dandouras I, Fazakerley AN, Fear RC, Frey HU, Grocott A, Kadokura A, Lucek E, Rème H, Milan SE, Watermann J (2008) Observed tail current systems associated with bursty bulk flows and auroral streamers during a period of multiple substorms. Ann Geophys 26(1):167. http://www.ann-geophys.net/26/167/2008/
Gabrielse C, Angelopoulos V, Runov A, Kepko L, Glassmeier KH, Auster HU, McFadden J, Carlson CW, Larson D (2008) Propagation characteristics of plasma sheet oscillations during a small storm. Geophys Res Lett 35:L17S13. doi:10.1029/2008GL033664
Galeev AA, Zelenyi LM (1976) Tearing instability in plasma configurations. Sov Phys JETP Engl Transl 43:1113
Haijima K, Tanaka K, Fujimoto M, Shinohara I (2008) Electron temperature anisotropy effects on tearing mode in ion-scale current sheets. Adv Space Res 41:1643
Hasegawa H, Nakamura R, Fujimoto M, Sergeev VA, Lucek EA, Rème H, Khotyaintsev Y (2007) Reconstruction of a bipolar magnetic signature in an earthward jet in the tail: flux rope or 3D guide-field reconnection? J Geophys Res 112:A11206. doi:10.1029/2007JA012492
Henderson MG (2009) Observational evidence for an inside-out substorm onset scenario. Ann Geophys 27(5):2129. http://www.anngeophys.net/27/2129/2009/
Hesse M, Birn J (1991) On dipolarization and its relation to the substorm current wedge. J Geophys Res 96:19417
Israelevich PL, Ershkovich AI (2008) Bifurcation of the tail current sheet and ion temperature anisotropy. Ann Geophys 26(7):1759. http://www.anngeophys.net/26/1759/2008/
Israelevich PL, Ershkovich AI, Oran R (2008) Current carriers in the bifurcated tail current sheet: ions or electrons? J Geophys Res 113:A04215. doi:10.1029/2007JA012541
Juusola L, Amm O, Frey HU, Kauristie K, Nakamura R, Owen CJ, Sergeev V, Slavin JA, Walsh A (2008) Ionospheric signatures during a magnetospheric flux rope event. Ann Geophys 26(12):3967. http://www.anngeophys.net/26/3967/2008/87
Keiling A, Angelopoulos V, Runov A, Weygand J, Apatenkov SV, Mende S, McFadden J, Larson D, Amm O, Glassmeier KH, Auster HU (2009) Substorm current wedge driven by plasma flow vortices: THEMIS observations. J Geophys Res 114:A00C22. doi:10.1029/2009JA014114
Lapenta G, King J (2007) Study of current intensification by compression in the Earth magnetotail. J Geophys Res 112:A12204. doi:10.1029/2007JA012527
Liang J, Donovan EF, Liu WW, Jackel B, Syrjasuo M, Mende SB, Frey HU, Angelopoulos V, Connors M (2008) Intensification of preexisting auroral arc at substorm expansion phase onset: wave-like disruption during the first tens of seconds. Geophys Res Lett 35:L17S19. doi:10.1029/2008GL033666
Liu WW, Liang J (2009) Disruption of magnetospheric current sheet by quasi-electrostatic field. Ann Geophys 27(5):1941. http://www.anngeophys.net/27/1941/2009/
Liu WW, Liang J, Donovan EF (2008) Interaction between kinetic ballooning perturbation and thin current sheet: Quasi-electrostatic field, local onset, and global characteristics. Geophys Res Lett 35:L20107. doi:10.1029/2008GL035757

Lui ATY (2009) Comment on "tail reconnection triggering substorm onset" Science 324:1391

Lui ATY, Mankofsky A, Chang C, Papadopoulos K, Wu CS (1990) A current disruption mechanism in the neutral sheet: a possible trigger for substorm expansions. Geophys Res Lett 17:745

Lui ATY, Angelopoulos V, LeContel O, Frey H, Donovan E, Sibeck DG, Liu W, Auster HU, Larson D, Li X, Nosé M, Fillingim MO (2008a) Determination of the substorm initiation region from a major conjunction interval of THEMIS satellites. J Geophys Res 113:A00C04. doi:10.1029/2008JA013424

Lui ATY, Volwerk M, Dunlop MW, Alexeev IV, Fazakerley AN, Walsh AP, Lester M, Grocott A, Mouikis C, Henderson MG, Kistler LM, Shen C, Shi JK, Zhang TL, H. Rème (2008b) Near-Earth substorm features from multiple satellite observations. J Geophys Res 113:A07S26. doi:10.1029/2007JA012738

Lui ATY, Yoon PH, Mok C, Ryu CM (2008c) Inverse cascade feature in current disruption. J Geophys Res 113:A00C06. doi:10.1029/2008JA013521

Ma YD, Cao JB, Nakamura R, Zhang TL, Rème H, Dandouras I, Lucek E, Dunlop M (2009) Statistical analysis of earthward flow bursts in the inner plasma sheet during substorms. J Geophys Res 114:A07215. doi:10.1029/2009JA014275

Malova HV, Zelenyi LM, Popov VY, Delcourt DC, Petrukovich AA, Runov AV (2007) Asymmetric thin current sheets in the earth's magnetotail. Geophys Res Lett 34:L16108. doi:10.1029/2007GL030011

Matsui T, Daughton W (2008) Kinetic theory and simulation of collisionless tearing in bifurcated current sheets. Phys Plasmas 15:012901

McPherron RL, Russell CT, Aubry MA (1973) Satellite studies of magnetospheric substorms on August 15, 1968, 9, phenomenological model for substorms. J Geophys Res 78:3131

Mende S, Angelopoulos V, Frey HU, Donovan E, Jackel B, Glassmeier KH, Mc-Fadden JP, Larson D, Carlson CW (2009) Timing and location of substorm onsets from themis satellite and ground based observations. Ann Geophys 27(7):2813. http://www.anngeophys.net/27/2813/2009/

Miura A (2007) A magnetospheric energy principle for hydromagnetic stability problems. J Geophys Res 112:A06234. doi:10.1029/2006JA011992

Miura A (2009) Pressure-driven and ionosphere-driven modes of magnetospheric interchange instability. J Geophys Res 114:A02224. doi:10.1029/2008JA013663

Nakamura R, Retin A, Baumjohann W, Volwerk M, Erkaev N, Klecker B, Lucek EA, Dandouras I, Andr M, Khotyaintsev Y (2009) Evolution of dipolarization in the near-earth current sheet induced by Earthward rapid flux transport. Ann Geophys 27(4):1743. http://www.ann-geophys.net/27/1743/2009/

Ohtani S, Miyashita Y, Singer H, Mukai T (2009) Tailward flows with positive bz in the near-Earth plasma sheet. J Geophys Res 114:A06218. doi:10.1029/2009JA014159

Ohtani SI, Shay MA, Mukai (2004) Temporal structure of the fast convective flow in the plasma sheet: comparison between observations and two-fluid simulations. J Geophys Res 109:A03210. doi:10.1029/2003JA010002

Pellat R, Coroniti FV, Pritchett PL (1991) Does ion tearing exist? Geophys Res Lett 18:143

Petrukovich AA, Baumjohann W, Nakamura R, Runov A (2008) Formation of current density profile in tilted current sheets. Ann Geophys 26(12):3669. http://www.ann-geophys.net/26/3669/2008/

Pontius DH Jr, Wolf RA (1990) Transient flux tubes in the terrestrial magnetosphere. Geophys Res Lett 17:49

Rae IJ, Mann IR, Murphy KR, Milling DK, Parent A, Angelopoulos V, Frey HU, Kale A, Watt CEJ, Mende SB, Russell CT (2009a) Timing and localization of ionospheric signatures associated with substorm expansion phase onset. J Geophys Res 114:A00C09. doi:10.1029/2008JA013559

Rae IJ, Mann IR, Angelopoulos V, Murphy KR, Milling DK, Kale A, Frey HU, Rostoker G, Russell CT, Watt CEJ, Engebretson MJ, Moldwin MB, Mende SB, Singer HJ, Donovan EF (2009b) Near-earth initiation of a terrestrial substorm. J Geophys Res 114:A07220. doi:10.1029/2008JA013771

Runov A, Angelopoulos V, Sergeev VA, Glassmeier KH, Auster U, McFadden J, Larson D, Mann I (2009a) Global properties of magnetotail current sheet flapping: themis perspectives. Ann Geophys 27(1):319. http://www.anngeophys.net/27/319/2009/

Runov A, Angelopoulos V, Sitnov MI, Sergeev VA, Bonnell J, McFadden JP, Larson D, Glassmeier K, Auste U (2009b) THEMIS observations of an earthward propagating dipolarization front. Geophys Res Lett 36:L14106. doi:10.1029/2009GL038980

Saito MH, Miyashita Y, Fujimoto M, Shinohara I, Saito Y, Mukai T (2008a) Modes and characteristics of low-frequency MHD waves in the near-Earth magnetotail prior to dipolarization: fitting method. J Geophys Res 113:A06201. doi:10.1029/2007JA012778

Saito MH, Miyashita Y, Fujimoto M, Shinohara I, Saito Y, Mukai T (2008b) Ballooning mode waves prior to substorm-associated dipolarizations: geotail observations. Geophys Res Lett 35:L07103. doi:10.1029/2008GL033269

Schindler K (1974) A theory of the substorm mechanism. J Geophys Res 79:2803

Schindler K (2007) Space plasma activity. Cambridge University Press, Cambridge, England

Schindler K, Birn J (2002) Models of two-dimensional embedded thin current sheets from Vlasov theory. J Geophys Res 107:SMP20. doi:10.1029/2001JA000304

Schindler K, Hesse M (2008) Formation of thin bifurcated current sheets by quasisteady compression. Phys Plasmas 15:042902

Sergeev V, Elphic RC, Mozer FS, Saint-Marc A, Sauvaud JA (1992) A two-satellite study of nightside flux transfer events in the plasma sheet. Planet Space Sci 40:15511572

Sergeev VA, Sormakov DA, Apatenkov SV, Baumjohann W, Nakamura R, Runov AV, Mukai T, Nagai T (2006) Survey of large-amplitude flapping motions in the mid-tail current sheet. Ann Geophys 24(7):2015. http://www.anngeophys.net/24/2015/2006/

Sergeev V, Kubyshkina M, Alexeev I, Fazakerley A, Owen C, Baumjohann W, Nakamura R, Runov A, Vörös Z, Zhang TL, Angelopoulos V, Sauvaud JA, Daly P, Cao JB, Lucek E (2008) J Geophys Res 113:A07S36. doi:10.1029/2007JA012902

Sharma AS, Nakamura R, Runov A, Grigorenko EE, Hasegawa H, Hoshino M, Louarn P, Owen CJ, Petrukovich A, Sauvaud

JA, Semenov VS, Sergeev VA, Slavin JA, Sonnerup BU, Zelenyi LM, Fruit G, Haaland S, Malova H, Snekvik K (2008) Transient and localized processes in the magnetotail: a review. Ann Geophys 26(4):955. http://www.ann-geophys.net/26/955/2008/

Shen C, Rong ZJ, Li X, Dunlop M, Liu ZX, Malova HV, Lucek E, Carr C (2008) Magnetic configurations of the tilted current sheets in magnetotail. Ann Geophys 26(11):3525. http://www.ann-geophys.net/26/3525/2008/

Shue JH, Ieda A, Lui ATY, Parks GK, Mukai T, Ohtani S (2008) Two classes of earthward fast flows in the plasma sheet. J Geophys Res 113:A02205. doi:10.1029/2007JA012456

Sitnov MI, Guzdar PN, Swisdak M (2003) A model of the bifurcated current sheet. Geophys Res Lett 30:L1712. doi:10.1029/2003GL017218

Sitnov MI, Swisdak M, Divin AV (2009) Dipolarization fronts as a signature of transient reconnection in the magnetotail. J Geophys Res 114:A04202. doi:10.1029/2008JA013980

Spanswick E, Donovan E, Liu W, Liang J, Blake JB, Reeves G, Friedel R, Jackel B, Cully C, Weatherwax A (2009) Global observations of substorm injection region evolution: 27 August 2001. Ann Geophys 27(5):2019. http://www.anngeophys.net/27/2019/2009/

Steinhauer LC, McCarthy MP, Whipple EC (2008) Multifiuid model of a one-dimensional steady state magnetotail current sheet. J Geophys Res 111:A04207. doi:10.1029/2007JA012578

Takada T, Nakamura R, Asano Y, Baumjohann W, Runov A, Volwerk M, Zhang T, Vös Z, Keika K, Klecker B, Reme H, Lucek E, Carr C, Frey H (2008) Plasma sheet oscillations and their relation to substorm development: cluster and double star TC1 case study. Adv Space Res 41:1585

Tsyganenko NA (1995) Modeling the earth's magnetospheric magnetic field confined within a realistic magnetopause. J Geophys Res 100:5599–5612

Walsh AP, Fazakerley AN, Wilson RJ, Alexeev IV, Henderson PD, Owen CJ, Lucek E, Carr C, Dandouras I (2007) Near-simultaneous magnetotail flux rope observations with cluster and double star. Ann Geophys 25(8):1887. http://www.anngeophys.net/25/1887/2007/

Walsh AP, Fazakerley AN, Lahiff AD, Volwerk M, Grocott A, Dunlop MW, Lui ATY, Kistler LM, Lester M, Mouikis C, Pu Z, Shen C, Shi J, Taylor MGGT, Lucek E, Zhang TL, Dandouras I (2009) Cluster and double star multipoint observations of a plasma bubble. Ann Geophys 27(2):725. http://www.anngeophys.net/27/725/2009/

Wing S, Johnson JR (2009) Substorm entropies. J Geophys Res 114:A00D07. doi:10.1029/2008JA013989

Wolf RA, Wan Y, Xing X, Zhang JC, Sazykin S (2009) Entropy and plasma sheet transport. J Geophys Res 114:A00D05. doi:10.1029/2009JA014044

Xing X, Wolf RA (2007) Criterion for interchange instability in a plasma connected to a conducting ionosphere. J Geophys Res 112:A12209. doi:10.1029/2007JA012535

Yoon PH, Lui ATY, Bonnell JW (2009) Identification of plasma instability from wavelet spectra in a current disruption event. J Geophys Res 114:A04207. doi:10.1029/2008JA013816

Zelenyi LM, Sitnov MI, Malova HV, Sharma AS (2000) Thin and superthin ion current sheets. quasi-adiabatic and nonadiabatic models. Nonlin Processes Geophys 7:127. http://www.nonlin-processes-geophys.net/7/127/2000/

Zelenyi LM, Malova HV, Popov VY, Delcourt D, Sharma AS (2004) Nonlinear equilibrium structure of thin currents sheets: influence of electron pressure anisotropy. Nonlin Processes Geophys 11:579587

Zelenyi L, Artemiev A, Malova H, Popov V (2008) Marginal stability of thin current sheets in the earth's magnetotail. JASTP 70:325

Zesta E, Lyons L, Wang CP, Donovan E, Frey H, Nagai T (2006) Auroral poleward boundary intensifications (PBIs): their two-dimensional structure and associated dynamics in the plasma. J Geophys Res 111:A05201. doi:10.1029/2004JA010640

Zhang YC, Liu ZX, Shen C, Fazakerley A, Dunlop M, Rème H, Lucek E, Walsh AP, Yao L (2007) The magnetic structure of an earthward-moving flux rope observed by cluster in the near-tail. Ann Geophys 25(7):1471. http://www.ann-geophys.net/25/1471/2007/

Zhang LQ, Liu ZX, Baumjohann W, Ma ZW, Pu ZY, Dunlop MW, Lu L, Shi JK, Carr C, Rème H, Wang JY (2009) Convective bursty flows in the near-earth magnetotail inside 13 re. J Geophys Res 114:A02202. doi:10.1029/2008JA013125

Zhou XZ, Angelopoulos V, Runov A, Sitnov MI, Coroniti F, Pritchett P, Pu ZY, Zong QG, McFadden JP, Larson D, Glassmeier KH (2009) Thin current sheet in the sub-storm late growth phase: modeling of THEMIS observations. J Geophys Res 114:A03223. doi:10.1029/2008JA013777

Zou S, Lyons LR, Wang CP, Boudouridis A, Ruohoniemi JM, Anderson PC, Dyson PL, Devlin JC (2009) On the coupling between the harang reversal evolution and substorm dynamics: A synthesis of SuperDARN, DMSP, and IMAGE observations. J Geophys Res 114:A01205. doi:10.1029/2008JA013449

Physical Processes for Magnetospheric Substorm Expansion Onsets

5

Anthony T.Y. Lui

Abstract

A major challenge in magnetospheric research is to identify the physical processes for magnetospheric substorm expansion onsets. Recent abundance of observations from Geotail, Cluster, and Themis missions has added impetus to substorm research. Observations that are linked to substorm expansion onsets are discussed. Topics encompassed in this review are (1) the external conditions in the solar wind for substorm onset, (2) observations prior to onset, (3) observations immediately after onset, (4) time history approach, and (5) system-wide approach that can reveal general characteristics of the physical processes for onset. The implications for the substorm onset processes are discussed based on these observations.

5.1 Introduction

Plasmas in the near-earth space environment exhibit a rich variety of phenomena that challenge our ability to comprehend the underlying physical processes. The space plasma phenomena that arguably attract the most attention in the space plasma community are those associated with magnetospheric substorm expansion onset. The substorm concept was introduced through observations compiled from a network of ground-based all-sky-cameras to construct the evolution of a global auroral pattern in the polar region during this episodic disturbance (Akasofu 1964). This concept was developed with the guidance of the late Sydney Chapman and the term 'substorm' is meant to imply that it is an elementary building block for a geomagnetic storm that causes worldwide depression of the geomagnetic field on the ground. Shortly after the inception of this concept, disturbances throughout the ionosphere and the magnetosphere were recognized to be manifestation of a substorm in the near-earth space (Akasofu 1968). Since then, identifying the physical processes responsible for a substorm expansion onset becomes arguably the 'holy grail' of magnetospheric physics and remains to be one of the most controversial issues in magnetospheric research.

A brief review of substorm expansion onset phenomena is in order for better understanding of the topic and appreciation on how some controversies arise. There is a general consensus that the episodic substorm cycle consists of three phases, namely, growth, expansion, and recovery (Akasofu 1964; McPherron 1970). The growth phase pertains to the period in which energy is accumulated gradually in the magnetosphere. Research on the physical processes for substorm onset is implicitly on the onset of the expansion

A.T.Y. Lui (✉)
Applied Physics Laboratory, The Johns Hopkins University, Laurel, MD, USA
e-mail: tony.lui@jhuapl.edu

W. Liu, M. Fujimoto (eds.), *The Dynamic Magnetosphere*, IAGA Special Sopron Book Series 3,
DOI 10.1007/978-94-007-0501-2_5, © Springer Science+Business Media B.V. 2011

phase that exhibits a sudden release of energy in the magnetosphere. Hereafter, substorm onset refers to the substorm expansion onset unless specified otherwise.

The classical identification of substorm onset is based on auroral observations. The schematic diagram describing the development of auroral morphology in a polar view is shown in Fig. 5.1. Typically seen before substorm onset are quiet auroral arcs oriented more or less parallel to the magnetic latitudes. These arcs move generally equatorward during the substorm growth phase. At substorm onset, an auroral arc typically in the pre-midnight local time sector brightens suddenly and begins to break up into irregular patches. This is described as an initial auroral breakup for the ensuing substorm expansion. The disturbance subsequently expands poleward as well as to other local time sectors. Note that there may be a certain time delay, as long as $\sim$5 min, between the initial brightening onset and the start of poleward motion of the auroral disturbance. The expansion of auroral activity, i.e., expansion phase, may last for $\sim$0.5 h before it begins to subside during the recovery phase. The durations of these phases are for guidance only and can vary considerably. For highly active periods such as magnetic storms, substorms may occur so frequently that they overlap in time, leading to a more complex temporal development of the global auroral pattern.

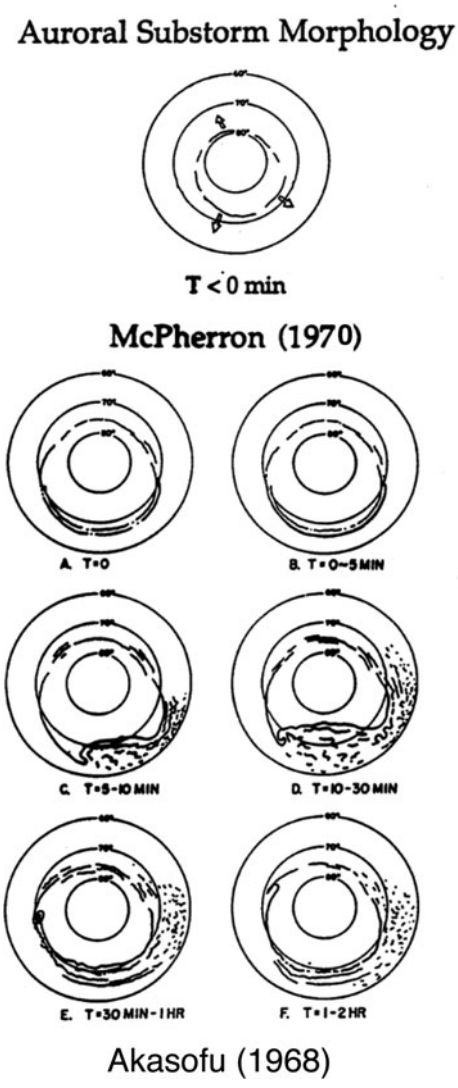

Fig. 5.1 Development of global auroral morphology during the three phases of substorm, namely, the growth phase when the auroral oval expands equatorward, followed by the expansion phase consisting of initial brightening of an auroral arc (**a** to **b**), poleward and local time expansion of auroral activity (**c** to **d**), and finally the recovery phase when auroral activity subsides and retreats equatorward (**e** to **f**)

Some key substorm phenomena, which will be addressed in more detail in later sections, are illustrated in Fig. 5.2.

Besides the auroral activity described earlier, the *H*-component at high-latitude ground magnetic stations show large negative excursions while those at mid-latitude and equatorial stations show small positive excursions (Fig. 5.2b). Micropulsations with periods in the 40–150 s range, called Pi2, are often observed in these magnetograms. Shorter period micropulsations (1–40 s) have also been observed. In the near-tail region (Fig. 5.2c) and at the geosynchronous altitude (Fig. 5.2d), the magnetic field configuration being tail-like prior to substorm onset relaxes abruptly to a dipolar-like configuration. This field relaxation is often accompanied by large magnetic fluctuations suggestive of a turbulent state due to disruption of the cross-tail current (current disruption). Earthward injection of energetic particles and thickening of the plasma sheet are seen after substorm onset. Transient fast plasma flows along with impulsive and highly fluctuating electric and magnetic fields occur in the mid-tail region around this time (Fig. 5.2e). Further down in the tail, the magnetic field shows a northward then southward swing, often accompanied by tailward plasma flows (Fig. 5.2f). These features are often interpreted as signatures of a plasmoid in which magnetic field lines form closed loops entrapping energetic particles within.

In this review, the external solar wind condition for substorm onsets is examined first in Section 5.2.

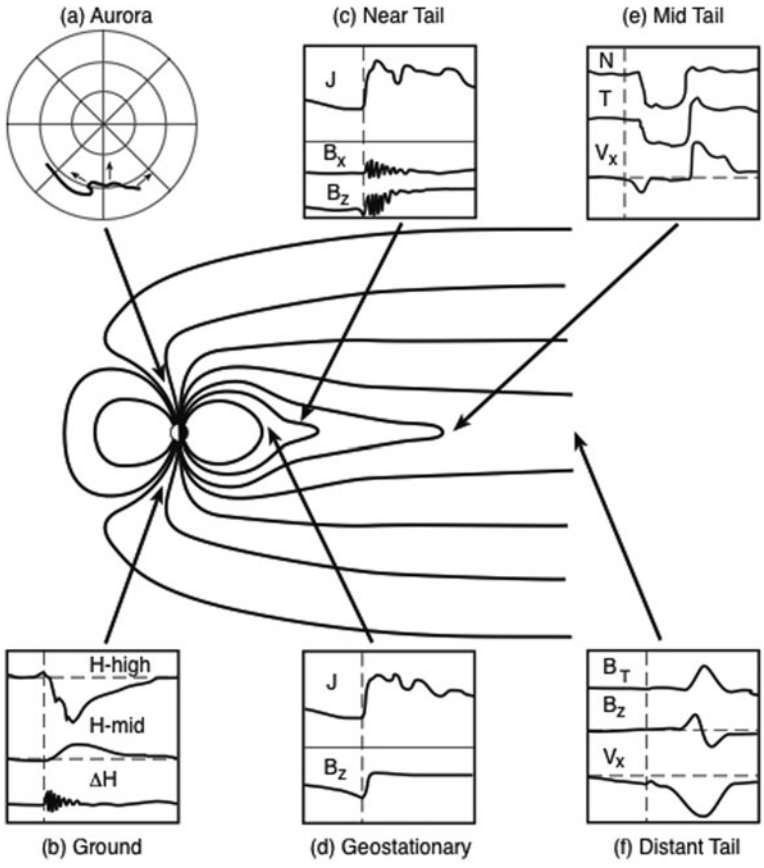

Fig. 5.2 A diagram to illustrate several key substorm phenomena. The substorm onset time is indicated in each panel by the *vertical dashed line*. The micropulsation is indicated by the ΔH trace in (**b**). The increased fluxes of energetic particles at the geosynchronous altitude and in the near-tail region are indicated by the J traces in (**c**) and (**d**). Plasma sheet thinning in the mid-tail is often seen by drops in number density (N) and temperature (T). Plasma flow (V_x) may occasionally be tailward before dropout and become earthward at plasma sheet recovery. Signatures attributed to plasmoids in (**f**) are a transient increase in the total magnetic field magnitude (B_T), a north-then-south swing of the B_Z component, and tailward plasma flow (Lui et al. 2000)

This research topic is important in order to distinguish whether a substorm is an externally driven event or an internal one. Some key substorm phenomena prior to substorm onset are discussed in Section 5.3 to provide clues for the conditions under which the substorm processes can be initiated. The plural form of 'process' is adopted to indicate that different substorm process may occur under different external solar wind condition and past history of magnetospheric activity. It also conveys the plausibility that multiple physical processes may be tightly coupled to produce a substorm. Section 5.4 deals with key substorm phenomena immediately after substorm onset so that the consequences of the onset processes can be identified. Section 5.5 reviews some efforts using time history of disturbances to evaluate substorm processes. Section 5.6 discusses a system-wide approach to extract general characteristics of substorm processes. The phenomena discussed in Sections 5.3–5.6 thus provide valuable insights and observational constraints to identify the relevant physical processes. Section 5.7 provides an assessment of potential onset processes based on observations discussed in previous sections, followed by concluding remarks in Section 5.8.

5.2 External Conditions

The energy accumulation in the growth phase is related to the coupling between the solar wind and the magnetosphere with a dominant role played by the southward component of the interplanetary magnetic field (IMF) (Fairfield and Cahill 1966; Burton et al. 1975; Perreault and Akasofu 1978; Newell et al. 2008). As a result, magnetic field in the near-earth magnetotail changes from a dipolar-like to a tail-like configuration. This reconfiguration can be visualized as dayside magnetic reconnection transporting magnetic flux to the tail (Coroniti and Kennel 1972) or as strengthening of the IMF connection with the Earth's magnetic field to power an enhanced cross-tail current (Atkinson 1967; Siscoe and Cummings 1969; Alfvén 1977; Lui 1991).

5.2.1 Northward Turning of IMF as a Substorm Trigger

Since the north-south component of IMF (IMF B_Z) plays a major role in the growth phase, its variation around the onset time may give a clue on the necessary condition for the external condition. Indeed, it was pointed out by Rostoker (1983) that northward turning of IMF seems to be a common feature in several statistical studies of external condition for onset (Foster et al. 1971; Caan et al. 1977; Blanchard et al. 2000) even though the earlier studies (Foster et al. 1971; Caan et al. 1977) did not recognize or emphasize this finding.

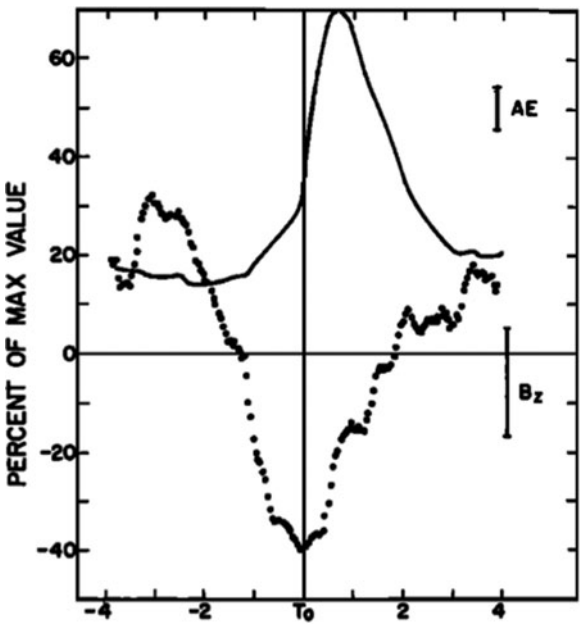

Fig. 5.3 Superposed epoch analysis of AE and IMF B_Z. AE was sampled at 2.5 min and IMF B_Z was sampled at 3 min. Data plotted are 5-point averages normalized to the maximum values (Foster et al. 1971)

Figure 5.3 shows a superposed epoch analysis relating the auroral electrojet index AE to the IMF B_Z for 54 isolated large substorms (Foster et al. 1971). The onset time is marked by *To* and the reference time to *To* is given in units of hour. Northward turning of IMF coincided well with *To*. The AE development preceding *To* was interpreted as the convection enhancement during the growth phase that typically lasts for ~1 h. The association exemplified in Fig. 5.3 was regarded as evidence for northward turning of IMF to be an external trigger for substorm onset and led to the development of a substorm model built on the thesis that most, if not all, substorms are caused by convection reduction as a result of northward turning of IMF (Lyons et al. 2003).

Recently, statistical association between substorm onset and IMF variations is examined with the minimum substorm model (Freeman and Morley 2004, 2009; Morley and Freeman 2007). Figure 5.4 shows one test from this work. In this test, a set of times $\{ti\}$ is selected randomly from real IMF data for which the IMF B_Z is below some threshold: $B_Z(ti) \leq 0.7$ nT. These times are not required to show a coincident rapid

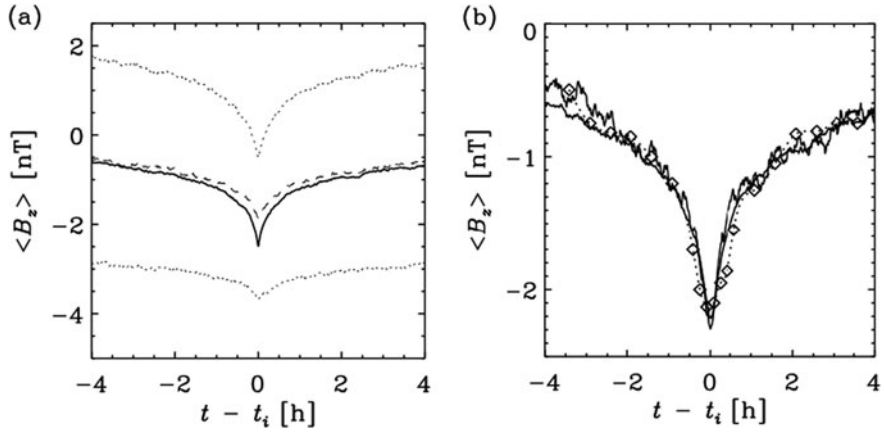

Fig. 5.4 (**a**) Superposed epoch analysis of IMF B_Z selected with a biased upper limit. The mean and medium are shown in *solid* and *dashed lines*. The upper and lower quartiles are shown in *dotted lines*. (**b**) Comparison of this superposed epoch analysis (*heavy solid line*) with the observed data set related to substorm onsets (*dashed line* and *diamonds*). Also shown is a subset of events (given in *light solid line*) equal to the number of events in the observed data set (Freeman and Morley 2009)

northward IMF turning and most of them are found not to correspond to substorm onsets. The threshold is chosen to match the average value in an earlier statistical study that showed the association of substorm onset with northward IMF turning. The statistical time profile of IMF B_Z is shown in Fig. 5.4a. This trend is then compared with the observed trend of IMF B_Z in Fig. 5.4b that was reported to be associated with substorm onsets. The near identity of these two trends indicates that northward turning may be a result of biased selection of times when the IMF B_Z is below a given threshold.

In addition, different interpretations of the result in Fig. 5.3 have been suggested. When the association was re-examined (Hsu and McPherron 2002) based on an automatic technique that used the numerical criteria put forth in Lyons et al. (1997), it was found that only about half of all substorms were associated with a northward IMF turning trigger. In other words, northward IMF turning is not necessary for substorm onset. Consistent with this deduction is that there are substorms without any indication of an external trigger (Horwitz 1985; Henderson et al. 1996). This result can rule out substorm models that rely on northward turning as the only substorm trigger (Lyons et al. 1997; Russell 2000) but not substorm models that have other external solar wind conditions besides northward IMF turning for association with substorm onsets (e.g., Lui 2001).

5.2.2 Interplanetary Shock as a Substorm Trigger

Another possible external trigger for substorms is an interplanetary shock that gives rise to a sudden storm commencement (SSC) or a sudden impulse (Schieldge and Siscoe 1970; Kawasaki et al. 1971; Burch 1972). At the early stage of substorm research, negative bays in high-latitude magnetic stations were used to identify the occurrence of substorms. It was shown that both the amplitude of SSC and the direction of the IMF are important in determining whether or not a negative bay will be triggered (Burch 1972). This result is given in Fig. 5.5, which shows that (1) no negative bays were triggered by an SSC with amplitude < 10 nT, (2) all SSC with amplitude > 10 nT preceded by at least a half-hour of southward IMF averaging > 1 nT triggered negative bays simultaneously, and (3) no negative bays were triggered by SSC with amplitude >10 nT when they were not preceded by either a half-hour of southward IMF averaging >1 nT or an averaged IMF magnitude > 9 nT.

However, negative bays could be caused by enhanced convection also. This issue was examined with the global auroral observations from Polar UVI (Liou et al. 2003). From a study of 43 interplanetary shock events, it was found that while ~52% of the shocks produced high-latitude negative bays and enhanced auroral luminosities, only 4 events (~9%)

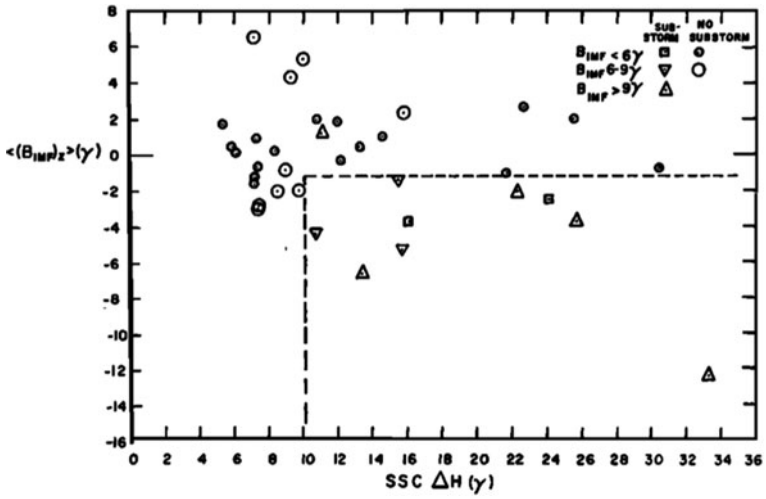

Fig. 5.5 The IMF B_Z averaged over six 5.46-min samples versus the amplitude of 36 SSCs. *Squares* and *triangles* indicate SSC producing simultaneous high-latitude negative bays; *circles* indicate SSC that did not trigger negative bays. Different symbols are used to denote different strength of the total IMF **B** field. Note that $1\gamma = 1$ nT (Burch 1972)

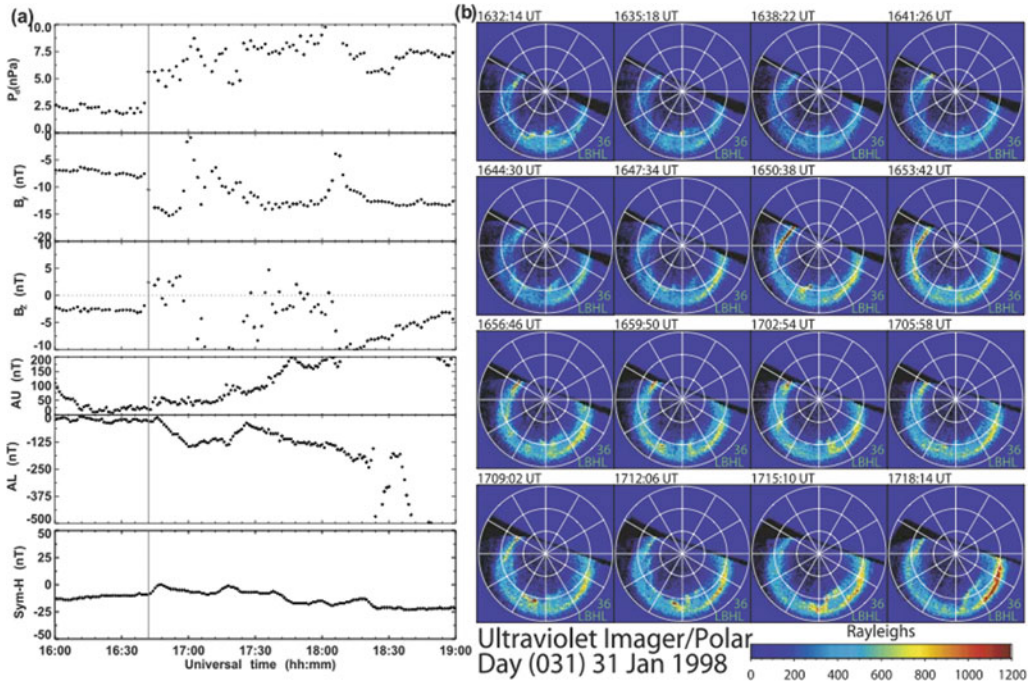

Fig. 5.6 (**a**) Solar wind parameters (dynamic pressure *P*d, IMF B_Y and B_Z) and geomagnetic indices (AU/AL, SymH). The arrival of the interplanetary shock is indicated by the *vertical line* (**b**) A sequence of auroral images from Polar UVI showing no substorm development after arrival of an interplanetary shock (Liou et al. 2003)

showed development of a substorm within the subsequent 20-min window.

One case of no substorm development after arrival of an interplanetary shock is shown in Fig. 5.6. The interplanetary parameters are given on the left of the figure, showing the arrival of an interplanetary shock at ~1640 UT on January 31, 1998. The sequence of global auroral images from Polar UVI is given on the right. For the subsequent ~28 min after shock arrival, there was no auroral pattern that suggests the occurrence of a substorm even though there was a small coincident perturbation of the AL index as seen on the left of the figure.

Interestingly, although an increase in the solar wind dynamic pressure rarely triggers a substorm, its decrease has a higher probability for association with substorm occurrence (3 out of 13 events within a 20-min window) than pressure increase (4 out of 43 events within a 20-min window) (Liou 2007). This association was interpreted as the effect of a solar wind discontinuity when the magnetosphere is in a metastable state, rendering it susceptible to small agitations to achieve its relaxation to a more stable state through a substorm.

5.2.3 Overall Assessment

While there is no doubt that energy of the magnetospheric system comes from the solar wind interaction with the Earth's magnetosphere, it is doubtful that an external trigger in the solar wind is necessary for substorm occurrence. At the very least, previous studies indicate that substorms may occasionally be initiated by an internal instability. Note that the perception of an internal instability as the substorm onset process is not inconsistent with observations of some substorms being initiated by an external agent. In such situations, the environment at the onset region may be near the threshold of the instability onset and an external agent adds a small perturbation for the instability to go off.

5.3 Activity Prior to Onset

The changes during the substorm growth phase provide important clues not only on the location where the substorm onset processes occur but also on the environment under which the physical processes responsible for the sudden energy release in substorm

onsets may be activated. In this section, several key observational features that occur just prior to local onset of substorm activity are discussed.

Although the classical substorm onset timing is based on auroral observations, the rare availability of such observations, especially on a global scale, has led many researchers to substitute this onset indicator with other ones. Unfortunately, this practice is the root of many controversies (Meng and Liou 2004).

Figure 5.7 illustrates the timing accuracy of substorm onset time based on other substorm onset indicators. Among them, the auroral kilometric radiation (AKR) onset is probably the closest one to the auroral breakup onset. Most of the delays in other indicators are due to the propagation time required for a localized substorm disturbance to reach the observing site. The first 'fast flow' line in Fig. 5.7 is based on plasmoid identification by Ieda et al. (2001). The second 'fast flow' line in Fig. 5.7 is based on Nakamura et al. (2001) who have shown that fast plasma flows, which are often regarded as evidence of magnetic reconnection, are not always associated with substorm onset but can be associated with localized auroral brightenings. In addition,

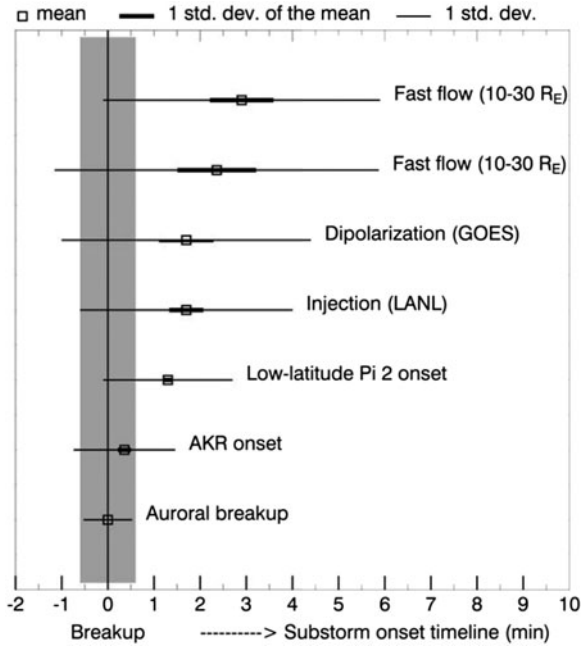

Fig. 5.7 Various substorm onset indicators are compared with the classical onset signature of auroral breakup determined by global auroral imaging from Polar UVI (Meng and Liou 2004)

Liou et al. (2000) showed that ~30% of large, isolated Pi2 onset are not associated with substorm onset, which can account for some events (30–40%) with fast flows preceding the Pi2 onsets. Therefore, caution is needed to judge substorm onset timing based on indicators other than auroral breakup.

5.3.1 Magnetic Field Reconfiguration

One of the most dramatic changes in the magnetosphere during the substorm growth phase is the nightside region where the magnetic field configuration transitions from a dipolar-like to a tail-like geometry (Walker et al. 1976; Sauvaud and Winckler 1980). The transition region, referred to as the nightside cusp, has been inferred as the substorm onset location in the magnetotail based on the examination of the onset location in relation to the low-altitude magnetospheric plasma boundaries. It was found to be adjacent to the trapping boundary of the energetic electrons ($E >$ 40 keV) (Lui and Burrows 1978) and slightly poleward of the proton aurora intensity peak (Donovan et al. 2008). Its location in the magnetotail is estimated to be typically at the downtail distance of 6–12 R_E (1 R_E (Earth's radius) = 6378 km), with the closer location to the Earth for a highly stressed state of the magnetosphere. Note that in the inner magnetotail, the equatorial plane is not necessarily the location where the magnetic field has the minimum strength, leading to a splitting of the cross-tail current into two latitude locations away from the equatorial plane. The cross-tail current in this feature has been referred to as the cut-ring current (Antonova et al. 2009a).

At the geosynchronous altitude, the magnetic field reconfiguration during the substorm growth phase is often seen and has been modeled by Kaufmann (1987). Figure 5.8 shows how the magnetic field at a geosynchronous satellite (marked by a cross in each panel) can be affected by different locations of a cross-tail current sheet with a fixed width along the tail axis (2 R_E) and a fixed magnitude (300 mA/m). This simple model indicates that the magnetic field at the geosynchronous altitude can become tail-like only when the cross-tail current is intensified nearby (panels b and c) and not further downtail (panel a) or much closer in where the local magnetic field is so strong that it is not affected much by the enhanced cross-tail current (panel d).

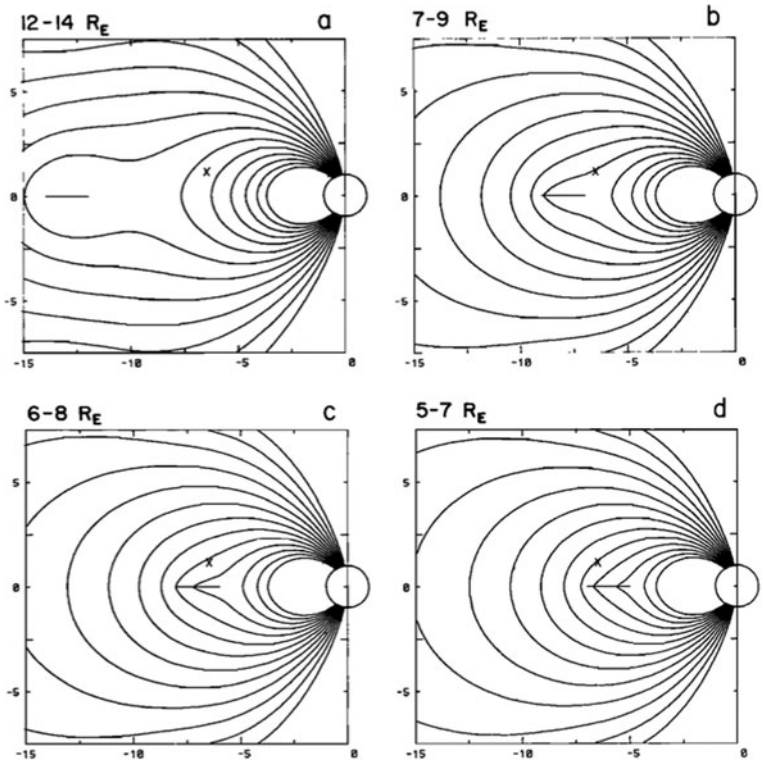

Fig. 5.8 Magnetic field configuration for four different locations of an enhanced cross-tail current (Kaufmann 1987)

5.3.2 Plasma Sheet Thinning and Poynting Flux Consideration

Stretching of the magnetic field in the inner magnetotail is often accompanied by a plasma dropout in satellite observations, interpreted as thinning of the plasma sheet (Sauvaud and Winckler 1980). This thinning is related to the enhancement of Poynting flux during the growth phase (Papadopoulos et al. 1993; Machida et al. 2009). It was shown from a simple magnetic field model that the magnetosphere acts as a lens for MHD waves, focusing the incident energy from the solar wind in the form of Poynting flux to the near-earth magnetotail in the downtail distance range of 8–16 R_E (Papadopoulos et al. 1993).

This novel idea is later confirmed from a novel superposed epoch analysis of Geotail data (Machida et al. 2009). In that study, substorm onsets are determined by auroral breakups observed in global auroral images from Polar or IMAGE spacecraft. A total of 234 events located in the region $-9 > X\ (R_E) > -31$ and $-3 < Y\ (R_E) < 8$ in GSM coordinates are distributed evenly into columns of 2 R_E width. The vertical axis Z is sorted by the plasma beta (using B_X for the magnetic field in calculating plasma beta), with decreasing plasma beta away from the $Z = 0$ plane. The temporal developments on the change in the total pressure ΔPt and the Poynting flux Fpoyz in two different regions within the constructed grid are shown in Fig. 5.9. The time $t = 0$ corresponds to substorm onset time. Region I is defined by $13 > X\ (R_E) > -17$ and $0 < Z < 2$, i.e., the high latitude plasma sheet in the inner magnetotail. Region IV is defined by $-13 > X$

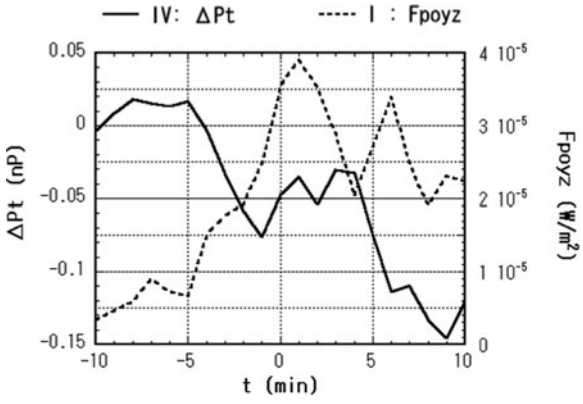

Fig. 5.9 The temporal development of the total pressure (ΔPt) in the central plasma sheet just outside the inner magnetosphere and the Poynting flux (Fpoyz) in the high latitude plasma sheet in the inner magnetotail (Machida et al. 2009)

(R_E) > –17 and 0 < Z < 2, i.e., the central plasma sheet just outside the inner magnetotail. The result shows that the Poynting flux propagates toward the central plasma sheet at least 10 min before substorm onset. The decrease in the total pressure in the central plasma sheet starting at ~5 min before substorm onset, a signature of rarefaction wave, will be discussed further in Section 5.4.3.

5.3.3 Ion Temperature Drop

New features of the near-earth plasma sheet have been revealed by observations from the THEMIS (Time History of Events and Macroscale Interactions during Substorms) mission (Angelopoulos 2008). From a statistical study of a special class of near-earth (7–11 R_E downtail) events in which current disruption (CD) was not preceded by fast earthward plasma flows and was detected near the plasma sheet boundary, it was found that a significant ion temperature drop generally occurred in a few minutes before local CD onset based on 15 substorm events and 20 measurement sequences (Liang et al. 2009).

One such example is given in Fig. 5.10, showing the magnetic field in VDH coordinates, plasma flow components, ion density, and ion temperatures. The gray lines in the flow panels denote convective flows. The

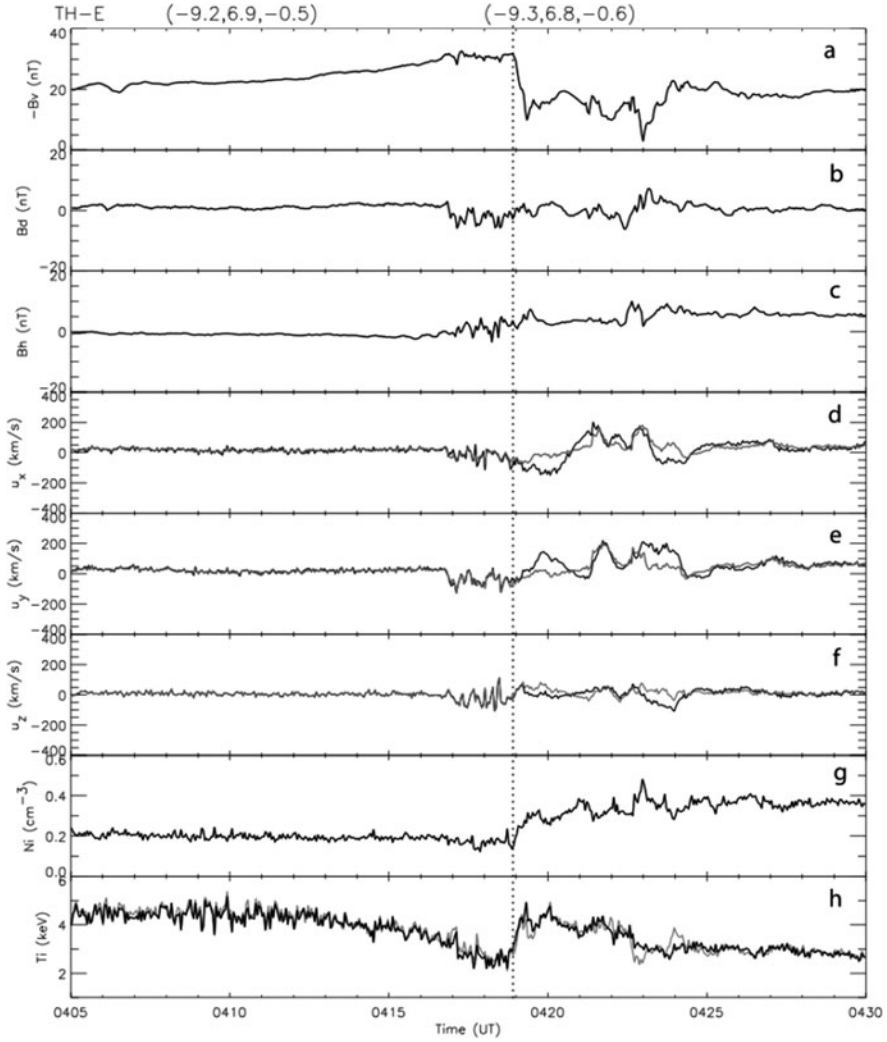

Fig. 5.10 Plasma measurements in the inner magnetosphere for the March 15, 2008 substorm event to show a significant ion temperature drop just prior to CD onset (Liang et al. 2009)

black and gray lines in the temperature panel denote perpendicular and parallel temperatures, respectively. The observations were taken from THEMIS E on March 15, 2008 at the downtail distance of ~9 R_E. The local CD onset is indicated by the vertical dotted line. It can be seen that there was no significant plasma flow prior to local CD onset. On the other hand, substantial ion temperature drop can be discerned for ~2–3 min prior to the local CD onset.

5.3.4 Neutral-Sheet-Pointing Electric Field

For the same event of Fig. 5.10, a neutral-sheet-pointing electric field concurrent with significant ion temperature drop occurred as well (Liang et al. 2009). Figure 5.11 shows electric field measurements determined in three different ways. The electric field in DSL (Despun Sun L-vectorZ) coordinates is given in Fig. 5.11a–c. In this event, the DSL-Y is about 30° from the GSM-Y direction

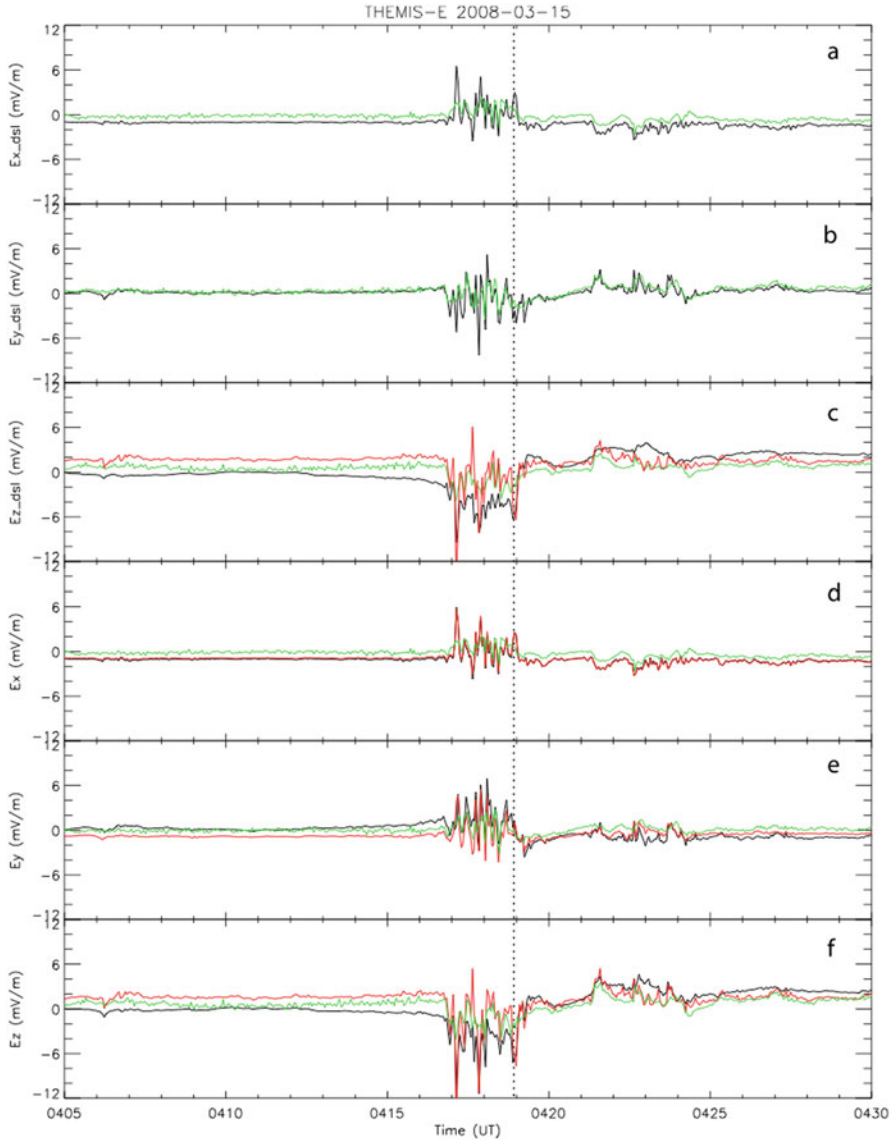

Fig. 5.11 Electric field measurements in the inner magnetosphere for the March 15, 2008 substorm event to show the occurrence of quasi-electrostatic field pointing towards the neutral sheet prior to CD onset (Liang et al. 2009)

and tilted north. In Fig. 5.11a–f, black lines are from raw measurements with an adjusted level (12 mV/m is applied to E_{DSLz} as an ad hoc correction of the instrumental offset). The green line shows $-\mathbf{u}_i \times \mathbf{B}$ ($\mathbf{u}_i$ is the plasma bulk flow and $\mathbf{B}$ is the vector magnetic field). In Fig. 5.11c–f, the red line shows the $\mathbf{E}$ components calculated based on $\mathbf{E} \cdot \mathbf{B} = 0$ ($\mathbf{E}$ is the electric field vector). Again, the local CD onset is indicated by the vertical dotted line. It can be seen that all three estimates of the electric field show a similar variation pattern, i.e., high oscillations with negative bias starting generally from ~2 min before CD onset. The E_Z component was in general negative, i.e., pointing towards the neutral sheet since the satellite was above the neutral sheet. Again, note that this event and the other events studied by Liang et al. (2009) are cases when the satellites were near the plasma sheet boundary at CD onset.

The recent result of ion temperature drop with neutral-sheet-pointing quasi-electrostatic field in the high-latitude plasma sheet prior to substorm onsets leads to the development of a new current sheet model invoking two separate populations – one hot plasma forming the thin current sheet and one cold plasma governed largely by MHD processes (Liu et al. 2010).

5.3.5 Dimming of Auroral Arcs

Dimming of auroral arcs is often seen before substorm onset (Pellinen and Heikkila 1978; Kauristie et al. 1997). This phenomenon was examined with Hβ emission from the Gillam meridian-scanning photometer (MSP) for 50 events (Liu et al. 2007), as shown in the keogram form for each event in Fig. 5.12. The time axis starts with 45 min prior to and ends 30 min after the auroral onset. Timing accuracy is ~2 min in this study. The general trend of auroral luminosity moving equatorward before the development of an auroral bulge at substorm onset is well demonstrated in each event. The event encircled by the dashed curve was examined in Liu et al. (2007) with high-latitude and mid-latitude magnetograms to show simultaneous Pi2 onsets.

Figure 5.13 gives the superposed epoch analysis on the temporal developments of the proton aurora brightness (top panel) and the optical b2i boundary

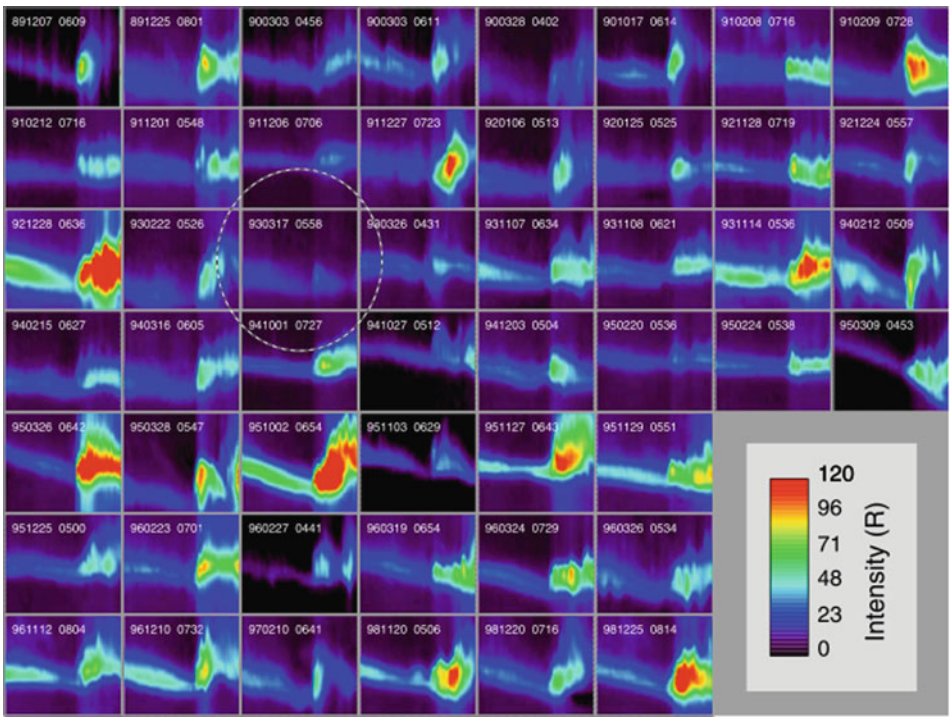

Fig. 5.12 Montage of keograms in H-beta emissions from Gillam station for 50 events used to examine the auroral brightness around substorm onset. The event enclosed by a *dashed circle* was examined further with ground-based magnetograms in Liu et al. (2007)

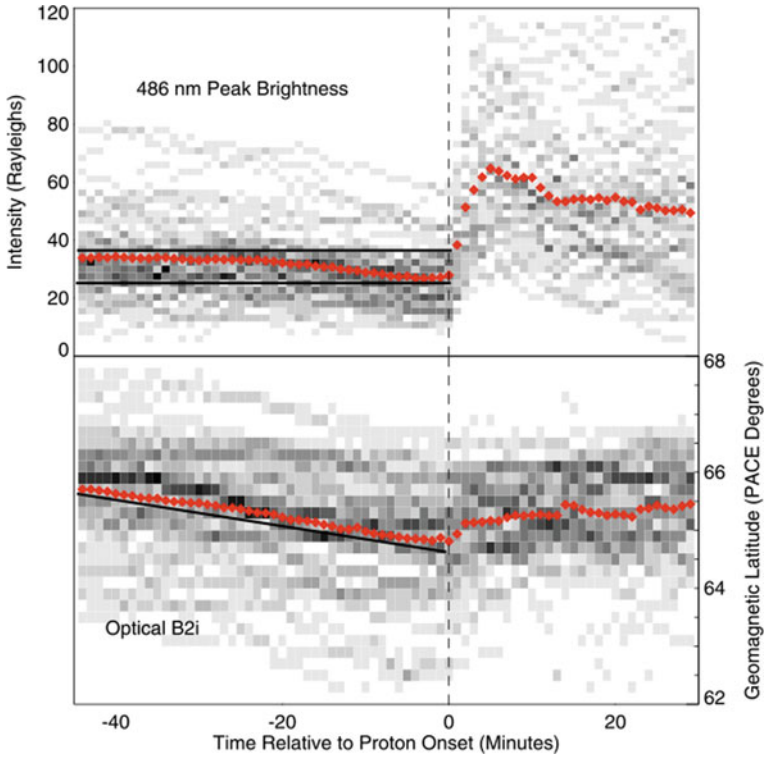

Fig. 5.13 Superposed epoch analysis of the occurrence probabilities (increasing with *darker color*) of auroral intensity and b2i location relative to substorm onset time (Liu et al. 2007)

(bottom panel). The optical b2i is the optical projection of the earthward limit of strong pitch angle scattering in the central plasma sheet, corresponding to the ion isotropy boundary (IB) (Donovan et al. 2003; Mende et al. 2003). The average values of these two parameters are shown by the red dotted curves. The general trend of the proton aurora intensity shows a systematic decrease ~15–20 min before onset. The latitude of the optical b2i also decreases systematically prior to onset and increases rapidly after. Since b2i and IB correlate with magnetic field stretching that reduces the solid angle of the loss cone, the auroral dimming as well as the equatorward movement of auroral arcs seen prior to substorm onsets may be explained naturally, which is confirmed with a quantitative estimate of the precipitating proton flux (Liu et al. 2007).

5.3.6 Auroral Activity Poleward of Breakup Arc

Since the auroral breakup typically occurs at the most equatorward arc (Akasofu 1968), it is of great interest to investigate whether the breakup activity is caused by disturbances poleward of the breakup arc that move equatorward. Several Geotail events in the mid-tail region that mapped close to the meridian of ground-based all-sky TV cameras observing the auroral breakups were examined (Yahnin et al. 2000). In spite of occasional high-speed (400–600 km/s) earthward plasma flows seen in the mid-tail by Geotail, timing analysis showed that there was no causal relationship between fast plasma flow in the mid-tail region and auroral breakup. Furthermore, there was no indication of any auroral precursor poleward of the breakup arc even with special methods to process TV camera data to detect weak aurora. Such negative result was later confirmed by similar TV observations (Antonova et al. 2009b).

However, recent reports seem to suggest the contrary, i.e., there are typically north-south auroral arcs moving equatorward to approach the vicinity of the breakup arc location before substorm onset (Nishimura et al. 2010; Lyons et al. 2010).

Figure 5.14 shows an example on February 29, 2008 in which the substorm onset, identified by breakup of

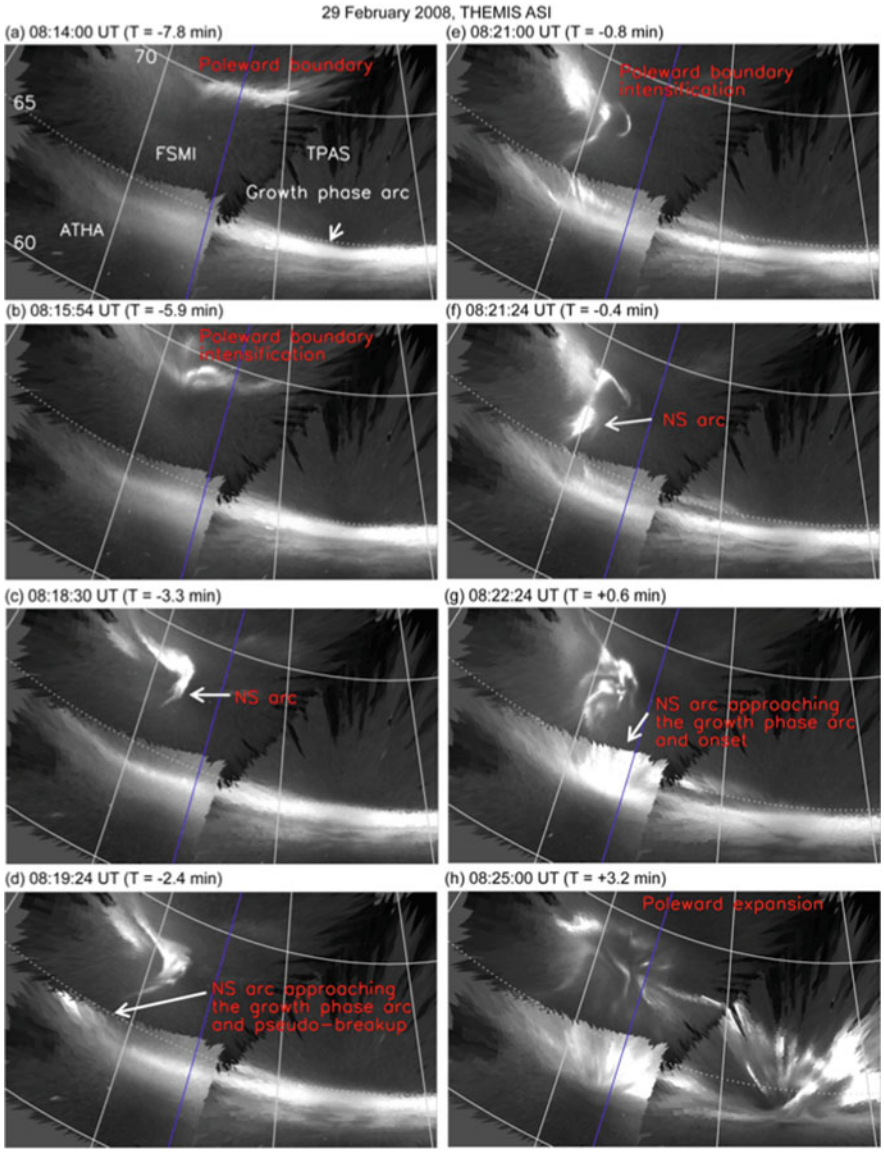

Fig. 5.14 A sequence of combined all-sky-camera images of aurora from the THEMIS GBO showing the progression of PBI to form a north-south auroral arc to approach the growth phase auroral arc before substorm onset (Nishimura et al. 2010)

an auroral arc, occurred when the poleward boundary intensification (PBI) approached the location of the auroral breakup arc. These observations were made from the network of ground-based all-sky-cameras (ASCs) set up for the THEMIS mission. For this event, the BPI appeared ~6 min before onset (Fig. 5.14b). The north-south auroral arc (NSA), which was linked to the PBI, developed and started to travel equatorward to the growth phase auroral arc (Fig. 5.14c–f). The substorm onset started when the NSA approached the growth phase arc (Fig. 5.14g). It is claimed that this precursory activity occurred in 84% for all 209 events studied and 96% for events when there was good coverage from all-sky-imagers in the THEMIS ground-based observatory (GBO).

Figure 5.15 shows the statistics on some time delays, i.e., time difference between (a) PBI appearance and substorm onset, (b) PBI appearance and NSA reaching equatorward portion of the auroral oval, and (c) NSA arrival at the equatorward portion of the

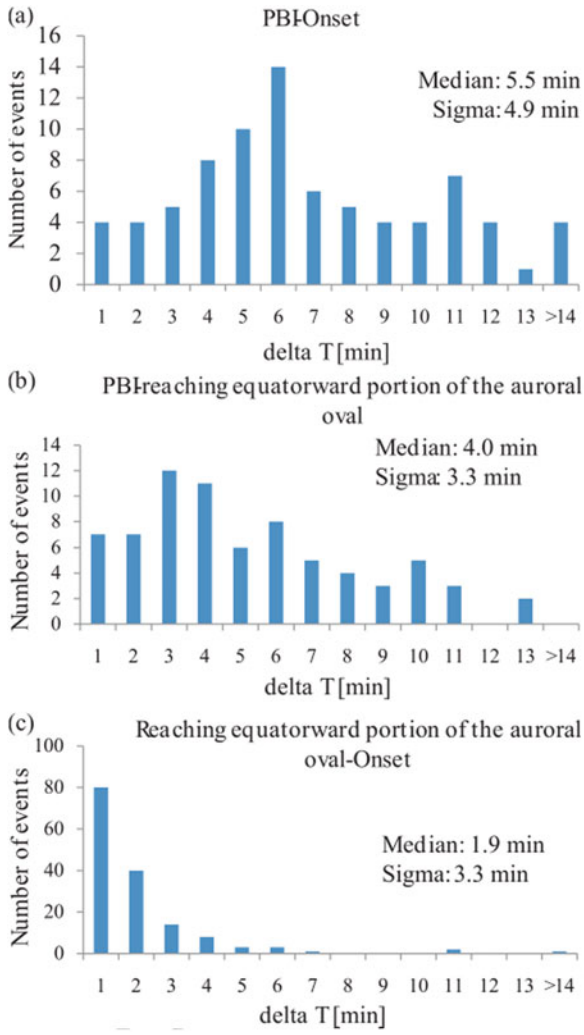

Fig. 5.15 Time evolution of pre-onset auroral forms: time difference between (**a**) PBI and substorm onset, (**b**) PBI appearance and north-south arc reaching the equatorward portion of the auroral oval, and (**c**) pre-onset arc reaching the equatorward portion of the auroral oval and substorm onset (Nishimura et al. 2010)

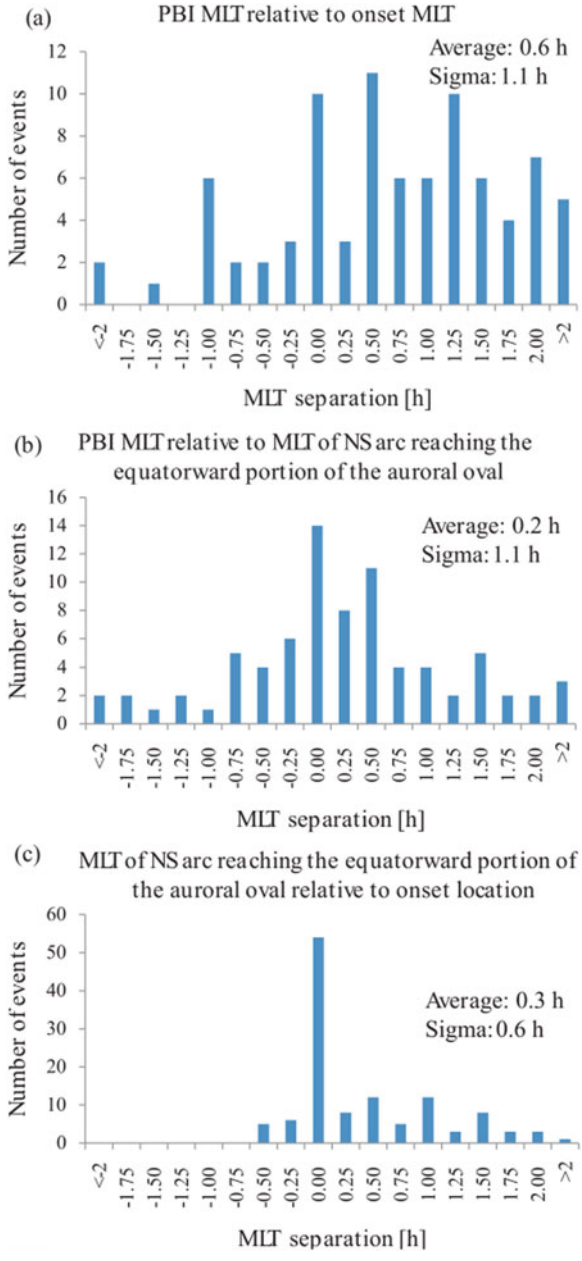

Fig. 5.16 MLT evolution of pre-onset auroral forms: MLT difference between (**a**) PBI and onset, (**b**) PBI and NS arc reaching the equatorward portion of the auroral oval, and (**c**) pre-onset arc approaching onset location (Nishimura et al. 2010)

auroral oval and substorm onset. The median values of these time delays are relatively short, from ~1.9 to ~5.5 min.

The magnetic local time difference between PBI/NSA and substorm onset is also small, from 0.2 to 0.6 h as shown in Fig. 5.16. It is suggested that the NSA brings in new plasma to the inner magnetotail, setting up condition favorable for an unspecified near-earth instability (Nishimura et al. 2010; Lyons et al. 2010).

5.3.7 Azimuthal Auroral Forms and Waves

An extensive study of auroral morphology around substorm onset from Viking satellite found that 26 out of 37 substorm onsets showed azimuthal auroral forms (AAF) along the arc system prior to its poleward

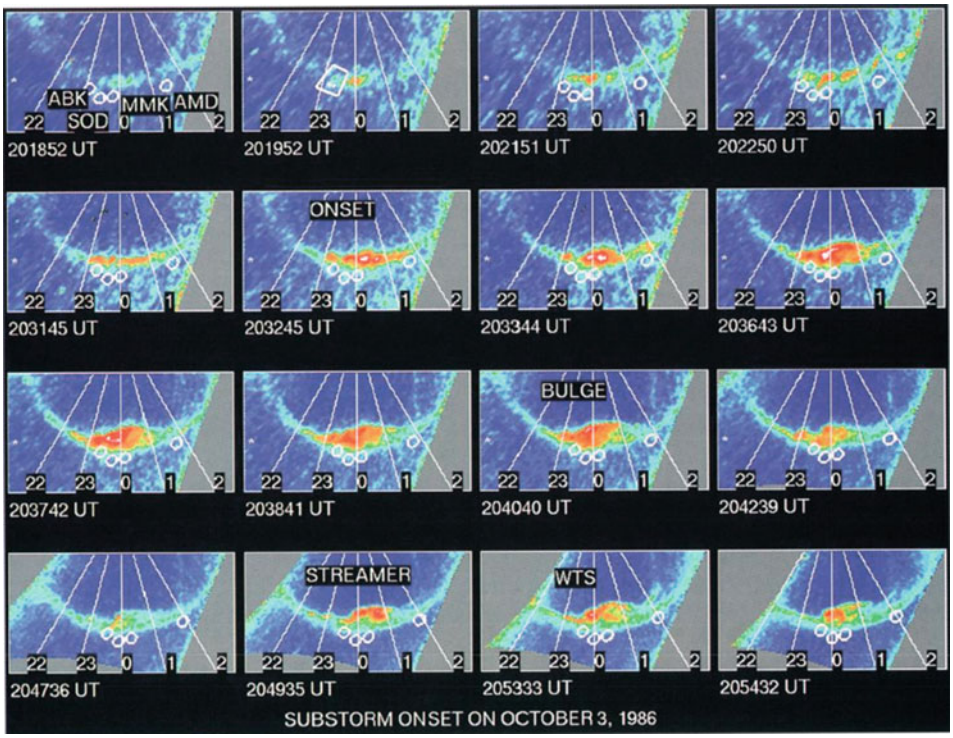

Fig. 5.17 Auroral images from Viking on October 3, 1986 to show the occurrence of azimuthal auroral forms at ~2023 UT (Elphinstone et al. 1995)

expansion (Elphinstone et al. 1995). An example is shown in Fig. 5.17 for the October 3, 1986 event. The AAF developed at ~202250 UT and substorm onset occurred at ~203145 UT, i.e., ~9 min later.

From the 26 events studied, the observed wavelength is in the range of ~130–580 km, with a mean of ~310 km. The AAF can span over a wide local time of ~8 h and generally propagates eastward in the morning sector. However, the onset itself is localized to ~1 h local time.

Several later studies confirmed this pre-onset feature (Friedrich et al. 2001; Donovan et al. 2006a, b, 2008; Liang et al. 2008; Henderson 2009; Rae et al. 2009). For example, it was found from THEMIS all-sky-camera (ASC) network that (a) the longitudinal pattern is wave-like with a wave number of ~100–300, and (b) the subsequent breakup spreads rapidly to 1 h local time within 10 s of substorm onset (Liang et al. 2008).

In the premidnight sector, the longitudinal pattern on a growth phase arc propagates with a wave velocity of 2–10 km/s and has a time period of 40–110 s during 10–20 min before auroral breakup (Uritsky et al. 2009). An example of the longitudinally propagating arc wave is shown in Fig. 5.18 by the slant patterns in the ewogram and auroral intensity at different magnetic longitudes (Fig. 5.18b–d) for the event on March 3, 2008. An ewogram is similar to a keogram except that the vertical axis is magnetic longitude instead of magnetic latitude for a keogram.

Intense waves at low frequencies (much below the ion gyrofrequency) have been observed prior to substorm onsets near the magnetic equator in the near-earth magnetotail (Cheng and Lui 1998; Saito et al. 2008a). Figure 5.19 shows the perturbed magnetic field measured by the Charge Composition Explorer (CCE) satellite around CD onset marked by the vertical dashed line. CCE was at ~9 R_E in the magnetotail near the midnight meridian. The low frequency magnetic perturbations were extracted by successive smoothing of the raw data with normalized binomial coefficients as used in Lui and Najmi (1997). They are then converted into components in the ambient magnetic field coordinate system. The components δB_ϕ and $\delta B_{||}$ point eastward and along the mean magnetic field, respectively. The component δB_L forms the right-hand

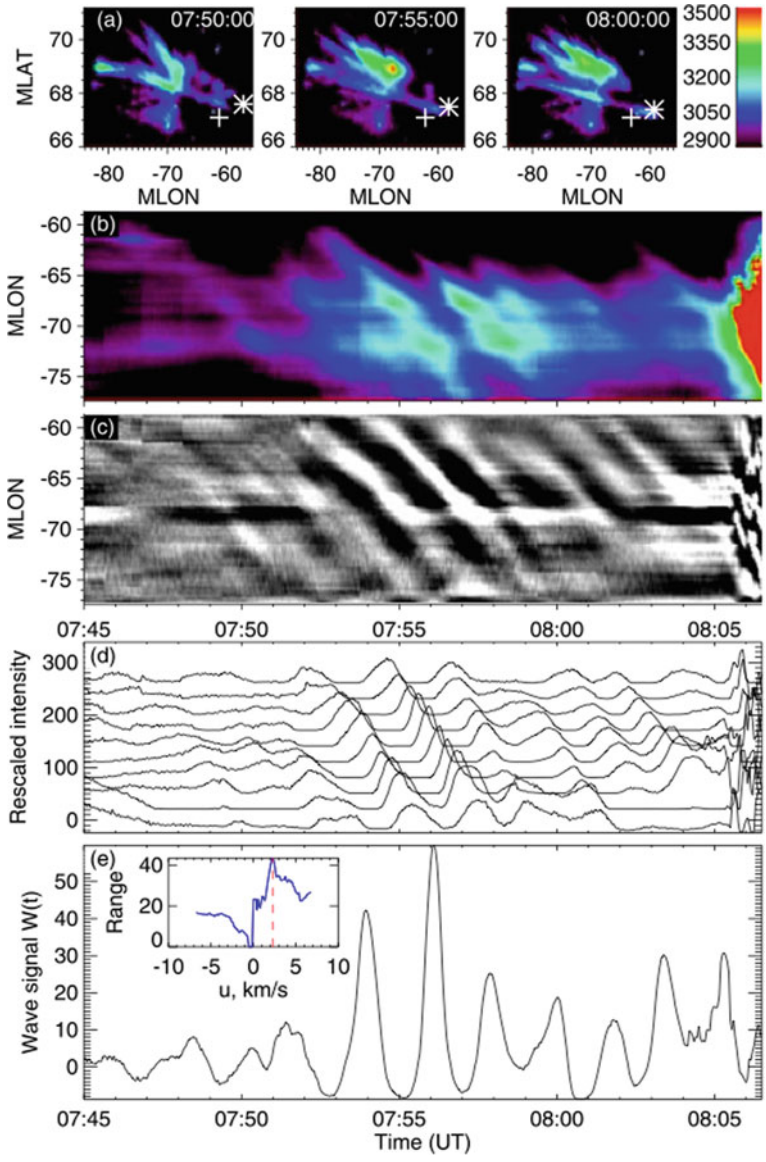

Fig. 5.18 (**a**) Sample images of the pre-onset aurora observed on March 3, 2008. Ionospheric footprints of THEMIS P2 and P4 are shown with *stars* and *crosses*, respectively; (**b**) raw ewogram representing time evolution of the northern arc seen in (**a**); (**c**) detrended ewogram exhibiting westward-propagating periodic fronts of auroral intensity; (**d**) stack plot of time-varying auroral intensity at different magnetic longitudes; (**e**) wave signal extracted using the surfing average technique; the insert shows the dynamic range (Uritsky et al. 2009)

orthogonal coordinate. The wave started ∼1.5 min prior to CD onset.

Quasi-electrostatic waves have also been observed a few minutes before local CD onset (Liu et al. 2008). Its generation is suggested to arise from a kinetic ballooning instability interacting with the local current sheet. The interaction pattern was observed to be constant across the downtail distance between 10 and 20 R_E for the reported events. It is proposed that the quasi-electrostatic field may modify the local stability condition to induce local CD.

Low frequency waves have also been found at other locations in the magnetotail. Six Geotail events in which continuous observations of the inner magnetotail ($-8 > X\,(R_E) > -12$) near the equator around CD onset have been examined by Saito et al. (2008a). The wave mode was identified with the technique developed in Saito et al. (2008b). The fluctuation in the x-component of the magnetic field $\delta \mathrm{B}_{\perp x}$ was compared with the fluctuation in the ion velocity perpendicular to the magnetic field $\delta v_{\perp}$. According to the linear MHD theory, for the wave to have almost zero frequency in the plasma rest frame, $\delta B_{\perp \mathrm{x}}$ fluctuates with very small $\delta v_{\perp}$.

Figure 5.20 shows four events (a, c, e, and f) satisfying the condition for almost zero-frequency wave

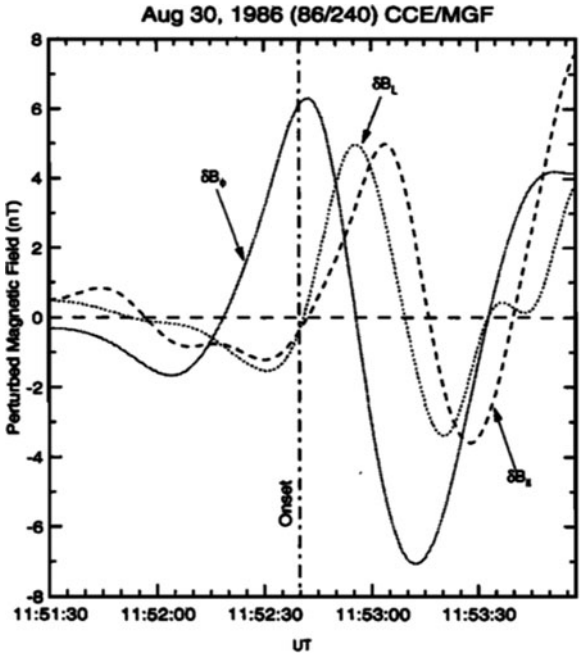

Fig. 5.19 Magnetic perturbations in the inner magnetotail observed by CCE at ~9 R_E in the midnight sector around CD onset time (Cheng and Lui 1998)

that occurred prior to local CD onset (from –4 to –1 min before). This result lends support to an earlier report from WIND observation of low frequency waves driven by earthward pressure gradient being enhanced before substorm onset and reduced after onset, developments expected from the ballooning instability activity at substorm onset (Chen et al. 2003).

5.4 Activity After Onset

The expansion onset manifests in an explosive manner and is the most intriguing as well as challenging phase of a substorm to understand. The observational features at this phase are as valuable as those prior to onset in providing insights into the physical processes responsible for the sudden energy release.

5.4.1 Magnetic Field Dipolarization and Current Disruption

The magnetic field reconfiguration in the near-earth magnetotail prior to substorm onset discussed in Section 5.3.1 is reversed abruptly at substorm onset with significant magnetic fluctuation and increase in the B_Z component. This change indicates the magnetic field becoming more dipolar-like, a phenomenon known as dipolarization. The field fluctuation is a typical signature of CD. An example of CD and dipolarization is shown in Fig. 5.21 (Takahashi et al. 1987). The observing satellite is CCE located at ~9 R_E in the midnight sector during the event. The onset of CD preceded the ground onset of Pi2 at the Kakioka station, located at the same MLT as CCE, by ~1 min. This short time delay is expected to be the travel time delay from the near-earth magnetotail to the ionosphere.

The near-earth CD and dipolarization is associated with substorm injection found at the geosynchronous altitude (McIlwain 1974; Sauvaud and Winckler 1980; Lui et al. 1988), implying that it progresses earthward, as indicated by substorm injection signatures in space and on the ground (Spanswick et al. 2009). In addition, CD is also found to develop at progressively further downtail distances. This tailward development of substorm disturbance was inferred from multi-satellite observations (Lopez and Lui 1990) and detailed analyses of magnetic field variations after substorm onset (Jacquey et al. 1991, 1993; Ohtani et al. 1992). Note that tailward progression of CD does not imply tailward plasma flows. On the contrary, this leads to a succession of earthward plasma flows accompanied by particle energization.

Figure 5.22 shows a schematic diagram illustrating the time evolution of CD region in the magnetotail from four satellites, namely, GOES 5 and 6, CCE, and IRM (Lopez and Lui 1990). This tailward development of substorm disturbance is later confirmed with other multi-satellite observations (Vogiatzis et al. 2005; Lui et al. 2007a, 2008a). In particular, Vogiatzis et al. used data from synchronous satellites, Polar, and Cluster to show that CD took place inside the geosynchronous orbit and expanded both in local time and tailward. Plasma flow from magnetic reconnection in the mid-tail may have contributed to the environment inducing the excitation of near-earth instability for CD. Similarly, Lui et al. (2007a, 2008a) examined data from synchronous satellites, Polar, Double Star 1, Geotail, and Cluster and found substorm disturbances to be initiated in the near-earth region and spread to further downtail subsequently. It is important to note that the result of the near-earth initiation of

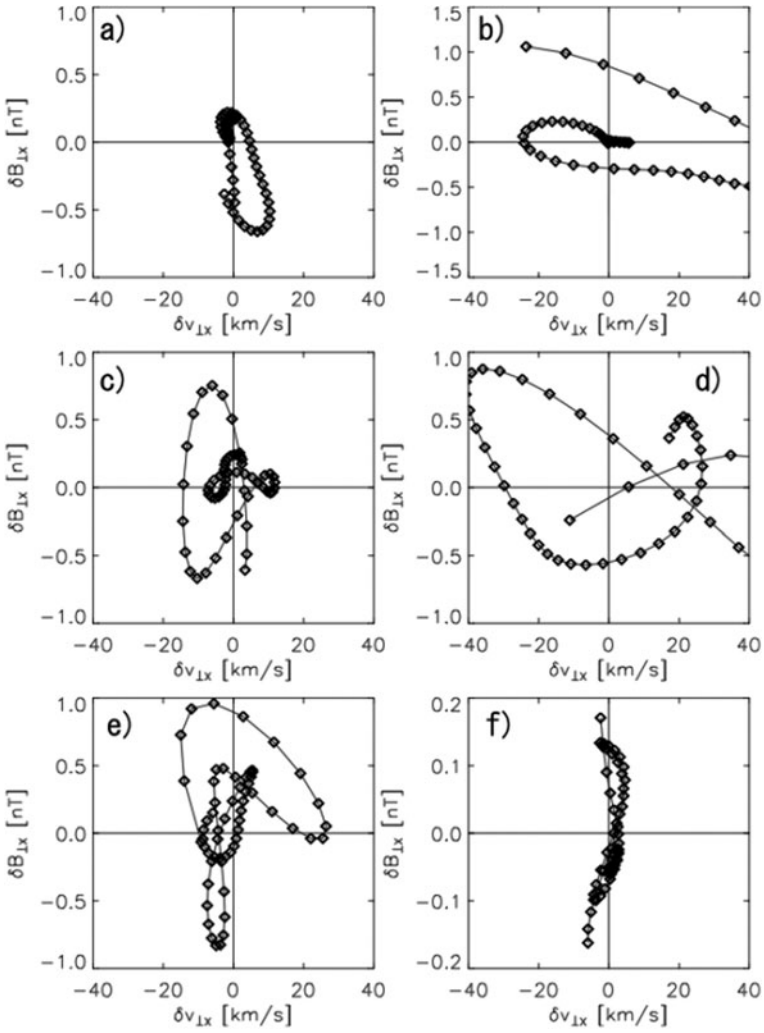

Fig. 5.20 Hodograms of magnetic field and ion velocity fluctuations in the inner magnetotail observed by Geotail to show, for cases (**a**), (**c**), (**e**) and (**f**), that the magnetic field fluctuations do not accompany those in the velocity component, implying zero frequency in the plasma rest frame and consistency with the ballooning instability signature (Saito et al. 2008a)

substorm onset is obtained by studies that cover both ground-based and space-based measurements.

Detailed analyses of magnetic field variation during substorms also lead to inference of tailward development of dipolarization. This is illustrated in Fig. 5.23 with variations of B_Z versus B_X in the near-earth magnetotail being reproduced well by modeling the tailward retreat of the CD region (Jacquey et al. 1991).

Dipolarization is also observed in the mid-tail region during substorms and it often appears in the form of a front (Nakamura et al. 2002; Runov et al. 2009; Sergeev et al. 2009). An example of such a dipolarization front (DF) observed by THEMIS satellites during a major tail conjunction interval, i.e., time when all THEMIS satellites were roughly aligned along the tail axis, is shown in Fig. 5.24. The satellite P1 furthest from the Earth was located at the downtail distance of ~20 R_E (Runov et al. 2009); see the top two panels of Fig. 5.24 that show the projected locations on the XZ- and the XY-planes of all THEMIS satellites. The DF was observed first at P1 and was subsequently detected by satellites at progressively closer distance to the Earth. Distinct from tailward propagation of CD, all reports of DF show them advancing earthward. The DF was associated with a very thin (below ion inertial length) current sheet aligned perpendicular to the neutral sheet, acting as an interface between the two adjacent plasmas with different densities and temperatures. Strong bursts of electric field (>50 mV/m) in the lower-hybrid time scale were found at this interface (Runov et al. 2009; Sergeev et al. 2009).

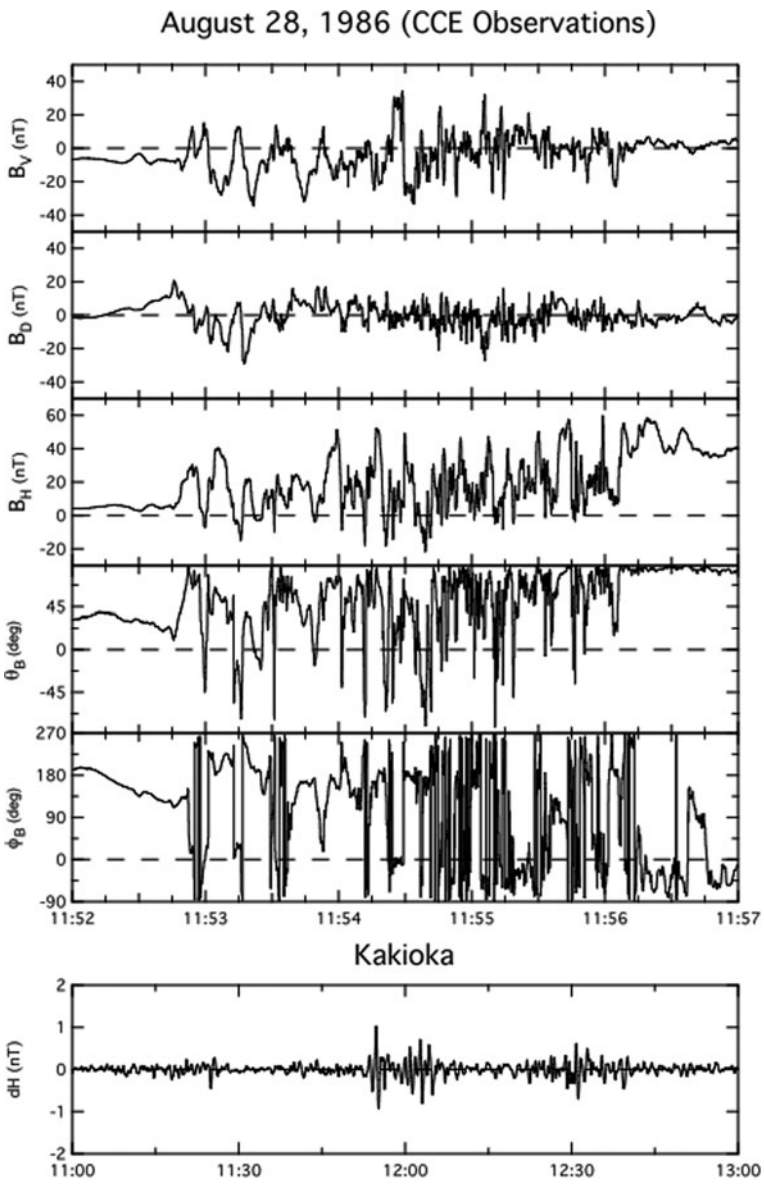

Fig. 5.21 Large magnetic fluctuations near the neutral sheet in the inner magnetosphere, signature of current disruption, observed by CCE just prior to Pi2 onset on the ground (Takahashi et al. 1987)

For the relevance of the DF to substorm onset, one should note that this sequence of earthward movement of DF shown in Fig. 5.24 occurred after substorm onset as indicated by the auroral activity. This is demonstrated in Fig. 5.25 by the auroral observation at Fort Smith.

The auroral breakup occurred at ~0744 UT, followed by dramatic poleward expansion of aurora typical of auroral behavior for substorm expansion. This onset time was ~7 min before the first appearance of DF at ~0751 UT by P1 and ~10 min before the latest appearance of DF at the inner satellite P4. In other words, the DF reported in Runov et al. (2009) was detected well after substorm onset even before it reached the inner magnetosphere. Therefore, it cannot be the cause of substorm onset for this event. This contrasts with near-earth dipolarization (NED) that can occur shortly before substorm onset (see, e.g., the case shown in Fig. 5.21). Furthermore, if the DF were caused by magnetic reconnection (MR) in the midtail (~20–30 R_E downtail distance), then the delayed onset of MR relative to substorm onset is exactly what the CD model predicts.

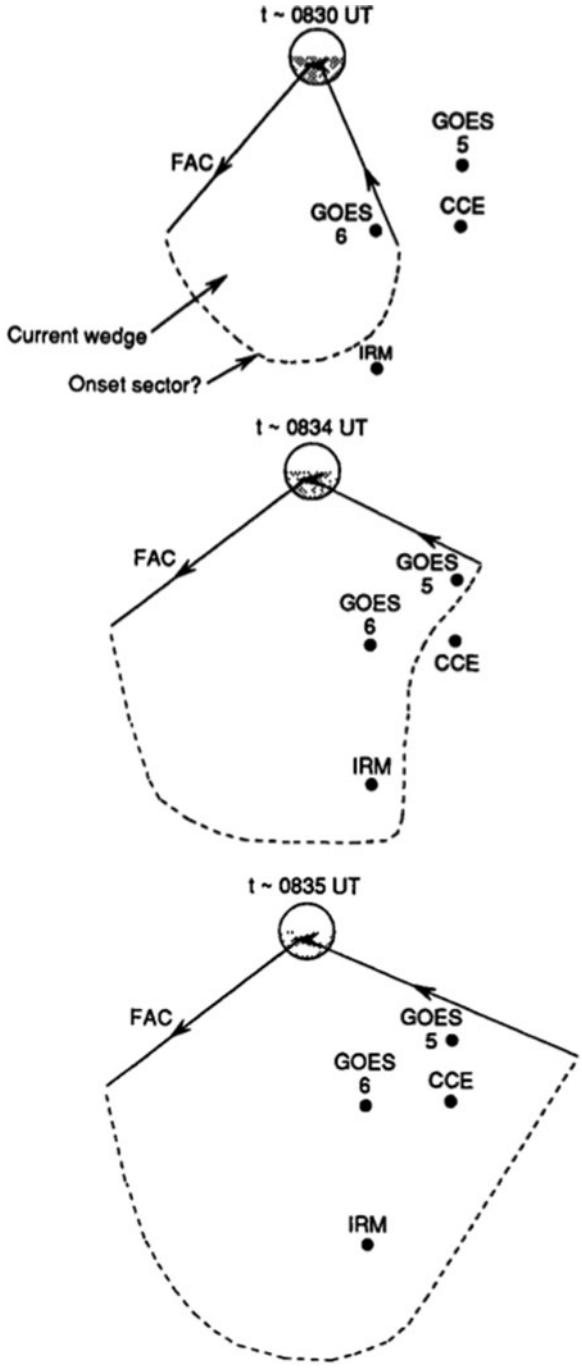

Fig. 5.22 A schematic illustration to show the progressive expansion of the CD region observed by multi-satellites in the inner magnetosphere during a substorm on April 19, 1985 (Lopez and Lui 1990)

Besides the opposite directions in the major development of B_Z increase between NED and DF, there are two additional major differences from the comparison of the temporal profile of B_Z in these dipolarizations. First, the NED starts with large magnetic fluctuations while the DF does not exhibit this variability. Second, the NED settles for a relatively steady B_Z over a prolonged period. In contrast, the B_Z increase in DF is very transient. These differences raise the plausibility that there may be two different types of dipolarization during a substorm.

Two different types of dipolarization was proposed by Nakamura et al. (2009) based on Cluster observations on 2007 October 27 at the downtail distances of ~10 R_E. These are schematically illustrated in Fig. 5.26. For this event, C4 was separated from C1 by only (8340, 12, 363) km. The first type (D1) is a dipolarization pulse transported by earthward fast flow followed by a short interval of B_Z fluctuations, plasma sheet thinning, and ~15 s period oscillation. The second type (D2) occurs after D1 where dipolarization has strong B_Z enhancement and not much B_Z fluctuations. However, this description does not fit well with the features seen in dipolarization fronts reported by Runov et al. (2009) and shown in Fig. 5.24, especially for B_Z variation of dipolarization at the innermost satellite P5.

A close look of the dipolarization at ~0907 UT for the Cluster event indicates a possible alternative interpretation. Figure 5.27 shows some Cluster measurements relevant to the data interpretation. Indeed, the B_Z fluctuations started earlier at C1 than C4. However, the dipolarization described in Nakamura et al. (2009) as type 1 dipolarization can be equally interpreted as a part of CD in which large fluctuations in all magnetic field components are produced. The large B_X fluctuations are another signature of CD, due possibly to current filamentation. Lui and Najmi (1997) have identified waves at ~15 s period in B_X (equivalent to B_V used in Lui and Najmi) during CD. Note also that the V_Z component of the plasma flow at C1 shows that the plasma was steadily moving northward, contrary to the interpretation of plasma sheet oscillation that would give V_Z sign change every ~15 s. At ~090845 UT (the vertical dashed line), the magnetic flux transported in the x-direction, calculated based on E_Y and B_Z, was much larger at C4 than at C1 even though both

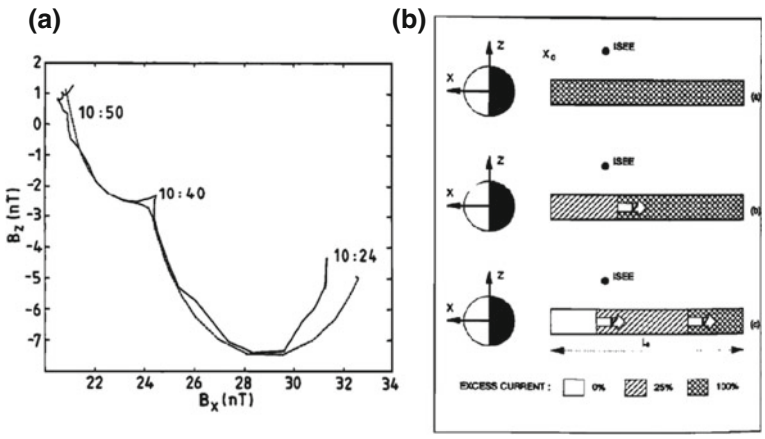

Fig. 5.23 (**a**) Modeling the variation of B_Z versus variation of B_X observed by ISEE satellite for a retreating CD region; (**b**) schematic representation of the current sheet used to model the B_Z versus B_X variations during a substorm (Jacquey et al. 1991)

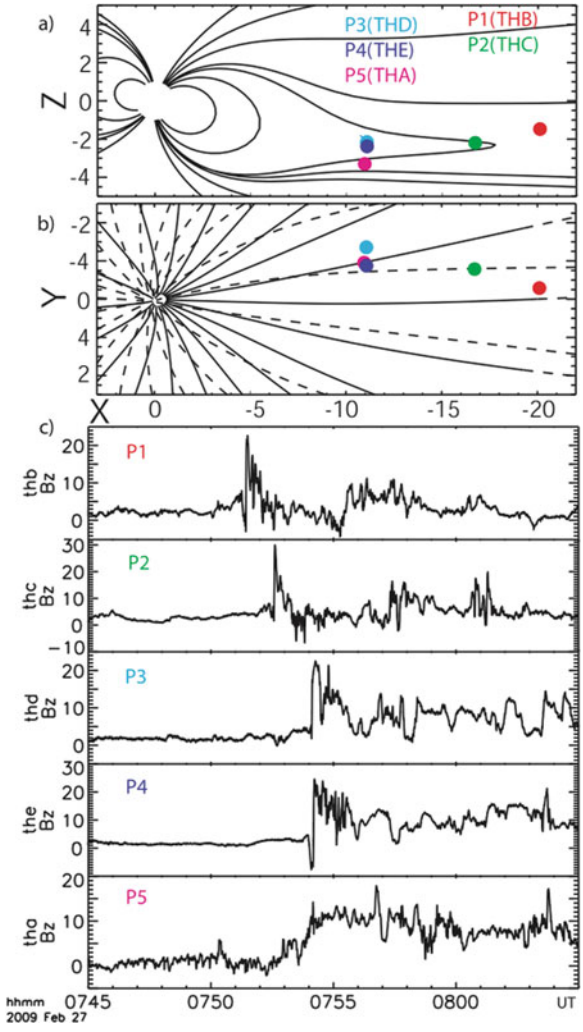

Fig. 5.24 Observation of dipolarization front during a major tail conjunction of THEMIS satellites (Runov et al. 2009)

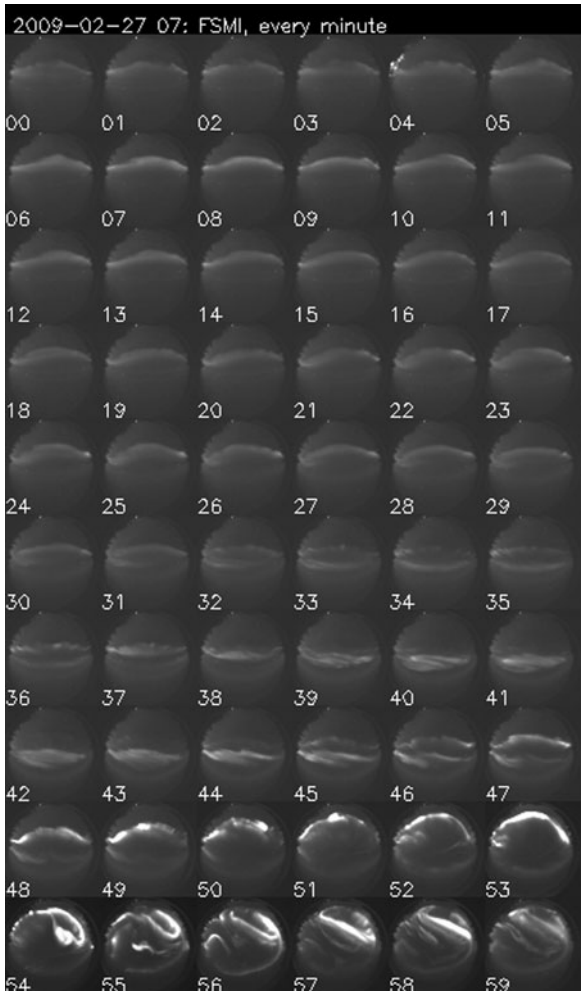

Fig. 5.25 Auroral images from Fort Smith for 0700-0800 UT on February 27, 2009 to show the dipolarization fronts observed by THEMIS occurred well after substorm onset at ~0744 UT. The earliest detection of dipolarization front at the most distant THEMIS satellite from Earth was at ~0751 UT (Lui, 2011a)

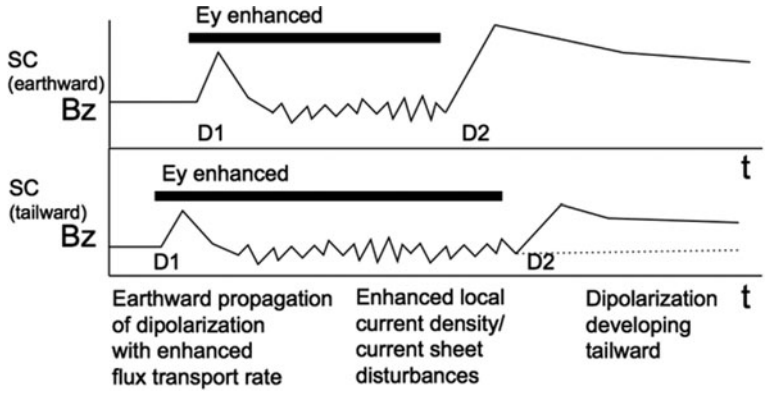

Fig. 5.26 Two types of dipolarization proposed by Nakamura et al. (2009)

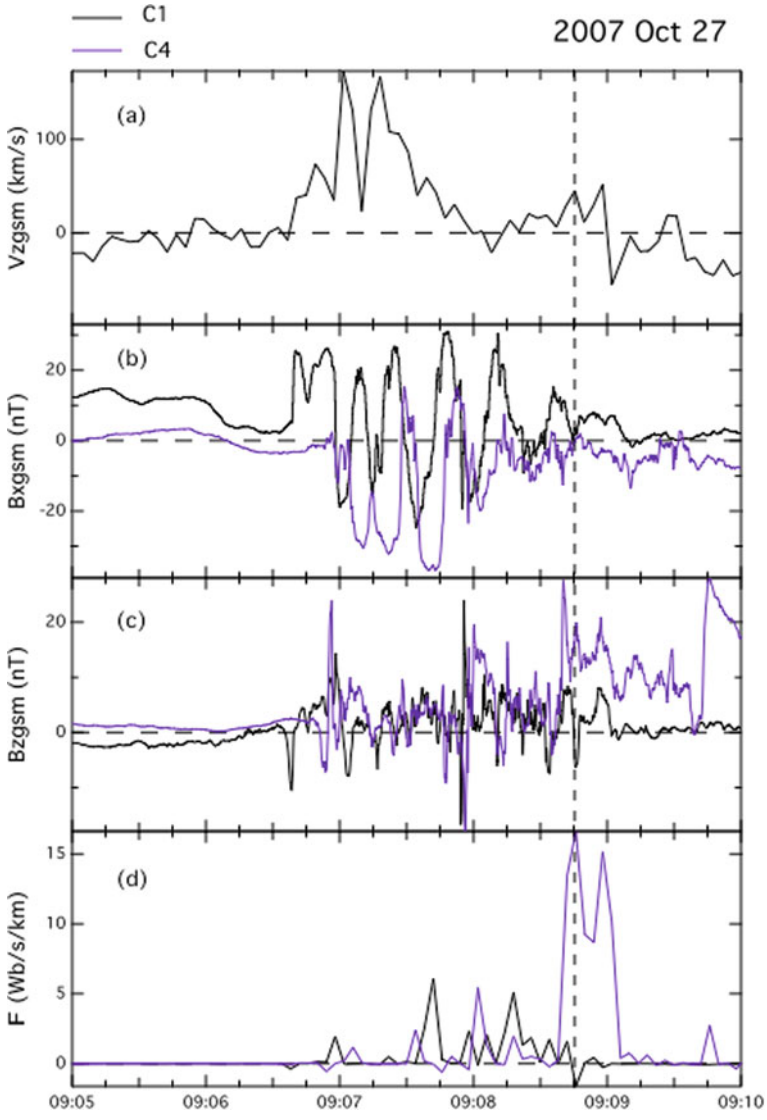

Fig. 5.27 Cluster data: (**a**) Vz at C1, (**b**) B_X at C1 and C4, (**c**) B_Z at C1 and C4, and (**d**) magnetic flux transport at C1 and C4. The B_X and B_Z fluctuations may be interpreted as magnetic perturbations from excited waves and current filamentation in current disruption phenomenon. The *vertical dashed line* marks the maximum magnetic flux transported earthward at C4. No similar value was seen in C1 further tailward

satellites were almost right at the neutral sheet where B_X was very small. This disparity does not fit well with the interpretation of magnetic flux transported earthward from C1 to C4.

5.4.2 Plasma Flows

Plasma flows are considered to be an integral part of dipolarization from the MHD point of view, i.e., magnetic flux is carried to various regions of the magnetotail by plasma flows perpendicular to the magnetic field. There are many studies of plasma flows in the magnetotail during substorms (e.g., Hones 1973; Lui et al. 1977a, 1998; Hones and Schindler 1979; Baumjohann et al. 1990; Angelopoulos et al. 1992, 1994; Nagai et al. 1998; Frank et al. 2001; Shue et al. 2008; Machida et al. 2009). The term burst bulk flow (BBF) was introduced to indicate the transient nature of the fast plasma flows (Angelopoulos et al. 1994) although such a transient nature was recognized earlier by Baumjohann et al. (1990). There are individual events that show plasma flow reversal from tailward to sunward after substorm onset that was identified by Pi2 pulsation onset (Nagai et al. 1998). However, statistical studies such as Machida et al. (2009) show its occurrence to be rare. DFs are often associated with the perpendicular plasma flow, as shown in Fig. 5.28 from Cluster observations (Nakamura et al. 2002). The four Cluster satellites were at ~15 R_E in the magnetotail for this event. Note the transient nature of dipolarization associated with the BBF.

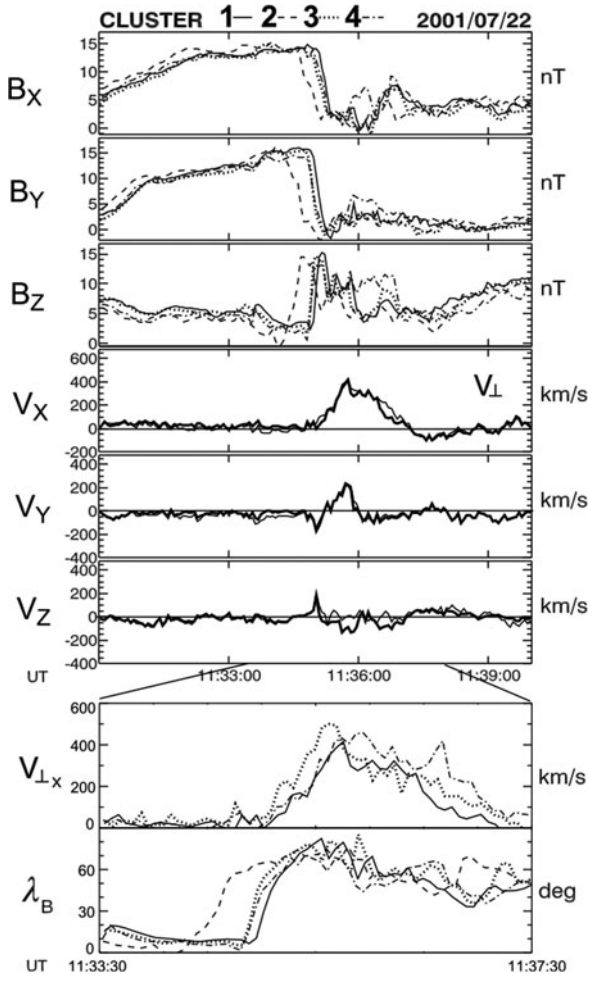

Fig. 5.28 Dipolarization front observed by Cluster satellites located at ~18 R_E in the magnetotail on August 12, 2001 (Nakamura et al. 2002)

At times, dipolarization near the neutral sheet occurs without any BBF (Lui et al. 1999). An example of this non-association of BBF and dipolarization from Geotail is shown in Fig. 5.29. Geotail was at ~10 R_E in the midnight sector of the magnetotail during this time. The times of the three dipolarizations are marked by vertical dashed lines, showing the lack of BBF and frequent occurrence of dawnward E_Y at dipolarization. Dawnward E_Y is opposite in direction to the expectation that earthward BBFs are responsible for dipolarization.

A systematic study involving 68 plasma flow events from Geotail revealed two classes of fast earthward plasma flows in the magnetotail (Shue et al. 2008). The first class consists of events observed near 10 R_E in the magnetotail. They were associated with high auroral powers and auroral substorm development seen by Polar UVI. The other class consists of events tailward of 15 R_E in the magnetotail. They were associated with low auroral powers with auroral features such as PBI and pseudobreakups. The spatial distribution of these two classes in relation to auroral power is shown in Fig. 5.30. Ohtani et al. (2006) showed that most BBFs seen in the mid-tail region do not reach geosynchronous altitude to cause dipolarization, a result consistent with the finding of two classes of BBFs. On the other hand, CD at downtail distances near 10 R_E can reach the geosynchronous altitude. Phenomena described as flow braking near 10 R_E may be related to plasma flows generated by CD at the near-earth distances rather than by magnetic reconnection beyond 15 R_E. The lack of association between

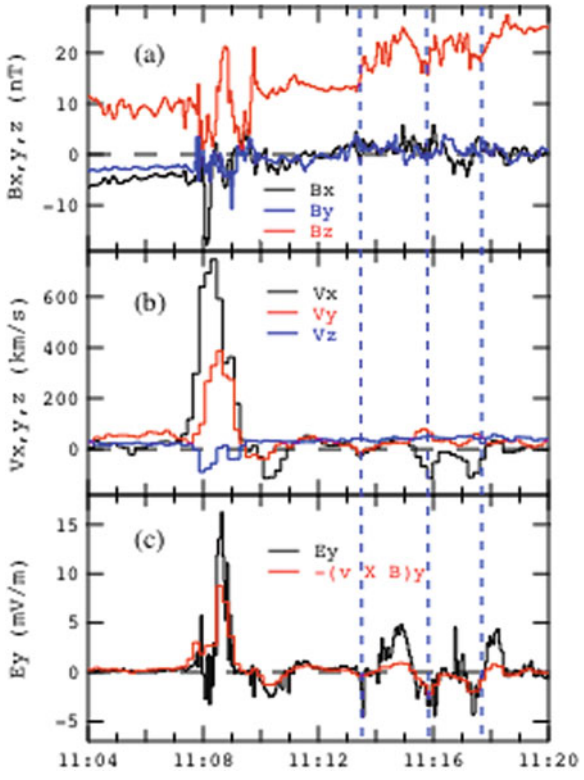

Fig. 5.29 Observation of dipolarization in the near-earth magnetotail by Geotail showing the absence of fast plasma flows associated with dipolarization (Lui et al. 1999)

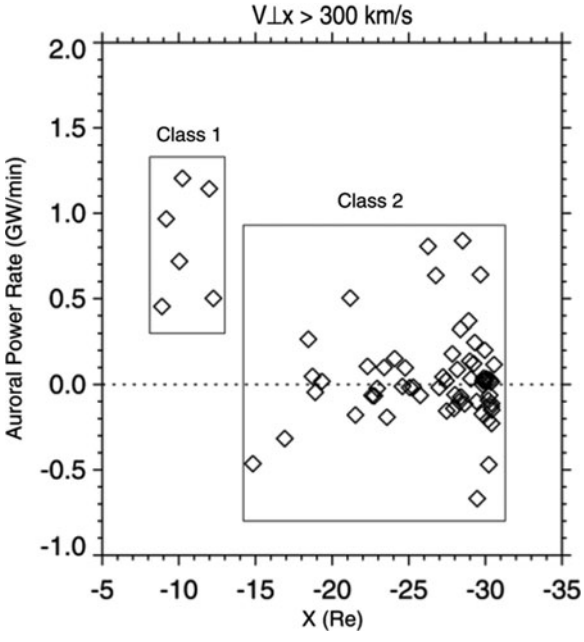

Fig. 5.30 Two classes of BBF in relation to auroral power output rate (Shue et al. 2008)

plasma flows in the near-earth region and the mid-tail region is illustrated well in statistical studies of plasma dynamics near substorm onset (Machida et al. 2009).

Tailward plasma flows with positive B_Z in the central plasma sheet within the downtail distance of ~31 R_E have been examined statistically with Geotail observations (Ohtani et al. 2009). Superposed epoch analysis shows that fast tailward flows last typically 1 min, occur more often in the near-earth ($X > -15\ R_E$) than in the mid-tail ($X < -15\ R_E$) plasma sheet, are often accompanied by negative E_y, and appear after fast earthward flows. These features suggest that fast tailward flows are rebounds of fast earthward flows.

5.4.3 Mid-Tail Plasma Sheet Thinning and Rarefaction Wave

Since CD causes substorm injection that displaces plasma earthward, its occurrence creates a reduction of plasma pressure locally. The partial void would be filled by surrounding plasma. This can lead to dipolarization in the central plasma sheet and thinning at the plasma sheet boundary layer, as observed in some occasions (e.g., Liang et al. 2009; Liu and Liang 2009; Sergeev et al. 2008). Furthermore, another consequence is a tailward progression of earthward plasma flow and plasma sheet thinning in the mid-tail, as observed by Lui et al. (1977b) and modeled in Chao et al. (1977). These plasma characteristics are consistent with a rarefaction wave launched by CD in the near-earth magnetotail. The rarefaction wave is revealed by the decrease in total pressure in the mid-tail from the superposed epoch analysis on Geotail observations (Machida et al. 2009).

This progressive plasma sheet thinning in the mid-tail is schematically illustrated in Fig. 5.31, together with the change in magnetic field orientation at several downtail distances. Stages 1, 2, and 3 of plasma sheet thinning in Fig. 5.31 correspond to the intervals before onset, shortly after onset, and well into substorm expansion, respectively. The magnetic field shows the largest southward dipping when the thinning wave front approaches the observation site (Lui et al. 1977b).

An example of such transient southward dipping from Cluster measurements is shown in Fig. 5.32 (Sergeev et al. 2007). Cluster was at the downtail

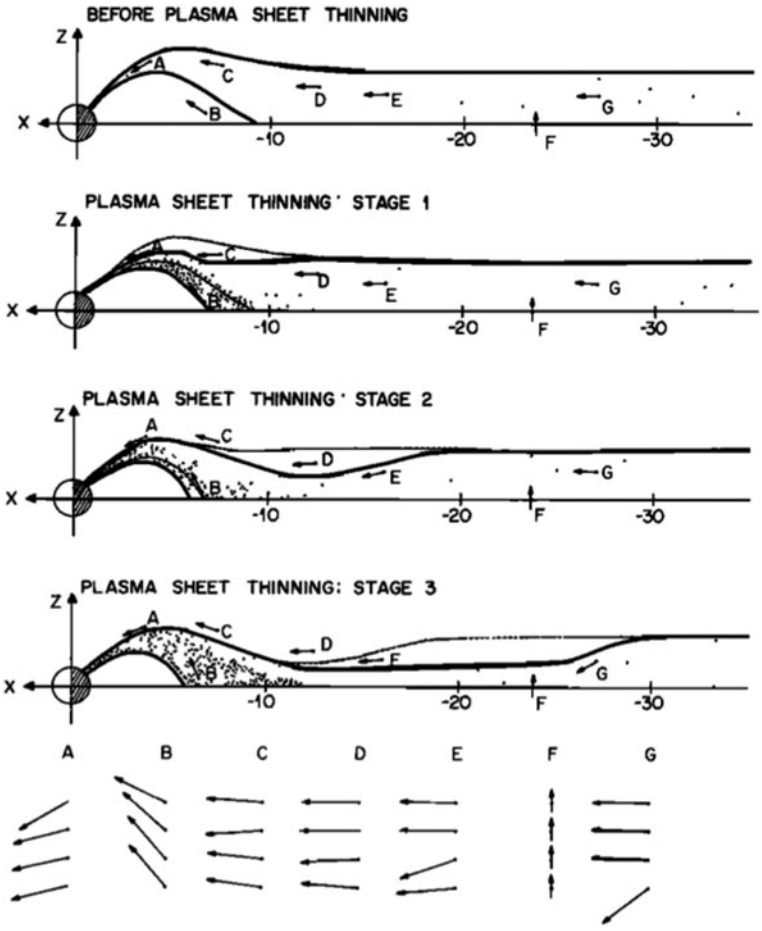

Fig. 5.31 Plasma sheet thinning and the associated magnetic field deflection at various magnetotail locations during a substorm. The largest deflection is at the plasma sheet boundary when the rarefaction wave that thins the plasma sheet reaches that downtail distance (Lui et al. 1977b)

distance of ∼15 R_E and TC2 was near the geosynchronous altitude when a small auroral bulge was observed by IMAGE WIC camera at ∼0845 UT on September 26, 2005. Substorm injection of energetic particles were detected by near-geosynchronous satellites (LANL 084 and TC2). Southward dipping of the magnetic field was found in all four Cluster satellites, with C2 showing the most negative B_Z. During the last two auroral activations at ∼0930 UT and ∼0940 UT, large magnetic fluctuations indicative of turbulence were observed both in the mid-tail region (Cluster) and at the near-geosynchronous altitude (TC2).

5.4.4 Plasma Waves and Turbulence

Intense plasma waves at frequencies near and above the ion gyrofrequency are often observed in association with CD. As an example, Fig. 5.33 shows the magnetic and electric fluctuations seen around CD onset by THEMIS P5 at ∼8 R_E in the magnetotail on January 29, 2008 (Yoon et al. 2009). The magnetic fluctuations of this event were first reported by Lui et al. (2008b), showing the inverse cascade feature in the B_Z component with wavelet analysis. Evidence of inverse cascade in the quasi-periodic auroral structures was also reported (Rae et al. 2009).

Vörös et al. (2010) later debated on this feature using discrete empirical mode analysis from the Hilbert-Huang transform (HHT) analysis. Even though their result showed high-frequency mode evolving to low-frequency mode, the presence of other trends indicative of multi-scale processes led them to assert the simple inverse cascade scenario to be incorrect. Also, they associated the inverse cascade as due to sudden jumps in the signal. These criticisms are not well founded. First, unlike the continuous wavelet analysis, the discrete output from HHT is unsuitable to

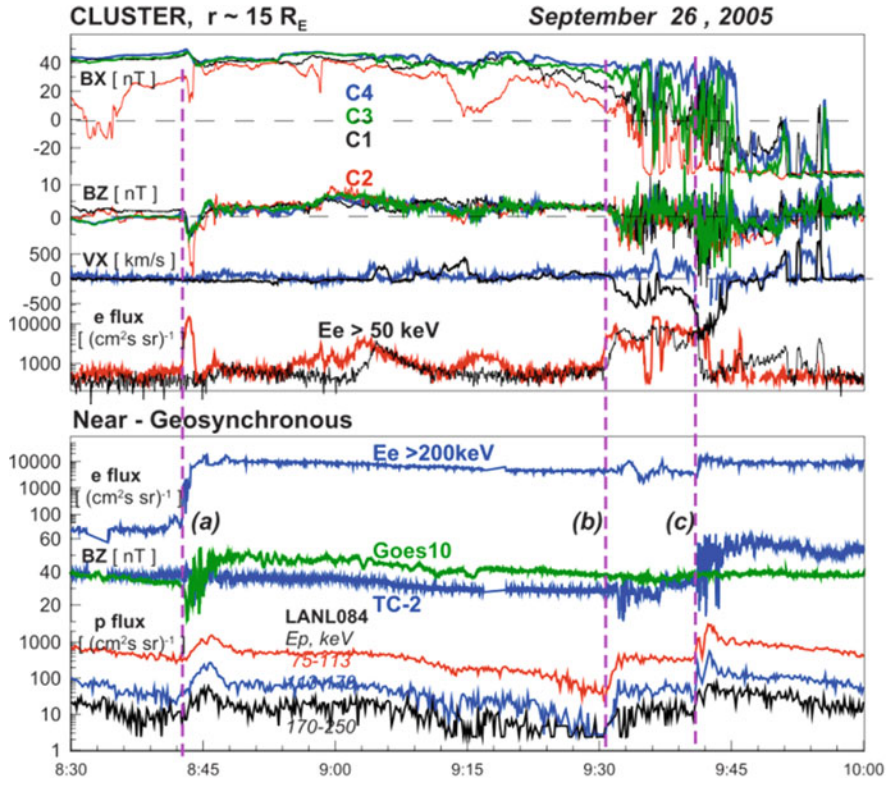

Fig. 5.32 Occurrence of magnetic reconnection and current disruption during a substorm on September 26, 2005 (Sergeev et al. 2007)

identify inverse cascade in a contiguous frequency scale. Second, the instantaneous frequency definition in HHT is not universally accepted. Third, a sudden jump in signal produces a 'pyramid' shape in the frequency-time domain, completely different from the inverse cascade shape. Fourth, Lui et al. (2008b) never claimed the inverse cascade feature to be a simple one since CD is a multi-scale phenomenon (Consolini et al. 2005; Lui 2002). Therefore, the criticisms of Vörös et al. are based on a simplistic notion of CD and inaccurate understanding of wavelet analysis. In addition, there is important underlying physics that can be extracted from the wavelet analysis results as shown in Yoon et al. (2009) that is totally unattainable by the Vörös et al. analysis.

For the CD event examined by Yoon et al. (2009), the corresponding wavelet analyses of these field components are shown in Figs. 5.34 and 5.35. When the perturbations were tested with the wave dispersion equation based on the Maxwell's equation, it was found that the wave characteristics match with those generated by the Alfvén ion cyclotron instability with propagation angles nearly perpendicular to the magnetic field.

Waves at frequencies much higher than the ion gyrofrequency have also been observed with dipolarization (Le Contel et al. 2009; Zhou et al. 2009). Quasi-parallel whistler waves were found throughout a local dipolarization interval on January 29, 2008 in the near-earth magnetotail (Le Contel et al. 2009). The measured electron temperature anisotropy, with perpendicular temperature larger than the parallel temperature, was sufficient to drive the whistler mode unstable. Poynting vector calculation indicates that the whistler waves were excited near the neutral sheet where the temperature anisotropy was the highest. These waves can be related to small-scale current sheets.

In another interval of multiple DFs during a substorm on February 15, 2008, large wave fluctuations extending from below the lower hybrid frequency to above the electron gyrofrequency were observed in the near-earth magnetotail (Zhou et al. 2009). Intense electric field wave packets were observed at the DF,

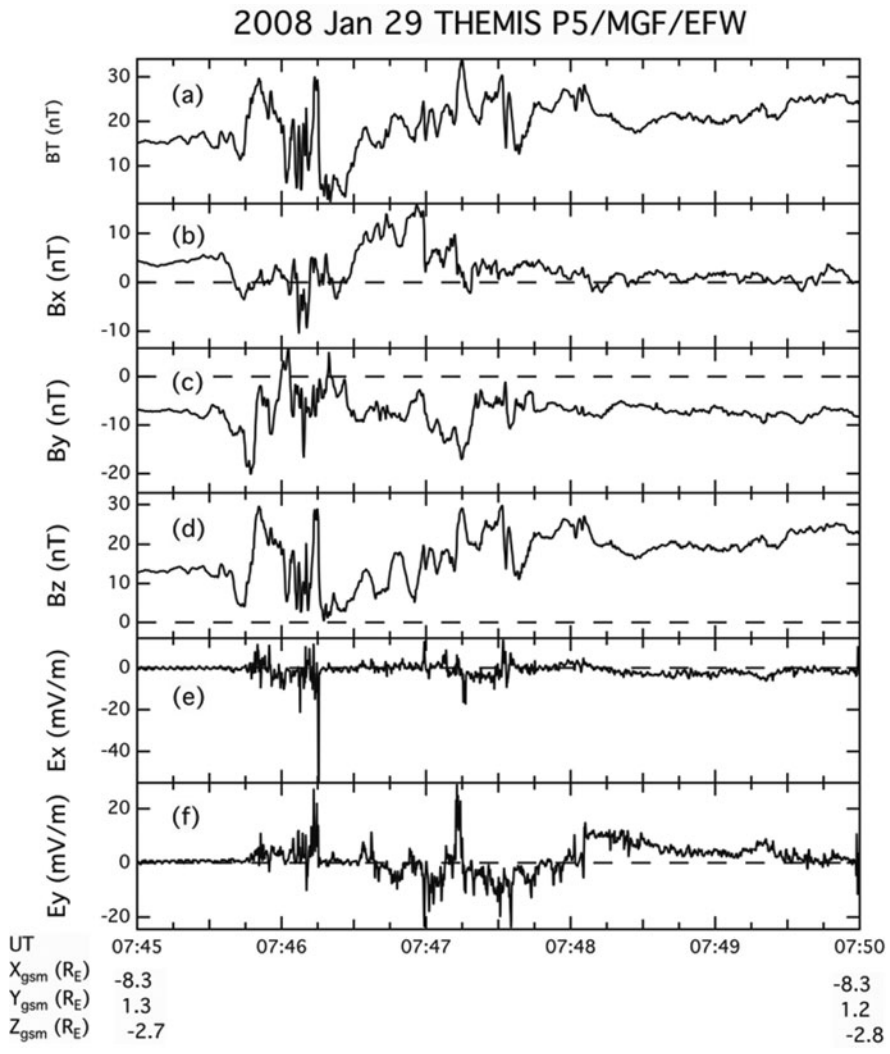

Fig. 5.33 Magnetic and electric field measurements by THEMIS P5 in the inner magnetosphere for a CD onset on January 29, 2008 (Yoon et al. 2009)

which was estimated to have a thin current sheet with a size on the order of the ion inertial length. Electrostatic electron cyclotron harmonic waves, possibly generated by the positive slope of the electron perpendicular velocity distribution, were observed slightly after the DF. The power spectrum, waveform, and electron distribution function for the event are shown in Fig. 5.36.

Panel (a) shows the power spectrum of electric field and the vertical dashed line indicates the electron gyro-frequency. Waveforms in field-aligned coordinate filtered between 800 and 3000 Hz are shown in panels (b) and (c). 1D cut of the electron phase space density as a function of perpendicular velocity at $V_{||} = 0$ is shown in panel (d).

The multiscale nature of plasma waves excited at CD onset is demonstrated well by the wavelet analysis shown in Figs. 5.34 and 5.35. More detail analysis of CD events shows CD to be non-MHD turbulence (Consolini et al. 2005). The validity of the term turbulence to describe the large magnetic and electric fluctuations during CD is also demonstrated by the multiscale and multifractal nature of these disturbances (Lui 2002).

Plasma turbulence can lead to the breakdown of the frozen-in condition assumed in the MHD theory. This is captured by Cluster observations during a substorm on August 22, 2001 when it was in the downtail distance of $\sim$19 R_E in the midnight sector

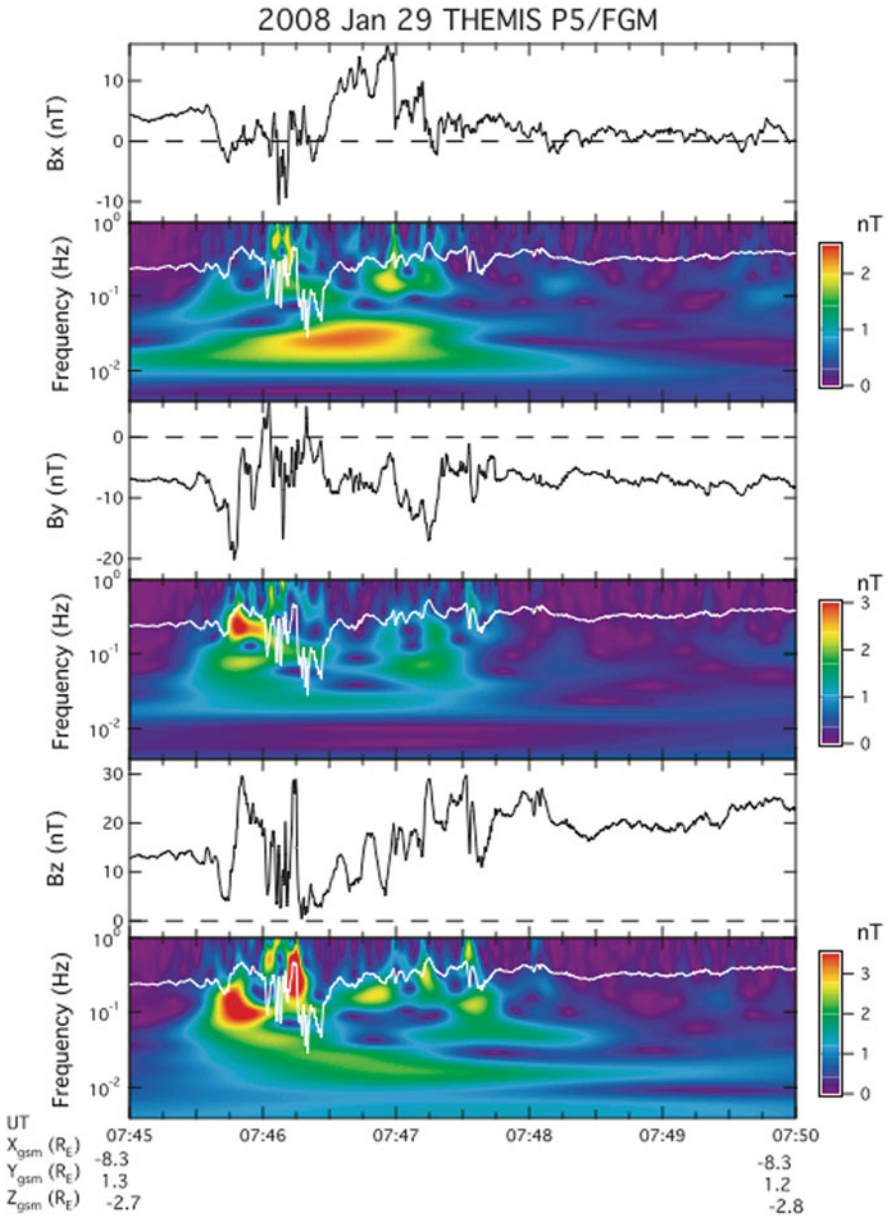

Fig. 5.34 Wavelet analysis of magnetic fluctuations during the CD event observed by THEMIS P5 on January 29, 2008. Inverse cascade of wave energy from high to low frequencies is evident in the B_Z component and, perhaps, in the B_Y component as well (Yoon et al. 2009)

(Lui et al. 2007b). Figure 5.37 shows observation in the breakdown of frozen-in condition at C1, identified by the difference between E_Y and $-(\mathbf{V}\times\mathbf{B})_y$, where $\mathbf{V}$ is the plasma bulk flow. The breakdown was very intermittent and occurred during high plasma flows.

The high-time resolution electric field measurement during the breakdown interval showed large variability as shown in Fig. 5.38. The electric field magnitude reached almost 200 mV/m. The breakdown occurred at other intervals at C1 as well as at another location sampled by C3, where the frozen-in condition can be checked.

The terms in the generalized Ohm's law can be estimated for this event. The current density $\mathbf{J}$ can be evaluated by the curlometer technique (Dunlop et al. 1988; Chanteur 1998), so can its time derivative (the inertial

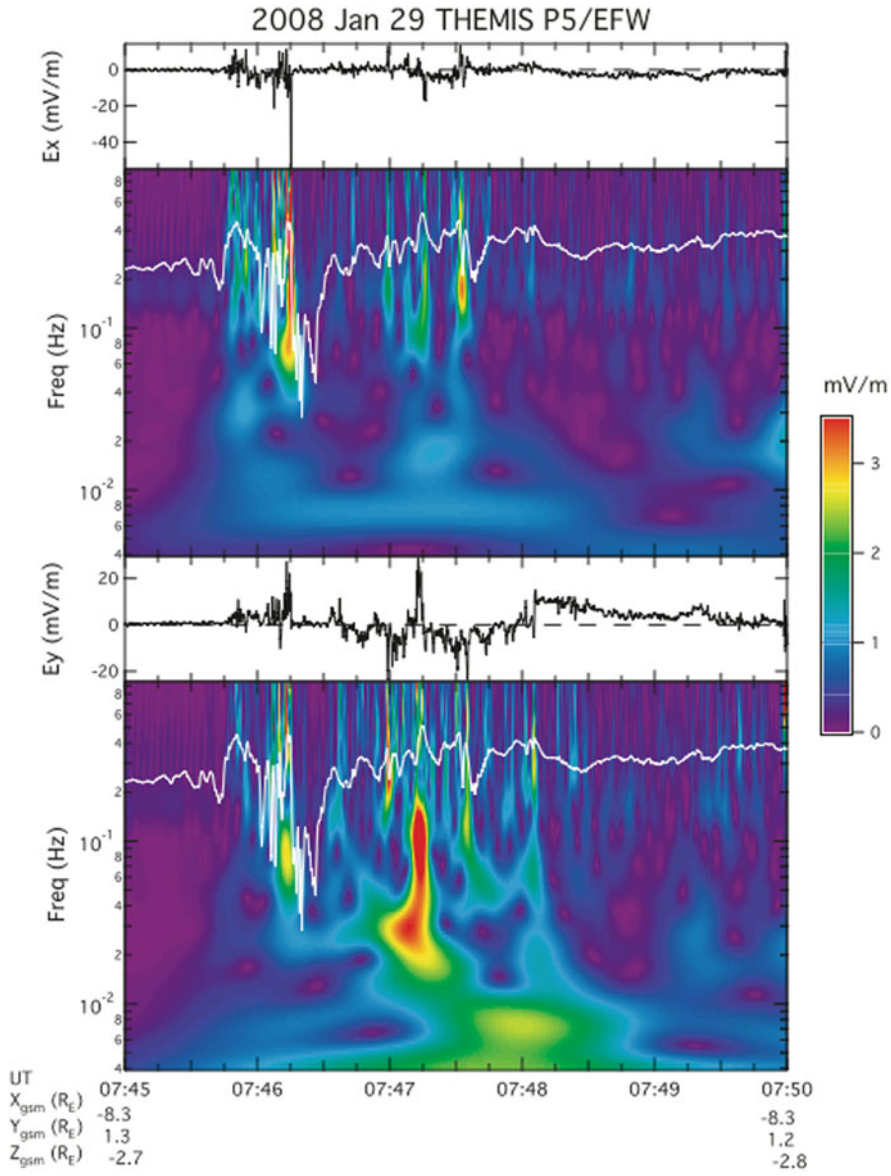

Fig. 5.35 Wavelet analysis of electric fluctuations during the CD event observed by THEMIS P5 on January 29, 2008 (Yoon et al. 2009)

term). The Hall term $\mathbf{J} \times \mathbf{B}$ can be calculated with the averaged $\mathbf{B}$. Since $\partial/\partial x \ll \partial/\partial z$ in the tail, the dominant terms in electron viscosity $(\nabla \bullet \mathrm{P_e})_y$ are $\partial \mathrm{P_{eyy}}/\partial y$ and $\partial \mathrm{P_{eyz}}/\partial z$. They can be estimated by the gradients of $\mathrm{P_{eyy}}$ and $\mathrm{P_{eyz}}$ between C1 and C2. The anomalous resistivity terms can be estimated by the fluctuations in $\mathbf{B}$, $\mathbf{E}$, and number density. With these estimates, it is found that the anomalous resistivity contribution arising from field fluctuations is the most significant, followed by the Hall, electron viscosity, and inertial contributions in descending order of importance. The values of these terms are shown in Fig. 5.39 for the time interval encompassing the breakdown. It can be seen that these terms only have significant values during the interval of frozen-in condition breakdown.

Electron diffusion region is where electrons do not satisfy the frozen-in condition. This occurs when the frozen-in condition is broken due to significant values from any of the three terms in the generalized Ohm's law, i.e., electron viscosity, inertial, and resistivity

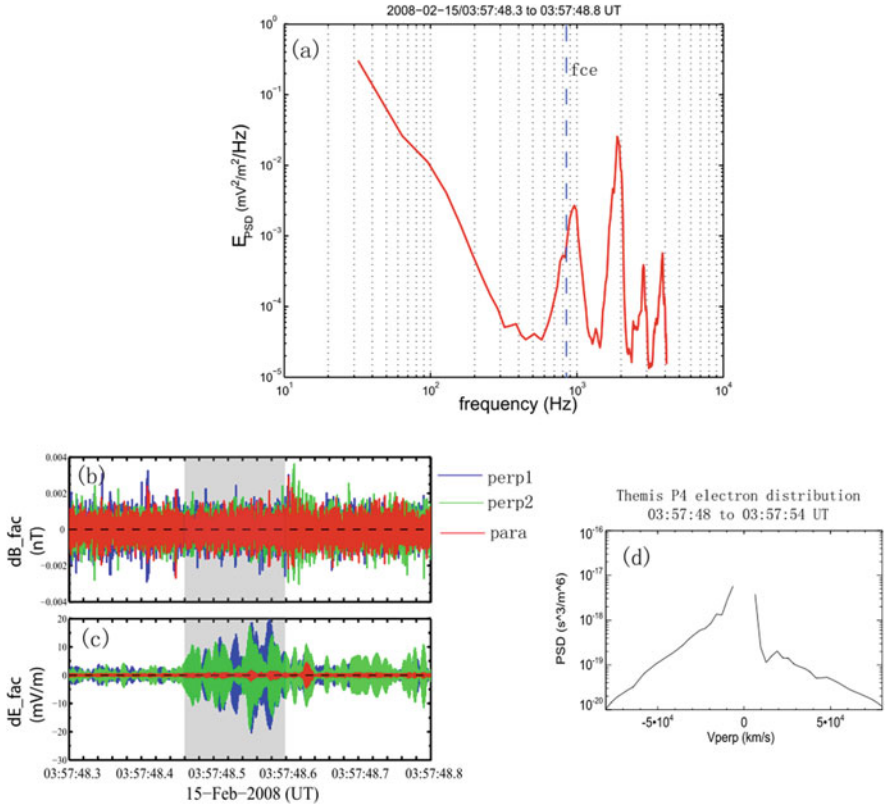

Fig. 5.36 Power spectrum, waveform, and electron distribution function for waves identified as electron cyclotron harmonic waves around dipolarization observed by THEMIS P4 on February 15, 2008 (Zhou et al. 2009)

from field fluctuations. A schematic diagram illustrating the electron diffusion region encountered during this event is shown in Fig. 5.40, emphasizing the strong turbulence and the complex magnetic field configuration in the closed magnetic field line region. The spatial separation of the Cluster satellites and the simultaneous detection of the frozen-in condition breakdown at two Cluster satellite locations give the approximate dimensions (>1000 km) for the electron diffusion region in both the radial and the north-south directions, which is much larger than the electron inertial scale for this event. The different symbol sizes of current density J_Y and electric field E_Y illustrate the different magnitude of these quantities, which have mostly positive values but occasionally negative values as well. The electron diffusion region is thus mostly dissipative but occasionally is a dynamo in localized regions.

Similar breakdown was reported in another substorm interval on August 28, 2005 when Cluster was in the downtail distance of ~17 R_E (Runov et al. 2008). This breakdown occurred during significant plasma flows also. However, the inability to estimate all the terms of the generalized Ohm's law for this event by Runov et al. (2008) leads only to the assessment of the ion diffusion region rather than the electron diffusion region. Furthermore, the north-south dimension of this breakdown region was estimated to be less than 900 km. This smaller dimension should not be surprising since different events have different plasma parameters in the breakdown region. Therefore, the dimensions from one event cannot be considered applicable to other events. Furthermore, it is also possible that the north-south distance separation between the Cluster satellites for that event did not span the entire ion diffusion region. For example, if the Cluster satellite nearest to the neutral sheet had a substantial distance from it or the Cluster satellite furthest from the neutral sheet was not at the outermost reconnection layer, then the separation between Cluster satellites does not yield an accurate determination of the ion diffusion dimension. As a result, a smaller dimension than the actual one would be inferred instead. In any

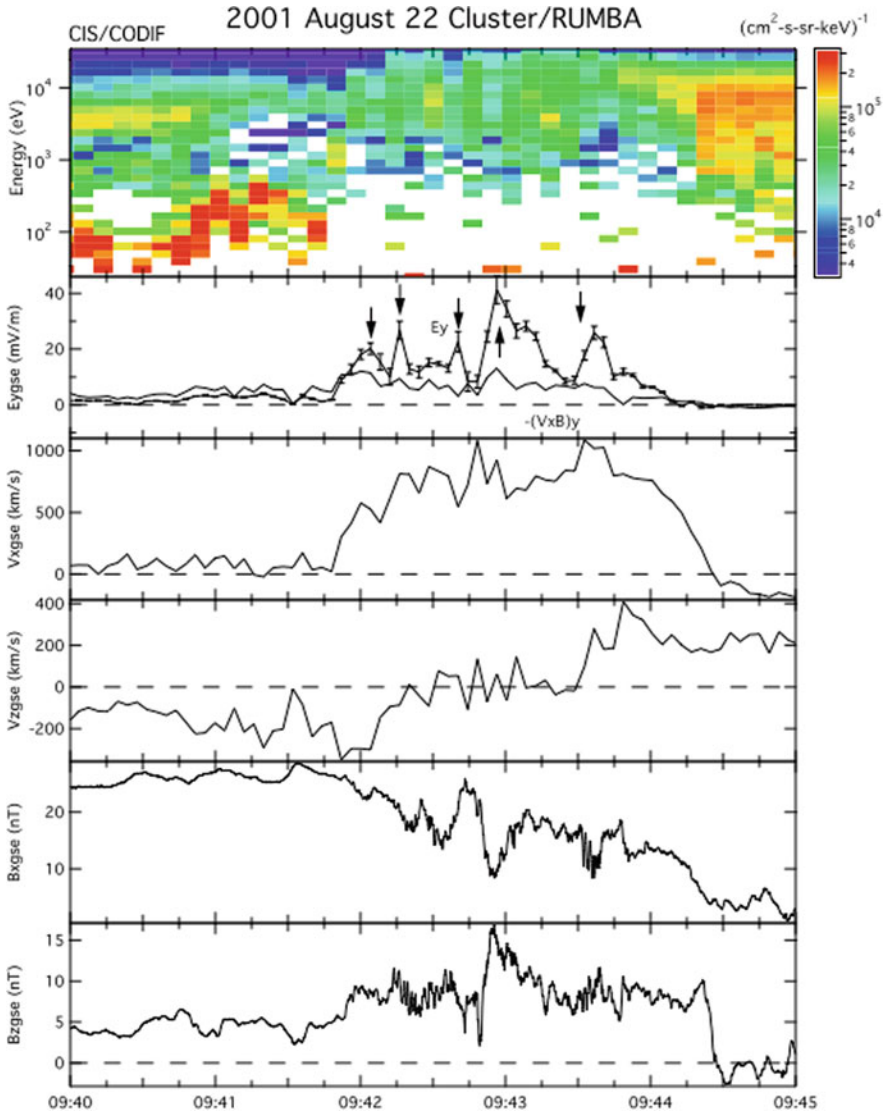

Fig. 5.37 Cluster observations of a breakdown of the frozen-in condition at ~19 R_E in the magnetotail (Lui et al. 2007b)

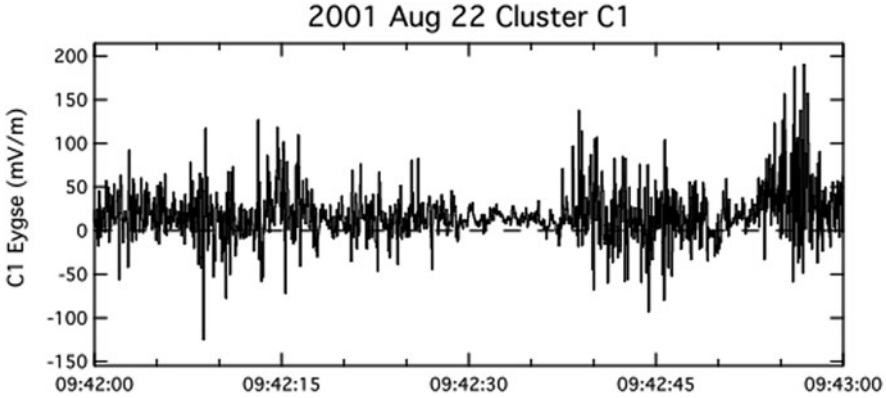

Fig. 5.38 Electric field fluctuations seen by Cluster during the breakdown of the frozen-in condition (Lui et al. 2007b)

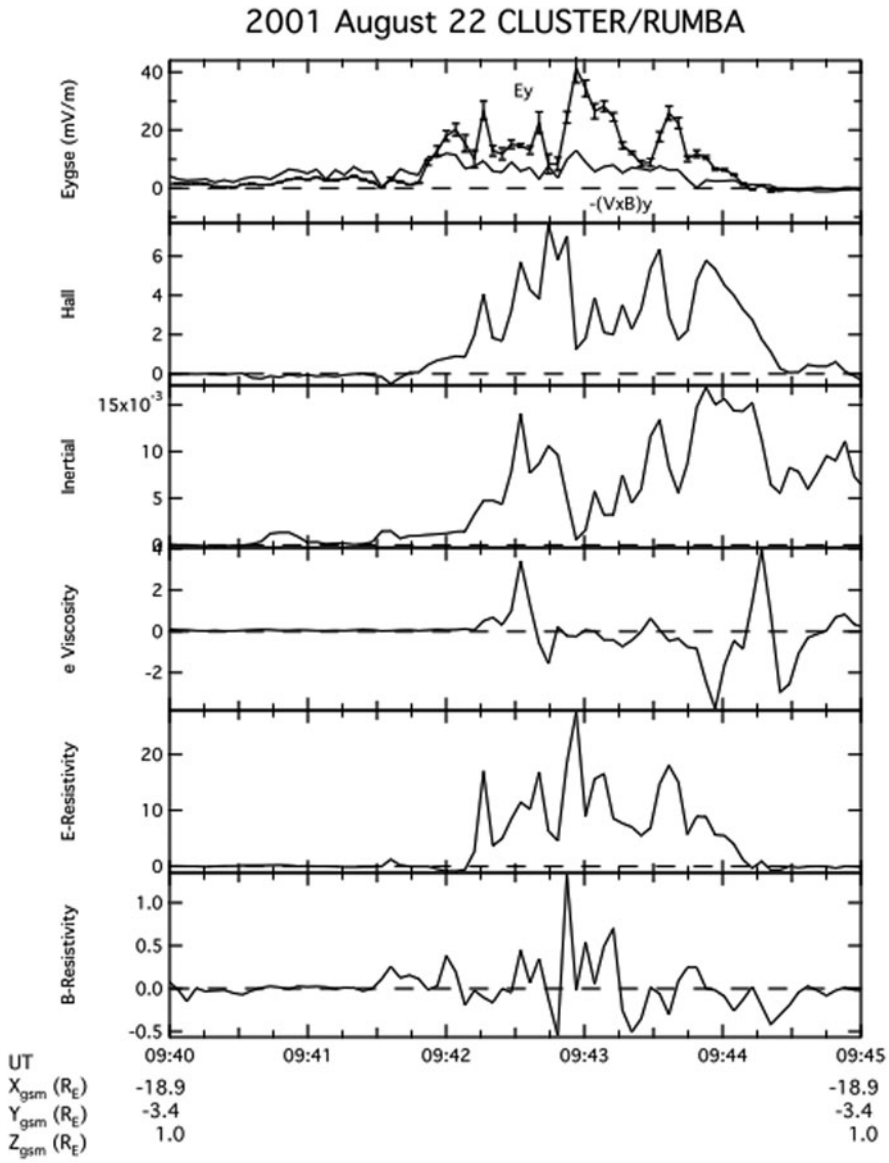

Fig. 5.39 Evaluation of the terms in the generalized Ohm's law that lead to the breakdown of the frozen-in condition (Lui et al. 2007b)

case, it is important to recognize that the dimensions found in Lui et al. (2007b) event are larger than the theoretical expectation.

5.5 Time History Analysis

A recent trend in substorm research is motivated by the THEMIS mission whose goal is to differentiate two main competing substorm models, one based on MR (magnetic reconnection) and the other on current disruption instability (CDI). The approach is to examine the time history of substorm disturbances within the magnetotail using five THEMIS satellites aligned nearly along the tail axis during major tail conjunction intervals, i.e., when all THEMIS satellites are aligned roughly along the tail axis. When substorm disturbance is first detected by a satellite in the mid-tail region, followed subsequently by disturbance seen at satellites closer to the Earth according to the downtail distance, then it is the 'outside-in' scenario. Otherwise,

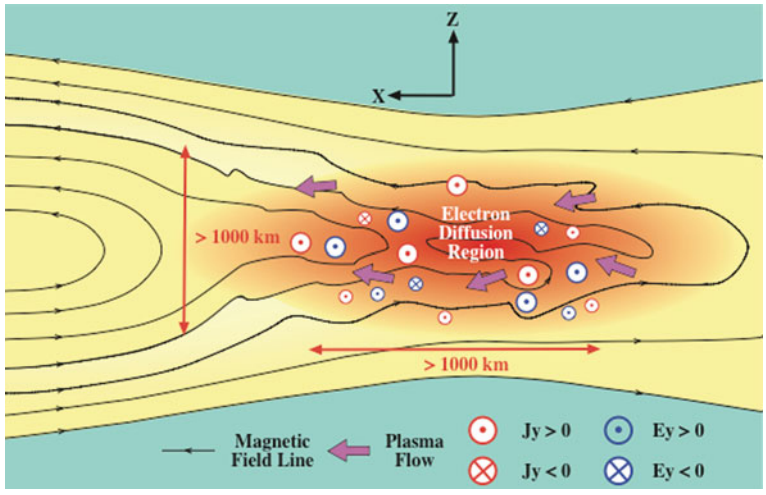

Fig. 5.40 A schematic diagram to show the breakdown of the frozen-in condition in the magnetotail, emphasizing the size (>1000 km) in the *X*- and *Z*-directions of the electron diffusion region and its immersion in fast earthward plasma flow region for this event. The irregularities in the magnetic field lines in the electron diffusion region illustrate the high fluctuation nature of the magnetic field (Lui et al. 2007b)

it is the 'inside-out' scenario. It is implicitly assumed that the 'outside-in' scenario implies the substorm onset process to be MR while the 'inside-out' scenario implies the substorm onset process to be CDI. Three individual substorm events (Sections 5.5.1–5.5.3) are presented here and the usefulness of this approach will be evaluated in Section 5.5.4.

5.5.1 2008 February 26 Event

Analysis of substorm disturbances on 2008 February 26 was conducted by Angelopoulos et al. (2008) based on the time history approach. The THEMIS satellites were aligned well along the tail axis; see right column of Fig. 5.41. The signatures at P1 used for MR

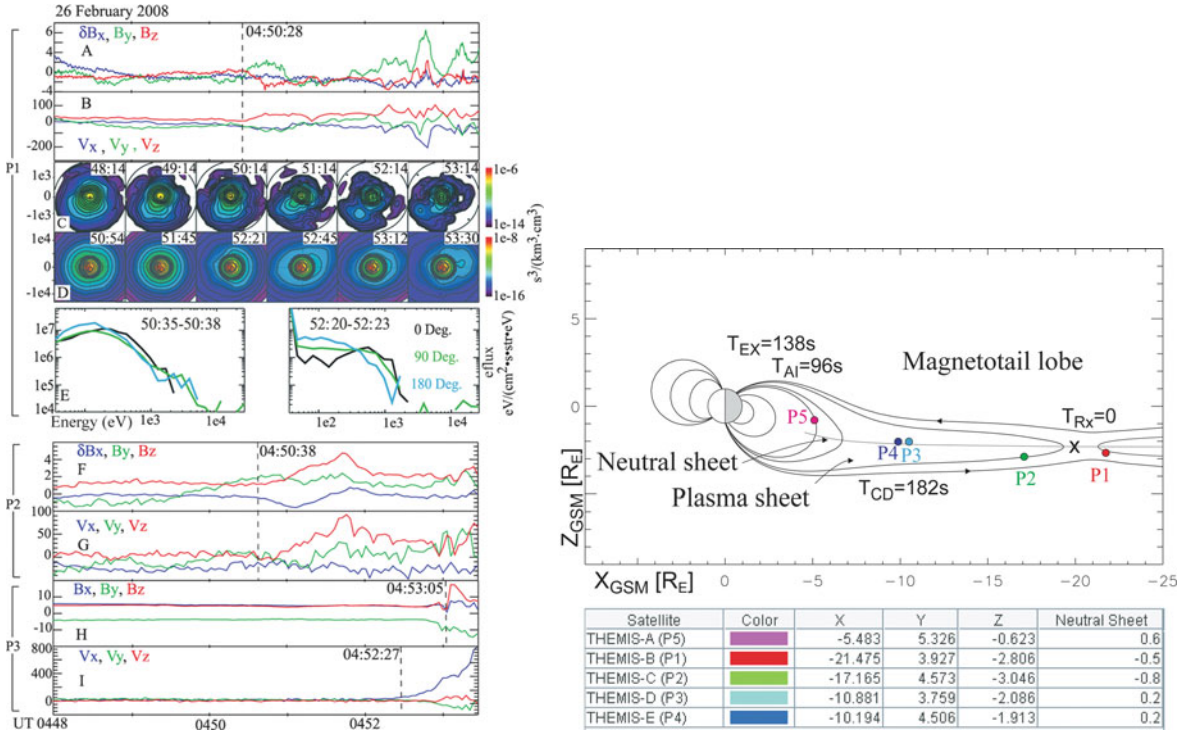

Satellite	Color	X	Y	Z	Neutral Sheet
THEMIS-A (P5)		-5.483	5.326	-0.623	0.6
THEMIS-B (P1)		-21.475	3.927	-2.806	-0.5
THEMIS-C (P2)		-17.165	4.573	-3.046	-0.8
THEMIS-D (P3)		-10.881	3.759	-2.086	0.2
THEMIS-E (P4)		-10.194	4.506	-1.913	0.2

Fig. 5.41 Observations of substorm disturbances from three THEMIS satellites on 2008 February 26 (Angelopoulos et al. 2008)

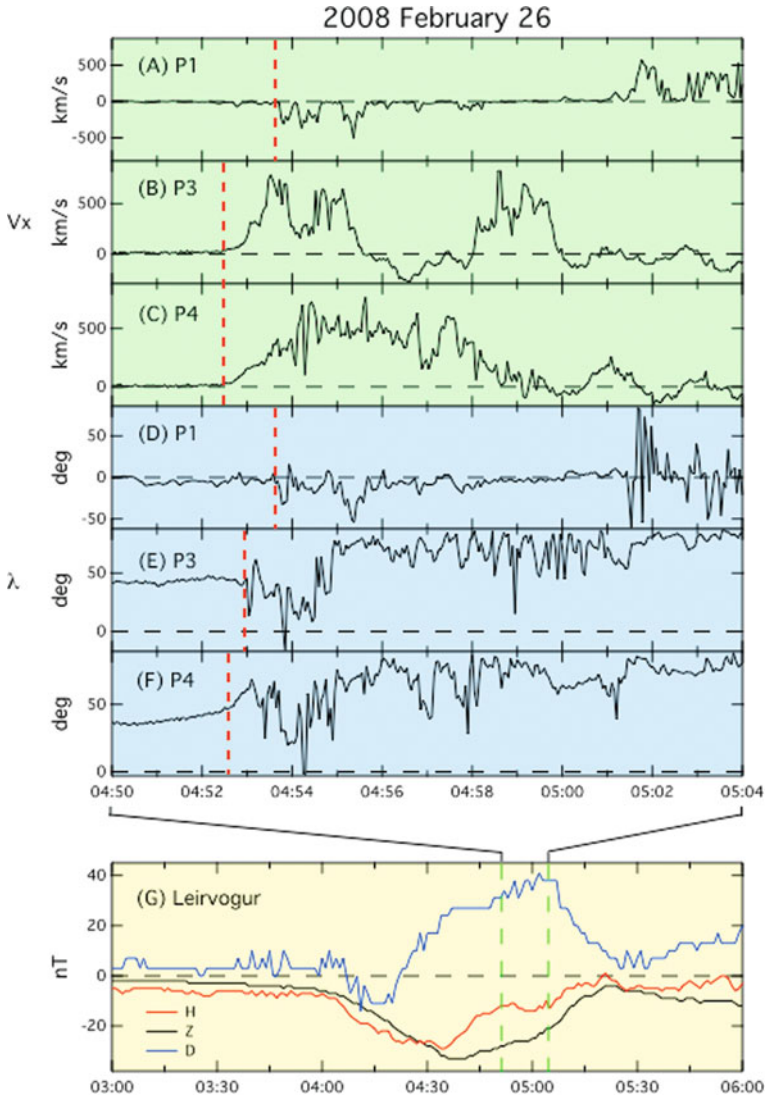

Fig. 5.42 Observations of significant substorm disturbances on 2008 February 26 from P1, P3, and P4. Panels (**a**)–(**c**) show the *x*-component of the convective flow from P1, P3, and P4, (**d**)–(**f**) show the elevation angle of the magnetic field from P1, P3, and P4, and (**g**) shows the perturbation at the ground magnetic station Leirvogur (Lui 2009)

identification are slight southward dipping of the magnetic field (Fig. 5.41a), slight northward plasma flow toward the neutral sheet (Fig. 5.41b), and opposite anisotropy between cold and hot electrons (Fig. 5.41e). MR signature used for P2 was a slight positive swing of B_Z (Fig. 5.41f). However, it was unaccompanied by earthward plasma flow or any noticeable change in the plasma flow signature (Fig. 5.41g), contrary to the expected MR signature. The larger disturbances at P3 occurred later (Fig. 5.41h, i). From this time history, it was concluded that MR near $X = -20\ R_E$ was the substorm onset trigger.

However, Lui (2009) pointed out several interpretation problems in addition to the discrepancy at P2. A close look of Fig. 5.42 at the significant disturbances at the THEMIS satellites using the standard MR signatures shows that tailward plasma flow and southward B_Z at P1 (Fig. 5.42a, d) occurred later than earthward plasma flow and CD activities at P3 and P4 (Fig. 5.42b, c, e, f). P2 observations are not included in the figure because significant changes occurred much later. Thus, the time history indicates the 'inside-out' scenario instead.

Other potential problems exist for MR as a substorm trigger:

(1) CD/dipolarization associated with the substorm current system occurred at P3 and P4, which were at ~10 R_E earthward of postulated MR site. If the

MR site were linked to the auroral onset arc, then it would imply that the substorm westward electrojet, which is a part of the substorm current system, would form well equatorward of the auroral onset arc. This expected feature has never been observed for an isolated substorm.

(2) If one relates the energy flux of electrons ejected from the postulated MR site to the intensity of auroral onset arc, then the energy flux is at least one order of magnitude below what is needed to account for the observed auroral intensity. In contrast, the electrons ejected from dipolarization region at P3 and P4 have the energy flux in the right order of magnitude (Lui, 2011b). Again, since P3 and P4 were ∼10 R_E earthward of the MR site, one would expect that if the MR site were linked with the auroral onset arc, then there would be another bright arc substantially equatorward of the onset arc, contrary to observation.

(3) The time delay between the postulated MR onset and the arc brightening is too short to be consistent with the Alfvén transit time between the two sites. If one invokes the Tamao path (Tamao 1964; Chi et al. 2009) to reduce the time delay, then one would expect an auroral arc (even though it might be weak) to move from high to low latitudes to reach the onset arc. This feature was not seen.

(4) Angelopoulos et al. (2009) tried to justify the use of unconventional features as MR signatures by stating that P1 was near the plasma sheet boundary and not near the neutral sheet. However, the positive swing of B_Z and the absence of change in the tailward plasma flow at P2 cannot be reconciled with MR interpretation even for a location near the plasma sheet boundary. Furthermore, since CDs are spatially localized (Ohtani et al. 1998), slow increases in earthward flow at P3 and P4 are CD signatures when the satellites are not close to the neutral sheet and not at the CD site. Stronger earthward flows and high field fluctuations will only occur when CD reaches the locations of these satellites.

(5) Although Angelopoulos et al. (2008, 2009) and Pu et al. (2010) interpreted the substorm activity at ∼0450 UT as distinct from the early one at ∼0400 UT, this interpretation is inconsistent with the disturbances at the ground magnetic station Leirvogur. The *H*- and *Z*-perturbations were recovering from the disturbance initiated at ∼0400 UT and the *D*-perturbation was near its peak at ∼0450 UT (Fig. 5.42g). In addition, for this earlier onset, the time history indicates substorm disturbances occurring in the near-earth region earlier than in the mid-tail, as illustrated in Fig. 5.43.

Note that strong earthward plasma flows as well as dipolarization based on the elevation angle of the magnetic field occurred first at P4, then P3, then finally P1. Pu et al. (2010) have noted that P1 detected tailward flows with a maximum speed of ∼300 km/s at ∼0358 UT. However, those flows were mainly field-aligned and the convective part was only ∼60 km/s. Field-aligned tailward flow and slight southward field dipping may equally be interpreted as thinning in the near-earth region where the plasma sheet is thinner than in the mid-tail (causing southward dipping). These features have been modeled by Chao et al. (1977) and have been shown in a statistical study of IMP-6 observations in the magnetotail (Lui et al. 1977b).

With the above reservations, this event cannot be considered as a compelling case for MR being the substorm trigger.

5.5.2 2008 February 16 Event

Gabrielse et al. (2009) conducted another study using the time history approach during a minor tail conjunction on 2008 February 16 when four of the five THEMIS were aligned nearly along the tail axis. The satellite locations in the magnetotail are shown at the right column of Fig. 5.44.

The substorm onset based on auroral brightening was determined to be at 045018 UT. It was preceded by several auroral brightenings and Pi2 onsets, e.g., at 044135, 044327, and 044815 UT, which were interpreted as pseudobreakups and not substorm onsets. P2, the most tailward satellite for this tail conjunction, observed a positive swing of B_Z at 044935 UT, followed by a significant negative B_Z at ∼0452 UT accompanied by tailward plasma flows. These signatures were interpreted as initial generation of a plasmoid. P3, closer to the Earth than P2, observed dipolarization starting at 045015 UT, as shown in Fig. 5.45. Detailed timing analysis suggests that MR started at 044907-044914 UT and its location was between 15.6 and 15.9 R_E downtail. Dipolarization at P3 started

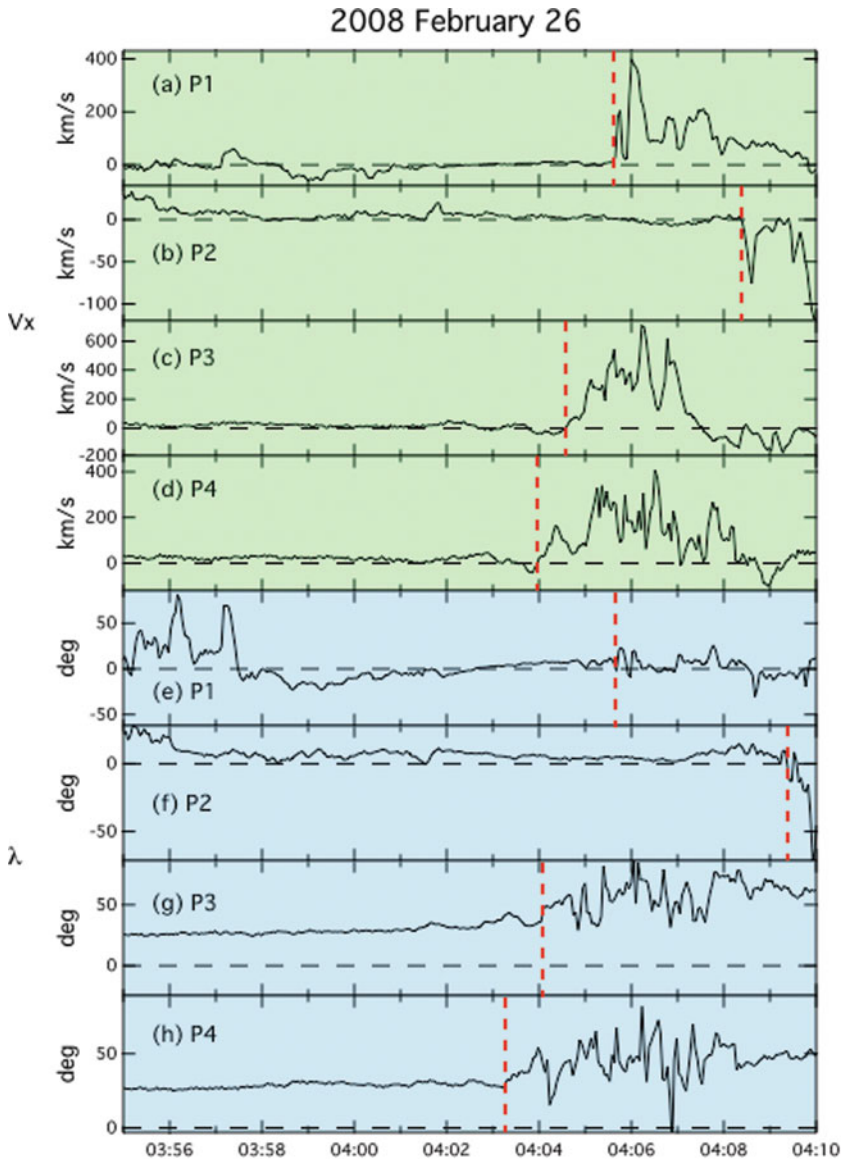

Fig. 5.43 Observations of significant substorm disturbances on 2008 February 26 from P1, P2, P3, and P4. Panels (**a**)–(**d**) show the *x*-component of the convective flow and (**e**)–(**h**) show the elevation angle of the magnetic field from P1, P2, P3, and P4 (Lui 2011a)

at 045019 UT, 68 s after MR onset, supporting the 'outside-in' scenario.

However, different interpretations can be made with these observations. For example, the positive B_Z swing at P2 can be interpreted as the satellite moving closer to the neutral sheet as indicated by the decrease in the B_X component. Such sign change in B_Z as a satellite approaches the neutral sheet has been reported in Lui et al. (1977b) and reproduced here in Fig. 5.46. Therefore negative B_Z at the high latitude plasma sheet may not necessarily imply MR occurring earthward of the location.

The highlighted time interval in Fig. 5.45 shows that dipolarization at P3 occurred in the absence of any plasma flow, which has also been reported in CD that exhibits non-MHD behavior (Lui et al. 1999). Therefore, the dipolarization at P3 is not due to earthward flow from MR reaching the near-earth region, contrary to the 'outside-in' scenario. Furthermore, multiple activations prior to the MR onset at 044947 UT may indicate that the substorm had already started before MR onset. The subsequent disturbances are associated with substorm intensifications, not substorm onset.

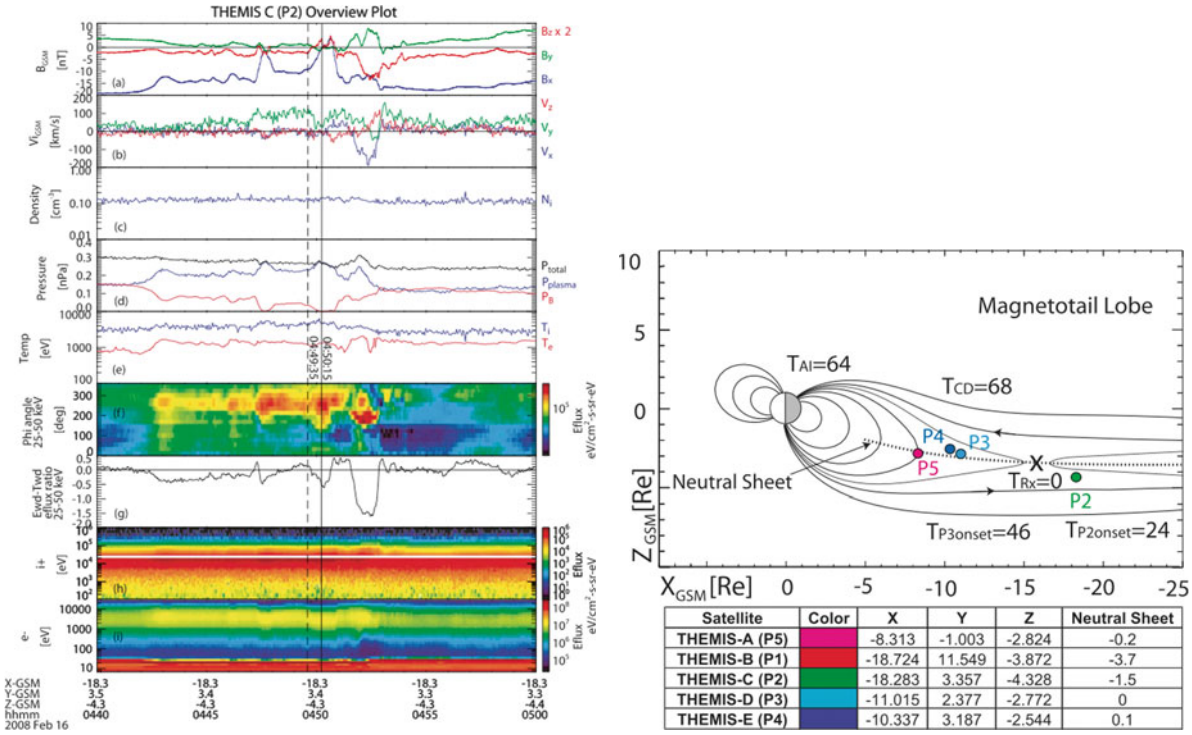

Satellite	Color	X	Y	Z	Neutral Sheet
THEMIS-A (P5)		-8.313	-1.003	-2.824	-0.2
THEMIS-B (P1)		-18.724	11.549	-3.872	-3.7
THEMIS-C (P2)		-18.283	3.357	-4.328	-1.5
THEMIS-D (P3)		-11.015	2.377	-2.772	0
THEMIS-E (P4)		-10.337	3.187	-2.544	0.1

Fig. 5.44 Locations of THEMIS satellites and observations of substorm disturbances from P2 satellite on 2008 February 16 (Gabrielse et al. 2009)

5.5.3 2008 February 25 Event

A recent study using a very short time history was reported by Kepko et al. (2009) who showed the ground auroral observation on 2008 February 25 in conjunction with data from two THEMIS satellites and GOES 12. Figure 5.47 shows the time series of auroral data using multi-spectral and white light all sky imagers at Gillam, Canada for this event. The satellite projections are indicated in the upper left image (P3: black; P4: white; GOES 12: grey) based on the T01 magnetic field model (Tsyganenko 2002). Letters A–C represent the low (A), mid (B), and high (C) latitude features.

For the 630.0 nm emission column, an auroral feature was seen in the middle of the frame starting at 052650 UT, which intensified drastically at 053002 UT. To the west of this feature, an auroral arc became noticeable at 052715 UT and intensified in the subsequent frames. For the 557.7 nm emission, there was a noticeable connection between the high latitude feature and the low latitude one as early as 052647 UT. This connection seems to disappear at 052735 UT to give rise to a weak auroral arc at 052759 UT, which later joined with the low latitude feature when it started to expand poleward at 052935 UT. Similar evolution of auroral activity can be seen in the 427.8 nm emission. For the white light, an auroral arc at the east edge of the frame was brightening as early as at 052655 UT and eventually expanded poleward at 053007 UT.

Corresponding satellite observations are shown in Fig. 5.48. THEMIS P3 and P4 were located in GSM coordinates at (X, Y) = (–11.1, 2.1) and (–10.6, 2.9) R_E, respectively. GOES 12 was in the post-midnight sector. Plasma flows were observed by P3 and P4 starting at 052850 UT, before auroral poleward expansion.

Onsets of several features are marked on the top of Fig. 5.48 and are used to assert that plasma flows preceded auroral expansion onset by ~90 s. However, this inference is rather misleading since substorm onset is defined by the initial auroral brightening time (see Fig. 5.1). For this event, the initial brightening can be seen to start at 052647 UT in 557.7 emission prior to poleward expansion. Therefore, plasma flows seen by P3 and P4 were ~2 min later than the initial brightening time. If one adds the Alfvén transit time

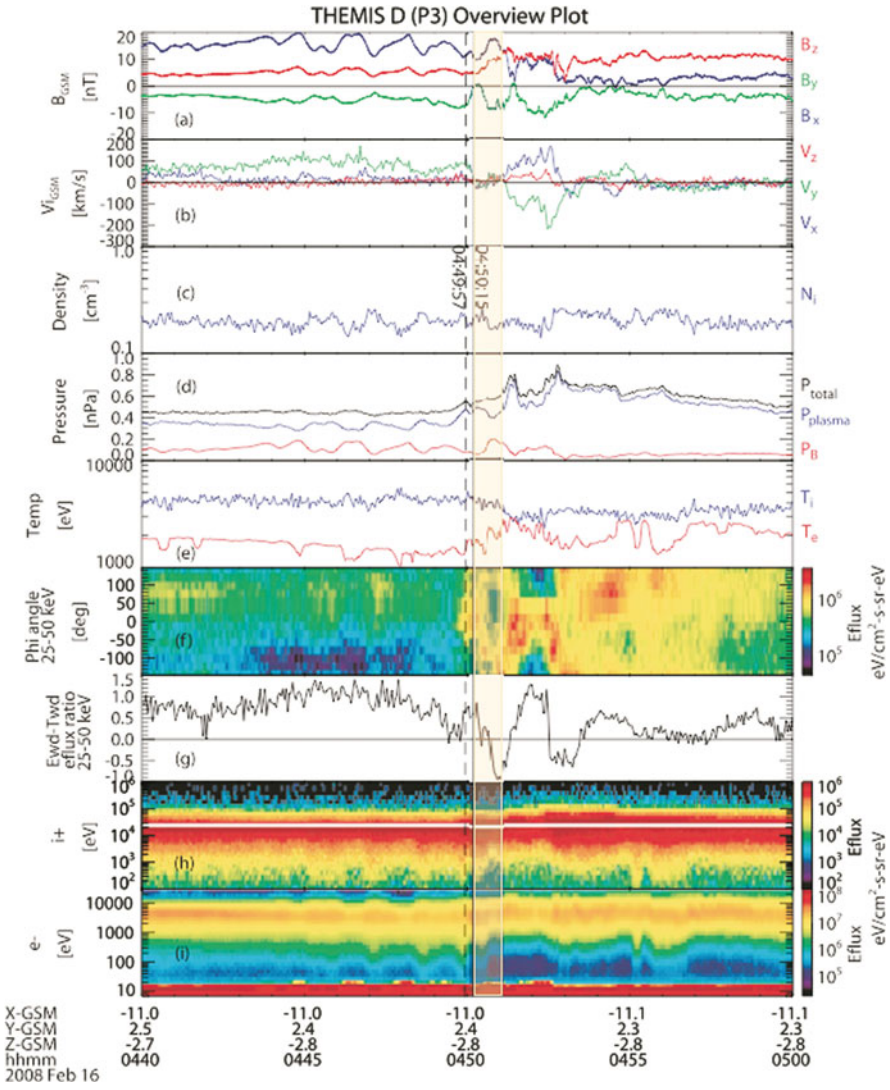

Fig. 5.45 Observations of substorm disturbances from P3 on 2008 February 16 (Gabrielse et al. 2009)

from the magnetosphere to the ionosphere, the plasma flow onset was ~3–4 min after substorm onset, i.e., substorm onset could not be caused by the flow bursts. It was stated in the article that the results are consistent with the scenario advocated by Angelopoulos et al. (2008). This is inaccurate since observations in Figs. 5.47 and 5.48 are more consistent with the scenario of plasma flow braking in the inner magnetotail to trigger a substorm (Haerendel 1992; Shiokawa et al. 1997) than the initial brightening arc being directly linked to the MR site without the intermediate step of flow braking in the inner magnetotail as advocated in Angelopoulos et al. (2008).

5.5.4 Weaknesses in the Time History Approach

The time history analysis relies on the progression of substorm disturbances in the tail region to determine the substorm initiation location in the tail and to imply the physical process for substorm onset. This implicit assumption can be very misleading in ascertaining substorm onset processes. For example, Fig. 5.32 shows two auroral activations in the interval ~0930–0945 UT at 15 R_E in the magnetotail. MR was invoked for the onset process based on a general trend of Hall magnetic perturbations (in spite of very large deviations) at that

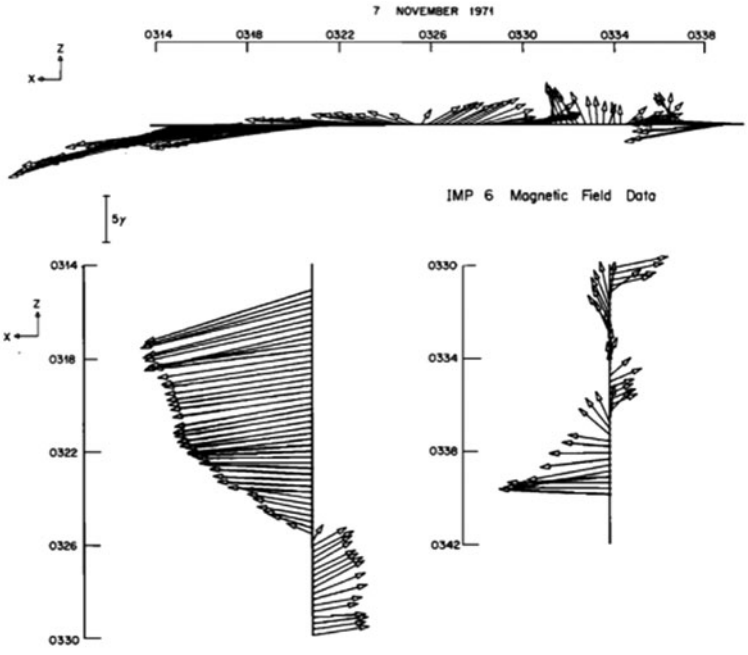

Fig. 5.46 Magnetic field observation from IMP-6 plotted in a vector form to show B_Z sign change as the satellite approaches the neutral sheet (Lui et al. 1977b)

time. However, the large fluctuations in the magnetic field are indicative of CD and the general trend of Hall perturbations could arise simply from electrons exiting the turbulence region further than the ions, thus setting up the Hall current system mimicking the MR site.

The observed large magnetic fluctuations differ from the orderly magnetic configuration expected for MR, as shown in Fig. 5.49. Therefore, this 'outside-in' scenario may imply CDI as the onset process. Furthermore, the auroral activation at ~0841 UT was attributed to MR at ~9 R_E in the magnetotail, consistent with the magnetic field configuration modeled and shown in Fig. 5.50 (Sergeev et al. 2007). This 'inside-out' scenario then implies MR rather than CDI as the substorm onset process.

The time history approach also has another pitfall. Since CD and MR are spatially localized in the dawn-dusk direction, there is no guarantee that satellite observation of CD or MR for a particular event is the initial disturbance from these processes for substorm onset. This leads to conflicting results even for the interpretation of a given event, as discussed in Sections 5.5.1–5.5.3. In addition, time history analysis for multiple events shows a wide range of possibilities, leading to the suggestion that a global Alfvénic interaction model is more appropriate than the two scenarios (Lin et al. 2009). On top of this is the possibility of new plasma intrusion from MR approaching the near-earth magnetotail to initiate substorm onset by a near-earth instability, which can be considered as a hybrid between the two scenarios (Vogiatzis et al. 2005; Nishimura et al. 2010; Lyons et al. 2010).

Another problem with the time history approach is whether the onset identified is in fact the start of the substorm expansion or onset of a substorm intensification well after onset. If the identified onset is a substorm intensification onset, then the observations will give inappropriate timing sequence for substorm disturbances. A case in point is the ambiguity for the February 26, 2008 substorm event examined by both Angelopoulos et al. (2008) and Lui (2009). The former interpreted ~0452 UT as the substorm onset while the latter suggested the actual substorm onset to be at ~0400 UT with ~0452 UT as the substorm intensification time, as discussed at length in Section 5.5.1. Therefore, the time history approach distracts research efforts in identifying the substorm onset processes.

One may compare the time history approach with a different approach that does not have the weaknesses inherent in the time history approach. This is to examine the plasma pressure at the auroral onset arc from low altitude measurements (see Fig. 5.51), as done by Dubyagin et al. (2003). They conducted a detailed study of an isolated substorm with the FAST satellite

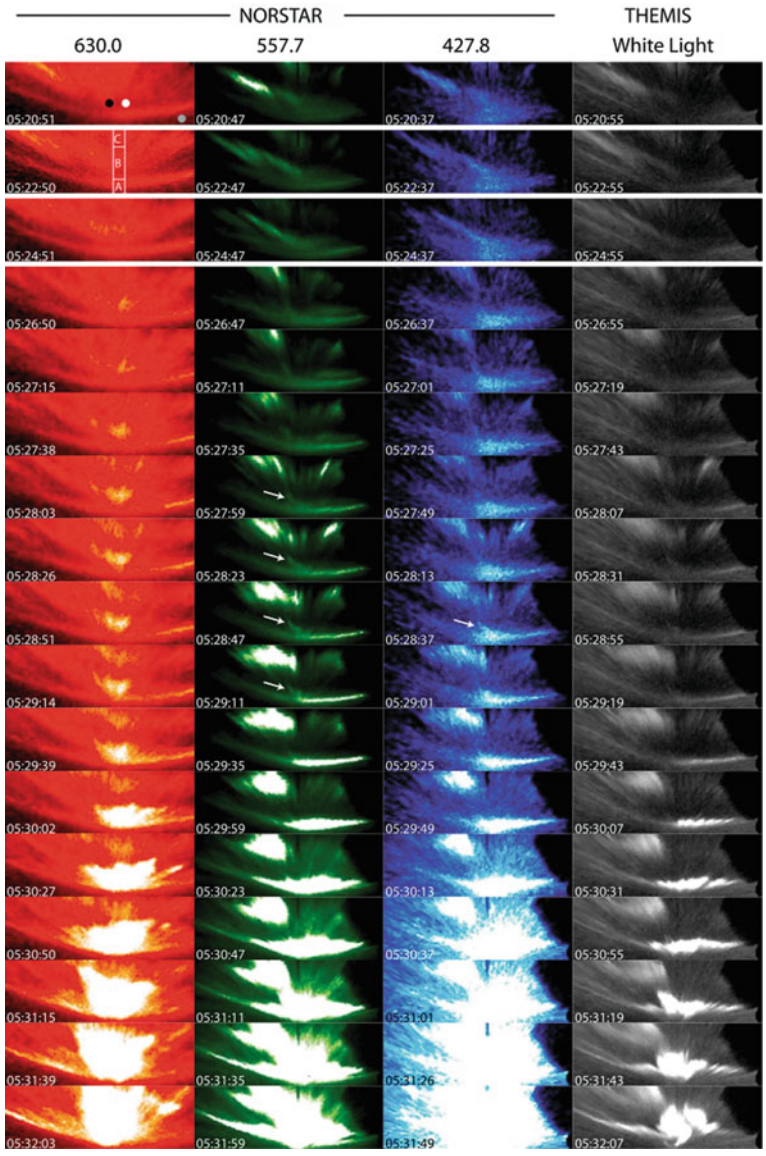

Fig. 5.47 Auroral images from the multispectral all-sky and THEMIS white light cameras at Gillam on 2008 February 25. North is up and west is to the left (Kepko et al. 2009)

crossing the most equatorward auroral arc just at the time of its breakup. It is found that (1) the arc flux tube was in the region of considerable pressure gradient where the pressure was ∼1–2 nPa; (2) the arc was just 0.4° poleward of the proton isotropic (b2i) boundary and close to the peak of the diffuse auroral electron precipitation, and (3) Tsyganenko 96 model maps the arc to the equatorial distance of ∼ 8 R_E. These results are indicative of the near-earth initiation for substorms, i.e., the 'inside-out' scenario.

5.6 System-Wide Approach

It is useful to extract further properties of the substorm onset processes from a system-wide approach. This different approach is pioneered theoretically by Chang (1992) and observationally by Consolini et al. (1996) and Consolini (1997). It motivated Lui et al. (2000) to study the analogy between the dynamic magnetosphere and an avalanche system with global auroral power dissipation as a measure of the power output of the magnetosphere.

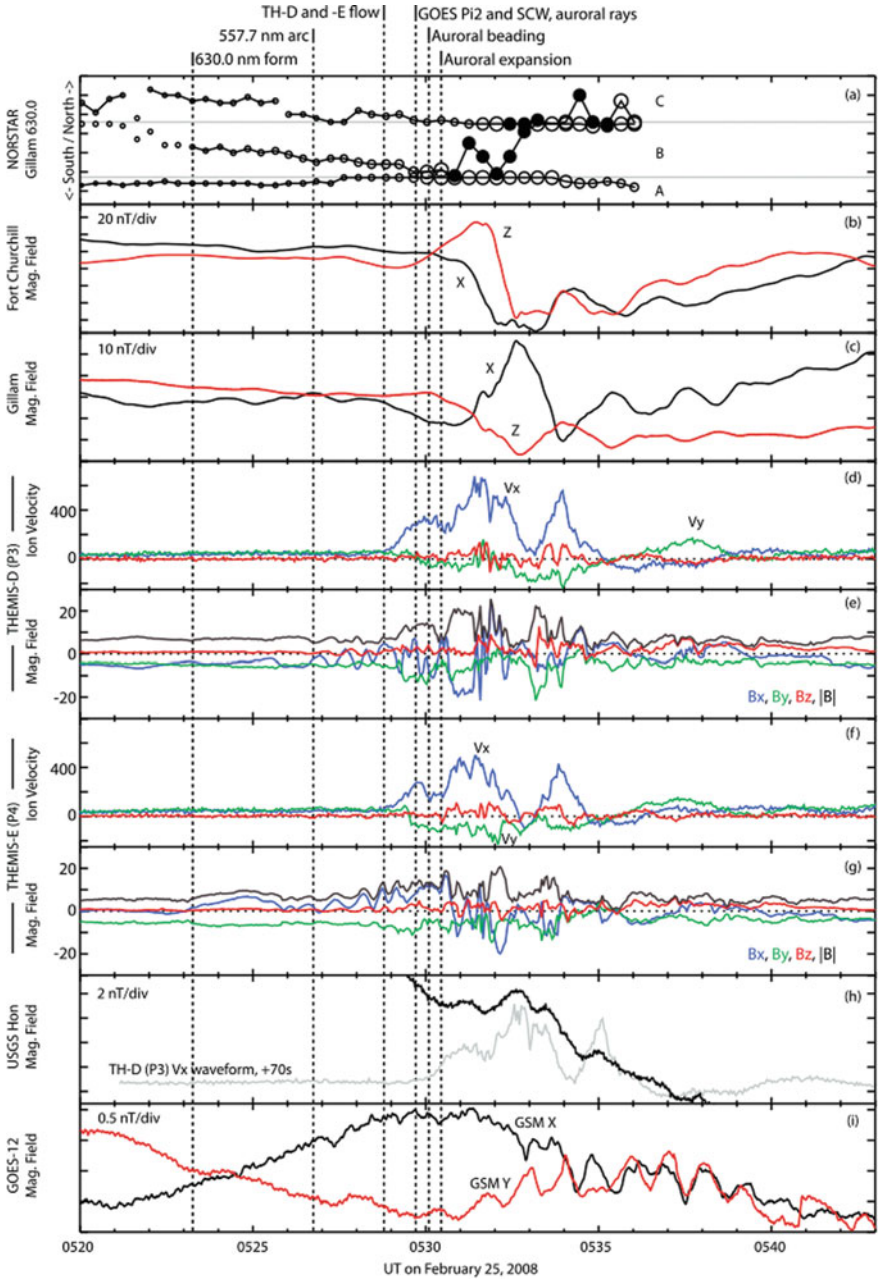

Fig. 5.48 Satellite observations on 2008 February 25 (Kepko et al. 2009). The *red curve* in the bottom panel should be labeled as GSM Z instead

Figure 5.52 shows the result from analyzing ~9000 images to generate the normalized occurrence for auroral dissipation area and power. Quiet times and substorm intervals were separately examined. Two types of energy dissipation were revealed: those internal to the magnetosphere occurring at all activity levels without an intrinsic scale and those occurring during active times with a characteristic scale. The internal events exhibit the same power law index in both active and quiet times, consistent with the behavior of a simple avalanche system. This approach enables 2D cellular automata modeling of the substorm disturbances in the magnetotail (Lui and Consolini 2005) to reproduce the skew distribution on the propagation of auroral activity site reported by Carbary et al. (2000).

This work was further extended to predict the probability of an auroral feature yielding a given total energy

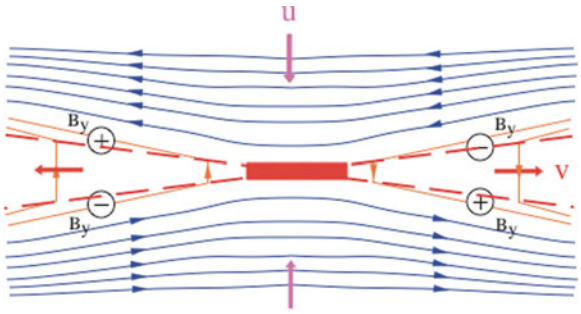

Fig. 5.49 A schematic diagram of the magnetic configuration for magnetic reconnection to illustrate its orderly pattern (Lui 2010b)

dissipation throughout its lifetime (Lui et al. 2003). The prediction algorithm is based on the instantaneous values of four attributes of the auroral feature, namely, its area, its power, and their rates of change.

Figure 5.53 shows the probability distribution function of the total dissipation and the resulting true skill score (TSS) based on the adopted prediction algorithm. The values of TSS range from 0.70 to 0.88, indicating that fairly reliable predictions can be made based on the probability density distribution. The higher TSS score is obtained from the prediction of a higher total dissipation of an auroral form.

The plausible energy avalanche in the central plasma sheet has also been examined with 1D cellular automaton (Liu et al. 2006). The simulation shows that a central plasma sheet driven by a spatially non-uniform energy loading to mimic convection is in a self-organized critical state. Its energy avalanches obey a scale-free distribution and exhibit quasi-periodic intermittencies, which are correlated to ring current injections. On the other hand, the strong avalanches bear no apparent correlation with tailward energy injection.

5.7 Implications on Substorm Onset Theories

If one disassociates the time history approach from identifying the substorm onset processes due to its weaknesses elaborated in Section 5.5.4, then the observations presented in Sections 5.3 and 5.4 reveal one prominent candidate, namely, a form of ballooning instability (BI) discussed by many substorm researchers (Roux et al. 1991; Samson et al. 1992a, b, 1996; Voronkov et al. 1997; Liu 1997; Pu et al. 1997, 1999; Bhattacharjee et al. 1998; Cheng and Lui 1998; Erickson et al. 2000; Cheng 2004; Zhu et al. 2004; Samson and Dobias 2005; Donovan et al. 2006b, Liu et al. 2008; Saito et al. 2008a; Henderson 2009).

Evidence for BI being a favorable candidate includes the analyses on the pressure gradient (Chen et al. 2003), associated wave properties in CD in the near-earth magnetotail (Cheng and Lui 1998; Erickson et al. 2000; Saito et al. 2008a) as well as the spatially periodic auroral spots just prior to substorm onset (Elphinstone et al. 1995; Donovan et al. 2006b, 2008; Henderson 2009). The range of wavelength inferred from these auroral spots is consistent with BI characteristics. One study on the threshold for BI triggering CD gives the magnitude of a quasi-electrostatic field to be at ~4 mV/m (Liu and Liang 2009).

The features from BI in the ionosphere and in the magnetospheric equatorial plane are illustrated in Fig. 5.54 (Henderson 2009). The positive feedback on an initial surface perturbation on the transition region arises from amplification of an azimuthal electric field by the ∇B drift. The ∇B drift is higher in the tail-like field region than in the dipolar-like field region. As a result, an induced duskward electric field is produced along the boundary of the perturbed intrusion that feeds field-aligned currents at the duskward

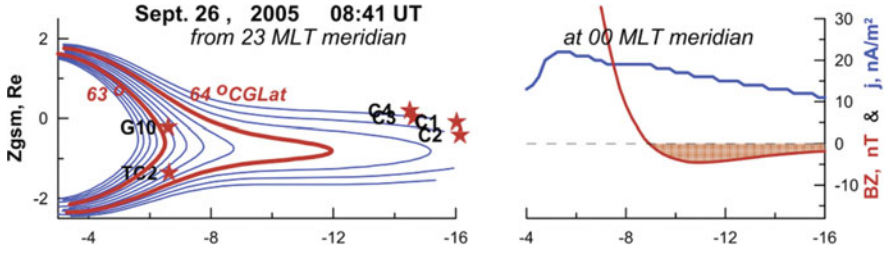

Fig. 5.50 Magnetic field configuration based on a magnetic field model showing the occurrence of magnetic reconnection at 9 R_E in the magnetotail for a weak substorm disturbance on September 26, 2008 (Sergeev et al. 2007)

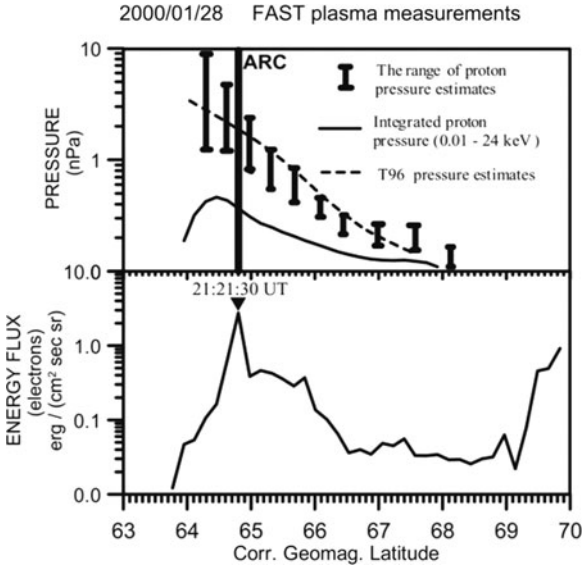

Fig. 5.51 Latitudinal profiles of proton pressure (*top*) and the precipitating electron energy flux (*bottom*) from FAST observations. *Vertical line* indicates the breakup arc position (Dubyagin et al. 2003)

boundary to produce the spatially periodic brightening on the substorm onset arc system. Note that although the azimuthal electric field in Henderson (2009) is attributed to the ∇B drift current, from the perspective of the guiding center orbit theory, it is more appropriate to attribute the azimuthal electric field to the diamagnetic current instead since the ∇B current is cancelled completely by part of the magnetization current (Longmire 1963).

Another instability for CD that has the same wavelength range as observed for the periodic auroral spots is the cross-field current instability (CCI: Lui et al. 1991). The corresponding excited waves near the ion gyrofrequency at local CD onset have been identified with wavelet analysis and are consistent with those predicted by CCI (Lui and Najmi 1997; Yoon et al. 2009). Donovan et al. (2006b) reported that the motion of these periodic auroral spots could be westward, stationary, or eastward. The variable direction of spot movement can be explained in terms of the relative importance of electrons as current carriers in the magnetospheric frame of reference. Note that the CCI theory is formulated in the reference frame where the electron drift is zero. Based on this theory, the predicted motion of these spots will be westward, nearly stationary, and eastward with increasing dominance of electrons as the current carriers in the cross-tail current at the instability location.

It is pointed out by Haerendel (1992) that BI converts particle energy to magnetic energy as it develops. Substorm onset requires the opposite conversion, i.e., from magnetic energy to particle energy to release the magnetic stress built up in the growth phase. This conversion can be accomplished by CCI, which can generate a meridional current system (Lui 2004). From this consideration, it is likely that BI and CCI may act in unison to produce local CD, with BI causing thinning of the current sheet explosively to trigger CCI onset. Onset locations of both BI and CCI have been shown to coincide with an auroral arc (Roux et al. 1991; Samson et al. 1992a, b, 1996; Voronkov et al. 1997; Lui and Murphree 1998; Samson and Dobias 2005), satisfying one of the observational constraints that substorm onset starts on an auroral arc.

Rae et al. (2010) recently conducted a detailed analysis of the optical frequency and azimuthal spatial structure of a substorm onset arc. The observational results provide extremely powerful constraints to date on the ionospheric manifestation of the physical processes occurring near substorm onset. Based on the extracted frequency, growth rates, and spatial scales, they found that these values to be consistent with the CCI and/or BI (collectively included in the term CDI) as the substorm onset mechanism.

All the above considerations (observations and theories) point to most, if not all, substorm onsets being caused by CDI operative near the nightside cusp (transition region between the dipolar field and tail-like field configurations) and MR is a consequence of this initial disturbance. It is important to realize that the conclusion of the nightside cusp being the substorm onset location is reached by studies that cover both ground-based and space-based measurements. However, MR starting earlier than substorm onset may provide indirectly a favorable environment in the nightside cusp for the CDI onset. The observations that an auroral arc lying poleward of the substorm onset arc remains typically undisturbed are consistent with this temporal development (e.g., Akasofu et al. 2010).

One might consider the possibility that a plasma process at low-altitudes generates the spatially periodic auroral spots. However, such a hypothesis has to be backed up by identifying the low-altitude process as well as showing that it could reproduce the phenomena

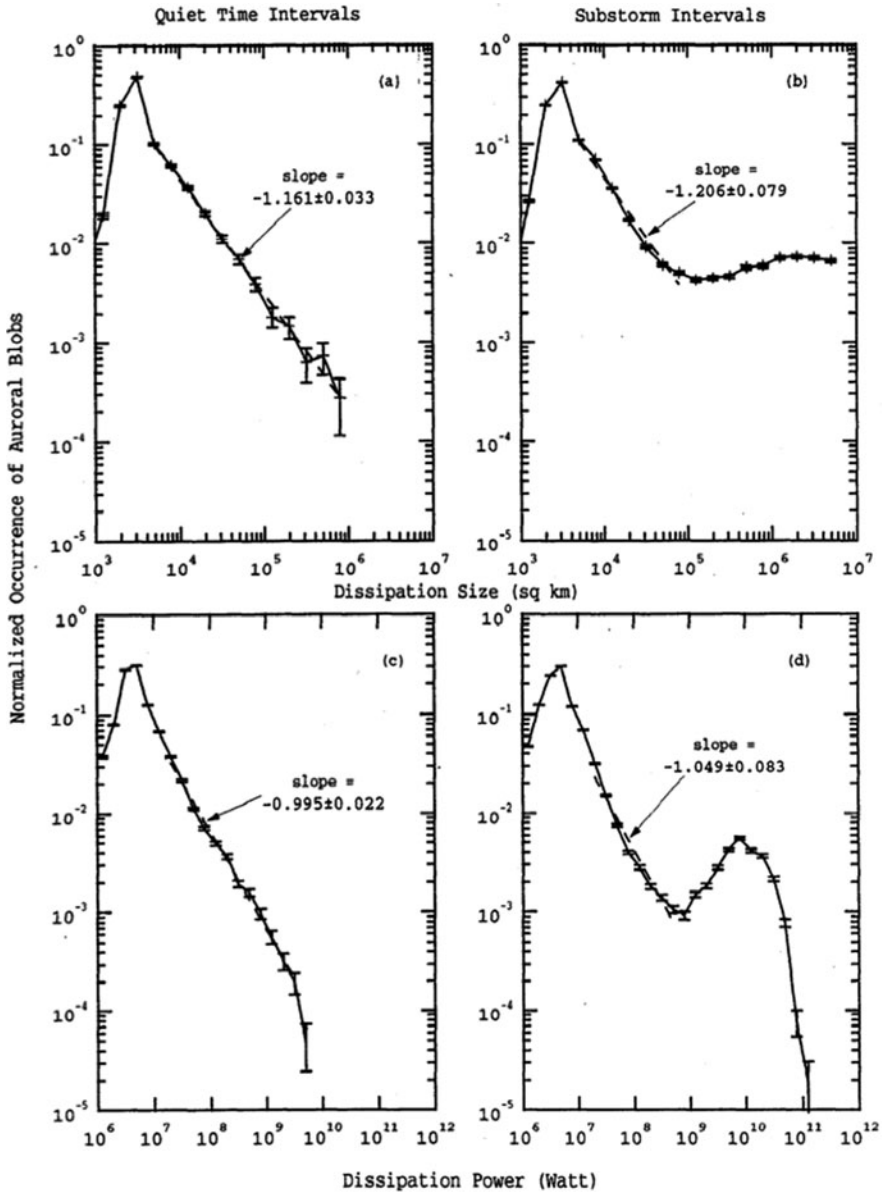

Fig. 5.52 The probability distribution functions of power and area size of auroral blobs during quiet and substorm times (Lui et al. 2000)

observed in the magnetotail as well as the wavelength and motion of these auroral spots in the ionosphere.

It is important to note that CDI can occur in mid-tail, as shown in Figs. 5.32 and 5.37–5.40. Anomalous resistivity from mid-tail CDI activity can enable mid-tail MR. Also, both MR and CDI can produce fast plasma flows and dipolarization. DF therefore cannot be taken as a unique signature for MR even though MR can give rise to DF (Sitnov et al. 2009).

Many global MHD simulations have claimed success in reproducing observed substorms (Lyon et al. 1998; Raeder et al. 2008; Zhu et al. 2009). One cause of concern on these simulations is the lack of grid convergence, i.e., the demonstration that the evolution of the system remains the same from duplicate runs with finer and finer grid resolutions in the simulation runs. Another concern is that some simulations rely on numerical resistivity for substorm initiation. Whether

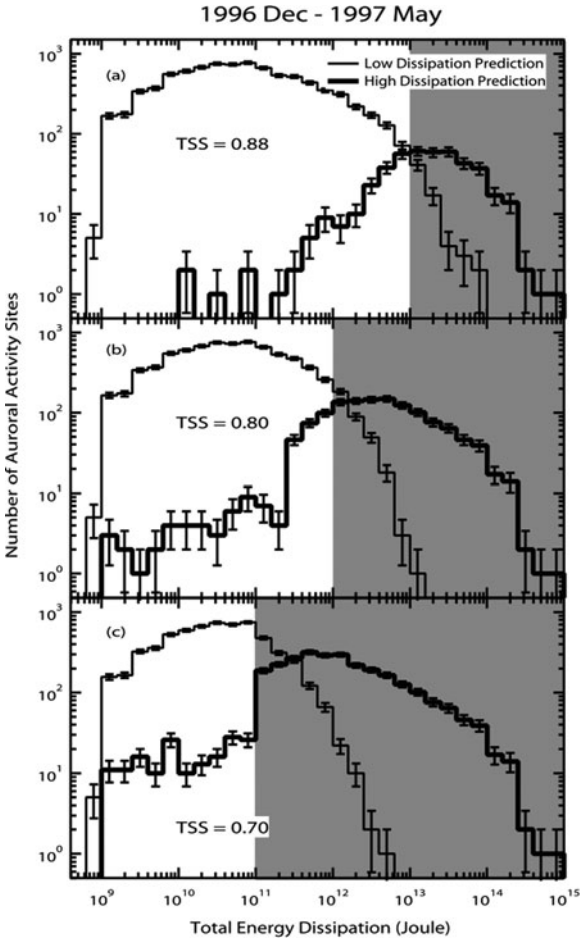

Fig. 5.53 The probability distribution functions of total energy dissipation of individual auroral blobs with prediction algorithm based on four attributes of the auroral blobs (Lui et al. 2003)

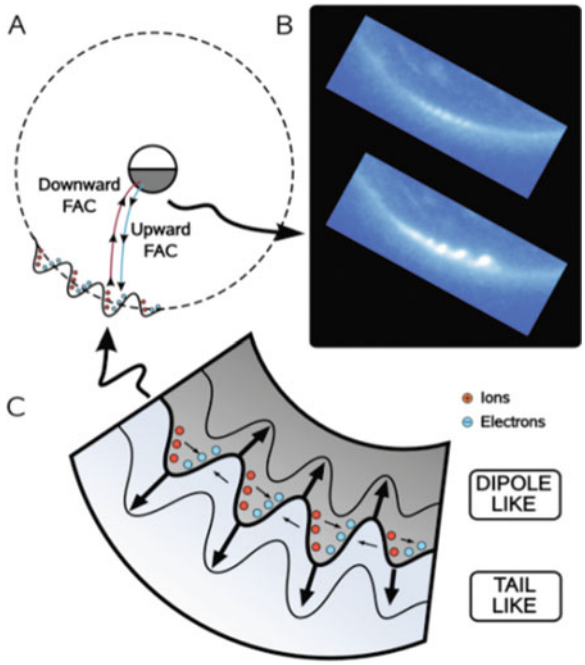

Fig. 5.54 A schematic diagram of the ballooning instability showing the development of an initial perturbation in the transition region separating dipolar and tail-like magnetic field configuration in the near-earth magnetotail (Henderson 2009)

such procedure corresponds to a realistic physical process is uncertain. It is desirable to examine these global simulations in terms of their predictions on the system-wide properties of the magnetospheric substorm, such as the probability density function of power dissipation and area of auroral sites as shown in Fig. 5.52.

While plasma instabilities have short time- and spatial-scales, especially the kinetic ones, transient and localized substorm activities can generally be considered as consistent with these characteristics. On the other hand, it is unclear how MR in the magnetotail is transient and spatially localized in nature unless the occurrence of MR critically depends on anomalous resistivity from plasma instabilities. Along this line of thought, it should be noted that several analysis of substorm activity shows the robust nature of avalanche in substorm activity, as discussed in Section 5.6. Therefore, the avalanching aspects should not be ignored. Otherwise, one would have a short duration of substorm activity and the global substorm evolution of the magnetotail will not be adequately portrayed. For example, if one were to artificially remove plasma content in a flux tube in the inner magnetosphere to mimic the local effects of CD (note that this procedure does not encompass all the effects of CD), then one should ensure that this would instigate the onset of CDI in an adjacent region, allowing plasma and magnetic flux to enter the initial CD region. CD in the adjacent region should then instigate CDI onset in another adjacent region, producing the chain reaction of avalanche. Without this chain reaction, the global evolution of the magnetotail from a localized CD will not be adequately modeled.

Ground-based observations of substorm activity provide a global evolution of substorm activity over extended periods. Satellite point-wise observations in space can never match such complete and simultaneous coverage. Attempts to use ground-based observations to infer magnetospheric disturbances are well

justified. Most investigations along this line use modified magnetic field model to gain insight on this link. However, magnetic field variations around substorm onset intervals are difficult to model and such models often provide representation with large uncertainties. It is highly desirable to overcome this limitation by using natural plasma boundaries or parameters to relate ionospheric features to magnetospheric features and vice versa. These natural reference frames include the trapping boundary of energetic particles, the inner edge of the cross-tail current and/or plasma sheet, the isotropic boundary, the proton temperature profile, the plasma pressure profile, and the phase space density profile. Examples using these natural boundaries to infer the substorm onset location in the magnetotail can be found in, e.g., Lui and Burrows (1978), Dubyagin et al. (2003), and Donovan et al. (2008).

5.8 Concluding Remarks

The substorm concept was introduced more than four decades ago. Many studies on substorm phenomena have been conducted. It is conceivable that the results from these studies have already provided sufficient clues to identify the physical processes for substorm onset. It is vital to consolidate observations from the ground and various regions in space to gain insight on the onset processes. An ingredient for success in this pursuit is to evaluate all potential candidates with observations at hand and not to interpret observations always in the framework of one particular candidate as done in several past studies.

Acknowledgments This work was supported by the NSF grant ATM-0630912 and NASA grants NNX09AI53G and NNX07AQ50G to The Johns Hopkins University Applied Physics Laboratory. We acknowledge E. Donovan for NORSTAR data, S. B. Mende and E. Donovan for THEMIS GBO ASC data, H. Réme for Cluster/CIS data and V. Angelopoulos for THEMIS data through CDAWeb. Section 5.5 was added at the request of the reviewer.

References

Akasofu S-I (1964) The development of the auroral substorm. Planet Space Sci 12:273–282

Akasofu S-I (1968) Polar and magnetospheric substorms. D. Reidel, Norwell, MA

Akasofu S-I, Lui ATY, Meng C-I (2010) The importance of auroral features in search for substorm onset processes. J Geophys Res 115:A08218. doi:10.1029/2009JA014960

Alfvén, H. (1977) Electrical currents in cosmic plasmas. Rev Geophys 15:271–284

Angelopoulos V (2008) The THEMIS mission. Space Sci Rev. doi:10.1007/s11214-008-9336-1

Angelopoulos V, Baumjohann W, Kennel CF, Coroniti FV, Kivelson MG, Pellat R, Lühr H, Paschmann G (1992) Bursty bulk flow in the inner central plasma sheet. J Geophys Res 97:4027–4039

Angelopoulos V, Kennel CF, Coroniti FV, Pellat R, Kivelson MG, Walker RJ, Russell CT, Baumjohann W, Feldman WC, Gosling JT (1994) Statistical characteristics of bursty bulk flow events. J Geophys Res 99:21257–21280

Angelopoulos V, McFadden JP, Larson D, Carlson CW, Mende SB, Frey H, Phan T, Sibeck DG, Glassmeier K-H, Auster U, Donovan E, Mann IR, Rae IJ, Russell CT, Runov A, Zhou X-Z, Kepko L (2008) Tail reconnection triggering substorm onset. Science 321:931–935. doi:10.1126/science.1160495

Angelopoulos V, McFadden JP, Larson D, Carlson CW, Mende SB, Frey H, Phan T, Sibeck DG, Glassmeier K-H, Auster U, Donovan E, Mann IR, Rae IJ, Russell CT, Runov A, Zhou X-Z, Kepko L (2009) Response to Comment on "Tail reconnection triggering substorm onset." Science 324:1391-c, doi:10.1126/science.1168045

Antonova EE, Kirpichev IP, Ovchinnikov IL, Orlova KG, Stepanova MV (2009a) High latitude magnetospheric topology and magnetospheric substorm. Ann Geophys 27:4069–4073

Antonova EE, Kornilov IA, Kornilova TA, Kornilov OI, Stepanova MV (2009b) Features of auroral breakup obtained using data of ground-based television observations: case study. Ann Geophys 27:1413–1422

Atkinson G (1967) An approximate flow equation for geomagnetic flux tubes and its application to polar substorms. J Geophys Res 72:5373–5382

Baumjohann W, Paschmann G, Luhr H (1990) Characteristics of high-speed ion flows in the plasma sheet. J Geophys Res 95:3801–3809

Bhattacharjee A, Ma ZW, Wang X (1998) Ballooning instability of a thin current sheet in the high-Lundquist number magnetotail. Geophys Res Lett 25:861–864

Blanchard GT, Lyons LR, Spann J (2000) Predictions of substorms following northward turnings of the interplanetary magnetic field. J Geophys Res 105:375–384

Burch JL (1972) Preconditions for the triggering of polar magnetic substorms by storm sudden commencements. J Geophys Res 77:6529–5632

Burton RK, McPherron RL, Russell CT (1975) An empirical relationship between interplanetary conditions and Dst. J Geophys Res 80:4204–4214

Caan MN, McPherron RL, Russell CT (1977) Characteristics of the association between the interplanetary magnetic field and substorms. J Geophys Res 82:4837–4842

Carbary JF, Liou K, Lui ATY, Newell PT, Meng CI (2000) "Blob" analysis of auroral substorm dynamics. J Geophys Res 105:16083–16091

Chang T (1992) Low dimensional behavior and symmetry breaking of stochastic systems near criticality – can these effects be observed in space and in the laboratory? IEEE Trans Plasma Sci 20:691–694

Chanteur G (1998) Spatial interpolation for four spacecraft: theory. In: Paschmann G, Daly P (eds) Analysis methods for multi-spacecraft data. ISSI Sci Rep SR-001, European Space Agency, Paris, pp 349–369

Chao JK, Kan JR, Lui ATY, Akasofu S-I (1977) A model for thinning of the plasma sheet. Planet Space Sci 25: 703–710

Chen L-J, Bhattacharjee A, Sigsbee K, Parks G, Fillingim M, Lin R (2003) Wind observations pertaining to current disruption and ballooning instability during substorms. Geophys Res Lett 30:68-1. doi:10.1029/2002GL016317

Cheng CZ (2004) Physics of substorm growth phase, onset, and depolarization. Space Sci Rev 113:207–270

Cheng CZ, Lui ATY (1998) Kinetic ballooning instability for substorm onset and current disruption observed by AMPTE/CCE. Geophys Res Lett 25:4091–4094

Chi PJ, Russell CT, Ohtani S (2009) Substorm onset timing via traveltime magnetoseismology. Geophys Res Lett 36:L08107. doi:10.1029/2008GL036574

Consolini G (1997) Intermittency and turbulence in magnetospheric dynamics. In: Mallamace F, Stanley HE (eds) Proceedings of the international school of physics "Enrico Fermi", IOS Press, Amsterdam, pp 657–660

Consolini G, Marcucci MF, Candidi M (1996) Multifractal structure of auroral electrojet index data. Phys Rev Lett 76(21):4082–4085

Consolini G, Kretzschmar M, Lui ATY, Zimbardo G, Macek WM (2005) On the magnetic field fluctuations during magnetospheric tail current disruption: a statistical approach. J Geophys Res 110:A07202. doi:10.1029/2004JA010947

Coroniti FV, Kennel CF (1972) Changes in magnetospheric configuration during the substorm growth phase. J Geophys Res 77:3361–3370

Donovan E, Jackel B, Voronkov I, Sotirelis T, Creutzbert F, Nicholson N (2003) Ground-based optical determination of the b2i boundary: a basis for an optical MT-index. J Geophys Res 108(A3):1115. doi:10.1029/2001JA009198

Donovan E, Mende S, Jackel B, Frey H, Syrjäsuo M, Voronkov I, Trondsen T, Peticolas L, Angelopoulos V, Stewart H, Greffen M, Connors M (2006a) The THEMIS all-sky imaging array – system design and initial results from the prototype imager. J Atmos Sol Terr Phys 68:1472–1487

Donovan E, Mende S, Jackel B, Syrjäsuo M, Meurant M, Voronkov I, Frey H, Angelopoulos V, Connors M (2006b) The azimuthal evolution of the substorm expansive phase onset aurora. In: Syrjäsuo M, Donovan E (eds) Proceedings of ICS-8. University of Calgary, Calgary, AB, pp 55–60

Donovan E, Liu W, Liang J, Spanswick E, Voronkov I, Connors M, Syrjäsuo M, Baker G, Jackel B, Trondsen T, Greffen M, Angelopoulos V, Russell CT, Mende SB, Frey HU, Keiling A, Carlson CW, McFadden JP, Glassmeier K-H, Auster U, Hayashi K, Sakaguchi K, Shiokawa K, Wild JA, Rae IJ (2008) Simultaneous THEMIS in situ and auroral observations of a small substorm. Geophys Res Lett 35:L17S18. doi:10.1029/2008GL033794

Dubyagin SV, Sergeev VA, Carlson CW, Marple SR, Pulkkinen TI, Yahnin AG (2003) Evidence of near-Earth breakup location. Geophys Res Lett 30:1282. doi:10.1029/2002GL016569

Dunlop MW, Southwood DJ, Glassmeier K-H, Neubauer FM (1988) Analysis of multipoint magnetometer data. Adv Space Res 8:273–277

Elphinstone RD, Hearn DJ, Cogger LL, Murphree JS, Singer H, Sergeev V, Mursula K, Klumpar DM, Reeves GD, Johnson M, Ohtani S, Potemra TA, Sandahl I, Nielsen E, Persson M, Opgenoorth H, Newell PT, Feldstein YI (1995) Observations in the vicinity of substorm onset: implications for the substorm process. J Geophys Res 100:7937–7969

Erickson GM, Maynard NC, Burke WJ, Wilson GR, Heinemann MA (2000) Electromagnetics of substorm onsets in the near-geosynchronous plasma sheet. J Geophys Res 105:25265–25290

Fairfield DH, Cahill LJ Jr (1966) Transition region magnetic field and polar magnetic disturbances. J Geophys Res 71:155–169

Foster JC, Fairfield DH, Ogilvie KW, Rosenberg TJ (1971) Relationship of interplanetary parameters and occurrence of magnetospheric substorms. J Geophys Res 76:6971–6975

Frank LA, Paterson WR, Sigwarth JB, Mukai T (2001) Observations of plasma sheet dynamics earthward of the onset region with the Geotail spacecraft. J Geophys Res 106:18823–18841

Freeman MP, Morley SK (2004) A minimal substorm model that explains the observed statistical distribution of times between substorms. Geophys Res Lett 31:L12807. doi:10.1029/2004GL019989

Freeman MP, Morley SK (2009) No evidence for externally triggered substorms based on superposed epoch analysis of IMF Bz. Geophys Res Lett 36:L21101. doi:10.1029/2009GL040621

Friedrich E, Samson JC, Voronkov I (2001) Ground-based observations and plasma instabilities in auroral substorms. Phys Plasmas 8(4):1104–1110

Gabrielse C, Angelopoulos V, Runov A, Frey HU, McFadden J, Larson DE, Glassmeier K-H, Mende S, Russell CT, Apatenkov S, Murphy KR, Rae IJ (2009) Timing and localization of near-Earth tail and ionospheric signatures during a substorm onset. J Geophys Res 114:A00C13. doi:10.1029/2008JA013583

Haerendel G (1992) Disruption, ballooning or auroral avalanche. In: Proceedings of the first international conference on substorms, ESA SP-335, Paris, 23–27 Mar 1992, pp 417–420

Henderson MG (2009) Observational evidence for an inside-out substorm onset scenario. Ann Geophys 27:2129–2140

Henderson MG, Reeves GD, Belian RD (1996) Observations of magnetospheric substorms occurring with no apparent solar wind/IMF trigger. J Geophys Res 101:10773–10791

Hones EW Jr (1973) Plasma flow in the plasma sheet and its relation to substorms. Radio Sci 8:979–990

Hones EW Jr, Schindler K (1979) Magnetotail plasma flow during substorms: a survey with IMP 6 and IMP 8. J Geophys Res 84:7155–7169

Horwitz JL (1985) The substorm as an internal magnetospheric instability: substorms and their characteristic time scales during intervals of steady interplanetary magnetic field. J Geophys Res 90:4164–4170

Hsu TS, McPherron RL (2002) An evaluation of the statistical significance of the association between northward

turnings of the interplanetary magnetic field and substorm expansion onsets. J Geophys Res 107(A11):1398. doi:10.1029/2000JA000125

Ieda A, Fairfield DH, Mukai T, Saito Y, Kokubun S, Liou K (2001) Plasmoid ejection and auroral brightenings. J Geophys Res 106:3845–3858

Jacquey C, Sauvaud JA, Dandouras J (1991) Location and propagation of the magnetotail current disruption during substorm expansion: analysis and simulation of an ISEE multi-onset event. Geophys Res Lett 18:389–392

Jacquey C, Sauvaud JA, Dandouras J, Korth A (1993) Tailward propagating cross-tail current disruption and dynamics of near-earth tail: a multi-point measurement analysis. Geophys Res Lett 20:983–986

Kaufmann RL (1987) Substorm currents: growth phase and onset. J Geophys Res 92:7471–7486

Kauristie K, Pulkkinen TI, Huuskonen A, Pellinen RJ, Opgenoorth HJ, Baker DN, Korth A, Syrjäsuo M (1997) Auroral precipitation fading before and at substorm onset: ionospheric and geostationary signatures. Ann Geophys 15:967–983

Kawasaki K, Akasofu S-I, Yasuhara F, Meng C-I (1971) Storm sudden commencements and polar magnetic substorms. J Geophys Res 76:6781–6789

Kepko L, Spanswick E, Angelopoulos V, Donovan E, McFadden J, Glassmeier K-H, Raeder J, Singer HJ (2009) Equatorward moving auroral signatures of a flow burst observed prior to auroral onset. Geophys Res Lett 36:L24104. doi:10.1029/2009GL041476

Le Contel O, Roux A, Jacquey C, Robert P, Berthomier M, Chust T, Grison B, Angelopoulos V, Sibeck D, Chaston CC, Cully CM, Ergun B, Glassmeier K-H, Auster U, McFadden J, Carlson C, Larson D, Bonnell JW, Mende S, Russell CT, Donovan E, Mann I, Singer H (2009) Quasi-parallel whistler mode waves observed by THEMIS during near-earth dipolarizations. Ann Geophys 27:2259–2275

Liang J, Donovan EF, Liu WW, Jackel B, Syrjasuo M, Mende SB, Frey HU, Angelopoulos V, Connors M (2008) Intensification of pre-existing auroral arc at substorm expansion phase onset: Wave-like disruption during the first tens of seconds. Geophys Res Lett 35:L17S19. doi:10.1029/2008GL033666

Liang J, Liu WW, Donovan EF (2009) Ion temperature drop and quasi-electrostatic electric field at the current sheet boundary minutes prior to the local current disruption. J Geophys Res 114:A10215. doi:10.1029/2009JA014357

Lin N, Frey HU, Mende SB, Mozer FS, Lysak RL, Song Y, Angelopoulos V (2009) Statistical study of substorm timing sequence. J Geophys Res 114:A12204. 10.1029/2009JA014381

Liou K (2007) Large, abrupt pressure decreases as a substorm onset trigger. Geophys Res Lett 34(14):L14107. doi:10.1029/2007GL029909

Liou K, Meng C-I, Newel PT, Takahashi K, Ohtani S-I, Lui ATY, Brittnacher M, and Parks G (2000) Evaluation of low-latitude Pi2 pulsations as indicators of substorm onset using Polar ultraviolet imagery. J Geophys Res 105:2495–2505

Liou K, Newell PT, Meng C-I, Wu C-C, Lepping RP (2003) Investigation of external triggering of substorms with Polar ultraviolet imager observations. J Geophys Res 108:1364. doi:10.1029/2003JA009984

Liu WW (1997) Physics of the explosive growth phase: ballooning instability revisited. J Geophys Res 102:4927–4931

Liu WW, Liang J (2009) Disruption of magnetospheric current sheet by quasi-electrostatic field. Ann Geophys 27: 1941–1950

Liu WW, Charbonneau P, Thibault K, Morales L (2006) Energy avalanches in the central plasma sheet. Geophys Res Lett 33:L19106. doi:10.1029/2006GL027282

Liu WW, Donovan EF, Liang J, Voronkov I, Spanswick E, Jayachandran PT, Jackel B, Meurant M (2007) On the equatorward motion and fading of proton aurora during substorm growth phase. J Geophys Res 112:A10217. doi:10.1029/2007JA012495

Liu WW, Liang J, Donovan EF (2008) Interaction between kinetic ballooning perturbation and thin current sheet: quasi-electrostatic field, local onset, and global characteristics. Geophys Res Lett 35:L20107. doi:10.1029/2008GL035757

Liu WW, Liang J, Donovan EF (2010) Electrostatic field and ion temperature drop in thin current sheets: a theory. J Geophys Res 115:A03211. doi:10.1029/2009JA014359

Longmire CL (1963) Elementary plasma physics. Interscience Publishers, New York, NY, p 54

Lopez RE, Lui ATY (1990) A multisatellite case study of the expansion of a substorm current wedge in the near-earth magnetotail. J Geophys Res 95:8009–8018

Lui ATY, Chang C-L, Mankofsky A, Wong H-K, Winske D (1991) A cross-field current instability for substorm expansions. J Geophys Res 96:11389–11401

Lui ATY (2001) A multiscale model for substorms. Space Sci Rev 95:325–345

Lui ATY (2002) Multiscale phenomena in the near-earth magnetosphere. J Atmos Sol Terr Phys 64:125–143

Lui ATY (2004) Potential plasma instabilities for substorm expansion onset. Space Sci Rev 113:127–206

Lui ATY (2009) Comment on "Tail reconnection triggering substorm onset." Science 324:1391-b. doi:10.1126/science.1167726

Lui ATY (2011a) Revisiting THEMIS substorm events implying magnetic reconnection as the substorm trigger. J Geophys Res 116:A03211. doi:10.1029/2010JA016078

Lui ATY (2011b) Energy source for auroral electrons from two proposed substorm onset processes. J Geophys Res 116:A04214. doi:10.1029/2010JA016332

Lui ATY, Burrows JR (1978) On the location of auroral arcs near substorm onset. J Geophys Res 83:3342–3348

Lui ATY, Consolini G (2005) Substorm disturbance propagation from a two-dimensional cellular automaton model. In: Lui ATY, Kamide Y, Consolini G (eds) Multiscale coupling of sun-earth processes. Elsevier, Amsterdam, The Netherlands, pp 357–364

Lui ATY, Murphree JS (1998) A substorm model with onset location tied to an auroral arc. Geophys Res Lett 25: 1269–1272

Lui ATY, Najmi A-H (1997) Time-frequency decomposition of signals in a current disruption event. Geophys Res Lett 24:3157–3160

Lui ATY, Frank LA, Ackerson KL, Meng C-I, Akasofu S-I (1977a) Systematic study of plasma flow during plasma sheet thinnings. J Geophys Res 82:4815–4825

Lui ATY, Meng C-I, Akasofu S-I (1977b) Search for the magnetic neutral line in the near-earth plasma sheet, 2. Systematic study of IMP-6 magnetic field observations. J Geophys Res 82:1547–1565

Lui ATY, Lopez RE, Krimigis SM, McEntire RW, Zanetti LJ, Potemra TA (1988) A case study of magnetotail current sheet disruption and diversion. Geophys Res Lett 15: 721–724

Lui ATY, Liou K, Newell PT, Meng C-I, Ohtani S-I, Kokubun S, Ogino T, Brittnacher M, Parks G (1998) Plasma and magnetic flux transport associated with auroral breakups. Geophys Res Lett 25:4059–4062

Lui ATY, Liou K, Nosé M, Ohtani S, Williams DJ, Mukai T, Tsuruda K, Kokubun S (1999) Near-earth dipolarization: evidence for a non-MHD process. Geophys Res Lett 26:2905–2908

Lui ATY, Chapman SC, Liou K, Newell PT, Meng C-I, Brittnacher M, Parks GK (2000) Is the dynamic magnetosphere an avalanching system? Geophys Res Lett 27:911–914

Lui ATY, Lai WW, Liou K, Meng CI (2003) A new technique for short-term forecast of auroral activity. Geophys Res Lett 30(5):1258. doi:10.1029/2002GL016505

Lui ATY, Zheng Y, Zhang Y, Angelopoulos V, Parks GK, Mozer FS, Rème H, Kistler LM, Dunlop MW, Gustafsson G, Henderson MG (2007a) Prelude to THEMIS tail conjunction. Ann Geophys 25:1001–1009

Lui ATY, Zheng Y, Rème H, Dunlop MW, Gustafsson G, Owen CJ (2007b) Breakdown of the frozen-in condition in the Earth's magnetotail. J Geophys Res 112:A04215. doi:10.1029/2006JA012000

Lui ATY, Volwerk M, Dunlop MW, Alexeev IV, Fazakerley AN, Walsh AP, Lester M, Grocott A, Mouikis C, Henderson MG, Kistler LM, Shen C, Shi J-K, Zhang T-L, Rème H (2008a) Near-earth substorm features from multiple satellite observations. J Geophys Res 113:A07S26. doi:10.1029/2007JA012738

Lui ATY, Yoon PH, Mok C, Ryu C-M (2008b) Inverse cascade feature in current disruption. J Geophys Res 113:A00C06. doi:10.1029/2008JA013521

Lyons LR, Blanchard GT, Samson JC, Lepping RP, Yamamoto T, Moretto T (1997) Coordinated observations demonstrating external substorm triggering. J Geophys Res 102:27039–27051

Lyon JG, Lopez RE, Goodrich CC, Wiltberger M, Papadopoulos K (1998) Simulation of the March 9, 1995, substorm: auroral brightening and the onset of lobe reconnection. Geophys Res Lett 25:3039–3042

Lyons LR, Nishimura Y, Shi Y, Zou S, Kim H-J, Angelopoulos V, Heinselman C, Nicolls MJ, Fornacon K-H (2010) Substorm triggering by new plasma intrusion: incoherent-scatter radar observations. J Geophys Res 115:A07223. doi:10.1029/2009JA015168

Machida S, Miyashita Y, Ieda A, Nosé M, Nagata D, Liou K, Obara T, Nishida A, Saito Y, Mukai T (2009) Statistical visualization of the Earth's magnetotail based on Geotail data and the implied substorm model. Ann Geophys 27:1035–1046

McIlwain CE (1974) Substorm injection boundaries. In: McCormac BM (ed) Magnetospheric physics. D. Reidel, Hingham, MA, pp 143–154

McPherron RL (1970) Growth phase of magnetospheric substorms. J Geophys Res 75:5592–5599

Mende SB, Frey HU, Morsony BJ, Immel TJ (2003) Statistical behavior of proton and electron auroras during substorms. J Geophys Res 108(A3):1339. doi:10.1029/2002JA009751

Meng C-I, Liou K (2004) Substorm timings and timescales: a new aspect. Space Sci Rev 113:41–75

Morley SK, Freeman MP (2007) On the association between northward turnings of the interplanetary magnetic field and substorm onsets. Geophys Res Lett 34:L08104. doi:10.1029/2006GL028891

Nagai T, Fujimoto M, Saito Y, Machida S, Terasawa T, Nakamura R, Yamamoto T, Mukai T, Nishida A, Kokubun S (1998) Structure and dynamics of magnetic reconnection for substorm onsets with Geotail observations. J Geophys Res 103:4419–4440

Nakamura R, Baumjohann W, Brittnacher M, Sergeev VA, Kubyshkina M, Mukai T, Liou K (2001) Flow bursts and auroral activations: onset timing and foot point location. J Geophys Res 106:10777–10790

Nakamura R, Baumjohann W, Klecker B, Bogdanova Y, Balogh A, Rème H, Bosqued JM, Dandouras I, Sauvaud JA, Glassmeier K-H, Kistler L, Mouikis C, Zhang TL, Eichelberger H, Runov A (2002) Motion of the dipolarization front during a flow burst event observed by Cluster. Geophys Res Lett 29(20):1942. doi:10.1029/2002GL015763

Nakamura R, Retinò A, Baumjohann W, Volwerk M, Erkaev N, Klecker B, Lucek EA, Dandouras I, André M, Khotyaintsev Y (2009) Evolution of dipolarization in the near-Earth current sheet induced by Earthward rapid flux transport. Ann Geophys 27:1743–1754

Newell PT, Sotirelis T, Liou K, Rich FJ (2008) Pairs of solar wind-magnetosphere coupling functions: combining a merging term with a viscous term works best. J Geophys Res 113:A04218. doi:10.1029/2007JA012825

Nishimura Y, Lyons L, Zou S, Angelopoulos V, Mende S (2010) Substorm triggering by new plasma intrusion: THEMIS all-sky imager observations. J Geophys Res 115:A07222. doi:10.1029/2009JA015166

Ohtani S, Takahashi K, Russell CT (1992) Radial expansion of the tail current disruption during substorms: a new approach to substorm onset region. J Geophys Res 97:3129–3136

Ohtani S, Takahashi K, Higuchi T, Lui ATY, Spence HE (1998) AMPTE/CCE – SCATHA simultaneous observations of substorm-associated magnetic fluctuations. J Geophys Res 103:4671–4682

Ohtani S, Singer HJ, Mukai T (2006) Effects of the fast plasma sheet flow on the geosynchronous magnetic configuration: Geotail and GOES coordinated study. J Geophys Res 111:A01204. doi:10.1029/2005JA011383

Ohtani S, Miyashita Y, Singer H, Mukai T (2009) Tailward flows with positive Bz in the near-earth plasma sheet. J Geophys Res 114:A06218. doi:10.1029/2009JA014159

Papadopoulos K, Sharma AS, Valdivia JA (1993) Is the magnetosphere a lens for MHD waves? Geophys Res Lett 20:2809–2812

Pellinen RJ, Heikkila WJ (1978) Observations of auroral fading before breakup. J Geophys Res 83:4207–4217

Perreault P, Akasofu S-I (1978) A study of geomagnetic storms. Geophys J R Astron Soc 54:547–573

Pu ZY, Korth A, Chen ZX (1997) MHD drift ballooning instability near the inner edge of the near-earth plasma sheet and its application to the substorm onset. J Geophys Res 102:14397

Pu ZY, Korth A, Kang KB, Zong QG, Fu SY, Hong MH, Liu ZX, Mouikis CG, Friedel RWH, Pulkknien T (1999) Drift ballooning instability in the presence of a plasma flow: a synthesis of tail reconnection and current disruption for the initiation of substorms. J Geophys Res 104: 10235–10248

Pu ZY, Chu XN, Cao X, Mishin V, Angelopoulos V, Wang J, Wei Y, Zong QG, Fu SY, Xie L, Glassmeier K-H, Frey H, Russell CT, Liu J, McFadden J, Larson D, Mende S, Mann I, Sibeck D, Sapronova LA, Tolochko MV, Saifudinova TI, Yao ZH, Wang XG, Xiao CJ, Zhou XZ, Reme H, Lucek E (2010) THEMIS observations of substorms on 26 February 2008 initiated by magnetotail reconnection. J Geophys Res 115:A02212. doi:10.1029/2009JA014217

Rae IJ, Mann IR, Angelopoulos V, Murphy KR, Milling DK, Kale A, Frey HU, Rostoker G, Russell CT, Watt CEJ, Engebretson MJ, Moldwin MB, Mende SB, Singer HJ, Donovan EF (2009) Near-earth initiation of a terrestrial substorm. J Geophys Res 114:A07220. doi:10.1029/2008JA013771

Rae IJ, Watt CEJ, Mann IR, Murphy KR, Samson JC, Kabin K, Angelopoulos VA (2010) Optical characterization of the growth and spatial structure of a substorm onset arc. J Geophys Res 115:A10222. doi:10.1029/2010JA015376

Raeder, Larson JD, Li W, Kepko L, Fuller-Rowell T (2008) OpenGGCM simulations for the THEMIS mission. Space Sci Rev 141:535–555. doi:10.1007/s11214-008-9421-5

Rostoker G (1983) Triggering of expansion phase intensifications of magnetospheric substorms by northward turnings of the interplanetary magnetic field. J Geophys Res 88:6981–6993

Roux A, Perraut S, Robert P, Morane A, Pedersen A, Korth A, Kremser G, Aparicio B, Rodgers D, Pellinen R (1991) Plasma sheet instability related to the westward traveling surge. J Geophys Res 96:17697–17714

Runov A, Baumjohann W, Nakamura R, Sergeev VA, Amm O, Frey H, Alexeev I, Fazakerley AN, Owen CJ, Lucek E, André M, Vaivads A, Dandouras I, Blecker B (2008) Observations of an active thin current sheet. J Geophys Res 113:A07S27. doi:10.1029/2007JA012685

Runov A, Angelopoulos V, Sitnov MI, Sergeev VA, Bonnell J, McFadden JP, Larson D, Glassmeier K-H, Auster U (2009) THEMIS observations of an earthward-propagating dipolarization front. Geophys Res Lett 36:L14106. doi:10.1029/2009GL038980

Russell CT (2000) How northward turnings of the IMF can lead to substorm expansion onsets. Geophys Res Lett 27:3257–3259

Saito MH, Miyashita Y, Fujimoto M, Shinohara I, Saito Y, Liou K, Mukai T (2008a) Ballooning mode waves prior to substorm-associated dipolarizations: Geotail observations. Geophys Res Lett 35:L07103. doi:10.1029/2008GL033269

Saito MH, Miyashita Y, Fujimoto M, Shinohara I, Saito Y, Mukai T (2008b) Modes and characteristics of low-frequency MHD waves in the near-earth magnetotail prior to dipolarization: fitting method. J Geophys Res 113:A06201. doi:10.1029/2007JA012778

Samson JC, Dobias P (2005) Explosive instabilities and substorm intensifications in the Earth's magnetotail. In: Lui ATY, Kamide Y, Consolini G (eds) Multiscale coupling of sun-earth processes. Elsevier, Amsterdam, pp 235–251

Samson JC, Lyons LR, Newell PT, Creutzbert F, Xu B (1992a) Proton aurora and substorm intensifications. Geophys Res Lett 19:2167–2170

Samson JC, Wallis DD, Hughes TJ, Creutzberg F, Ruohoniemi JM, Greenwald RA (1992b) Substorm intensifications and field line resonances in the nightside magnetosphere. J Geophys Res 97:8495

Samson JC, Cogger LL, Pao Q (1996) Observations of field line resonances, auroral arcs, and auroral vortex structures. J Geophys Res 101:17373

Sauvaud J-A, Winckler JR (1980) Dynamics of plasma, energetic particles, and fields near synchronous orbit in the nighttime sector during magnetospheric substorms. J Geophys Res 85:2043–2056

Schieldge JP, Siscoe GL (1970) A correlation of the occurrence of simultaneous sudden magnetospheric compressions and geomagnetic bay onsets with selected geophysical indices. J Atmos Sol Terr Phys 32:1819–1830

Sergeev V, Semenov V, Kubyshkina M, Ivanova V, Baumjohann W, Nakamura R, Penz T, Runov A, Zhang TL, Glassmeier K-H, Angelopoulos V, Frey H, Sauvaud J-A, Daly P, Cao JB, Singer H, Lucek E (2007) Observation of repeated intense near-earth reconnection on closed field lines with Cluster, Double Star, and other spacecraft. Geophys Res Lett 34:L02103. doi:10.1029/2006GL028452

Sergeev VA, Apatenkov SV, Angelopoulos V, McFadden JP, Larson D, Bonnell JW, Kuznetsova M, Partamies N, Honary F (2008) Simultaneous THEMIS observations in the near-tail portion of the inner and outer plasma sheet flux tubes at substorm onset. J Geophys Res 113:A00C02. doi:10.1029/2008JA013527

Sergeev V, Angelopoulos V, Apatenkov S, Bonnell J, Ergun R, Nakamura R, McFadden J, Larson D, Runov A (2009) Kinetic structure of the sharp injection/dipolarization front in the flow-braking region. Geophys Res Lett 36:L21105. doi:10.1029/2009GL040658

Shiokawa K, Baumjohann W, Haerendel G (1997) Braking of high-speed flows in the near-Earth tail. Geophys Res Lett 24:1179–1182

Shue J-H, Ieda A, Lui ATY, Parks GK, Mukai T, Ohtani S (2008) Two classes of earthward fast flows in the plasma sheet. J Geophys Res 113:A02205. doi:10.1029/2007JA012456

Siscoe GL, Cummings WD (1969) On the cause of geomagnetic bays. Planet Space Sci 17:1795–1802

Sitnov MI, Swisdak M, Divin AV (2009) Dipolarization fronts as a signature of transient reconnection in the magnetotail. J Geophys Res 114:A04202. doi:10.1029/2008JA013980

Spanswick E, Donovan E, Liu W, Liang J, Blake JB, Reeves G, Friedel R, Jackel B, Cully C, Weatherwax A (2009) Global observations of substorm injection region evolution: 27 August 2001. Ann Geophys 27:2019–2025

Takahashi K, Zanetti LJ, Lopez RE, McEntire RW, Potemra TA, Yumoto K (1987) Disruption of the magnetotail current sheet observed by AMPTE/CCE. Geophys Res Lett 14: 1019–1022

Tamao T (1964) The structure of three-dimensional hydromagnetic waves in a uniform cold plasma. J Geomagnetism Geoelectricity 18:89–114

Tsyganenko NA (2002) A model of the near magnetosphere with a daw-dusk asymmetry, 2. Parameterization and fitting to observations. J Geophys Res 107:A8. 10.1029/2001JA000220

Uritsky VM, Liang J, Donovan E, Spanswick E, Knudsen D, Liu W, Bonnell J, Glassmeier KH (2009) Longitudinally propagating arc wave in the pre-onset optical aurora. Geophys Res Lett 36:L21103. doi:10.1029/2009GL040777

Vogiatzis II, Fritz TA, Zong Q-G, Baker DN, Sarris ET, Daly PW (2005) Fine-time energetic electron behavior observed by Cluster/RAPID in the magnetotail associated with X-line formation and subsequent current disruption. Ann Geophys 23:2265–2280

Voronkov I, Rankin R, Frycz P, Tikhonchuk VT, Samson JC (1997) Coupling of shear flow and pressure gradient instabilities. J Geophys Res 102:9639–9650

Vörös Z, Runov A, Leubner MP, Baumjohann W, Volwerk M (2010) Is current disruption associated with an inverse cascade? Nonlinear Processes Geophys 17:287–292

Walker RJ, Erickson KN, Swanson RL, Winckler JR (1976) Substorm-associated particle boundary motion at synchronous orbit. J Geophys Res 81:5541–5550

Yahnin AG, Kornilov IA, Kornilova TA, Sergeev VA, Lui ATY, Liou K, Meng C-I, Pajunpaa A (2000) Do the observations confirm the high-speed flow braking model for substorms? In: Proceedings of the fifth international conference on substorms, ESA SP-443, Paris, pp 345–348

Yoon PH, Lui ATY, Bonnell JW (2009) Identification of plasma instability from wavelet spectra in a current disruption event. J Geophys Res 114:A04207. doi:10.1029/2008JA013816

Zhou M, Ashour-Abdalla M, Deng X, Schiver D, El-Alaoui M, Pang Y (2009) THEMIS observation of multiple dipolarization fronts and associated wave characteristics in the near-earth magnetotail. Geophys Res Lett 36:L20107. doi:10.1029/2009GL040663

Zhu P, Bhattacharjee A, Ma ZW (2004) Finite ky ballooning instability in the near-earth magnetotail. J Geophys Res 109:A11211. doi:10.1029/2004JA010505

Zhu P, Raeder J, Germaschewski K, Hegna CC (2009) Initiation of ballooning instability in the near-Earth plasma sheet prior to the 23 March 2007 THEMIS substorm expansion onset. Ann Geophys 27:1129–1138

Cluster Observations of Plasma Bubbles, BBFs and Their Wakes

6

Andrew P. Walsh and Colin Forsyth

Abstract

Bursty Bulk Flows (BBFs) are an important means of transporting magnetic flux and plasma through the Earth's magnetosphere and can be explained as entropy depleted flux tubes (plasma bubbles) propagating earthward under the action of the interchange instability. For 10 years ESA's Cluster spacecraft have been making measurements of BBFs in the magnetotail at spacecraft separations ranging from 100 to 10,000 km. Here we compare three BBFs observed by Cluster at three different spacecraft separations and discuss some of the similarities and differences between the features observed during each event, with particular reference to field-aligned currents and the newly-discovered wake region observed behind and around earthward moving flux tubes.

6.1 Introduction

The transport of magnetic flux and plasma through the magnetotail during periods of enhanced geomagnetic activity is predominantly carried out during transient events known as Bursty Bulk Flows, or BBFs (Angelopoulos et al. 1992). BBFs are defined as periods of earthward plasma flow and enhanced B_Z detected by spacecraft in the magnetotail that last ~10 min and are often comprised of several so-called "flow bursts" each lasting ~1 min.

A theoretical framework that reproduces the observational features of BBFs is the plasma bubble theory of Chen and Wolf (1993) wherein each flow burst can be represented as a plasma bubble – an entropy depleted flux tube that propagates earthward under the action of the interchange instability. At its simplest, the plasma bubble theory predicts that BBFs have a lower plasma pressure than surrounding flux tubes, compensated for by a higher magnetic pressure than surrounding flux tubes. The bubble theory also predicts regions of field-aligned current (FAC) should be present at the edges of the plasma bubble, associated with the magnetic field shear caused by the bubble's motion through the ambient magnetic field. The sense of the magnetic field shear (i.e. the sign of $B_X \cdot \delta B_Y$) at the edge of the bubble is indicative of the direction of FAC. Currents into the ionosphere are expected at the dawnward edge of the bubble and currents out of the ionosphere are expected at the duskward edge of a bubble (Sergeev et al. 1996), in the same manner as the Substorm Current Wedge. Thus by measuring the direction of FAC using multi-spacecraft techniques, or through examining any magnetic field shear seen

A.P. Walsh (✉)
Mullard Space Science Laboratory, University College London, Dorking, Surrey, RH5 6NT, UK
e-mail: apw@mssl.ucl.ac.uk

W. Liu, M. Fujimoto (eds.), *The Dynamic Magnetosphere*, IAGA Special Sopron Book Series 3,
DOI 10.1007/978-94-007-0501-2_6,

by a single spacecraft, the location of a spacecraft relative to the bubble centre line can be determined. Tailward directed return flows have also been predicted to be found around the edges of the depleted flux tube. Various spacecraft observations have been made of these features (Forsyth et al. 2008; Walsh et al. 2009).

The plasma bubble theory does not offer any explanation as to the source of depletion, although recent simulation work (Sitnov et al. 2005, 2009) suggests that reconnection of closed field lines may be responsible. Here we compare and contrast, with particular reference to return flows and wake structures, two of the more detailed observational studies of BBFs/plasma bubbles based on Cluster observations. The first study (Walsh et al. 2009) reported observations made during the 2005 tail season, when the separation of the Cluster spacecraft was ~10,000 km, while the second (Forsyth et al. 2008) reported observations made during the 2003 tail season when the Cluster spacecraft were separated by 100 km. A third event from the 2004 (1000 km separation) tail season is also included.

6.2 Case Study One: 21 September 2005

The data in this section were first presented by Walsh et al. (2009) and concern a plasma bubble observed on 21 September 2005, when Cluster 1 was located at GSM(–15.9, 1.8, 1.1) R_E. During the interval the Cluster spacecraft were configured in a 10,000 km triangle in the plane of a model tail neutral sheet with one spacecraft (C4) offset from that triangle by 1000 km. During this interval, C2 was located 10,000 km duskward of C1. Data from the interval are plotted in Fig. 6.1. Panel a shows magnitude and GSM components (all data are presented in GSM unless otherwise stated) of magnetic field from Cluster 1 FGM (Balogh et al. 2001). Panel b shows total, magnetic and

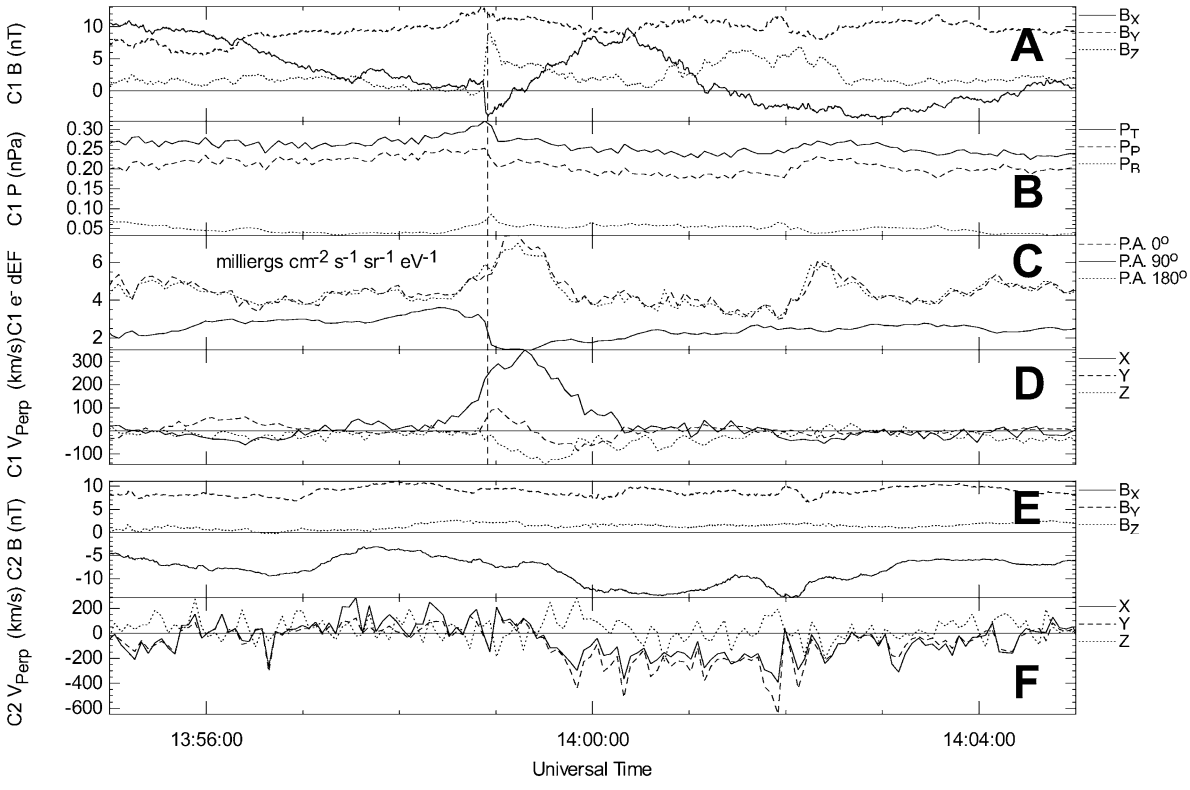

Fig. 6.1 Data from 21st September 2005. Panel (**a**) shows GSM components of magnetic field from C1; Panel (**b**) the proton, magnetic and total pressures from C1; Panel (**c**) electron energy fluxes from PEACE for particles with pitch angles of 0°, 90° and 180° and Panel (**d**) GSM components of $V_\perp$ from C1. Panels (**e**) and (**f**) are equivalent to Panels (**a**) and (**d**) but for C2

ion pressure from C1 FGM and CIS-HIA (Rème et al. 2001). Panel c shows total electron energy flux for particles with pitch angles of 0°, 90° and 180° from C1 PEACE (Johnstone et al. 1997). Panel d shows GSM components of ion velocity perpendicular to the magnetic field velocity ($V_\perp$) from C1 CIS-HIA. Panels e and f are equivalent to A and D for C2 with velocities derived from PEACE electron measurements.

The minute-long period of enhanced $V_{\perp X}$ detected by C1 beginning at ~13:58:55 UT (Panel a). During the period of enhanced B_Z, which was longer than the flow burst, the plasma pressure was reduced and the magnetic pressure enhanced, resulting in approximately constant total pressure (Panel c), consistent with the plasma bubble theory. Furthermore, a magnetic shear (δB_Y) was detected as the spacecraft passed into the low plasma pressure region consistent with C1 passing through the dawnward side of a plasma bubble (Panel a). What is not predicted by theory is the extended region of reduced plasma pressure behind the bubble that forms a depleted "wake". This wake is partially stagnant and partially tailward flowing. In contrast, no B_Z enhancement was detected by C2, instead there was an enhancement in B_X (Panel e) contemporaneous with tailward- and dawnward-directed flows (Panel f). Since B_Z was positive, it is likely that the C2 spacecraft missed the bubble itself and made the first direct detection of the expected return flows around the edges of a plasma bubble. The enhanced B_X in the return flow region means there is an enhanced magnetic pressure, so the return flow region may also have been depleted in the same manner as the wake behind the bubble that was observed by C1. A decrease in perpendicular electron flux (not shown) was observed and is consistent with this. No ion measurements are available from C2, however, thus it is not possible to directly compare the pressures in return flow region and wake region directly.

The earthward flow at C1 was first detected before the magnetic field dipolarization and before the depletion in plasma pressure. This was interpreted as a region of magnetic flux and plasma pileup in front of the plasma bubble. The increase in magnetic pressure seen before the dipolarization (Panel c) is also consistent with this. Once within the plasma bubble, the spacecraft detected a negative $V_{\perp Z}$ (Panel d) consistent with the contraction of the flux tube as it propagated towards the Earth into higher field strength regions.

The dimensions of this particular plasma bubble can be estimated because of the relative locations of C1 and C2. The spacecraft were separated by approximately 10,000 km in Y GSM, with C2 located duskward of C1. Thus if C1 passed through the plasma bubble on its dawnward side, consistent with the sign of $B_X \cdot \delta B_Y$ just prior to bubble entry, assuming approximate symmetry either side of the bubble centre line, the bubble can be no wider than twice the spacecraft separation, i.e. ~20,000 km or $3R_E$ (Walsh et al. 2009), consistent with previous observations (Nakamura et al. 2004).

6.3 Case Study Two: 25 August 2003

The data in this section were first presented by Forsyth et al. (2008) and concern a BBF observed on 25 August 2003. During the event, the Cluster spacecraft were located at GSM(–18.7, –3.6, –1.1)R_E in a formation close to a regular tetrahedron and separated by 120 km. Data from Cluster 4 are plotted in Fig. 6.2. Due to their close separation, data from all four spacecraft were similar throughout the event (Forsyth et al. 2008). Panel a shows the magnetic field components in GSM. Panel b shows the proton (dashed line), magnetic (dotted line) and total (based on the proton and magnetic) pressures. Panel c shows the total energy flux for electrons with 0°, 90°, and 180° pitch angles. Panel d shows the proton velocity perpendicular to the magnetic field in GSM coordinates. Panel e shows the field-aligned current (FAC) calculated using the curlometer method (Dunlop et al. 1988) for both the 5 Hz (dotted line) and spin resolution (solid line) magnetic field data. Proton data are from the CIS-CODIF instrument (Rème et al. 2001).

From 01:24:25 UT, $V_\perp$ was enhanced for 2 min (Fig. 6.2, Panel d), associated with a dipolarization of the magnetic field (Panel a) and a decrease in the plasma pressure (Panel b) driven by a drop in density. The magnetic field and proton pressure indicate that the BBF was made up of two individual flow bursts (i.e. two regions of reduced proton and enhanced magnetic pressure), separated by a region of enhanced (relative to each flow burst) proton pressure and reduced magnetic pressure. This is confirmed by the presence of two bi-polar FAC signatures (Panel e), indicating that the spacecraft passed from the dusk to dawn sides of the flow bursts, consistent with results from minimum

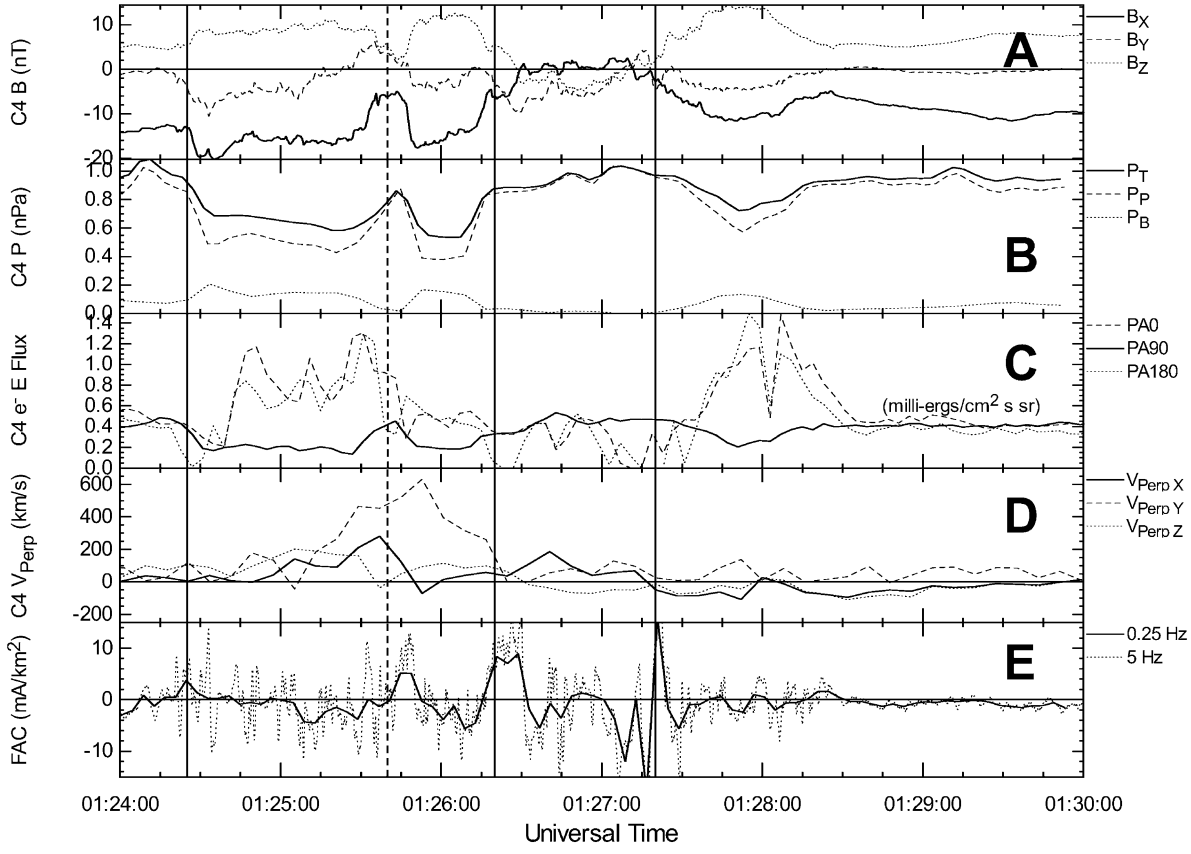

Fig. 6.2 Data from 8 August 2003. Panels (**a**) to (**d**) are the same as for Fig. 6.1 while Panel (**e**) shows *j//* calculated using the curlometer technique from spin resolution and 5 Hz FGM data. *Solid vertical lines* delimit the BBF and wake regions. The *dashed vertical line* marks the boundary between the two flow bursts

variance analysis and multi-spacecraft timing analysis (Forsyth et al. 2008). During the two flow bursts, it can be seen that the electron energy flux was enhanced in the parallel and anti-parallel directions over the perpendicular direction. Following the BBF, there were 45 s during which time B_Z turned negative and B_X turned positive.

From 01:27:20 UT, $V_{\perp X}$ and $V_{\perp Z}$ were negative, indicating tailward flow away from the centre of the plasma sheet, associated with enhanced field parallel electron energy flux. This is similar to the wake region behind the BBF discussed above and had not previously been noted. Within this region, the field-aligned currents were directed earthwards, consistent with currents on the dawn side of a flow. These Earthward field-aligned currents are expected, given that Cluster exited the last flow burst on the dawnward side (Forsyth et al. 2008). Compared to the currents within the BBF, these currents show less variability (in both the 5 Hz and spin resolution data) although they are somewhat smaller than the currents in the flow region.

6.4 Case Study Three: 24 September 2004

During the 2004 tail season, the Cluster spacecraft were orbiting in a regular tetrahedral formation, separated by approximately 1000 km. To complement the above studies, we present observations of a BBF from 24 September 2004 when Cluster was located at GSM(–17.3, 4.2, –2.3) R_E. Data from Cluster 1 from the event are plotted in Fig. 6.3. Panel a shows the magnetic field components in GSM. Panel b shows the proton (dashed line), magnetic (dotted line) and total (based on the proton and magnetic) pressures. Panel c shows the total energy flux for electrons with pitch angles of 0°, 90°, and 180°. Panel d shows the

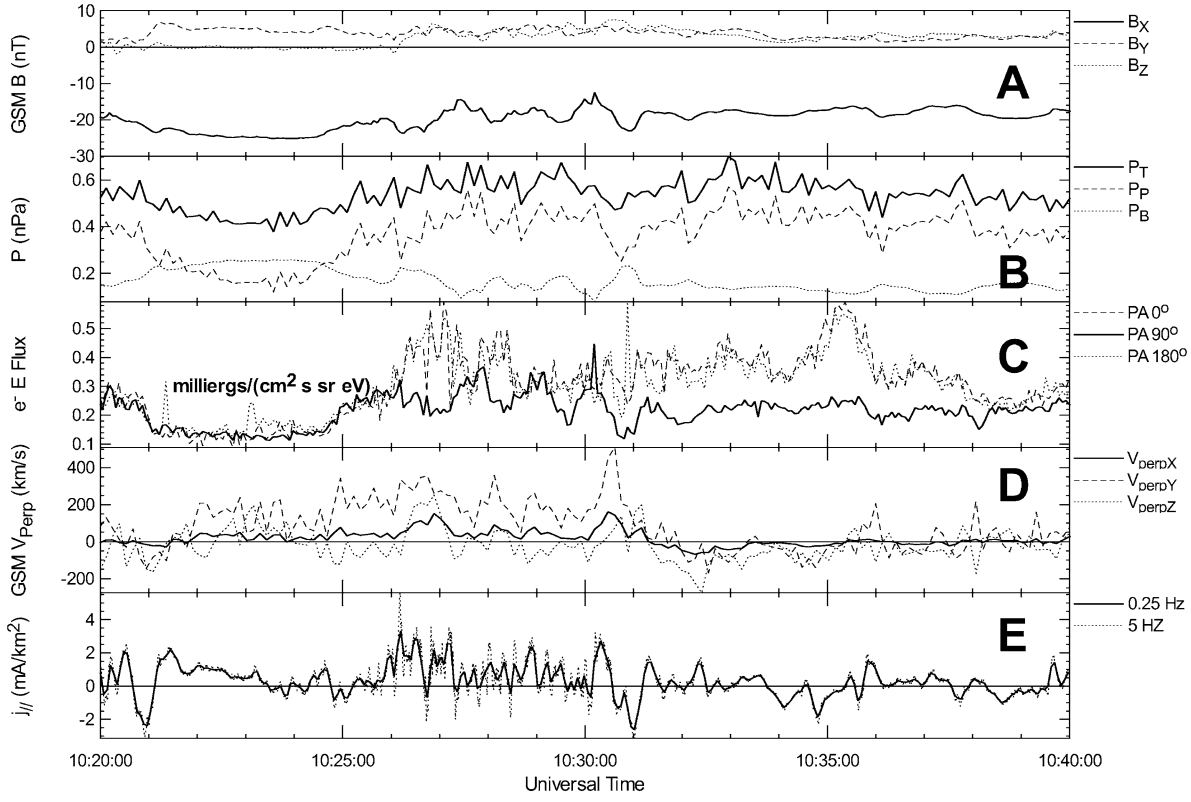

Fig. 6.3 Data taken by C1 on 24th September 2004. Panels are the same as for Fig. 6.2

ion velocities perpendicular to the magnetic field in GSM coordinates. Panel e shows the field-aligned current calculated using the curlometer method (Dunlop et al. 1988) for both the 5 Hz (dotted line) and spin resolution (solid line) magnetic field data.

The transport of magnetic flux ($V_\perp$) was enhanced from 10:22:00 to 10:31:00, predominantly in the positive Y direction (Fig. 6.3, Panel d), associated with a decrease in Bx and an increase in Bz (Panel a), consistent with the definition of a BBF. During the $V_\perp$ enhancement, there were four distinct intervals during which time the parallel electron flux was enhanced above the perpendicular electron flux (Panel c), coinciding with enhancements in the Earthward magnetic flux transport ($V_\perp x$, Panel d) and dipolarizations of the magnetic field and indicating the presence of four separate flow bursts. During the flow bursts the magnetic pressure was also enhanced and proton pressure appeared reduced (Panel b), although noisy CODIF data mean this is not as clear as for the 2003 and 2005 events. Also during the flow bursts, the field-aligned currents were enhanced, showing tailward flowing currents for each of the flow bursts apart from the last, which showed a bipolar current signature, indicative of the spacecraft staying on the duskward side of each of the first three flow bursts and passing from the duskward to the dawnward side of the final flow burst. The duskward direction of $V_\perp Y$ throughout the BBF is consistent with this interpretation.

After 10:31:00, all components turned negative, indicating that the spacecraft entered the wake region behind the BBF. In this region, the parallel electron flux remained elevated above the perpendicular electron flux and the field-aligned currents were variable, showing no apparent tendency to be earthward or tailward.

6.5 Discussion

We have presented the results from three case studies of BBFs using the Cluster spacecraft when the spacecraft were separated by 100, 1000, and 10,000 km, two of which have previously been examined individually

(Forsyth et al. 2008; Walsh et al. 2009). In the following, we discuss the similarities and differences between the observations. Wake regions were observed, albeit with slightly different characteristics, during all three of the presented events. Only in case study one was the return flow region observed, which is thought to form the wake behind the plasma bubble (Walsh et al. 2009). This was observed concurrently with the earthward moving plasma bubble. The wake/return flow region was most obviously different from the bubble itself in the 2005 case, possibly because that event represented a single flow burst whilst multiple flow bursts were observed within the 2003 and 2004 BBFs. This may indicate that the ambient plasma between the flow bursts interacts in a more complex manner with the earthward moving flux tubes. In all cases the perpendicular electron fluxes were higher in the wake regions than within the depleted flux tubes themselves.

In the 2004 and 2005 cases, the (anti)parallel electron fluxes observed in the wake regions were reduced with respect to those seen within the plasma bubbles, while in the 2003 case the (anti)parallel electron fluxes resembled those seen during the flow bursts. In this case, the wake region was separated from the flow bursts by a region of negative *Bz* which was not present in either of the other cases. Enhanced (anti)parallel electron fluxes were, however observed at the interface between the wake and undisturbed plasma sheet in the 2004 and 2005 cases (Figs. 6.3 and 6.1, Panels c). It would appear, then, that the wake regions behind BBFs and flow bursts show significant variability in magnetic field, plasma properties, field-aligned currents and substructure that require further, statistical, study in order to be properly understood.

It has previously been shown that the curlometer technique (Dunlop et al. 1988) can be used to examine the current systems of BBFs using data from the Cluster spacecraft when the spacecraft are in a regular, tetrahedral formation (Forsyth et al. 2008). However, studies have shown that when the spacecraft formation deviates strongly from a regular tetrahedron, the curlometer provides less meaningful results (Robert et al. 1998). As such, we only have curlometer data from the events in 2003 (100 km scale) and 2004 (1000 km scale). Both events consist of multiple flow bursts within a period of enhanced magnetic flux transport and both show enhancements of the field-aligned currents associated with the flow bursts. During the 2004 event, Cluster observed only tailward currents (field-parallel in the southern plasma sheet) for the first three flow bursts, whereas the last flow burst, and both flow bursts in the 2003 event, had bipolar current signatures. The currents from the 2003 event were larger than that of the 2004 event and showed greater variability between the results from the spin resolution and 5 Hz magnetic field data. Modelling studies (Forsyth et al. 2010) have shown that, for a fixed width line current, the curlometer will detect more of the current when the spacecraft are deployed in a smaller tetrahedron than a larger tetrahedron relative to the current width. As such, we would expect that the currents in 2003 would be larger, assuming that currents within flow bursts do not vary significantly between events. In both the 2003 and 2004 cases, FAC were observed in the wake regions behind the BBF, albeit of lower magnitude than during the flow bursts. For the 2005 event, an examination of the electron fluxes in the parallel and antiparallel directions in the wake observed by C2 did not reveal any significant flux imbalance (Walsh et al. 2009), contrary to the fluxes observed in the plasma bubble itself (Fig. 6.1, Panel c), hence it was not possible to infer the presence of significant FAC in that case.

In each case the velocities of the BBFs were slightly different. In 2003 and 2004 $V_{\perp Y}$ dominated while in 2005 $V_{\perp X}$ was dominant. In all cases however, the component of $V_{\perp Z}$ was consistent with that of a contracting flux tube: negative when the spacecraft was located north of the tail neutral sheet (2005), positive when the spacecraft were located south of the neutral sheet (2003, 2004). The magnitude of $V_{\perp Z}$ was higher for those events where the spacecraft were located further from the neutral sheet, as expected for the contracting flux tube scenario. The observed asymmetry in electron pitch angle distributions, i.e. enhanced (anti)parallel flux and reduced perpendicular flux, within all three plasma bubbles can be explained in context of the contracting flux tube scenario. Particle populations frozen to contracting flux tubes can be Fermi accelerated in order to conserve the bounce invariant, provided the contraction happens on a time scale longer than the particle bounce time. Alternatively, if the plasma bubbles were first formed by localised reconnection of open, lobe field lines, one might expect the electrons frozen to those field lines to have a more (anti)field-aligned (i.e. PSBL-like) character (Forsyth et al. 2008).

The events from 2004 and 2005 showed little change in the total pressure observed by the Cluster spacecraft passing through the flows. In the 2004 event,

the ion pressure increased slightly, and the magnetic pressure dropped slightly and vice versa for the 2005 event. In contrast, the event from 2003 had a distinct drop in the total pressure, driven by a drop in the ion pressure that was not fully compensated for by an increase in the magnetic pressure. MHD models of plasma bubbles (Birn et al. 2004) have predicted that during the early life of plasma bubbles, the particle pressure is depleted and forces act to re-establish pressure balance between the bubble and its surroundings. Later on, once pressure balance has been restored, the particle pressure along the flux tube further from the neutral sheet may increase above its surroundings.

Based on this, we suggest that events from 2004 and 2005 are relatively mature bubbles compared to the event from 2003, which shows the characteristics of a young bubble.

In the 2004 case particularly, $V_{\perp Z}$ was northward during each of the individual flow bursts within the BBF, in contrast to the "ambient" BBF plasma which had a southward directed $V_{\perp Z}$ (Fig. 6.3, Panel d). This highlights the difference between the flow bursts and the rest of the BBF. The flow bursts (i.e. plasma bubbles) had significantly different $V_{\perp X}$ and $V_{\perp Z}$ components than the "ambient" BBF, despite all of the plasma having a significant $V_{\perp Y}$, hinting that different physical processes govern their motion and evolution. Indeed, if one compares the velocity profile of a single flow burst from the 2004 event with the 2005 event one sees similar features in $V_{\perp X}$ and $V_{\perp Z}$, despite the very different $V_{\perp Y}$ behaviour. Furthermore, the 2003 and 2004 events make clear that the regions between the individual flow bursts that make up a BBF do not have reduced plasma pressure (Figs. 6.2 and 6.3, Panels b) and the electron fluxes in these regions are not as parallel-dominated as during the flow bursts/bubbles themselves. An important, question, then, is what is the difference between these regions, and what causes them to move if not the same interchange mechanism as the plasma bubbles themselves? Interaction between earthward-moving magnetic structures in the magnetotail and the ambient plasma and magnetic field might be expected to cause the ambient plasma to move (Slavin et al. 2003), indeed the moving pile-up region in front of the flow burst in the 2005 event (Fig. 6.1, Panel d) is evidence that this can occur, however in the 2003 and 2004 cases the dominant $V_{\perp Y}$ is not consistent with plasma and flux being driven before a more earthward-moving plasma bubble or flow burst such as those observed in the 2004 event. A more detailed investigation into the interaction between flow bursts and the rest of a BBF is beyond the scope of this paper, however further theoretical and simulation work focusing on the this topic and more detailed multi-scale measurements would both be necessary in answering this question and shedding light on the generation mechanism of BBFs.

Recent work (Panov et al. 2010) based on data from the THEMIS spacecraft has interpreted tailward flows observed directly after earthward flows as the rebounding of earthward propagating flux tubes. It is important to make a distinction between tailward directed return flows (i.e. bubble wakes) that are a result of interchange motion and rebounding flux tubes that have been observed closer to the Earth than the events reported here. The tailward flows observed by both C1 and C2 in the 2005 event certainly do not represent a rebounding flux tube: The same bubble was observed by Double Star TC-2 near geosynchronous orbit some 3 min later (Walsh et al. 2009), thus one might expect to see bubble wakes in the near-tail region where rebounding flux tubes have been detected. Further work is required to determine what proportion of tailward flows with positive Bz observed in the near-earth tail are bubble wakes and what proportion are rebounding flux tubes.

6.6 Summary and Conclusions

We have presented three case studies of BBFs using data from the Cluster spacecraft. Each of the three case studies had several common features, yet there were also some significant differences between them. In the 2003 and 2004 cases each BBF was made up of several flow bursts, the 2005 event was just one flow burst. Each flow burst conformed to the plasma bubble model and had associated with it field-aligned currents consistent with those expected (Sergeev et al. 1996) and each had a reduction in plasma pressure, increase in magnetic pressure and transient dipolarization.

Whilst the 2004 and 2005 plasma bubbles were generally in pressure balance with their surroundings, the 2003 bubble was not. This was interpreted as being because the 2003 bubble was detected earlier in its lifetime than the 2004 and 2005 bubbles. In all cases individual flow bursts had a component of $V_{\perp Z}$ consistent with the depleted flux tube contracting as it propagated earthward. Each flow burst had enhanced (anti)parallel electron fluxes and reduced perpendicular electron

fluxes within it, possibly a result of Fermi acceleration of the particles as the flux tube contracted, or evidence the flux tube was made up of reconnected PSBL field lines. Between the flow bursts in the "ambient BBF" there was no reduction in plasma pressure and the anti(parallel) electron fluxes reduced. The motion of the "ambient BBF" seems to be different from that of the flow bursts, particularly in the 2004 case when there was a dominant $V_{\perp Y}$ throughout the BBF.

Previously, wakes had only been reported for the 2005 event (Walsh et al. 2009). In this study, wakes were identified behind each BBF and, in the case of the 2005 event, the expected return flow region around its sides. Where it was possible to use the curlometer to detect FACs, currents with a lower current density were detected in the wake regions than at the boundaries of the plasma bubbles.

While wakes were detected in all three cases it was only during the 2005 event, that the wake and the flow burst were observed simultaneously and the dimensions of the flow burst estimated. With this tetrahedron configuration, determination of FACs using the curlometer was not possible. Conversely, for the 2003 and 2004 events, the field-aligned current density could be determined through the curlometer, however details of the interaction between the flow bursts and the wake was not able to be determined, nor the dimensions of the flow bursts and BBFs. In order to fully understand BBFs and plasma bubbles then; and determine how and/or whether the magnitude of FACs are related to bubble size, density, velocity or other parameters, detailed measurements made simultaneously at multiple scales are required. The planned Scope mission should provide this capability.

Acknowledgements The authors wish to acknowledge the ESA Cluster Active Archive and the FGM, CIS and PEACE instrument teams for providing the data employed in this study. Some data analysis was done with QSAS. The authors were funded by UK STFC grant number PP/E/001173/1.

References

Angelopoulos V, Baumjohann W, Kennel CF, Coronti FV, Kivelson MG, Pellat R, Walker RJ, Luehr H, Paschmann G (1992) Bursty bulk flows in the inner central plasma sheet. J Geophys Res 97:4027

Balogh A, Carr CM, Acuna MH, Dunlop MW, Beek TJ, Brown P, Fornaçon KH, Georgescu E, Glassmeier KH, Harris J, Musmann G, Oddy T, Schwingenschuh K (2001) The Cluster Magnetic Field Investigation: overview of in-flight performance and initial results. Ann Geophys 19:1207

Birn J, Raeder J, Wang Y, Wolf R, Hesse M (2004) On the propagation of bubbles in the geomagnetic tail. Ann Geophys 22:1773

Chen CX, Wolf RA (1993) Interpretation of high-speed flows in the plasma sheet. J Geophys Res 98:21409

Dunlop MW, Southwood DJ, Glassmeier K, Neubauer FM (1988) Analysis of multipoint magnetometer data. Adv Space Res 8:273. doi:10.1016/0273-1177(88)90141-X

Forsyth C, Lester M, Cowley SWH, Dandouras I, Fazakerley AN, Fear RC, Frey HU, Grocott A, Kadokura A, Lucek E, Rème H, Milan SE, Watermann J (2008) Observed tail current systems associated with bursty bulk flows and auroral streamers during a period of multiple substorms. Ann Geophys 26:167

Forsyth C, Lester M, Fazakerley AN, Owen CJ, Walsh AP (2010) Planet Space Sci 59(7): 598–605

Johnstone AD, Alsop C, Burge S, Carter PJ, Coates AJ, Coker AJ, Fazakerley AN, Grande M, Gowen RA, Gurgiolo C, Hancock BK, Narheim B, Preece A, Sheather PH, Winningham JD, Woodliffe RD (1997) PEACE: A Plasma Electron and Current Experiment. Space Sci Rev 79:351

Nakamura R, Baumjohann W, Mouikis C, Kistler LM, Runov A, Volwerk M, Asano Y, Z. Vörös, Zhang TL, Klecker B, Rème H, Balogh A (2004) Spatial scale of high-speed flows in the plasma sheet observed by Cluster. Geophys Res Lett 31:9804. doi:10.1029/2004GL019558

Panov EV, Nakamura R, Baumjohann W, Angelopoulos V, Petrukovich AA, Retinò A, Volwerk M, Takada T, Glassmeier K, McFadden JP, Larson D (2010) Multiple overshoot and rebound of a bursty bulk flow. Geophys Res Lett 37:L08103. doi:10.1029/2009GL041971

Rème H et al (2001) First multispacecraft ion measurements in and near the Earth's magnetosphere with the identical Cluster ion spectrometry (CIS) experiment. Ann Geophys 19:1303

Robert P, Dunlop MW, Roux A, Chanteur G (1998) Accuracy of Current Density Determination. In: Pashmann G, Daly PW (eds) Analysis methods for multi-spacecraft data. International Space Science Institute, Bern, p 395

Sergeev VA, Angelopoulos V, Gosling JT, Cattell CA, Russell CT (1996) Detection of localized, plasma-depleted flux tubes or bubbles in the midtail plasma sheet. J Geophys Res 101:10817. doi:10.1029/96JA00460

Sitnov MI, Guzdar PN, Swisdak M (2005) On the formation of a plasma bubble. Geophys Res Lett 32:16103. doi:10.1029/2005GL023585

Sitnov MI, Swisdak M, Divin AV (2009) Dipolarization fronts as a signature of transient reconnection in the magnetotail. J Geophys Res 114(A13):4202. doi:10.1029/2008JA013980

Slavin JA, Lepping RP, Gjerloev J, Fairfield DH, Hesse M, Owen CJ, Moldwin MB, Nagai T, Ieda A, Mukai T (2003) Geotail observations of magnetic flux ropes in the plasma sheet. J Geophys Res 108:1015

Walsh AP, Fazakerley AN, Lahiff AD, Volwerk M, Grocott A, Dunlop M, Lui T, Kistler L, Lester M, Mouikis C, Pu Z, Shen C, Shi J, Taylor MG, Lucek E, Zhang TL, Dandouras I (2009) Cluster and Double Star Multipoint Observations of a Plasma Bubble. Ann Geophys 27:725

A Statistical Study of Pressure Changes in the Near-Earth Magnetotail Associated with Substorm Expansion Onsets

7

Y. Miyashita, S. Machida, and A. Ieda

Abstract

We have statistically studied substorm-associated evolution of the near-Earth magnetotail to understand the substorm triggering mechanism. In the present chapter we focus on changes in the total and plasma pressures. We find that energy release is more significant between the regions of the magnetic reconnection and the initial dipolarization, i.e., at $-12 > X > -18$ R_E than in the surrounding regions. Unlike previously reported results, the plasma pressure increases in association with the initial dipolarization at $X > -12$ R_E, the increase largely contributed by high-energy particles. This result suggests that the rarefaction wave scenario proposed in the current disruption model is questionable.

7.1 Introduction

The triggering mechanism of a substorm expansion onset is a major issue in magnetospheric research. Substorm models proposed so far include the near-Earth neutral line (NENL) model (e.g., Russell 1972, 1974; Hones 1976; Baker et al. 1996; Shiokawa et al. 1997, 1998), the current disruption (CD) model (e.g., Lui 1996), the magnetosphere-ionosphere coupling model (Kan et al. 1988; Rothwell et al. 1988; Kan 2007), the convection reduction model (Lyons 1995), the boundary layer dynamics model (Rostoker and Eastman 1987; Rostoker 1996), and the thermal catastrophe model (Smith et al. 1986; Goertz and Smith 1989).

Y. Miyashita (✉)
Solar-Terrestrial Environment Laboratory, Nagoya University, Furo-cho, Chikusa-ku, Nagoya, Aichi 464-8601, Japan
e-mail: miyasita@stelab.nagoya-u.ac.jp

Among these models, the NENL model and the CD model are thought to be the principal candidates. These models are different in the initial process, its location, and the propagation direction of the resultant flows or waves. In the NENL model, the magnetic reconnection first occurs in the midtail at $X \sim -20$ R_E, generating a tailward moving plasmoid and a fast earthward flow. The fast earthward flow propagates to the near-Earth tail at $X \sim -10$ R_E, causing the dipolarization or the current disruption. On the other hand, the CD model predicts that the current disruption first occurs in the near-Earth tail at $X \sim -10$ R_E, resulting in the dipolarization. This process is accompanied by a plasma pressure reduction, generating a rarefaction wave. It then propagates tailward and leads to plasma sheet thinning and weakening of the north-south magnetic field. As a result, the magnetic reconnection takes place in the midtail at a later time (Lui 1991). Recently, however, Machida et al. (2009) have proposed a new model called a "catapult (slingshot) current sheet relaxation model", in which the initial process occurs between

W. Liu, M. Fujimoto (eds.), *The Dynamic Magnetosphere*, IAGA Special Sopron Book Series 3,
DOI 10.1007/978-94-007-0501-2_7,

the regions of the magnetic reconnection and the initial dipolarization, leading to the two processes.

For clarifying the relative timing and the causal relationship of substorm-associated processes in the magnetotail, it is helpful to employ a timing analysis, such as superposed epoch analysis (e.g., Lui et al. 1998; Nagai et al. 1998; Machida et al. 1999, 2009; Miyashita et al. 2000, 2003, 2009). Miyashita et al. (2009) have revealed an overall picture of substorm-associated evolution of the near-Earth magnetotail: The magnetic reconnection occurs at $X \sim -16$ to $-20\ R_E$ at least 2 min before onset to create a plasmoid tailward of $X \sim -20\ R_E$. Almost simultaneously with the magnetic reconnection, or within a few min, the dipolarization begins at $X \sim -7$ to $-10\ R_E$.

Further detailed studies, however, are needed to understand the causal relationship between the magnetic reconnection and the current disruption as well as processes midway between the regions of the two processes, such as fast earthward flow and rarefaction wave. There are possibly various approaches to understanding the causal relationship, such as timing analysis of multispacecraft observations (e.g., Angelopoulos et al. 2008; Lui et al. 2008). In the present study, we focus on changes in the total and plasma pressures in the magnetotail in association with substorm onsets. The pressure is one of the key parameters for the substorm dynamics.

In the present chapter, after showing the main results of Miyashita et al. (2009), we show some of the statistical results of the plasma pressure and discuss the rarefaction wave scenario proposed in the CD model in connection with the triggering of the magnetic reconnection in the midtail. More details about the plasma pressure changes can be found in Miyashita et al. (2010).

7.2 Superposed Epoch Analysis

In this section, we show the results of superposed epoch analysis of the plasma flow, the north-south magnetic field, the total pressure (Miyashita et al. 2009), and the plasma (ion) pressure (Miyashita et al. 2010), which are fundamental to the understanding of the magnetotail dynamics. The variations that we show are on the X–Y plane, while Machida et al. (2009) showed those on the X–Z plane. Figure 7.1 shows a summary of the results of Miyashita et al. (2009).

We utilized a total of 3787 substorm events that were determined from the auroral breakup observed by Polar UVI (Liou et al. 2000) or IMAGE FUV (Frey et al. 2004; Frey and Mende 2007). The substorm expansion onset times ($t = 0$) were determined with an accuracy of less than or equal to 2 min, which was why we used 2 min averages for the superposed epoch analysis. During each of the selected events, any of the Geotail, Polar, and GOES spacecraft was located in the nightside sector: $-5 \geq X \geq -31\ R_E$ and $|Y| \leq 15\ R_E$ in GSM coordinates for Geotail, $-3.5 \geq X \geq -10\ R_E$, $|Y| \leq 9\ R_E$, and $|Z| \leq 5\ R_E$ for Polar, and $-3.5 \geq X \geq -6.6\ R_E$ and $|Y| \leq 6\ R_E$ for GOES. For the Geotail data, we used the LEP ion moments, the MGF magnetic field, and the

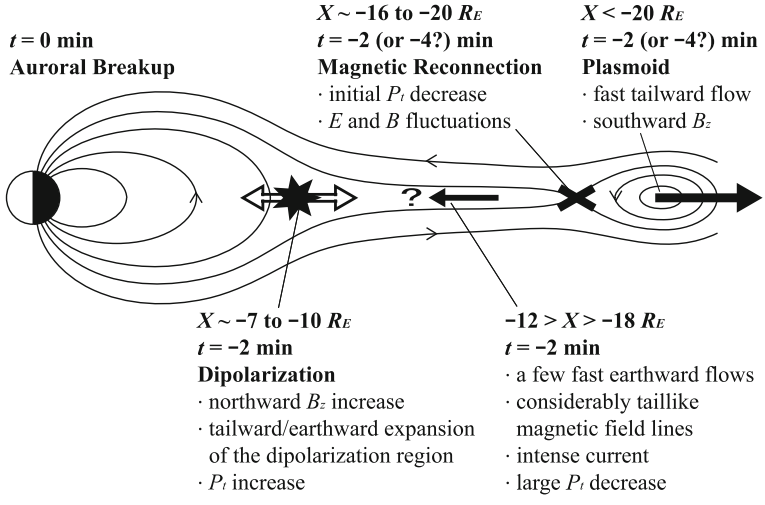

Fig. 7.1 Summary of the magnetotail evolution associated with substorm onsets. The figure is not exactly scaled (from Miyashita et al. 2009)

EPIC-STICS high-energy particle data. Note that the ion pressure was calculated by combining the LEP (a few tens of eV/q to ~40 keV/q) and EPIC-STICS (44–265 keV) data. The classification of the Geotail data into the plasma sheet (PS), the plasma sheet boundary layer (PSBL), and the lobe was based on the ion β (see Miyashita et al. 2000). We also used the Polar MFE and GOES magnetic field data for the near-Earth region. More details about the data set and the method were described in Miyashita et al. (2009).

Figure 7.2 shows the results of the X component of the plasma (ion) flow V_X in the PS and PSBL, the deviation of the north-south magnetic field ΔB_z in the PS, PSBL, and lobe, and the normalized deviation of the total pressure $\Delta Pt/\overline{P_t}$ in the PS, PSBL, and lobe (Miyashita et al. 2009). Here the baseline of the deviation ($\overline{B_z}$ and $\overline{P_t}$) is the average value over the interval from t = –11 to –7 min, calculated for each event. The total pressure is the sum of the ion and magnetic pressures.

Fast tailward flows begin to grow significantly in the premidnight sector at $X < -20\ R_E$ at onset ($t = 0$), associated with the formation and evolution of the plasmoid. They further develop continuously, with the region of fast tailward flow expanding in the Y direction due to the plasmoid expansion. In contrast, more fast earthward flows appear at $X < -12\ R_E$ after $t = -2$ min, but they are not distributed very widely even immediately after onset, probably due to the localization of the flows in the Y and Z directions. Some earthward flows slightly grow at $t = 2$ min at $(X, Y) \sim (-8, 0)\ R_E$, where there are very slow flows and even tailward flows (see Miyashita et al. 2000, 2003).

For the north-south magnetic field, at onset the negative ΔB_z substantially grows, that is, B_z decreases in the premidnight sector tailward of $X \sim -20\ R_E$. A detailed analysis shows that the development of the negative ΔB_z already begins at t = –2 or possibly –4 min at $X < -23\ R_E$. In this region the fast tailward flows are seen, so that the negative ΔB_z is associated with the plasmoid in the PS and the traveling compression region in the PSBL and the lobe. On the other hand, simultaneously with the plasmoid evolution, the positive ΔB_z begins to grow, that is, B_z substantially increases first at $X \sim$ –7 to –10 R_E and $Y \sim 4\ R_E$ at t = –2 min in association with the dipolarization. The dipolarization region then successively expands tailward, duskward, dawnward, and earthward. Another interesting feature of ΔB_z is that the relatively large negative ΔB_z appears in the premidnight sector at $X \sim$ –5 to –20 R_E and $Y \sim 2 - 12\ R_E$ before onset, implying that magnetic field lines become considerably taillike and the cross-tail current is significantly intensified there before onset.

For the total pressure, before and at t = –4 min, the positive $\Delta Pt/\overline{P_t}$ enhances, that is, the total pressure increases in the entire tail. At t = –2 min, however, the values of the positive $\Delta Pt/\overline{P_t}$ become small in the premidnight sector at $X \sim -16$ to –20 R_E and $Y \sim 0 - 5\ R_E$, followed by the appearance and growth of the negative $\Delta Pt/\overline{P_t}$. Namely, the total pressure decreases first in this region. This change relates to the magnetic reconnection. Subsequently the total pressure also decreases in the surrounding regions, except the dipolarization region at $X > -10\ R_E$, at or immediately after onset. In contrast, the total pressure generally increases, rather than decreases, in the near-Earth region at $X > -10\ R_E$ and $-5 < Y < 8\ R_E$ simultaneously with or a few min after the beginning of the dipolarization. Tailward of $X \sim -10\ R_E$, the total pressure decreases before the dipolarization region reaches there, but the total pressure continues to decrease or begins to increase when the dipolarization occurs.

The fast tailward flow and the significant growth of the negative ΔB_z due to the plasmoid, as well as the initial total pressure decrease, obtained from our statistical analysis suggest that the magnetic reconnection first occurs in the premidnight tail, on average, at $X \sim$ –16 to –20 R_E at least 2 min before onset. Almost simultaneously with the magnetic reconnection (with 2 min resolution), the dipolarization begins first at $X \sim$ –7 to –10 R_E 2 min before onset.

Furthermore, we examined the pressure changes in more detail. The left column of Fig. 7.3 shows the total pressure deviation ΔPt. The negative ΔPt begins to grow in the premidnight sector at $-10 > X > -20\ R_E$ at t = –4 or –2 min. In particular, this decrease in the absolute value of the total pressure is more significant at $X \sim$ –12 to –18 R_E, i.e., on the earthward side of the magnetic reconnection region than in the surrounding regions. This result suggests that energy release is more significant between the two regions of the magnetic reconnection and the initial dipolarization.

The right column of Fig. 7.3 shows the plasma (ion) pressure deviation ΔP_p in the PS. The plasma pressure increases, rather than decreases, in the initial dipolarization region at $X > -12\ R_E$ and $-2 < Y < 6\ R_E$

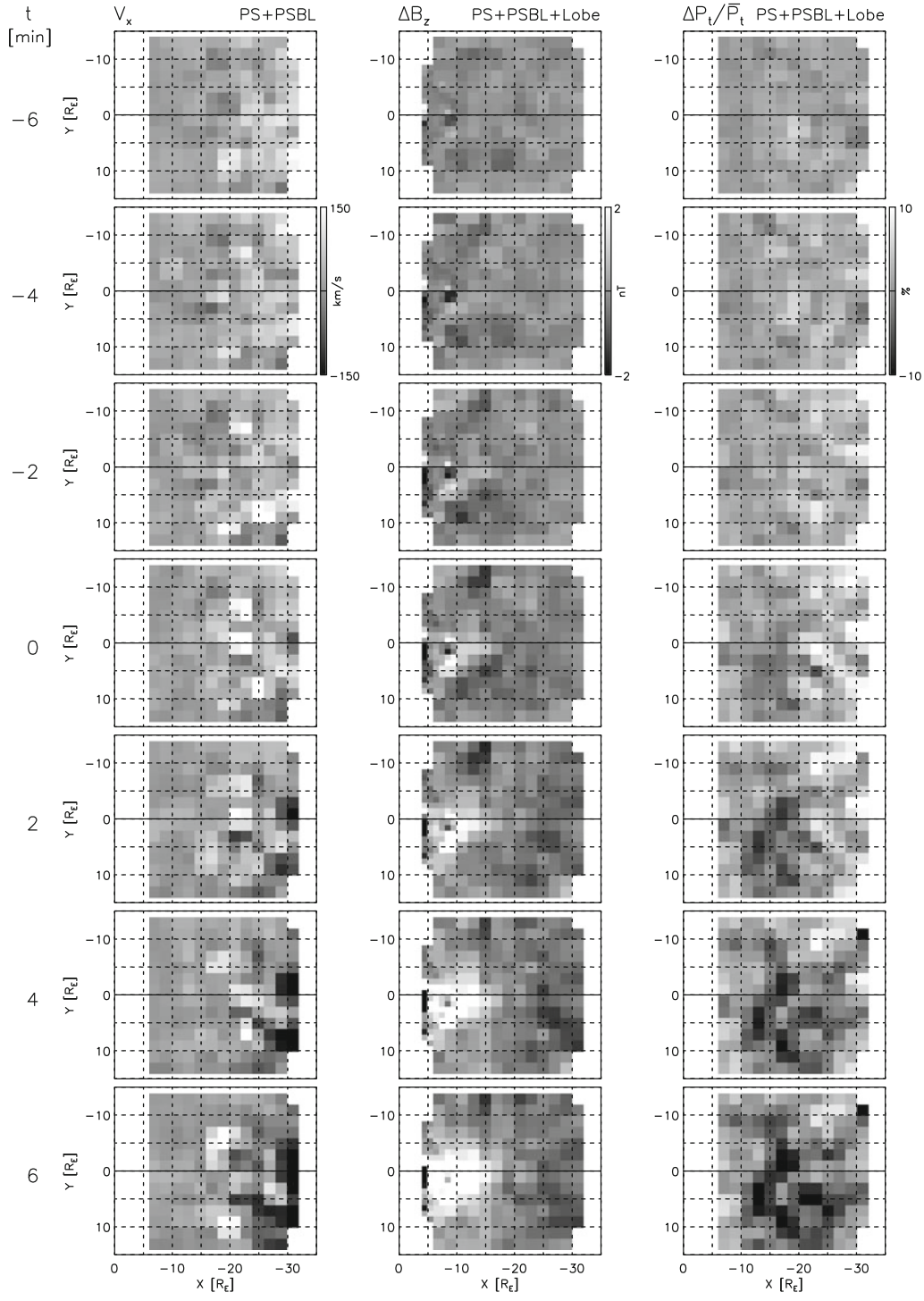

Fig. 7.2 Two-dimensional plots of (*left*) the *X* component of the plasma (ion) flow *Vx* on the GSM *X*–*Y* plane in the plasma sheet (PS) and plasma sheet boundary layer (PSBL), (*middle*) the deviation of the north-south magnetic field ΔB_z in the PS, PSBL, and lobe, and (*right*) the normalized total pressure deviation $\Delta Pt/\overline{P_t}$ in the PS, PSBL, and lobe from $t = -6$ to 6 min. The size of bins is 4 $R_E \times 4$ R_E, except for ΔB_z in the inner magnetospheric region, 2 $R_E \times 2$ R_E. The 4 $R_E \times 4$ R_E (2 $R_E \times 2$ R_E) bins are slid by 2 R_E (1 R_E) on the *X*–*Y* plane, so that only their central parts of 2 $R_E \times 2$ R_E (1 $R_E \times 1$ R_E) are shown in the figure not to overlap each other. The times shown are the centers of the averaging intervals. The original color version can be found in Miyashita et al. (2009)

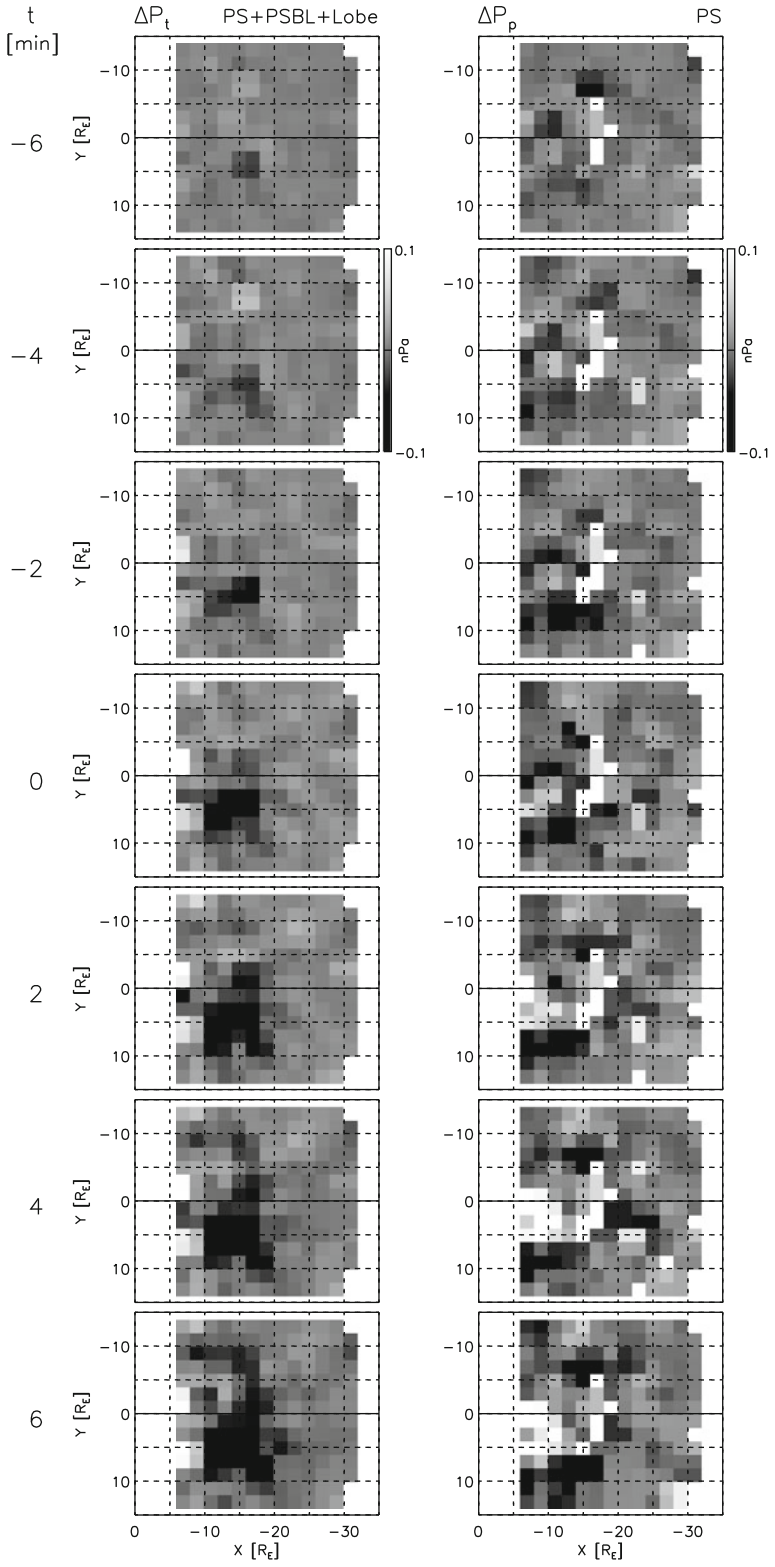

Fig. 7.3 Two-dimensional plots of the deviations of (*left*) the total pressure Δ *Pt* in the PS, PSBL, and lobe and (*right*) the plasma (ion) pressure Δ P_p in the PS in 4 R_E × 4 R_E bins from t = –6 to 6 min. The original color version can be found in Miyashita et al. (2009, 2010)

simultaneously with or just after the beginning of the dipolarization. Outside this region, particularly tailward and duskward of this region, the plasma pressure decreases just before onset, i.e., before the dipolarization region reaches there; when the dipolarization occurs at later times, the plasma pressure tends to increase.

We also examined the contribution of each of high-energy (EPIC-STICS) and low-energy (LEP) particles to the plasma pressure (figures are not shown). In the initial dipolarization region, the plasma pressures from both high- and low-energy particles generally increase. In particular, high-energy particles largely contribute to the plasma pressure increase in association with the dipolarization. Furthermore, the plasma pressure from high-energy particles increases just outside the initial dipolarization region, but it does not significantly change further away from this region. The plasma pressure from low-energy particles generally decreases outside the initial dipolarization region, particularly duskward and tailward of this region.

The plasma pressure increase in association with the dipolarization is consistent with recent THEMIS observations (Xing et al. 2010; Dubyagin et al. 2010). Kistler et al. (1992) also reported that the plasma pressure increases, associated with "energetic particle injection", although because of the lack of the magnetic field data, it was not clear whether or not the change that they reported related to the dipolarization. On the other hand, our result is obviously different from that of Lui et al. (1992) and Lyons et al. (2003), who reported that the plasma pressure in the plasma sheet decreased in association with the dipolarization.

7.3 Discussion

We have statistically studied substorm-associated evolution of the near-Earth magnetotail to understand the substorm triggering mechanism. In the present chapter we focused on changes in the total and plasma pressures. In this section we discuss the significant decrease in the total pressure between the regions of the magnetic reconnection and the initial dipolarization, and an implication of the plasma pressure increase in association with the initial dipolarization.

We found that the total pressure decrease is more significant between the regions of the magnetic reconnection and the initial dipolarization, suggesting that energy release is more significant there. This may be a key to the understanding of the causal relationship between the two processes and the substorm triggering mechanism. A possible explanation for the energy release is as follows: Magnetic energy in the lobe is released and converted to plasma kinetic and thermal energy in the plasma sheet. Part of the plasma energy is transported by fast earthward flows. Meanwhile, the region of the significant energy release is located near the earthward edge of a region of fast earthward flows, or probably the flow braking region. The low-frequency magnetic and electric field fluctuations are seen at $X \sim -14$ to -20 R_E around onset (see Miyashita et al. 2009). Hence the fast flow is coupled with the Alfvén wave or other kinds of waves to convert the plasma energy into the wave energy, leading to acceleration and heating of electrons (Angelopoulos et al. 2002; Zhou et al. 2009). In addition, some process other than the fast flow may be involved in the energy release, since the region of the total pressure decrease is wider than that of the fast earthward flow, as shown in the left columns of Figs. 7.2 and 7.3. In the near-Earth region the plasma pressure enhances in association with the initial dipolarization. Some portion of the energy for this near-Earth process may be transported from the region of the significant energy release, although a large portion can be transported by the Poynting flux from the lobe (Miyashita et al. 2001). It is an open question, however, whether the carrier is the plasma flow or some types of wave, i.e., how the energy is released, transported, and spent.

As mentioned in the introduction, Lui (1991) proposed that the tailward propagating rarefaction wave, generated by the plasma pressure reduction associated with the current disruption or the dipolarization in the near-Earth region, leads to the magnetic reconnection in the midtail. However, there seems to be no solid evidence to support the rarefaction wave scenario, as discussed below in terms of the plasma pressure decrease, the propagation direction of the fast earthward flow, and the plasma sheet behavior.

For discussion about the possibility, it is very important to clarify the duration of the rarefaction wave and the necessary growth time of an instability resulting in the magnetic reconnection. The thin plasma/current sheet and a very small B_z for some duration are required for efficient triggering of the magnetic reconnection. In simulations by Shinohara et al. (2007),

it takes ∼1 min for the magnetic reconnection to be triggered. If the rarefaction wave scenario is true, the magnetic reconnection should be caused instantaneously or within ∼1 min after the arrival of the rarefaction wave, considering that the propagation time of the rarefaction wave from the initial dipolarization region to the magnetic reconnection region is ∼1–2 min and that the two processes occur nearly simultaneously, as shown above. However, our statistical study with 2 min resolution data and our case studies with 1 min resolution data (not shown) demonstrated that the plasma pressure increases in association with the dipolarization, without a transient decrease. Recent THEMIS observations with 3 s resolution data (Xing et al. 2010; Dubyagin et al. 2010) have also shown the same result. Hence, even if the plasma pressure decrease occurs, it should be very transient, lasting for less than a few seconds, and the resultant rarefaction wave should also be very transient. Because of the finite Larmor radius effect, this small-scale structure may not be sustained long enough to propagate to the midtail and trigger the magnetic reconnection. Even if a very transient rarefaction wave can be sustained, it is questionable that the magnetic reconnection can be effectively triggered by the short-duration plasma sheet thinning and B_z decrease. Otherwise, it is debatable whether or not waves generated at different sites successively reach the midtail region, leading effectively to the magnetic reconnection within ∼1 min, even if the duration of each wave is very short.

Meanwhile, fast earthward flows at ∼400 km/s associated with the tailward propagating rarefaction wave should appear first on the earthward side and then on the tailward side. However, recent THEMIS observations (Runov et al. 2009; Takada et al. 2009) and a Geotail statistical study (Machida et al. 2009) showed that fast earthward flows appear in reverse order, i.e., first on the tailward side and then on the earthward side; the fast earthward flow propagates earthward from the tailward region, before the dipolarization region expands tailward (Machida et al. 2009; Takada et al. 2009). Furthermore, the plasma pressure decrease begins away from the initial dipolarization region, i.e., in the midtail region before the expected arrival of the rarefaction wave, as shown by our statistical studies. In addition, the plasma sheet expands in the Z direction, rather than thins, at $R < \sim 15$ R_E at or immediately after onset (Hones et al. 1984; Baumjohann et al. 1992). Thus these observations of the plasma pressure, flow, and plasma sheet behavior are not consistent with the rarefaction wave scenario.

In conclusion, a number of substorm models have been proposed for the triggering mechanism of an expansion onset, as mentioned in the introduction. Each of them can explain part of the observed substorm processes, but none of them can perfectly explain all the processes. For fully understanding the substorm triggering mechanism, it is necessary in future studies to clarify what each model, not exclusively the NENL and CD models, can explain and what it cannot explain, as well as why it can or cannot, and establish an integrated model or an entirely new model which can truly explain all the observed processes.

Acknowledgments The Geotail LEP ion moment data were provided by T. Mukai and Y. Saito. The Geotail MGF magnetic field data were provided by S. Kokubun and T. Nagai. The Geotail EPIC high-energy particle data were provided by R. W. McEntire, S. P. Christon, and A. T. Y. Lui. The Polar MFE and GOES magnetic field data were provided by C. T. Russell and H. J. Singer, respectively, through the Coordinated Data Analysis Web (CDAWeb) at NASA. The auroral breakup lists used in the present study were provided by K. Liou and H. U. Frey. We thank D. Nagata, Y. Kamide, M. Fujimoto, M. Nosé, K. Liou, C. T. Russell, S. P. Christon, T. Mukai, M. H. Saito, and I. Shinohara for their useful comments.

References

Angelopoulos V, Chapman JA, Mozer FS et al (2002) Plasma sheet electromagnetic power generation and its dissipation along auroral field lines. J Geophys Res 107:1181. doi:10.1029/2001JA900136

Angelopoulos V, McFadden JP, Larson D et al (2008) Tail reconnection triggering substorm onset. Science 321:931–935

Baker DN, Pulkkinen TI, Angelopoulos V et al (1996) Neutral line model of substorms: past results and present view. J Geophys Res 101:12,975–13,010

Baumjohann W, Paschmann G, Nagai T (1992) Thinning and expansion of the substorm plasma sheet. J Geophys Res 97:17173–17175

Dubyagin S, Sergeev V, Apatenkov S et al (2010) Pressure and entropy changes in the flow-braking region during magnetic field dipolarization. J Geophys Res 115:A10225. doi:10.1029/2010JA015625

Frey HU, Mende SB (2007) Substorm onsets as observed by IMAGE-FUV. In: Syrjäsuo M, Donovan E (eds) Proceedings of international conference on substorms-8. University of Calgary, AB, pp 71–75

Frey HU, Mende SB, Angelopoulos V et al (2004) Substorm onset observations by IMAGE-FUV. J Geophys Res 109:A10304. doi:10.1029/2004JA010607

Goertz CK, Smith RA (1989) The thermal catastrophe model of substorms. J Geophys Res 94:6581–6596

Hones EW Jr (1976) The magnetotail: its generation and dissipation. In: Williams DJ (ed) Physics of solar planetary environments. AGU, Washington, DC, pp 558–571

Hones EW Jr, Pytte T, West HI Jr (1984) Associations of geomagnetic activity with plasma sheet thinning and expansion: a statistical study. J Geophys Res 89:5471–5478

Kan JR (2007) On the formation of near-Earth X-line at substorm expansion onset. J Geophys Res 112:A01207. doi:10.1029/2006JA012011

Kan JR, Zhu L, Akasofu SI (1988) A theory of substorms: onset and subsidence. J Geophys Res 93:5624–5640

Kistler LM, Möbius E, Baumjohann W et al (1992) Pressure changes in the plasma sheet during substorm injections. J Geophys Res 97:2973–2983

Liou K, Meng CI, Newell PT et al (2000) Evaluation of low-latitude Pi2 pulsations as indicators of substorm onset using Polar ultraviolet imagery. J Geophys Res 105:2495–2505

Lui ATY (1991) A synthesis of magnetospheric substorm models. J Geophys Res 96:1849–1856

Lui ATY (1996) Current disruption in the Earth's magnetosphere: observations and models. J Geophys Res 101:13,067–13,088

Lui ATY, Lopez RE, Anderson BJ et al (1992) Current disruptions in the near-Earth neutral sheet region. J Geophys Res 97:1461–1480

Lui ATY, Liou K, Newell PT et al (1998) Plasma and magnetic flux transport associated with auroral breakups. Geophys Res Lett 25: 4059–4062

Lui ATY, Angelopoulos V, LeContel O et al (2008) Determination of the substorm initiation region from a major conjunction interval of THEMIS satellites. J Geophys Res 113:A00C04. doi:10.1029/2008JA013424

Lyons LR (1995) A new theory for magnetospheric substorms. J Geophys Res 100:19,069–19,081

Lyons LR, Wang CP, Nagai T et al (2003) Substorm inner plasma sheet particle reduction. J Geophys Res 108:1426. doi:10.1029/2003JA010177

Machida S, Miyashita Y, Ieda A et al (1999) GEOTAIL observations of flow velocity and north-south magnetic field variations in the near and mid-distant tail associated with substorm onsets. Geophys Res Lett 26:635–638

Machida S, Miyashita Y, Ieda A et al (2009) Statistical visualization of the Earth's magnetotail based on Geotail data and the implied substorm model. Ann Geophys 27: 1035–1046

Miyashita Y, Machida S, Mukai T et al (2000) A statistical study of variations in the near and middistant magnetotail associated with substorm onsets: GEOTAIL observations. J Geophys Res 105:15913–15930

Miyashita Y, Machida S, Mukai T et al (2001) Mass and energy transport in the near and middistant magnetotail around substorm onsets: Geotail observations. J Geophys Res 106:6259–6274

Miyashita Y, Machida S, Liou K et al (2003) Evolution of the magnetotail associated with substorm auroral breakups. J Geophys Res 108:1353. doi:10.1029/2003JA009939

Miyashita Y, Machida S, Kamide Y et al (2009) A state-of-the-art picture of substorm-associated evolution of the near-Earth magnetotail obtained from superposed epoch analysis. J Geophys Res 114:A01211. doi:10.1029/2008JA013225

Miyashita Y, Machida S, Ieda A et al (2010) Pressure changes associated with substorm dipolarization in the near-Earth plasma sheet. J Geophys Res 115:A12239. doi:10.1029/2010JA015608

Nagai T, Fujimoto M, Saito Y et al (1998) Structure and dynamics of magnetic reconnection for substorm onsets with Geotail observations. J Geophys Res 103:4419–4440

Rostoker G (1996) Phenomenology and physics of magnetospheric substorms. J Geophys Res 101:12,955–12,973

Rostoker G, Eastman T (1987) A boundary layer model for magnetospheric substorms. J Geophys Res 92:12,187–12,201

Rothwell PL, Block LP, Silevitch MB et al (1988) A new model for substorm onsets: the pre-breakup and triggering regimes. Geophys Res Lett 15:1279–1282

Runov A, Angelopoulos V, Sitnov MI et al (2009) THEMIS observations of an earthward-propagating dipolarization front. Geophys Res Lett 36:L14106. doi:10.1029/2009GL038980

Russell CT (1972) The configuration of the magnetosphere. In: Dyer ER (ed) Critical problems of magnetospheric physics. IUCSTP Secretariat, Washington, DC, pp 1–16

Russell CT (1974) The solar wind and magnetospheric dynamics. In: Page DE (ed) Correlated interplanetary and magnetospheric observations. D. Reidel Publishing Company, Dordrecht, Holland, pp 3–47

Shinohara I, Tanaka KG, Fujimoto M (2007) Quick triggering of magnetic reconnection in magnetotail. Earth Moon Planet 100:225–232

Shiokawa K, Baumjohann W, Haerendel G (1997) Braking of high-speed flows in the near-Earth tail. Geophys Res Lett 24:1179–1182

Shiokawa K, Baumjohann W, Haerendel G et al (1998) High-speed ion flow, substorm current wedge, and multiple Pi 2 pulsations. J Geophys Res 103:4491–4507

Smith RA, Goertz CK, Grossmann W (1986) Thermal catastrophe in the plasma sheet boundary layer. Geophys Res Lett 13:1380–1383

Takada T, Miyashita Y, Hasegawa H et al (2009) Tailward propagation of dipolarization following earthward fast flows. Paper presented at LASP THEMIS 2009 Workshop, Laboratory for Atmospheric and Space Physics, University of Colorado, Boulder, CO

Xing X, Lyons LR, Angelopoulos V et al (2010) Plasma sheet pressure evolution related to substorms. J Geophys Res 115:A01212. doi:10.1029/2009JA014315

Zhou M, Ashour-Abdalla M, Deng X et al (2009) THEMIS observation of multiple dipolarization fronts and associated wave characteristics in the near-Earth magnetotail. Geophys Res Lett 36:L20107. doi:10.1029/2009GL040663

8 Categorization of the Time Sequence of Events Leading to Substorm Onset Based on THEMIS All-Sky Imager Observations

Y. Nishimura, L.R. Lyons, S. Zou, V. Angelopoulos, and S.B. Mende

Abstract

The sequence of events leading to substorm auroral onset has been a long-standing issue in substorm research. Based on statistical studies using THEMIS all-sky imager data, we have recently reported evidence that most substorm onset events are preceded by a pre-onset auroral form which is a distinct north-south arc originating from an poleward boundary intensification (PBI) and reaches the auroral onset region just before onset. This onset sequence was found to be a repetitive process; it is detected in 84% of 249 events between November 2007 and April 2008. A high occurrence of PBIs (84%) emphasizes an abrupt flux transport across the open-closed field line as initiation of the onset sequence. Here we present a variation of the onset sequence we have previously reported and two less frequently observed types of onset time sequence: poleward boundary contact and Harang aurora deformation. While poleward boundary contact events also start with PBIs, the auroral oval width becomes much narrower (∼2° MLAT) prior to onset, indicating that the plasma sheet is thin and the nightside magnetic separatrix is located closer to the near-Earth onset region. Harang auroral deformation events are not associated with an observed PBI, but the equatorward portion of a pre-existing Harang aurora bends equatorward, which indicates a rapid convection change leading to onset. All of those three categories of events suggest that new plasma intrusion toward onset location changes the pressure profile in the near-Earth region and leads to onset instability.

8.1 Introduction

Determination of the sequence of events that lead to substorm onset has been a critical problem and the subject of much debate since the discovery of the substorm more than 40 years ago. Substorm onset can be identified by its ionospheric manifestation, an auroral onset, which starts along an arc near the equatorward boundary of the auroral oval and likely maps along magnetic field lines toward the near-Earth portion of the electron plasma sheet (Samson et al. 1992; Zou et al. 2009a, b).

Y. Nishimura (✉)
Department of Atmospheric and Ocean Sciences, University of California, Los Angeles, CA 90095-1565, USA;
Solar-Terrestrial Environment Laboratory, Nagoya University, Furocho, Chikusa, Nagoya 464-8601, Japan
e-mail: toshi@atmos.ucla.edu

W. Liu, M. Fujimoto (eds.), *The Dynamic Magnetosphere*, IAGA Special Sopron Book Series 3,
DOI 10.1007/978-94-007-0501-2_8,

The main debate has been whether substorm onset is initiated by magnetic reconnection in the mid-tail plasma sheet (~20–30 R_E, downtail from the Earth) or by an instability along the near-Earth plasma sheet field lines (~10 R_E downtail) (Angelopoulos 2008).

However, a potential resolution to this long-term problem was recently given by Nishimura et al. (2010, hereafter referred to as Paper 1). They examined observations from the THEMIS all-sky imager (ASI) array, which provides unprecedented high spatial and temporal resolution of auroral observations together with broad latitudinal and longitudinal coverage. Their analysis showed a distinct and repeatable sequence of events leading to onset which has similarities but also important differences from each of the above ideas for substorm onset. In the present chapter, we separate the pre-onset time sequence into three classifications. The most common of these was shown and described in Paper 1; this type of sequence, including an occasionally seen variation of this type, and two others less common types are discussed here.

Recent THEMIS spacecraft observations during radially aligned spacecraft configurations in the magnetotail have given evidence that tail reconnection occurs prior to substorm onset (Angelopoulos et al. 2008). Mid-tail reconnection is expected to lead to onset by driving longitudinally localized flows from the reconnection region toward the near-Earth onset region (e.g., Birn et al. 1999). A statistical study using Geotail spacecraft observations shows evidence for enhancements of the plasma flow in the plasma sheet soon before auroral onset (Miyashita et al. 2009), though onsets in this study where determined from global auroral images from space, which cannot reliably detect the initial brightening of a thin breakup auroral arc. On the other hand, localized plasma sheet flows are known to cause auroral activity. Specifically, poleward boundary intensifications (PBIs) have been related to enhanced equatorward flows that carry plasma across the nightside separatrix (de la Beaujardiere et al. 1994) into the plasma sheet (Lyons et al. 1999). Some PBIs develop into equatorward moving auroral arcs roughly north-south (NS) orientated, which have been related to channels of enhanced earthward flows within the plasma sheet (Rostoker et al. 1987; Sergeev et al. 1999, 2000; Nakamura et al. 2001; Zesta et al. 2002; Henderson et al. 2002). Thus, if mid-tail reconnection were able to lead to onset, the flows coming from the reconnection location to the near-Earth onset should lead to north-south (NS) aurora moving equatorward toward onset latitudes. Elphinstone et al. (1995) suggested that NS arcs may precede some substorm onsets and recently Kepko et al. (2009) noted an equatorial moving diffuse aurora feature prior to onset for one event, suggesting it might be related to mid-tail reconnection. However, neither of these features has been verified as a common pre-cursor to onset. This lent support for a near-Earth instability process leading to onset, in order to explain auroral onset occurring near the equatorward boundary of the auroral oval (Samson et al. 1992; Donovan et al. 2008).

The pre-onset auroral sequence described in Paper 1 is initiated by a PBI, which is followed by an NS arc moving equatorward towards the onset latitude. Because of the linkage of fast magnetotail flows to PBIs and to NS auroras, this sequence gives strong support to an idea that onset is preceded by enhanced earthward flows of plasma from the distant magnetotail to the near-Earth region. That the sequence is initiated by PBIs indicates that the enhanced flow enters the plasma sheet from the open field line region in association with enhanced reconnection near the pre-existing open-closed field line boundary rather than being from a mid-tail reconnection region. Since such earthward flow enhancements have been linked to under-populated flux tubes (Wolf et al. 2009), Paper 1 suggested that the arrival of new flux tubes with reduced entropy from the Earth's magnetotail to the near-Earth magnetosphere leads to the expansion phase of substorms via a near-Earth instability.

Also important fact is that the substorm onset location has been linked to the plasma convection pattern. Lyons et al. (2010) used Sondrestrom incoherent scatter radar and showed that plasma flows near the poleward boundary of the auroral oval are enhanced several minutes prior to substorm onset, and SuperDARN (Miyashita et al. 2008) and Poker Flat incoherent scatter radar observations (Lyons et al. 2010) have detected a plasma flow enhancement near the onset latitude a few minutes preceding onset. These ionospheric flow responses are consistent with inferences given in Paper 1 that newly-injected plasma across the open-closed boundary is transported toward the near-Earth region and leads to substorm onset.

The following case studies illustrate three different types of the pre-onset aurora sequence: PBI and NS arc

related (described in Paper 1), and the less common poleward boundary contact and Harang aurora deformation events. We show statistics indicating that most of the events are associated with PBIs followed by westward-moving auroral forms turning from NS arcs. We suggest that enhanced plasma flows injected into the onset location leads to substorm onset, and that the convection pattern developed during the growth phase governs motion of the enhanced flows that lead to onset.

8.2 Case Study

In this section, we present three examples illustrating the sequence of events in the ASI that we have repeatedly found to lead to onset. Here substorm onset refers to the initiation of substantial intensification of an auroral arc near the equatorward boundary followed by a poleward expansion lasting more than 3 min (Akasofu 1964; Angelopoulos et al. 2008) together with enhancements of the westward electrojet identified by ground magnetometers. Arc intensification near the equatorward boundary lasting less than 3 min is classified as a pseudo-breakup.

8.2.1 15 February 2008 Auroral Breakup

Figure 8.1 presents a sequence of selected images from four ASIs during a substorm auroral onset that occurred at 6:13:39 UT on 15 February 2008 near the Churchill meridian (See movie S1 for the entire image sequence). A faint, pre-existing growth phase arc initially extended azimuthally at ~67° magnetic latitude (MLAT) (Fig. 8.1a). The poleward boundary of the auroral oval was located at ~74° MLAT.

After multiple PBIs, a PBI occurred at 06:09:24 UT, ~5 min prior to auroral onset, identified as a bright auroral form near the center of the RANK imager field-of-view (FOV) in Fig. 8.1a. The auroral form expanded both eastward and westward, and then an NS arc extending from the eastern edge of the PBI drifted equatorward and westward, forming an arc rotating clockwise (Fig. 8.1b). The NS arc contacted the growth phase arc in the FOV of the GILL imager. Finally, auroral onset started on the pre-existing growth phase arc to the west of the NS arc at 06:13:39 UT,

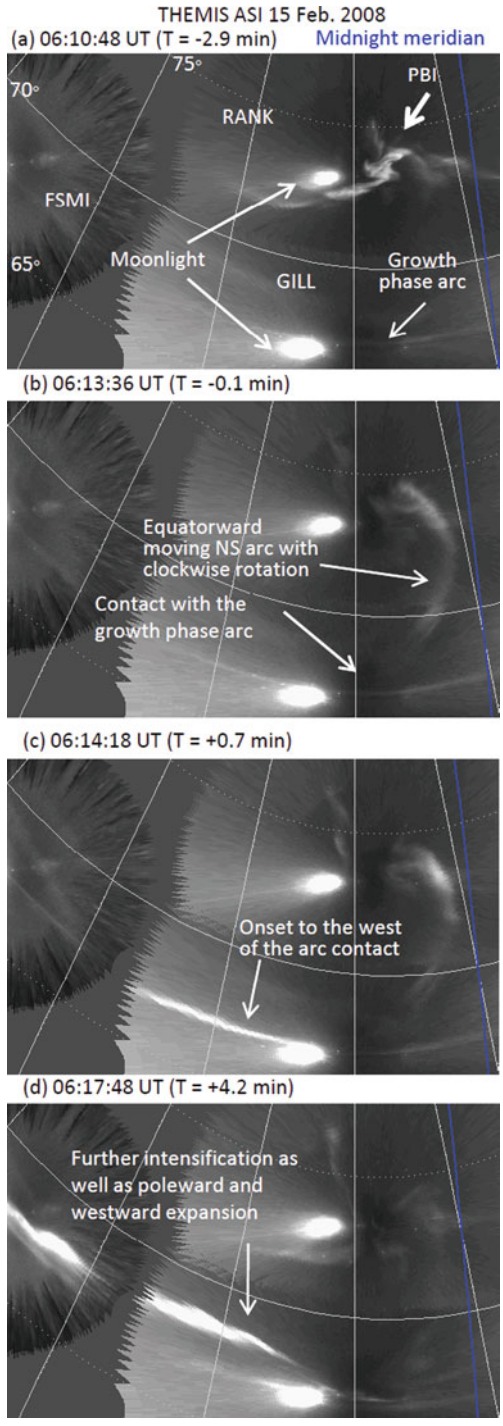

Fig. 8.1 THEMIS ASI data during an auroral onset on 15 February 2008. ASIs used are RANK, FSMI, and GILL. White lines are isocontours of magnetic latitude (every 10° in *solid lines*) and longitude (every 15°). The *blue line* in each panel is the magnetic midnight meridian. The onset occurred at 06:13:39 UT. The entire sequence is shown in movie S1

immediately after the NS aurora contacted the growth phase arc. The auroral onset and small poleward and westward expansion can be seen clearly in Fig. 8.1d (images taken 4.2 min after onset).

The time evolution of the pre-onset auroral form can also be identified in the keogram shown in Fig. 8.5a–d. The onset marked by the vertical line is characterized by substantial auroral intensification followed by a poleward expansion observed within the GILL imager FOV (Fig. 8.5c) and an enhancement of the westward electrojet (Fig. 8.5d). Multiple PBIs occurred (Fig. 8.5a) and the NS arc marked by the arrows moved equatorward and was associated with the brightest PBI. The onset followed the contact of the NS arc with the growth-phase arc.

The above time sequence clearly demonstrates the connection between auroral onset and the pre-onset aurora starting at the poleward boundary. Based on the association of PBIs and NS arcs with flow channels in the magnetotail, the temporal evolution of the pre-onset auroral form can be regarded as motion of magnetospheric plasma. First, new plasma, presumably with lower entropy than the surrounding plasma (Wolf et al. 2009), is supplied across the open-closed field line boundary. This plasma is then transported earthward along an azimuthally narrow flow channel, with upward field-aligned currents and the NS aurora measured by the ASIs along its westward edge. While interchange motion is presumably responsible for the flow channel that brings the low-entropy plasma earthward, a separate instability, which could also be an interchange mode, is triggered near the inner edge of the electron plasma sheet by the intrusion of the new plasma. Auroral brightening occurs within the ionospheric footprint of this instability, followed by either a pseudo-breakup or full onset.

We emphasize that the pre-onset auroral form did not move equatorward along the onset magnetic meridian, but instead approached the onset location from the east. The NS arc reached the growth phase arc ∼1 h in magnetic local time (MLT) to the east of the onset location and subsequently approached the onset location along a pre-existing growth phase arc. Together with the clockwise motion of the NS-oriented arc, the two-dimensional evolution of the onset time sequence seen in the pre-midnight sector is similar to the Harang flow shear in duskside ionospheric convection. This suggests that motion of the pre-onset (substorm precursor) auroral form was organized by the two-cell ionospheric convection developed during the growth phase. As in many of our events, an NS arc formed in the dusk convection cell at the poleward boundary of the auroral oval and then moved equatorward and eastward around the poleward portion of the Harang aurora. It then turned westward and continued moving around the equatorward portion of the flow shear within the dusk convection cell leading to onset in the premidnight sector.

8.2.2 4 February 2008 Auroral Breakup

Figure 8.2 shows ASI data from four imagers located in the central region of Northern America during an auroral onset on 4 February 2008, and illustrate a relative uncommon type of event where an unusually narrow auroral oval develops near the onset longitude. The full sequence is shown in movie S2. As seen in Fig. 8.2a prior to the onset, the auroral oval was narrow in latitude near the magnetic midnight meridian with the poleward and equatorward boundaries at ∼71° and ∼68° MLAT, respectively. As described below, the oval width (∼3°) was much narrower than that of the quiet time found ∼2 h before during the NOAA-18 observation. A PBI was detected at ∼72° MLAT in the FSMI imager 2.6 min prior to the auroral onset (seen clearly in Fig. 8.2b). The onset occurred at 08:37:25 UT soon after the PBI expanded equatorward and contacted the growth phase arc (Fig. 8.2c). The oval width decreased down to ∼2° at onset. The aurora then expanded poleward with clockwise rotation (Fig. 8.2d), indicating existence of the Harang flow shear around the onset arc.

The narrow auroral oval feature detected in ASIs is supported by a simultaneous observation of precipitating electrons by the NOAA-18 spacecraft. Figure 8.3a, b show a comparison of the approximately latitudinal distribution of the precipitating electron energy flux ∼2 h (moderately disturbed) and ∼10 min (growth phase) before onset, respectively. The precipitating region during the growth phase is much narrower than that detected ∼2 h before. When using 0.1 mW/m^2 as a reference, the poleward boundary moved equatorward from 77.4° to 73.4° MLAT and the equatorward boundary shifted poleward from 63.6° to 65.8° MLAT. The latitudinal range in Fig. 8.3b corresponds quite well to the poleward and equatorward boundaries (∼74° and 67° MLAT) seen in the auroral

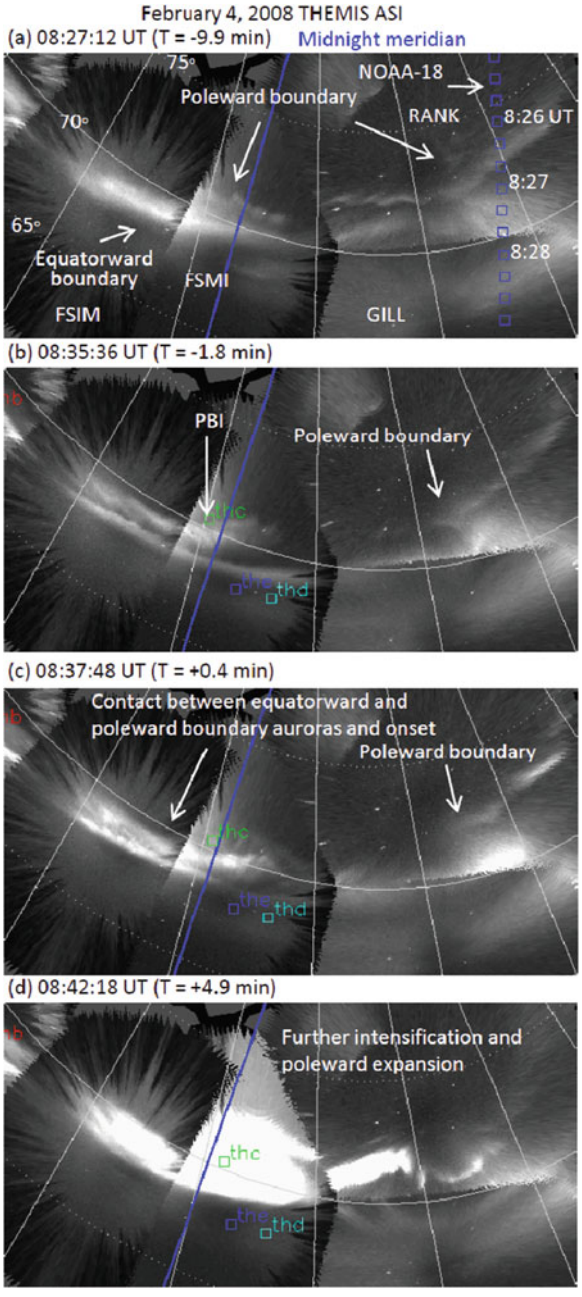

Fig. 8.2 THEMIS ASI data during an auroral onset on 4 February 2008. The format is same as Fig. 8.1. ASIs used are FSIM, FSMI, GILL and RANK. The onset occurred at 08:37:25 UT. The whole sequence is shown in movie S2

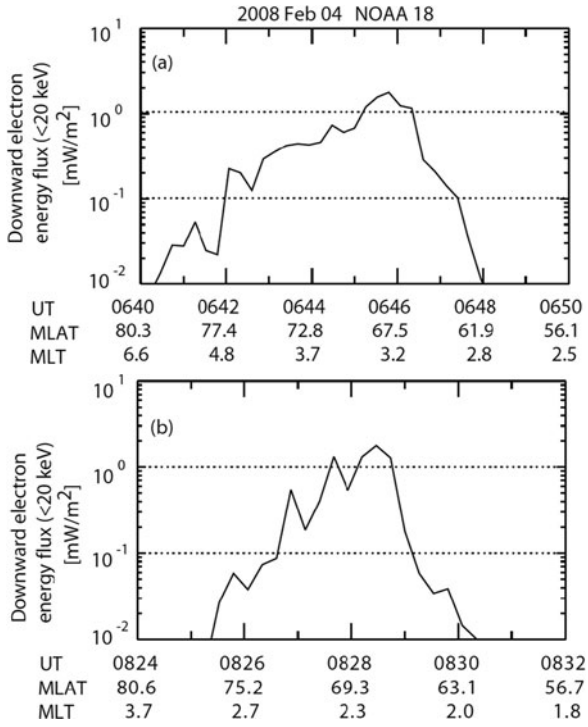

Fig. 8.3 NOAA-18 observations of the downward energy flux of electrons with energies below 20 keV. Data shown in panel (**b**) were obtained during the growth phase of the substorm shown in Fig. 8.2, while data in panel (**a**) were taken during the previous pass

image along the footprint of the spacecraft in Fig. 8.2a. This agreement leads us to suggest that, based on the auroral observations, the plasma sheet width became narrow near the onset longitude during the growth phase and that the poleward boundary aurora contacted the equatorward boundary aurora just prior to onset.

The time evolution of the pre-onset auroral form can also be identified in the keograms shown in Fig. 8.5e–f. Onset (second vertical line) is marked by substantial auroral intensification and poleward expansion (Fig. 8.5e) and enhancement of the westward electrojet identified as further changes in all of the magnetic field components detected in YKC located near the PBI (Fig. 8.5f). Variations in the D and H components starting earlier than the auroral breakup are possibly due to the current associated with PBIs, which occurred at latitudes overlapping those of the westward electrojet because of the latitudinally narrow oval extending from ~67° to ~68.8° MLAT as seen in Fig. 8.5e just prior to onset. A PBI started at ~8:35 UT and extended equatorward while the poleward boundary stayed at ~68.5° MLAT. The onset started just after the PBI reached the equatorward boundary of the auroral oval.

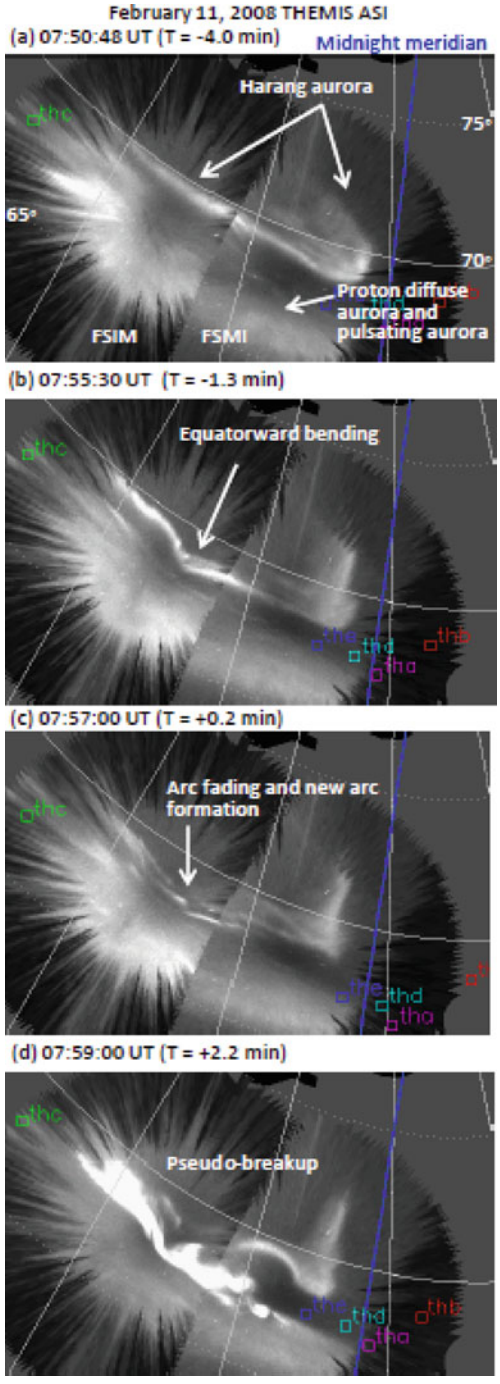

Fig. 8.4 THEMIS ASI data for an auroral onset on 11 February 2008 auroral onset. The format is same as Fig. 8.1. ASIs used are FSIM and FSMI. Onset occurred at 07:56:48 UT. The entire sequence is shown in movie S3

8.2.3 11 February 2008 Pseudo-breakup

The three events discussed above are associated with PBIs and enhanced auroral brightness moving toward the onset locations. A small number of events, however, do not have such precursor auroral forms but instead show a sudden change in auroral motion near the onset location just before onset. Such an example is shown in Fig. 8.4. The entire sequence is presented in movie S3. As clearly seen in the movie and Fig. 8.4a, the auroral arc in the premidnight sector prior to the onset, marked as Harang aurora, rotated clockwise with southeastward and westward motion in the poleward and equatorward halves of the auroral form. Similar to the clockwise-rotating arc seen in Fig. 8.1, this arc motion also presumably follows the Harang flow shear. There is evidence of fast equatorward flows in SuperDARN radar observations near the eastern boundary of the poleward portion of the Harang aurora (not shown), indicating the existence of a flow channel supplying new plasma toward onset location.

The pre-onset feature in this event is characterized as equatorward bending of the equatorward portion of the Harang aurora, as seen in Fig. 8.4b. The arc then started to fade and a new arc appeared just equatorward (Fig. 8.4c). The pre-existing Harang arc merged into the new arc, and the new arc developed as a pseudo-breakup, which did not show a remarkable poleward expansion as seen in Fig. 8.4d. The sequence suggests that an abrupt change in the plasma convection pattern and the current system initiate onset instability; a direct connection to flows from the polar cap boundary is not evident from the auroral observations.

The time sequence described above can also be seen in the keogram in Fig. 8.5g. The equatorward portion of the Harang aurora located at ~68°69° MLAT started to fade when the breakup arc appeared just equatorward. It expanded poleward only for a minute, and the westward electrojet (see Fig. 8.5h) also stopped increasing in ~1.5 min.

8.3 Statistical Study

Nishimura et al. (2010) performed a statistical study of the occurrence probability of the pre-onset auroral forms using 249 auroral onset events occurred within FOVs of THEMIS ASIs from November 2007 to April 2008. They classified events into the four

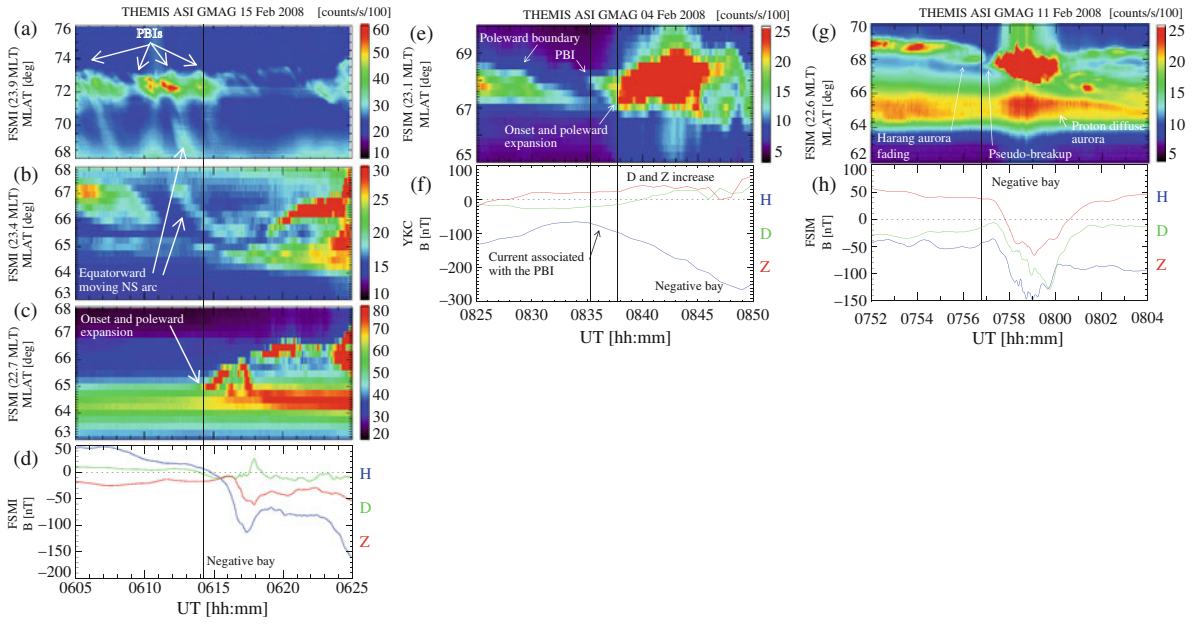

Fig. 8.5 Keograms and magnetograms of (**a**–**d**) 15 February 2008, (**e**–**f**) 4 February 2008, and (**g**–**h**) 11 February, 2008 onsets corresponding to ASI data shown in Figs. 8.1, 8.2 and 8.4. MLTs at the central times of each keogram are shown in the labels

categories and showed that the majority (84.1%) of substorm onset events fall into the sequence associated with NS or east-west (EW) arcs moving toward onset location as precursors as represented in Fig. 8.1. As shown below, pre-onset auroral forms in this category typically originated from auroral activity at or near the poleward boundary of the auroral oval. An NS arc extends from the poleward boundary and reaches the onset location directly or after turning into an EW arc. The second category, auroral stream pattern change events, contains most of the remaining events (10.7%). Sudden changes in auroral motion patterns as described in Section 8.2.3, possibly related to changes in magnetospheric convection prior to onset, can thus also be a precursor of auroral onset. Category 3 events, for which no pre-onset auroral activity was detected (4.8%), include many in which bright moonlight or partly cloudy skies might have obscured faint auroral forms. Thus, it can be concluded that substorm auroral onset in the absence of a precursor is rare, and most auroral substorms are associated with pre-onset auroral forms moving toward the onset location.

Figure 8.6 presents detection probabilities of the different types of pre-onset auroral forms in category 1 (209 events). The existence of NS or EW arcs or the poleward boundary contacting the onset location was determined for all events. Here, NS arcs occasionally

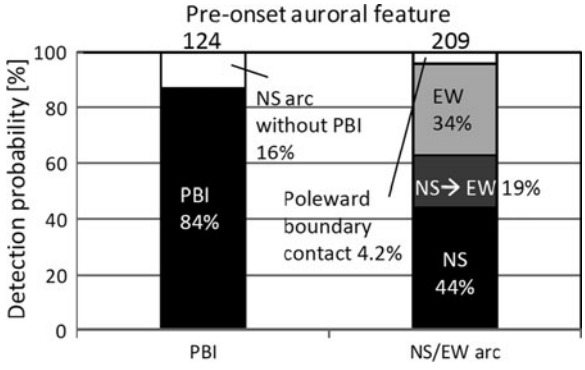

Fig. 8.6 Occurrence rates of pre-onset phenomena: (**a**) pre-onset auroral forms related to those contacting with onset locations just prior to onset, and (**b**) pre-onset phenomena related to region 2 FACs. Grey areas correspond where EW arcs turned from NS arcs contact onset locations. Total number of events and number of events matching each condition are shown on the top of each area

turn into EW arcs after contacting growth phase arcs. PBI occurrence was obtained for all events where the FOVs of imagers covered at least 2 h of MLT of the poleward boundary centered on the MLT of the NS arcs. For 84% of such events, a PBI was seen connected to the NS arcs leading to onset. Thus, enhanced flows that brought newly-supplied plasma across the open-closed boundary were a frequent precursor to

onset. PBIs were followed by NS arcs extending equatorward, and the NS arcs were observed to directly reach the onset location for about half of the onset events (48%). For 19% of onset events, NS arcs contacting a growth phase arc merged with EW arcs, and the associated auroral enhancement contacted the onset location by moving azimuthally along the pre-existing growth phase arc. EW auroral enhancements come from outside the imager FOVs along growth phase arcs without detection of a PBI or NS arc for 34% of events. Those events may also be connected to NS arcs, but such arcs would have extended equatorward to the growth phase arc outside of the FOVs of the available ASIs. The high occurrence rate (53% as pre-onset aurora indicates that it is approximately as common for the plasma populations leading to near-Earth onset to have turned and drifted roughly azimuthally toward the onset locations as for onset to occur at the first contact point with the growth phase arc. The rest of the events (4.2%) are not associated with NS or EW arc but the poleward boundary moves equatorward and contacts with the onset location just prior to onset.

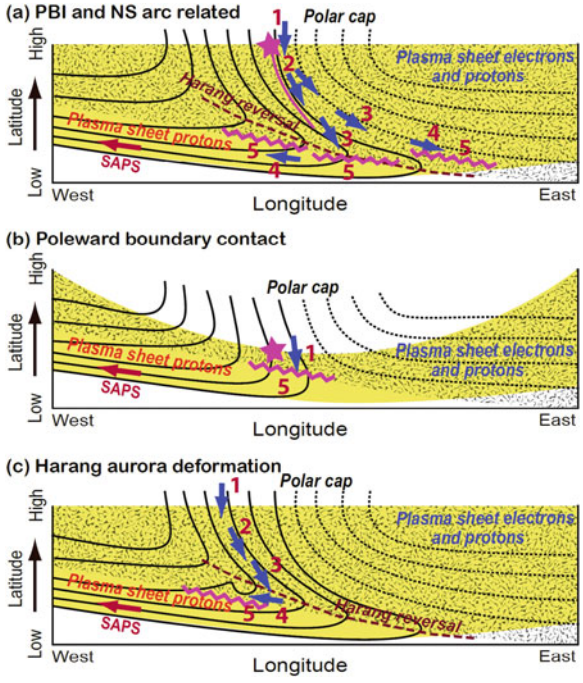

Fig. 8.7 Schematic illustration of motion of pre-onset auroral forms and their relation to nightside ionospheric convection. (**a**) The time sequence for PBI and NS arc related, (**b**) poleward boundary contact, and (**c**) Harang aurora deformation onset events. *Pink stars*, NS-oriented *pink line*, and azimuthally-extended wavy lines indicate PBIs, NS-oriented arc and onset arcs, respectively. *Blue arrows* illustrate the plasma flow pattern inferred from pre-onset auroral motion. Numbers 1–5 show time evolution of pre-onset aurora (see text). *Yellow* and *gray* areas correspond to proton and electron precipitations

Conclusion

This study presents classifications of the time sequence of events leading to substorm onset using the THEMIS ASI array. The onset time sequence can be classified into three major types: PBI and NS arc related, poleward boundary contact, and Harang aurora deformation events. The most dominant sequence detected in 84% of the events where the FOV of the imagers cover up to the poleward boundary, starts from a PBI, indicating an abrupt injection of a new plasma and magnetic flux from the lobe to the plasma sheet through magnetic reconnection. The sequence is summarized in Fig. 8.7a and below:

1. The initial feature of pre-onset auroral activity is a PBI.
2. An NS arc extending from the PBI then moves equatorward, roughly following the preexisting flow pattern around the Harang flow shear.
3. The NS arc contacts a growth phase arc within the equatorward portion of the auroral oval. For about half of the events, onset occurs at the contact location.
4. For the other half, the NS arc turns into EW auroral form with enhanced auroral brightness that moves azimuthally (according to the ionospheric convection pattern, dominantly westward leading to premidnight onset) along the growth phase arc.
5. Onset occurs when the azimuthally-moving brightened EW auroral form reaches the onset location.

Although each auroral feature in the above sequence is well known, the present study links these features together, giving evidence that a connection between the poleward and equatorward boundaries of the aurora oval leads to substorm onset.

The high incidence of PBIs (84%) observed to initiate the sequence, together with the known relation between PBIs and NS arcs and flow channels, leads to the inference that the pre-onset sequence starts with the enhanced transport of new plasma across the open-closed field line boundary.

This enhanced transport corresponds to a localized enhancement of the reconnection rate, which would reflect an enhancement in reconnection preceding substorm onset as has been observed by the THEMIS spacecraft (Angelopoulos et al. 2008). This then leads to a channel of enhanced earthward flow carrying the new plasma earthward, which is manifested by the NS arc seen moving equatorward in the ionosphere.

A minor population of onset events (4.2% out of the cases where precursor auroral forms are detected) shows a narrow auroral oval width which decreases to ∼2° just prior to onset. The sequence is summarized in Fig. 8.7b. The poleward boundary near the magnetic midnight moves equatorward, and the auroral oval near midnight becomes much narrower than the dawn and dusk regions. PBIs with a finite latitudinal width directly reach onset location. This sequence indicates that magnetic reconnection is enhanced when the plasma sheet becomes extremely thin and plasma is rapidly transported toward the near-Earth region leading to onset.

Contrary to the PBI-associated events described above, auroral onsets are not associated with any PBI or enhanced brightness moving toward onset location for a small fraction of events (10.7%). As illustrated in Fig. 8.7c, the pre-onset feature in this category is characterized as equatorward bending of the equatorward portion of the Harang aurora. The pre-existing arc then generally starts to fade and a new arc appears equatorward and develops as an auroral brightening. Although the cause of the bending of the pre-existing aurora cannot be identified from ASIs, it suggests that an abrupt change in the plasma convection pattern associated with enhanced plasma flows leads to initiation of onset instability. We cannot exclude the possibility that the convection change results from new plasma intruding from the polar cap boundary, but we see no evidence for this intrusion in the auroral observations.

The events and statistics presented in this study suggest that enhanced plasma flows into the onset location lead to substorm onset and that the convection pattern during the growth phase governs motion of the enhanced flow. Using observations from incoherent scatter radars, Lyons et al. (2010) showed a plasma flow enhancement near the open-closed field line boundary associated with PBIs is commonly observed at a time preceding onset. Pre-onset flow enhancements are also observed by radar observations a few minutes prior to onset near the onset location (Miyashita et al. 2008; Lyons et al. 2010). These radar observations thus support the above suggestion based on ASI observations that an influx of new plasma crossing the nightside separatrix and intruding to the near-Earth magnetosphere along channels of enhanced flow leads to substorm onset. The new plasma injection from the open-closed field line boundary toward the near-Earth region can be observed by *in-situ* spacecraft observations and radar observations in conjunction with the aurora forms that lead to onset, and such a study is currently in progress (Xing et al. 2010; S. Zou, personal communication 2009).

Acknowledgments This work was supported by National Science Foundation grants ATM-0646233 and ATM-0639312, NASA grant NNX07AF66, NASA contract NAS5-02099, and JSPS Research Fellowships for Young Scientists. Deployment of the THEMIS ASIs was partly supported by CSA contract 9F007-046101. Alaska magnetometer data were obtained from Geophysical Institute of University of Alaska, Fairbanks. NOAA satellite data were provided through the NOAA's National Geophysical Data Center.

References

Akasofu S-I (1964) The development of the auroral substorm. Planet Space Sci 12:273

Angelopoulos V (2008) The THEMIS mission. Space Sci Rev 321:47

Angelopoulos V et al (2008) Tail reconnection triggering substorm onset. Science 321:931

Birn J, Hesse M, Haerendel G, Baumjohann W, Shiokawa K (1999) Flow braking and the substorm current wedge. J Geophys Res 104:19895–19904

de la Beaujardiere O et al (1994) Quiet-time intensifications along the poleward auroral boundary near midnight. J Geophys Res 99:287–298

Donovan E et al (2008) Simultaneous THEMIS in situ and auroral observations of a small substorm. Geophys Res Lett 35:17

Elphinstone RD et al (1995) Observations in the vicinity of substorm onset: implications for the substorm process. J Geophys Res 100:7937–7969

Henderson et al (2002) The evolution of northsouth aligned auroral forms into auroral torch structures: the generation of omega bands and ps6 pulsations via flow bursts. In: Winglee RM (ed) Sixth international conference on substorms. University of Washington, Seattle, WA, pp 169–174

Kepko L et al (2009) Equatorward moving auroral signatures of a flow burst observed prior to auroral onset. Geophys Res Lett 36(24):L24104

Lyons LR, Nagai T, Blanchard GT, Samson JC, Yamamoto T, Mukai T, Nishida A, Kokobun S (1999) Association between Geotail plasma flows and auroral poleward boundary intensifications observed by CANOPUS photometers. J Geophys Res 104:4485–4500

Lyons L, Nishimura Y, Shi Y, Kim H-J, Zou S, Heinselman C, Nicolls M, Angelopoulos V (2010) Substorm onset by earthward intrusion of new plasma: incoherent scatter radar observations. J Geophys Res 115(A7):A07223

Miyashita Y et al (2008) Response of large-scale ionospheric convection to substorm expansion onsets: a case study. J Geophys Res 113:A12309

Miyashita Y et al (2009) A state-of-the-art picture of substorm-associated evolution of the near-Earth magnetotail obtained from superposed epoch analysis. J Geophys Res 114(A13):1211

Nakamura R et al (2001) Earthward flow bursts, auroral streamers, and small expansions. J Geophys Res 106:10791–10802

Nishimura Y, Lyons L, Zou S, Angelopoulos V, Mende S (2010) Substorm triggering by new plasma intrusion: THEMIS all-sky imager observations. J Geophys Res 115(A7):A07222

Rostoker G, Lui ATY, Anger CD, Murphree JS (1987) North-south structures in the midnight sector auroras as viewed by the Viking imager. Geophys Res Lett 14:407–410

Samson JC, Lyons LR, Newell PT, Creutzberg F, Xu B (1992) Proton aurora and substorm intensifications. Geophys Res Lett 19:2167–2170

Sergeev VA, Liou K, Meng C-I, Newell PT, Brittnacher M, Parks G, Reeves GD (1999) Development of auroral streamers in association with localized impulsive injections to the inner magnetotail. Geophys Res Lett 26:417–420

Sergeev VA et al (2000) Multiple-spacecraft observation of a narrow transient plasma jet in the Earth's plasma sheet. Geophys Res Lett 27:851–854

Wolf RA, Wan Y, Xing X, Zhang J-C, Sazykin S (2009) Entropy and plasma sheet transport. J Geophys Res 114:A00D05

Xing X, Lyons L, Nishimura Y, Angelopoulos V, Larson D, Carlson C, Bonnell J, Auster U (2010) Substorm onset by new plasma intrusion: THEMIS spacecraft observations. J Geophys Res 115(A10):A10246

Zesta E, Donovan E, Lyons L, Enno G, Murphree JS, Cogger L (2002) Twodimensional structure of auroral poleward boundary intensifications. J Geophys Res 107:1350

Zou S et al (2009a) On the coupling between the Harang reversal evolution and substorm dynamics: a synthesis of SuperDARN, DMSP, and IMAGE observations. J Geophys Res 114:A01205

Zou S, Lyons LR, Nicolls MJ, Heinselman CJ, Mende SB (2009b) Nightside ionospheric electrodynamics associated with substorms: PFISR and THEMIS ASI observations. J Geophys Res 114(114):A12301

Part III
Inner Magnetospheric Processes

Dynamic Inner Magnetosphere: A Tutorial and Recent Advances

9

Y. Ebihara and Y. Miyoshi

Abstract

The purpose of this chapter is to present a tutorial and recent advances on the Earth's inner magnetosphere, which includes the plasmasphere, warm plasma, ring current, and radiation belts. Recent analysis and modeling efforts have revealed the detailed structure and dynamics of the inner magnetosphere. It has been clearly recognized that elementary processes can affect and be affected by each other. From this sense, the following two different approaches enable us to fully understand the inner magnetosphere and magnetic storms. The first is to investigate its elementary processes, which would include the transport of single particles, interaction between particles and waves, and collisions. The other approach is to integrate the elementary processes in terms of cross energy and cross region couplings. Multi-satellite observations along with ground-network observations and comprehensive simulations are one of the promising avenues to incorporate the two approaches and treat the inner magnetosphere as a non-linear, compound system.

9.1 Preface

The inner magnetosphere is a natural cavity in which various types of charged particles are trapped by a planet's intrinsic magnetic field. With regard to the Earth, the kinetic energy of these trapped particles ranges from ~eV to $\sim 10^8$ eV. These particles undergo different physical processes and are never stable, even in geomagnetically quiet times, due to variations in the solar wind and self-excited instabilities in the inner magnetosphere.

Y. Ebihara (✉)
Institute for Advanced Research, Nagoya University, Aichi, Japan (Now at Research Institute for Sustainable Humanosphere, Kyoto University, Uji, Japan)
e-mail: ebihara@rish.kyoto-u.ac.jp

The following terms have traditionally been used to identify the Earth's energy regimes. In the order of low to high energies, they are the plasmasphere (~ eV), ring current (~ 1–100 keV), and radiation belts (>~100 keV) (Fig. 9.1). In a broad sense, the plasmasphere is the region where the number density of particles is high. The ring current is the torus-like region where the energy density (or the plasma pressure) is high. Van Allen radiation belts consist of energetic particles of electrons and ions of more than a few hundred keV (Van Allen and Frank 1959). The electron radiation belts consist of inner and outer belts. There exists a slot region between them, in which electron flux is small. The proton/ion radiation belt consists of a single belt.

These energy regimes are directly or indirectly coupled with one another. Mass and energy are transported

W. Liu, M. Fujimoto (eds.), *The Dynamic Magnetosphere*, IAGA Special Sopron Book Series 3,
DOI 10.1007/978-94-007-0501-2_9, © Springer Science+Business Media B.V. 2011

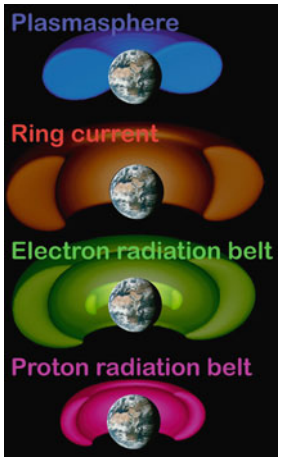

Fig. 9.1 Energy structure of particles trapped in the inner magnetosphere

to the other regions such as the outer magnetosphere and the ionosphere. Research efforts directed toward cross energy and cross region couplings are therefore needed for a comprehensive understanding and modeling of the inner magnetosphere. In this chapter, we review the progress of research on the inner magnetosphere and offer perspectives on future research directions in terms of the elementary processes involved and their role in the coupled evolution of the inner magnetospheric system.

9.2 Plasmasphere

9.2.1 Structure of Plasmasphere

The region where the number density of the plasma is higher than the ambient number density is called the plasmasphere. The plasmasphere consists of cold and dense plasmas that originate in the topside ionosphere. The number density of these plasmas exceeds $\sim 10^3$ cm^{-3} at $L = 2$ and gradually decreases with L (e.g., Carpenter and Anderson 1992). The typical temperature of the ions is ~1–2 eV, a value which increases with L (Farrugia et al. 1989). At a certain L, the density shows a sharp drop by an order of magnitude; this region is called the plasmapause (Carpenter 1963). The L-value of the plasmapause depends on the magnetic local time (MLT) (Carpenter 1966) and magnetic activity (Chappell et al. 1970; Carpenter and Anderson 1992; Carpenter and Lemaire 1997; Moldwin et al. 2002). During magnetically quiet times, the plasmapause is located at $L \approx 7$. During active times, it moves to $L \approx 2$. Baker et al. (2004) have indicated that the plasmapause was shrunk to $L = 1.5$ during the Halloween storm of October 2003.

On average, the plasmapause has a bulge on the duskside when mapped to the equatorial plane (Fig. 9.2a; see Carpenter 1966). Nishida (1966) and Brice (1967) have pointed out that the shape of the plasmasphere is understood to be a combination of the convection electric field and the corotation electric field (Fig. 9.2b). Grebowsky (1970) has suggested that the plasmasphere is elongated sunward on the duskside when the convection electric field becomes strong (Fig. 9.2c). In-situ satellite observations sometimes show a "detached" dense plasma cloud outside the plasmapause (Chappell 1974). Chen and Grebowsky (1974) have suggested that this "detached" plasma cloud can be explained by the elongated form of the plasmasphere, which has what is called a plasma tail (Fig. 9.2d). This "detached" feature can also be formed by a strong poleward electric field in the subauroral region (Ober et al. 1997), or by an interchange instability (Lemaire 2001).

Schematic density profile patterns of the plasmasphere are summarized by Singh and Horwitz (1992) and displayed in Fig. 9.3, indicating that identification of the plasmapause is not always easy. Moldwin et al. (2002) investigated the thermal plasma density acquired by the CRRES satellite near the equatorial plane. They found that the plasmapause could be identified in ~73% of all the inbound and outbound trajectories of CRRES, and only ~16% of them displayed a "classical" plasmapause. The difficulty in identifying the plasmapause arises from its small density gradient, and the relatively smooth and highly structured variations in density. Irregular variations in density are often observed near the plasmapause (Chappell 1972; Oya and Ono 1987; Koons 1989; Horwitz et al. 1990b; Singh and Horwitz 1992; Carpenter et al. 2000; Darrouzet et al. 2004; Green and Fung 2005). Due to the complex nature of the plasmapause, Carpenter and Lemaire (2004) encourage the use of the term Plasmasphere Boundary Layer (PBL) instead of the conventional term plasmapause.

In the late 1990s, semiglobal imaging of the plasmasphere was achieved for the first time by the Japanese NOZOMI (PLANET-B) Mars spacecraft (Nakamura et al. 2000a). After the launch of NASA's IMAGE satellite in 2000 (Burch et al. 2001), the Extreme

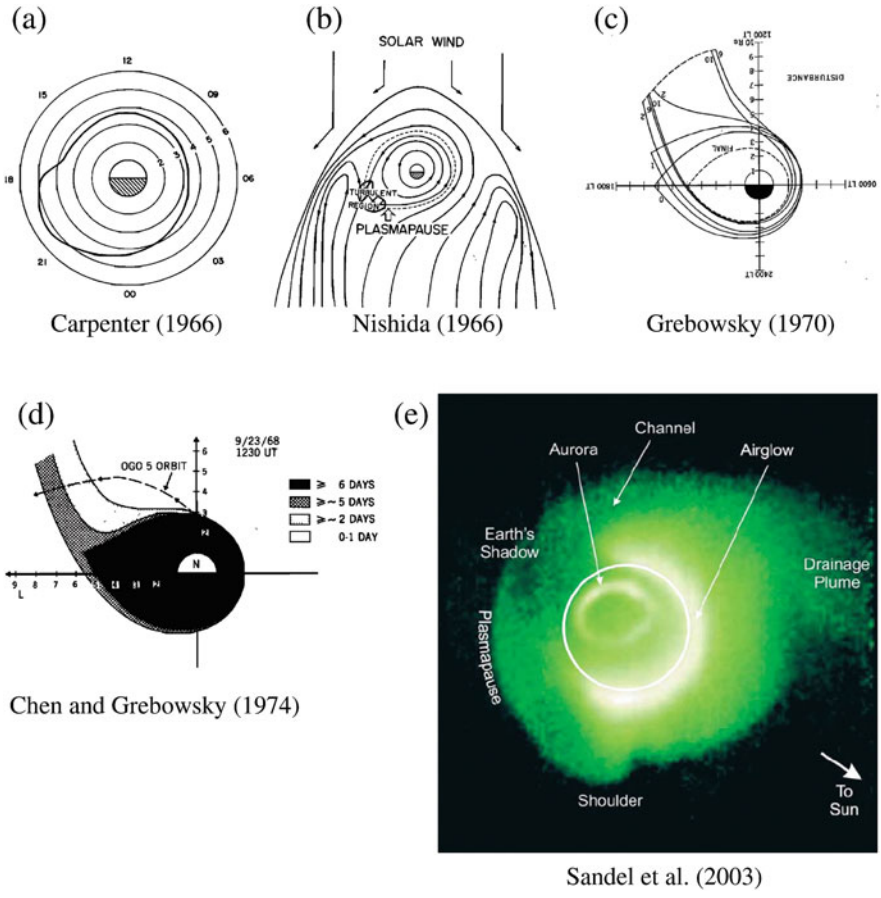

Fig. 9.2 Shape of the plasmasphere

Ultraviolet Image (EUV) instrument on board the satellite provided completely global images of the emission of He^+ with a time resolution of 10 min and a spatial resolution of 0.1 Re (Sandel et al. 2003). The brightness of the He^+ emission is proportional to the line-of-sight density of He^+. The images from IMAGE/EUV reveal more complicated and dynamic features of the plasmasphere (Fig. 9.2e), such as a shoulder (Burch et al. 2001), notch/bite-out (Green and Reinisch 2002), channel (Sandel et al. 2001), and plume (Sandel et al. 2001). For the determination of the equatorial plasmapause from the IMAGE/EUV observations, at least two algorithms have been used: the Edge Algorithm (Roelof and Skinner 2000) and the Minimum *L* Algorithm (Wang et al. 2007). In the late 2000s, the Japanese KAGUYA (SELENE) Lunar satellite, from its lunar orbit, succeeded in capturing images of emissions from the plasmasphere (Yoshikawa et al. 2010; Murakami et al. 2010). Yoshikawa et al. (2010) found a large depression of the plasmaspheric plasma near the equatorial plane.

In general, identifying the plasmapause at a low altitude (in the ionosphere) is more difficult than identifying it at a high altitude (in the magnetosphere). A close coincidence between the ionospheric trough and the plasmapause has been suggested by Grebowsky et al. (1976, 2009) and Yizengaw et al. (2005). When an electron density trough cannot be identified, the H^+ density can be used to identify a mid-latitude trough (Taylor 1972; Morgan et al. 1976; Grebowsky et al. 2009 and references therein). Anderson et al. (2008) developed a 7-step method to identify the plasmapause location from the low-altitude satellite DMSP in the topside ionosphere. Their results agree well with those derived from IMAGE/EUV observations. Foster et al. (2004b) reconstructed a two-dimensional distribution of the total electron contents (TEC) using a network of GPS TEC receivers. When mapped on the equatorial

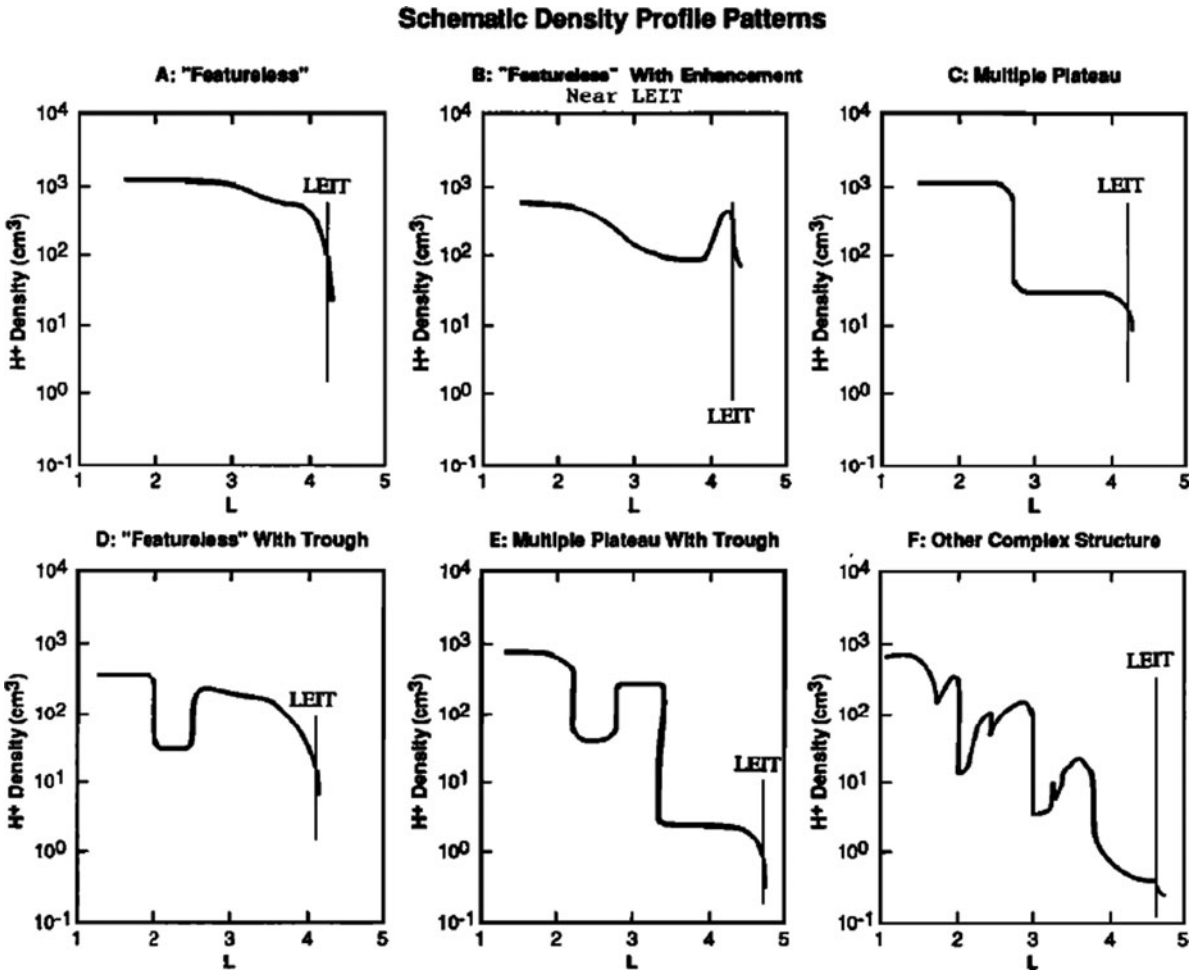

Fig. 9.3 Six schematic plasmaspheric density profiles (Horwitz et al. 1990a)

plane, the TEC distribution is similar to the global distribution of the He^+ plasmasphere derived from the IMAGE/EUV images. GPS TEC is the line-of-sight integral from the GPS satellite (20,220 km altitude) to the ground, so that GPS TEC includes contributions from both the plasmasphere and the ionosphere. Yizengaw et al. (2008) compared the GPS signals received by the low Earth-orbiting satellite JASON 1 (1,335 km altitude) with those received by ground-based stations. They concluded that the plasmasphere contributes significantly to ground-based GPS TEC, especially at night, when its contribution reaches 60% at low latitudes.

The plasmasphere consists of H^+, He^+, O^+, O^{++}, D^+, N^+, N^{++}, and other minor ionic species. Their composition ratios are highly variable (Chappell 1972; Chappell et al., 1982; Horwitz et al. 1986, 1990b; Farrugia et al. 1989). The most frequent values given for the He^+/H^+ ratio in the plasmasphere are ~2–6% (Farrugia et al. 1989) and ~20% (Horwitz et al. 1990b), but it has also been indicated that the ratio ranges from ~1% to, on occasion, over 100% (Farrugia et al. 1989). The He^+/H^+ ratio decreases with L (Farrugia et al. 1989). O^+ is in general minor, but the O^+/H^+ ratio occasionally increases to ~100% in the outer plasmasphere during a storm recovery phase (Horwitz et al. 1984, 1986). The N^+/O^+ ratio is ~5–10%, and the N^{++}/N^+ ratio is ~1–5% (Chappell et al. 1982). As understood using a magnetoseismology technique, O^+ becomes important in the plasmatrough (Takahashi et al. 2008), or during a large magnetic storm (Takasaki et al. 2006; Kale et al. 2009).

The temperature of the thermal plasma increases with L (Farrugia et al. 1989). The difference in the

thermal structure of the inner and outer regions of the plasmasphere has been pointed out by Kotova et al. (2008). On the basis of data from Interball 2 and Magion 5, they showed that on the nightside, the plasmaspheric temperatures are quite close to the ionospheric temperature at $1.4 < L < 2.8$. At $L > 3$, the plasmaspheric temperature is higher than the ionospheric temperature. They suggested that there is a heating source at high L, particularly in the noon-to-dusk sector.

The field-aligned density distribution of plasmaspheric electrons has also been studied (Reinisch et al. 2009 and references therein). Theoretical studies have predicted that the field-aligned density will obey the hydrostatic assumption if the plasmasphere is in a steady condition. If the temperatures of the plasmaspheric plasma are constant and isotropic along a field line, the density distribution is in an exponential form, which is consistent with the result obtained by time-dependent simulation within ±40° MLAT (Rasmussen et al. 1993). Statistical studies have suggested that the field-aligned density can be well fitted to a power law form on the basis of data from Polar (Goldstein et al. 2001; Denton et al. 2002). Radio sounding of the plasmasphere was performed by a radio plasma imager (RPI) on the IMAGE satellite. Huang et al. (2004) and Tu et al. (2006) suggested a mathematical form in order to explain the field-aligned density profile that was observed remotely by IMAGE/RPI. By measuring Alfvén wave harmonic frequencies, Denton et al. (2009) inferred a field-aligned mass density profile, and fitted to a polynomial function. The physical meaning of the field-aligned density distribution of the thermal plasma is not well understood.

9.2.2 Formation of Plasmasphere

It has been suggested that the plasmasphere is formed by three principal processes: (1) the supply of thermal plasma from the ionosphere along a field line (e.g., Singh and Horwitz 1992), (2) pitch angle scattering of the supplied plasma (e.g., Schulz and Koons 1972; Lemaire 1989), and (3) large-scale electric fields that act on the drift motion of thermal plasma (e.g., Nishida 1966).

The main source of H^+ in the plasmasphere is the reaction $O^+ + H \rightarrow O + H^+$ that takes place in the topside ionosphere. The reverse reaction, $O + H^+ \rightarrow O^+ + H$, also takes place with almost the same speed, which is the main sink for H^+. When the plasmasphere is completely empty, the former process will proceed, and H^+ will be supplied into the magnetosphere with a maximum flux. The limiting flux of H^+ is a weak function of a neutral temperature, but is directly proportional to the neutral hydrogen density and to the O^+ scale height and O^+ density at a lower boundary altitude of the production region (Richards and Torr 1985). The lower boundary altitude increases from 500 km for a solar minimum to 1000 km for a solar maximum because of an increase in the neutral density scale height and O^+ density. When the lower boundary altitude increases, the density of the neutral hydrogen decreases, so that the limiting flux is decreased. Thus, the refilling time is longer at a solar maximum than at a solar minimum. The opposite tendency is expected for He^+, according to the simulation performed by Krall et al. (2008). The refilling of He^+ is more rapid at a solar maximum than at a solar minimum because the He^+ density generally increases with solar activity due to photo ionization. The idea that He^+ density is largely controlled by photo ionization is supported by the diurnal variation in the He^+ density observed by IMAGE/EUV (Galvan et al. 2008).

Based on whistler wave observations in Antarctica, the time required to reach an equilibrium was obtained to be ∼1 day at $L = 2.5$ and ∼8 days at $L = 4$ (Park 1970, 1974). Using cold ion data from the GEOS-2 satellite at geosynchronous orbit, Song et al. (1988) found that the refilling time constants range from ∼3 to ∼7 days with refilling rates depending on the *Dst* index. The first global imaging of a refilling process was accomplished by Sandel and Denton (2007) using data from IMAGE/EUV. In the early stage of the refilling process, the interior of the He^+ plasmasphere is structured in azimuth and the plasmapause is diffuse, suggesting that the refilling may take place nonuniformly in azimuth. The refilling rates were inferred to be ∼1 He^+ cm^{-3} h^{-1} at $L = 3.3$, and $\sim 7 \times 10^{-2}$ He^+ cm^{-3} h^{-1} at $L = 6$, rates which are consistent with those reported in previous studies.

Electric fields play a major role in the formation of the plasmasphere (Nishida 1966; Brice 1967; Kavanagh et al. 1968; Grebowsky 1970; Chen and Grebowsky 1974). The corotation electric field captures the thermal plasma originating from the ionosphere. The convection electric field peels away the outer layer of the thermal plasma. When the electric

fields are stationary, the transition between them is precisely determined by the combination of the corotation and convection electric fields. The last-closed equipotential corresponds to the plasmapause. The situation, however, is not as simple as this suggests because the electric fields are never stationary. Major changes in the convection electric field result in the formation of a plasma tail (drainage plume) (Grebowsky 1970; Chen and Grebowsky 1974). Even though the large-scale convection electric field is relatively stable, small fluctuations in the convection electric fields result in a leakage of plasma (Matsui et al. 1999, 2000). Additional electric fields driven by magnetosphere-ionosphere coupling also result in deformation of the plasmapause (Goldstein et al. 2003b, c).

The plasmasphere can be used as a diagnostic tool to investigate the magnetosphere's electric fields because its structure is highly sensitive to the electric fields. The strength of the large-scale convection electric field was modeled using the location of the plasmapause (Maynard and Chen 1975). The degree of shielding was investigated using the shape of the plasmapause (Ejiri 1981; Ebihara and Ejiri 2003). The corotation lag (∼10%) was evaluated using a distinguishable structure of the plasmapause (Burch et al. 2004). The response time between the solar wind electric field and the electric field in the inner magnetosphere has been evaluated (Goldstein et al. 2003a). Using two-dimensional images of the plasmasphere, snapshots of the electric fields were obtained for the entire plasmasphere (Gallager and Adrian 2007), and also along the plasmapause (Goldstein et al. 2004b).

9.2.3 Fate of Plasmaspheric Plasma

Erosion is the most drastic large-scale phenomenon in the plasmasphere. The erosion takes place when the enhanced convection electric field peels away the outer layer of the plasmaspheric plasma with a time delay of ∼30 min (Goldstein et al. 2003a). A plasma tail (Grebowsky 1970, or Fig. 9.2c) or a drainage plume (Sandel et al. 2001, or Fig. 9.2e) is thought to be a manifestation of the path of the peeled plasma. In the noon-dusk sector, sunward drifting cold ions have already been observed at geosynchronous orbit (Freeman 1969; Borovsky and Denton 2008). Borovsky and Denton (2008) confirmed that the drainage plume plasma moves sunward with flow speeds that decrease as storms progress. According to their calculation, the integrated mass fluxes in the plumes are $\sim 2\times10^{26}$ ions/s in the early stage of magnetic storms. It is estimated that ultimately, a total of $\sim 2\times10^{31}$ ions (34 tons of protons) is drained from the main body of the plasmasphere during a magnetic storm. Plumes exhibit large velocity fluctuations, suggesting a turbulent condition, as was previously suggested by Matsui et al. (1999).

The fate of the drained plasma is not well known. During magnetic storms, cold ions have been observed on, or just outside the magnetopause (e.g., Freeman 1969; Elphic et al. 1996; Borovsky et al. 1997). Foster et al. (2004a) observed a cold plume plasma with its leading edge making contact with a cusp region at the ionospheric altitude. The transport rates of the plasmaspheric material were estimated to be $\sim 10^{26}$ ions/s (Elphic et al. 1997) and $>10^{26}$ ions/s (Foster et al. 2004a). Recently, McFadden et al. (2008) have shown clear evidence that the cold plume plasma exists in open flux tubes, suggesting that the cold plume plasma participates in the magnetic reconnection at the dayside magnetopause. This observed fact supports the idea that the cold plume plasma changes from a closed field line to an open field line at the dayside magnetopause and moves antisunward through the lobe region (Borovsky et al. 1997; Elphic et al. 1997).

Moore et al. (2008) used the term "plasmaspheric wind" to describe the cold plasma population that originates from the plasmasphere. They investigated the fate of the plasmaspheric wind by test particle simulation under the 3-D magnetospheric fields provided by a global MHD simulation. The plasmaspheric wind escapes from the magnetosphere downstream, rather than being recycled through the inner magnetosphere. They found that the contribution from the plasmaspheric wind to the inner magnetosphere is negligible in comparison with the solar wind protons for the southward IMF condition but becomes significant for the subsequent northward IMF condition.

The plasmasphere is of importance in the dispersion relations of waves, which lead to scattering of the energetic particles trapped in the inner magnetosphere (e.g., Lam et al. 2007; Shprits et al. 2008b; Varotsou et al. 2008; Gamayunov and Khazanov 2008; Gamayunov et al. 2009; Breneman et al. 2009). Chen et al. (2009) evaluated the path-integrated gain of electromagnetic ion cyclotron (EMIC) waves and found that the minimum cyclotron-resonant electron energy

occurs in the plasmaspheric plume. The minimum resonant electron energies are several MeV in plumes and near the plasmapause, and > 8 MeV in the low-density trough. See Sections 9.6.3.2 and 9.6.4.2 for a more detailed description in this regard.

9.3 Warm Plasma

In situ measurements have shown the presence of a variety of ions whose temperatures ranging between a few eV and hundreds of eV (e.g., DeForest and McIlwain 1971; Comfort and Horwitz 1981; Kaye et al. 1981; Fennell et al. 1981; Olsen 1981; Quinn and Johnson 1982a, b; Sojka et al. 1983; Nagai et al. 1983; Sagawa et al. 1987; Olsen et al. 1987; Collin et al. 1993; Yamauchi et al. 1996). Chappell et al. (2008) have clarified that the warm plasma represents an intermediate energy population (a few eV to hundreds of eV) that is too high in energy to be a direct upward flow of the ionosphere (0.1 to a few eV) and too low in energy to be accepted as part of the dominant plasma sheet (1–10 keV) or ring current (10–100 keV) populations. The warm plasma population tends to appear in the morning to early afternoon sector, which is called the "warm plasma cloak" (Chappell et al. 2008). The pitch angle distribution of the warm ions is isotropic, bidirectional field-aligned, unidirectional field-aligned, or pancake-like, and their occurrence rates depend on the local time, magnetic activity, and ionic species (Comfort and Horwitz 1981; Nagai et al. 1983; Collin et al. 1993).

Origin of the warm ions is a subject of debate. The uncertainty arises from the fact that these ions can be accelerated, heated, and transported by different means. The acceleration mechanisms include quasi-static parallel electric fields in the ionosphere (Mizera and Fennell 1977; Frahm et al. 1986), substorm-associated induction electric fields in the magnetosphere (Quinn and McIlwain 1979), and ion cyclotron waves (Klumpar 1979). The heating mechanism includes cyclotron turbulence near the equatorial plane (Olsen et al. 1987). The transport mechanisms include convection from the nightside (Fennell et al. 1981; Chappell et al. 2008) and substorms (Moore et al. 1981). In addition, it has been suggested that the ring current population becomes warm ions due to its interaction with thermal plasmas, that is, due to Coulomb drag (Jordanova et al. 1996).

It has been pointed out that a field-aligned pitch angle distribution of ions does not always indicate a direct supply from the ionosphere (Nagai et al. 1983). The presence of ions in the loss cone is the best indication of such a direct supply.

Warm ions are sometimes accompanied by a wedge-like energy dispersion in energy vs. time spectrograms. These wedge-like structures have been observed by Viking (Yamauchi et al. 1996; Ebihara et al. 2001), Equator-S (Ebihara et al. 2008b), and Cluster (Yamauchi et al. 2009) when the satellites traverse the inner magnetosphere in the radial direction. The shape of this dispersion is well understood to represent a convective transport from the nightside plasmasphere (Ebihara et al. 2001), and the source population of the warm H^+ is estimated to be ∼10 eV in the near-Earth plasma sheet (Ebihara et al. 2008b), which is obviously distinct from the typical plasma sheet population (∼keV).

Warm (suprathermal) electrons are also supplied from not only the ionosphere (Peterson et al. 1977; Khazanov et al. 1996) but also the plasma sheet (Khazanov et al. 1996). Bortnik et al. (2007) have shown that fluxes of the warm electrons at all energies increase with increasing magnetic activity. It has been suggested that the warm electrons tend to be more likely associated with ECH (Electrostatic Cyclotron Harmonic) emissions and upper-band whistler-mode chorus waves (e.g., Horne et al. 2003; Ni et al. 2008).

9.4 Ring Current

9.4.1 Carrier of Ring Current

A complete or incomplete ring-like region where the plasma pressure (energy density) is high is hereinafter termed a ring current. The general expression of the ring current is given by Parker (1957) as follows:

$$\begin{aligned}\mathbf{J} &= \mathbf{J}_M + \mathbf{J}_B + \mathbf{J}_c \\ &= \frac{\mathbf{B}}{B^2} \times \left[\nabla P_\perp + \left(P_{||} - P_\perp \right) \frac{\mathbf{B} \cdot \nabla \mathbf{B}}{B^2} \right]\end{aligned} \tag{9.1}$$

where $\mathbf{J}_M, \mathbf{J}_B, \mathbf{J}_C, P_\perp, P_{||}, \mathbf{B}$ are the magnetization current (due to gyration), grad-B drift current, curvature drift current, perpendicular pressure, parallel pressure, and magnetic field, respectively. The inertial current

is usually negligible in the inner magnetosphere. The pressure terms are given by

$$P_{\perp} = \frac{1}{2}\sum_i \int F_i(v,\alpha)\, m_i v^2 \cos^2\alpha dv d\alpha \qquad (9.2)$$

$$P_{||} = \sum_i \int F_i(v,\alpha)\, m_i v^2 \sin^2\alpha dv d\alpha \qquad (9.3)$$

where F, i, m, v, and α are the distribution function of particles, particle species, mass, speed, and pitch angle, respectively. Positively (negatively) charged particles drift westward (eastward) due to the grad-B and curvature drifts. Thus, the drift currents $\mathbf{J}_B$ and $\mathbf{J}_C$ flow westward in the Earth's magnetosphere. For isotropic pressure ($P = P_{\perp} = P_{||}$), the contributions from $\mathbf{J}_B$ and $\mathbf{J}_C$ are canceled by a part of $\mathbf{J}_M$, and the resultant electric current is simply expressed as $\mathbf{J}_{\perp} = \mathbf{B} \times \nabla P / B^2$. Thus, the contribution from $\mathbf{J}_M$ is significant, while the drift currents ($\mathbf{J}_B$ and $\mathbf{J}_C$) are less so. In this particular case, the pressure peak ($dP/dL = 0$) is located along the shear of the electric currents, that is, a westward current in the outer region and an eastward current in the inner region. The idea that "the ring current flows westward because ions drift westward and electrons drift eastward" is incorrect.

In-situ observations have shown that the plasma pressure is primarily sustained by ions with an energy that ranges from ~1 keV to ~a few hundred keV (Frank 1967; Smith and Hoffman 1973; Williams 1981; Daglis et al. 1993). The H^+ ions usually make the greatest contribution to the plasma pressure, though the energy density of O^+ ions occasionally dominates that of H^+ ions during particular magnetic storms (Lundin et al. 1980; Lennartsson et al. 1981; Krimigis et al. 1985; Hamilton et al. 1988; Daglis et al. 1999). Other ionic species such as He^+, He^{++}, O^{++} (Krimigis et al. 1985), N^+ (Liu et al. 2005b), and $O^{\geq+3}$ (Ebihara et al. 2009a), have also been identified in the ring current region. The N^+/O^+ ratio is ~0.314 during quiet times, and it decreases with $F_{10.7}$ (Liu et al. 2005b).

He^+ and O^+ ions are thought to originate in the Earth, while He^{++} and $O^{\geq+3}$ ions are thought to originate in the Sun. Using data from the Polar satellite, Ebihara et al. (2009a) found that $O^{\geq+3}$ and $O^{+,++}$ are almost simultaneously enhanced in the heart of the ring current during magnetic storms. This observational fact indicates that both contributions from the solar wind and the ionosphere are important for the storm-time ring current. However, transport, acceleration, and loss processes of these ions are not fully understood.

The contribution of electrons to the ring current is uncertain. During quiet times, ~1–50 keV electrons have been found to contribute to 1% (Liu et al. 2005a) of the ring current. During active times, these electrons have been found to contribute to ~25% (Frank 1967), and 8–19% (Liu et al. 2005a) of the ring current. A simulation has also predicted that the electrons contribute to and ~2% during quiet times and ~10% during active times (Jordanova and Miyoshi 2005). The reason for their small contribution to the ring current is unknown. The smallness may come from the relatively low temperature of the electrons in the nightside plasma sheet (Baumjohann et al. 1989) or from rapid losses of electrons.

Dessler and Parker (1959) and Sckopke (1966) developed a formula that relates the total energy of trapped particles to the magnetic field perturbation at the center of the Earth. Greenspan and Hamilton (2000) confirmed that this formula holds true on average when using the *Dst* index as a proxy for the magnetic field perturbation at the center of the Earth. On the other hand, Turner et al. (2001) have shown that the ring current ions contribute, on average, half of the *Dst* index.

9.4.2 Structure of Ring Current

Chapman and Ferraro (1933) predicted the existence of a circular ring of current surrounding the Earth. In our time, a detailed picture of the ring current has been obtained by the following different observational means.

1. *Ground-based measurements of the magnetic deflection induced by the ring current* (e.g., Akasofu and Chapman 1964; Kamide and Fukushima 1971; Kamide 1974; Clauer and McPherron 1980). The averaged magnetic field deflection observed at a geomagnetically low latitude is used to derive the *Dst* index (Sugiura 1964). The local time asymmetry of the ground magnetic deflection can be used to measure the asymmetry of the ring current (Akasofu and Chapman 1964; Cahill 1966), though one must be careful to take into account the contribution of the field-aligned current (Ohtani et al. 2007a).

2. *In-situ measurements of energetic particles*. The plasma pressure (energy density of plasma) distribution has been observed (e.g., Frank 1967; Smith and Hoffman 1973; Lui et al. 1987; Spence et al. 1989; De Michelis et al. 1997; Milillo et al. 2001, 2003; Korth et al. 2000; Ebihara et al. 2002; Lui 2003). The observed pressure is always underestimated because of the finite energy window of the instrument used to measure particles.
3. *In-situ measurements of the magnetic fields induced by the ring current* (Cahill 1966; Sugiura et al. 1971; Hoffman 1973; Terada et al. 1998; Lui 2003; Le et al. 2004; Vallat et al. 2005; Ohtani et al. 2007a).
4. *Remote sensing of energetic neutral atoms (ENAs) emitted from the ring current* (Jorgensen et al. 1997; Pollock et al. 2001; Brandt et al. 2004; Ohtani et al. 2006; Scime et al. 2002).

On average, the plasma pressure (or the energy density) is fairly symmetric during geomagnetically quiet times (De Michelis et al. 1999; Ebihara et al. 2002; Lui 2003). The plasma pressure (or the energy density) becomes asymmetric during high *AE* (De Michelis et al. 1999), low *Dst* (Ebihara et al. 2002), and high K_p (Lui 2003) periods. The H^+ pressure is the highest in the dusk-midnight sector (Lui 2003). Ebihara et al. (2002) found that the degree of the pressure asymmetry depends on the storm phase. During the storm main phase, the energy density of H^+ shows an increase on the nightside and a decrease on the dayside (Ebihara et al. 2002, 2004a). During the storm recovery phase, the energy density evolves in the opposite direction and becomes asymmetric. The same tendency has been observed by in-situ particle measurements (Stüdemann et al. 1987; Korth et al. 2000) and by ENA measurements (Brandt et al. 2002a).

On average, the anisotropy of the plasma pressure ($A = P_\perp/P_\parallel - 1$) is large on the dayside (or inner region), and small on the nightside (or outer region) (Lui et al. 1994; De Michelis et al. 1999). At midnight, the anisotropy index A is ~2, ~1, and ~0.5 at $L = 3$, 4, and 6, respectively (Lui et al. 1994). Thus, the second term in Eq. (9.1) is important when one evaluates the intensity and force balance of the ring current (Lui et al. 1987, 1994; De Michelis et al. 1999). The pitch angle distribution depends on L and energy (Lyons 1977; Collin et al. 1993; Ganushkina et al. 2005; De Benedetti et al. 2005; Ebihara et al. 2008a).

Tinsley (1981) predicted the existence of a secondary ring current belt that results from ENAs that travel from the core of the ring current. Years later, Søraas et al. (2003) and Sørbø et al. (2006) observed an inner belt of ring current during magnetic storms by using data from the low-altitude satellite NOAA. They termed this inner belt the Storm-Time Equatorial Belt (STEB). The STEB appears at an extremely low L-value near the magnetic equator. Convective transport cannot account for the formation of the STEB. It is plausible that the STEB results from ENAs traveling earthward from the core of the ring current without any influence by the magnetic field. The ENAs can become ions through charge exchange with dense neutral hydrogen and oxygen.

It should be noted that the ring current does not perfectly encircle the Earth as might inferred from the name. The plasma pressure distribution is not axisymmetric with respect to Earth's dipole moment. The asymmetry of the pressure distribution results in uneven current density of the ring current. The rest of the current is thought to flow into/away from the ionosphere along a field line, called field-aligned currents. The electric currents that might be associated with ring current are drawn in Fig. 9.4.

9.4.3 Transport and Acceleration of Ring Current Particles

9.4.3.1 Convection

A long-lasting main phase of magnetic storms is associated with a prolonged southward IMF (Kokubun 1972), which results in the enhancement of the large-scale convection (Dungey 1961; Baumjohann and Haerendel 1985; Weimer 2001, 2005; Matsui et al. 2008). A large-scale, dawn-to-dusk convection electric field conveys charged particles from the near-Earth plasma sheet to the dayside magnetopause (Kavanagh et al. 1968). As the particles drift earthward, they gain kinetic energy in order to conserve the first two adiabatic invariants. The first and second adiabatic invariants (μ and J) are respectively expressed as (Roederer 1970)

$$\mu = \frac{p_\perp^2}{2m_0 B} \tag{9.4}$$

$$J = \oint p_{||} dl \tag{9.5}$$

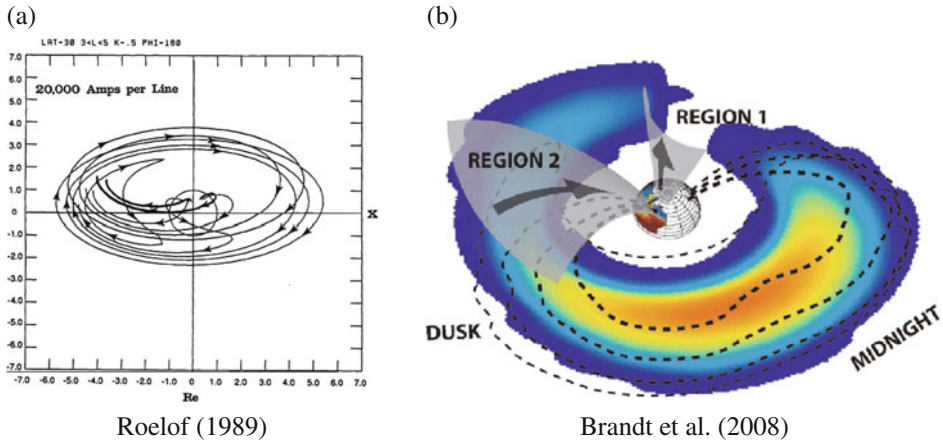

Fig. 9.4 (**a**) Global electric current lines deduced from model ring current pressure distribution (Roelof 1989), and (**b**) ring current plasma pressure deduced from energetic neutral atom observation and possible field-aligned current generated by the plasma pressure (Brandt et al. 2008)

where m_0 is the rest mass, p is the momentum, and dl is a line element along a field line. If the magnetic field is the dipole, the kinetic energy will be proportional to L^{-3} for an equatorial pitch angle of 90° and to L^{-2} for an equatorial pitch angle of 0° (Ejiri 1978). The ions tend to drift westward due to grad-B and curvature drifts as they gain kinetic energy. As a consequence, the plasma pressure (or the energy density) of ions is increased in the premidnight sector. The convection electric field also conveys the preexisting particles on the dayside to the dayside magnetopause, resulting in the decrease in the plasma pressure in the prenoon sector (Ebihara et al. 2002). The increase in the pressure in the dusk-midnight sector and the decrease in the pressure in the prenoon sector results in an asymmetric distribution of the plasma pressure, namely "asymmetric ring current." The global evolution of the asymmetric distribution was measured by IMAGE/HENA (Brandt et al. 2002a).

It has been confirmed that enhancements of the convection electric field can reasonably account for observations regarding the morphology of the ring current, ion flux enhancements, and observed variations in the *Dst* (Ejiri et al. 1980; Roeder et al. 1999; Korth et al. 2000; Brandt et al. 2002b; Ebihara et al. 2004; Miyoshi and Kataoka 2005; Burke et al. 2007), and numerical simulations (Wolf et al. 1982; Fok et al. 1996; Kozyra et al. 1998a; Ebihara and Ejiri 1998, 2000, Jordanova et al. 1999; Liemohn et al. 1999, 2001; Brandt et al. 2002b; Garner et al. 2004; Ebihara and Fok 2004; Liemohn et al. 2005). During the super storm of November 2003, the intensified convection electric field could account for the ion injection deep into $L = 1.5$ (Ebihara et al. 2005a).

When the convection electric field becomes weak during a storm's recovery phase, these particles tend to drift azimuthally, resulting in symmetric distribution of the plasma pressure, namely "symmetric ring current" (Korth et al. 2000; Ebihara et al. 2002).

The rate of increase of kinetic energy due to the electrostatic field is given by $q\mathbf{V}\cdot\mathbf{E}$, where q is charge, $\mathbf{V}$ is the drift velocity, and $\mathbf{E}$ is the electric field. The upper limit of the particle energy to be accelerated is determined by the total electric potential imposed on the magnetosphere. The cross polar cap potential, which is a measure of the net electric potential, shows saturation for a large solar wind electric field (Reiff et al. 1981; Wygant et al. 1983; Siscoe et al. 2002; Ober et al. 2003; Hairston et al. 2005). DMSP satellite measurements indicate that the saturation limit of the cross polar cap potential was about 260 kV for the severe storms of October–November 2003 (Hairston et al. 2005). This saturation is thought to have resulted from the Region 1 field-aligned current (Siscoe et al. 2002), ionospheric conductance (Merkin et al. 2005), the impedance mismatch between the solar wind and ionosphere (Kivelson and Ridley 2008), and a current-limited voltage generator (Borovsky et al. 2009). Lopez et al. (2009) have proposed a mechanism that explains the nonsaturated behavior of the ring current intensification under a saturated condition of the polar cap potential.

The details of structure and generation mechanism of the electric field in the inner magnetosphere remain controversial. The electric field measured near the plasmapause is highly variable and its amplitude increases with magnetic activity (Maynard et al. 1983). When averaged, the electric fields are qualitatively in agreement with ionospheric observations (Maynard et al. 1983; Baumjohann and Haerendel 1985; Rowland and Wygant 1998; Matsui et al. 2008). The cause of fluctuations in the electric fields in the inner magnetosphere has not yet been determined. Hori et al. (2005) have pointed out that no systematic increase was found in plasma sheet electric fields (>9 Re) during a storm's main phase. Their result may introduce ambiguity to the idea that enhanced convection conveys the plasma sheet particles into the inner magnetosphere during the main phase of a storm. A large spike in the amplitude of the poleward electric field has frequently been observed in the magnetosphere at subauroral latitudes (e.g., Maynard et al. 1980) and is described in detail in Section 9.4.6.1.

The response time of the inner magnetospheric convection electric field to the solar wind electric field is also uncertain. On the basis of their observation of plasmaspheric erosion, Goldstein et al. (2003a) obtained a response time of ~30 min. They suggested that the propagation time from the magnetopause to the ionosphere takes ~3–15 min, followed by ~10–25 min for complete reconfiguration of the ionospheric convection. Kikuchi et al. (1996, 2008) have shown that the dawn-to-dusk convection electric field is "immediately" transmitted from the polar ionosphere to the equatorial ionosphere. This suggests that reconfiguration of the ionospheric convection can be accomplished quickly, at the speed of light, by the TM_0 mode waves in an Earth-ionosphere waveguide (Kikuchi et al. 1978).

9.4.3.2 Substorm

Impulsive enhancements of particle fluxes have frequently been observed near geosynchronous orbit (Konradi et al. 1967; DeForest and McIlwain 1971; McIlwain 1974) and inside the geosynchronous orbit (Reeves et al. 1996; Ohtani et al. 2007b). These enhancements are associated with substorms that are identified by ground magnetic fields (Konradi et al. 1967; DeForest and McIlwain 1971; Kamide and McIlwain 1974). Because of the sudden appearance of particles, this phenomenon is called a "substorm injection."

A "substorm injection" that is not accompanied by energy dispersion is called a "dispersionless" injection. Such an injection has been observed at least at $4 \leq L \leq 8$ (Friedel et al. 1996). After injection, a cloud of the injected particles begins to display energy dispersion due to drift velocities, depending on its energy (DeForest and McIlwain 1971). Mauk and McIlwain (1974) specified a zero-energy boundary of the injected cloud at the geosynchronous orbit, and found that the location of the boundary depends on MLT and K_p. They suggested a spiral-shaped boundary of injection, called an injection boundary. Konradi et al. (1975) extended the injection boundary to the morning quadrant by reflecting the spiral-shaped evening boundary about the midnight meridian. As a consequence of the reflection, the injection boundary has a dented form, shaped somewhat like the Arabic numeral "3". Following the study of Konradi et al., this 3-shaped boundary is commonly referred to as an injection boundary (e.g., Mauk and Meng 1983; Lopez et al. 1990; Reeves et al. 1996). However, the existence of the 3-shaped boundary is still a controversial subject. Zhang et al. (2009) simulated a plasma bubble ejected by a substorm and demonstrated that the inner edge of the plasma sheet has a 3-shaped boundary.

A "substorm injection" is thought to be caused by the relaxation of the magnetic field associated with a substorm (Walker et al. 1976). In the course of such relaxation (dipolarization), a strong dawn-dusk induction electric field was observed (Aggson et al. 1983). A 2-min envelope of the dawn-dusk electric field having an amplitude of 30 mV/m correlates with that of the inductive fields of the collapsing magnetic field. Low-frequency (t~10 s) and high-frequency ($t < 1$ s) wave variations were also present throughout the event.

At geosynchronous altitude, the ion temperature increases significantly, while the ion density remains almost constant during the course of a substorm (Birn et al. 1997a). This quite likely suggests that the particles are significantly accelerated. A test particle simulation performed in the three-dimensional MHD field showed that ions with an energy >20 keV are accelerated by the cross-tail electric field under nonadiabatic motion during dipolarization (Birn et al. 1997b). Particles can also be accelerated by a parallel component of the induction electric field (Quinn and Southwood 1982), and by magnetic field fluctuations

having frequencies that are close to the gyrofrequencies of the ions (Ono et al. 2009). The test particle simulation performed by Birn et al. (1997b) showed that ions with an energy <20 keV are not effectively accelerated by this process because the $E \times B$ drift dominates the cross-tail drifts. A substorm-associated dipolarization event probably results in both a local acceleration (as was observed by Lopez et al. 1990) and the inward transport of particles (as was observed by DeForest and McIlwain 1971; Mauk and McIlwain 1974). Sergeev et al. (1998) have emphasized that one can observe an increase, a decrease, or no variation of flux after a substorm, and that particle flux variation depends on the energy and radial flux gradient.

The net result of a "substorm injection" on the ring current is still being debated. Mitchell et al. (2003) observed intensifications of H^+ and O^+ immediately following substorms. H^+ and O^+ were not simultaneously enhanced, suggesting that a mass-dependent acceleration process probably takes place. Simulations have shown that a substorm results in net intensification of the ring current (Fok et al. 1999; Zhang et al. 2009). Further observations and simulations are awaited that will quantitatively evaluate the overall influence of a substorm on the development of the ring current.

9.4.3.3 Compression of Magnetosphere

Sometimes the magnetosphere is compressed by an abrupt enhancement of the solar wind dynamic pressure prior to the main phase of a storm. This is called storm sudden commencement (SSC), which is followed by a storm's initial phase. Due to magnetospheric compression, ions having an energy between keV and hundreds-of-keV are increased by ~25–40% due to adiabatic energization (Lee et al. 2007). Due to an azimuthal induction electric field (Shinbori et al. 2004), preexisting particles are expected to drift in the radial direction. The magnetospheric state established in the initial phase may also play an important role in the subsequent development of the ring current during the main phase of a storm.

9.4.3.4 Wave-Particle Interaction

EMIC waves can be excited by cyclotron resonant instability with anisotropic ring current H^+, leading to heavy ion heating perpendicular to the ambient magnetic field (e.g., Gendrin and Roux 1980; Anderson and Fuselier 1994; Thorne and Horne 1994; Horne and Thorne 1997). This process may be efficient when the concentration of O^+ is significantly enhanced, and contribute to the observed acceleration of O^+ up to the ring current energy. Recently, Pickett et al. (2010) found the triggered emission of EMIC waves in the inner magnetosphere. Omura et al. (2010) developed a nonlinear wave growth theory of this triggered emissions, which may cause efficient acceleration of ions in the inner magnetosphere.

9.4.4 Source of Ring Current Particles

The importance of the number density in the plasma sheet has been suggested based on observations (Thomsen et al. 1998; Smith et al. 1999; Liemohn et al. 2008), and simulations (Chen et al. 1994; Kozyra et al. 1998b; Ebihara and Ejiri 1998, 2000; Kozyra and Liemohn 2003; Ebihara et al. 2005a). In stronger storms, the plasma sheet density at geosynchronous altitude becomes high (Liemohn et al. 2008). In super storms, on average, density peaks appear 9 h before the storm peak, and around the storm peak. For the super storm of November 20, 2003, the enhancement of the plasma sheet density around the storm peak is necessary in order to account for the large development of the ring current (Ebihara et al. 2005a).

On average, the plasma sheet density is fairly well correlated with the solar wind density (Terasawa et al. 1997; Borovsky et al. 1998; Ebihara and Ejiri 2000). Terasawa et al. (1997) found that the plasma sheet becomes dense and cold when the IMF is northward. The best correlations between the plasma sheet parameters and the IMF are obtained when the solar wind density is averaged over 5–12 h prior to the plasma sheet observations. For given plasma pressure in the plasma sheet, cold-dense plasma sheet results in deeper penetration of the plasma sheet ions (Garner 2003; Lavraud and Jordanova 2007). At geosynchronous altitude, the density is usually 0.4–2 cm^{-3}, though it sometimes exceeds 2 cm^{-3} (Borovsky et al. 1997; Thomsen et al. 2003; Lavraud et al. 2005). This is called a super dense plasma sheet. A hot and super dense plasma sheet is detected at geosynchronous orbit for ~20 h following the convection onset that is led by high-speed coronal hole streams (CHS) (Denton and Borovsky 2008).

Some entry processes from the solar wind into the magnetosphere have been suggested; magnetic

reconnection near the subsolar point under a southward IMF (Dungey 1961), double lobe reconnection under a northward IMF (Song and Russell 1992; Song et al. 1999), diffusive entry (Terasawa et al. 1997; Fujimoto et al. 1998), Kelvin-Helmholtz instability (Hasegawa et al. 2004), and cusp entry (Fritz et al. 2003). Once it has entered, the plasma is transported to the inner magnetosphere by the convection electric field through the plasma sheet (Spence and Kivelson 1993), eddy diffusion (Borovsky et al. 1998), and convection through the lobe (Ebihara et al. 2009a).

The Earth's ionosphere is also a significant source of ring current particles, as evidenced by in-situ observations of O^+ in the heart of the ring current (Lundin et al. 1980; Lennartsson et al. 1981; Krimigis et al. 1985; Hamilton et al. 1988; Daglis et al. 1999; Pulkkinen et al. 2001). At least three distinct time scales for the supply of O^+ have been determined: ~10s of minutes (Daglis and Axford 1996; Daglis et al. 2000; Mitchell et al. 2003), ~days (Hamilton et al. 1988; Daglis et al. 1999), and ~years (Young et al. 1982; Pulkkinen et al. 2001; Greenspan and Hamilton 2002).

On a short time scale (~10s of minutes), the variation of O^+ ions is associated with a substorm expansion. This variation may be attributed to a rapid supply of ions from the ionosphere to the equatorial plane (Daglis and Axford 1996), or to a localized energization of preexisting ions (Mitchell et al. 2003). Mitchell et al. (2003) stressed that the rapid enhancement of O^+ just after substorms cannot be explained by a rapid supply from the ionosphere. Trajectory tracing of O^+ predicts that it usually takes ~1–2 h to reach the equatorial plane from the ionosphere (Cladis and Francis 1992). Nosé et al. (2009a) have presented observational evidence that during magnetic storms, the O^+ outflow commences in the topside ionosphere within several minutes immediately following a substorm, and that subsequently, O^+ is increased in the near-Earth plasma sheet on a time scale of 1 h.

The medium time-scale (~days) variation is associated with a magnetic storm. During magnetic storms, O^+ ions are enhanced in the ring current (Krimigis et al. 1985; Hamilton et al. 1988; Daglis et al. 1999; Pulkkinen et al. 2001). The O^+ concentration is also increased in the plasma sheet (Lennartsson and Sharp 1982), which can be attributed to an enhancement of the auroral and polar outflow of O^+ (Yau et al. 1985a; Abe et al. 1996). In situ observations have suggested that O^+ can be directly introduced from the ionosphere into the inner magnetosphere during magnetic storms (Kaye et al. 1981; Sheldon et al. 1998; Yao et al. 2008).

The long time scale (~years) variation is associated with the solar cycle. Outflowing O^+ from the topside ionosphere is increased with $F_{10.7}$ (Yau et al. 1985b). O^+ concentration is also increased with increasing $F_{10.7}$ in the plasma sheet in the energy 0.1–16 keV/e (Lennartsson et al. 1989) and 9.4–212.1 keV/e (Nosé et al. 2009b).

Ebihara et al. (2006) emphasized the importance of the thinness of the current sheet in transporting O^+ from the ionosphere to the inner magnetosphere. When outflowing O^+ first encounters the current sheet, it moves in a meandering path and undergoes nonadiabatic acceleration in the current sheet where the gyroradius is close to the curvature radius of a field line (Sergeev et al. 1983; 1993). When the current sheet is thick, the O^+ gains more energy and undergoes grad-B and curvature drifts. When energized too much, O^+ is difficult to drift earthward by the $E \times B$ drift (Ebihara and Ejiri 2000; Garner 2003; Lavraud and Jordanova 2007). In order to effectively supply O^+ from the current sheet to the inner magnetosphere, a thin current sheet and strong convection are needed (Ebihara et al. 2006). During magnetic storms, the magnetic field is stretched further (Ohtani et al. 2007a) and the current sheet becomes thin (Sitnov et al. 2008). The storm-time current sheet structure would help the O^+ efficiently propagate into the inner magnetosphere.

9.4.5 Loss of Ring Current Ions

9.4.5.1 Charge Exchange

A fast ion captures an electron from a neutral atom to become a fast neutral atom. In the neutral state, a fast atom becomes free of any control by a magnetic field, as has been observed by the IMAGE satellite (e.g., Mitchell et al. 2003). The charge exchange occurs frequently in the region where there is a high concentration of neutral atoms. In the topside ionosphere, oxygen atom is the dominant neutral species. With increasing altitude, hydrogen becomes dominant (Rairden et al. 1986). The number density of neutral hydrogen is ~500–1000 cm^{-3} at 3 Re, and ~50–100 cm^{-3} at 6 Re (Rairden et al. 1986; Østgaard et al. 2003). The cross sections for the charge exchange have been

suggested by Janev and Smith (1993) for the H^+–H reaction, by Barnett (1990) for the He^+–H reaction, and by Phaneuf et al. (1987) for the O^+–H reaction. Because the geocoronal hydrogen is dense at a low altitude, ions with small equatorial pitch angles readily undergo charge exchange. Smith and Bewtra (1976) suggest that the bounce-averaged lifetime is as follows:

$$\langle \tau \rangle = \frac{\cos^{3.5\pm0.2}\lambda_m}{n_H v \sigma_{ch}}, \tag{9.6}$$

where $<\tau>$, n_H, v, σ_{ch}, and λ_m are the bounce-averaged lifetime, neutral hydrogen density in the equatorial plane, velocity of the ion, charge exchange cross section, and mirror latitude, respectively. The lifetime of H^+ is shorter than that of O^+ for energy less than 45 keV, while it is longer than that of O^+ for energy greater than 45 keV (Fok et al. 1991).

Ebihara and Ejiri (2003) calculated the ring current evolution during weak magnetic storms, and showed that the *Dst* variation is well explained by the ring current simulation with the charge exchange loss. When the charge exchange loss is excluded, the *Dst* variation is obviously different from that observed.

Hamilton et al. (1988) demonstrated a rapid recovery of *Dst* (*e*-folding time scale of ~9.3 h) and a rapid decay of O^+ ions (30–310 keV/e) during the intense storm of February 1986. They suggested that the rapid decay of O^+ could be attributed to the short charge exchange lifetime of O^+. The two-step recovery of *Dst* can be attributed to the rapid decay of O^+ followed by the slow decay of H^+. Fok et al. (1995) simulated the ring current during the February 1986 storm and encountered a problem in the interpretation of the rapid recovery of *Dst*. Kozyra et al. (1998a) pursued the rapid recovery, and suggested that, in addition to charge exchange, precipitation loss plays an important role in the ion loss.

9.4.5.2 Coulomb Drag

Ions are decelerated by Coulomb collisions with thermal plasma. This is called Coulomb drag. The decay rate has been formulated by Fok et al. (1991) and Jordanova et al. (1996). The Coulomb drag results in redistribution of the ions in the velocity space, and it enhances the low-energy ion precipitating fluxes inside the plasmasphere (Jordanova et al. 1996). The kinetic energy of the ions is transferred to the thermal electrons (Kozyra et al. 1987) and to the ionosphere, contributing emissions at 630 nm. The resultant glow of these emissions manifests in what are termed stable auroral red (SAR) arcs (Cole 1965; Kozyra et al. 1997). Coulomb drag is insignificant in ring current decay because the loss rate is much smaller than that of the charge exchange at energy >10 keV (Fok et al. 1991) and because the plasmasphere shrinks during magnetic storms.

9.4.5.3 Coulomb Scattering

Ions are scattered by Coulomb collisions with thermal plasma and are precipitated into the ionosphere in what is called Coulomb scattering. Jordanova et al. (1996) found that, in general, the decay rates are small. The decay rates due to Coulomb scattering are much smaller than those due to Coulomb drag by two orders of magnitude.

9.4.5.4 Wave-Particle Interaction

Ions are scattered by the EMIC waves (e.g., Cornwall et al. 1970; Summers 2005; Summers et al. 2007) that are frequently observed in the inner magnetosphere (e.g., Anderson et al. 1992; Mursula et al. 2001; Engebretson et al. 2007). EMIC waves are primarily caused by the temperature anisotropy of ions with an energy of 10–50 keV (Cornwall 1977). Such temperature anisotropy can be easily established by the charge exchange as represented by Eq. (9.6), as well as by convective transport. Jordanova et al. (1997) calculated the growth of EMIC waves and the evolution of the ring current with pitch angle diffusion due to wave-particle interaction. They found that EMIC waves are readily developed near the plasmapause on the duskside, resulting in scattering of the ions. The localized precipitation of ions results in the proton auroral emission associated with plumes, and is remotely monitored by an auroral imager onboard the IMAGE satellite (Fuselier et al. 2004; Spasojevic et al. 2005; Jordanova et al. 2007).

Thorne and Horne (1997) showed that the EMIC waves are absorbed efficiently at high magnetic latitudes via cyclotron resonant interactions with energetic O^+. When the fractional composition of ring current O^+ exceeds 60%, cyclotron absorption by resonant O^+ can become so severe to totally suppress wave excitation. The storm-time development of the ring current may be modulated by the relative composition of energetic O^+ through resonant interaction with EMIC waves.

9.4.5.5 Adiabatic Loss Cone Loss

When ions drift earthward, their equatorial pitch angle shifts toward 90° due to the conservation of the first two adiabatic invariants. The loss cone angle is also rapidly widended as the ions drift earthward, so that ions with a small pitch angle encounter the loss cone at a certain L-value without any pitch angle scattering (cf., figure 9 of Ebihara and Ejiri 2003). This is called adiabatic loss cone loss. Jordanova et al. (1996) have suggested that adiabatic loss cone loss is sufficient to explain the ion precipitation observed by satellites. Ebihara and Ejiri (2003) precisely calculated the precipitating ion flux and found that the energy flux of the precipitating flux is much smaller than that observed by the DMSP satellite. The calculated loss rate of the ring current due to the adiabatic loss cone loss is ∼1–2% for a weak storm. The importance of the adiabatic loss cone loss is yet to be conclusively determined.

9.4.5.6 Violation of First Adiabatic Invariant

The first adiabatic invariant of ions is no longer conserved when the ions are situated in a stretched magnetic field line. The pitch angle is scattered and the ions are precipitated into the ionosphere when the first adiabatic invariant is violated. The characteristics of such scattering due to field line curvature (FLC) have been theoretically studied (Sergeev et al. 1983; Büchner and Zelenyi 1989; Delcourt et al. 1996). The FLC scattering is thought to be responsible for the global precipitation of ions with a pitch angle distribution that is almost isotropic (Sergeev et al. 1993). The equatorward edge of the isotropic precipitation is called the isotropic boundary (IB), whose latitude, they suggest, is a manifestation of the stretching of the magnetic field on the nightside.

9.4.5.7 Magnetopause Loss

When ions encounter the magnetopause, they are thought to escape from it (Möbius et al. 1986; Zong and Wilken 1999; Christon et al. 2000; Keika et al. 2004). Herein, we refer to two types of magnetopause loss of ring current particles. In Type 1, the plasma sheet density suddenly decreases on the nightside. In Type 2, the dayside magnetopause shrinks.

Type 1. Liemohn et al. (2001) calculated the evolution of the ring current by changing the convection electric field and suggested that most of the ions that constitute the ring current during the storm main phase have open drift paths. This implies that under a strong convection electric field, the ions are injected from the plasma sheet on the nightside and ejected to the dayside magnetopause. The compensation between the inflow and the outflow determines the budget of the total energy of particles within the inner magnetosphere, that is, the ring current. When the plasma sheet density abruptly decreases, this change is transmitted sunward so that the total energy of the particles decreases (Ebihara and Ejiri 1998, 2003; Liemohn et al. 2001; Jordanova et al. 2003). The transit time involved depends entirely on the strength of the convection electric field. When the plasma sheet density and the convection electric field simultaneously decrease, the transit time will be very long and the change in the plasma sheet density is not effectively transmitted into the inner magnetosphere because the last-closed equipotential is expanded (Ejiri 1978). In the case of Type 1, the degree of loss depends on the plasma sheet density on the nightside and the strength of the convection electric field.

Type 2. Keika et al. (2004) have shown that the energetic ions originating from the magnetosphere are frequently observed outside the magnetopause during magnetic storms. The energy flux of outflowing ions is well correlated with the square root of the solar wind dynamic pressure, rather than the solar wind electric field (Keika et al. 2005). The energy flux of outflowing ions during the recovery phase is comparable to that during the main phase. Keika et al. (2005) have suggested that the magnetospheric ions are lost due to magnetic drift, rather than the $E \times B$ drift. In the case of Type 2, the degree of the loss depends on the standoff distance of the dayside magnetopause.

9.4.6 Influence on Other Regions and Other Energy Regimes

9.4.6.1 Ring Current-Ionosphere Coupling

The electric current (ring current) cannot be completely closed in the inner magnetosphere. Vasyliunas (1970) and Wolf (1970) have suggested the following conceptual framework regarding the closure of the electric current. The convection electric field conveys hot plasma into the inner magnetosphere, and enhances the plasma pressure. A remnant of the current must flow into/away from the ionosphere along a field line to complete the closure. To conduct away the space charge deposited by the field-aligned current,

an additional electric field must be developed in the ionosphere. This electric field is fed back into the magnetosphere, affecting the $E \times B$ drift velocity of the trapped particles. Thus, the electric field induced by the ring current potentially influences the dynamics of the inner magnetosphere.

The ring current tends to generate a downward (magnetosphere to ionosphere) field-aligned current on the duskside, and an upward (ionosphere to magnetosphere) current on the dawnside. This current system resembles the Region 2 field-aligned current (Iijima and Potemra 1976). The direction of the resultant electric field is eastward on the nightside, which is opposite to that of the convection electric field. Thus, the resultant electric field is called a shielding electric field, whose existence has been supported by ground-based observations (Fejer et al. 1979; Kelley et al. 1979; Spiro et al. 1988; Kikuchi et al. 2008, 2010; Ebihara et al. 2008c). An overshielding condition can be established immediately following an abrupt decay of the Region 1 current (Spiro et al. 1988; Peymirat et al. 2000; Ebihara et al. 2008c), an abrupt decay of the aurora oval (Ebihara et al. 2004), or an abrupt contraction of the auroral oval (Kikuchi et al. 2008), because the ring current-associated field-aligned current cannot decay as quickly as the Region 1 current.

The shielding electric field may elongate the pattern of the duskside convection cell toward the equatorward of the dawnside convection cell. The resultant convection cell resembles the Harang discontinuity (Erickson et al. 1991; Ebihara et al. 2005a; Gkioulidou et al. 2009). During a storm, the ring current intensifies and the elongation is further developed. Finally, a flow reversal on the dawnside develops (Ebihara et al. 2005a), which was observed by a satellite (Ebihara et al. 2005a) and by HF radar (Kataoka et al. 2007) at subauroral latitudes. It appears that a strong westward electric field is established near the eastern edge of the flow reversal, resulting in the intensification of the tens-of-keV proton fluxes in the inner magnetosphere (Fok et al. 2001; Ebihara and Fok 2004). Such unusual dawnside enhancements of tens-of-keV proton fluxes were first confirmed by IMAGE satellite observations (Brandt et al. 2002b). It has also been suggested that the shielding electric field impedes the development of the ring current (Ebihara et al. 2005b). The intensity of the ring current was previously thought to be simply proportional to the plasma sheet density (N_{ps}) (Chen et al. 1994; Ebihara and Ejiri 1998, 2000; Liemohn et al. 2001), but the shielding may result in the intensity being proportional to the square root of N_{ps} (Ebihara et al. 2004). The degree of the impediment may depend upon the conductivity (Spiro and Wolf 1984; Ebihara et al. 2004).

In the premidnight sector, the downward Region 2 current tends to flow into the ionosphere equatorward of the auroral oval. The upward Region 1 current tends to flow away from the auroral oval. A poleward electric field is then established on the duskside to complete the closure of the Region 1 and Region 2 currents. The conductivity is high in the auroral oval due to the precipitation of energetic particles, while the conductivity is low in the subauroral region. The poleward electric field is strengthened in the subauroral region because of low conductivity, resulting in a rapid, westward plasma flow in the subauroral region (Anderson et al. 1993). This phenomenon has been described by various terms: Polarization Jet (PJ) (Galperin et al. 1973), SubAuroral Ion Drift (SAID) (Spiro et al. 1979), Drift Spike (DS) (Unwin and Cummack 1980), SubAuroral Electric Field (SAEF) (Maynard et al. 1980; Karlsson et al. 1998), and SubAuroral Polarization Stream (SAPS) (Foster and Vo 2002). PJ, SAID, and DS probably refer to a subregion of SAPS.

Data from the DMSP satellites showed that the latitude of the SAPS channel decreases with a decrease in the *Dst* index, suggesting that the SAPS is related to the ring current (Huang and Foster 2007). Seasonal variations in the SAPS have also been noted. There is a strong correlation between the subauroral integrated conductivity and the latitude of the SAPS channel, and there is a strong anticorrelation between the conductivity and the SAPS velocity (Wang et al. 2008). This suggests that the SAPS is a part of the current system caused by a current generator. The SAPS is intensified after a substorm following a delay of >30 min (Anderson et al. 2001), ~10 min (Mishin and Puhl-Quinn 2007), and ~30 s (Nishimura et al. 2008). If a substorm results in a localized enhancement of the plasma pressure, a blob of the plasma pressure will travel inward under the influence of the convection electric field, enhancing the SAPS speed. When this is the case, the delay time can be explained by the traveling time between the source and the observation point. Quasi-periodic variations in the speed of the SAPS have been observed during a time of disturbance (Foster et al. 2004b; Ebihara et al. 2009b), and these may be interpreted in terms of structured, multiple ring currents moving earthward (Ebihara et al. 2009b). Different types of subauroral flows have recently been

reported. One study reported is that a westward flow is sandwiched in between eastward flows, a configuration which was termed a mirror eastward flow channel (Makarevich et al. 2009). A rapid, eastward plasma flow was also found, which was termed an abnormal SAID (Voiculescu and Roth 2008).

9.4.6.2 Ring Current-Thermosphere Coupling

In the course of the precipitation of energetic protons deep into the atmosphere, the protons undergo electron capture, neutral excitation, and electron loss processes. The hydrogen atoms can be left in an excited state so that Lyman, Balmer, or other H series may be radiated (Vallance Jones 1974). The proton aurora is thus considered to be a direct manifestation of proton precipitation from the magnetosphere. A patch of proton aurora in the subauroral region was first observed by Ono et al. (1987). A similar patch was also observed together with intensification of geomagnetic ULF waves that manifest in bursts, the so-called Pc 1 pulsations (Sakaguchi et al. 2007, 2008, Yahnin et al. 2007; Yahnina et al. 2008). The close relationship between the proton auroral spot and the bursts of Pc 1 pulsations implies that the source of the proton precipitation is probably the EMIC waves excited in the ring current. This excitation of the EMIC waves is stimulated by compression of the dayside magnetosphere (Zhang et al. 2008; Yahnina et al. 2008; Usanova et al. 2008) and convective transport (Jordanova et al. 1997), which causes temperature anisotropy or some other instabilities. Jordanova et al. (2006, 2007) simulated the growth rate of the EMIC waves with the evolving ring current H^+, O^+, and He^+ ion distributions. The global distribution of the simulated proton precipitation is similar to that of the proton aurora taken by IMAGE/FUV.

Hardy et al. (1989) have documented the global distribution of precipitating ions. The hemispheric energy input from the ions is 11–17% of that from the electrons. The precipitating ions, however, are the major source of ionization and conductance in the evening sector (Senior et al. 1987; Senior 1991; Galand and Richmond 2001), along with Joule heating, an increase in the *E* and *F* region temperature, and strong neutral winds in the lower thermosphere (Galand et al. 2001).

The ENAs emitted from the ring current are suggested to strike the thermosphere and cause the ionization at low latitudes. Rowe (1974) presented the observation that the electron density in the nightside *E* region at Arecibo was significantly enhanced during magnetic storms. Precipitating ENAs may be sufficient to account for the electron density enhancement (Lyons and Richmond 1978). Spectrographic photometers onboard TIMED detected anomalous auroral emissions from the nightside thermosphere at low latitudes during intense magnetic storms (Zhang et al. 2006). The brightness of these anomalous emissions is correlated with $|Dst|$. Zhang et al. (2006) suggest that the source of the anomalous emissions is ENAs.

9.4.6.3 Ring Current-Plasmasphere Coupling

The ring current interacts with the plasmasphere both directly and indirectly. Theoretically, the inner edge of the ion plasma sheet and the plasmasphere can coexist in the "nose" energy dispersion structure (Ejiri et al. 1980; Kozyra et al. 1993). The kinetic energy of the ions is degraded by the Coulomb drag and transferred to the thermal plasma. The heat flux is then propagated to the topside ionosphere along a field line, resulting in a glow of emissions that are called SAR arcs (Cole 1965; Kozyra et al. 1987) (see Section 9.4.5.2). SAR arcs can last for ∼28 h (Craven et al. 1982) and can be a very bright (∼13 k Rayleighs) (Baumgardner et al. 2007).

The ring current induces additional electric fields in the ionosphere, known as SAPS and overshielding (Section 9.4.6.1). The deformation of the ionospheric electric field is transmitted to the magnetosphere, and is also thought to result in deformation of the plasmasphere (Goldstein et al. 2003c, 2004a).

9.4.6.4 Ring Current-Ring Current Coupling

The electric field deformed by the ring current can also deform the ring current itself. Post-midnight enhancements of tens-of-keV ions (Brandt et al. 2002b) can be explained by the electric potential deformed by the ring current (Fok et al. 2001; Ebihara and Fok 2004). The convection electric field is weakened by the ring current, and the strength of the ring current is no longer proportional to the plasma sheet density (Spiro and Wolf. 1984; Ebihara et al. 2004). For a detailed explanation, see Section 9.4.6.1.

Lyons and Williams (1976) have shown that during the main phase of a storm, the flux of the equatorially mirroring ions at >200 keV decreases. Lyons (1977) found that the pitch angle distribution of the ions shows a butterfly pattern having a minimum flux at a 90° pitch angle in association with a reduction in the equatorial

magnetic field. They have attributed the decrease in the 90° ions to adiabatic deceleration (betatron deceleration). Ebihara et al. (2008a) have demonstrated that during the main phase of a storm, the H^+ flux at >80 keV at pitch angles near 90° decreases, while the H^+ flux at near 0° and 180° increases. Ebihara et al. (2008a) have suggested that these variations can be explained by a combination of the betatron deceleration (due to a depression of the equatorial magnetic fields), and the Fermi acceleration (due to a shortening of the distance between mirror points). Zaharia et al. (2006) have predicted that the pressure anisotropy ($A = P_\perp/P_\parallel - 1$) is reduced mainly due to the Fermi acceleration under the magnetic field that is depressed by the ring current.

9.4.6.5 Ring Current-Radiation Belt Coupling

Relativistic trapped particles sometimes show an abrupt decrease during magnetic storms (McIlwain 1966; Williams et al. 1968), in what is called a *Dst* effect, or a ring current effect. The *Dst* effect may be understood, in part, as energy deceleration due to the betatron deceleration and radial displacement due to the conservation of the third invariant (Dessler and Karplus 1961). This process may be valid when the field deformation proceeds slowly enough (Northrop and Teller 1960). For a detailed explanation, see Section 9.6.4.1.

EMIC waves generated from the ring current ions cause pitch angle scattering of the radiation belt electrons (see Section 9.6.4.2), which is another example of ring current-radiation belt coupling. ULF waves driven by ring current ions also have an impact on the radial transport and energization of radiation belt electrons (Ozeke and Mann 2008).

9.5 Proton Radiation Belt

9.5.1 Time Variation of Proton Radiation Belt

The inner part of the proton belt, $L < 2.0$, is very stable. Secular changes in the Earth's magnetic field may gradually increase the proton intensity by a factor of 10 due to contacting drift shells (Selesnick et al. 2007). Therefore, the reduction of the Earth's intrinsic magnetic field exerts an impact upon the proton belt. During solar cycles, solar activity causes expansion of the scale height of upper atmosphere, and the collision rate increases at a low altitude. The proton flux shows solar cycle variations that are anti-correlated with solar activities (Miyoshi et al. 2000).

In the outer part of the proton belt ($L > 2$), dramatic variations have been observed, especially during strong interplanetary shocks. For example, during a record SSC event on March 24, 1991, a new proton belt was formed within just 3 min (Blake et al. 1992). A similar shock-associated enhancement of the proton belt was observed in 2003 (Looper et al. 2005).

9.5.2 Source and Loss of Relativistic Protons

It has been though that Cosmic Ray Albedo Neutron Decay (CRAND) is mainly responsible for energies >100 MeV protons. In CRAND, the cosmic ray flux on the atmosphere is backscattered as neutrons which decay into protons and electrons trapped in the inner magnetosphere. Solar protons during proton events are a source of protons of the radiation belt (Hudson et al. 1995, 2004; Kress et al. 2005). The inward transport of protons by radial diffusion is important for their acceleration (Albert et al. 1998; Jordanova and Miyoshi 2005). The dominant causes of loss of protons are Coulomb collisions with plasmaspheric thermal plasma and atmospheric absorption, which have been modeled in a three-dimensional Fokker-Planck simulation for the proton radiation belt (Beutier et al. 1995). The precipitation into the ionosphere due to the pitch angle scattering is also important.

In the outer part of the proton belt, shock-related compression of the magnetosphere can accelerate solar protons to energies of more than tens of MeV on timescales of tens of seconds (Hudson et al. 1995).

9.6 Electron Radiation Belt

9.6.1 Time Variation of Electron Radiation Belt

In the inner belt, the electron flux is usually stable, while the electron flux sometimes increases in association with large magnetic storms. During the strong SSC event on March 24, 1991, injections and drift echoes of

tens of MeV electrons were observed at $L = 2$ (Blake et al. 1992; Li et al. 1993; Gannon et al. 2005).

In the slot region and the outer belt, the electron flux shows dynamical time variations on various scales. Electron flux variations in the radiation belts are the result of achieving a balance between source (transport/acceleration) and loss processes (Reeves et al. 2003). Different processes for acceleration/transportation and loss occur simultaneously during storms (see figure 2 of Reeves 2007, and reviews Friedel et al. 2002; Millan and Thorne 2007; Shprits et al. 2008a, b, Hudson et al. 2008 and references therein).

9.6.1.1 Storm-Time Variations

Typically, the outer belt flux decreases/disappears during the main phase of a storm then returns to its prestorm level during the early recovery and recovery phases (e.g., Baker et al. 1986; Nagai 1988; Reeves et al. 2003; Miyoshi and Kataoka 2005; Li et al. 2005). The flux sometimes increases to a degree that is higher than its prestorm level. The typical time scale for the flux enhancement of the outer belt is a few days (Nagai 1988; Reeves et al. 1998), depending on the L-shell (e.g., Li et al. 1997; Vassiliadis et al. 2003, 2005), while it has been observed that rapid flux enhancement in the inner portion of the outer belt and in the slot region takes place within a few hours (Baker et al. 1998b; Nagai et al. 2006). As will be discussed later, the decrease and increase in the electrons of the outer radiation belt frequently occur not only in storms but also associated with solar wind disturbances.

Magnetic storms are caused by large scale interplanetary structures. Coronal Mass Ejections (CMEs) and Corotating Interaction Regions (CIRs) have intense electric fields that can drive magnetic storms, though there are several differences between CME- and CIR-driven storms (Borovsky and Denton 2006). CMEs have a strong magnetic field in the sheath as well as the ejecta and exert an interplanetary shock that causes the sudden commencement of the storm. CIRs have a strong magnetic field that is the interface between slow and fast streams, and they are followed in time by CHS. All intense storms ($Dst < -150$ nT) are driven by CMEs during solar cycle 23. Therefore, it is expected that the outer belt will respond differently to CME- vs. CIR-driven storms. Note that the outer belt flux variation is independent of the storm size as measured by the *Dst* index (Reeves et al. 2003). CIR-driven storms are more effective than CME-driven storms for the large flux enhancement of MeV electrons in the outer portion as well as at geosynchronous orbit (Miyoshi and Kataoka 2005). Large flux enhancements of MeV electrons occur at geosynchronous orbit in 80% of intense CIR-driven storms ($Dst < -100$ nT), and in ~50% of CME-driven storms (Kataoka and Miyoshi 2006). On the other hand, large flux enhancement in the inner portion and the slot region occur during CME-driven great-storms of Dst < –150 nT (Miyoshi and Kataoka 2005). These findings are consistent with the peak *L*-shell dependence on the storm amplitude (e.g., Tverskaya et al. 2003; O'Brien et al. 2003).

It is noteworthy that a large number of multiple storms occur during the solar maximum. The size of these multiple storms tends to be large and sometimes exceeds –400 nT (Kataoka and Miyoshi 2006). For example, the largest flux enhancement observed was in the inner portion and the slot region in the famous Halloween event, which occurred in October 2003 (Baker et al. 2004; Horne et al. 2005b; Loto'aniu et al. 2006). The largest flux enhancement during solar cycle 23 at geosynchronous orbit was observed in July 2004 during the recovery phase of intense multiple storms driven by a series of CMEs (Kataoka and Miyoshi 2008a, b). These multiple storms might not have any notable effect on the solar cycle variations of the outer belt since subsequent solar wind structures produce new variations in the outer belt. In the inner belt, however, long-lasting flux enhancements which persist for more than a few years have been observed following intense storms triggered by events such as those of March 1991 and October/November 2003 (Li and Temerin 2001; Looper et al. 2005).

9.6.1.2 Semiannual Variations

Besides variations ranging from a few days to a week, there are other timescales for flux variation of the radiation belts. During the solar declining phase, recurrent flux variations of 27 days and 13.5 days are significantly associated with the arrival of recurrent high-speed CHS. There are also semiannual variations in which the flux increases in the spring and autumn (Baker et al. 1999; Li et al. 2001; Miyoshi et al. 2004). The origin of this semiannual variation in the radiation belts is geomagnetic activities that are driven by the Russell-McPherron effect (Russell and McPherron 1973; Baker et al. 1999; Miyoshi et al. 2004).

9.6.1.3 Solar Cycle Variations

The outer belt and slot region vary with the solar cycle (Miyoshi et al. 2004; Li et al. 2006; Fung et al. 2006; Maget et al. 2007; Baker and Kanekal 2008). During the solar declining phase, the flux in the outer portion of the outer belt tends to increase in association with small storms (and also with no storms), while the flux in the inner portion of the outer belt and the slot region tends to decrease. During the solar active period, the flux tends not to increase in the outer portion, and vice versa in the inner portion. These long-term variations in each position correspond to long-term structural shifts of the outer belt; the outer belt moves outward during the solar declining phase and moves inward during the solar active period (Miyoshi et al. 2004). These long-term structural variations are the result of occurrence variations of CME-driven great storms and high-speed coronal hole streams. That is, CME-driven great storms tend to increase electrons in the inner portions, while CHS causes a large flux enhancement in the outer portion (Miyoshi and Kataoka 2005; Baker and Kanekal 2008).

In the inner belt ($L < 2$), energetic electrons increase during the solar active period at $L > 1.4$ (Abel et al. 1994; Miyoshi et al. 2004), while they decrease at $L < 1.3$ (Abel et al. 1994).

9.6.2 Response to Solar Wind and IMF

9.6.2.1 Solar Wind Speed

Solar wind speed is a primary driver of the large flux enhancement of the outer belt (e.g., Paulikas and Blake 1979). Since ULF pulsations in the Pc 5 range have been well correlated with solar wind speed (e.g., Mathie and Mann 2001) through Kelvin-Helmholtz instability (Claudepierre et al. 2008) and/or fluctuations in the solar wind dynamic pressure (Takahashi and Ukhorskiy 2007), correlations between the solar wind speed and MeV electron flux enhancement may indicate that radial diffusion is a dominant process in flux enhancement (see Section 9.6.3.1).

9.6.2.2 IMF

Because the outer belt electrons do not always increase greatly when high-speed streams arrive at the Earth (e.g., Kim et al. 2006), there must be parameters other than solar wind speed that control flux enhancement.

Flux enhancement tends to occur during the predominantly southward IMF (Blake et al. 1997; Iles et al. 2002; Miyoshi et al. 2007). Statistical studies focused upon CHS have shown that the large flux enhancement of MeV electrons depends on the Russell-McPherron effect; that is, the flux tends to increase largely in the southward B_z dominant CHS (Miyoshi and Kataoka 2008a, b; McPherron et al. 2009). It should be noted that the average amplitude of the minimum *Dst* in the coronal hole stream is small, greater than –50 nT, which means that intense flux enhancements at GEO occur regardless of whether or not a magnetic storm takes place (Kim et al. 2006; Miyoshi and Kataoka 2008a). A statistical survey revealed that 90% (50%) of the fast CHSs (average solar wind speed faster than 500 km/s) display a large flux enhancement at geosynchronous orbit when the southward (northward) B_z is dominant (Miyoshi and Kataoka 2008b).

9.6.2.3 Solar Wind Density and Dynamic Pressure

The enhancement of solar wind dynamic pressure causes the adiabatic acceleration of the energetic particles due to the compression of the background magnetic field. On the other hand, flux decreases at the outer portion of the outer belt (e.g., geosynchronous orbit) tend to occur in large dynamic pressure (Onsager et al. 2007; Ohtani et al. 2009). Same tendency about flux decrease has been found in the solar wind density (Lyatsky and Khazanov 2008).

9.6.3 Transport and Acceleration of Relativistic Electrons

9.6.3.1 Radial Diffusion

Since the typical energy of radiation belt particles exceeds the upper limit of the particle energy to be accelerated by the convection electric field (Section 9.4.3.1), radiation belt particles are usually not affected by the convection electric field.

Radial diffusion is regarded as one of the plausible mechanisms that could cause flux enhancement of the radiation belts. The elemental process of radial diffusion is a "drift resonance" that occurs between electrons drifting around the Earth and fluctuations in the electric/magnetic field. Considering the typical electron drift period, the ULF pulsation in the Pc 5 frequency range (~a few minutes) is the most plausible driver for electron diffusion (e.g., Elkington et al. 1999, 2003, 2006; Perry et al. 2005; Sarris et al.

2006). The origin of Pc-5 ULF waves has been variously attributed to Kelvin-Helmholtz instability (e.g., Chen and Hasegawa 1974), fluctuations in the solar wind dynamic pressure (e.g., Takahashi and Ukhorskiy 2007), and the drift-bounce resonance of ring current ions (e.g., Southwood et al. 1969). In radial diffusion, the first two adiabatic invariants (Eqs. (9.3) and (9.4)), μ and J, are always conserved, so the electron energy and pitch angle must change when the electrons move in a radial direction. The particle energy increases and the pitch angle of a particle shifts to 90° when a particle moves earthward and vice versa when a particle moves outward.

Since a random resonance with fluctuations has been assumed, the following Fokker-Planck equation has been used to describe radial diffusion (e.g., Schulz and Lanzerotti 1974; Schulz 1991; Shprits et al. 2008a and references therein):

$$\frac{\partial f}{\partial t} = L^2 \frac{\partial}{\partial L}\left(\frac{D_{\mathrm{LL}}}{L^2}\frac{\partial f}{\partial L}\right) + \text{Source} - \text{Loss}, \qquad (9.7)$$

where f is the phase space density of electrons, D_{LL} is the radial diffusion coefficient, and t is time. As shown in this equation, the direction of particle flow is determined entirely by the particle distribution, following Fick's law, and is independent of the mechanism given by the radial diffusion coefficient. If there is no source inside the radiation belts, the phase space density for any μ and J in the plasma sheet will be larger than that in the radiation belts, thus producing flux enhancements. Therefore, the positive gradient of the phase space density will be observed. In contrast to the diffusive model, coherent resonance with narrow-band waves has also been studied (Degeling et al. 2008).

Drift-resonance acceleration has been confirmed by observation (Tan et al. 2004). Many studies have shown a correlation between flux enhancement and the ULF Pc 5 power (e.g., Rostoker et al. 1998; Baker et al. 1998a, b; O'Brien et al. 2001; Mathie and Mann 2001; Green and Kivelson 2001; Kim et al. 2006; Sarris et al. 2007).

9.6.3.2 In Situ Accelerations by Wave-Particle Interactions

There are other mechanisms that produce relativistic electrons in the radiation belts: Some plasma waves; whistler, magnetosonic (ion Bernstein), free-space mode waves such as auroral kirometric radiation; and fast MHD waves can resonate with electrons by violation of adiabatic invariants, causing an acceleration (Horne and Thorne 1998; Summers and Ma 2000; Summers et al. 1998, 2001; Horne et al. 2007; Xiao et al. 2007, 2010b). A recirculation process (Nishida 1976) driven by both radial transport and pitch angle scattering, which causes a violation of all adiabatic invariants, has been applied for the energization of electrons (Fujimoto and Nishida 1990; Liu et al. 1999). Here, we focus on whistler-mode wave particle interactions, which are thought to be the mechanism responsible for producing MeV electrons.

Whistler-mode chorus waves generated outside the plasmapause can accelerate the electrons of the outer radiation belt by Doppler-shifted cyclotron resonance (e.g., Horne and Thorne 1998; Summers et al. 1998; Horne 2002; Shprits et al. 2008b and references therein). The resonance condition of relativistic electrons can be given by

$$\omega - kv = n\frac{\Omega}{\gamma}, \qquad (9.8)$$

where ω is the wave-frequency, k is the wave number vector, v is the particle velocity, n is the harmonic number, Ω is the electron gyro-frequency, and γ is the relativistic factor. Since a faster phase speed is required to effectively accelerate electrons, the low plasma density outside the plasmapause provides an environment that is conducive to this acceleration.

In this process, plasma/particles with different energy ranges are coupled to generate chorus waves and subsequent electron accelerations. Whistler-mode chorus waves are generated by the temperature anisotropy of injected plasma sheet electrons of a few tens of keV, and are then amplified largely due to the subsequent nonlinear process (Santolik et al. 2003; Katoh and Omura 2007a; Omura et al. 2008). A global simulation has successfully reproduced chorus enhancement during the storm (Jordanova et al. 2010). Generated whistler-mode chorus waves can resonate with subrelativistic electrons that might be coming from the plasma sheet and accelerate these electrons to the level of relativistic energies. Therefore, the chorus wave acts as a mediating agent. The wave growth occurs by absorbing a free energy of the low energy electrons, and then the wave transfers the energies to the high energy electron acceleration. Since the wave-dispersion relations as well as the resonance condition

are strongly affected by the ambient plasma density and magnetic field, the variations in thermal plasma density greatly changes the electron acceleration. That is, the cross-energy coupling of particles whose energies differ by more than 6 orders is essential to produce relativistic electrons of the outer belt in regard to the internal acceleration (Miyoshi et al. 2003, 2007; Bortnik and Thorne 2007; Horne 2007).

The acceleration process of wave-particle interactions as well as pitch angle scattering has been often described by the Fokker-Planck equations in the velocity space.

$$\frac{\partial f}{\partial t} = \frac{1}{v \sin\alpha} \frac{\partial}{\partial \alpha} \sin\alpha \left(D_{\alpha\alpha} \frac{1}{v} \frac{\partial f}{\partial \alpha} + D_{\alpha v} \frac{\partial f}{\partial v} \right) + \frac{1}{v^2} \frac{\partial}{\partial v} v^2 \left(D_{v\alpha} \frac{1}{v} \frac{\partial f}{\partial \alpha} + D_{vv} \frac{\partial f}{\partial v} \right), \tag{9.9}$$

where α is the pitch angle. The diffusion coefficients D_{vv}, $D_{\alpha\alpha}$, $D_{\alpha v}$, and $D_{v\alpha}$ are given by the quasi-linear theory, considering the resonance condition of a given wave spectrum (e.g., Lyons 1974; Albert 1999). Based upon a detailed estimation of the diffusion coefficients (e.g., Horne et al. 2005a; Li et al. 2007) in the realistic plasma environment during storms, electron acceleration caused by wave-particle interaction is considered to be possible.

Over the last few years, several research efforts have supported the concept of accelerations being caused by wave-particle interactions. Chorus wave power is most intense outside the plasmapause at midnight and is distributed to the dawn sector and early afternoon sector. In this region, the cold plasma density is low, which fulfills the condition required for efficient electron diffusion (e.g., Meredith et al. 2003b; Li et al. 2008, 2009). The large flux enhancement of the outer belt occurs concurrently with chorus wave enhancement (e.g., Meredith et al. 2001, 2003a; Miyoshi et al. 2003, 2007; Kasahara et al. 2009), and recent comprehensive numerical simulations and the modeling of diffusion coefficients using the observed plasma parameters have accounted for electron acceleration on the order of 1–2 days, which is comparable to the observed times scale for acceleration (e.g., Miyoshi et al. 2003; Varotsou et al. 2005, 2008; Fok et al. 2008; Albert et al. 2009; Shprits et al. 2009; Xiao et al. 2010a; Subbotin et al. 2010). The flat-top pitch angle distributions that are predicted by the wave-particle interaction process have been observed during storms (Horne et al. 2003). Some of the solar wind parameter dependence of the outer belt electrons (Section 9.6.2) can be explained by acceleration via wave-particle interactions.

Although most studies of local acceleration processes have focused on the whistler-mode chorus waves using quasi-linear diffusion theory, strong nonlinear interactions with individual chorus elements (Katoh and Omura 2007b; Omura et al. 2007; Katoh et al. 2008; Bortnik et al. 2008) are also important for the acceleration.

9.6.3.3 Which Mechanism Is Important?

From the standpoint of radial diffusion, the close correlation between solar wind speed and the MeV electron flux enhancement as described in Section 9.6.2 supports the idea that radial diffusion is a primary mechanism for the flux enhancement of the outer belt (e.g., Rostoker et al. 1998; Baker et al. 1998a, b; O'Brien et al. 2001; Mathie and Mann 2001; Green and Kivelson 2001; Mann et al. 2004; Kim et al. 2006; Sarris et al. 2006), because the solar wind speed is the main driver for the Pc 5 ULF activities in the magnetosphere. During a CHS, the plasma sheet temperature is high (Borovsky et al. 1997; Denton et al. 2006), so that seed populations with a large magnetic moment may be stored in the plasma sheet. These electrons may be diffused inward by continuous enhanced radial diffusion to produce large flux enhancements during a CHS.

From the standpoint of the internal acceleration by VLF waves, the dependence on solar wind speed and IMF described in Section 9.6.2 can be understood as follows. The acceleration by VLF waves is especially effective when a continuous source of hot electrons can be maintained to produce a chorus for the several-day period required to accelerate electrons to relativistic energies. This suggests that a prolonged period of enhanced convection/substorms is required for acceleration (Meredith et al. 2002; Miyoshi et al. 2003; Bortnik and Thorne 2007; Horne 2007). The southward IMF and high-speed solar wind causes continuous substorm/convection activities (the so-called HILDCAAs: High Intensity Long Duration Continuous AE Activities, e.g., Tsurutani et al. 2006) in which continuous hot electron injections from the plasma sheet into the inner magnetosphere can be seen (Obara et al. 2000; Denton et al. 2006).

The close relationship between CHS and accelerations by VLF waves was conducted in two CIR storms in November 1993 by polar-orbit Akebono and POES satellites. Observations showed that the outer belt electron flux increased largely during the recovery phase of the first storm when the Russell-McPherron effect was at work and did not increase during the recovery phase of the second storm when it was not at work. The differences in hot electrons, subrelativistic electrons, VLF waves, and substorm/convection activities are consistent with the scenario according to which the internal acceleration by VLF waves is important to flux enhancement (Miyoshi et al. 2007).

Some observations (Lyons et al. 2005; 2009) have shown the correlations between VLF waves measured on the ground and MeV electron flux enhancement during CHS, which can be explained by this scenario. The southward IMF dependence of MeV electrons (Miyosh and Kataoka 2008a; McPherron et al. 2009) is also consistent with this scenario.

Observations of the phase space density profile are critical for discriminating between radial diffusion and internal accelerations. Equation (9.7) shows that the phase space density gradient should be possible if the inward radial diffusion contributes to flux enhancement, because the direction of particle movement is determined by the slope of the phase space density. On the other hand, the appearance of local peaks and the subsequent local evolution of the phase space density indicate that the internal acceleration process contributes to flux enhancement (see figure 2 of Green and Kivelson 2004). Equation (9.5) is described in variables of the first and second adiabatic invariants and L-value, so that it is essential to obtain the accurate phase space density at a certain μ and J.

There are several observational reports of local peaks of the phase space density inside the outer belt, which suggests an internal acceleration (e.g., Brautingam and Albert 2000; Selesnick and Blake 2000; Miyoshi et al. 2003; Green and Kivelson 2004; Iles et al. 2006; Chen et al. 2006, 2007; Fennell and Roeder 2008). Some studies have reported the positive gradient of the phase space density, suggesting that radial diffusion is the primary mechanism of flux enhancement during a storm (e.g., Hilmer et al. 2000; Onsager et al. 2004). Due to certain problems that are addressed below, the subject of phase space density profiles during a storm is still being debated. However, it may be natural to consider that both radial diffusion and in-situ acceleration contribute to flux enhancement, though during a storm, one process might play a more dominant role than the other.

It should be noted here that some problems attend the derivation of accurate phase space density values (see also Green and Kivelson 2004). The magnetic field model is necessary in order to derive the second adiabatic invariant and L^* (Roederer 1970). The results of the phase space density profile depend largely on the magnetic field model that is used for the calculation (Selesnick and Blake 2000; Ni et al. 2009a). Since the interesting period about the large flux variation is often magnetic storms, a strong distortion of the magnetic field is to be expected, which in turn makes it more difficult to derive an accurate phase space density profile. Another problem in the calculation of phase space density is the coverage of the equatorial pitch angle. It has been reported that flux variations depend on the pitch angle (Seki et al. 2005) and that the phase space density profile depends on the second adiabatic invariant even when the first adiabatic invariant is the same (Fennell and Roeder 2008). Therefore, a reliable empirical and physical magnetic field model that can be applied in intense magnetic storms is one of the keys to an accurate phase space density profile. Moreover, observations around the magnetic equator that can cover a wide range of equatorial pitch angles, that is, a wide range of the second invariant, are important and necessary for future missions.

Note that the data assimilation technique for the radiation belt studies has recently developed, which couples the radial diffusion model (Eq. (9.7)) with the satellite data, to derive more accurate phase space density profile and specify the physical processes that cause the flux enhancement (e.g., Koller et al. 2007; Kondrashov et al. 2007; Shprits et al. 2007; Ni et al. 2009a, b). The data assimilation would become useful and important tool for better understanding of radiation belt physics.

9.6.4 Loss of Relativistic Electrons

9.6.4.1 Adiabatic Effect

Electron fluxes decrease in a certain L-shell in a fixed energy window during magnetic storms (McIlwain 1966; Kim and Chan 1997). This is the so-called the *Dst* effect or ring current effect (Section 9.4.6.5), which causes no change in the phase space density

in the adiabatic coordinate space. This process causes flux reduction during the main phase and subsequent flux recovery to the prestorm level if only adiabatic processes take place. Due to the ring current effect, the pitch angle distribution of electrons conserving the first and second adiabatic invariants exhibits butterfly distribution due to betatron acceleration (Lyons 1977) and a combination of betatron acceleration and Fermi acceleration (Ebihara et al. 2008a).

In about a quarter of magnetic storms, however, the flux of the outer belt electrons does not recover to the prestorm level (Reeves et al. 2003), in which case other nonadiabatic loss processes must occur (see Millan and Thorne 2007 and references therein).

9.6.4.2 Precipitation into Atmosphere

Pitch angle scattering with plasma waves causes the precipitation of particles into the atmospheric loss cone, which is one of the important processes in outer belt electron loss. This precipitation of MeV electrons depletes ozone through the enhancement of NOx (Thorne 1977), which may affect the climate (e.g., Rozanov et al. 2005).

Pitch angle scattering has been described by the first term of Eq. (9.7). Whistler-mode waves such as plasmaspheric hiss and chorus resonate with radiation belt electrons (Kennel and Petschek 1966; Lyons et al. 1972). Whistler-mode hiss waves are responsible for the formation of the slot region. The equilibrium structure of the radiation belts – the inner belt, outer belt, and slot region – has been successfully reproduced considering the wave-particle interactions with plasmaspheric hiss (Lyons et al. 1972; Lyons and Thorne 1972; Albert 1994, 1999; Abel and Thorne 1998a, b). The measured decay rates following storms show good agreement with the estimated life times (Albert 2000; Meredith et al. 2006) and a one-dimensional radial diffusion simulation (e.g., Lam et al. 2007). The top-hat shape of the pitch angle distribution is another piece of evidence for the pitch angle scattering by hiss waves (e.g., West et al. 1973; Lyons and Williams. 1975a, b, Morioka et al. 2001). The close correlation between the plasmapause and the outer belt position also supports the idea that whistler-mode hiss is an important loss process (O'Brien et al. 2003; Miyoshi et al. 2004; Goldstein et al. 2005; Li et al. 2006). Lightning whistler becomes more important, as do the VLF transmitters at lower L (Abel and Thorne 1998a, b) and the outer belt (Bortnik et al. 2006a, b).

Another kind of wave for the pitch angle scattering of relativistic electrons is EMIC waves in the region where the plasmasphere overlaps with the ring current (e.g., Cornwall et al. 1970; Jordanova et al. 1997). The rapid pitch angle scattering by EMIC waves when electron energies become relativistic has been predicted theoretically, (Thorne and Kennel 1971; Lyons et al. 1972; Summers and Thorne 2003; Albert 2003). There have also been several observations that suggest EMIC-relativistic electron interactions (e.g., Foat et al. 1995; Lorentzen et al. 2000; Millan et al. 2002; Meredith et al. 2003c; Sandanger et al. 2007). In addition, recent satellite-ground conjunction observations as well as theoretical checks have identified that EMIC waves actually cause the coincident precipitation of tens of keV ions and MeV electrons into the ionosphere near the plasmapause (Miyoshi et al. 2008). A self-consistent simulation that included convection, radial diffusion, and pitch angle scattering by whistlers and EMIC waves showed that EMIC waves cause the pitch angle scattering of both ring current ions and MeV electrons, but the dominant process in the global loss of the outer belt during the main phase is the outward diffusion, as shown in Section 9.6.4.3 (Jordanova et al. 2008).

Outside the plasmapause, whistler-mode chorus causes the pitch angle scattering of electrons as well as acceleration (Thorne et al. 2005). It has been suggested that the microbursts of MeV electrons that occur on the dawn-side between $L = 4$–6 (e.g., Nakamura et al. 1995, 2000b; Lorentzen et al. 2001) are the result of scattering by whistler-mode chorus waves. Microbursts occur frequently during the storm recovery phase, but losses are much stronger during the main phase, and are capable of emptying the outer belt in one day or less (O'Brien et al. 2004).

9.6.4.3 Magnetopause Loss

It has been suggested that electron loss from the magnetopause is the mechanism responsible for electron flux dropouts. Three-dimensional test particle simulations (Kim et al. 2008; Saito et al. 2010) showed that magnetopause shadowing (MPS) causes the abrupt loss of the outer portion of the outer belt and changes in the trapping boundary. Two-dimensional test particle simulations showed that the storm-time partial ring current produces a nightside depression of the magnetic field, causing an outward expansion of the outer belt and the loss of electrons in the

outer portion (Ukhorskiy et al. 2006). If the phase space density of the outer portion decreases due to MPS, then electrons move outward due to the outward diffusion (Eq. (9.5)). Some simulation studies (Brautingam and Albert 2000; Miyoshi et al. 2003, 2006; Jordanova and Miyoshi 2005; Shprits et al. 2006) found that the outward diffusion triggered by the flux decrease in the outer portion leads to changes in the lower *L*-shells, which in turn contributes to the flux decrease during the main phase. Recently, Ohtani et al. (2009) have shown observational evidence that some flux loss observed at geosynchronous orbit can be explained by MPS (see Section 9.6.2.3). It is worthwhile to note that such outward diffusion also occurs through the negative phase space density gradient when the internal acceleration causes the peak phase space density inside the outer radiation belt (Shprits et al. 2009).

9.6.4.4 Which Mechanism Is Important?

During the time of a storm, it is understood that the various loss processes take place simultaneously, but it has not been quantitatively understood which process predominates in the net loss of the outer belt. Different processes work at different L-shell and local times. Green et al. (2004) suggest that precipitation may account for a part of the loss processes, rather than MPS, but they do not identify the exact mechanism by which this takes place. Bortnik et al. (2006c) indicated that both MPS (for high *L*) and precipitation by EMIC waves (for low *L*) may have been active in the November 2003 storm.

The effective solar wind parameters that would cause a loss have been debated. Onsager et al. (2007) found that the onset of southward IMF is an important cause of flux dropouts, while Ohtani et al. (2009) showed that dynamic pressure enhancement is also essential, due to MPS. Borovsky and Denton (2009) showed that the onset of the flux dropouts associated with CIRs tends to occur after the crossing of the IMF sector boundary, and they investigated how the pitch angle scattering by EMIC waves inside the drainage plumes could be an important factor. Quantitative physics-based models that take into consideration these mechanisms would be necessary in order to identify the effective loss mechanisms.

9.6.5 Cross-Energy Couplings for Acceleration of Relativistic Electrons

Figure 9.5 summarizes these transport/acceleration mechanisms in the *L*-energy diagram of the inner magnetosphere. In radial diffusion (indicated by blue lines), the electrons move earthward with increasing energy due to the conservation of the first two adiabatic invariants. In this process, the ULF waves that are driven by solar wind and ring current instability are essential for driving the particle transport. The ambient plasma density has an effect on the condition of the drift-bounce resonance (Ozeke and Mann 2008). On the other hand, in the in-situ acceleration by waves (indicated by red lines), subrelativistic electrons are

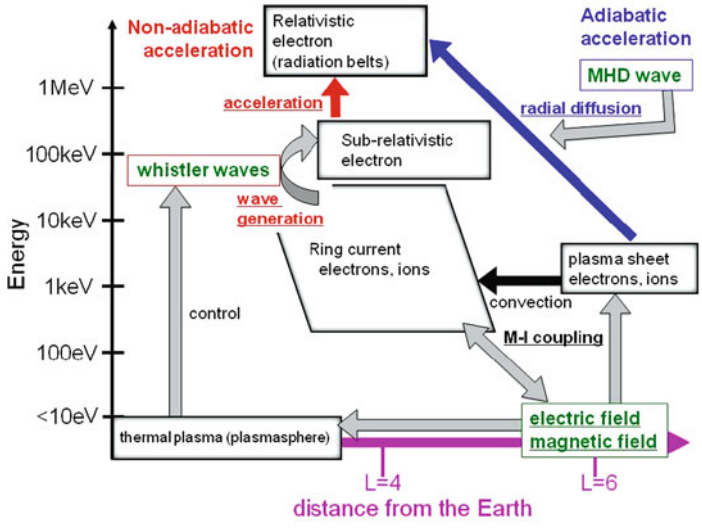

Fig. 9.5 Possible formation processes for the electron radiation belt

accelerated to MeV energies by whistler-mode waves that are generated by the plasma instability of the ring current electrons. In this process, the thermal plasma density plays an essential role as the ambient medium. Because the transport of ring current electrons and thermal plasma are predominantly controlled by convective electric fields (see Sections 9.2, 9.3, and 9.4), the process of convection may affect the relativistic electron dynamics in this process. In the loss process, different energy electrons and ions affect the dynamics of the relativistic electrons through wave-particle interactions as well as the field distortion. Therefore, the formation of the radiation belt including both flux enhancement and decrease is one of the manifestations of cross-energy/cross-region couplings in the inner magnetosphere.

9.7 Concluding Remarks

The physical processes involved in the structure and dynamics of the inner magnetosphere are schematically summarized in Fig. 9.6. While the diagram is admittedly incomplete, it may provide an essential context for understanding the inner magnetosphere and magnetic storms. Each element is directly or indirectly coupled with one another, so that the inner magnetosphere should be treated as a nonlinear, compound system. Once studied a particular element in detail, one should take into account its physical connection with the others as a system network.

During magnetic storms, each element is activated and the network of the inner magnetospheric system is dynamically stimulated. The following processes are expected to occur simultaneously:

1. The convection electric field is enhanced by southward IMF and fast solar wind.
2. Plasma sheet particles are transported into the inner magnetosphere by the convection electric field.
3. The ring current is developed on the nightside, and the plasmasphere shrinks.
4. The inner magnetospheric magnetic field is inflated by the ring current, resulting in deformation of the ring current and the radiation belts.
5. The inner magnetospheric electric field is deformed by the ring current, resulting in further deformation of the ring current and the plasmasphere.

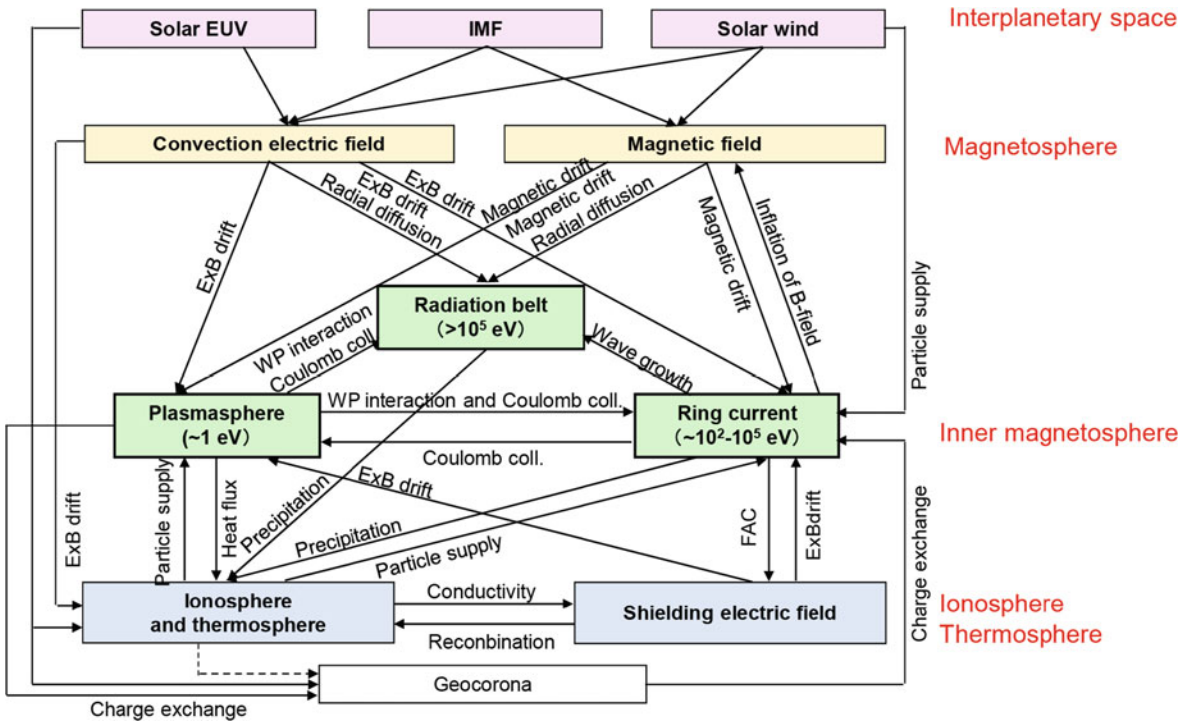

Fig. 9.6 Possible cross energy and cross region couplings in the inner magnetosphere

6. Waves are excited, resulting in the acceleration and scattering of particles.
7. Magnetic and electric fields fluctuate greatly, enhancing the radial diffusion of energetic particles.
8. The ionospheric conductivity is enhanced by the precipitation of protons, electrons and ENAs.
9. The ionosphere is heated by the ring current, resulting in the glow of a SAR arc.
10. Various types of auroras are excited by the precipitating protons, electrons and ENAs.

The inner magnetosphere is so dynamic and complicated that only a system-based approach can promise to offer an overall understanding of the inner magnetosphere and the Sun-Earth connection. To achieve a comprehensive understanding of the dynamics of the inner magnetosphere, several interesting missions are now in progress and are being planned. An international fleet of inner magnetosphere exploration satellites will consist of THEMIS (US), RBSP (US), ORBITALS (Canada), RESONANCE (Russia), and ERG (Japan) around the next solar maximum. Well-networked ground-based observations by instruments such as the magnetometer and SuperDARN HF-radar are powerful remote-sensing tools for exploring the inner magnetosphere. Simulations that can comprehend cross region and cross energy couplings, such as the Radiation Belt Environment (RBE) model (Fok et al. 2008) and the ring current-atmosphere interactions model (RAM) (Jordanova et al. 2010), are also valid to investigate the tightness of the coupling.

References

Abel B, Thorne RM (1998a) Electron scattering loss in the Earth's inner magnetosphere, 1. Dominant physical processes. J Geophys Res 103:2385–2396

Abel B, Thorne RM (1998b) Electron scattering loss in the Earth's inner magnetosphere, 2. Sensitivity to model parameters. J Geophys Res 103:2397–2407

Abel B, Thorne RM, Vampola AL (1994) Solar cycle behavior of trapped energetic electrons in Earth's radiation belt. J Geophys Res 99:19427–19431

Abe T, Watanabe S, Whalen BA, Yau AW, Sagawa E (1996) Observations of polar wind and thermal ion outflow by Akebono/SMS. J Geomagn Geoelectr 48:319–325

Aggson TL, Heppner JP, Maynard NC (1983) Observations of large magnetospheric electric fields during the onset phase of a substorm. J Geophys Res 88:3981–3990

Akasofu S-I, Chapman S (1964) On the asymmetric development of magnetic storm fields in low and middle latitudes. Planet Space Sci 12:607–626

Albert JM (1994) Quasi-linear pitch angle diffusion coefficients: Retaining high harmonics. J Geophys Res 99:23741–23745

Albert JM (1999) Analysis of quasi-linear diffusion coefficients. J Geophys Res 104:2429–2441

Albert JM (2000) Pitch angle diffusion as seen by CRRES. Adv Space Res 12:2343–2346

Albert JM (2003) Evolution of quasi-linear diffusion coefficients for EMIC waves in a multispecies plasma. J Geophys Res. doi:10.1029/2002JA009792

Albert JM, Ginet G, Gussenhoven M (1998) CRRES observations of radiation belt protons 1. Data overview and steady state radial diffusion. J Geophys Res 103:9261–9273

Albert JM, Meredith NP, Horne RB (2009) Three-dimensional diffusion simulation of outer radiation belt electrons during the 9 October 1990 magnetic storm. J Geophys Res. doi:10.1029/2009JA014336

Anderson BJ, Fuselier SA (1994) Response of thermal ions to electromagnetic ion cyclotron waves. J Geophys Res 99:19413–19425

Anderson BJ, Erlandson RE, Zanetti LJ (1992) A statistical study of pc 1–2 magnetic pulsations in the equatorial magnetosphere, 1. Equatorial occurrence distributions. J Geophys Res 97:3075–3088

Anderson PC, Hanson WB, Heelis RA, Craven JD, Baker DN, Frank LA (1993) A proposed production model of rapid subauroral ion drifts and their relationship to substorm evolution. J Geophys Res 98:6069–6078

Anderson PC, Carpenter DL, Tsuruda K, Mukai T, Rich FJ (2001) Multisatellite observations of rapid subauroral ion drifts (SAID). J Geophys Res 106:29585–29599. doi:10.1029/2001JA000128

Anderson PC, Johnston WR, Goldstein J (2008) Observations of the ionospheric projection of the plasmapause. Geophys Res Lett. doi:10.1029/2008GL033978

Baker DN, Blake JB, Klebesadel RW, Higbie PR (1986) Highly relativistic electrons in the Earth's outer magnetosphere, 1. Lifetimes and temporal history 1979–1984. J Geophys Res 91:4265–4276

Baker DN, Pulkkinen T, Li X, Kanekal S, Blake JB, Selesnick RS, Henderson MG, Reeves GD, Spence HE, Rostoker G (1998a) Coronal mass ejection, magnetic clouds, and relativistic electron events: ISTP. J Geophys Res 103:17279–17291

Baker DN, Pulkkinen TI, Li X, Kanekal SG, Ogilivie KW, Lepping RP, Blake JB, Callis LB, Rostoker G, Singer HJ, Reeves GD (1998b) A strong CME-related magnetic cloud interaction with the Earth's magnetosphere: ISTP observations of rapid relativistic electron acceleration on May 15:1997. Geophys Res Lett 25:2975–2978

Baker DN, Kanekal SG, Pulkkinen TI, Blake JB (1999) Equinoctial and solstitial averages of magnetospheric relativistic electrons: a strong semiannual modulation. Geophys Res Lett 26:3163–3196

Baker DN, Kanekal SG, Li X, Monk SP, Goldstein J, Burch JL (2004) An extreme distortion of the Van Allen belt arising from the "Halloween" solar storm in 2003. Nature 432:878–881

Baker DN, Kanekal SG (2008) Solar cycle changes, geomagnetic variations, and energetic particle properties in the inner magnetosphere. J Atmos Solar-Terr Phys 70:195–206

Barnett CF (1990) Atomic data for fusion, vol I, Collisions of H, H2, He and Li atoms and ions with atoms and molecules. Technical Report ORNL–6086/VI, Oak Ridge National Laboratory, Oak Ridge, TN

Baumgardner J, Wroten J, Semeter J, Kozyra J, Buonsanto M, Erickson P, Mendillo M (2007) A very bright SAR arc: implications for extreme magnetosphere-ionosphere coupling. Ann Geophys 25:2593–2608

Baumjohann W, Haerendel G (1985) Magnetospheric convection observed between 0600 and 2100 LT: solar wind and IMF dependence. J Geophys Res 90:6370–6378

Baumjohann W, Paschmann G, Cattell CA (1989) Average plasma properties in the central plasma sheet. J Geophys Res 94:6597

Beutier T, Boscher D, France M (1995) SALAMMBO: a three-dimensional simulation of the proton radiation belt. J Geophys Res 100:17181–17188

Birn J, Thomsen MF, Borovsky JE, Reeves GD, McComas DJ, Belian RD (1997a) Characteristic plasma properties during dispersionless substorm injections at geosynchronous orbit. J Geophys Res 102:2309–2324

Birn J, Thomsen MF, Borovsky JE, Reeves GD, McComas DJ, Belian RD, Hesse M (1997b) Substorm ion injections: geosynchronous observations and test particle orbits in three-dimensional dynamic MHD fields. J Geophys Res 102:2325–2341

Blake JB, Baker DN, Turner N, Ogilvie KW, Lepping RP (1997) Correlation of changes in the outer zone relativistic electron population with upstream solar wind and magnetic field measurements. Geophys Res Lett 24:927–929

Blake JB, Kolasinski WA, Fillius RW, Mullen EG (1992) Injection of electrons and protons with energies of tens of MeV into L < 3 on 24 March 1991. Geophys Res Lett 19:821–824

Borovsky JE, Denton MH (2006) Differences between CME-driven storms and CIR-driven storms. J Geophys Res. doi:10.1029/2005JA011447

Borovsky JE, Denton MH (2008) A statistical look at plasmaspheric drainage plumes. J Geophys Res. doi:10.1029/2007JA012994

Borovsky JE, Denton MH (2009) Relativistic-electron dropouts and recovery: a superposed epoch study of the magnetosphere and the solar wind. J Geophys Res. doi:10.1029/2008JA013128

Borovsky JE, Thomsen MF, McComas DJ (1997) The superdense plasma sheet: Plasmaspheric origin, solar wind origin or ionospheric origin? J Geophys Res 102:22089–22097

Borovsky JE, Thomsen MF, Elphic RC (1998) The driving of the plasma sheet by the solar wind. J Geophys Res 103:17617–17639

Borovsky JE, Lavraud B, Kuznetsova MM (2009) Polar cap potential saturation, dayside reconnection, and changes to the magnetosphere. J Geophys Res. doi:10.1029/2009JA014058

Bortnik J, Thorne RM (2007) The dual role of ELF/VLF chorus waves in the acceleration and precipitation of radiation belt electrons. J Atmos Solar-Terr Phys 69:378–376

Bortnik J, Inan US, Bell TF (2006a) Temporal signatures of radiation belt electron precipitation induced by lightning-generated MR whistler waves: 1. Methodology. J Geophys Res. doi:10.1029/2005JA01182

Bortnik J, Inan US, Bell TF (2006b) Temporal signatures of radiation belt electron precipitation induced by lightning-generated MR whistler waves: 2. Global signatures. J Geophys Res. doi:10.1029/2005JA011398

Bortnik J, Thorne RM, O'Brien TO, Green JC, Strangeway RJ, Shprits YY, Baker DN (2006c) Observation of two distinct rapid loss-mechanisms during the November 20:2003 radiation belt dropout event. J Geophys Res. doi:10.1029/2006JA011802

Bortnik J, Thorne RM, Meredith NP (2007) Modeling the propagation characteristics of chorus using CRRES suprathermal electron fluxes. J Geophys Res. doi:10.1029/2006JA012237

Bortnik J, Thorne RM, Inan US (2008) Nonlinear interaction of energetic electrons with large amplitude chorus. Geophys Res Lett. doi:10.1029/2008GL035500

Brandt PC, Mitchell DG, Ebihara Y, Sandel BR, Roelof EC, Burch JL, Demajistre R (2002a) Global IMAGE/HENA observations of the ring current: Examples of rapid response to IMF and ring current-plasmasphere interaction. J Geophys Res. doi:10.1029/2001JA000084

Brandt PC, Ohtani S, Mitchell DG, Fok M-C, Roelof EC, Demajistre R (2002b) Global ENA observations of the storm mainphase ring current: Implications for skewed electric fields in the inner magnetosphere. Geophys Res Lett. doi:10.1029/2002GL015160

Brandt PC, Roelof EC, Ohtani S, Mitchell DG, Anderson B (2004) IMAGE/HENA: pressure and current distributions during the 1 October 2002 storm. Adv Space Res 33. Streamers, slow solar wind, and the dynamics of the magnetosphere, pp 719–722

Brandt PC, Zheng Y, Sotirelis TS, Oksavik K, Rich FJ (2008) The linkage between the ring current and the ionosphere system. In: Kintner PM, Coster AJ, Fuller-Rowell T, Mannucci AJ, Mendillo M, Heelis R (eds) Midlatitude ionospheric dynamics and disturbances. Geophysical monograph series, vol 181. AGU, Washington, DC, pp 135–143

Breneman AW, Kletzing CA, Pickett J, Chum J, Santolik O (2009) Statistics of multispacecraft observations of chorus dispersion and source location. J Geophys Res. doi:10.1029/2008JA013549

Brice NM (1967) Bulk Motion of the Magnetosphere. J Geophys Res 72:5193–5211

Burch JL et al (2001) Views of the Earth's magnetosphere with the IMAGE satellite. Science 291:619

Burch JL, Goldstein J, Sandel BR (2004) Cause of plasmasphere corotation lag. Geophys Res Lett. doi:10.1029/2003GL019164

Burke WJ, Gentile LC, Huang CY (2007) Penetration electric fields driving main phase Dst. J Geophys Res. doi:10.1029/2006JA012137

Büchner J, Zelenyi L (1989) Regular and chaotic charged particle motion in magnetotaillike field reversals, 1. Basic theory of trapped motion. J Geophys Res 94:11821–11842

Cahill LJ (1966) Inflation of the inner magnetosphere during a magnetic storm. J Geophys Res 71:4505–4519

Carpenter DL (1963) Whistler evidence of a 'knee' in the magnetospheric ionization density profile. J Geophys Res 68:1675–1682

Carpenter DL (1966) Whistler studies of the plasmapause in the magnetosphere 1. Temporal variations in the position of the knee and some evidence on plasma motions near the knee. J Geophys Res 71:693–709

Carpenter DL, Anderson RR (1992) An ISEE/whistler model of equatorial electron density in the magnetosphere. J Geophys Res 97:1097–1108

Carpenter DL, Lemaire J (1997) Erosion and recovery of the plasmasphere in the plasmapause region. Space Sci Rev 80:153–179

Carpenter DL, Lemaire J (2004) The plasmasphere boundary layer. Ann Geophys 22:4291–4298

Carpenter DL, Anderson RR, Calvert W, Moldwin MB (2000) CRRES observations of density cavities inside the plasmasphere. J Geophys Res 105:23323–23338

Chappell CR (1972) Recent satellite measurements of the morphology and dynamics of the plasmasphere. Rev Geophys 10:951–979

Chappell CR (1974) Detached plasma regions in the magnetosphere. J Geophys Res 79:1861–1870

Chappell CR, Harris KK, Sharp GW (1970) A study of the influence of magnetic activity on the location of the plasmapause as measured by OGO 5. J Geophys Res 75:50–56

Chappell CR, Olsen RC, Green JL, Johnson JFE, Waite JH Jr (1982) The discovery of nitrogen ions in the Earth's magnetosphere. Geophys Res Lett 9:937–940

Chappell CR, Huddleston MM, Moore TE, Giles BL, Delcourt DC (2008) Observations of the warm plasma cloak and an explanation of its formation in the magnetosphere. J Geophys Res. doi:10.1029/2007JA012945

Chapman S, Ferraro VCA (1933) A new theory of magnetic storms. Terr Magn Atmos Electr 38:79–96

Chen AJ, Grebowsky JM (1974) Plasma tail interpretations of pronounced detached plasma regions measured by Ogo 5. J Geophys Res 79:3851–3855

Chen L, Hasegawa A (1974) A theory of long-period magnetic pulsations: Impulse excitation of surface eigenmode. J Geophys Res 79:1033–1037

Chen M, Lyons L, Schulz M (1994) Simulations of phase space distributions of storm time proton ring current. J Geophys Res 99:5745–5759

Chen Y, Friedel RHW, Reeves GD (2006) Phase space density distributions of energetic electrons in the outer radiation belt during two Geospace Environment Modeling Inner Magnetosphere/Storms selected storms. J Geophys Res. doi:10.1029/2006JA011703

Chen Y, Reeves GD, Friedel RHW (2007) The energization of relativistic electrons in the outer Van Allen radiation belt. Nat Phys. doi:10.1038/nphys655

Chen L, Thorne RM, Horne RB (2009) Simulation of EMIC wave excitation in a model magnetosphere including structured high-density plumes. J Geophys Res. doi:10.1029/2009JA014204

Christon SP, Desai MI, Eastman TE, Gloeckler G, Kokubun S, Lui ATY, McEntire RW, Roelof EC, Williams DJ (2000) Low-charge-state heavy ions upstream of Earth's bow shock and sunward flux of ionospheric O+1, N+1, and O+2 ions: geotail observations. Geophys Res Lett 27:2433–2436

Cladis JB, Francis WE (1992) Distribution in magnetotail of O+ ions from cusp/cleft ionosphere: a possible substorm trigger. J Geophys Res 97:123–130

Claudepierre SG, Elkington SR, Wiltberger M (2008) Solar wind driving of magnetospheric ULF waves: Pulsations driven by velocity shear at the magnetopause. J Geophys Res. doi:10.1029/2007JA012890

Clauer CR, McPherron RL (1980) The relative importance of the interplanetary electric field and magnetospheric substorms on partial ring current development. J Geophys Res 85:6747–6759

Cole KD (1965) Stable auroral red arcs, Sinks for energy of Dst main phase. J Geophys Res 70:1689–1706

Collin HL, Quinn JM, Cladis JB (1993) An empirical static model of low energy ring current ions. Geophys Res Lett. 20:141–144

Comfort RH, Horwitz JL (1981) Low energy ion pitch angle distributions observed on the dayside at geosynchronous altitudes. J Geophys Res 86:1621–1627

Cornwall JM (1977) On the role of charge exchange in generating unstable waves in the ring current. J Geophys Res 82:1188–1196

Cornwall JM, Coroniti FV, Thorne RM (1970) Turbulent loss of ring current protons. J Geophys Res 75:4699–4709

Craven JD, Frank LA, Ackerson KL (1982) Global observations of a SAR arc. Geophys Res Lett 9:961–964

Daglis IA, Axford WI (1996) Fast ionospheric response to enhanced activity in geospace: ion feeding of the inner magnetotail. J Geophys Res 101:5047–5065

Daglis IA, Sarris ET, Wilken B (1993) AMPTE/CCE CHEM observations of the ion population at geosynchronous altitudes. Ann Geophys 11:685

Daglis IA, Kasotakis G, Sarris ET, Kamide Y, Livi S, Wilken B (1999) Variations of the ion composition during an intense magnetic storm and their consequences. Phys Chem Earth 24:229–232

Daglis IA, Kamide Y, Monikis C, Reeves GD, Sarris ET, Shiokawa K, Wilken B (2000) 'Fine structure' of the storm-substorm relationship: ion injections during DST decrease. Adv Space Res 25:2369–2372

Darrouzet, F, Décréau PME, De Keyser J, Masson A, Gallagher DL, Santolik O, Sandel BR, Trotignon JG, Rauch JL, Le Guirriec E, Canu P, Sedgemore F, André M, Lemaire JF (2004) Density structures inside the plasmasphere: Cluster observations. Ann Geophys 22:2577–2585

De Benedetti J, Milillo A, Orsini S, Mura A, De Angelis E, Daglis IA (2005) Empirical model of the inner magnetosphere H+ pitch angle distributions. In: Pulkkinen TI, Tsyganenko NA, Friedel RHW (eds) The inner magnetosphere: physics and modeling. Geophysical monograph series, vol 38. AGU, Washington, DC, pp 283–291

DeForest SE, McIlwain CE (1971) Plasma clouds in the magnetosphere. J Geophys Res 76:3587

Degeling AW, Ozeke LG, Rankin R, Mann IR, Kabin K (2008) Drift resonance generation of peaked relativistic electron distributions by Pc5 ULF waves. J Geophys Res. doi:10.1029/2007JA012411

Delcourt D, Sauvaud J-A, Martin R Jr, Moore T (1996) On the nonadiabatic precipitation of ions from the near-Earth plasma sheet. J Geophys Res 101:17409–17418

De Michelis P, Daglis IA, Consolini G (1997) Average terrestrial ring current derived from AMPTE/CCE–CHEM measurements. J Geophys Res 102:14103–14111

De Michelis P, Daglis IA, Consolini G (1999) An average image of proton plasma pressure and of current systems in the equatorial plane derived from AMPTE/CCE-CHEM measurements. J Geophys Res 104:28615–28624

Denton MH, Borovsky JE (2008) Superposed epoch analysis of high-speed-stream effects at geosynchronous orbit: hot plasma, cold plasma, and the solar wind. J Geophys Res. doi:10.1029/2007JA012998

Denton RE, Goldstein J, Menietti JD (2002) Field line dependence of magnetospheric electron density. Geophys Res Lett. doi:10.1029/2002GL015963

Denton MH, Borovsky JE, Skoug RM, Thomsen MF, Lavraud B, Henderson MG, McPherron RL, Zhang JC, Liemohn MW (2006) Geomagnetic storms driven by ICME- and CIR-dominated solar wind. J Geophys Res. doi:10.1029/2005JA011436

Denton RE, Décréau P, Engebretson MJ, Darrouzet F, Posch JL, Mouikis C, Kistler LM, Cattell CA, Takahashi K, Schäfer S, Goldstein J (2009) Field line distribution of density at L = 4.8 inferred from observations by CLUSTER. Ann Geophys 27:705–724.

Dessler AJ, Parker EN (1959) Hydromagnetic theory of geomagnetic storms. J Geophys Res 64:2239–2252.

Dessler AJ, Karplus R (1961) Some effects of diamagnetic ring currents on Van Allen radiation. J Geophys Res 66:2289–2295

Dungey JW (1961) Interplanetary magnetic field and the auroral zones. Phys Rev Lett 6:47–48

Ebihara Y, Ejiri M (1998) Modeling of solar wind control of the ring current buildup: A case study of the magnetic storms in April 1997. Geophys Res Lett 25:3751–3754

Ebihara Y, Ejiri M (2000) Simulation study on fundamental properties of the storm-time ring current. J Geophys Res 105:15843–15859

Ebihara Y, Ejiri M (2003) Numerical simulation of the ring current: review. Space Sci Rev 105:377–452

Ebihara Y, Fok M-C (2004) Postmidnight storm–time enhancements of tens-of-keV proton flux. J Geophys Res. doi:10.1029/2004JA010523

Ebihara Y, Yamauchi M, Nilsson H, Lundin R, Ejiri M (2001) Wedge-like dispersion of sub-keV ions in the dayside magnetosphere: particle simulation and Viking observation. J Geophys Res 106:29571–29584

Ebihara Y, Ejiri M, Nilsson H, Sandahl I, Milillo A, Grande M, Fennell JF, Roeder JL (2002) Statistical distribution of the storm–time proton ring current: POLAR measurements. Geophys Res Lett. doi:10.1029/2002GL015430

Ebihara Y, Ejiri M, Sandahl I, Nilsson H, Grande M, Fennell JF, Roeder JL, Ganushkina N Yu, Milillo A (2004a) Structure and dynamics on the proton energy density in the inner magnetosphere. Adv Space Res 33:711–718

Ebihara Y, Fok M-C, Wolf RA, Immel TJ, Moore TE (2004b) Influence of ionosphere conductivity on the ring current. J Geophys Res. doi:10.1029/2003JA010351

Ebihara Y, Fok M-C, Sazykin S, Thomsen MF, Hairston MR, Evans DS, Rich FJ, Ejiri M (2005a) Ring current and the magnetosphere–ionosphere coupling during the super storm of 20 November 2003. J Geophys Res. doi:10.1029/2004JA010924

Ebihara Y, Fok M-C, Wolf RA, Thomsen MF, Moore TE (2005b) Nonlinear impact of the plasma sheet density on the ring current. J Geophys Res. doi:10.1029/2004JA010435

Ebihara Y, Yamada M, Watanabe S, Ejiri M (2006) Fate of outflowing suprathermal oxygen ions that originate in the polar ionosphere. J Geophys Res. doi:10.1029/2005JA011403

Ebihara Y, Fok M-C, Blake JB, Fennell JF (2008a) Magnetic coupling of the ring current and the radiation belt. J Geophys Res. doi:10.1029/2008JA013267

Ebihara Y, Kistler LM, Eliasson L (2008b) Imaging cold ions in the plasma sheet from the Equator-S satellite. J Geophys Res Lett. doi:10.1029/2008GL034357

Ebihara Y, Nishitani N, Kikuchi T, Ogawa T, Hosokawa K, Fok M-C (2008c) Two-dimensional observations of overshielding during a magnetic storm by the Super Dual Auroral Radar Network (SuperDARN) Hokkaido radar. J Geophys Res. doi:10.1029/2007JA012641

Ebihara Y, Kasahara S, Seki K, Miyoshi Y, Fritz TA, Chen J, Grande M, Zurbuchen TH (2009a) Simultaneous entry of oxygen ions originating from the Sun and Earth into the inner magnetosphere during magnetic storms. J Geophys Res. doi:10.1029/2009JA014120

Ebihara Y, Nishitani N, Kikuchi T, Ogawa T, Hosokawa K, Fok M-C, Thomsen MF (2009b) Dynamical property of storm time subauroral rapid flows as a manifestation of complex structures of the plasma pressure in the inner magnetosphere. J Geophys Res. doi:10.1029/2008JA013614

Ejiri M (1978) Trajectory traces of charged particles in the magnetosphere. J Geophys Res 83:4798–4810

Ejiri M (1981) Shielding of the magnetospheric convection electric field and energetic charged particle penetrations towards the Earth. In: Magnetospheric Dynamics, Proceedings of the 1980 ISAS Symposium on Magneto-Ionosphere. Institute of Space and Aeronautical Science, University of Tokyo, Tokyo, p. 113

Ejiri M, Hoffman RA, Smith PH (1980) Energetic particle penetrations into the inner magnetosphere. J Geophys Res 85(A2):653–663

Elkington SR (2006) A review of ULF interactions with radiation belt electrons. In: Takahashi K, Chi PJ, Denton RE, Lysak RL (eds) Magnetospheric ULF waves: synthesis and new directions. AGU, Washington, DC, pp 177–193

Elkington SR, Hudson MK, Chan AA (1999) Acceleration of relativistic electrons via drift-resonant interaction with toroidal-mode Pc-5 ULF oscillations. Geophys Res Lett 26:3273–3276

Elkington SR, Hudson MK, Chan AA (2003) Resonant acceleration and diffusion of outer zone electrons in an asymmetric geomagnetic field. J Geophys Res. doi:10.1029/2001JA009202

Elphic RC, Weiss LA, Thomsen MF, McComas DJ, Moldwin MB (1996) Evolution of plasmaspheric ions at geosynchronous orbit during times of high geomagnetic activity. Geophys Res Lett 23:2189–2192

Elphic RC, Thomsen MF, Borovsky JE (1997) The fate of the outer plasmasphere. Geophys Res Lett 24:365–368

Engebretson MJ et al (2007) Cluster observations of Pc 1-2 waves and associated ion distributions during the October and November 2003 magnetic storms. Planet Space Sci 55:829–848

Erickson GM, Spiro RW, Wolf RA (1991) The physics of the Harang discontinuity. J Geophys Res 96:1633–1645

Farrugia CJ, Young DT, Geiss J, Balsiger H (1989) The composition, temperature, and density structure of cold ions in the

quiet terrestrial plasmasphere: GEOS 1 results. J Geophys Res 94:11865–11891
Fejer BG, Gonzales CA, Farley DT, Kelley MC, Woodman RF (1979) Equatorial electric fields during magnetically disturbed conditions, 1. The effect of the interplanetary magnetic field. J Geophys Res 84:5797–5802
Fennell JF, Croley DR Jr, Kaye SM (1981) Low-energy ion pitch angle distribution in the magnetosphere: ion zipper distributions. J Geophys Res 86:3375
Fennell JF, Roeder JL (2008) Storm time phase space density radial profiles of energetic electrons for small and large K values: SCATHA results. J Atmos Solar-Terr Phys 70:1760–1773
Foat JE, Lin RP, Smith DM, Fenrich F, Millan R, Roth I, Lorentzen KR, McCarthy MP, Parks GK, Treilhou JP (1995) First detection of a terrestrial MeV X-ray burst. Geophys Res Lett 25:4109–4112
Fok M-C, Kozyra JU, Nagy A, Cravens T (1991) Lifetime of ring current particles due to coulomb collisions in the plasmasphere. J Geophys Res 96:7861–7867
Fok M-C, Moore TE, Kozyra JU, Ho GC, Hamilton DC (1995) Three-dimensional ring current decay model. J Geophys Res 100:9619–9632
Fok M-C, Moore TE, Greenspan ME (1996) Ring current development during storm main phase. J Geophys Res 101:15311–15322
Fok M-C, Moore TE, Delcourt DC (1999) Modeling of inner plasma sheet and ring current during substorms. J Geophys Res 104:14557–14569
Fok M-C, Wolf RA, Spiro RW, Moore TE (2001) Comprehensive computational model of Earth's ring current. J Geophys Res 106:8417–8424
Fok M-C, Horne RB, Meredith NP, Glauert SA (2008) Radiation Belt Environment model: application to space weather nowcasting. J Geophys Res. doi:10.1029/2007JA012558
Foster JC, Vo HB (2002) Average characteristics and activity dependence of the subauroral polarization stream. J Geophys Res. doi:10.1029/2002JA009409
Foster JC, Coster AJ, Erickson PJ, Rich FJ, Sandel BR (2004a) Stormtime observations of the flux of plasmaspheric ions to the dayside cusp/magnetopause. Geophys Res Lett. doi:10.1029/2004GL020082
Foster JC, Erickson PJ, Lind FD, Rideout W (2004b) Millstone Hill coherent-scatter radar observations of electric field variability in the sub-auroral polarization stream. Geophys Res Lett. doi:10.1029/2004GL021271
Frahm RA, Reiff PH, Winningham JD, Burch JL (1986) Banded ion morphology: main and recovery storm phases. In: Chang T et al (eds) Ion acceleration in the magnetosphere and ionosphere. Geophysical monograph series, vol 38. AGU, Washington, DC, pp 98–107
Frank LA (1967) On the extraterrestrial ring current during geomagnetic storms. J Geophys Res 72:3753–3767
Freeman JW Jr (1969) Magnetospheric wind. Science 63:1061–1062
Friedel RHW, Korth A, Kremser G (1996) Substorm onsets observed by CRRES: Determination of energetic particle source regions. J Geophys Res 101:13137–13154
Friedel RH, Reeves GD, Obara T (2002) Relativistic electron dynamics in the inner magnetosphere – a review. J Atmos Solar-Terr Phys 64:265–282
Fritz TA, Chen J, Siscoe GL (2003) Energetic ions, large diamagnetic cavities, and Chapman-Ferraro cusp. J Geophys Res. doi:10.1029/2002JA009476
Fujimoto M, Nishida A (1990) Energization and anisotropization of energetic electrons in the Earth's radiation belt by the recirculation process. J Geophys Res 95:4265–4270
Fujimoto M, Terasawa T, Mukai T, Saito T, Yamamoto T, Kokubun S (1998) Plasma entry from the flanks of the near-Earth magnetotail: geotail observations. J Geophys Res 103:4391–4408
Fung SF, Shao X, Tan LC (2006) Long-term variations of the electron slot region and global radiation belt structure. Geophys Res Lett. doi:10.1029/2005GL024891
Fuselier SA, Gary SP, Thomsen MF, Claflin ES, Hubert B, Sandel BR, Immel T (2004) Generation of transient dayside subauroral proton precipitation. J Geophys Res. doi:10.1029/2004JA010393
Galand M, Fuller-Rowell TJ, Codrescu MV (2001) Response of the upper atmosphere to auroral protons. J Geophys Res 106:127–139
Galand M, Richmond AD (2001) Ionospheric electrical conductances produced by auroral proton precipitation. J Geophys Res 106:117–125
Gallager DL, Adrian ML (2007) Two-dimensional drift velocities from the IMAGE EUV plasmaspheric imager. J Atmos Solar-Terr Phys 69:341–350
Galperin YI, Ponomarev VN, Zosimova AG (1973) Direct measurements of drift rate of ions in upper atmosphere during a magnetic storm. II. Results of measurements during magnetic storm of November 3:1967. Cosmic Res Engl Transl 11:249–258
Galvan DA, Moldwin MB, Sandel BR (2008) Diurnal variation in plasmaspheric He inferred from extreme ultraviolet images. J Geophys Res. doi:10.1029/2007JA013013
Gamayunov KV, Khazanov GV (2008) Crucial role of ring current H+ in electromagnetic ion cyclotron wave dispersion relation: results from global simulations. J Geophys Res. doi:10.1029/2008JA013494
Gamayunov KV, Khazanov GV, Liemohn MW, Fok M-C, Ridley AJ (2009) Self-consistent model of magnetospheric electric field, ring current, plasmasphere, and electromagnetic ion cyclotron waves: initial results. J Geophys Res. doi:10.1029/2008JA013597
Ganushkina N Yu, Pulkkinen TI, Kubyshkina MV, Sergeev VA, Lvova EA, Yahnina TA, Yahnin AG, Fritz TA (2005) Proton isotropy boundaries as measured on mid- and low-altitude satellites. Ann Geophys 23:1839–1847
Garner TW (2003) Numerical experiments on the inner magnetospheric electric field. J Geophys Res. doi:10.1029/2003JA010039
Garner TW, Wolf RA, Spiro RW, Burke WJ, Fejer BG, Sazykin S, Roeder JL, Hairston MR (2004) Magnetospheric electric fields and plasma sheet injection to low L-shells during the 4–5 June 1991 magnetic storm: Comparison between the Rice Convection Model and observations. J Geophys Res. doi:10.1029/2003JA010208
Gannon JL, Li X, Temerin M (2005) Parametric study of shock-induced transport and energization of relativistic electrons in the magnetosphere. J Geophys Res. doi:10.1029/2004JA010679

Gendrin R, Roux A (1980) Energization of Helium ions by proton-induced hydromagnetic waves. J Geophys Res 85:4577–4586

Gkioulidou M, Wang C-P, Lyons LR, Wolf RA (2009) Formation of the Harang reversal and its dependence on plasma sheet conditions: rice convection model simulations. J Geophys Res. doi:10.1029/2008JA013955

Goldstein J, Denton RE, Hudson MK, Miftakhova EG, Young SL, Menietti JD, Gallagher DL (2001) Latitudinal density dependence of magnetic field lines inferred from Polar plasma wave data. J Geophys Res 106:6195–6201

Goldstein J, Sandel BR, Forrester WT, Reiff PH (2003a) IMF-driven plasmasphere erosion of 10 July 2000. Geophys Res Lett. doi:10.1029/2002GL016478

Goldstein J, Sandel BR, Hairston MR, Reiff PH (2003b) Control of plasmaspheric dynamics by both convection and sub-auroral polarization stream. Geophys Res Lett. doi:10.1029/2003GL018390

Goldstein J, Spiro RW, Sandel BR, Wolf RA, Su S-Y, Reiff PH (2003c) Overshielding event of 28–29 July 2000. Geophys Res Lett. doi:10.1029/2002GL016644

Goldstein J, Sandel BR, Hairston MR, Mende SB (2004a) Plasmapause undulation of 17 April 2002. Geophys Res Lett. doi:10.1029/2004GL019959

Goldstein J, Wolf RA, Sandel BR, Reiff PH (2004b) Electric fields deduced from plasmapause motion in IMAGE EUV images. Geophys Res Lett. doi:10.1029/2003GL018797

Goldstein J, Kanekal SG, Baker DN, Sandel BR (2005) Dynamic relationship between the outer radiation belt and the plasmapause during March-May 2001. Geophys Res Lett. doi:10.1029/2005GL023431

Green JC, Kivelson MG (2001) A tale of two theories: how the adiabatic response and ULF waves affect relativistic electrons. J Geophys Res 106:25777–25791

Green JL, Reinisch BW (2002) An overview of results from RPI on IMAGE. Space Sci Rev 145:231–261

Green JC, Kivelson MG (2004) Relativistic electrons in the outer radiation belt. Differentiating between acceleration mechanisms. J Geophys Res. doi:10.1029/2003JA010153

Green JL, Fung SF (2005) Advances in inner magnetosphere passive and active wave research. In: Pulkkinen TI, Tsyganenko NA, Friedel HW (eds) The inner magnetosphere physics and modeling. AGU, Washington, DC. doi:10.1029/155GM21

Green JC, Onsager TG, O'Brien TP, Baker DN (2004) Testing loss mechanisms capable of rapidly depleting relativistic electron flux in the Earth's outer radiation belt. J Geophys Res. doi:10.1029/2004JA010579

Greenspan ME, Hamilton DC (2000) A test of the Dessler-Parker-Sckopke relation during magnetic storms. J Geophys Res 105:5419–5430

Greenspan ME, Hamilton DC (2002) Relative contributions of H^+ and O^+ to the ring current energy near magnetic storm maximum. J Geophys Res. doi:10.1029/2001JA000155

Grebowsky JM (1970) Model study of plasmapause motion. J Geophys Res 75:4329–4333

Grebowsky JM, Maynard NC, Tulunay YK, Lanzerotti LJ (1976) Coincident observations of ionospheric troughs and the equatorial plasmapause. Planet Space Sci 24:1177–1185

Grebowsky JM, Benson RF, Webb PA, Truhlik V, Bilitza D (2009) Altitude variation of the plasmapause signature in the main ionospheric trough. J Atmos Solar-Terr Phys 71:1669–1676

Hamilton DC, Gloeckler G, Ipavich FM, Stüdemann W, Wilken B, Kremser G (1988) Ring current development during the great geomagnetic storm of February 1986. J Geophys Res 93:14343–14355

Hairston MR, Drake KA, Skoug R (2005) Saturation of the ionospheric polar cap potential during the October-November 2003 superstorms. J Geophys Res. doi:10.1029/2004JA010864

Hardy DA, Gussenhoven MS, Brautigam D (1989) A statistical model of auroral ion precipitation. J Geophys Res 94:370–392

Hasegawa H et al (2004) Rolled-up Kelvin-Helmholtz vortices and associated solar wind entry at Earth's magnetopause. Nature 430:755–758

Hilmer RV, Ginet GP, Cayton TE (2000) Enhancement of equatorial energetic electron fluxes near L=4.2 as a result of high speed solar wind streams. J Geophys Res 105:23311–23322

Hoffman RA (1973) Particle and field observations from Explorer 45 during the December 1971 magnetic storm period. J Geophys Res 78:4771–4777

Hori T et al (2005) Storm-time convection electric field in the near-Earth plasma sheet. J Geophys Res. doi:10.1029/2004JA010449

Horne RB (2002) The contribution of wave-particle interactions to electron loss and acceleration in the earth's radiation belts during geomagnetic storms. In: Stone WR (ed) Rev Radio Sci., 1999–2002, Wiley, pp 801–829

Horne RB (2007) Plasma astrophysics: acceleration of killer electrons. Nat Phys 3:590–591

Horne RB, Thorne RM (1997) Wave heating of He+ by electromagnetic ion cyclotron waves in the magnetosphere: Heating near the H^+-He^+ bi-ion resonance frequency. J Geophys Res 102:11457–11471

Horne RB, Thorne RM (1998) Potential waves for relativistic electron scattering and stochastic acceleration during magnetic storms. Geophys Res Lett 25:3011–3014

Horne RB, Meredith NP, Thorne RM, Heynderickx D, Iles RHA, Anderson RR (2003) Evolution of energetic electron pitch angle distributions during storm time electron acceleration to megaelectronvolt energies. J Geophys Res. doi:10.1029/2001JA009165

Horne RB, Thorne RM, Glauert SA, Albert JM, Meredith NP, Anderson RR (2005a) Timescale for radiation belt electron acceleration by whistler mode chorus waves. J Geophys Res. doi:10.1029/2004JA010811

Horne RB, Thorne RM, Shprits YY, Meredith NP, Glauert SA, Smith AJ, Kanekal SG, Baker DN, Engebretson MJ, Posch JL, Spasojevic M, Inan US, Pickett JS, Decreau PMM (2005b) Wave acceleration of electrons in the Van Allen radiation belts. Nature 437:227–230

Horne RB, Thorne RM, Glauert SA, Meredith NP, Pokhotelov D, Santolik O (2007) Electron acceleration in the Van Allen radiation belts by fast magnetosonic waves. Geophys Res Lett. doi:10.1029/2007GL030267

Horwitz JL, Comfort RH, Chappell CR (1984) Thermal ion composition measurements of the formation of the new outer plasmasphere and double plasmapause during storm recovery phase. Geophys Res Lett 11:701–704

Horwitz J, Brace L, Comfort R, Chappell C (1986) Dual-spacecraft measurements of plasmasphere-ionosphere coupling. J Geophys Res 91:11203–11216

Horwitz JL, Comfort RH, Chappell CR (1990a) A statistical characterization of plasmasphere density structure and boundary locations. J Geophys Res 95:7937–7947

Horwitz JL, Comfort RH, Richards PG, Chandler MO, Chappell CR, Anderson P, Hanson WB, Brace LH (1990b) Plasmasphere-ionosphere coupling, 2. ion composition measurements at plasmaspheric and ionospheric altitudes and comparison with modeling results. J Geophys Res 95:7949–7959

Huang C-S, Foster JC (2007) Correlation of the subauroral polarization streams (SAPS) with the Dst index during severe magnetic storms. J Geophys Res 112. doi:10.1029/2007JA012584

Huang X, Reinisch BW, Song P, Green JL, Gallagher DL (2004) Developing an empirical density model of the plasmasphere using IMAGE/RPI observations. Adv Space Res 33:829–832

Hudson MK, Kotelnikov AD, Li X, Roth I, Temerin M, Wygant J, Blake JB, Gussenhoven MS (1995) Simulation of proton radiation belt formation during the March 24:1991 SSC. Geophys Res Lett 22:291–294

Hudson MK, Kress BT, Mazur JE, Perry KL, Slocum PL (2004) 3D modeling of shock-induced trapping of solar energetic particles in the Earth's magnetosphere. J Atmos Solar-Terr Phys 66:1389–1397

Hudson MK, Kress BT, Mueller H-R, Zastrow JA, Blake JB (2008) Relationship of the Van Allen radiation belts to solar wind drivers. J Atmos Solar-Terr Phys 70:708–729

Iijima T, Potemra TA (1976) The amplitude distribution of field-aligned currents at northern high latitudes observed by Triad. J Geophys Res 81:2165–2174

Iles RH, Meredith NP, Fazakerley AN, Horne RB (2006) Phase space density analysis of the outer radiation belt energetic electron dynamics. J Geophys Res. doi:10.1029/2005JA011206

Iles RHA, Fazakerley AN, Johnstone AD, Meredith NP, Buhler P (2002) The relativistic electron response in the outer radiation belt during magnetic storms. Ann Geophys 20:957–965.

Janev RK, Smith JJ (1993) Cross sections for collision processes of hydrogen atoms with electrons, protons, and multiply-charged ions. In: Atomic and plasma-material interaction data for fusion. Int Atmos Energ Agency 4:1–80

Jordanova VK, Miyoshi Y (2005) Relativistic model of ring current and radiation belt ions and electrons: initial results. Geophys Res Lett. doi:10.1029/2005GL023020

Jordanova VK, Kistler LM, Kozyra JU, Khazanov GV, Nagy AF (1996) Collisional losses of ring current ions. J Geophys Res 101:111–126

Jordanova VK, Kozyra JU, Nagy AF, Khazanov GV (1997) Kinetic model of the ring current-atmosphere interactions. J Geophys Res 102:14279–14291

Jordanova VK, Farrugia CJ, Quinn JM, Torbert RB, Borovsky JE, Sheldon RB, Peterson WK (1999) Simulation of off-equatorial ring current ion spectra measured by Polar for a moderate storm at solar minimum. J Geophys Res 104:429–436

Jordanova VK, Kistler LM, Thomsen MF, Mouikis CG (2003) Effects of plasma sheet variability on the fast initial ring current decay. Geophys Res Lett. doi:10.1029/2002GL016576

Jordanova VK, Miyoshi Y, Zaharia S, Thomsen MF, Reeves GD, Evans DS, Moukis CG, Fennell JF (2006) Kinetic simulations of ring current evolution during the Geospace Environment Modeling challenging events. J Geophys Res. doi:10.1029/2006JA011644.

Jordanova VK, Spasojevic M, Thomsen MF (2007) Modeling the electromagnetic ion cyclotron wave-induced formation of detached subauroral proton arcs. J Geophys Res. doi:10.1029/2006JA012215

Jordanova VK, Albert J, Miyoshi Y (2008) Relativistic electron precipitation by EMIC waves from self-consistent global simulations. J Geophys Res. doi:10.1029/2008JA013239

Jordanova VK, Thorne RM, Li W, Miyoshi Y (2010) Excitation of whistler-mode chorus from global ring current simulations. J Geophys Res. doi:10.1029/2009JA014810

Jorgensen AM, Spence HE, Henderson MG, Reeves GD, Sugiura M, Kamei T (1997) Global energetic neutral atom (ENA) measurements and their association with the Dst index. Geophys Res Lett 24:3173–3176

Kale ZC, Mann IR, Waters CL, Vellante M, Zhang TL, Honary F (2009) Plasmaspheric dynamics resulting from the Hallowe'en 2003 geomagnetic storms. J Geophys Res 114. doi:10.1029/2009JA014194

Kamide Y (1974) Association of DP and DR fields with the interplanetary magnetic field variation. J Geophys Res 79:49–55

Kamide Y, Fukushima N (1971) Analysis of magnetic storms with DR indices for equatorial ring-current field. Radio Sci 6:277–278

Kamide Y, McIlwain CE (1974) The onset time of magnetospheric substorms determined from ground and synchronous satellite records. J Geophys Res 79:4787–4790

Karlsson T, Marklund G, Blomberg L, Mälkki A (1998) Subauroral electric fields observed by the Freja satellite: a statistical study. J Geophys Res 103:4327–4341

Kasahara Y, Miyoshi Y, Omura Y, Berkhoglyadova O, Nagano I, Kimura I, Tsurutani B (2009) Simultaneous satellite observations of VLF chorus, hot and relativistic electrons in a magnetic storm "recovery phase". Geophys Res Lett. doi:10.1029/2008GL036454

Kataoka R, Miyoshi Y (2006) Flux enhancement of radiation belt electrons during geomagnetic storms driven by coronal mass ejections and corotating interaction regions. Space Weather. doi:10.1029/2005SW000211

Kataoka R, Miyoshi Y (2008a) Magnetosphere inflation during the recovery phase of geomagnetic storms as an excellent magnetic confinement of killer electrons. Geophys Res Lett. doi:10.1029/2007GL031842

Kataoka R, Miyoshi Y (2008b) Average profiles of the solar wind and outer radiation belt during the extreme flux enhancement of relativistic electrons at geosynchronous orbit. Ann Geophys 26:1335–1339

Kataoka R, Nishitani N, Ebihara Y, Hosokawa K, Ogawa T, Kikuchi T, Miyoshi Y (2007) Dynamic variations of a convection flow reversal in the subauroral postmidnight sector as seen by the SuperDARN Hokkaido HF radar. Geophys Res Lett. doi:10.1029/2007GL031552

Katoh Y, Omura Y (2007a) Computer simulation of chorus wave generation in the Earth's inner magnetosphere. Geophys Res Lett. doi:10.1029/2006GL028594

Katoh Y, Omura Y (2007b) Relativistic particle acceleration in the process of whistler-mode chorus wave generation. Geophys Res Lett. doi:10.1029/2007GL029758

Katoh Y, Omura Y, Summers D (2008) Rapid energization of radiation belt electrons by nonlinear wave trapping. Ann Geophys 26:3451–3456

Kavanagh LD Jr, Freeman JW Jr, Chen AJ (1968) Plasma flow in the magnetosphere. J Geophys Res 73:5511–5519

Kaye SM, Shelley EG, Sharp RD, Johnson RG (1981) Ion composition of zipper events. J Geophys Res 86:3383–3388

Keika K, Nosé M, Christon SP, McEntire RW (2004) Acceleration sites of energetic ions upstream of the Earth's bow shock and in the magnetosheath: statistical study on charge states of heavy ions. J Geophys Res. doi:10.1029/2003JA009953

Keika K, Nosé M, Ohtani S-I, Takahashi K, Christon SP, McEntire RW (2005) Outflow of energetic ions from the magnetosphere and its contribution to the decay of the storm time ring current. J Geophys Res. doi:10.1029/2004JA010970

Kelley MC, Fejer BG, Gonzales CA (1979) An explanation for anomalous equatorial ionospheric electric fields associated with a northward turning of the interplanetary magnetic field. Geophys Res Lett 6:301–304

Kennel C, Petschek H (1966) Limit on stably trapped particle fluxes. J Geophys Res 71:1–28

Khazanov GV, Moore TE, Liemohn MW, Jordanova VK, Fok M-C (1996) Global, collisional model of high-energy photoelectrons. Geophys Res Lett 23:331–334

Kikuchi T, Araki T, Maeda H, Maekawa K (1978) Transmission of polar electric fields to the equator. Nature 273: 650–651

Kikuchi T, Lühr H, Kitamura T, Saka O, Schlegel K (1996) Direct penetration of the polar electric field to the equator during a DP 2 event as detected by the auroral and equatorial magnetometer chains and the EISCAT radar. J Geophys Res 101:17161–17173

Kikuchi T, Hashimoto KK, Nozaki K (2008) Penetration of magnetospheric electric fields to the equator during a geomagnetic storm. J Geophys Res. doi:10.1029/2007JA012628

Kikuchi T, Ebihara Y, Hashimoto K, Kataoka R, Hori T, Watari S, Nishitani N (2010) Penetration of the convection and overshielding electric fields to the equatorial ionosphere during a quasi-periodic DP2 geomagnetic fluctuation event. J Geophys Res. doi:10.1029/2008JA013948

Kim H-J, Chan AA (1997) Fully adiabatic changes in storm time relativistic electron fluxes. J Geophys Res 102:22107–22116

Kim H-J, Kim KC, Lee D-Y, Rostoker G (2006) Origin of geosynchronous relativistic electron events. J Geophys Res. doi:10.1029/2005JA011469

Kim KC, Lee D-Y, Kim H-J, Lyons LR, Lee ES, Ozturk MK, Choi CR (2008) Numerical calculations of relativistic electron drift loss effect. J Geophys Res. doi:10.1029/2007JA013011

Kivelson MG, Ridley AJ (2008) Saturation of the polar cap potential: Inference from Alfvén wing arguments. J Geophys Res. doi:10.1029/2007JA012302

Klumpar DM (1979) Transversely accelerated ions: an ionospheric source of hot magnetospheric ions. J Geophys Res 84:4229–4237

Kokubun S (1972) Relationship of interplanetary magnetic field structure with development of substorm and storm main phase. Planet Space Sci 20:1033–1049

Koller J, Chen Y, Reeves GD, Friedel RHW, Cayton TE, Vrugt JA (2007) Identifying the radiation belt source region by data assimilation. J Geophys Res. doi:10.1029/2006JA012196

Kondrashov D, Shprits Y, Ghil M, Thorne R (2007) A Kalman filter technique to estimate relativistic electron lifetimes in the outer radiation belt. J Geophys Res. doi:10.1029/2007JA012583.

Konradi A (1967) Proton events in the magnetosphere associated with magnetic bays. J Geophys Res 72:3829–3841

Konradi A, Semar CL, Fritz TA (1975) Substorm-injected protons and electrons and the injection boundary model. J Geophys Res 80:543–552

Koons HC (1989) Observations of large-amplitude, whistler mode wave ducts in the outer plasmasphere. J Geophys Res 94:15393–15397

Korth A, Friedel RHW, Mouikis CG, Fennell JF, Wygant JR, Korth H (2000) Comprehensive particle and field observations of magnetic storms at different local times from the CRRES spacecraft. J Geophys Res 105:18729–18740

Kotova G, Bezrukikh V, Verigin M, Smilauer J (2008) New aspects in plasmaspheric ion temperature variations from INTERBALL 2 and MAGION 5 measurements. J Atmos Solar-Terr Phys 70:399–406

Kozyra JU, Shelley EG, Comfort, RH, Brace LH, Cravens TE, Nagy AF (1987) The role of ring current O^+ in the formation of stable auroral red arcs. J Geophys Res 92:7487–7502

Kozyra JU, Chandler MO, Hamilton DC Peterson WK, Klumpar DM, Slater DW, Buonsanto MJ, Carlson HC (1993) The role of ring current nose events in producing stable auroral red arc intensifications during the main phase: Observations during the September 19–24:1984, equinox transition study. J Geophys Res 98:9267–9283

Kozyra JU, Nagy AF, Slater DW (1997) High-altitude energy source(s) for stable auroral red arcs. Rev Geophys 35:155–190

Kozyra JU, Fok M-C, Sanchez ER, Evans DS, Hamilton DC, Nagy AF (1998a) The role of precipitation losses in producing the rapid early recovery phase of the great magnetic storm of February 1986. J Geophys Res 103:6801–6814

Kozyra JU, Jordanova VF, Borovsky JE, Thomsen MF, Knipp D, Evans DS, McComas D, Cayton T (1998b) Effects of a high-density plasma sheet on ring current development during the November 2–6:1993, magnetic storm. J Geophys Res 103:26285–26305

Kozyra JU, Liemohn MW (2003) Ring current energy input and decay. Space Sci Rev 109:105–131

Krall J, Huba JD, Fedder JA (2008) Simulation of field-aligned H+ and He+ dynamics during late-stage plasmasphere refilling. Ann Geophys 26:1507–1516

Kress BT, Hudson MK, Slocum PL (2005) Impulsive solar energetic ion trapping in the magnetosphere during geomagnetic storms. Geophys Res Lett. doi:10.1029/2005GL022373

Krimigis SM, Gloeckler G, McEntire RW, Potemra TA, Scarf FL, Shelley EG (1985) Magnetic storm of September 4:1984: a synthesis of ring current spectra and energy densities measured with AMPTE/CCE. Geophys Res Lett 12: 329–332

Lam MM, Horne RB, Meredith NP, Glauert SA (2007) Modeling the effects of radial diffusion and plasmaspheric hiss on outer radiation belt electrons. Geophys Res Lett 34. doi:10.1029/2007GL031598

Lavraud B, Jordanova VK (2007) Modeling the effects of cold-dense and hot-tenuous plasma sheet on proton ring current energy and peak location. Geophys Res Lett. doi:10.1029/2006GL027566.

Lavraud B, Denton MH, Thomsen MF, Borovsky JE, Friedel RHW (2005) Superposed epoch analysis of dense plasma access to geosynchronous orbit. Ann Geophys 23:2519–2529. doi:10.5194/angeo-23-2519-2005.

Le G, Russell CT, Takahashi K (2004) Morphology of the ring current derived from magnetic field observations. Ann Geophys 22:1267–1295

Lee D-Y, Ohtani S, Brandt PC, Lyons LR (2007) Energetic neutral atom response to solar wind dynamic pressure enhancements. J Geophys Res. doi:10.1029/2007JA012399

Lemaire J (1989) Plasma distribution models in a rotating magnetic dipole and refilling of plasmaspheric flux tubes. Phys Fluids B 1:1519–1525.

Lemaire J (2001) The formation of the light ion trough and peeling off the plasmasphere. J Atmos Terr Phys 63: 1285–1291

Lennartsson W (1989) Energetic (0.1- to 16-keV/e) magnetospheric ion composition at different levels of Solar F10.7. J Geophys Res 94:3600–3610

Lennartsson W, Sharp RD (1982) A comparison of the 0.1–17 keV/e ion composition in the near equatorial magnetosphere between quiet and disturbed conditions. J Geophys Res 87:6109–6120

Lennartsson W, Sharp RD, Shelley EG, Johnson RG, Balsiger H (1981) Ion composition and energy distribution during 10 magnetic storms. J Geophys Res 86:4628–4638

Li X, Temerin MA (2001) The electron radiation belt. Space Sci Rev 95:569–580

Li X, Roth I, Temerin M, Wygant JR, Hudson MK, Blake JB (1993) Simulation of the prompt energization and transport of radiation belt particles during the March 24:1991 SSC. Geophys Res Lett 20:2423–2426

Li X, Baker DN, Temerin M, Cayton TE, Reeves GD, Christensen RA, Blake JB, Looper MD, Nakamura R, Kanekal SG (1997) Multisatellite observations of the outer zone electron variation during the November 3–4:1993, magnetic storm. J Geophys Res 102:14123–14140

Li X, Baker DN, Kanekal SG, Looper M, Temerin M (2001) Long term measurements of radiation belts by SAMPEX and their variations. Geophys Res Lett 28:3827–3830

Li X, Baker DN, Temerin M, Reeves G, Friedel R, Shen C (2005) Energetic electrons, 50 keV to 6 MeV, at geosynchronous orbit: their responses to solar wind variations. Space Weather. doi:10.1029/2004SW000105

Li X, Baker DN, O'Brien TP, Xie L, Zong QG (2006) Correlation between the inner edge of outer radiation belt electrons and the innermost plasmapause location. Geophys Res Lett. doi:10.1029/2006GL026294.

Li W, Shprits YY, Thorne RM (2007) Dynamic evolution of energetic outer zone electrons due to wave-particle interactions during storms. J Geophys Res. doi:10.1029/2007JA012368

Li W, Thorne RM, Angelopoulos V, Bortnik J, Cully CM, Ni B, LeContel O, Roux A, Auster U, Magnes W (2009) Global distribution of whistler mode chorus waves observed on the THEMIS spacecraft. Geophys Res Lett. doi:10.1029/2009GL037595

Li W, Thorne RM, Meredith NP, Horne RB, Bortnik J, Shprits YY, Ni B (2008) Evaluation of whistler mode chorus amplication during an injection event observed on CRRES. J Geophys Res. doi:10.1029/2008JA013129

Liemohn MW, Kozyra JU, Jordanova VK, Khazanov GV, Thomsen MF, Cayton TE (1999) Analysis of early phase ring current recovery mechanisms during geomagnetic storms. Geophys Res Lett 26:2845–2848

Liemohn MW, Kozyra JU, Thomsen MF, Roeder JL, Lu G, Borovsky JE, Cayton TE (2001) Dominant role of the asymmetric ring current in producing the stormtime Dst. J Geophys Res 106:10883–10904

Liemohn MW, Ridley AJ, Brandt PC, Gallagher DL, Kozyra JU, Mitchell DG, Roelof EC, DeMajistre R (2005) Parametric analysis of nightside conductance effects on inner magnetospheric dynamics for the 17 April 2002 storm. J Geophys Res. doi:10.1029/2005JA011109

Liemohn MW, Zhang J-C, Thomsen MF, Borovsky JE, Kozyra JU, Ilie R (2008) Plasma properties of superstorms at geosynchronous orbit: how different are they? Geophys Res Lett. doi:10.1029/2007GL031717

Liu W, Rostoker G, Baker D (1999) Internal acceleration of relativistic electrons by large-amplitude ULF pulsations. J Geophys Res 104:17391–17407

Liu S, Chen MW, Roeder JL, Lyons LR, Schulz M (2005a) Relative contribution of electrons to the stormtime total ring current energy content. Geophys Res Lett. doi:10.1029/2004GL021672

Liu WL, Fu SY, Zong Q-G, Pu ZY, Yang J, Ruan P (2005b) Variations of N+/O+ in the ring current during magnetic storms. Geophys Res Lett. doi:10.1029/2005GL023038

Looper MD, Blake JB, Mewaldt RA (2005) Response of the inner radiation belt to the violent Sun-Earth connection events of October-November 2003. Geophys Res Lett. doi:10.1029/2004GL021502

Lopez RE, Sibeck DG, McEntire RW, Krimigis SM (1990) The energetic ion substorm injection boundary. J Geophys Res 95:109–117

Lopez RE, Lyon JG Mitchell E, Bruntz R, Merkin VG, Brogl S, Toffoletto F, Wiltberger M (2009) Why doesn't the ring current injection rate saturate? J Geophys Res. doi:10.1029/2008JA013141.

Lorentzen KR, McCarthy MP, Parks GK, Foat JE, Millan RM, Smith DM, Lin RP, Treilhou JP (2000) Precipitation of relativistic electrons by interaction with electromagnetic ion cyclotron waves. J Geophys Res 5381–5389

Lorentzen KR, Blake JB, Inan US, Bortnik J (2001) Observations of relativistic electron microbursts in association with VLF chorus. J Geophys Res 106:6017–6027

Loto'aniu TM, Mann IR, Ozeke LG, Chan AA, Dent ZC, Milling DK (2006) Radial diffusion of relativistic electrons into the radiation belt slot region during the 2003 Halloween geomagnetic storms. J Geophys Res. doi:10.1029/2005JA011355

Lui ATY (2003) Inner magnetospheric plasma pressure distribution and its local time asymmetry. Geophys Res Lett. doi:10.1029/2003GL017596

Lui ATY, McEntire RW, Krimigis SM (1987) Evolution of the ring current during two geomagnetic storms. J Geophys Res 92:7459–7470

Lui ATY, Spence HE, Stern DP (1994) Empirical modeling of the quiet time nightside magnetosphere. J Geophys Res 99:151–157

Lundin R, Lyons LR, Pissarenko N (1980) Observations of the ring current composition at L < 4. Geophys Res Lett 7:425–428

Lyatsky W Khazanov GV (2008) Effect of solar wind density on relativistic electrons at geosynchronous orbit. Geophys Res Lett. doi:10.1029/2007GL032524

Lyons LR (1974) General relations for resonant particle diffusion in pictcn angle and decay. J Plasma Phys 12:45–49

Lyons LR (1977) Adiabatic evolution of trapped particle pitch angle distributions during a storm main phase. J Geophys Res 82:2428–2432

Lyons LR, Thorne RM (1972) Parasitic pitch angle diffusion of radiation belt particles by ion cyclotron waves. J Geophys Res 77:5608–5616

Lyons LR, Thorne RM (1973) Equilibrium structure of radiation belt electrons. J Geophys Res 78:2142–2149

Lyons LR, Williams DJ (1975a) The quiet time structure of energetic (35–560 keV) radiation belt electrons. J Geophys Res 80:943–950

Lyons LR, Williams DJ (1975b) The storm and poststorm evolution of energetic (35–560 keV) radiation belt electron distributions. J Geophys Res 80:3985–3994

Lyons L, Williams D (1976) Storm-associated variations of equatorially mirroring ring current protons, 1–800 keV, at constant first adiabatic invariant. J Geophys Res 81: 216–220

Lyons LR, Richmond AD (1978) Low-latitude E region ionization by energetic ring current particles. J Geophys Res 83:2201–2204

Lyons LR, Thorne RM, Kennel CF (1972) Pitch-angle diffusion of radiation belt electrons within the plasmasphere. J Geophys Res 77:3455–3474

Lyons LR, Lee D-Y, Thorne RM, Horne RB, Smith AJ (2005) Solar wind–magnetosphere coupling leading to relativistic electron energization during high–speed streams. J Geophys Res. doi:10.1029/2005JA011254

Lyons LR, Lee D-Y, Kim H-J, Hwang JA, Thorne RM, Horne RB, Smith AJ (2009) Solar-wind-magnetosphere coupling, including relativistic electron energization, during high-speed streams. J Atmos Solar-Terr Phys 71:1059–1072

Maget V, Bourdarie S, Boscher D, Friedel RHW (2007) Data assimilation of LANL satellite data into the Salammbo electron code over a complete solar cycle by direct insertion. Space Weather. doi:10.1029/2007SW000322

Makarevich RA, Kellerman AC, Bogdanova YV, Koustov AV (2009) Time evolution of the subauroral electric fields: a case study during a sequence of two substorms. J Geophys Res. doi:10.1029/2008JA013944

Mann IR, O'Brien TP, Milling DK (2004) Correlations between ULF wave power, solar wind speed, and relativistic electron flux in the magnetosphere: solar cycle dependence. J Atmos Solar-Terr Phys 66:187–198

Mathie RA, Mann IR (2001) On the solar wind control of Pc5 ULF pulsation power at mid-latitudes: implications for MeV electron acceleration in the outer radiation belt. J Geophys Res 106:29783–29796

Matsui H, Mukai T, Ohtani S, Hayashi K, Elphic RC, Thomsen MF, Matsumoto H (1999) Cold dense plasma in the outer magnetosphere. J Geophys Res 104:25077–25095

Matsui H, Nakamura M, Terasawa T, Izaki Y, Mukai T, Tsuruda K, Hayakawa H, Matsumoto H (2000) Outflow of cold dense plasma associated with variation of convection in the outer magnetosphere. J Atmos Solar–Terr Phys 62: 521–526

Matsui H, Puhl-Quinn PA, Jordanova VK, Khotyaintsev Y, Lindqvist P-A, Torbert RB (2008) Derivation of inner magnetospheric electric field (UNH–IMEF) model using Cluster data set. Ann Geophys 26:2887–2898

Mauk BH, McIlwain CE (1974) Correlation of Kp with the substorm-injected plasma boundary. J Geophys Res 79:3193–3196

Mauk BH, Meng C-I (1983) Characterization of geostationary particle signatures based on the 'injection boundary' model. J Geophys Res 88:3055–3071

Maynard NC, Chen AJ (1975) Isolated cold plasma regions: observations and their relation to possible production mechanisms. J Geophys Res 80:1009–1013

Maynard NC, Aggson TL, Heppner JP (1980) Magnetospheric observation of large sub-auroral electric fields. Geophys Res Lett 7:881–884

Maynard NC, Aggson TL, Heppner JP (1983) The plasmaspheric electric field as measured by ISEE 1. J Geophys Res 88:3991–4003

McFadden JP, Carlson CW, Larson D, Bonnell J, Mozer FS, Angelopoulos V, Glassmeier K, Auster U (2008) Structure of plasmaspheric plumes and their participation in magnetopause reconnection: first results from THEMIS. Geophys Res Lett. doi:10.1029/2008GL033677

McIlwain CE (1966) Ring current effects on trapped particles. J Geophys Res 71:3623–3628

McIlwain CE (1974) Substorm injection boundaries, In: McComac BM (ed) Magnetospheric physics, D. Reidel, Hingham, MA, p 143

McPherron RL, Baker DN, Crooker NU (2009) Role of the Russell-McPherron effect in the acceleration of relativistic electrons. J Atmos Solar-Terr Phys 71:1032–1044

Meredith NP, Horne RB, Anderson RR (2001) Substorm dependence of chorus amplitudes: implications for the acceleration of electrons to relativistic energies. J Geophys Res 106:13165–13178

Meredith NP, Horne RB, Summers D, Thorne RM, Iles RHA, Heynderickx D, Anderson RR (2002) Evidence for acceleration of outer zone electrons to relativistic energies by whistler mode chorus. Ann Geophys 20:967–979

Meredith NP, Cain M, Horne RB, Thorne RM, Summers D, Anderson RR (2003a) Evidence for chorus-driven electron acceleration to relativistic energies from a survey of geomagnetically disturbed periods. J Geophys Res. doi:10.1029/2002JA009764

Meredith NP, Horne RB, Thorne RM, Anderson RR (2003b) Favored regions for chorus-driven electron acceleration to relativistic energies in the Earth's outer radiation belt. Geophys Res Lett. doi:10.1029/2003GL017698

Meredith NP, Thorne RM, Horne RB, Summers D, Fraser BJ, Anderson RR (2003c) Statistical analysis of relativistic electron energies for cyclotron resonance with EMIC waves on CRRES. J Geophys Res. doi:10.1029/2002JA009700

Meredith NP, Horne RB, Glauert SA, Thorne RM, Summers D, Albert JM, Anderson RR (2006) Energetic outer zone electron loss timescales during low geomagnetic activity. J Geophys Res. doi:10.1029/2005JA011516

Merkin VG, Sharma AS, Papadopoulos K Milikh G, Lyon J, Goodrich C (2005) Global MHD simulations of the strongly driven magnetosphere: modeling of the transpolar potential saturation. J Geophys Res. doi:10.1029/2004JA010993

Milillo A, Orsini S, Daglis IA (2001) Empirical model of proton fluxes in the equatorial inner magnetosphere: development. J Geophys Res 106:25713–25729

Milillo A, Orsini S, Delacourt DC, Mura A, Massetti S, De Angelis E, Ebihara Y (2003) Empirical model of proton fluxes in the equatorial inner magnetosphere: 2. Properties and applications. J Geophys Res. doi:10.1029/2002JA009581

Millan RM, Thorne RM (2007) Review of radiation belt electron losses. J Atmos Solar-Terr Phys 69:362–377

Millan RM, Lin RP, Smith DM, Lorentzen KR, McCarthy MP (2002) X-ray observations of MeV electron precipitation with a balloon-borne germanium spectrometer. Geophys Res Lett. doi:10.1029/2002GL015922.

Mishin EV, Puhl-Quinn PA (2007) SAID: plasmaspheric short circuit of substorm injections. Geophys Res Lett. doi:10.1029/2007GL031925

Mitchell DG, Brandt PC, Roelof EC, Hamilton DC, Retterer KC, Mende S (2003) Global imaging of O^+ from IMAGE/HENA. Space Sci. Rev. 109:63– 75

Miyoshi Y, Kataoka R (2005) Ring current ions and radiation belt electrons during geomagnetic storms driven by coronal mass ejections and corotating interaction regions. Geophys Res Lett. doi:10.1029/2005GL024590

Miyoshi Y, Kataoka R (2008a) Flux enhancement of the outer radiation belt electrons after the arrival of stream interaction regions. J Geophys Res. doi:10.1029/2007JA012506

Miyoshi Y, Kataoka R (2008b) Probabilistic space weather forecast of the relativistic electron flux enhancement at geosynchronous orbit. J Atmos Solar-Terr Phys 70: 475–481

Miyoshi Y, Morioka A, Misawa H (2000) Long term modulation of low altitude proton radiation belt by the Earth's atmosphere. Geophys Res Lett 27:2169–2172

Miyoshi Y, Morioka A, Obara T, Misawa H, Nagai T, Kasahara Y (2003) Rebuilding process of the outer radiation belt during the November 3:1993, magnetic storm – NOAA and EXOS-D observations. J Geophys Res. doi:10.1029/2001JA007542

Miyoshi Y, Jordanova VK, Morioka A, Evans DS (2004) Solar cycle variations of the electron radiation belts: observations and radial diffusion simulation. Space Weather. doi:10.1029/2004SW000070

Miyoshi YS, Jordanova VK, Morioka A, Thomsen MF, Reeves GD, Evans DS, Green JC (2006) Observations and modeling of energetic electron dynamics during the Oct. 2001 storm. J Geophys Res. doi:10.1029/2005JA011351

Miyoshi Y, Morioka A, Kataoka R, Kasahara Y, Mukai T (2007) Evolution of the outer radiation belt during the November 1993 storms driven by corotating interaction regions. J Geophys Res. doi:10.1029/2006JA012148

Miyoshi Y, Sakaguchi K, Shiokawa K, Evans D, Albert J, Connors M, Jordanova V (2008) Precipitation of radiation belt electrons by EMIC waves, observed from ground and space. Geophys Res Lett. doi:10.1029/2008GL035727

Mizera PF, Fennell JF (1977) Signatures of electric fields from high and low altitude particles distributions. Geophys Res Lett 4:311–314

Möbius D, Hovestadt D, Klecker B, Scholer M, Ipavich FM, Carlson CW, Lin RP (1986) A burst of energetic O^+ ions during an upstream particle event. Geophys Res Lett 13:1372–1375

Moldwin MB, Downward L, Rassoul HK, Amin R, Anderson RR (2002) A new model of the location of the plasmapause: CRRES results. J Geophys Res. doi:10.1029/2001JA009211

Moore TE, Arnoldy RL, Feynman J, Hardy DA (1981) Propagating substorm injection fronts. J Geophys Res 86:6713–6726

Moore TE, Fok M-C, Delcourt DC, Slinker SP, Fedder JA (2008) Plasma plume circulation and impact in an MHD substorm. J Geophys Res. doi:10.1029/2008JA013050

Morgan MG, Maynard NC (1976) Evidence of dayside plasmaspheric structure through comparisons of ground-based whistler data and Explorer 45 plasmapause data. J Geophys Res 81:3992–3998

Morioka A, Misawa H, Miyoshi Y, Oya H, Iizima M, Nagai T (2001) Pitch angle distribution of relativistic electrons in the inner radiation belt and its relation to equatorial plasma wave turbulence phenomena. Geophys Res Lett 28:931–934

Murakami G, Yoshikawa I, Obana Y, Yoshikawa K, Ogawa G, Yamazaki A, Kagitani M, Taguchi M, Kikuchi M, Kameda S, Nakamura M (2010) First sequential images of the plasmasphere from the meridian perspective observed by KAGUYA. Earth Planet Space 62, e9–e13

Mursula K, Braysy T, Niskala, K, Russell CT (2001) Pc1 pearls revisited: structured electromagnetic ion cyclotron waves on Polar satellite and on the ground. J Geophys Res 106:29543–29533

Nagai T (1988) "Space Weather Forecast": prediction of relativistic electron intensity at synchronous orbit. Geophys Res Lett 15:425–428

Nagai T, Johnson JFE, Chappell CR (1983) Low-energy (less than 100 eV) ion pitch angle distributions in the magnetosphere by ISEE 1. J Geophys Res 88:6944–6960

Nagai T, Yukimatu AS, Matsuoka A, Asai KT, Green JC, Onsager TG, Singer HJ (2006) Timescales of relativistic electron enhancements in the slot region. J Geophys Res. doi:10.1029/2006JA011837

Nakamura R, Baker DN, Blake JB, Kanekal S, Klechker B, Hovestadt D (1995) Relativistic electron precipitation enhancements near the outer edge of the radiation belt. Geophys Res Lett 22:1129–1132

Nakamura M, Yoshikawa I, Yamazaki A, Shiomi K, Takizawa Y, Hirahara M, Yamashita K, Saito Y, Miyake W (2000a) Terrestrial plasmaspheric imaging by an Extreme Ultraviolet Scanner on Planet-B. Geophys Res Lett 27: 141–144

Nakamura R, Isowa M, Kamide Y, Baker DN, Blake JB, Looper M (2000b) SAMPEX observations of precipitation bursts in the outer radiation belt. J Geophys Res 105:15875–15885

Ni B, Thorne RM, Shprits YY, Bortnik J (2008) Resonant scattering of plasma sheet electrons by whistler-mode chorus: contribution to diffuse auroral precipitation. Geophys Res Lett 35. doi:10.1029/2008GL034032.

Ni B, Shprits Y, Thorne R, Friedel R, Nagai T (2009a) Reanalysis of relativistic radiation belt electron phase space density using multisatellite observations: sensitivity to empirical magnetic field models. J Geophys Res. doi:10.1029/2009JA014438

Ni B, Shprits Y, Nagai T, Thorne R, Chen Y, Kondrashov D, Kim H-J (2009b) Reanalysis of the radiation belt electron phase space density using nearly equatorial CRRES and polar-orbiting Akebono satellite observations. J Geophys Res. doi:10.1029/2008JA013933

Nishida A (1966) Formation of plasmapause, or magnetospheric plasma knee, by the combined action of magnetospheric convection and plasma escape from the tail. J Geophys Res 71:5669–5679

Nishida A (1976) Outward diffusion of energetic particles from the Jovian radiation belt. J Geophys Res 81:1771–1773

Nishimura Y, Wygant J, Ono T, Iizima M, Kumamoto A, Brautigam D, Friedel R (2008) SAPS measurements around the magnetic equator by CRRES. Geophys Res Lett. doi:10.1029/2008GL033970

Northrop TG, Teller E (1960) Stability of the adiabatic motion of charged particles in the Earth's field. Phys Rev 117:215–225

Nosé M, Ieda A, Christon SP (2009a) Geotail observations of plasma sheet ion composition over 16 years: on variations of average plasma ion mass and O+ triggering substorm model. J Geophys Res. doi:10.1029/2009JA014203

Nosé M, Taguchi S, Christon SP, Collier MR, Moore TE, Carlson CW, McFadden JP (2009b) Response of ions of ionospheric origin to storm time substorms: coordinated observations over the ionosphere and in the plasma sheet. J Geophys Res. doi:10.1029/2009JA014048

Obara T, Nagatsuma T, Den M, Miyoshi Y, Morioka A (2000) Main–phase creation of "seed" electrons in the outer radiation belt. Earth Planet Space 52:41–47

Ober DM, Horwitz JL, Gallagher DL (1997) Formation of density troughs embedded in the outer plasmasphere by subauroral ion drift events. J Geophys Res 102:14595–14602

Ober DM, Maynard NC, Burke WJ (2003) Testing the Hill model of transpolar potential saturation. J Geophys Res. doi:10.1029/2003JA010154

O'Brien TP, McPherron RL, Sornette D, Reeves GD, Friedel R, Singer HJ (2001) Which magnetic storms produce relativistic electrons at geosynchronous orbit? J Geophys Res 106:15533–15544

O'Brien TP, Lorentzen KR, Mann IR, Meredith NP, Blake JB, Fennell JF, Looper MD, Milling DK, Anderson RR (2003) Energization of relativistic electrons in the present of ULF power and MeV microbursts: evidence for dual ULF and VLF acceleration. J Geophys Res. doi:10.1029/2002JA009784

O'Brien TP, Looper MD, Blake JB (2004) Quantification of relativistic electron microburst losses during the GEM storms. Geophys Res Lett. doi:10.1029/2003GL018621

Ohtani S, Brandt PC, Singer HJ, Mitchell DG, Roelof EC (2006) Statistical characteristics of hydrogen and oxygen ENA emission from the storm-time ring current. J Geophys Res. doi:10.1029/2005JA011201

Ohtani S, Ebihara Y, Singer HJ (2007a) Storm-time magnetic configurations at geosynchronous orbit: comparison between the main and recovery phases. J Geophys Res. doi:10.1029/2006JA011959

Ohtani S et al (2007b) Cluster observations in the inner magnetosphere during the 18 April 2002 sawtooth event: dipolarization and injection at r = 4.6 RE. J Geophys Res. doi:10.1029/2007JA012357

Ohtani S, Miyoshi Y, Singer H, Weygand J (2009) On the loss of relativistic electrons at geosynchronous altitude: its dependence on magnetic configurations and external conditions. J Geophys Res. doi:10.1029/2008JA013391

Olsen RC (1981) Equatorially Trapped plasma populations. J Geophys Res 86:11235–11245

Olsen RC, Shawhan SD, Gallagher DL, Green JL, Chappell CR, Anderson RR (1987) Plasma observations at the Earth's magnetic equator. J Geophys Res 92:2385–2407

Omura Y, Furuya N, Summers D (2007) Relativistic turning acceleration of resonant electrons by coherent whistler mode waves in a dipole magnetic field. J Geophys Res. doi:10.1029/2006JA012243

Omura Y, Katoh Y, Summers D (2008) Theory and simulation of generation of whistler-mode chorus. J Geophys Res. doi:10.1029/2007JA012622

Omura Y, Pickett J, Grison B, Santolik O, Dandouras I, Engebretson M, Décréau PME, Masson A (2010) Theory and observation of electromagnetic ion cyclotron triggered emissions in the magnetosphere. J Geophys Res. doi:10.1029/2010JA015300

Ono T, Hirasawa T, Meng CI (1987) Proton auroras observed at the equatorward edge of the duskside auroral oval. Geophys Res Lett 14:660–663

Ono Y, Nosé M, Christon SP, Lui ATY (2009) The role of magnetic field fluctuations in nonadiabatic acceleration of ions during depolarization. J Geophys Res. doi:10.1029/2008JA013918

Onsager TG, Chan AA, Fei Y, Elkington SR, Green JC, Singer HJ (2004) The radial gradient of relativistic electrons at geosynchronous orbit. J Geophys Res. doi:10.1029/2003JA010368

Onsager TG, Green JC, Reeves GD, Singer HJ (2007) Solar wind and magnetospheric conditions leading to abrupt loss of outer radiation belt electrons. J Geophys Res. doi:10.1029/2006JA011708

Østgaard N, Mende SB, Frey HU, Gladstone GR, Lauche H (2003) Neutral hydrogen density profiles derived from geocoronal imaging. J Geophys Res. doi:10.1029/2002JA009749

Oya H, Ono T (1987) Stimulation of plasma waves in the magnetosphere using satellite JIKIKEN (EXOS B) Part II: plasma density across the plasmapause. J Geomagn Geoelectr 39:591–607

Ozeke LG, Mann IR (2008) Energization of radiation belt electrons by ring current ion driven ULF waves. J Geophys Res. doi:10.1029/2007JA012468

Park CG (1970) Whistler observations of the interchange of ionization between the ionosphere and the protonosphere. J Geophys Res 75:4249–4260

Park CG (1974) Some features of plasma distribution in the plasmasphere deduced from Antarctic whistlers. J Geophys Res 79:169–173

Parker EN (1957) Newtonian development of the dynamical properties of ionized gases of low density. Phys Rev 107:924–933

Paulikas GA, Blake JB (1979) Effects of the solar wind on magnetospheric dynamics: energetic electrons at the synchronous orbit. In: Olson WP (ed) Quantitative modeling of magnetospheric processes. AGU, Washington, DC, pp 180–202

Perry KL, Hudson MK, Elkington SR (2005) Incorporating spectral characteristic of Pc5 waves into three-dimensional radiation belt modeling and the diffusion of relativistic electrons. J Geophys Res. doi:10.1029/2004JA010760

Peterson WK, Doering JP, Potemra TA, McEntire RW, Bostrom CO (1977) Conjugate photoelectron fluxes observed on Atmosphere Explorer C. Geophys Res Lett 4:109–112

Peymirat C, Richmond AD, Kobea AT (2000) Electrodynamic coupling of high and low latitudes: simulations of shielding/overshielding effects. J Geophys Res 105:22991–23003

Phaneuf RA, Janev RK, Pindzola MS (1987) Atomic data for fusion, vol. V, Collisions of carbon and oxygen ions with electrons, H, H_2 and He. Technical Report ORNL–6090/V5, Oak Ridge National Laboratory, Oak Ridge, TN

Pickett JS, Grison B, Engebretson MJ, Dan douras I, Masson A, Adrian ML, Decreau PME, Cornilleau-Wehrlin N, Constantinescu D (2010) Cluster observations of EMIC triggered emissions in association with Pc1 waves near Earth′s plasmapause. Geophys Res Lett 37:L09104. doi:10.1029/2010GL042648

Pollock CJ et al (2001) First medium energy neutral atom (MENA) Images of Earth′s magnetosphere during substorm and storm-time. Geophys Res Lett 28:1147–1150

Pulkkinen TI, Ganushkina NYu, Baker DN, Turner NE, Fennell JF, Roeder J, Fritz TA, Grande M, Kellett B, Kettmann G (2001) Ring current ion composition during solar minimum and rising solar activity: polar/CAMMICE/MICS results. J Geophys Res 106:19131–19147

Quinn JM, McIlwain CE (1979) Bouncing ion clusters in the Earth's magnetosphere. J Geophys Res 84:7365–7370

Quinn JM, Johnson RG (1982a) Composition measurements of warm equatorially trapped ions near geosynchronous orbit. Geophys Res Lett 9:777–780

Quinn JM, Southwood DJ (1982) Observations of parallel ion energization in the equatorial region. J Geophys Res 87:10536–10540

Rairden RL, Frank LA, Craven JD (1986) Geocoronal imaging with dynamics explorer. J Geophys Res 91:13613–13630

Rasmussen CE, Guiter SM, Thomas SG (1993) A two-dimensional model of the plasmasphere: refilling time constants. Planet Space Sci 41:35–43

Reeves GD (2007) Radiation belt storm probes: a new mission for space weather forecasting. Space Weather. doi:10.1029/2007SW000341

Reeves GD, Henderson MG, McLachlan PS, Belian RD, Friedel RHW, Korth A (1996) Radial propagation of substorm injections, In: Proceedings of the Third International Conference on Substorms, Versailles, France, 12–17 May 1996. Eur. Space Agency Spec. Publ., ESA SP–389, pp 579–584

Reeves G, Friedel R, Belian R, Meier M, Henderson M, Onsager T, Singer H, Baker D, Li X, Blake J (1998) The relativistic electron response at geosynchronous orbit during the January 1997 magnetic storm. J Geophys Res 103:17559–17570

Reeves GD, McAdams KL, Friedel RHW, O'Brien TP (2003) Acceleration and loss of relativistic electrons during geomagnetic storms. Geophys Res Lett. doi:10.1029/2002GL016513

Reiff PH, Spiro RW, Hill TW (1981) Dependence of polar cap potential drop on interplanetary parameters. J Geophys Res 86:7639–7648

Reinisch BW, Moldwin MB, Denton RE, Gallagher DL, Matsui H, Pierrard V, Tu J (2009) Augmented empirical models of plasmaspheric density and electric field using IMAGE and CLUSTER Data. Space Sci Rev 145:231–261

Richards PG, Torr DG (1985) Seasonal, diurnal, and solar cyclical variations of the limiting H+ flux in the Earth's topside ionosphere. J Geophys Res 90:5261–5268

Roeder JL, Fennell JF, Grande M, Livi S, Sheldon R (1999) Ring current response to interplanetary magnetic cloud events. Phys Chem Earth, Part C: Solar Terr Planet Sci 24:83–87

Roederer JG (1970) Dynamics of geomagnetically trapped radiation. Springer, New York, NY

Roelof EC (1989) Remote sensing of the ring current using energetic neutral atoms. Adv Space Res 9:195–203

Roelof EC, Skinner AJ (2000) Extraction of ion distributions from magnetospheric ENA and EUV images. Space Sci Rev 91:437–459

Rostoker G, Skone S, Baker DN (1998) On the origin of relativistic electrons in the magnetosphere associated with some geomagnetic storms. Geophys Res Lett 25:3701–3704

Rowe JF Jr (1974) Magnetic activity variations of the nighttime E region at Arecibo. Radio Sci 9:175–182

Rowland D, Wygant J (1998) Dependence of the large-scale, inner magnetospheric electric field on geomagnetic activity. J Geophys Res 103:14959–14964

Rozanov E, Callis L, Schlesinger M, Yang F, Andronova N, Zubov V (2005) Atmospheric response to NOy source due to energetic electron precipitation. Geophys Res Lett. doi:10.1029/2005GL023041

Russell CT, McPherron RL (1973) Semiannual variation of geomagnetic activity. J Geophys Res 78:92–108

Sagawa E, Yau AW, Whalen BA, Peterson WK (1987) Pitch angle distributions of low-energy ions in the near-Earth magnetosphere. J Geophys Res 92:12241–12254

Saito S, Miyoshi Y, Seki K (2010) A split in the outer radiation belt by magnetopause shadowing: test particle simulations. J Geophys Res. doi:10.1029/2009JA014738

Sakaguchi K, Shiokawa K, Ieda A, Miyoshi Y, Otsuka Y, Ogawa T, Connors M, Donovan EF, Rich FJ (2007) Simultaneous ground and satellite observations of an isolated proton arc at subauroral latitudes. J Geophys Res. doi:10.1029/2006JA012135

Sakaguchi K, Shiokawa K, Miyoshi Y, Otsuka Y, Ogawa T, Asamura K, Connors M (2008) Simultaneous appearance of isolated aurora arcs and Pc1 geomagnetic pulsations at subauroral latitudes. J Geophys Res. doi:10.1029/2007JA012888

Sandanger M, Søraas F, Aarsnes K, Oksavik K, Evans DS (2007) Loss of relativistic electrons: evidence for pitch angle scattering by electromagnetic ion cyclotron waves excited by unstable ring current protons. J Geophys Res. doi:10.1029/2006JA012138

Sandel BR, Denton MH (2007) Global view of refilling of the plasmasphere. Geophys Res Lett. doi:10.1029/2007GL030669

Sandel BR, Goldstein J, Gallagher DL, Spasojevic M (2003) Extreme ultraviolet imager observations of the structure and dynamics of the plasmasphere. Space Sci. Rev 109:25–46

Sandel BR, King RA, Forrester WT, Gallagher DL, Broadfoot AL, Curtis CC (2001) Initial results from the IMAGE Extreme Ultraviolet Imager. Geophys Res Lett. doi:10.1029/2001GL012885

Santolik O, Gurnett DA, Pickett JS, Parrot M, Cornilleau-Wehrlin N (2003) Spatio-temporal structure of storm-time chorus. J Geophys Res. doi:10.1029/2002JA009791

Sarris TE, Li X, Temerin M (2006) Simulating radial diffusion of energetic (MeV) electrons through a model of fluctuating electric and magnetic fields. Ann Geophys 24:1–16

Sarris TE, Loto'aniu TM, Li X, Singer HJ (2007) Observations at geosynchronous orbit at a persistent Pc5 geomagnetic pulsation and energetic electron flux modulations. Ann Geophys 25:1653–1667

Schulz M (1991) The magnetosphere. In: Jacobs JA (ed) Geomagnetism. Academic, London, pp 87–293

Schulz M, Koons HC (1972) Thermalization of colliding ion streams beyond the plasmapause. J Geophys Res 77:248–254

Schulz M, Lanzerotti LJ (1974) Particle diffusion in the radiation belts. Sprinter, Heidelberg, Germany

Scime EE, Keesee AM Jahn J, Kline JL, Pollock CJ, Thomsen MF (2002) Remote ion temperature measurements of Earth's magnetosphere: medium energy neutral atom (MENA) images. Geophys Res Lett. doi:10.1029/2001GL013994

Sckopke N (1966) A general relation between the energy of trapped particles and the disturbance field near the Earth. J Geophys Res 71:3125–3135

Seki K, Miyoshi Y, Summers D, Meredith NP (2005) Comparative study of outer-zone relativistic electrons observed by Akebono and CRRes. J Geophys Res. doi:10.1029/2004JA010655

Selesnick RS, Blake JB (2000) On the source location of radiation belt electrons. J Geophys Res 105:2607–2624

Selesnick RS, Looper MD, Mewaldt RA (2007) A theoretical model of the inner proton radiation belt. Space Weather. doi:10.1029/2006SW000275

Senior C (1991) Solar and particle contributions to auroral height integrated conductivities from EISCAT data: a statistical study. Ann Geophys 9:449–460

Senior C, Sharber JR, de la Beaujardière O, Heelis RA, Evans DS, Winningham JD, Sugiura M, Hoegy WR (1987) E and F region study of the evening sector auroral oval: a Chatanika/Dynamics Explorer 2/NOAA 6 comparison. J Geophys Res 92:2477–2494

Sergeev VA, Sazhina EM, Tsyganenko NA, Lundblad JÅ, Søraas F (1983) Pitch-angle scattering of energetic protons in the magnetotail current sheet as the dominant source of their isotropic precipitation into the nightside ionosphere. Planet Space Sci 31:1147–1155

Sergeev VA, Malkov M, Mursula K (1993) Testing the isotropic boundary algorithm method to evaluate the magnetic field configuration in the tail. J Geophys Res 98:7609–7620

Sergeev VA, Shukhtina MA, Rasinkangas R, Korth A, Reeves GD, Singer HJ, Thomsen MF, Vagina LI (1998) Event study of deep energetic particle injections during substorm. J Geophys Res 103:9217–9234

Sheldon RB, Spence HE, Fennell JF (1998) Observation of the 40 keV field-aligned ion beams. Geophys Res Lett 25:1617–16i20

Shinbori A, Ono T, Iizima T, Kumamoto A (2004) SC related electric and magnetic field phenomena observed by the Akebono satellite inside the plasmasphere. Earth Planet Space 56:269–282

Shprits YY, Thorne RM, Friedel R, Reeves GD, Fennell J, Baker DN, Kanekal SG (2006) Outward radial diffusion driven by losses at magnetopause. J Geophys Res. doi:10.1029/2006JA011657

Shprits Y, Kondrashov D, Chen Y, Thorne R, Ghil M, Friedel R, Reeves G (2007) Reanalysis of relativistic radiation belt electron fluxes using CRRES satellite data, a radial diffusion model, and a Kalman filter. J Geophys Res. doi:10.1029/2007JA012579.

Shprits YY, Elkington SR, Meredith NP, Subbotin DA (2008a) Review of modeling of losses and sources of relativistic electrons in the outer radiation belt I: radial transport. J Atmos Solar-Terr Phys 70:1679–1693

Shprits YY, Subbotin DA, Meredith NP, Elkington SR (2008b) Review of modeling of losses and sources of relativistic electrons in the outer radiation belt II: local acceleration and loss. J Atmos Solar-Terr Phys 70:1694–1713

Shprits YY, Subbotin DA, Ni B (2009) Evolution of electron fluxes in the outer radiation belt computed with the VERB code. J Geophys Res 114. doi:10.1029/2008JA013784.

Singh N, Horwitz JL (1992) Plasmasphere refilling: recent observations and modeling. J Geophys Res 97:1049–1079

Siscoe GL, Crooker NU, Siebert KD (2002) Transpolar potential saturation: roles of region 1 current system and solar wind ram pressure. J Geophys Res. doi:10.1029/2001JA009176

Sitnov MI, Tsyganenko NA, Ukhorskiy AY, Brandt PC (2008) Dynamical data-based modeling of the storm-time geomagnetic field with enhanced spatial resolution. J Geophys Res. doi:10.1029/2007JA013003

Smith PH, Hoffman RA (1973) Ring current particle distributions during the magnetic storms of December 16–18:1971. J Geophys Res 78:4731–4737

Smith PH, Bewtra NK (1976) Dependence of the charge exchange lifetimes on mirror latitude. Geophys Res Lett 3:689–692

Smith JP, Thomsen MF, Borovsky JE, Collier M (1999) Solar wind density as a driver for the ring current in mild storms. Geophys Res Lett 26:1797–1800

Sojka J, Schunk R, Johnson J, Waite J, Chappell C (1983) Characteristics of Thermal and suprathermal ions associated with the dayside plasma trough as measured by the dynamics explorer retarding ion mass spectrometer. J Geophys Res 88:7895–7911

Song P, Russell C (1992) Model of the formation of the low-latitude boundary layer for strongly northward interplanetary magnetic field. J Geophys Res 97:1411–1420

Song XT, Gendrin R, Caudal G (1988) Refilling process in the plasmasphere and its relation to magnetic activity. J Atmos Terr Phys 50:185–195

Song P, DeZeeuw DL, Gombosi TI, Groth CPT, Powell KG (1999) A numerical study of solar wind-magnetosphere interaction for northward interplanetary magnetic field. J Geophys Res 104:28361–28378

Southwood DJ, Dungey JW, Etherington RJ (1969) Bounce resonant interaction between pulsations and trapped particles. Planet Space Sci 17:349–361

Spasojevic M, Thomsen MF, Chi PJ, Sandel BR (2005) Afternoon subauroral proton precipitation resulting from ring current-plasmasphere interaction. In: Burch J, Schulz M, Spence H (eds) Inner magnetosphere interactions: new perspective from imaging. doi: 10.1029/159GM12. AGU, Washington DC

Spence HE, Kivelson MG (1993) Contributions of the low-latitude boundary layer to the finite width magnetotail convection model. J Geophys Res 98:15487–15496

Spence HE, Kivelson MG, Walker RJ, McComas DJ (1989) Magnetospheric plasma pressures in the midnight meridian: observations from 2.5 to 35 RE. J Geophys Res 94:5264–5272

Spiro RW, Wolf RA (1984) Electrodynamics of convection in the inner magnetosphere. In: Potemra TA (ed) Magnetospheric currents. Geophysical monograph series, vol 28. AGU, Washington, DC, p 248

Spiro RW, Heelis RA, Hanson WB (1979) Rapid subauroral ion drifts observed by Atmospherics Explorer C. Geophys Res Lett 6:657–660

Spiro RW, Wolf RA, Fejer BG (1988) Penetration of high-altitude-electric-field effects to low latitudes during SUNDIAL 1984. Ann Geophys 6:39–49

Stüdemann W et al (1987) The May 2–3:1986 magnetic storm: first energetic ion composition observations with the MICS instrument on Viking. Geophys Res Lett 14:455–458

Subbotin D, Shprits Y, Ni B (2010) Three-dimensional VERB radiation belt simulations including mixed diffusion. J Geophys Res. doi:10.1029/2009JA015070.

Sugiura M (1964) Hourly values of equatorial Dst for IGY. In: Berkner LV(eds) Annals of the International Geophysical Year, 35. Pergamon Press, Oxford, pp 9–45

Sugiura M, Ledley B, Skillman T, Heppner J (1971) Magnetospheric-field distortions observed by Ogo 3 and 5. J Geophys Res 76:7552–7565

Summers D (2005) Quasi-linear diffusion coefficients for field-aligned electromagnetic waves with applications to the magnetosphere. J Geophys Res 110. doi:10.1029/2005JA011159

Summers D, Ma C (2000) Rapid acceleration of electrons in the magnetosphere by fast-mode MHD waves. J Geophys Res 105:15887–15895

Summers D, Thorne RM (2003) Relativistic electron pitch-angle scattering by electromagnetic ion cyclotron waves during geomagnetic storms. J Geophys Res 108. doi:10.1029/2002JA009489

Summers D, Thorne RM, Xiao F (1998) Relativistic theory of wave-particle resonant diffusion with application to electron acceleration in the magnetosphere. J Geophys Res 103:20487–20500

Summers D, Thorne RM, Xiao F (2001) Gyroresonant acceleration of electrons in the magnetosphere by superluminous electromagnetic waves. J Geophys Res 106:10853–10868

Summers D, Ni B, Meredith NP (2007) Timescales for radiation belt electron acceleration and loss due to resonant wave-particle interactions: 1. Theory. J Geophys Res 112. doi:10.1029/2006JA011801.

Søraas F, Oksavik K, Aarsnes K, Evans DS, Greer MS (2003) Storm time equatorial belt-an "image" of RC behavior. Geophys Res Lett. doi:10.1029/2002GL015636

Sørbø M, Søraas F, Aarsnes K, Oksavik K, Evans DS (2006) Latitude distribution of vertically precipitating energetic neutral atoms observed at low altitudes. Geophys Res Lett 33. doi:10.1029/2005GL025240

Takahashi K, Ukhorskiy AY (2007) Solar wind control of Pc5 pulsation power at geosynchronous orbit. J Geophys Res. doi:10.1029/2007JA012483

Takahashi K, Ohtani S, Denton RE, Hughes WJ, Anderson RR (2008) Ion composition in the plasma trough and plasma plume derived from a combined release and radiation effects satellite magnetoseismic study. J Geophys Res. doi:10.1029/2008JA013248

Takasaki S, Kawano H, Tanaka Y, Yoshikawa A, Seto M, Iizima M, Obana Y, Sato N, Yumoto K (2006) A significant mass density increase during a large magnetic storm in October 2003 obtained by ground-based ULF observations at L $\sim$ 1.4. Earth Planet Space 58:617–622

Tan LC, Fung SF, Shao X (2004) Observation of magnetospheric relativistic electrons accelerated by Pc–5 ULF waves. Geophys Res Lett. doi:10.1029/2004GL019459

Taylor HA Jr (1972) The light ion trough. Planet Space Sci 20:1593–1599

Terada N, Iyemori T, Nose M, Nagai T, Matsumoto H, Goka T (1998) Storm–time magnetic field variations observed by the ETS-VI satellite. Earth Planet Space 50:853–864

Terasawa T et al (1997) Solar wind control of density and temperature in the near-Earth plasma sheet: WIND/GEOTAIL collaboration. Geophys Res Lett 24:935–938

Thomsen M, Borovsky J, McComas D, Collier M (1998) Variability of the ring current source population. Geophys Res Lett 25:3481–3484

Thomsen MF, Borovsky JE, Skoug RM, Smith CW (2003) Delivery of cold, dense plasma sheet material into the near-Earth region. J Geophys Res. doi:10.1029/2002JA009544

Thorne RM, Kennel CF (1971) Relativistic electron precipitation during magnetic storm main phase. J Geophys Res 76:4446–4453

Thorne RM (1977) Energetic radiation belt electron precipitation: a natural depletion mechanism for stratospheric ozone. Science 195:287–289

Thorne RM, Horne RB (1994) Energy transfer between energetic ring current H^+ and O^+ by electromagnetic ion cyclotron waves. J Geophys Res 99:17275–17282

Thorne RM, Horne RB (1997) Modulation of electromagnetic ion cyclotron instability due to interaction with ring current O^+ during magnetic storms. J Geophys Res 102:14155–14163

Thorne RM O'Brien TP, Shprits YY, Summers D, Horne RB (2005) Timescale for MeV electron microburst loss during geomagnetic storms. J Geophys Res. doi:10.1029/2004JA010882

Tinsley BA (1981) Neutral atom precipitation – a review. J Atmos Terr Phys 43:617–632,

Tsurutani BT, Gonzalez WD, Gonzalez ALC, Guarnieri FL, Gopalswamy N, Grande M, Kamide Y, Kasahara Y, Lu G, Mann I, McPherron R, Sorass F, and Vasyliunas V (2006) Corotating solar wind streams and recurrent geomagnetic activity: a review. J Geophys Res. doi:10.1029/2005JA011273

Tu J, Song P, Reinisch BW, Green JL, Huang X (2006) Empirical specification of field–aligned plasma density profiles for plasmasphere refilling. J Geophys Res 111. doi:10.1029/2005JA011582

Turner NE, Baker DN, Pulkkinen TI, Roeder JL Fennell JF, Jordanova VK (2001) Energy content in the storm time ring current. J Geophys Res 106:19149–19156

Tverskaya LV, Pavlov NN, Blake JB, Selesnick RS, Fennell JF (2003) Predicting the L-position of the storm-injected relativistic electron belt. Adv Space Res 31:1039–1044

Ukhorskiy AY, Anderson BJ, Takahashi K, Tsyganenko NA (2006) Impact of ULF oscillations in solar wind dynamic pressure on the outer radiation belt electrons. Geophys Res Lett. doi:10.1029/2005GL024380

Unwin RW, Cummack CH (1980) Drift spikes: the ionospheric signature of large poleward directed electric fields at subauroral latitudes. Mem Natl Inst Polar Res 16:72 (Special Issue "IMS in Antarctica")

Usanova ME, Mann IR, Rae IJ, Kale ZC, Angelopoulos V, Bonnell JW, Classmeier K-H, Auster HU, Singer HJ (2008) Multipoint observations of magnetospheric compression-related EMIC Pc1 waves by THEMIS and CARISMA. Geophys Res Lett. doi:10.1029/2008GL034458

Vallance Jones A (1974) Aurora D. Reidel, Norwell, MA

Vallat et al (2005) First current density measurements in the ring current region using simultaneous multi-spacecraft Cluster-FGM data. Ann Geophys 23:1849–1865

Van Allen JA, Frank LA (1959) Radiation around the earth to a radial distance of 107400 km. Nature 183:430–434

Varotsou A, Boscher D, Bourdarie S, Horne RB, Glauert SA, Meredith NP (2005) Simulation of the outer radiation belt electrons near geosynchronous orbit including both radial diffusion and resonant interaction with whistler-mode chorus waves. Geophys Res Lett. doi:10.1029/2005GL023282

Varotsou A, Boscher D, Bourdarie S, Horne RB, Meredith NP, Glauert SA, Friedel RH (2008) Three-dimensional test simulations of the outer radiation belt electron dynamics including electron-chorus resonant interactions. J Geophys Res. doi:10.1029/2007JA012862

Vassiliadis D, Klimas AJ, Weigel RS, Baker DN, Rigler EJ, Kanekal SG, Nagai T, Fung SF, Friedel RWH, Cayton TE (2003) Structure of Earth's outer radiation belt inferred from long-term electron flux dynamics. Geophys Res Lett. doi:10.1029/2003GL017328

Vassiliadis D, Fung SF, Klimas AJ (2005) Solar, interplanetary, and magnetospheric parameters for the radiation belt energetic electron flux. J Geophys Res. doi:10.1029/2004JA010443

Vasyliunas VM (1970) Mathematical models of magnetospheric convection and its couplingt to the ionosphere, In: McCormac BM (ed) Particles and fields in the magnetosphere. D. Reidel, New York, NY pp. 60–71

Voiculescu M, Roth M (2008) Eastward sub-auroral ion drifts or ASAID. Ann Geophys 26:1955–1963

Walker RJ, Erickson KN, Swanson RL, Winckler JR (1976) Substorm-associated particle boundary motion at synchronous orbit. J Geophys Res 81:5541–5550

Wang C, Newman TS, Gallagher DL (2007) Plasmapause equatorial shape determination via the Minimum L Algorithm: description and evaluation. J Geophys Res. doi:10.1029/2006JA012202

Wang H, Ridley AJ, Lühr H, Liemohn MW, Ma SY (2008) Statistical study of the subauroral polarization stream: its dependence on the cross-polar cap potential and subauroral conductance. J Geophys Res. doi:10.1029/2008JA013529

West H Jr, Buck R, Walton J (1973) Electron Pitch Angle Distributions throughout the Magnetosphere as Observed on Ogo 5. J Geophys Res 78:1064–1081

Weimer DR (2001) An improved model of ionospheric electric potentials including substorm perturbations and application to the Geospace Environment Modeling November 24:1996, event. J Geophys Res 106:407–416

Weimer DR (2005) Improved ionospheric electrodynamic models and application to calculating Joule heating rates. J Geophys Res. doi:10.1029/2004JA010884

Williams DJ (1981) Ring current composition and sources: an update. Planet Space Sci 29:1195–1203

Williams DJ, Arens JF, Lanzerotti LJ (1968) Observations of trapped electrons at low and high altitudes. J Geophys Res 73:5673–5696

Wolf RA (1970) Effects of ionospheric conductivity on convective flow of plasma in the magnetosphere. J Geophys Res 75:4677–4698

Wolf RA, Harel M, Spiro RW, Voigt G-H, Reiff PH, Chen C-K (1982) Computer simulation of inner magnetospheric dynamics for the magnetic storm of July 29:1977. J Geophys Res 87:5949–5962

Wygant JR, Torbert RB, Mozer FS (1983) Comparison of S3-3 polar cap potential with the interplanetary magnetic field and models of magnetospheric reconnection. J Geophys Res 88:5727–5735

Xiao F, Thorne RM, Summers D (2007) Higher-order gyroresonant acceleration of electrons by superluminous (AKR) wave modes. Planet Space Sci 55:1257–1271

Xiao F, Su Z, Zheng H, Wang S (2010a) Three-dimensional simulations of outer radiation belt electron dynamics including cross-diffusion terms. J Geophys Res. doi:10.1029/2009JA014541

Xiao F, Su Z, Chen L, Zheng H, Wang S (2010b) A parametric study on outer radiation belt electron evolution by superluminous R-X mode waves. J Geophys Res. doi:10.1029/2010JA015374

Yahnin AG, Yahnina TA, Frey HU (2007) Subauroral proton spots visualize the Pc1 source. J Geophys Res. doi:10.1029/2007JA012501

Yahnina TA, Frey HU, Bösinger T, Yahnin AG (2008) Evidence for subauroral proton flashes on the dayside as the result of the ion cyclotron interaction. J Geophys Res. doi:10.1029/2008JA013099

Yamauchi M, Lundin R, Mursula K, Marklund G, Potemra TA (1996) Dayside Pc5 pulsation detected by Viking ion data at L=4. Geophys Res Lett 23:2517–2520

Yamauchi M, Ebihara Y, Dandouras I, Rème H (2009) Dual source populations of substorm-associated ring current ions, Ann Geophys 27:1431–1438

Yao Y, Seki K, Miyoshi Y, McFadden JP, Lund EJ, Carlson CW (2008) Statistical properties of the multiple ion band structures observed by the FAST satellite. J Geophys Res. doi:10.1029/2008JA013178

Yau AW, Beckwith PH, Peterson WK, Shelley EG (1985a) Long-term (solar cycle) and seasonal variations of upflowing ionospheric ion events at DE 1 Altitudes. J Geophys Res 90:6395–6407

Yau AW, Shelley EG, Peterson WK, Lenchyshyn L (1985b) Energetic auroral and polar ion outflow at DE 1 altitudes: magnitude, composition, magnetic activity dependence, and long-term variations. J Geophys Res 90:8417–8432

Yizengaw E, Wei H, Moldwin MB, Galvan D, Mandrake L, Mannucci A, Pi X (2005) The correlation between

mid-latitude trough and the plasmapause. Geophys Res Lett. doi:10.1029/2005GL022954

Yizengaw E, Moldwin MB, Galvan D, Iijima BA, Komjathy A, Mannucci AJ (2008) Global plasmaspheric TEC and its relative contribution to GPS TEC. J Atmos Solar-Terr Phys 70:1541–1548

Yoshikawa I, Murakami G, Ogawa G, Yoshioka K, Obana Y, Taguchi M, Yamazaki A, Kameda S, Nakamura M, Kikuchi M, Kagitani M, Okano S, Miyake W (2010) Plasmaspheric EUV images seen from lunar orbit: initial results of the extreme ultraviolet telescope on board the Kaguya spacecraft. J Geophys Res. doi:10.1029/2009JA014978

Young DT, Balsiger H, Geiss J (1982) Correlations of magnetospheric ion composition with geomagnetic and solar activity. J Geophys Res 87:9077–9096

Zaharia S, Jordanova VK, Thomsen MF, Reeves GD (2006) Self-consistent modeling of magnetic fields and plasmas in the inner magnetosphere: application to a geomagnetic storm. J Geophys Res. doi:10.1029/2006JA011619

Zhang Y, Paxton LJ, Kozyra JU, Kil H, Brandt PC (2006) Nightside thermospheric FUV emissions due to energetic neutral atom precipitation during magnetic superstorms. J Geophys Res. doi:10.1029/2005JA011152

Zhang Y, Paxton LJ, Zheng Y (2008) Interplanetary shock induced ring current auroras. J Geophys Res. doi:10.1029/2007JA012554

Zhang J-C, Wolf RA, Spiro RW, Erickson GM, Sazykin S, Toffoletto FR, Yang J (2009) Rice convection model simulation of the substorm-associated injection of an observed plasma bubble into the inner magnetosphere: 2. Simulation results. J Geophys Res. doi:10.1029/2009JA014131

Zong Q-G, Wilken B (1999) Bursty energetic oxygen events in the dayside magnetosheath: geotail observations. Geophys Res Lett 26:3349–3352

Self-Consistent Simulations of Plasma Waves and Their Effects on Energetic Particles

10

Vania K. Jordanova

Abstract

Understanding wave-particle interactions and their effects on energetic particle dynamics in near-Earth space is needed to develop models with predictive space weather capabilities. The local acceleration and/or loss of relativistic electrons are associated with two dominant magnetospheric plasma waves, whistler mode chorus emissions and electromagnetic ion cyclotron (EMIC) waves. The generation and propagation characteristics of EMIC waves depend strongly on the presence of both cold and energetic heavy ions (mainly He^+ and O^+) in the plasmas, which varies significantly with geomagnetic and solar activity. We present self-consistent studies of the excitation of these waves during geomagnetic storms after the fresh injection of plasma sheet particles into the inner magnetosphere. We use our four-dimensional (4D) kinetic ring current-atmosphere interactions model (RAM), which includes time-dependent convective transport and radial diffusion, all major loss processes, and is coupled with a dynamic (2D) plasmasphere model. The boundary conditions are specified by a plasma sheet source population at geosynchronous orbit that varies both in space and time. We calculate the pitch angle anisotropy of ring current ions and electrons and identify equatorial regions for potential growth of EMIC waves and whistler mode chorus, respectively. We show that He^+ band EMIC wave excitation may be significantly reduced by ring current O^+ ions during storm peak conditions when O^+ contribution increases. We find that the linear growth rate of chorus waves maximizes at large L shells in the midnight-to-dawn local time sector, while EMIC waves are most intense in the afternoon sector in agreement with previous satellite observations.

10.1 Introduction

The dynamics of energetic particles in the inner magnetosphere has been an important subject of near-Earth space studies in recent years. Observations, theory, and modeling of the ring current indicate that a thorough understanding of the mechanisms involved in particle injection, trapping, and loss could be achieved

V.K. Jordanova (✉)
Space Science and Applications, Los Alamos National Laboratory, Los Alamos, NM 87545, USA
e-mail: vania@lanl.gov

W. Liu, M. Fujimoto (eds.), *The Dynamic Magnetosphere*, IAGA Special Sopron Book Series 3,
DOI 10.1007/978-94-007-0501-2_10, © Springer Science+Business Media B.V. 2011

only with global scale studies including coupling with adjacent regions. The motion of charged particles in the inner magnetosphere is determined by the ambient electric and magnetic fields. Precise specification of the spatial structure and temporal development of the highly variable convection electric field is required for simulating the storm time ring current. High resolution empirical models have been developed such as the Assimilative Mapping of Ionospheric Electrodynamics (AMIE) (Richmond 1992) involving the synthesis of ground-based and satellite data, and the Weimer (2001) convection model derived from measurements of the Vector Electric Field Instrument (VEFI) on the DE 2 spacecraft. Similarly, detailed knowledge of the magnetic field is needed for accurate modeling of particle drifts since in non-dipolar magnetic fields drift-shell splitting occurs, resulting in non-isotropic electron and ion pitch angle distributions. Complex empirical models of the magnetic field have been developed as well, like the present state of the art T04S model (Tsyganenko and Sitnov 2005). These empirical models have provided much insight in geomagnetic storm dynamics and have been employed in many numerical studies of particle trajectory tracings. However, for a more realistic storm time description of the ring current and the radiation belts and to achieve predictive modeling capabilities, the modification of the fields by the plasma pressure in the inner magnetosphere has to be included. One of the challenges is thus to develop ring current models that calculate self-consistently the electric and magnetic fields in which the particles drift. An example of such an effort is the Rice Convection Model (RCM) which computes the electric potential by solving the fundamental equations of magnetosphere-ionosphere coupling assuming an electron-proton plasma with isotropic pitch angle distributions (Toffoletto et al. 2003). Another example is the addition of a self-consistently calculated magnetic field to the ring current-atmosphere interactions model (RAM) (Jordanova et al. 2006; Zaharia et al. 2006). In these first studies an equilibrium magnetic field was computed using as input anisotropic pressure from the kinetic RAM, indicating significant magnetic field depressions near Earth at the storm peak. Preserving the storm time pressure anisotropy in the inner magnetosphere is essential for the excitation of various plasma waves that affect the dynamics of both ring current ions and radiation belt electrons.

Observations from geosynchronous Los Alamos National Laboratory (LANL) satellites show that the relativistic electron fluxes increase during the solar quiet period and decrease during the solar active period. Although such an increase is well correlated with solar wind speed (Paulikas and Blake 1979), it shows weaker correlation with geomagnetic activity (Reeves et al. 2003), the cause for which is not well understood. The dynamics of relativistic electrons in the radiation belts of the Earth during storm times are affected by a large number of processes, causing electron fluxes with energy $E > 100$ keV to vary by several orders of magnitude. Even for modest geomagnetic storms, radiation belt electron fluxes can be rapidly enhanced within the Earth's inner magnetosphere. The majority of radiation belt enhancements occur in association with high-speed solar wind streams, which produce an intense seed population of 10–300 keV electrons (Miyoshi et al. 2007). These ring current-energy electrons are subsequently accelerated (on time scales of hours to days) to relativistic energies either by ultralow-frequency (ULF) waves (Rostoker et al. 1998), higher-frequency (VLF) chorus waves (Summers et al. 1998), or magnetosonic waves (Horne et al. 2007). On the other hand, the radiation belt fluxes decrease due to a combination of electron loss to the magnetopause (Kim and Chan 1997) and to electron precipitation to the atmosphere (Millan et al. 2002). The main loss process causing the slot region is pitch angle scattering by plasmaspheric hiss (Lyons et al. 1972). Electron loss from the outer zone occurs from electromagnetic ion cyclotron (EMIC) waves (Thorne and Kennel 1971) and whistler mode chorus (Thorne et al. 2005). Detailed description of the loss and source mechanisms for relativistic electrons in the outer radiation belt can be found in recent reviews by Shprits et al. 2008a, b. Additional complexity in studying energetic particle dynamics thus comes from the fact that their evolution depends on the interactions with plasma waves. The free energy for plasma wave excitation in the inner magnetosphere is provided by the anisotropic ring current ion and electron distributions. When plasma sheet ions and electrons are injected into the ring current region, their pitch angle distribution is relatively isotropic. As particles drift in, the pitch angle anisotropy increases due to energization by betatron acceleration, as well as to losses by charge exchange, Coulomb collisions, and collisions at low altitudes with the dense atmosphere (Jordanova et al.

1999). Another challenge for the space weather modeling community is the development of a self-consistent treatment of particle transport and wave dynamics in order to address the full physical coupling between the plasma and the fields. Such an approach has been used by Jordanova et al. (2001, 2008) to show the effectiveness of EMIC waves in scattering ring current and radiation belt particles and is discussed in the next section.

In this paper we evaluate the dynamics of the inner magnetosphere using our kinetic ring current-atmosphere interactions model (RAM) to simulate the earthward penetration of plasma sheet ions and electrons during geomagnetic storms. Our model is not drift-averaged and retains four dimensions (4D) by solving the bounce-averaged kinetic equation as a function of radial distance in the equatorial plane, magnetic local time (MLT), energy, and pitch angle (Jordanova et al. 1997). RAM includes time-dependent convective transport, all major loss processes for ring current ions and electrons, and is coupled with a dynamic 2D plasmasphere model (Rasmussen et al. 1993). The RAM code was recently extended to relativistic energies using a convection-diffusion approach (Jordanova et al. 2006; Miyoshi et al. 2006). The fluxes at the nightside boundary and the convection electric field inside the simulation domain are supplied either from the Rice Convection Model (RCM) (Harel et al. 1981) or from empirical models. We calculate the linear growth rate of EMIC and whistler mode chorus waves in the equatorial plane due to the anisotropic ring current populations. We identify localized (L shell and MLT-dependent) regions where these plasma waves are excited, which is important in delineating prominent mechanisms for acceleration and loss of charged particles in the near-Earth space environment.

10.2 Global Simulations of Electromagnetic Ion Cyclotron Waves

10.2.1 Effects of Heavy Ions on EMIC Wave Generation and Propagation

During geomagnetic storms the ring current ion distributions become anisotropic and unstable to EMIC wave excitation in the equatorial magnetosphere (Cornwall 1977; Solomon and Picon 1981). The generation and propagation of EMIC waves are strongly influenced by the presence of both cold (plasmaspheric) and hot (ring current) heavy ions (mainly He^+ and O^+) in the plasmas (Rauch and Roux 1982; Kozyra et al. 1984). Heavy ions can modify the frequencies at which wave growth occurs as well as the growth rates themselves, and significantly decrease the group velocity. The presence of heavy ions results in stop bands above the gyrofrequency of given ion species. The width of the stop bands depends on the composition of both cold and hot plasmas. The hydrogen cyclotron instability is, therefore, suppressed as heavy ions begin to dominate the ring current, however, wave growth may still occur in the lower frequency (He^+ and O^+) wave bands. Reducing the energy of the hot components reduces the wave growth, while decreasing the magnetic field strength (at higher L shell) increases the wave growth. The regions where EMIC waves are present exhibit quite variable MLT dependence during storm time (Jordanova et al. 2001, 2008), with the strongest waves being usually excited near the plasmapause.

We use our kinetic RAM (Jordanova et al. 1997, 2006) to simulate ring current evolution and subsequent He^+ band (between the oxygen and helium gyrofrequencies) EMIC wave generation during the 21–23 April 2001 storm. This is a CME-driven geomagnetic storm with about 15-h long main phase and a minimum $Dst = -102$ nT reached at 16 UT on 22 April (Fig. 10.1, top panel). To model the inflow of plasma from the magnetotail we use geosynchronous data from LANL satellites, while the convection electric field is modeled after Weimer (2001) ionospheric potentials mapped to the equatorial plane using the Tsyganenko (2002) magnetic field model (for more details see Jordanova et al. 2006). After being injected at the nightside boundary, the plasma sheet ions are transported sunward, energized, and drift azimuthally around the Earth to form the ring current. The time-dependent variations of the convection electric field allow particles to move from open to closed drift paths and to become trapped. Particles that are not trapped and remain on open trajectories are lost at the dayside magnetopause. We calculate the EMIC wave growth in the equatorial plane as a function of L shell and MLT with storm evolution using the hot plasma dispersion relation and RAM input parameters. The dial plots in Fig. 10.1 show several test

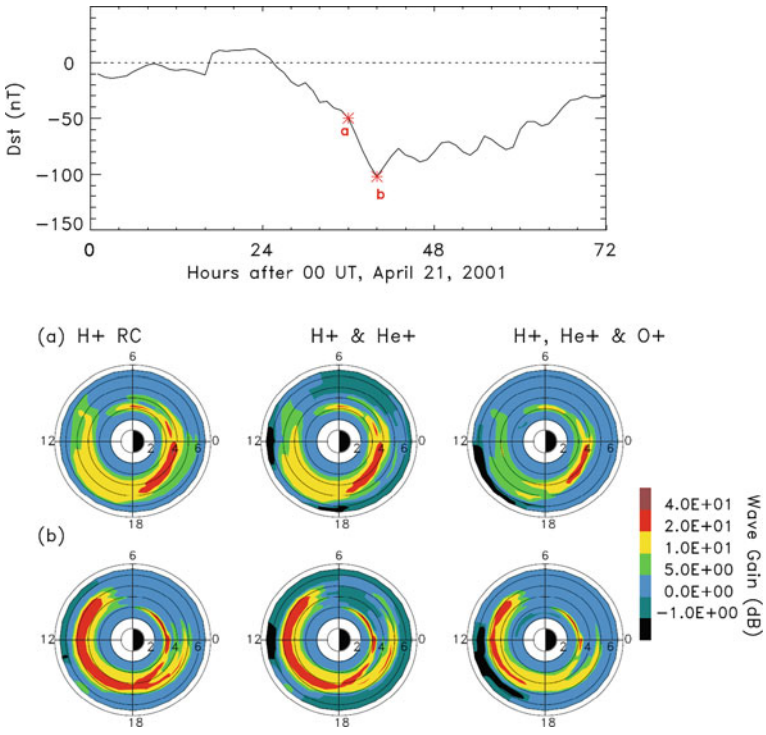

Fig. 10.1 Wave gain of He^+ band EMIC waves calculated with RAM at selected hours during the main phase of the 21–23 April 2001 storm indicated with stars on the *Dst* plot, considering H^+, and adding He^+, and O^+ ring current ions

simulations considering various ring current ion distributions calculated with RAM: only H^+ ions (left column), both H^+ and He^+ ions (middle column), and adding O^+ ring current ions as well (right column). The plasmaspheric density is obtained with the model of Rasmussen et al. (1993) and a cold ion composition of 77 % H^+, 20% He^+, and 3% O^+ is assumed during all simulations. The wave gain obtained after integrating the convective growth rates along field-aligned wave paths is shown in Fig. 10.1 for two universal times after 00 UT, 21 April. The wave growth maximizes during the storm main phase at first on the nightside (Fig. 10.1a) and then extends to the dayside (Fig. 10.1b) as ring current ions are injected and drift westward with storm development. Clearly, the wave gain in the He^+ band is reduced when heavy ring current ions are included. The damping due to ring current O^+ ions is more pronounced in this frequency range than that due to He^+ ions which is negligible; the effect is especially strong near minimum *Dst* (Fig. 10.1b) when O^+ concentration reaches maximum. These results indicate that the contribution from ring current O^+ ions has to be considered in EMIC wave simulations.

10.2.2 Observations and Modeling of Subauroral Proton Arcs

Global observations from the IMAGE FUV instrument (Mende et al. 2000) revealed detached subauroral proton arcs, separated from the main oval and extending over several hours of local time in the afternoon sector. Magnetically conjugate observations during some of the subauroral arc events demonstrated the presence of precipitating protons and the absence of precipitating electrons (Immel et al. 2002). Recent studies (Spasojeviç et al. 2004, 2005) indicated simultaneous observations of plasmaspheric plumes and EMIC waves during some of the events. Scattering by EMIC waves could lead to the precipitation of ring current ions and the excitation of subauroral arcs. Jordanova et al. (2007) investigated the mechanisms causing the proton precipitation during a subauroral arc event that occurred on 23 January 2001. The FUV images indicated signatures of subauroral precipitation in the afternoon sector beginning around 21 UT on 23 January until ~00 UT on 24 January; the proton aurora brightened significantly around 23 UT and separated from the main auroral arc. Jordanova et al. calculated the

growth rate of EMIC waves self-consistently with the evolving ring current H^+, O^+, and He^+ ion distributions simulated with RAM during the event. The convective growth rates were integrated along field-aligned wave paths to obtain the wave gain. A simple model (Jordanova et al. 2001) was used to relate the calculated wave gain to EMIC wave amplitude on the basis of statistical studies, since information on the background noise level from which the waves grow is unavailable. Quasi-linear diffusion coefficients from Jordanova et al. (1996) were used to calculate the pitch angle scattering of ring current protons into the loss cone due to resonant interactions with EMIC waves. RAM simulations (Fig. 10.2a) indicated enhancement of EMIC waves within regions of spatial overlap of energetic ring current protons and dayside plasmaspheric plumes, and along the plasmapause due to guiding of the waves by density gradients (Jordanova et al. 2007; Thorne and Horne 1997). Precipitating proton fluxes in the 10–40 keV range increased by several orders of magnitude between 23 UT and 24 UT when EMIC wave scattering was included (Fig. 10.2c) in comparison with the simulation when it wasn't (Fig. 10.2b). In agreement with observations, the precipitating fluxes decreased 1 h later (Fig. 10.2, right column) since the ring current proton anisotropy was reduced due to the pitch angle scattering, and there was no significant EMIC wave excitation. The location of the proton precipitation by EMIC waves thus matched very well the temporal and spatial evolution of FUV observations, indicated with diamond line in Fig. 10.2c. This self-consistent simulation of EMIC wave scattering of ring current protons and EMIC wave amplification/attenuation showed that cyclotron resonant wave-particle interactions are a viable mechanism for the generation of subauroral proton arcs.

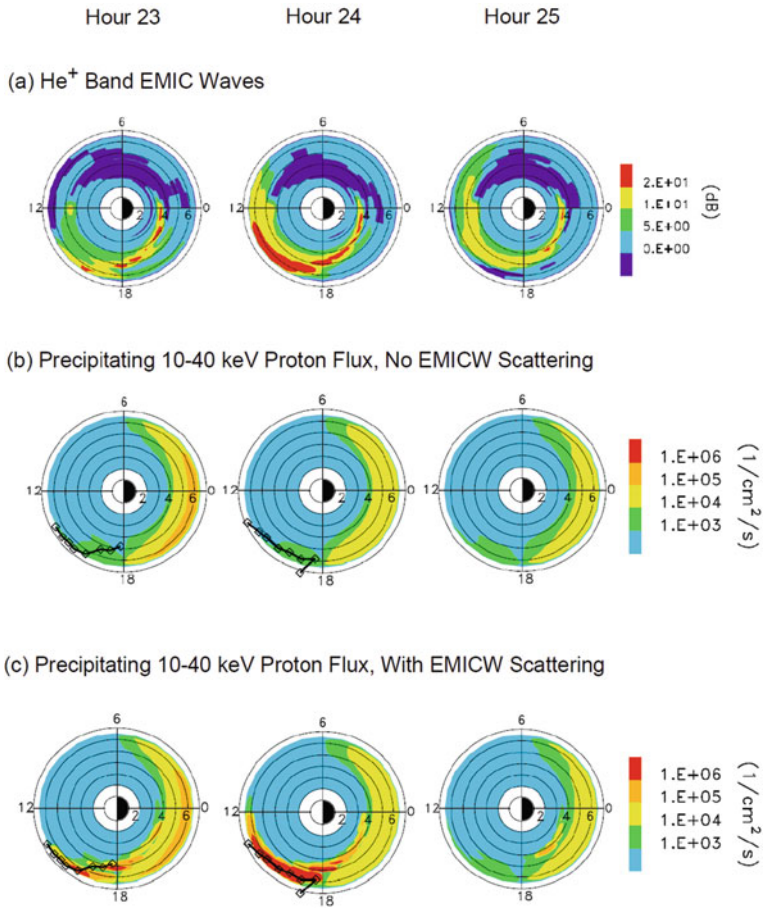

Fig. 10.2 (**a**) Calculated EMIC wave gain as a function of radial distance in the equatorial plane and MLT at selected hours after 00 UT on 23 January 2001. (**b**) Precipitating proton number flux considering drift and collisional losses without, and (**c**) with scattering by EMIC waves. The *diamond line* indicates the low-latitude boundary of FUV images of proton precipitation mapped to the SM equatorial plane

10.2.3 Scattering of Radiation Belt Electrons by EMIC Waves

EMIC waves affect strongly the loss of MeV electrons and knowledge of their global distribution and power are crucial for the accurate understanding of radiation belt dynamics. Jordanova et al. (2008) studied the effect of EMIC wave scattering on radiation belt electrons during the large geomagnetic storm of 21 October 2001 with minimum $Dst = -187$ nT (Fig. 10.3). LANL satellites provided very good

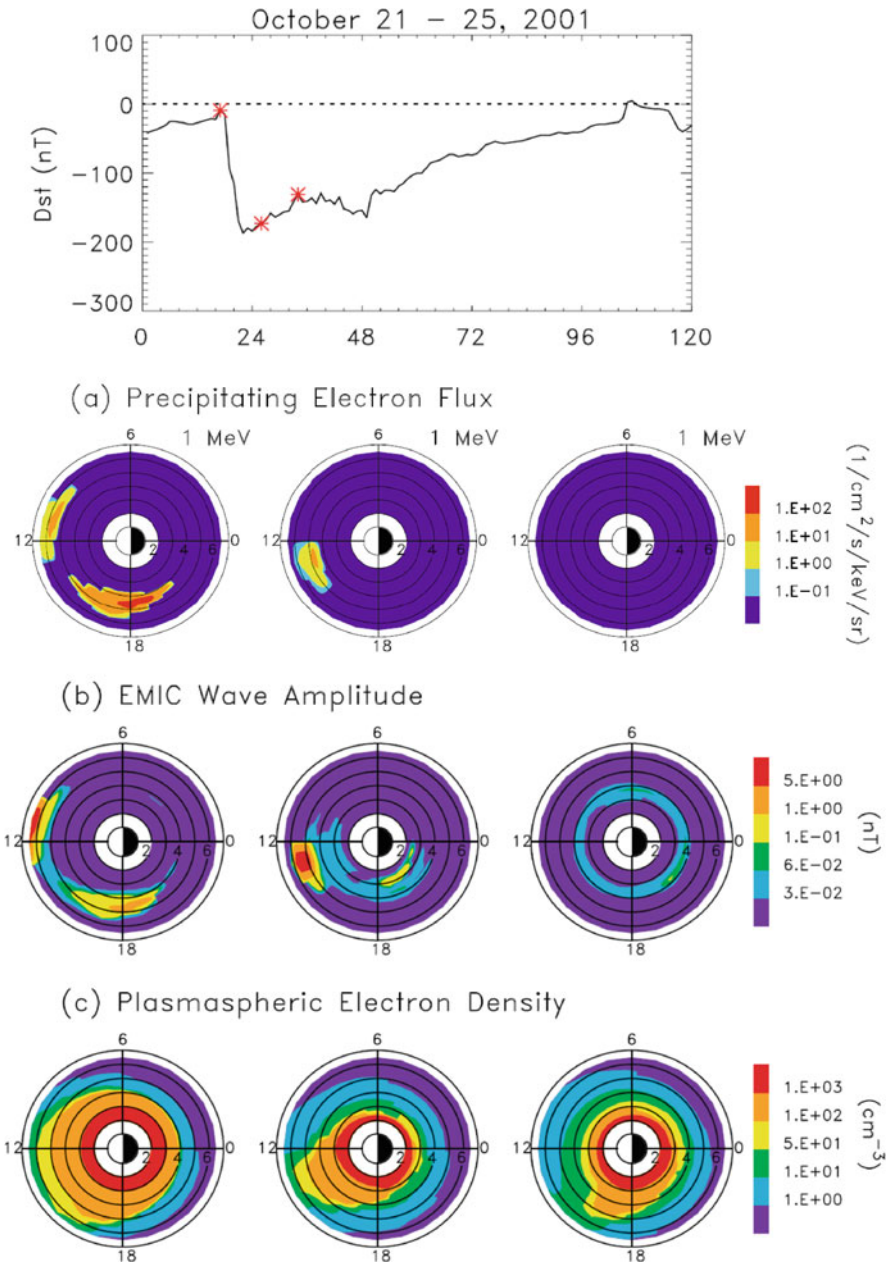

Fig. 10.3 (*top*) The *Dst* index during 21–25 October 2001. (**a**) Precipitating 1 MeV electron flux, (**b**) calculated amplitude of He^+ band EMIC waves, and (**c**) plasmaspheric electron density, as a function of radial distance in the equatorial plane and MLT at selected hours after 00 UT on 21 October 2001, shown with *stars* on the *Dst* plot

coverage of the time-varying conditions at geosynchronous orbit in response to solar wind changes, showing a large relativistic electron flux dropout during the main phase of this storm. The RAM code was used to calculate self-consistently the EMIC wave excitation from the anisotropic ring current ion populations, and the resulting precipitating ion and electron fluxes. Particle interactions with these waves were evaluated according to quasi-linear theory, using diffusion coefficients for a multi-species plasma and including not only field-aligned but also oblique EMIC wave propagation. The pitch angle diffusion coefficients increased from 0° to ~60° within the unstable regions and pitch angle scattering by EMIC waves caused significant loss of radiation belt electrons at $E \geq 1$ MeV and precipitation into the atmosphere. Figure 10.3a shows results from RAM simulations indicating large precipitating fluxes within regions of enhanced EMIC instability, whose location varied with time but was predominantly in the afternoon-dusk sector at $3 \leq L \leq 6$. Geoeffective (>0.1 nT) EMIC wave amplitudes (Fig. 10.3b) occurred during the main and early recovery storm phase inside plasmaspheric drainage plumes or along the plasmapause (Fig. 10.3c). The EMIC waves faded away at hour 34 (right column) owing to the wave scattering feedback and isotropization of the proton ring current, so there was no electron precipitation either. The precipitating electron fluxes were usually collocated with precipitating ion fluxes (not shown) but occurred at variable energy range and magnitude. The minimum resonant energy increased at low L and relativistic electrons at $E \leq 1$ MeV did not precipitate at $L < 3$ during this storm.

10.3 Global Simulations of Whistler Mode Chorus Waves

10.3.1 Evolution of Ring Current Electrons

Although there is an increased interest recently in the prediction of geomagnetic activity, the dynamics of ring current electrons have not been investigated in detail. An initial study of Frank (1967) estimated that the electron component may provide about 25% of the ring current energy during storm time. Using Explorer 45 data Liu et al. (2005) found that the electrons may contribute ~7.5% of the ring current energy, while the percentage obtained from their simulation results was 19%. Jordanova and Miyoshi (2005) evaluated the electron contribution to the ring current during the October 2001 storm and found it to be highly variable, being small (~2%) during quiet time and the largest near *Dst* peaks, resulting in ~10% of the total ring current energy content. Jordanova et al. (2010) simulated ring current electron dynamics during the 21–23 April 2001 storm (the *Dst* index for this storm is shown in Fig. 10.1, top) using the RAM extended to relativistic energies and electrons. RAM was driven by the RCM electric field which was updated every 10 min during the storm. The RCM provided as well the fluxes at the outer boundary of RAM ($L = 6.5$) every 10 min and with 1 h MLT dependence. Figure 10.4 shows the electron fluxes during the main phase of the storm at hours 31 and 37, simulated with RAM including only convective transport (top), and adding loss processes (bottom). Losses from wave-induced scattering inside the plasmasphere due to whistler mode hiss,

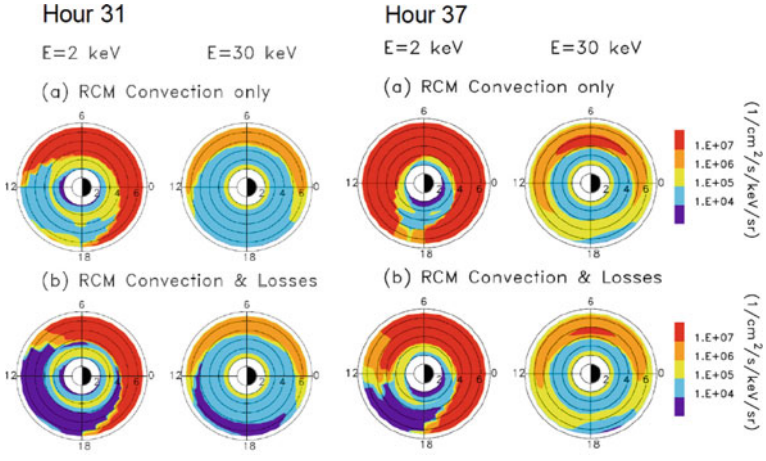

Fig. 10.4 Electron fluxes at hours 31 (two *left* columns) and 37 (two *right* columns) after 00 UT on 21 April, for 2 and 30 keV energy and 60° pitch angle, as a function of radial distance in the equatorial plane and MLT considering (**a**) only magnetospheric convection, and (**b**) convection and various losses

lightning whistler, and VLF transmitters (Abel and Thorne 1998; Albert 1999) and outside the plasmasphere due to whistler mode chorus (Chen and Schulz 2001) are included in this simulation using appropriate lifetimes. The ring current electrons drift eastward, so after injection from the plasma sheet on the nightside they surround the Earth toward dawn, and if not trapped leave the simulation domain through the dayside boundary. The electrons penetrate closer to Earth with storm evolution and reach L∼4 at hour 37. The ring current electron energy density peaks near dawn. When losses are included (Fig. 10.4b) the fluxes decrease significantly in the noon-to-dusk sector since the electrons are lost along their drift paths and cannot reach this location. A very asymmetric electron distribution is thus obtained.

10.3.2 Observations and Modeling of Chorus Waves

The injection of plasma sheet electrons into the ring current during geomagnetically disturbed conditions leads to distributions that are unstable to the generation of whistler mode waves (Kennel and Thorne 1967; Horne et al. 2003). Whistler mode chorus is observed mostly outside the plasmapause and its source region is located near the geomagnetic equator (Tsurutani and Smith 1974; Santolik et al. 2003). Statistical surveys indicate that nightside chorus is strongest in the near-equatorial region at $3 < L < 7$, peaking in the premidnight-to-dawn MLT quadrant, while dayside chorus peaks in the dawn-to-prenoon quadrant at L∼7–8 and propagates to higher latitudes (Meredith et al. 2001; Horne et al. 2005; Li et al. 2009). The chorus generation process contains both linear and nonlinear growth. The nonlinear growth plays an important role and Omura and Summers (2004) showed that whistler mode waves ultimately grow nonlinearly to a saturation level. Equally important is the linear growth since it provides the initial amplification that raises the weak signals to levels at which nonlinear trapping of electrons takes place (Nunn et al. 2003; Li et al. 2008). Jordanova et al. (2010) calculated the linear wave growth of whistler mode chorus in the equatorial plane due to the anisotropic electron population using the dispersion relation for whistler mode waves of Kennel and Petschek (1966). Figure 10.5a shows the

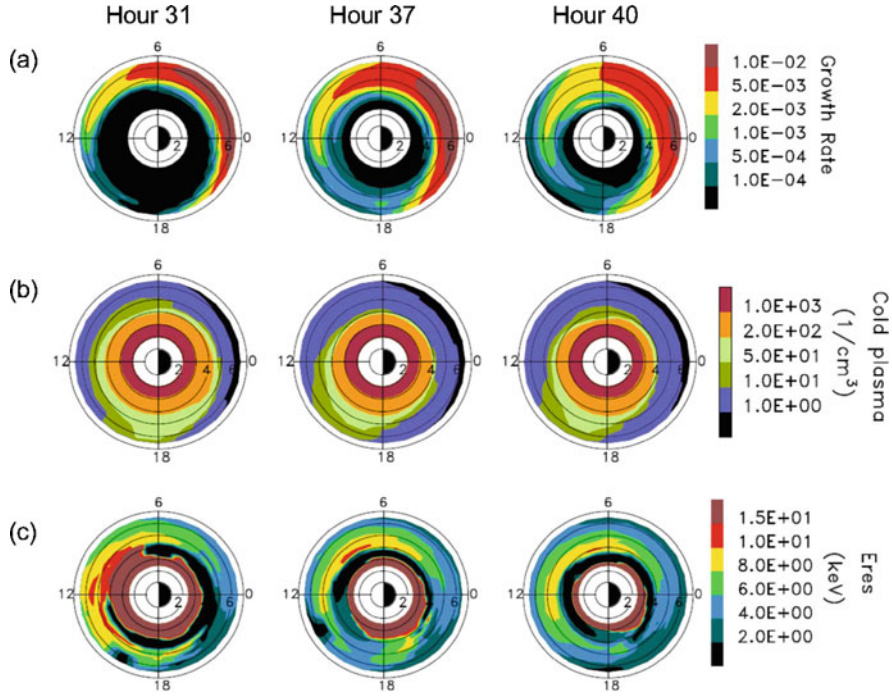

Fig. 10.5 Various parameters calculated with RAM at selected hours after 00 UT on 21 April 2001. From top to bottom the panels are (**a**) normalized growth rate of chorus waves, (**b**) plasmaspheric electron density, and (**c**) parallel energy of resonant particles

growth rate of whistler mode chorus calculated in the equatorial plane during the 21–23 April 2001 storm using the RAM electron distributions (Fig. 10.4) and the cold plasmaspheric density (Fig. 10.5b). At every equatorial location the wave growth was calculated as a function of frequency normalized to the electron cyclotron frequency and the maximum wave growth was selected. The growth rate increased on the nightside as the plasma sheet electrons were injected into the inner magnetosphere under storm time enhanced convection. At first the wave growth was large at $L > 5$ (hour 31) in the premidnight-to-dawn sector and then it extended earthward to $L \sim 4$ at storm peak (hour 40). The corresponding parallel energy of resonant electrons (Fig. 10.5c) was ~4–6 keV on the nightside where the largest growth rates were calculated, and ~8 to 10 keV on the dayside, respectively. Intense chorus waves were thus predicted by RAM outside the plasmasphere on the nightside, in agreement with previous chorus observations near the equator (Meredith et al. 2003; Li et al. 2009). The wave growth predicted by RAM on the dayside was weaker because the electron fluxes were significantly reduced. Larger pitch angle anisotropy due to increased scattering losses or drift-shell splitting may lead to the generation of enhanced chorus emissions in this sector and this will be investigated in future studies.

10.4 Summary and Conclusions

This paper addresses the challenge of incorporating in a self-consistent manner the transport of energetic particles and simultaneous wave-particle interactions in global models of inner magnetospheric dynamics. We show kinetic simulations with RAM that demonstrate highly variable EMIC wave excitation in the equatorial plane and subsequent localized electron and ion precipitation. The EMIC wave growth is calculated self-consistently with the evolving ring current ion populations and maximizes where the westward drifts of energetic ions pass through high-density plasmaspheric regions like dayside drainage plumes, or along the plasmapause. These waves scatter cyclotron resonant particles toward the loss cone and enhance the ring current ion and relativistic electron precipitation to the atmosphere. The proton precipitation causes the excitation of detached subauroral arcs that are observed by IMAGE mostly in the afternoon sector.

Similar self-consistent approach for the generation of chorus waves by the anisotropic ring current electrons is under development (Jordanova et al. 2010). We show RAM results illustrating chorus excitation in the equatorial plane after the fresh injection and eastward drift of plasma sheet electrons. The wave growth intensifies outside the plasmasphere in the midnight-to-dawn sector and reproduces reasonably well previous satellite observations. Future studies will consider the implementation of quasi-linear diffusion by chorus waves in RAM and the effects of these waves on the acceleration and loss of relativistic electrons.

Acknowledgments This work was conducted under the auspices of the U. S. Department of Energy, with partial support from the NASA Theory, LWS and GI programs, and from a Los Alamos National Laboratory Directed Research and Development grant.

References

Abel B, Thorne R (1998) Electron scattering loss in Earth's inner magnetosphere 1. Dominant physical processes. J Geophys Res 103:2385

Albert J (1999) Analysis of quasi-linear diffusion coefficients. J Geophys Res 104:2429

Chen M, Schulz M (2001) Simulations of diffuse aurora with plasma sheet electrons in pitch angle diffusion less than everywhere strong. J Geophys Res 106:28949

Cornwall JM (1977) On the role of charge exchange in generating unstable waves in the ring current. J Geophys Res 82:1188

Frank L (1967) On the extraterrestrial ring current during geomagnetic storms. J Geophys Res 72:3753

Harel M, Wolf R, Reiff P, Spiro R, Burke W, Rich F, Smiddy M (1981) Quantitative simulation of a magnetospheric substorm, 1. Model logic and overview. J Geophys Res 86:2217

Horne RB, Glauert SA, Thorne RM (2003) Resonant diffusion of radiation belt electrons by whistler mode chorus. Geophys Res Lett. doi:10.1029/2003GL016963

Horne RB, Thorne RM, Glauert SA, Albert JM, Meredith NP, Anderson RR (2005) Timescale for radiation belt electron acceleration by whistler mode chorus waves. J Geophys Res. doi:10.1029/2004JA010811

Horne RB, Thorne RM, Glauert SA, Meredith NP, Pokhotelov D, Santolík O (2007) Electron acceleration in the Van Allen radiation belts by fast magnetosonic waves. Geophys Res Lett. doi:10.1029/2007GL030267

Immel TJ, Mende SB, Frey HU, Peticolas LM, Carlson CW, Gerard J-C, Hubert B, Fuselier SA, Burch JL (2002) Precipitation of auroral protons in detached arcs. Geophys Res Lett. doi:10.1029/2001GL013847

Jordanova VK, Miyoshi Y (2005) Relativistic model of ring current and radiation belt ions and electrons: initial results. Geophys Res Lett. doi:10.1029/2005GL023020

Jordanova VK, Kozyra JU, Nagy AF (1996) Effects of heavy ions on the quasi-linear diffusion coefficients from resonant interactions with EMIC waves. J Geophys Res 101:19771

Jordanova VK, Kozyra JU, Nagy AF, Khazanov GV (1997) Kinetic model of the ring current-atmosphere interactions. J Geophys Res 102:14279

Jordanova VK, Farrugia CJ, Quinn JM, Torbert RB, Borovsky JE, Sheldon RB, Peterson WK (1999) Simulation of off-equatorial ring current ion spectra measured by POLAR for a moderate storm at solar minimum. J Geophys Res 104:429

Jordanova VK, Farrugia CJ, Thorne RM, Khazanov GV, Reeves GD, Thomsen MF (2001) Modeling ring current proton precipitation by electromagnetic ion cyclotron waves during the May 14–16, 1997, storm. J Geophys Res 106:7

Jordanova VK, Miyoshi YS, Zaharia S, Thomsen MF, Reeves GD, Evans DS, Mouikis CG, Fennell JF (2006) Kinetic simulations of ring current evolution during the geospace environment modeling challenge events. J Geophys Res. doi:10.1029/2006JA011644

Jordanova VK, Spasojeviç M, Thomsen MF (2007) Modeling the electromagnetic ion cyclotron wave-induced formation of detached subauroral proton arcs. J Geophys Res. doi:10.1029/2006JA012215

Jordanova VK, Albert J, Miyoshi Y (2008) Relativistic electron precipitation by EMIC waves from self-consistent global simulations. J Geophys Res. doi:10.1029/2008JA013239

Jordanova VK, Thorne RM, Li W, Miyoshi Y (2010) Excitation of whistler mode chorus from global ring current simulations. J Geophys Res. doi:10.1029/2009JA014810

Kennel C, Petschek H (1966) Limit on stably trapped particle fluxes. J Geophys Res, 71:1

Kennel CF, Thorne RM (1967) Unstable growth of unducted whistlers propagating at an angle to the geomagnetic field. J Geophys Res 72:871

Kim H-J, Chan AA (1997) Fully-adiabatic changes in storm-time relativistic electron fluxes. J Geophys Res 102:22107

Kozyra JU, Cravens TE, Nagy AF, Fontheim EG, Ong RSB (1984) Effects of energetic ions on electromagnetic ion cyclotron wave generation in the plasmapause region. J Geophys Res 89:2217

Li W, Thorne RM, Meredith NP, Horne RB, Bortnik J, Shprits YY, Ni B (2008) Evaluation of whistler mode chorus amplification during an injection event observed on CRRES. J Geophys Res doi:10.1029/2008JA013129

Li W, Thorne RM, Angelopoulos V, Bortnik J, Cully CM, Ni B, LeContel O, Roux A, Auster U, Magnes W (2009) Global distribution of whistler-mode chorus waves observed on the THEMIS spacecraft. Geophys Res Lett. doi:10.1029/2009GL037595

Liu S, Chen MW, Roeder JL, Lyons LR, Schulz M (2005) Relative contribution of electrons to the storm-time total ring current energy content. Geophys Res Lett. doi:10.1029/2004GL021672

Lyons LR, Thorne RM, Kennel CF (1972) Pitch angle diffusion of radiation belt electrons within the plasmasphere. J Geophys Res 77:3455

Mende SB et al (2000) Far ultraviolet imaging from the IMAGE spacecraft. 3. Spectral imaging of Lyman-a and OI 135.6 nm. Space Sci Rev 91:287

Meredith NP, Horne RB, Anderson RR (2001) Substorm dependence of chorus amplitudes: Implications for the acceleration of electrons to relativistic energies. J Geophys Res 106:13165

Meredith NP, Horne RB, Thorne RM, Anderson RR (2003) Favored regions for chorus-driven electron acceleration to relativistic energies in the Earth's outer radiation belt. Geophys Res Lett. doi:10.1029/2003GL017698

Millan RM, Lin RP, Smith DM, Lorentzen KR, McCarthy MP (2002) X-ray observations of MeV electron precipitation with a balloon-borne germanium spectrometer. Geophys Res Lett. doi:10.1029/2002GL015922

Miyoshi YS, Jordanova VK, Morioka A, Thomsen MF, Reeves GD, Evans DS, Green JC (2006) Observations and modeling of energetic electron dynamics during the October 2001 storm. J Geophys Res. doi:10.1029/2005JA011351

Miyoshi Y, Morioka A, Kataoka R, Kasahara Y, Mukai T (2007) Evolution of the outer radiation belt during the November 1993 storms driven by corotating interaction regions. J Geophys Res. doi:10.1029/2006JA012148

Nunn D, Demekhov A, Trakhtengerts V, Rycroft MJ (2003) VLF emission triggering by a highly anisotropic electron plasma. Ann Geophys 21:481

Omura Y, Summers D (2004) Computer simulations of relativistic whistler-mode wave-particle interactions. Phys Plasmas. doi:10.1063/1.1757457

Paulikas GA, Blake JB (1979) Effects of the solar wind on magnetospheric dynamics: energetic electrons at the synchronous orbit. In: Olson W (ed.) Quantitative modeling of the magnetospheric processes. Geophysical monograph series, vol 21. AGU, Washington, DC, p 180

Rasmussen CE, Guiter SM, Thomas SG (1993) Two-dimensional model of the plasmasphere: refilling time constants. Planet Space Sci 41:35

Rauch JL, Roux A (1982) Ray tracing of ULF waves in a multicomponent magnetospheric plasma: Consequences for the generation mechanism of the ion cyclotron waves. J Geophys Res 87:8191

Reeves GD, McAdams KL, Friedel RHW, O'Brien TP (2003) Acceleration and loss of relativistic electrons during geomagnetic storms. Geophys Res Lett. doi:10.1029/2002GL016513

Richmond AD (1992) Assimilative mapping of ionospheric electrodynamics. Adv Space Res 12:669

Rostoker G, Skone S, Baker DN (1998) On the origin of relativistic electrons in the magnetosphere associated with some geomagnetic storms. Geophys Res Lett 25:3701

Santolik O, Gurnett DA, Pickett JS, Parrot M, Cornilleau-Wehrlin N (2003) Spatio-temporal structure of storm-time chorus. J Geophys Res. doi:10.1029/2002JA009791

Shprits YY, Elkington SR, Meredith NP, Subbotin DA (2008a) Review of modeling of losses and sources of relativistic electrons in the outer radiation belt I: radial transport. J Atmos Sol Terr Phys. doi:10.1016/j.jastp.2008.06.008

Shprits YY, Subbotin DA, Meredith NP, Elkington SR (2008b) Review of modeling of losses and sources of relativistic electrons in the outer radiation belt II: local acceleration and loss. J Atmos Sol Terr Phys. doi:10.1016/j.jastp.2008.06.014

Solomon J, Picon O (1981) Charge exchange and wave-particle interaction in the proton ring current. J Geophys Res 86:3335

Spasojeviç M, Frey HU, Thomsen MF, Fuselier SA, Gary SP, Sandel BR, Inan US (2004) The link between a detached subauroral proton arc and a plasmaspheric plume. Geophys Res Lett. doi:10.1029/2003GL018389

Spasojeviç M, Thomsen MF, Chi PJ, Sandel BR (2005) Afternoon subauroral proton precipitation resulting from ring current–plasmasphere interaction. In: Burch J, Schulz M, Spence H (eds) Inner magnetosphere interactions: new perspectives from imaging. AGU, Washington, DC, p 85

Summers D, Thorne RM, Xiao F (1998) Relativistic theory of wave-particle resonant diffusion with application to electron acceleration in the magnetosphere. J Geophys Res 103:20487

Thorne RM, Kennel CF (1971) Relativistic electron precipitation during magnetic storm phase. J Geophys Res 76:4446

Thorne RM, Horne RB (1997) Modulation of electromagnetic ion cyclotron instability due to interaction with ring current O+ during magnetic storms. J Geophys Res 102:14155

Thorne RM, O'Brien TP, Shprits YY, Summers D, Horne RB (2005) Timescale for MeV electron microburst loss during geomagnetic storms. J Geophys Res. doi:10.1029/2004JA010882

Toffoletto F, Sazykin S, Spiro R, Wolf R (2003) Inner magnetospheric modeling with the Rice Convection Model. Space Sci Rev 107:175

Tsurutani B, Smith E (1974) Postmidnight chorus: a substorm phenomenon. J Geophys Res 79:118

Tsyganenko NA (2002) A model of the near magnetosphere with a dawn-dusk asymmetry: 2. Parameterization and fitting to observations. J Geophys Res. doi:10.1029/2001JA000220

Tsyganenko NA, Sitnov MI (2005) Modeling the dynamics of the inner magnetosphere during strong geomagnetic storms. J Geophys Res. doi:10.1029/2004JA010798

Weimer DR (2001) An improved model of ionospheric electric potentials including substorm perturbations and application to the Geospace Environment Modeling November 24, 1996, event. J Geophys Res 106:407

Zaharia S, Jordanova VK, Thomsen MF, Reeves GD (2006) Self-consistent modeling of magnetic fields and plasmas in the inner magnetosphere: application to a geomagnetic storm. J Geophys Res. doi:10.1029/2006JA011619

Topology of High-Latitude Magnetospheric Currents

11

Elizaveta E. Antonova, Igor P. Kirpichev, Ilya L. Ovchinnikov, Maria S. Pulinets, Svetlana S. Znatkova, Ksenia G. Orlova, and Marina V. Stepanova

Abstract

The structure and localization of high latitude transverse and field-aligned currents are analyzed using the data from the Themis satellite mission. A number of evidences resumed in this paper, including daytime compression of magnetic field lines and the existence of magnetic field minima far from the equatorial plane make necessary to reanalyze the traditional points of view about the topology of high-latitude magnetospheric currents. Comparison between the dayside integral transverse currents at the geocentric distances 7–10R_E, calculated assuming the validity of the condition of magnetostatic equilibrium and the nighttime transverse currents, showed that ordinary ring current has the high latitude continuation until geocentric distances ~10–13R_E. The problem of the location of Region 1 field-aligned current of Iijima and Potemra is discussed.

11.1 Introduction

To clarify the nature of magnetospheric activity, including the nature of magnetospheric substorms and storms, it is necessary to establish an adequate description of the topology of high latitude transverse and field-aligned currents. The auroral oval is a region of intense magnetosphere-ionosphere interactions where powerful field-aligned currents are closed inside the ionosphere. Traditionally it is considered that the auroral oval forms as a result of the plasma sheet mapping into the ionospheric altitudes. According to the most popular points of view, the geomagnetic substorms develop as a result of tail plasma dynamics (reconnection in the magnetotail or tail current disruption). At the same time, magnetic storms are traditionally connected to the ring current development, although, some authors try to demonstrate the significant contribution of the tail current into the Dst variation.

From our point of view, there are a number of recent findings, which could change significantly the traditional picture of high latitude magnetospheric currents. In this paper we will summarize such findings including distribution of plasma with tail properties inside the magnetosphere, structure of transverse currents at the geocentric distance from ~7 till ~10–13R_E and auroral oval mapping. We also discuss the topology of Region 1 currents of Iijima and Potemra and the location of the region of isolated substorm onset. We try to show that the reanalysis of the topology of high latitude magnetospheric currents can help to create a

E.E. Antonova (✉)
Skobeltsyn Institute of Nuclear Physics, Moscow State University, Moscow, Russia; Space Research Institute RAS, Moscow, Russia
e-mail: antonova@orearm.msk.ru

W. Liu, M. Fujimoto (eds.), *The Dynamic Magnetosphere*, IAGA Special Sopron Book Series 3,
DOI 10.1007/978-94-007-0501-2_11,

non-contradictory picture of high latitude magnetospheric processes.

11.2 Auroral Oval and Plasma Distribution in the High Latitude Magnetosphere

Rather good coincidence between thermal particle fluxes measured by high altitude satellites in the plasma sheet and by low altitude satellites crossing the auroral oval was the base for the statement that the auroral oval forms as a result of plasma sheet particle precipitations and therefore the oval is a result of the plasma sheet mapping into the ionospheric altitudes. Mapping of the near Earth plasma sheet into the ionospheric altitudes using very popular Tsyganenko-87 magnetic field model also produced a nearly ring structure. For example, Fig. 2 of the paper Stasiewicz (1991) shows the results of straight line $X = \text{const} = 10R_E$ mapping into ionospheric altitudes using Tsyganenko (1987) magnetic field model. Stasiewicz (1991) stressed that a cross-tail band maps into an ionospheric structure simulating the auroral oval. It is only necessary to mention that daytime part of the ring, shown in Fig. 2 of the paper Stasiewicz (1991) must be obtained as a result of low latitude boundary layer (LLBL) mapping.

However, even the first observations of the auroral oval showed that the auroral oval has a closed quasi-ring structure. For example, Feldstein and Galperin (1985) defined auroral oval precipitation region (AOR) as a region with the structured precipitations. They also selected diffuse auroral zone (DAZ) as a region of diffuse precipitation located equatorward from the auroral oval and the soft diffuse precipitation region (SOD) as a region of soft diffuse precipitation adjoining to the AOR at the poleward border. AOR in this study has the closed structure near noon. These results were supported by a vast number of observations (see Vorobjev et al. (2007) and references therein).

In particular, Newell and Meng (1992) carefully analyzed a near-noon particle precipitation region. They showed that plasma sheet particle precipitations near noon come from a region situated at the equator from the low latitude boundary layer. Newell et al. (2009) have developed an auroral precipitation model, which separately categorizes the discrete aurora and both the electron and ion diffuse aurora. Newell et al. (2009) model supports the existence of closed ring of plasma sheet like precipitations. Therefore, the low altitude observations show the existence of surrounding the Earth closed ring of plasma sheet like plasma.

Results of plasma observations near equatorial plane totally agree with the existence of surrounding the Earth plasma sheet like plasma domain. AMPTE/CCE observations give the possibility to obtain the distribution of plasma pressure at the equatorial plane (see, Lui and Hamilton 1992; DeMichelis et al. 1999). The global picture of magnetospheric plasma pressure distribution at $L<9$ demonstrates the presence of nearly azimuthally symmetric plasma distribution at $L\sim7$–9 and plasma pressure isotropy. Latest THEMIS results can be used for the verification of this picture as all five THEMIS satellites make measurements nearly at the equatorial plane (see, Angelopoulos 2008). Figure 11.1 obtained from (http://www.nasa.gov/mission_pages/themis/) illustrates the results of THEMIS satellite crossings of the magnetopause near noon on July 18, 2007. Figure 11.1a shows orbit positions, Fig 11.1b the electron and ion spectrograms of TEMIS-C, -D and -E satellite, obtained using the ESA instrument. It is possible to see analyzing Fig. 11.1 that the magnetopause at subsolar point is rather sharp, and a mixture of magnetosheath and plasma sheet like plasma (low latitude boundary layer) is observed just at the inner boundary of the magnetopause. It is also possible to see the plasma sheet like plasma at the equator from the LLBL.

Analysis of the variation of the strength of magnetic field along the magnetic field line is very important for the determination of the distribution of transverse currents. In this context, it is necessary to mention that minimal values of magnetic field at the magnetic field line are observed at the equatorial plane near midnight. Nevertheless, such minima are significantly shifted from the equatorial plane near noon. A region from the geostationary orbit till $\sim10R_E$ was named the region of quasi trapping at the first stages of magnetospheric studies. From that time, it is well known that energetic particle trajectories cross the magnetopause when the particle pitch angle is equal to 90°. On the other side, the drift shell splitting effect is observed for particles with smaller pitch angles (Shabansky and Antonova 1968). Drift trajectories of such particles are closed inside the magnetosphere (see, for example, the discussion in the papers, Delcourt and Sauvaud (1999);

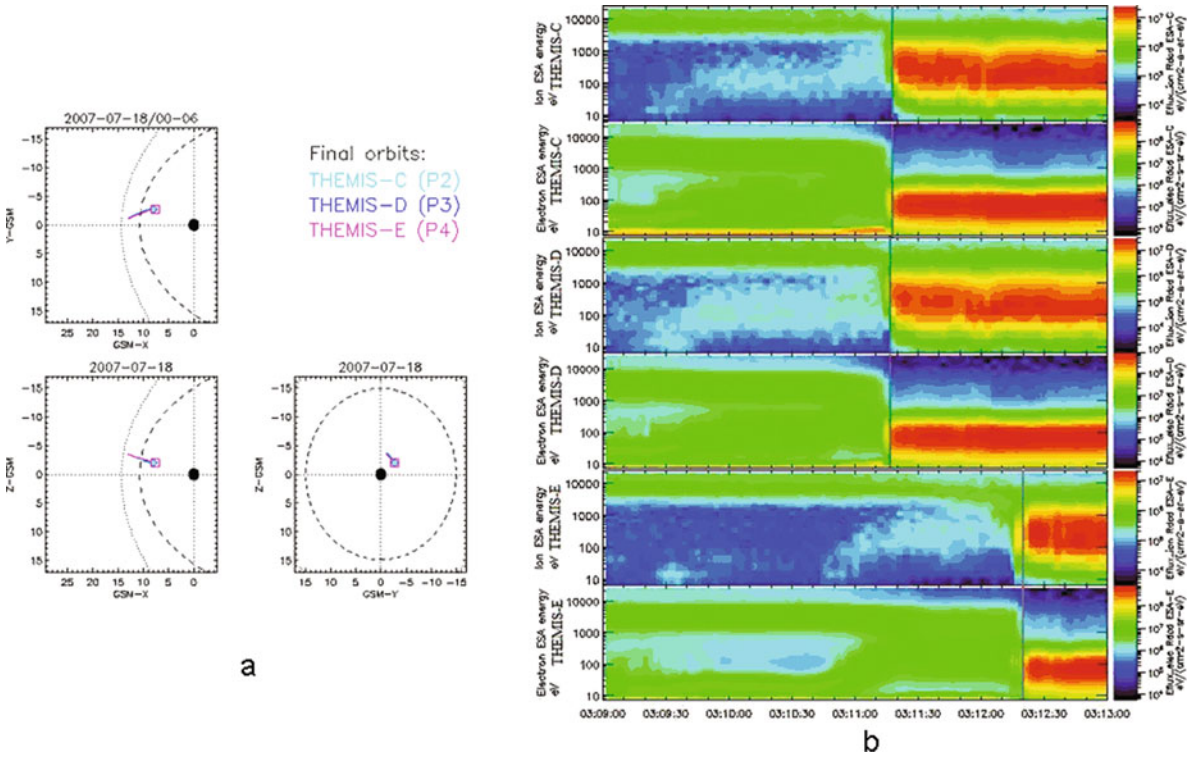

Fig. 11.1 Positions of the orbits of THEMIS satellites for the event 18 July 2007 (**a**), and ion and electron spectrograms of THEMIS-C, D, E satellite for the event July 18, 2007

Öztürk and Wolf (2007)). It was detected by observing the drift echo effect. Hori et al. (2003) observed this effect until geocentric distances ∼12–13R_E near midnight, using the data from the Geotail satellite. This fact indicates that the region of the quasi trapping extends up to 12–13R_E.

Therefore the results of low altitude and high altitude observations demonstrate the existence of the surrounding the Earth plasma sheet like plasma structure in which trajectories of energetic particles are closed inside the magnetosphere up to the low latitude boundary layer near noon and up to ∼12–13R_E near midnight. However, the distribution of currents in this structure was not analyzed in details.

11.3 Transverse Currents at Geocentric Distances >7R_E

Values of current densities and integral transverse current can be estimated assuming the validity of the condition of magnetostatic equilibrium when distribution of plasma pressure is nearly isotropic, as observed at large geocentric distances (see, DeMichelis et al. 1999). In such a case, transverse current $j_\perp$ is equal to

$$\mathbf{j}_\perp = \mathbf{B} \times \nabla p / B^2, \tag{11.1}$$

where ∇p is the plasma pressure gradient, $\mathbf{B}$ is the magnetic field. Equation (11.1) indicates that surrounding the Earth plasma domain contains transverse westward current when the plasma pressure gradient has the earthward direction. Taking into consideration that the plasma pressure has a constant value along magnetic field line in accordance with the condition of magnetostatic equilibrium, it is possible to evaluate current density at any point of the field line, if plasma pressure distribution at the equatorial plane is known, using one of the magnetic field models. Although such approach is not self consistent, it makes it possible to estimate current densities far from the equatorial plane.

The plasma pressure gradient obtained by Lui and Hamilton (1992; DeMichelis et al. (1999) has an earthward direction, which implies the existence of a westward transverse current. DeMichelis et al. (1999) reproduced current density in the equatorial plane

using values of plasma pressure gradients derived from AMPTE/CCE satellite and the Tsyganenko-87 magnetic field model (Tsyganenko 1987). The nighttime part of the picture obtained by DeMichelis et al. (1999) corresponds to comparatively large current densities ~3–5 nA/m^2 and was attributed to the partial ring current. Daytime current densities were smaller ~1 nA/m^2. These values can be used for the estimation of integral transverse current near noon only at the geocentric distances smaller than $7R_E$ where field lines are not compressed. Dayside field lines are very compressed, and the minima of geomagnetic field on these field lines are located far from the equatorial plane. Therefore, the values of the daytime current densities obtained by DeMichelis et al. (1999) are smaller than the largest possible current densities for the same field lines.

Antonova et al. (2009a) estimated daytime current densities using radial pressure distribution obtained by Lui and Hamilton (1992) and Tsyganenko-2001 field line model (Tsyganenko 2002a, b). The values of plasma pressure measured by Lui and Hamilton (1992) were used for geocentric distances up to $9R_E$. The radial dependence of plasma pressure from 9 to $10R_E$ was approximated used the exponential dependence. It was shown that the integral daytime current at geocentric distances from 7.5 to $10R_E$ is comparable with the nighttime current at the same geocentric distances. The possibility to obtain radial plasma pressure gradients at geocentric distances $>9R_E$ appeared with the beginning of the operation of the THEMIS satellite mission. To obtain the estimations of radial plasma pressure gradients Antonova et al. (2009b) used the data from the THEMIS-B satellite for the period between June 2, 2007 and October 29, 2007 (http://www.nasa.gov/mission_pages/themis/) at the equatorial plane near noon. Parts of trajectories were selected at the geocentric distances $7 < r < 12R_E$ with limitation of the azimuthal angle in ±20°. Figure 11.2 shows the obtained radial plasma pressure profile (a), the position of minima of the magnetic field at the daytime magnetic field lines and the calculated values of current densities in the regions of magnetic field minima (b). An exponential fit of the obtained plasma pressure profile was used for the calculation of current densities at every point of the field line. The resulting integral quiet time current from $7.5R_E$ till the magnetopause in both hemispheres is 5.8×10^5 A. The center of transverse currents is situated at $X_{eff} = 7.3R_E$, $Z_{eff} = \pm2.7R_E$ (the star on Fig. 11.2b). Antonova et al. (2009b) concluded analyzing near Earth tail current distribution in Tsyganenko quiet time models that considerable part of near Earth tail current can be closed inside the magnetosphere by dayside transverse currents at the same geocentric distances. Results obtained by Antonova et al. (2009a, b) support the assumption made by Antonova and Ganushkina (2000); Antonova (2003, 2004) about the existence of high latitude continuation of the ordinary ring current split into two branches in the dayside magnetosphere and named the

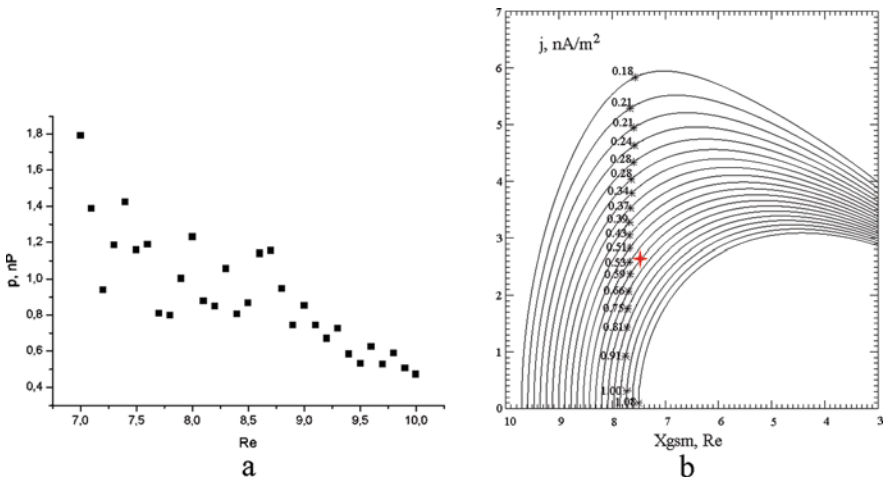

Fig. 11.2 Dayside radial plasma pressure profile obtained from the THEMIS-B satellite data (**a**), positions of minima of the magnetic field at the daytime magnetic field lines and calculated transverse current densities in the regions of magnetic field minima (**b**)

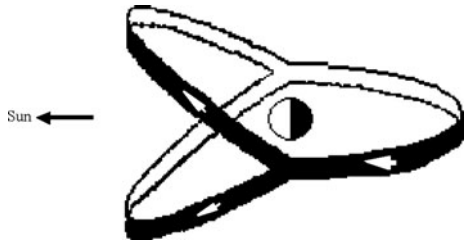

Fig. 11.3 Scheme illustrating the configuration of the Cut Ring Current (CRC)

cut ring current (CRC). Figure 11.3 shows the scheme illustrating CRC configuration. White arrows show the current direction. Topologically, this current is the high latitude continuation of the ordinary ring current and it is generated by plasma pressure gradients directed to the Earth. It is possible to mention that current sheet bifurcation sometimes is observed in the midnight magnetosphere as well (see Asano et al. (2005) and references therein). However, such bifurcation is connected to the fast plasma flows and nongyrotropy of plasma pressure. The nature of the effect of the nighttime current bifurcation is completely different from the dayside transverse current splitting. The last effect takes place due to daytime magnetic field compression even in the in case of isotropic plasma pressure.

The daytime part of CRC is situated comparatively close to the magnetopause and is located far from the equatorial plane. This could be the reason why it was not included into the existing versions of Tsyganenko models. At the same time, the introduction of CRC to the magnetic field models can help to improve such models during both quiet and disturbed periods.

11.4 Auroral Oval and Field-Aligned Currents

Iijima et al. (1990) analyzed the magnetic field data from the AMPTE/CCE satellite obtained at geocentric distances $< 8.8R_E$ and concluded that the equatorial currents, primarily the westward ring current, and the Region 2 current system are closely connected. It is very interesting to understand whether the Region 1 currents of Iijima and Potemra or part of these currents can be supported by the divergence of CRC currents.

Mapping of Iijima and Potemra (1976) picture of the field-aligned currents to the equatorial plane using different magnetic field models (see, Potemra (1976) and Antonova et al. (2006)) shows that the source of the major part of the Region 1 currents is located inside the magnetosphere. Potemra (1976) used the Fairfield and Mead model (Fairfield and Mead 1975), Antonova et al. (2006) used Tsyganenko-1996 and 2001 models (Tsyganenko and Stern 1996; Tsyganenko 2002a, b). Comparison of obtained pictures shows that Tsyganenko models produce such mapping at much larger geocentric distances, which is explained by well known overstretching of Tsyganenko models. The location of the source of Region 1 currents inside the magnetosphere leads to the natural suggestion that such currents are the result of the divergence of large-scale transverse magnetospheric currents.

Considerable part of Region 1 currents in accordance with the picture obtained by Potemra (1976) is mapped into geocentric distances smaller than $13R_E$ near midnight. Therefore, the picture obtained by Potemra (1976) gives the possibility to suggest that significant part of Region 1 currents of Iijima and Potemra is supported due to CRC divergence.

The value of field-aligned current in the condition of magnetostatic equilibrium at the ionospheric altitudes is determined by Grad-Vasyliunas-Boström-Tverskoy relation (Grad 1964; Vasyliunas 1970; Boström 1975; Tverskoy 1982)

$$j_{\text{II}} = 0.5\mathbf{n} \cdot [\nabla W \times \nabla p], \tag{11.2}$$

where ∇ is the two-dimensional gradient, $W = \int dl/B$ is the volume of the magnetic flux tube per unit flux, dl is the element of magnetic field line length, B is the magnetic field and the integration is produced between the conjugate ionospheres, $\mathbf{n}$ is the external normal to the ionosphere, and the positive sign is assigned to the upward field-aligned current. The generation of field-aligned current in accordance with (11.2) requires the noncoincidence of isosurfaces $W = \text{const}$ and $p = \text{const}$. The verification of the possibility of the action of plasma pressure mechanism of Region 1 current generation requires the analysis of the topology of the magnetic configuration (as was done by Antonova and Ganushkina (1997) using Tsyganenko magnetic field models) or measurements of plasma pressure gradients.

Results obtained by Wing and Newell (2000) and Stepanova et al. (2004) support the action of the plasma pressure mechanism. Low altitude observations were

used for obtaining the global picture of plasma distribution at the equatorial plane. Tsyganenko-89 magnetic field model was used by Wing and Newell (2000) for mapping the picture of plasma pressure gradients obtained at low altitudes into the equatorial plane. However, Peredo et al. (1993) and Reeves et al. (1996) demonstrated the overstretching of Tsyganenko-89 model. This means that plasma pressure gradients supported in accordance with Wing and Newell (2000) Region 1 currents are located at smaller geocentric distances than it is shown on Figure 1 of the paper Wing and Newell (2000). Stepanova et al. (2004) used the Tsyganenko-96 magnetic field model, which also is overstretched as shown by Antonova et al. (2006).

Successful launch of the Themis multisatellite mission makes possible to study pressure gradients in situ. Xing et al. (2009) have investigated the quiet-time azimuthal plasma pressure gradient in the plasma sheet at a radial distance between 10 and $12R_E$ using THEMIS spacecraft TH-D and TH-E. They identified the duskward pressure gradient as a source of the upward Region-2 current system in the post-midnight sector and the upward Region 1 current system in pre-midnight sector. These results were compared with the mappings of the Region 1 and Region 2 upward current systems of Iijima and Potemra (1976) made by Potemra (1976) and Antonova et al. (2006). It was shown that the mapping of Region 1 currents with the Fairfield and Mead model is consistent with the results of Xing et al. (2009), indicating the overstretching of Tsyganenko-1996 and -2001 models used for mapping by Antonova et al. (2006). Therefore, some inconsistencies of Wing and Newell (2000) results with Xing et al. (2009) are probably connected to the model-dependent mapping uncertainties. The localization of the source of upward Region 1 current of Iijima and Potemra at geocentric distances $\sim 11R_E$ obtained by Xing et al. (2009) support the possibility of the generation of part of Region 1 currents by divergence of CRC currents.

The suggestion of the mapping of Region 1 currents at comparatively small geocentric distances leads to the suggestion that auroral oval maps at comparatively small distances. Really, Tsyganenko models (Tsyganenko-Sitnov model will be discussed later) can not be used for proper auroral oval mapping due to their overstretching. CRC is not introduced in the existing models that can be the reason of such overstretching.

It is possible to obtain the global picture of upward field-aligned currents using data of auroral imagers. Maximal energy flux of precipitating electrons in the case of absence of field-aligned potential drop is equal to (see, Antonova 1981)

$$\varepsilon^* = n_0 T_e^{3/2} 2^{1/2} / (\pi m_e)^{1/2}, \qquad (11.3)$$

where n_0 is the electron density near the equatorial plane, T_e is the electron temperature (Maxwellian approximation is used for electron distribution function), m_e is the electron mass. For typical plasma sheet parameters $n_0 = 0.5$–$1\ \mathrm{cm}^{-3}$ and $T_e = 0.5$ keV, $\varepsilon^* \sim 0.4$–$0.8\ \mathrm{erg/cm^2 s}$. Such energy flux is close to a threshold of measurements of the imager of Polar satellite ($\sim 0.5\ \mathrm{erg/cm^2 s}$). Visually observed aurora of the I class of brightness requires $0.6\ \mathrm{erg/cm^2 s}$ (Akasofu and Chapman 1972). The existence of field aligned potential drop accelerating magnetospheric electrons up to ~3–10 keV at the altitude $\geq 1\ R_E$ leads to an one-two orders of magnitude increase of the energy flux value in accordance with Knight (1973) relation (see also, Antonova and Tverskoy (1975); Lyons et al. (1979)) and, correspondingly, to the appearance of II and III class of aurora. It is necessary to mention that the accelerated magnetospheric electrons with energies 1–10 keV cannot create polar aurora of IV class. They are produced by accelerated till 1–2 keV dense (with density $\sim 10^2$–$10^3\ \mathrm{cm}^{-3}$) electrons of inospheric origin. Region of downward accelerated magnetospheric electrons is the region of upward field-aligned current. That is why visible picture of polar aurora simultaneously represents the distribution of upward field-aligned currents. Such feature was used in KTH-model of magnetospheric convection by (Marklund et al. 1987) (see also references in the paper Cumnock and Blomberg (2004)).

Region of upward field-aligned currents in the picture of Iijima and Potemra (1976) has a horseshoe like form. It contains the daytime gap near noon. Such distribution of upward field-aligned current produces the horseshoe like distribution of bright aurora. Upward current region can be divided into the Iijima and Potemra sheets of upward Region 1 and Region 2 currents and substorm-connected currents near midnight. Sometimes it is possible to observe their development (see Chua et al. (1998); Shue et al. (2002)). Figure 11.4 contains an example of the comparison of Iijima and Potemra (1976) picture of field-aligned currents and

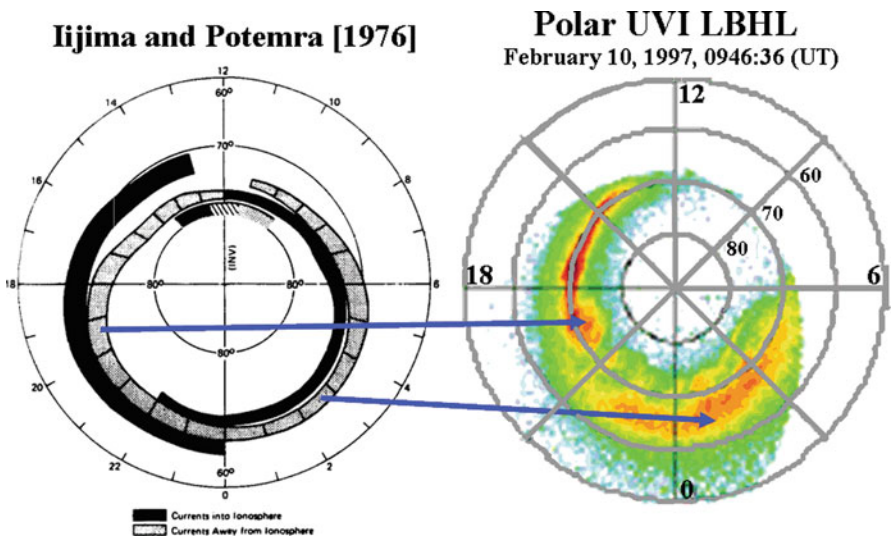

Fig. 11.4 Comparison of Iijima and Potemra (1976) picture of field-aligned currents with Polar UVI observations February 10, 1997

results of Polar UVI observations (http://www.nsstc.nasa.gov/) on February 10, 1997. Nightside gap in this picture is filled by auroral structures during substorms.

The existence of the horseshoe like structure of bright auroral forms can be considered as a proof of tail source of the auroral oval if it will be possible to forget that this is the picture of upward current. Therefore, the location of the source of upward current at the equatorial plane must coincide with the source of auroras in the auroral oval. The band of upward current is split into a definite number of structures if the value of upward current is larger than definite threshold (see, Antonova et al. 1998). The result of such splitting is the appearance of multiple inverted V auroral structures. Penetration of cold ionospheric plasma inside the region of field-aligned potential drop at the boundary of inverted V structure produces collimated field-aligned particle beam having the electron density $\sim 10^2$–10^3 cm^{-3} and energy $\sim$1–2 keV (see discussion in the paper Stepanova et al. (2002)). Therefore, the brightest auroral forms also appear in the region of upward current. Splitting of the upward current band and appearance of bright thin auroral arc makes the picture of the field-aligned currents more complex (appearance of small and medium scale downward field-aligned currents in the region of large-scale upward current). However, the region of discrete auroral forms continues to be the region of large-scale upward current. Therefore, the deep connection of large-scale upward current band of Iijima and Potemra (1976) with discrete auroral oval precipitation region gives the possibility to clarify the location of the source of AOR at the equatorial plane, taking into consideration that the situation with the formation of large-scale currents became clearer after Xing et al. (2009) findings.

11.5 Discussion and Conclusions

The results of particle observations give the possibility to introduce new structure of high latitude transverse currents – Cut Ring Current (CRC) which is the high latitude continuation of the ordinary ring current till magnetopause near noon and till $\sim$10–13R_E near midnight. Despite the necessity to continue with this research, introduction of the CRC system can significantly change the common point of view to the magnetospheric processes, showing that many processes that have been considered as a part of the tail dynamics become a part of the ring current dynamics.

In the first place, it is necessary to mention, that nearly ring structure of the CRC can produce significant contribution to the Dst variation, as discussed by Antonova et al. (2009a). In this context, it is necessary to reanalyze the well-known fact that the auroral oval moves to the lower latitudes during storms, which implies the movement of the upward current region

as well. This displacement can be an important factor for the solution of the problem of external radiation belt filling and appearance "electrons-satellite killers" during storm recovery phase.

Second problem is the location of isolated substorm onset. Lui et al. (2008) have found that the onset is located at the geocentric distances $< 10R_E$, confirming previous results (see also the discussion in the paper Antonova et al. (2009c)). Zou et al. (2009) show that the substorm auroral onset is seen to occur quite near the center of the Harang flow shear and stressed that the nightside Region 2 field-aligned current physics is closely related to substorm dynamics. Region 2 current source is located at geocentric distances smaller than $10R_E$ and ordinarily connected to partial ring current development. This means that isolated substorm onset is located in the quiet time CRC region and the processes giving such onset are connected to CRC dynamics. The processes of partial ring current formation are ordinarily connected to the development of Region 2 field-aligned current system during growth phase of magnetospheric substorm. At the same time, theories of current disruption during substorm consider the disruption of tail current. Partial ring current in such a case must be overlapped with tail current. Considering partial ring current as a stage of CRC development we have more natural picture in which the symmetrization of partial ring current produce the ring current surrounding the Earth.

The situation with Region 1 currents is not so clear. The location of "roots" of Region 1 currents at the equatorial plane requires very careful analysis in the future works as such currents create the dawn-dusk electric field in the polar cap. This field is ordinarily considered as the driver of many magnetospheric processes. Region 1 currents can appear as a result of CRC divergence at its polar boundary or tail current divergence at its equatorial boundary. However, the results obtained by Xing at al. (2009) clearly show that the source of Region 1 currents is not located at large distances in geomagnetic tail.

The introduction of CRC can help to improve magnetic field models based on the fitting of the selected current systems. At the same time, results of Xing et al. (2009) demonstrated very good accuracy of Fairfield and Mead model, which was created using any suggestion about existing current systems. Nearly the same approach was used in Tsyganenko-Sitnov model (Tsyganenko and Sitnov 2007; Sitnov et al. 2008) which show many interesting details of distribution of the magnetospheric currents. However, some difficulties appear with the localization of "roots" of field-aligned currents. In any case, it will be very interesting try to check Region 1 current nature and localization using latest multisatellite missions.

Mapping of the Region 1 currents and external boundary of the auroral oval at the external boundary of CRC, if the future studies will support the discussed findings, can be very important for the study of the problem of magnetosphere-ionosphere interactions. The analysis of the stability of plasma pressure distribution of the plasma ring surrounding the Earth leads to the solution describing the formation of Region 1 and Region 2 field-aligned currents and large-scale magnetospheric convection (see Antonova (2008) and references therein). Such approach gives the possibility to overcome difficulties connected to the hypothesis of solar wind electric field penetration inside the magnetosphere and considers the formation of magnetospheric convection as the process inside the magnetosphere modulated by the interplanetary magnetic field.

Acknowledgements We thank the teams who provided THEMIS and Polar data obtained via NSSDC CDAWEB online facility. The work is supported by FONDECYT grant 1070131, RFBR grant 10-05-00247-a.

References

Akasofu SI, Chapman S (1972) Solar-terrestrial physics. Clarendel, Oxford

Angelopoulos V (2008) The THEMIS mission. Space Sci Rev 141:5–34. doi:10.1007/s11214-008-9336-1

Antonova EE (1981) The reason why the field-aligned flow of electrons from to the ionosphere is a linear function of the field-aligned potential difference. Geomagn Aeron 21(6):1004–1008

Antonova EE (2003) Investigation of the hot plasma pressure gradients and the configuration of magnetospheric currents from INTERBALL. Adv Space Res 31(5):1157–1166. doi:10.1016/S0273-1177(03)00077-2

Antonova EE (2004) Magnetostatic equilibrium and current systems in the Earth's magnetosphere. Adv Space Res 33(5):752–760. doi:0.1016/S0273-1177(03)00636-7

Antonova EE (2008) Magnetospheric turbulence and properties of magnetospheric dynamics. Adv Space Res 41(10):1677–1681. doi:10.1016/j.asr.2007.05.057

Antonova EE, Tverskoy BA (1975) Nature of inverted-V electron precipitation band and Harang discontinuity in the evening sector of auroral ionosphere. Geomagn Aeron (Engl Transl) 15(1):85–90

Antonova EE, Ganushkina NY (1997) Azimuthal hot plasma pressure gradients and dawn-dusk electric field formation. J Atmos Terr Phys 59:1343–1354. doi:10.1016/S1364-6826(96)00169-1

Antonova EE, Ganushkina NYu (2000) Inner magnetospheric currents and their role in the magnetosphere dynamics. Phys Chem Earth(C) 25(1–2):23–26. doi:10.1016/S1464-1917(99)00028-8

Antonova EE, Stepanova MV, Teltzov MV, Tverskoy BA (1998) Multiple inverted-V structures and hot plasma pressure mechanism of plasma stratification. J Geophys Res 103:9317–9332. doi:10.1029/97JA03090

Antonova EE, Kirpichev IP, Stepanova MV (2006) Field-aligned current mapping and the problem of the generation of magnetospheric convection. Adv Space Res 38(8):1637–1641. doi:10.1016/j.asr.2005.09.042

Antonova EE, Kirpichev IP, Stepanova MV, Orlova KG, Ovchinnikov IL (2009a) Topology of the high latitude magnetosphere during large magnetic storms and the main mechanisms of relativistic electron acceleration. Adv Space Res 43(4):628–633. doi:10.1016/j.asr.2008.09.011

Antonova EE, Kirpichev IP, Ovchinnikov IL, Orlova KG, Stepanova MV (2009b) High latitude magnetospheric topology and magnetospheric substorm. Ann Geophys 27(10):4069–4073

Antonova EE, Kornilov IA, Kornilova TA, Kornilov OI, Stepanova MV (2009c) Features of auroral breakup obtained using data of ground-based television observations: case study. Ann Geophys 27(4):1413–1422.

Asano Y, Nakamura R, Baumjohann W, Runov A, Vörös Z, Volwerk M, Zhang TL., Balogh A, Klecker B, Rème H (2005) How typical are atypical current sheets? Geophys Res Lett 32:L03108. doi:10.1029/2004GL021834

Boström R (1975) Mechanism for driving Birkeland currents. In: Hultgvist B, Stenflo L (eds) Physics of the hot plasma in the magnetosphere. Proceedings of the thirtieth nobel symposium. Kiruna, Sweden, 2–4 Apr 1975, pp 341–365

Chua D, Brittnacher M, Parks G, Germany G, Spann J (1998) The new auroral feature: the nightside gap. Geophys Res Lett 25(2):3747–3750. doi:10.1029/98GL02806

Cumnock JA, Blomberg LG (2004) Transpolar arc evolution and associated potential patterns. Ann Geophys 22(4):1213–1231

De Michelis P, Daglis IA, Consolini G (1999) An average image of proton plasma pressure and of current systems in the equatorial plane derived from AMPTE/CCE-CHEM measurements. J Geophys Res 104(A12):28615–28624. doi:10.1029/1999JA900310

Delcourt DC, Sauvaud J-A (1999) Populating of the cusp and boundary layers by energetic (hundreds of keV) equatorial particles. J Geophys Res 104(A10):22635–22648. doi:10.1029/1999JA900251

Fairfield DH, Mead GD (1975) Magnetospheric mapping with quantitative geomagnetic field models. J Geophys Res 80(4):535–548

Feldstein YI, Galperin YuI (1985) The aurororal luminosity structure in the high-latitude upper atmosphere. Its dynamics and relationship to the large-scale structure of the Earth's magnetosphere. Rev Geophys 23(3):217–275

Grad H (1964) Some new variational properties of hydromagnetic equilibria. Phys Fluids 7:1283–1292. doi:10.1063/1.1711373

Hori T, Ohtani S, Lui ATY, McEntire RW, Maezawa K, Sato Y, Mukai TA (2003) Substorm associated drift echo of energetic protons observed by Geotail: radial density gradient structure. Geophys Res Lett 30(6):1330. doi:10.1029/20002GL016137

Iijima T, Potemra TA (1976) Field-aligned currents in the dayside cusp observed by TRIAD. J Geophys Res 81(12):5971–5979. doi:10.1029/JA081i034p05971

Iijima T, Potemra TA, Zanetti J (1990) Large-scale characteristics of magnetospheric equatorial currents. J Geophys Res 95(A2):991–999. doi: 10.1029/JA095iA02p00991

Knight LR (1973) Parallel electric fields. Planet Space Sci 21(5):741–750

Lui ATY, Hamilton DC (1992) Radial profile of quiet time magnetospheric parameters. J Geophys Res 97(A12):19325–19332. doi:10.1029/92JA01539

Lui ATY, Volwerk M, Dunlop MW, Alexeev IV et al (2008) Near-Earth substorm features from multiple satellite observations. J Geophys Res 113(A7):A07S26. doi:10.1029/2007JA012738

Lyons LR, Evans DS, Lundin R (1979) An observed relation between field aligned electric fields and downward electron energy fluxes in the vicinity of auroral forms. J Geophys Res 84(A2):457–461. doi:10.1029/JA084iA02p00457

Marklund GT, Blomberg LG, Potemra TA, Murphree JS, Rich JR, Stasiewicz K (1987) A new method to derive "instantaneous" high-latitude potential distributions from satellite measurements including auroral imager data. Geophys Res Lett 14(4):439–442. doi:10.1029/GL014i004p00439

Newell PT, Meng C-I (1992) Mapping the dayside ionosphere to the magnetosphere according to particle precipitation characteristics. Geophys Res Lett 19(6):609–612. doi:10.1029/92GL00404

Newell PT, Sotirelis T, Wing S (2009) Diffuse, monoenergetic, and broadband aurora: the global precipitation budget. J Geophys Res 114(A9):A09207. doi:10.1029/2009JA014326

Öztürk MK, Wolf RA (2007) Bifurcation of drift shells near the dayside magnetopause. J Geophys Res 112(A7):A07207. doi:10.1029/2006JA012102

Peredo M, Stern DP, Tsyganenko NA (1993) Are existing magnetic field models excessively stretched? J Geophys Res 98(A9):15343–15354

Potemra TA (1976) Large-scale characteristics of field-aligned currents determined from the Triad magnetometer experiment. In: Grandal B, Holtet JA (eds) Dynamical and chemical coupling between the neutral and ionized atmosphere. Proceedings of the advanced study institute. NATO Advanced Study Institute, Series C, vol 35. Spatind, Norway, 12–22 Apr 1977, pp 337–352

Reeves GD, Weiss LA, Thomsen MF, McComas DJ (1996) A quantitative test of different magnetic field models using conjunctions between DMSP and Geosynchronous orbit. Radiation belts: modeling and standards. Geophysical monograph, vol 97. pp 167–172

Shabansky VP, Antonova AE (1968) Topology of particle drift shells in the Earth's magnetosphere. Geomagn Aeron (in Russian) 8:993–997

Shue J-H, Newell PT, Liou K, Meng C-I, Kamide Y, Lepping RP (2002)Two-component auroras. Geophys Res Lett 29(10):CiteID 1379. doi:10.1029/2002GL014657

Sitnov MI, Tsyganenko NA, Ukhorskiy AY, Brandt PC (2008) Dynamical data-based modeling of the stormtime geomagnetic field with enhanced spatial resolution. J Geophys Res 113(A7):A07218. doi:10.1029/2007JA013003

Stasiewicz K (1991) A global model of gyroviscous field line merging at the magnetopause. J Geophys Res 96(1):77–86. doi: 10.1029/90JA02194

Stepanova MV, Antonova EE, Bosqued JM, Kovrazhkin RA, Aubel KR (2002) Asymmetry of auroral electron precipitations and its relationship to the substorm expansion phase onset. J Geophys Res 107(A7):CiteID 1134. doi:10.1029/2001JA003503

Stepanova MV, Antonova EE, Bosqued JM, Kovrazhkin R (2004) Azimuthal plasma pressure reconstructed by using the Aureol-3 satellite date during quiet geomagnetic conditions. Adv Space Res 33(5):737–741. doi:10.1016/S0273-1177(03)00641-0

Tsyganenko NA (1987) Global quantitative models of the geomagnetic field in the cislunar magnetosphere for different disturbance levels. Planet Space Sci 35(11):1347–1358. doi: 10.1016/0032-0633(87)90046-8

Tsyganenko NA (2002a) A model of the near magnetosphere with a dawn-dusk asymmetry: 1. Mathematical structure. J Geophys Res 107(A8):CiteID 1179. doi:10.1029/2001JA000219

Tsyganenko NA (2002b) A model of the near magnetosphere with a dawn-dusk asymmetry: 2. Parameterization and fitting to observations. J Geophys Res 107(A8):CiteID 1176. doi:10.1029/2001JA000220

Tsyganenko NA, Sitnov MI (2007) Magnetospheric configurations from a high-resolution data-based magnetic field model. J Geophys Res 112(A6):A06225. doi:10.1029/2007JA012260

Tsyganenko NA, Stern DP (1996) A new generation global magnetosphere field model, based on spacecraft magnetometer data. ISTP Newsletter 6(1):21

Tverskoy BA (1982) Field-aligned currents in the magnetosphere. Geomagn Aeron (Engl Transl) 22(6):812–815

Vasyliunas VM (1970) Mathematical models of magnetospheric convections and its coupling to the ionosphere. In: McCormac BM (ed) Particles and fields in the magnetosphere. D. Reidel, Hingham, MA, pp 60–71

Vorobjev VG, Iagodkina OY, Starkov GV, Feldstein YaI (2007): Features of the planetary distribution of auroral precipitation characteristics during substorms. Geomagn Aeron (in Russian) 47(2):193–204

Wing S, Newell PT (2000) Quiet time plasma sheet ion pressure contribution to Birkeland currents. J Geophys Res 105(A4):7793–7802. doi:10.1029/1999JA900464

Xing X, Lyons LR, Angelopoulos V, Larson D, McFadden J, Carlson C, Runov A, Auster U (2009) Azimuthal plasma pressure gradient in quiet time plasma sheet. Geophys Res Lett 36(14):L14105. doi:10.1029/2009GL038881

Zou S, Lyons LR, Wang C-P, Boudouridis A, Ruohoniemi JM, Anderson PC, Dyson PL, Devlin JC (2009) On the coupling between the Harang reversal evolution and substorm dynamics: a synthesis of SuperDARN, DMSP, and IMAGE observations. J Geophys Res 114(A1):A01205. doi:10.1029/2008JA013449

Detection of Dynamical Complexity Changes in *Dst* Time Series Using Entropy Concepts and Rescaled Range Analysis

12

Georgios Balasis, Ioannis A. Daglis,
Anastasios Anastasiadis, and Konstantinos Eftaxias

Abstract

Using an array of diagnostic tools including entropy concepts and rescaled range analysis, we establish that the *Dst* index time series exhibits long-range correlations, and that the underlying stochastic process can be modeled as fractional Brownian motion. We show the emergence of two distinct patterns in the geomagnetic variability of the terrestrial magnetosphere: (1) a pattern associated with intense magnetic storms, which is characterized by a higher degree of organization (i.e., lower complexity or higher predictability for the system) and persistent behavior, and (2) a pattern associated with normal periods, which is characterized by a lower degree of organization (i.e., higher complexity or lower predictability for the system) and anti-persistent behavior.

12.1 Introduction

Studies of entropy provide physical insight into space plasma transport, intermittency, turbulence, and information flow in the heliosphere and magnetosphere (Wing and Johnson 2010). Moreover, entropy-based information theory can be used to characterize the dynamics of complex magnetospheric phenomena (Balasis et al. 2008, 2009; Balasis and Eftaxias 2009).

Here we present a detailed investigation of the *Dst* index time variations using entropy measures and rescaled range analysis (via the Hurst exponent) to search for long-time correlations and dynamical changes in the complex system of the magnetosphere. In this context, we seek a "good" complexity measure, i.e., a statistic quantifying regularity and complexity, which has application to relatively brief and noisy data.

We consider 1 year of *Dst* data (2001) including two intense magnetic storms, which occurred on 31 March 2001 and 6 November 2001 with minimum *Dst* values −387 nT and −292 nT respectively, as well as a number of weaker events (e.g. May and August 2001 with $Dst \sim -100$ nT in both cases). More precisely, the temporal evolution of nonlinear characteristics is studied by applying a variety of recently proposed entropy techniques: the original *Dst* time series is projected to a symbolic sequence and then analyses in terms of the classical Shannon entropy, dynamical (Shannon-like) block entropy, *T*-complexity and non-extensive Tsallis entropy follow. For the purpose of comparison we also analyze the original *Dst* data by means of approximate entropy. Finally, for the first time, the rescaled range analysis method is applied to the *Dst* data to calculate the values of the Hurst exponent. This analysis verifies

G. Balasis (✉)
Institute for Space Applications and Remote Sensing, National Observatory of Athens, Athens, Greece
e-mail: gbalasis@space.noa.gr

W. Liu, M. Fujimoto (eds.), *The Dynamic Magnetosphere*, IAGA Special Sopron Book Series 3,
DOI 10.1007/978-94-007-0501-2_12,

the results of an earlier fractal spectral analysis of the *Dst* index based on wavelet transforms (Balasis et al. 2006).

12.2 Theoretical Background

In this section we briefly introduce concepts of entropy and tools of information theory which will be used in the present study.

12.2.1 Fundamentals of Symbolic Dynamics

For the sake of completeness and for later use, we compile here the basic points of symbolic dynamics. Symbolic time series analysis is a useful tool for modelling and characterization of nonlinear dynamical systems. It provides a rigorous way of looking at "real" dynamics with finite precision (Hao 1989; Karamanos and Nicolis 1999). Briefly, it is a way of coarse-graining or simplifying the description.

The basic idea is quite simple. One divides the phase space into a finite number of partitions and labels each partition with a symbol (e.g. a letter from some alphabet). Instead of representing the trajectories by infinite sequences of numbers-iterates from a discrete map or sampled points along the trajectories of a continuous flow, one watches the alteration of symbols. Of course, in so doing one loses an amount of detailed information, but some of the invariant, robust properties of the dynamics may be kept, e.g. periodicity, symmetry, or the chaotic nature of an orbit (Hao 1989).

In the framework of symbolic dynamics, time series are transformed into a series of symbols by using an appropriate partition which results in relatively few symbols. After symbolization, the next step is the construction of "symbol sequences" ("words" in the language symbolic dynamics) from the symbol series by collecting groups of symbols together in temporal order.

To be more precise, the simplest possible coarse-graining of a time series is given by choosing a threshold C (usually the mean value of the data considered) and assigning the symbols "1" and "0" to the signal, depending on whether it is above or below the threshold (binary partition). Thus, we generate a symbolic time series from a 2-letter ($\lambda = 2$) alphabet (0, 1), e.g. 0110100110010110.... We usually read this symbolic sequence in terms of distinct consecutive "blocks" (words) of length $n = 2$. In this case one obtains 01/10/10/01/10/01/01/10/.... We call this reading procedure "lumping".

The number of all possible kinds of words is $\lambda^n = 2^2 = 4$, namely 00, 01, 10, 11. The required probabilities for the estimation of an entropy, p_{00}, p_{01}, p_{10}, p_{11} are the fractions of the blocks (words) 00, 01, 10, 11 in the symbolic time series, namely, 0, 4/16, 4/16, and 0, correspondingly. Based on these probabilities we can estimate, for example, the probabilistic entropy measure H_S introduced by Shannon (1948)

$$H_S = -\sum p_i \ln p_i \tag{12.1}$$

where p_i are the probabilities associated with the microscopic configurations.

Various tools of information theory and entropy concepts are used to identify statistical patterns in the symbolic sequences, onto which the dynamics of the original system under analysis has been projected. For detection of an anomaly, it suffices that a detectable change in the pattern represents a deviation of the system from nominal behavior (Graben and Kurths 2003). Recent published work has reported novel methods for detection of anomalies in complex dynamical systems, which rely on symbolic time series analysis. Entropies depending on the word-frequency distribution in symbolic sequences are of special interest, extending Shannon's classical definition of the entropy and providing a link between dynamical systems and information theory. These entropies take a large/small value if there are many/few kinds of patterns, i.e., they decrease while the organization of patterns is increasing. In this way, these entropies can measure the complexity of a signal.

12.2.2 The Concept of Dynamical (Shannon-Like) Block Entropy

Block entropies, depending on the word-frequency distribution, are of special interest, extending Shannon's classical definition of the entropy of a single state to the entropy of a succession of states (Nicolis and Gaspard 1994).

Symbolic sequences, $\{A_1, \ldots, A_n, \ldots, A_L\}$ are composed of letters from an alphabet consisting of λ letters $\{A^{(1)}, A^{(2)}, \ldots, A^{(\lambda)}\}$. An English text, for example,

is written on an alphabet consisting of 26 letters $\{A, B, C, \ldots, X, Y, Z\}$.

A word of length $n < L$, $\{A_1, \ldots, A_n\}$, is defined by a substring of length n taken from $\{A_1, \ldots, A_n, \ldots, A_L\}$. The total number of different words of length n which exists in the alphabet is $N_{\lambda n} = \lambda^n$.

We specify that the symbolic sequence is to be read in terms of distinct consecutive "blocks" (words) of length n,

$$\ldots, \underbrace{A_1, \ldots, A_n}_{B_1} \underbrace{A_{n+1}, \ldots, A_{2n}}_{B_2}, \ldots, \underbrace{A_{jn+1}, \ldots, A_{(j+1)n}}_{B_{j+1}}, \ldots \tag{12.2}$$

As stated previously, we call this reading procedure *lumping*. *Gliding* is the reading of the symbolic sequence using a *moving frame*. It has been suggested that, at least in some cases, the entropy analysis by lumping is much more sensitive than classical entropy analysis (gliding) (Karamanos 2000, 2001).

The probability $p^{(n)}(A_1, \ldots, A_n)$ of occurrence of a block $A_1, \ldots, A_n$ is defined by the fraction,

$$\frac{\text{No. of blocks, } A_1, \ldots, A_n, \text{ encountered when lumping}}{\text{Total no. of blocks}} \tag{12.3}$$

starting from the beginning of the sequence.

From the quantities characterize the information content of the symbolic sequence (Khinchin 1957; Ebeling and Nicolis 1992) we focus on the Shannon n-block entropy. Following Shannon's approach (Shannon 1948) the n-block entropy, $H(n)$, is given by

$$H(n) = -\sum p^{(n)}(A_1, \ldots, A_n) \ln p^{(n)}(A_1, \ldots, A_n) \tag{12.4}$$

The entropy $H(n)$ is a measure of uncertainty and gives the average amount of information necessary to predict a sub-sequence of length n.

12.2.3 T-complexity

T-entropy is a novel grammar-based complexity/information measure defined for finite strings of symbols (Ebeling et al. 2001; Titchener et al. 2005). It is a weighted count of the number of production steps required to construct a string from its alphabet. Briefly, it is based on the intellectual economy one makes when rewriting a string according to some rules.

An example of an actual calculation of the *T*-complexity for a finite string is given by Ebeling et al. (2001). We briefly describe how the *T*-complexity is computed for finite strings. The *T*-complexity of a string is defined by the use of one recursive hierarchical pattern copying (RHPC) algorithm. It computes the effective number of *T*-augmentation steps required to generate the string. The *T*-complexity may thus be computed effectively from any string and the resultant value is unique.

The string $x(n)$ is parsed to derive constituent patterns $p_i \in A^+$ and associated copy-exponents, $k_i \in N^+$, $i = 1, 2, \ldots, q$, where $q \in A^+$ satisfying:

$$x = p_q^{k_q} p_{q-1}^{k_{q-1}} \ldots p_i^{k_i} \ldots p_1^{k_1} \alpha_0, \ \alpha_0 \in A \tag{12.5}$$

Each pattern p_i is further constrained to satisfy:

$$p_i = p_{i-1}^{m_{i,i-1}} p_{i-2}^{m_{i,i-2}}, \ldots, p_j^{m_{i,j}}, \ldots, p_1^{m_{i,1}} \alpha_i \tag{12.6}$$

$$\alpha_i \in A \text{ and } 0 \leq m_{i,j} \leq k_j \tag{12.7}$$

The *T*-complexity $C_T(x(n))$ is defined in terms of the copy-exponents k_i:

$$C(x(n)) = \sum_i^q \ln(k_i + 1) \tag{12.8}$$

One may verify that $C_T(x(n))$ is minimal for a string comprising a single repeating character.

The *T*-information $I_T(x(n))$ of the string $x(n)$ is defined as the inverse logarithmic integral, ${l_i}^{-1}$, of the *T*-complexity divided by a scaling constant ln 2:

$$I_T(x(n)) = {l_i}^{-1} \ln\left(\frac{C_T(x(n))}{\ln 2}\right) \tag{12.9}$$

In the limit $n \to \infty$ we have that $I_T(x(n)) \leq \ln(\#A^n)$.

The form of the right-hand side may be recognizable as the maximum possible n-block entropy of Shannon's definition. The Neperian logarithm implicitly gives to the *T*-information the units of nats. $I_T(x(n))$ is the *T*-information of string $x(n)$. The *average T-information rate per symbol*, referred to here as the

average T-entropy of $x(n)$ and denoted by $h_T(x(n))$, is defined along similar lines,

$$h_T\left(x\left(n\right)\right) = \frac{I_T\left(x\left(n\right)\right)}{n} \text{ (nats/symbol)} \tag{12.10}$$

12.2.4 Principles of Non-extensive Tsallis Entropy

It has been established that physical systems which are characterized by longrange interactions or long-term memories, or are of a multi-fractal nature, are best described by a generalized statistical-mechanical formalism proposed by Tsallis (1988, 2009). More precisely, inspired by multifractals concepts, Tsallis introduced an entropic expression characterized by an index q which leads to non-extensive statistics (1988, 2009):

$$S_q = k\frac{1}{q-1}\left(1 - \sum_{i=1}^{W} p_i^q\right) \tag{12.11}$$

where p_i are probabilities associated with the microscopic configurations, W is their total number, q is a real number and k is Boltzmann's constant. The entropic index q describes the deviation of Tsallis entropy from the standard Boltzmann-Gibbs entropy. Indeed, using $p_i^{(q-1)} = e^{(q-1)\ln(p_i)} \sim 1 + (q-1)\ln(p_i)$ in the limit $q \to 1$, we recover the usual Boltzmann-Gibbs entropy

$$S_1 = -k\sum_{i=1}^{W} p_i \ln\left(p_i\right) \tag{12.12}$$

The entropic index q characterizes the degree of non-extensivity reflected in the following pseudo-additivity rule:

$$S_q\left(A+B\right) = S_a\left(A\right) + S_q\left(B\right) + \frac{1-q}{k} S_q\left(A\right) S_q\left(B\right) \tag{12.13}$$

For subsystems that have special probability correlations, extensivity

$$S_{B-G} = S_{B-G}\left(A\right) + S_{B-G}\left(B\right) \tag{12.14}$$

is not valid for $SB{-}G$, but may occur for Sq with a particular value of the index q. Such systems are sometimes referred to as non-extensive (Tsallis 1988, 2009).

The cases $q > 1$ and $q < 1$, correspond to sub-additivity, or super-additivity, respectively. We may think of q as a bias-parameter: $q < 1$ privileges rare events, while $q > 1$ privileges prominent events (Zunino et al. 2008).

We clarify that the parameter q itself is not a measure of the complexity of the system but measures the degree of non-extensivity of the system. It is the time variations of the Tsallis entropy for a given q, (S_q), that quantify the dynamic changes of the complexity of the system. Lower S_q values characterize the portions of the signal with lower complexity.

In terms of symbolic dynamics the Tsallis entropy for the word length n is (Balasis et al. 2008):

$$S_q\left(n\right) = k\frac{1}{q-1}\left(1 - \sum_{(A_1,A_2,\ldots,A_n)} \left[p(n)_{A_1,A_2,\ldots,A_n}\right]^q\right) \tag{12.15}$$

12.2.5 Approximate Entropy

Approximate entropy (*ApEn*), has been introduced as a quantification of regularity in time series data, motivated by applications to a wide variety of relatively brief, noisy data sets. *ApEn* could serve as a valuable tool for dynamically monitoring "health" status in a wide range of non-stationary systems. Therefore, it is here adopted for examining the dynamic system of the Earth's magnetosphere.

Related to time series analysis, *ApEn* provides a measure of the degree of irregularity or randomness within a series of data (of length N). *ApEn* was pioneered by Pincus as a measure of system complexity (Pincus 1991). It was introduced as a quantification of regularity in relatively brief and noisy data. It is rooted in the work of Grassberger and Procaccia (1983) and has been widely applied to biological systems (Pincus and Goldberger 1994; Pincus and Singer 1996 and references therein).

The *ApEn* examines time series for similar epochs: more similar and more frequent epochs lead to lower values of *ApEn*.

For a qualitative point of view, given N points, the *ApEn*-like statistics is approximately equal to the negative logarithm of the conditional probability that two sequences that are similar for m points remain similar,

that is, within a tolerance r, at the next point. Smaller *ApEn*-values indicate a greater chance that a set of data will be followed by similar data (regularity), thus, smaller values indicate greater regularity. Conversely, a greater value for *ApEn* signifies a lesser chance of similar data being repeated (irregularity), hence, greater values convey more disorder, randomness and system complexity. Thus a low/high value of *ApEn* reflects a high/low degree of regularity. Notably, *ApEn* detects changes in underlying episodic behavior not reflected in peak occurrences or amplitudes (Pincus and Keefe 1992).

The following is a brief description of the calculation of *ApEn*. A more comprehensive description of *ApEn* may be found in (Pincus 1991; Pincus and Goldberger 1994; Pincus and Singer 1996).

Given any sequence of data points $u(i)$ from $i = 1$ to N, it is possible to define vector sequences $x(i)$, which consists of length m and are made up of consecutive $u(i)$, specifically defined by the following:

$$x(i) = (u[i], u[i+1], \ldots, u[i+m-1]) \quad (12.16)$$

In order to estimate the frequency that vectors $x(i)$ repeat themselves throughout the data set within a tolerance r, the distance $d(x[i], x[j])$ is defined as the maximum difference between the scalar components $x(i)$ and $x(j)$. Explicitly, two vectors $x(i)$ and $x(j)$ are "similar" within the tolerance or filter r, namely $d\left(x[i], x\left[j\right]\right) \leq r$, if the difference between any two values for $u(i)$ and $u(j)$ within runs of length m does not exceed r (i.e. $|u(i+k) - u(j+k)| \leq r\{\wr \nabla\ 0 \leq k \leq m$). Subsequently, the correlation sum of vector $x(i)$ is

$$C_i^m = \frac{\left[\text{number of } j \text{ such that } d\left(x[i], x\left[j\right]\right) \leq r\right]}{(N-m+1)}$$

where $j \leq (N-m+1)$.

The $C_i^m(r)$ values measure, within a tolerance r, the regularity (frequency) of patterns similar to a given one of window length m. The parameter r acts like a filter value: within resolution r, the numerator count the number of vectors that are approximately the same as a given vector $x(i)$. The quantity $C_i^m(r)$ is called the correlation sum because it quantifies the summed (or global) correlation of vector $x(i)$ with all other vectors.

Taking the natural logarithm of $C_i^m(r)$, the mean logarithmic correlation sum of all vectors is defined as:

$$\Phi^m(r) = \sum_i \ln C_i^m(r)/(N-m+1) \quad (12.17)$$

where Σ_i is a sum from $i = 1$ to $(N-m+1)$. $\Phi^m(r)$ is a measure of the prevalence of repetitive patterns of length m within the filter r. Briefly, $\Phi_m(r)$ represents the average frequency of all the m-point patterns in the sequence remain close to each other.

Finally, $ApEn(m, r, N)$, is defined as the natural logarithm of the relative prevalence of repetitive patterns of length m as compared with those of length $m+1$:

$$ApEn(m, r, N) = \Phi^m(r) - \Phi^{m+1}(r) \quad (12.18)$$

Thus, $ApEn(m, r, N)$ measures the logarithmic frequency that similar runs (within the filter r) of length m also remain similar when the length of the run is increased by 1. Small values of *ApEn* indicate regularity, given that increasing run length m by 1 does not decrease the value of $\Phi^m(r)$ significantly (i.e., regularity connotes that $\Phi^m[r] \approx \Phi^{m+1}(r)$). $ApEn(m, r, N)$ is expressed as a difference, but in essence it represents a ratio; note that $\Phi^m(r)$ is a logarithm of the averaged $C_i^m(r)$, and the ratio of logarithms is equivalent to their difference.

In summary, *ApEn* is a "regularity statistics" that quantifies the unpredictability of fluctuations in a time series. The presence of repetitive patterns of fluctuation in a time series renders it more predictable than a time series in which such patterns are absent. A time series containing many repetitive patterns has a relatively small *ApEn*; a less predictable (i.e., more complex) process has a higher *ApEn*.

12.2.6 Rescaled Range Analysis

Following the original work of Hurst (1951), the rescaled range (R/S)method is used to calculate the scaling exponent (Hurst exponent), H, to give quantitative measure of the persistence of a signal. First, when $0 < H < 1$ a signal can be modeled by fractional Brownian motion (fBm) (Henegham and McDarby 2000). $0.5 < H < 1$ is taken to indicate persistence, while $H = 0.5$ indicates an uncorrelated process. Persistence means that if the amplitude of the fluctuations increases in a time interval it is likely to continue increasing in the next interval. $0 < H < 0.5$ indicates anticorrelation or anti-persistence. Anti-persistence

implies a set of fluctuations tending to induce stability within the system.

The R/S analysis is a statistical method to analyse long records of natural phenomena (Vanouplines 1995). There are two factors used in this analysis: firstly the range R, this is the difference between the minimum and maximum "accumulated" values or cumulative sum of $X(t, \tau)$ of the natural phenomenon at discrete integervalued time t over a time span τ , and secondly the standard deviation S, estimated from the observed values $Xi(t)$. Hurst found that the ratio R/S is very well described for a large number of natural phenomena by the following empirical relation:

$$R/S = (c\tau)^H \tag{12.19}$$

where τ is the time span, and H the Hurst exponent. The coefficient c was taken equal to 0.5 by Hurst. R is defined as:

$$R(\tau) = \max(X(t, \tau)) - \min(X(t, \tau)) \tag{12.20}$$

where t takes values from [1 τ]. S is given by:

$$S = \left\{ \frac{1}{\tau} \sum_{t=1}^{\tau} \left[\xi(t) - \langle \xi \rangle_\tau \right]^2 \right\}^{1/2} \tag{12.21}$$

where $\langle \xi \rangle_\tau = \sum_{t-1}^{\tau} \xi(t)/\tau$ and $X(t, \tau) = \sum_{u=1}^{t} \left[\xi(u) - \langle \xi \rangle_\tau \right]$. This method handles observations in time. The graphical representation uses time in the abscissa, and the observed value in the ordinate.

12.3 Results

In Fig. 12.1 the *Dst* time series is presented. The 1 year *Dst* data (2001) are divided into 5 shorter time series (see triangles denoting 5 distinct time intervals in Fig. 12.1). The 2nd and 4th time windows include the *Dst* variations associated to the 2 intense magnetic storms of 31/3/2001 and 6/11/2001, respectively. In Fig. 12.1 the values of the H parameter calculated by two different methods (i.e., fractal spectral analysis using wavelets (see Balasis et al. 2006, 2008, 2009) and R/S analysis) are also shown for the *Dst* index data. Figure 12.1 shows that *Dst* variations follow the fBm model (H always lies between 0 and 1) and exhibit persistent properties ($0.5 < H < 1$) around 31 March and 6 November 2001 magnetic storms (c.f. parts of H plot calculated by fractal spectral analysis marked in red represent persistency). In general, there is good agreement with the results for the H exponent

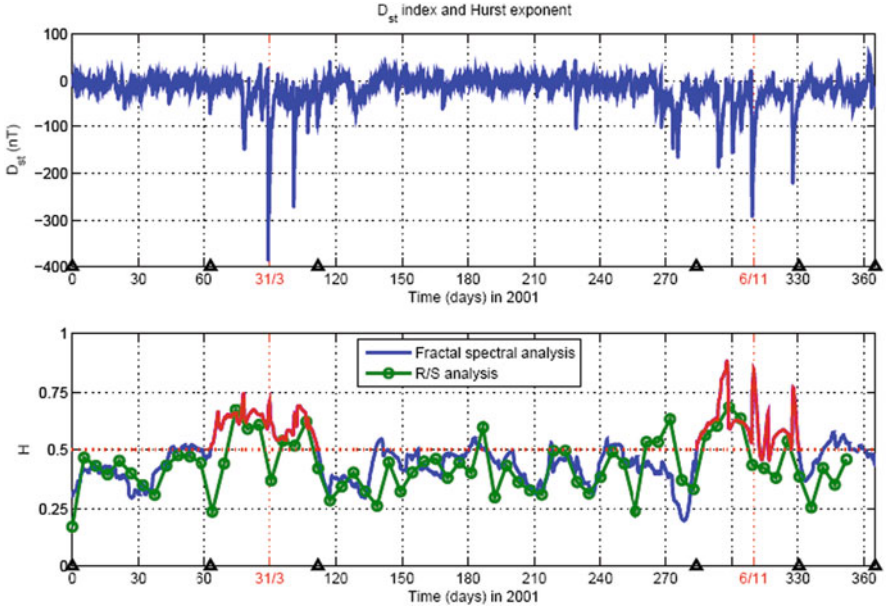

Fig. 12.1 *Dst* time series (*upper panel*) and Hurst exponents H (*lower panel*) calculated by fractal spectral analysis (*blue color*) and R/S analysis (*green color*). The 31 March and 6 November 2001 magnetic storms are marked with *red*. The *red dashed line* in H plot marks the transition between anti-persistent and persistent behavior. The triangles denote 5 time intervals corresponding to windows related to intense magnetic storms (2nd and 4th) and windows related to normal times (1st, 3rd and 5th)

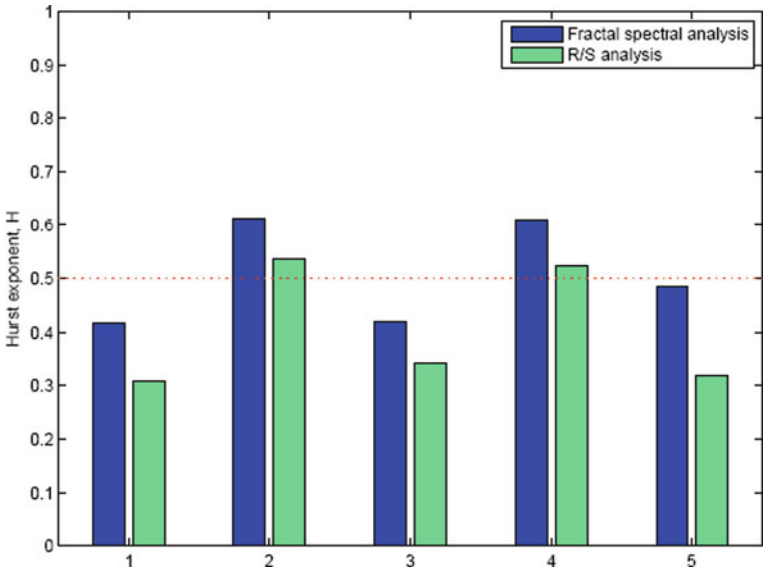

Fig. 12.2 Average values of the Hurst exponents H calculated by fractal spectral analysis (*blue color*) and R/S analysis (*green color*) at the 5 time windows indicated in Fig. 12.1. The *red dashed* line marks the transition between anti-persistent and persistent behavior. It is evident that time windows 1, 3 and 5 correspond to *Dst* index data with anti-persistent behavior, whereas, time windows 2 and 4 represent *Dst* time series with persistent behavior

from the R/S method. Thus, it is evident that the onset and development of the magnetic storms of 31/3/2001 and 6/11/2001 are associated with persistent behavior, which suggests that the underlying dynamics is governed by a positive feedback mechanism.

In Fig. 12.2 we show the average values of the Hurst exponents H calculated by fractal spectral analysis (blue color) and R/S analysis (green color) at the 5 time windows of Fig. 12.1. We stress that as both methods state the anti-persistent epochs ($0 < H < 0.5$)

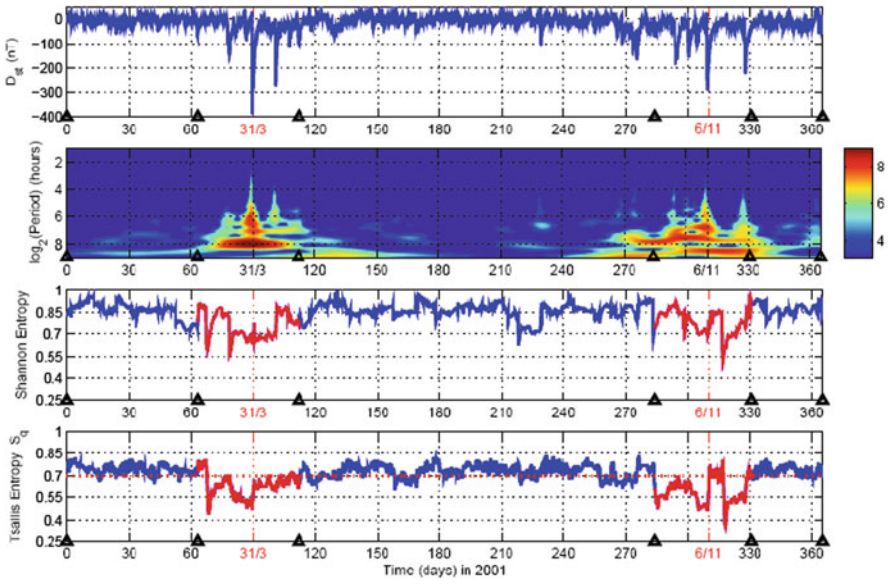

Fig. 12.3 From *top* to *bottom*: *Dst* time series along with its wavelet power spectrum for 2001 and time variations of Shannon entropies and Tsallis entropies, S_q. The 31 March and 6 November 2001 magnetic storms are marked with *red*. The *red dashed line* in S_q plot marks a possible boundary value for the transition to the lower complexity characterizing the different state of the magnetosphere. The triangles denote 5 time intervals (as in Fig. 12.1) in which: 1st, 3rd and 5th time windows correspond to anti-persistent ($0 < H < 0.5$) or high Tsallis entropies epochs; second and fourth time windows correspond to persistent ($0.5 < H < 1$) or lower Tsallis entropies epochs

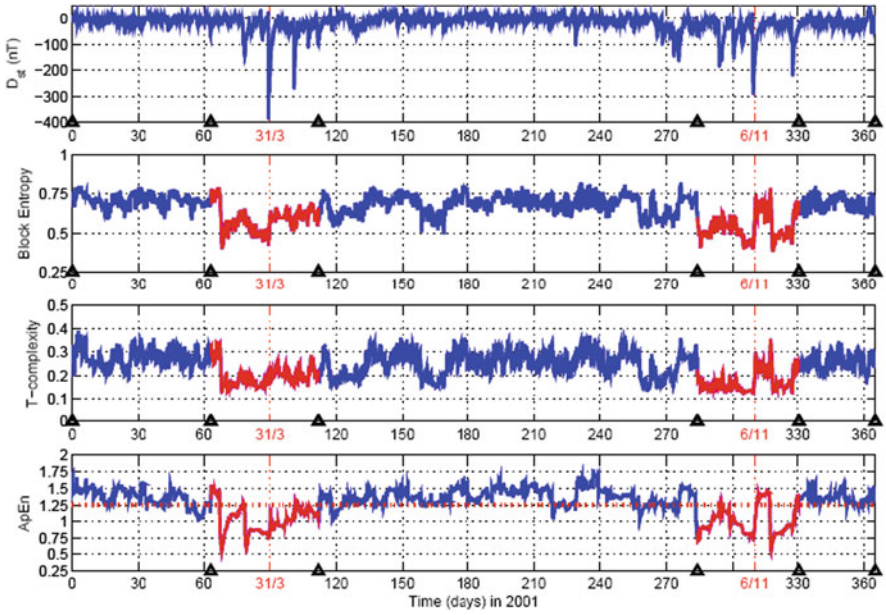

Fig. 12.4 From *top* to *bottom*: *Dst* time series along with time variations of block entropies, approximate entropies *ApEn* and *T*-complexities. The 31March and 6 November 2001 magnetic storms are marked with *red*. The *red dashed line* in *ApEn* plot marks a possible boundary value for the transition to the lower complexity characterizing the different state of the magnetosphere. The triangles denote 5 time intervals (as in Figs. 12.1 and 12.3)

correspond to the normal (quiet-time) magnetosphere (1st, 3rd and 5th time windows where H is below 0.5), while, the persistent epochs ($0.5 < H < 1$) correspond to the abnormal (storm-time) magnetosphere (2nd and 4th time windows where H is above 0.5). This finding supports the existence of two different epochs referring to two distinct states of the magnetic storm evolution.

Figure 12.3 gives the temporal evolution of *Dst* along with its wavelet power spectrum (Balasis et al. 2006) and corresponding time variations of Shannon entropy and Tsallis entropy for the whole year of 2001. In terms of entropy measures, we see how nicely Tsallis entropy variations identify the different complexity regimes in the *Dst* time series (c.f. red part of the corresponding plot). Figure 12.3 further demonstrates that Tsallis entropy yields superior results in comparison to Shannon entropy regarding the detection of dynamical complexity in the Earth's magnetosphere (i.e., offer a clearer picture of the transition from normal state to magnetic storms). A possible explanation for this is that Tsallis is an entropy obeying a non-extensive statistical theory, which is different from the usual Boltzmann-Gibbs statistical mechanics obeyed by Shannon entropy. Therefore, it is expected to better describe the dynamics of the magnetosphere, which is a nonequilibrium physical system with large variability.

Figure 12.4 gives the temporal evolution of *Dst* along with corresponding time variations of the block entropy, the *T*-complexity and, the *ApEn* for the whole year of 2001. We see how nicely the entropy measures identify the different complexity regimes in the *Dst* time series (c.f. red part of the corresponding plots). Figure 12.4 further demonstrates that the *ApEn* entropy yields superior results in comparison to the other entropy measures regarding the detection of dynamical complexity in the Earth's magnetosphere (i.e., offer a clearer picture of the transition). A possible explanation for this is that *ApEn* is more stable when dealing with nonstationary signals of dynamical systems (such the magnetospheric signal) than the rest of the entropy measures presented in Fig. 12.4.

12.4 Discussion and Conclusions

Entropy can provide the basis for information theory, which can be used to analyze the dynamics of a complex system. An example of such an application in the terrestrial magnetosphere is provided here. Our study uses several complexity measures (e.g. Tsallis

entropy, approximate entropy, and Hurst exponent) to analyze *Dst* during storm and nonstorm ("normal") times. Moreover, Hurst exponent can be used to characterize the persistence of a system, e.g., whether the trend of the fluctuations will continue ("persistent") or differ ("anti-persistent") in the next time interval. We also find that the nonstorm intervals have higher entropies and lower persistence than storm intervals. Tsallis entropy, which is based on a non-extensive statistical theory, rather than Boltzmann-Gibbs statistical mechanics, can better describe the dynamics of the magnetosphere because the latter is a nonequilibrium system with large variabilities.

We stress that the anti-persistent time windows correspond to the time windows of higher entropies, while the persistent time windows correspond to the time windows of lower entropies. Importantly, a recent analysis presented by Carbone and Stanley (2007) shows that anti-correlated time series, with Hurst exponent $0.5 < H < 1$, are characterized by entropies greater than correlated time series having $0.5 < H < 1$. This suggestion is in agreement with our results. Wanliss (2005) and Wanliss and Dobias (2007) analyzed fluctuations of the *SYM-H* index around magnetic storms and found that there was a rapid and unidirectional change in the Hurst scaling exponent at the time of storm onset indicating a nonequilibrium dynamical phase transition.

An important remark is the agreement of the results between the linear analysis in terms of the Hurst exponent and nonlinear entropy analyses. A combination of linear and nonlinear analysis techniques can offer a firm warning that the onset of an intense magnetic storm is imminent.

As an extension of this application, we will consider in the near future a basic space weather challenge (Daglis et al. 2001, 2003, 2009), i.e., the problem of continuous monitoring of the magnetospheric condition, where the time series is not a fixed and complete set, but is "streaming". If we can associate a change in signal complexity with a change in the condition of the system, then we can hope that an entropy-like measure will be able to detect a developing storm and potential problem for space systems (and possibly provide some warning before system failure).

This would be the ultimate task of our research efforts.

Acknowledgements The *Dst* data are provided by the World Data Center for Geomagnetism, Kyoto (http://swdcwww.kugi.kyoto-u.ac.jp/).

References

Balasis G, Eftaxias K (2009) A study of non-extensivity in the Earth's magnetosphere. Eur Phys J Special Topics 174:219–225

Balasis G, Daglis IA, Kapiris P, Mandea M, Vassiliadis D, Eftaxias K (2006) From prestorm activity to magnetic storms: a transition described in terms of fractal dynamics. Ann Geophys 24:3557–3567

Balasis G, Daglis IA, Papadimitriou C, Kalimeri M, Anastasiadis A, Eftaxias K (2008) Dynamical complexity in Dst time series using non-extensive Tsallis entropy. Geophys Res Lett. doi:10.1029/2008GL034743

Balasis G, Daglis IA, Papadimitriou C, Kalimeri M, Anastasiadis A, Eftaxias K (2009) Investigating dynamical complexity in the magnetosphere using various entropy measures. J Geophys Res. doi:10.1029/2008JA014035

Carbone A, Stanley H (2007) Scaling properties and entropy of long-range correlated time series. Physica A 384:267–271

Daglis IA, Baker DN, Galperin Y, Kappenman JG, Lanzerotti LJ (2001) Technological impacts of space storms: outstanding issues. Eos Trans AGU. doi:10.1029/01EO00340

Daglis IA, Kozyra J, Kamide Y, Vassiliadis D, Sharma A, Liemohn M, Gonzalez W, Tsurutani B, Lu G (2003) Intense space storms: critical issues and open disputes. J Geophys Res. doi:10.1029/2002JA009722

Daglis IA, Balasis G, Ganushkina N, Metallinou F-A, Palmroth M, Pirjola R, Tsagouri IA (2009) Investigating dynamic coupling in geospace through the combined use of modeling, simulations and data analysis. Acta Geophys. doi:10.2478/s11600-008-0055-5

Ebeling W, Nicolis G (1992) Word frequency and entropy of symbolic sequences: a dynamical Perspective. Chaos Solitons Fractals 2:635–650

Ebeling W, Steuer R, Titchener M (2001) Partition-based entropies of deterministic and stochastic maps. Stochast Dyn 1:45–61

Graben P, Kurths J (2003) Detecting subthreshold events in noisy data by symbolic dynamics. Phys Rev Lett 90:100602(1–4).

Grassberger P, Procaccia I (1983) Estimation of the Kolmogorov entropy from a chaotic signal. Phys Rev A 28:2591–2593

Hao B-L (1989) Elementary symbolic dynamics and chaos in dissipative systems. World Scientific, Singapore

Henegham C, McDarby G (2000) Establishing the relation between detrended fluctuation analysis and power spectral density analysis for stochastic processes. Phys Rev E 62:6103–6110

Hurst HE (1951) Long-term storage of reservoirs: an experimental study. Trans Am Soc Civ Eng 116:770–799

Karamanos K (2000) From symbolic dynamics to a digital approach: chaos and transcendence. Lect Notes Phys 550:357–371

Karamanos K (2001) Entropy analysis of substitutive sequences revisited. J Phys A: Math Gen 34:9231–9241

Karamanos K, Nicolis G (1999) Symbolic dynamics and entropy analysis of Feigenbaum limit sets. Chaos Solitons Fractals 10(7):1135–1150

Khinchin AI (1957) Mathematical foundations of information theory. Dover, New York, NY

Nicolis G, Gaspard P (1994) Toward a probabilistic approach to complex systems. Chaos Solitons Fractals 4(1):41–57

Pincus S (1991) Approximate entropy: a complexity measure for biologic time series data. In: Proceedings of IEEE 17th annual northeast bioengineering conference, IEE Press, New York, NY, p 35–36

Pincus S, Keefe D (1992) Quantification of hormone pulsatility via an approximate entropy algorithm. Am J Physiol (Endocrinol Metab) 262: E741–E754

Pincus S, Goldberger A (1994) Physiological time-series analysis: what does regularity quantify? Am J Physiol 266:H1643–H1656

Pincus S, Singer B (1996) Randomness and degree of irregularity. Proc Natl Acad Sci USA 93:2083–2088

Shannon CE (1948) A mathematical theory of communication. Bell Syst Tech J 27:379–423

Titchener M, Nicolescu R, Staiger L, Gulliver A, Speidel U (2005) Deterministic complexity and entropy. Fund Inform 64:443–461

Tsallis C (1988) Possible generalization of Boltzmann-Gibbs statistics. J Stat Phys 52:479–487

Tsallis C (2009) Introduction to nonextensive statistical mechanics, approaching a complex word. Springer, Berlin

Vanouplines P (1995) Rescaled range analysis and the fractal dimension of pi. University library, Free University Brussels, Brussels, Belgium. http://ftp.vub.ac.be/_pvouplin/pi/rswhat.htm

Wanliss JA (2005) Fractal properties of SYM-H during quiet and active times. J Geophys Res. doi:10.1029/2004JA010544.

Wanliss JA, Dobias P (2007) Space storm as a dynamic phase transition. J Atmos Sol Terr Phys 69:675–684

Wing S, Johnson J.R. (2010) Introduction to special section on entropy properties and constraints related to space plasma transport. J Geophys Res. doi:10.1029/2009JA014911

Zunino L, Perez D, Kowalski A, Martin M, Garavaglia M, Plastino A, Rosso O (2008) Fractional Brownian motion, fractional Gaussian noise and Tsallis permutation entropy. Physica A 387:6057–6068

Part IV

Waves and Turbulence in Magnetosphere-Ionosphere Coupling

Magnetospheric ULF Waves: A Review

13

Frederick W. Menk

Abstract

Ultra-low frequency (ULF; approx. 1 mHz $\leq f \leq$ 10 Hz) MHD plasma waves are readily recorded throughout the Earth's magnetosphere and on the ground. Generated by a variety of instabilities, ULF waves transport and couple energy throughout the system, and may play important roles in the energization and loss of radiation belt particles. ULF waves also provide a convenient probe and diagnostic monitor of the magnetosphere. The availability of multipoint measurements from spacecraft, ionospheric sounders and ground magnetometer arrays and the increasing sophistication of modeling tools have stimulated much recent progress in this area. Nevertheless, fundamental questions remain regarding the generation, propagation and consequences of these waves. This chapter reviews recent developments in these areas.

13.1 ULF Wave Sources

Ultra-low frequency (ULF) plasma waves are broadly of two types, depending on whether their energy source originates in the solar wind or from processes within the magnetosphere. Evidence for the former comes from the dependence of daytime power in the Pc3 (20–100 mHz), Pc4 (7–20 mHz) and Pc5 (1.7–7 mHz) ranges on solar wind speed and interplanetary magnetic field (IMF) clock angle (e.g. Odera 1986; Engebretson et al. 1987; Mathie and Mann 2001; Kessel et al. 2004; Francia et al. 2009). Solar wind density also plays an important role in controlling Pc3 activity (Heilig et al. 2010). Substorms and other instabilities in the tail form an important source of ULF waves on the nightside, but are considered elsewhere in this volume and the discussion here focuses on sources of waves on the dayside. Other recent reviews on ULF waves include Walker (2005), Kivelson (2006), Takahashi et al. (2006), Fraser (2007), and Villante (2007).

13.1.1 Sources in the Solar Wind

There are several ways in which ULF waves may be energized by the solar wind. A rich variety of plasma waves occurs in the magnetosheath, in particular Alfvén/ion cyclotron and mirror modes under low and high plasma β conditions respectively (Schwartz et al. 1996). Magnetospheric ULF waves occur most favorably under near-radial IMF conditions (Russell

F.W. Menk (✉)
School of Mathematical and Physical Sciences, The University of Newcastle, Callaghan, NSW 2308, Australia
e-mail: fred.menk@newcastle.edu.au

W. Liu, M. Fujimoto (eds.), *The Dynamic Magnetosphere*, IAGA Special Sopron Book Series 3,
DOI 10.1007/978-94-007-0501-2_13,

et al. 1983) when Alfvén/ion cyclotron waves may be produced upstream by the right-hand (RH) resonance instability with field-aligned backstreaming ions (Troitskaya et al. 1971; Takahashi et al. 1984; Le and Russell 1996; Blanco-Cano et al. 2009). Spatial properties of waves in the foreshock were described by Archer et al. (2005). The waves can convect downstream to the subsolar region of the magnetopause and into the magnetosphere without significant change to their spectrum (Greenstadt et al. 1983; Krauss-Varban 1994). The wave frequency depends on the strength and cone angle of the IMF but is typically in the Pc3 range (Takahashi et al. 1984).

Global two-dimensional hybrid (kinetic ions and fluid electrons) simulations for radial IMF conditions reveal the formation of a very perturbed foreshock region within which a slightly smaller ULF wave foreshock is embedded (Blanco-Cano et al. 2009). Weakly compressive sinusoidal waves in this region are RH polarized in the plasma frame but LH in the spacecraft frame. The extent of the foreshock over the dayside region decreases with increasing cone angle.

These ideas are supported by multisatellite observations of upstream waves entering and propagating through the magnetosphere as compressional waves (Sakurai et al. 1999; Constantinescu et al. 2007; Heilig et al. 2007; Clausen et al. 2008, 2009). By examining wavefront curvature and propagation properties for Pc3 waves recorded during an outbound magnetosheath crossing of the four Cluster satellites, Constantinescu et al. (2007) found that these waves mostly originated from the cusp and electron foreshock, but not especially from the ion fore-shock. This suggests that small Alfvén/ion cyclotron and mirror mode waves are initially stimulated in the electron foreshock and then couple to and are amplified by ion beam instabilities in the slightly downstream ion foreshock region.

In an independent study using the Cluster and Geotail spacecraft and ground magnetometers located near the Cluster footpoint, Clausen et al. (2009) found a 'cradle to grave' example of Pc3 event that was generated in the foreshock region after a sudden reduction in the solar wind cone angle, and was then observed in the outer magnetosphere and on the ground. The upstream waves were predominantly transverse but with a compressional component, relating (after a suitable propagation delay) to compressional waves in the outer magnetosphere that mode-converted to bandlimited field line guided toroidal Alfvén waves at the local field line eigenfrequency as verified using ground cross-phase measurements. The frequency of the upstream waves agreed precisely with the Takahashi et al. (1984) prediction.

Heilig et al. (2007) presented a detailed statistical survey of Pc3-4 compressional mode wave power at ~350 km altitude using the CHAMP spacecraft, finding that events between ±60° latitude are most likely generated in the upstream foreshock region, with wave frequency depending on IMF strength and a Doppler shift due to the Alfvénic mach number M_A, but not on the cone angle: $f_{peak}\,(\mathrm{mHz}) = (0.708 \cdot M_A + 0.64)\,(\mathrm{mHz/nT}) \cdot B_{IMF}\,(\mathrm{nT})$.

Periodic compressional or Alfvénic fluctuations in the solar wind may also directly drive discrete frequency ULF waves in the magnetosphere (e.g. Potemra et al. 1989; Prikryl et al. 1998; Stephenson and Walker 2002; Kepko and Spence 2003; Menk et al. 2003). Kessel (2008) examined the relationship between Pc5 wave power in the solar wind (ACE, Wind), near the magnetopause (Geotail), at geostationary orbit (GOES 8, 10), over the poles (Cluster), and on the ground near the Geotail and GOES footpoints, during high speed streams and coronal mass ejections. Over 80% of total Pc5 activity (including propagating compressional waves, field line resonances and global modes) during a 2 week interval was driven by solar wind pressure fluctuations, with the amplitude and power of Pc5 compressional fluctuations in the magnetosphere and on the ground being directly proportional to the amplitude and power of similar fluctuations in the solar wind.

A similar conclusion was reached by Takahashi and Ukhorskiy (2007, 2008) who conducted superposed epoch analyses of upstream solar wind parameters recorded by ACE, and Pc5 wave fields at GOES at solar maximum and solar minimum, finding that solar wind pressure variations are the major driver of Pc5 waves at geosynchronous orbit, where standing Alfvén waves are then established.

Recent event and statistical studies provide accumulating evidence that periodic variations in solar wind dynamic pressure are prompt drivers of some magnetospheric Pc5 ULF waves and field line resonances (FLRs) at the discrete 'magic' frequencies (0.7, 1.4, 2.0, 4.8 mHz) reported by Samson et al. (1992) and many others (e.g. Ziesolleck and McDiarmid 1994; Francia and Villante 1997) and ascribed to magnetospheric cavity/waveguide modes.

Examining a specific event, Fenrich and Waters (2008) used a phase coherence technique to show that 1.7 mHz oscillations in solar wind density were related, with 99% confidence and after a suitable propagation delay, to FLR signatures recorded near 62° magnetic latitude in the ionosphere with an HF SuperDARN radar. Villante et al. (2007) also used a phase coherence technique to examine the relationship between discrete frequency oscillations in the solar wind and at low latitudes on the ground, while Eriksson et al. (2006b) found that 9 out of 10 Pc5 events detected in the ionosphere by an HF radar exhibited high correlation coefficients with oscillations in the solar wind dynamic pressure. Such pressure-driven 'magic frequency' Pc5 pulsations can also be associated with auroral pulsations (Liou et al. 2008).

In an important study, Viall et al. (2009) examined the occurrence of discrete spectral peaks in the 0.5–5.0 mHz range for over 11 years of measurements of number density in the upstream solar wind (recorded by the Wind spacecraft) and for 10 years of magnetic field data in the magnetosphere within an hour of local noon (recorded by the geostationary GOES spacecraft). Using statistical tests on overlapping 6-h intervals, they found in both data sets discrete frequencies that occurred more often than other frequencies, and also determined that such discrete frequencies were seen in the magnetosphere 54% of the time they occurred in the solar wind. Their results are summarized in Fig. 13.1. The discrete frequencies are at or near the Samson 'magic' frequencies, although in both data sets there was some gradual evolution through the solar cycle. Viall et al. concluded that a clear physical relationship exists between some discrete, repeatable frequencies in solar wind number density and in the magnetosphere, although other discrete frequencies are also present in the magnetosphere due to other physical processes.

In conclusion, multipoint observations show that Pc3-4 ULF waves generated in the foreshock region

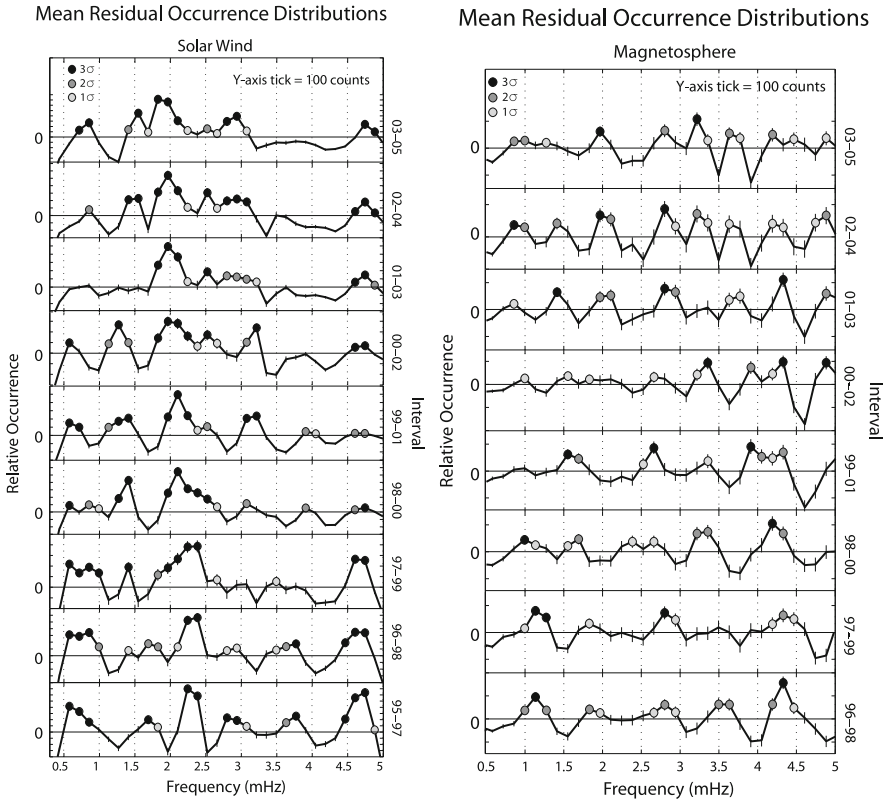

Fig. 13.1 Mean residuals of 3-year occurrence distribution of statistically significant frequencies over 1995–2005 in solar wind number density (*left*) and in the dayside magnetosphere (*right*). Vertical bars indicate ±1 s.d.; *y*-axis tick marks denote 100 counts (Figures 4 and 5 from Viall et al. 2009)

may be observed in the magnetosphere and on the ground, while there is also accumulating evidence that Pc5 waves may be directly driven by pressure oscillations in the solar wind. This may be an important source of magnetospheric ULF waves at low frequencies which are hard to reconcile with cavity/waveguide modes. Fundamental questions that arise include: (i) How important are these solar wind-related mechanisms as sources of Pc3-5 ULF waves in the daytime magnetosphere? (ii) Hence, how significant are cavity/waveguide modes? (iii) To what extent can these sources explain ULF waves seen on the ground in the polar cap and tail regions? (iv) Why and how should discrete frequencies be present in the solar wind?

13.1.2 Instabilities at the Magnetopause

The correlation between solar wind speed and ULF power in the magnetosphere suggests that the Kelvin-Helmholtz instability (KHI) resulting from the velocity shear at the magnetopause may be a significant source of ULF wave energy (e.g. Walker 1981; Pu and Kivelson 1983). The resultant surface waves propagate antisunward and are strongly evanescent within the magnetosphere. However, the shear flow between the plasma in the magnetosheath and magnetosphere also controls the reflection condition at the magnetopause, and when taking into account the boundary layer thickness this may result in the formation of over-reflection modes at the magnetopause (Mann et al. 1999; Walker 2000). Over-reflection occurs when the characteristic scales of the wave and the inhomogeneity are comparable, and may provide an efficient process for the extraction of energy from the magnetosheath to magnetospheric waveguide modes on the flanks during fast solar wind speed intervals (Wright and Mann 2006). This may explain the production of discrete frequency ULF waves in the magnetosphere and statistical correlations between Pc5 power on the ground and solar wind velocity (Mathie and Mann 2001; Mann et al. 2004; Pahud et al. 2009).

Numerical models now permit studies of the entire magnetosphere system under various conditions. Claudepierre et al. (2008) described a global three-dimensional (3-D) MHD simulation of the solar wind/magnetosphere interaction in which all solar wind parameters except driving velocity were held constant. Two coupled ULF surface modes were excited by the KHI near the dawn and dusk magnetopause, one propagating tailward along the magnetopause boundary and the other along the inner edge of the boundary layer. The phase velocities of the modes were different but the frequencies were the same and depended on the solar wind driving velocity. For both modes the preferred wavenumber was related to the boundary thickness, so that the KH waves are monochromatic.

Multispacecraft observations provide new opportunities for in situ studies of wave distributions and properties. Using 13 months' electric and magnetic field THEMIS data covering all local times but mostly under weak solar wind conditions, W. Liu et al. (2009a) found that wave power in the outer magnetosphere was greater in the Pc5 compared to the Pc4 range, being dominated by toroidal modes near the flanks and poloidal modes near noon. It was concluded that the KHI plays an important role in the excitation of Pc5 waves (especially near the flanks) during solar minimum years. During northward IMF conditions KHI events with particularly long wavelengths can be excited on the flanks of the equatorial magnetosphere (Hasegawa et al. 2009).

While Viall et al. (2009) suggested that solar wind perturbations drive ULF waves at certain frequencies, Plaschke et al. (2009a) presented results from an analysis of spline function interpolation of nearly 6700 THEMIS magnetopause crossings (to determine properties of magnetopause undulations) to suggest that Alfvénic waves propagating along the magnetopause surface may develop into standing Alfvén waves on the boundary due to reflection from the conjugate ionospheres (i.e. Kruskal-Schwarzschild modes). The surface waves are likely due to magnetopause displacements as a result of local pressure perturbations in the magnetosheath, while the eigenfrequencies of the standing modes are determined by the magnetopause geometry and are strikingly similar to the Samson 'magic' frequencies; see Fig. 13.2. Plaschke et al. (2009b) added solar wind observations to their dataset in order to determine the dependence of the observed spectrum of magnetopause oscillations on solar wind and IMF conditions and local time. They found that magnetopause oscillations occurred more favorably near noon and for northward IMF, low solar wind speed and low cone angle. This combination of conditions suggests that the oscillations are more likely

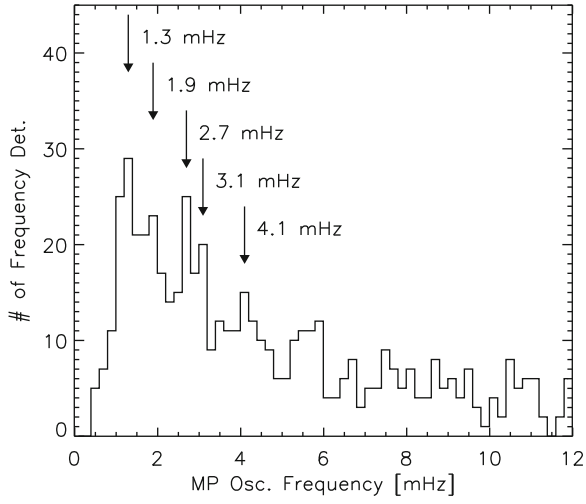

Fig. 13.2 Oscillation frequencies due to magnetopause motion (Figure 2 from Plaschke et al. 2009a)

due to Kruskal-Schwarzshild modes than solar wind pressure perturbations or the KHI at the flanks.

There have been few reports of the KHI in the magnetotail (e.g. Takagi et al. 2006). However, Volwerk et al. (2007) identified 5 min magnetic oscillations as the Cluster and Doublestar spacecraft entered a flow shear channel in magnetotail. The oscillations propagated Earthward at about half the plasma flow speed and increased in amplitude in agreement with KHI wave growth. These results also suggest that the KHI may play a role in the braking of fast flows in the magnetotail.

In conclusion, simulation and observational studies show that instabilities at the magnetopause are likely an important source of long period ULF wave activity. Further work is needed on both fronts to clarify the role of such instabilities as sources of 'everyday' wave activity. The significance of over-reflection and Kruskal-Schwarzshild modes requires particular investigation.

13.1.3 Interactions within the Magnetosphere

ULF waves can be generated by a variety of mechanisms internal to the magnetosphere, including drift-mirror instabilities due to pressure anisotropies, and drift-bounce resonance with trapped energetic ions (e.g. Walker 2005). These waves are often strongly compressional, have high azimuthal wave number, m, and are attenuated on the ground due to spatial integration, resulting in a 'hidden' wave population previously hinted at by radar observations (e.g. Yeoman et al. 2000) and fortuitous satellite conjunctions (e.g. Hughes et al. 1978). Recent radar observations are outlined in Section 13.4.

The drift-mirror instability occurs under high β conditions when there is significant perpendicular pressure anisotropy. The frequency of the growing mode depends on the diamagnetic drift frequency but the instability condition is affected by field line curvature and coupling to transverse shear Alfvén waves. The drift mirror waves will propagate slowly with the Larmor drift frequency. Rae et al. (2007) showed an example of a large amplitude compressional Pc5 wave event detected for some hours by Equator-S in the dawnside magnetopause under average solar wind conditions. The waves were most likely generated by a drift mirror instability near the equatorial plane and might also couple to local standing toroidal mode Alfvén waves.

High-m compressional Pc5 waves have been measured by the THEMIS spacecraft in the outer magnetosphere under average magnetic conditions near local dawn (Korotova et al. 2009) and dusk (Constantinescu et al. 2009). Both studies found the waves had wavelengths of ~2 R_E and propagated sunward at velocities of ~10–20 km/s, and both studies concluded that the waves were most likely generated by the drift mirror instability.

The availability of multipoint spacecraft observations has therefore provided new information on the source and generation of high-m waves in the outer magnetosphere.

13.2 Wave Generation and Propagation Mechanisms

The propagation of magnetospheric ULF plasma waves has been described in detail by many workers (e.g. Allan and Poulter 1992), usually in the context of standing shear Alfvén mode field line oscillations with low azimuthal wavenumber (e.g. Orr 1984) that are driven by energy coupling from incoming compressional fast mode waves (e.g. Odera et al. 1991). The latter may also excite global eigenoscillations of the magnetosphere (Kivelson and Southwood 1986; Allan

et al. 1986a) or the plasmasphere (Allan et al. 1986b; Waters et al. 2000). In fact, the coupling of cavity or waveguide eigenmodes to FLRs may explain how discrete spectra are produced across a range of latitudes (Kivelson and Southwood 1985; Samson et al. 1995; Menk et al. 2000), including at the 'magic' frequencies (e.g. Samson et al. 1992; Mathie et al. 1996; Villante et al. 1997). However, cavity modes are difficult to detect with spacecraft (Waters at al. 2002) and the existence of highly stable discrete frequency modes is still controversial. On the other hand, the existence of a peculiar, large, highly monochromatic wave mode called giant pulsations has been known for a long time (e.g. Chisham et al. 1990). Measurements with ionospheric sounders have shown that these high *m* poloidal mode waves may be fairly common after storms (e.g. Wright and Yeoman 1999). In this section we focus mainly on waves generated in the local daytime.

13.2.1 Global Cavity Modes

Many studies have suggested that global cavity modes may be responsible for the appearance of ULF signals with multiple discrete spectral peaks at the 'magic' frequencies and spanning a range of latitudes. During very large storms such discrete frequency modes may be detected throughout the magnetosphere (Lee et al. 2007). Figure 13.3 shows discrete frequency Pc5

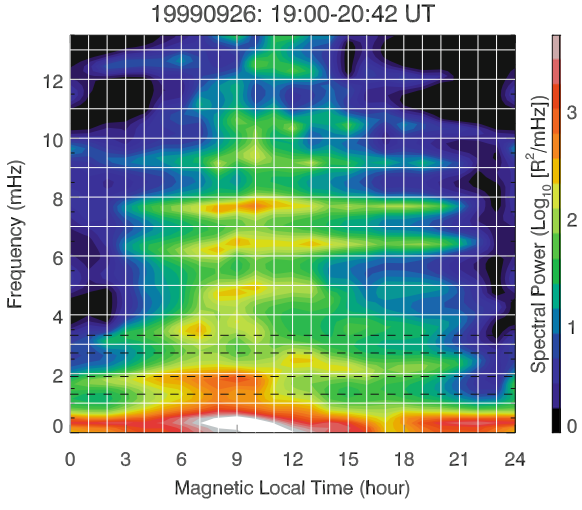

Fig. 13.3 Power spectrum of discrete frequency auroral pulsations. *Horizontal dashed lines* denote preferred Pc5 frequencies (Figure 2 from Liou et al. 2008)

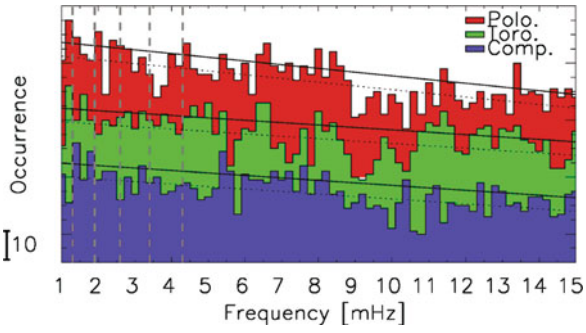

Fig. 13.4 Occurrence of spectral peaks in 1 year of Cluster magnetometer data (Adapted from Figure 11 of Clausen and Yeoman 2009)

pulsations and auroral modulations at frequencies up to 6–8 mHz, most likely produced by global cavity modes caused by solar wind pressure variations (Liou et al. 2008).

Using case studies and a 1-year statistical survey, Clausen and Yeoman (2009) examined FLRs recorded at the 'magic' frequencies by the Cluster spacecraft and at ground stations. As seen in Fig. 13.4, there was no preference for the set of 'magic' frequencies in the data, but there was a tendency for certain frequencies above 5 mHz, attributed to higher harmonics of waveguide/cavity modes.

Takahashi et al. (2009) reported the observation of global eigenmode oscillations near 15 mHz throughout the dayside plasmasphere (L∼1.7–3.1) under conditions favorable for the propagation of broadband compressional mode power from the solar wind into the magnetosphere. However, no distinct plasmapause signature was evident and they therefore termed the plasmaspheric global mode a virtual resonance. The existence of such virtual resonance modes was predicted by Lee and Lysak (1999) and Lee and Takahashi (2006), and they are believed to account for the observed spectral properties of night-time Pi2 pulsations (Kim et al. 2005; Teramoto et al. 2008).

Plasmaspheric cavity resonances are expected to be a fraction of an R_E apart (Samson et al. 1995), and it would be difficult to detect the resultant spectral fine structure using spacecraft, but this is easier with ground magnetometers. The structure of such trapped plasmaspheric modes was predicted using a simple 1-D waveguide model by Waters et al. (2000), confirming the observations of Menk et al. (2000). However, virtual resonance modes can extend beyond the plasmasphere and can exist even in the absence of

a clear plasmapause boundary. Takahashi et al. (2005) pointed out that nightside Pc4 pulsations at geomagnetically quiet times could result from plasmaspheric cavity modes excited by a dayside energy source. Similar Pc4 pulsations have been reported in HF radar signals (Ponomarenko et al. 2003).

In summary, the following key questions remain unresolved. (i) Is there clear evidence in spacecraft data for the existence of cavity modes? (ii) Do cavity modes preferably exist at the 'magic' Samson frequencies or higher frequencies or both? (iii) Under which conditions do global cavity modes exist – i.e. extreme or quiet conditions; frequent or infrequent occurrence; dependence on a solar wind driver; etc? (iv) Under which conditions and at what frequencies do virtual cavity resonances exist compared to plasmaspheric cavity modes?

13.2.2 Field Line Resonances (FLRs)

The physical principles of FLRs are well known (e.g. Waters et al. 2006). However, mathematical descriptions often assume a simple dipolar geometry which is not appropriate to high latitudes where field lines experience significant temporal distortion. This affects the frequency (Waters et al. 1996; Wild et al. 2005) and polarization properties of the FLRs (Kabin et al. 2007). The latter is important because wave-particle energy transfer involves the wave electric field component parallel to the drift velocity of particle, i.e. the azimuthal field (poloidal mode) in a dipolar magnetic field. In order to obtain a more realistic representation of the situation Elkington et al. (2003) used a non-axisymmeteric compressed magnetic field model, but assumed that the wave electric field was either exactly radial or azimuthal. However, Kabin et al. showed that in a 3-D compressed dipole background field (described in terms of Euler potentials) and using the Rankin et al. (2006) standing shear Alfvén wave model, the polarization of Alfvén modes can no longer be described as poloidal or toroidal but becomes increasingly mixed and changes with local time. This arises because the contours of constant magnetic field no longer coincide with contours of constant wave period for either mode in the equatorial plane, as shown in Fig. 13.5. This means that at high latitudes different Alfvénic modes may contribute to particle acceleration in different MLT sectors.

This work has been extended by Degeling et al. (2010) who modeled the propagation of MHD waves and the formation of FLRs in a compressed dipole geometry including day/night asymmetry. In addition to the MLT dependence of shear Alfvén wave eigenmode polarization, they found that the FLR properties depend strongly on the wave source location at the magnetopause boundary.

A further complication arises when the magnetospheric plasma is in relative motion, such as near a KHI site. Kozlov and Leonovich (2008) modeled this analytically and numerically through azimuthal rotation of the plasma, finding that monochromatic fast magnetosonic waves could then excite harmonics of standing Alfvén waves simultaneously on different resonant surfaces. The plasma motion effect is greatest near strong density gradients (magnetopause, plasmapause) and results in distorted phase and amplitude profiles.

Sarris et al. (2009a, c) examined the structure of FLRs in situ between 4 R_E and the magnetopause using the THEMIS constellation. The polarization characteristics of the observed FLRs were in striking agreement with the Kabin et al. (2007) predictions based on a non-axisymmetric field geometry.

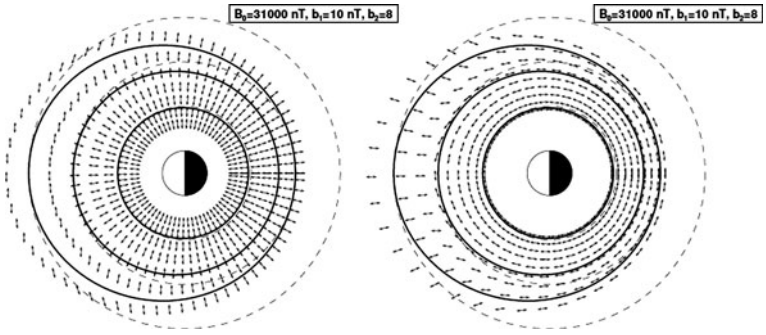

Fig. 13.5 Electric field polarization in the equatorial plane with a realistic magnetic field geometry and for the wave mode with radial electric field at midnight (*left*) and azimuthal field at midnight (*right*) (Figure 6 from Kabin et al. 2007)

Combined in situ observations with the 4 Cluster satellites and ground magnetometer measurements show (Liu et al. 2008) that Pc3 pulsations just inside the cusp have dominant transverse toroidal and poloidal components, wavelength $\sim 10^3$ km, and phase velocity $\sim 10^2$ km/s Earthward. The Poynting flux is field aligned and away from the equatorial plane. These waves likely arise from incoming compressional mode waves coupling to guided Alfvén waves on the last closed field lines, exciting FLRs at lower latitudes. In a follow-up study Y. Liu et al. (2009b) showed that the transverse scale size of these Pc3 waves near the cusp is ~ 0.14 R_E when using a threshold inter-spacecraft coherency of 0.65. There was also clear evidence of rotation of the polarization ellipse by 90° between the spacecraft and ground.

How much energy does a FLR deposit into the ionosphere? Estimates for large Pc5 FLR events include $\sim 6 \times 10^9$ W (Greenwald and Walker 1980), 10^{10}–10^{13} J (Allan and Poulter 1984), and 10^{10}–10^{11} J for high-m particle-driven FLRs (Baddeley et al. 2005a). Most recently, through combined Polar spacecraft, ground magnetometer and HF radar observations Rae et al. (2007) found that the energy dissipated into the ionosphere via Joule heating for a high solar wind speed-driven global Pc5 event was 10^{14}–10^{15} W, i.e. 30% of a substorm budget and much higher than previous estimates.

At low latitudes the source of FLRs is generally believed to be fast mode waves that propagate from the solar wind deep into the magnetosphere (e.g. Yumoto and Saito 1983; Yumoto et al. 1985; Matsuoka et al. 1997). The frequency of FLRs reverses near $L = 1.6$ due to ionospheric mass loading (Menk et al. 2000; Ndiitwani and Sutcliffe 2010), and the low latitude limit of FLRs is $L \approx 1.3$. In fact, recent observations have shown that discrete frequency fast mode waves are often present in the plasmasphere and couple to standing poloidal and toroidal modes causing FLRs that are detected on the ground (Menk et al. 2006; Ndiitwani and Sutcliffe 2009). In the former study poloidal mode flux tube oscillations at $L = 2.5$ were detected with VLF sounders, and coupled to FLRs that were recorded by ground magnetometers. The frequency of these signals corresponded with the frequency expected for waves generated in the upstream solar wind, although other discrete frequencies were also present in the spectra. The latter study used CHAMP low-Earth orbit spacecraft and ground magnetometer observations to show that discrete frequency fast mode oscillations above the ionosphere coupled to toroidal mode FLRs.

In summary, although the fundamental properties of FLRs are well known, many key questions still exist: (i) How do the properties of FLRs change at high latitudes in realistic field geometries? (ii) What is the effect of such changes (e.g. modified wave polarization) on particle acceleration? (iii) How significant is the effect of plasma motion on the properties of FLRs? (iv) There has been much discussion of the azimuthal wavenumber k_y. What are typical values for the meridional wavenumber k_x in FLRs? (v) How often do large FLRs occur that deposit significant energy into the ionosphere, and what are typical integrated values of energy deposition? (vi) What is the contribution of FLRs to the ULF wave spectrum at low latitudes? (vii) At high latitudes Pc3 signals are detected with clear FLR-like properties, with apparent poleward propagation (Howard and Menk 2005). Are these higher harmonics of FLRs, and if so what is the contribution of these to general ULF activity at high latitudes?

13.2.3 Other Alfvén Modes

Here we are concerned with poloidal mode waves, and coherent waves at high latitudes whose generation and propagation mechanisms are unclear. The compressional narrowband Pc4-5 waves described in Section 13.1.3 that are produced by drift-bounce resonance with trapped energetic ions have high azimuthal wave number m and induce poloidal mode (radial) field line perturbations. Most previous knowledge of these comes from HF radar measurements of wave fields in the ionosphere. Multipoint spacecraft observations are providing new information on these waves, which may persist up to days in the outer magnetosphere in the noon/postnoon sectors during the recovery phase of storms (Takahashi et al. 1985; Eriksson et al. 2005, 2006a; Sarris et al. 2007, 2009b; Schäfer et al. 2007, 2008). The waves are usually quite localized radially and have azimuthal wavenumbers as high as $m \sim 150$ (Eriksson et al. 2006a; Schäfer et al. 2008). The polarization of wave packets may also vary with time or spacecraft position, as predicted by Kabin et al. (2007).

Occasionally these waves are seen at quiet times when no energetic particles are present and drift or bounce resonance is unlikely (Eriksson et al. 2005). Sometimes high-m Pc4 waves are seen near the

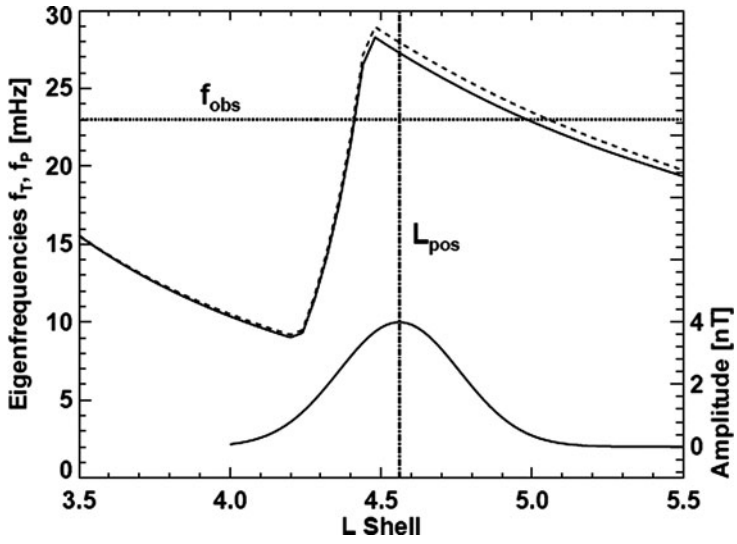

Fig. 13.6 Location of poloidal mode resonance region at the plasmapause. *Upper solid* and *dashed curves* show radial profiles of toroidal and poloidal mode eigenfrequencies; *horizontal dotted line* shows observed frequency $f_{obs} = 23$ mHz, and lower curve represents amplitude profile (Figure 14 from Schäfer et al. 2008)

plasmapause, suggesting they may be due to harmonics of poloidal mode eigenoscillations in a radially confined Alfvén resonance region at the inner (Schäfer et al. 2007) or outer edge of the plasmapause (Schäfer et al. 2008; Turkakin et al. 2008). This situation is illustrated schematically in Fig. 13.6 and was predicted by Klimushkin (1998). This is a new result not evident in ground records.

Observations of whistler mode waves with VLF sounders are sensitive to localized radial motions of flux tubes and show that poloidal mode field line oscillations are fairly common at quiet times, are related to fast mode ULF waves generated in the upstream solar wind, and couple to FLRs (Andrews 1977; Yearby and Clilverd 1996; Menk et al. 2006).

Questions that arise regarding new results on poloidal modes include: (i) How frequently do high-m poloidal mode particle-generated waves occur? (ii) Can such waves be generated at quiet times in the absence of energetic particle distributions? (iii) How common are high-m poloidal mode waves at the plasmapause and are they a signature of the plasmapause? (iv) What is the significance of these waves for the energization of ring current particles (see e.g. Ozeke and Mann 2008)? (v) Techniques such as VLF sounders and HF radars provide the possibility of ground-based monitoring of high-m poloidal mode waves. What new results could emerge?

An unresolved question is how coherent narrowband Pc3-4 waves arrive on open field lines in the polar regions (e.g. Santarelli et al. 2007); these signals may not just be a poleward extension of mid-latitude activity but relate to compressional waves in space (e.g. Engebretson et al. 2006). Pilipenko et al. (2008) suggested these pulsations may be due to the interaction of propagating magnetosonic and Alfvén waves. In a longitudinally inhomogeneous plasma the field-aligned wave vector components of travelling fast magnetosonic waves and Alfvén modes match, and fast mode energy may be resonantly converted to the latter. This may happen at frequencies much higher than the Alfvén resonance frequency.

An unexplained phenomenon is the existence of coherent low m waves that propagate sunward, away from the midnight sector. These have been observed in mid-latitude ground data (e.g. Mier-Jedrzejowicz and Southwood 1979) and now at large L with spacecraft (e.g. Erikkson et al. 2008). The latter reported observations of 1–2 mHz $m = 3$ toroidal waves at $L = 16$ post-midnight, with sunward propagation and Poynting flux, and wave frequency that changes with magnetic field strength. Wright and Allan (2008) reported numerical simulations of MHD wave coupling in the magnetotail waveguide that suggested 5–20 min fast mode waves generated in the magnetotail waveguide by substorms may couple to Earthward propagating Alfvén waves and produce field-aligned currents resulting in narrow auroral arcs that move equatorward at ~1 km/s. The Alfvén waves phasemix as they propagate Earthward, resulting in a rapid variation of wave fields perpendicular to B. The predicted wave properties agree with observations of Alfvén waves with local standing wave signatures in the PSBL and on the ground (Keiling et al. 2005). In summary,

these new results raise the following questions: (i) What is the source of coherent narrowband Pc3-4 waves in the polar caps? (ii) What is the source of coherent sunward propagating waves in the tail? (iii) How common are such waves? (iv) Can mechanisms such as that proposed by Wright and Allan play a role in the generation of these waves?

13.3 Electromagnetic Ion-Cyclotron Waves (EMICWs)

Until recently the origin of magnetospheric Pc1-2 (~0.2–5 Hz) waves was thought to be well understood. The waves are generally believed to be generated in the equatorial magnetosphere by ion-cyclotron resonance with unstable distributions of energetic ring current ions (e.g. Cornwall 1965; Criswell 1969) during the recovery phase of magnetic storms (Wentworth 1964). The characteristic fine structure appearance of 'pearl' Pc1 waves was attributed to dispersive field-aligned wave packet propagation in the LH ion mode on successive bounces between hemispheres (e.g. Jacobs and Watanabe 1964; Obayashi 1965). Non-propagation stop-bands occur at the local bi-ion frequencies in He^+ and O^+ rich plasmas (Fraser 1982). On reaching the ionosphere some of the wave energy couples to the RH mode and propagates in a horizontal waveguide centered on the ionospheric F2 region (Tepley and Landshoff 1966; Manchester 1970; Erlandson and Anderson 1996) from the source region near the plasmapause (e.g. Altman and Fijalkow 1980; Webster and Fraser 1985). IPDP are an unstructured subtype of Pc1-2 pulsations generated by resonant interaction with westward drifting energetic protons near the plasmapause in the evening sector (e.g. Horita et al. 1979). Figure 13.7 gives a schematic overview of the generation and propagation of structured Pc1 emissions.

Difficulties with the above picture of Pc1-2 generation were summarized by Demekhov (2007) and Mursala (2007), the main problem being lack of evidence of wave packet bouncing between conjugate points (Mursala et al. 1997). Spacecraft measurements have shown that EMICW propagation is almost exclusively away from the equator (Erlandson et al. 1996; Fraser et al. 1996) at latitudes greater than about 11° (Loto'aniu et al. 2005), with minimal reflection at the ionosphere. Furthermore, EMIC emissions can occur in the outer magnetosphere (Menk et al. 1992, 1993) in connection with solar wind perturbations (e.g. Olson and Lee 1983; Hansen et al. 1992, 1995; Arnoldy et al. 2005).

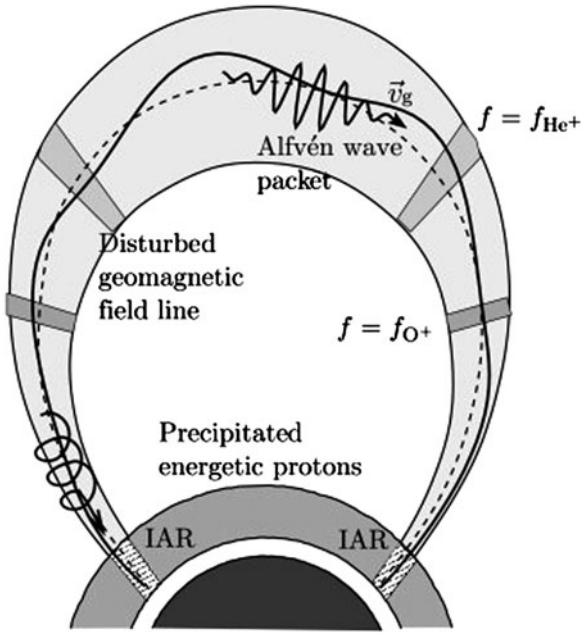

Fig. 13.7 Schematic picture of a magnetospheric flux tube in which Pc1 EMICWs are generated and propagate to the ground (Figure 2 from Demekhov 2007)

13.3.1 Observational Studies

Recent studies combining multipoint ground and in situ observations have confirmed that Pc1 EMICWs occur in localized L shells near the plasmapause (Usanova et al. 2008; Engebretson et al. 2008b) and are seen on the ground mostly after moderate and intense storms (Bortnik et al. 2008a; Engebretson et al. 2008a). The Usanova et al. study focused on emissions associated with a magnetospheric compression, detected by the THEMIS spacecraft in a narrow L range directly at the plasmapause, and with no evidence of wave packets bouncing back and forth to the ground. This work is important in the context of EMICW-particle interactions discussed later. The Bortnik et al. study examined 8 years of low latitude data using the automated detection algorithm mentioned in Section 13.5.4.

The association of EMICWs with energetic particle precipitation is reviewed in Section 13.5.3. Several

authors have suggested that subauroral proton spots may be caused by pitch angle scattering by EMICWs generated by the interaction between hot ring current protons and cold plasmaspheric ions (e.g. Fuselier et al. 2004) or the enhanced cold dense plasma associated with plasmaspheric plumes (Frey et al. 2004; Spasojević et al. 2004). A direct connection between proton aurora spots, which map to the vicinity of the plasmapause, and EMICWs was demonstrated by Yahnin et al. (2007).

A statistical study by Engebretson et al. (2008a) reinforced the likely association between Pc1-2 on the ground in the recovery phase of storms and plasmaspheric plumes and precipitating energetic particles.

A complete 'cradle-to-grave' case study of EMIC wave propagation was presented by Morley et al. (2009). They used conjunction observations in the equatorial magnetosphere, at low-Earth orbit, and on the ground, to study the propagation of a LH polarized EMIC wave from the source region to the ground in association with >6 keV ion precipitation. They also used a $2\frac{1}{2}$-D MHD model to clarify the observed travel times, showing that the wave and ion source region was at the edge of a plasma drainage plume.

An important question in the discussion of EMICW generation and the particular packet structure that gave rise to the bouncing wave packet idea, is the possibility that the wave generation process is modulated by compressional Pc5 ULF waves. This has been confirmed by case studies and a statistical analysis of data from CRRES (Loto'aniu et al. 2009). They found a good linear correlation between Pc1 wave packet duration and Pc5 wave period, shown in Fig. 13.8, although the wave packets were sometimes 180° out of phase and non-adiabatic and non-linear processes may play a role.

During very intense storms unusually polarized Pc1-2 waves may be produced, including purely compressional waves near the equator that propagate radially Earthward, and waves with power in the radial and compressional but not azimuthal components that may propagate oblique to B (Engebretson et al. 2007).

Pc1-2 waves in the plasmasheet have components perpendicular and parallel to the field and propagate perpendicular to it (Broughton et al. 2008). Counterstreaming ion beams are also associated with these waves. At high latitudes, near the cusp, Pc1-2 signals often have the appearance of discrete bursts and structured emissions whose distribution is indicative of the source region and magnetospheric topology (e.g. Menk et al. 1992; Dyrud et al. 1997; Engebretson et al. 2009). Such Pc1-2 bursts accompany most magnetic impulse events (Arnoldy et al. 1996; Kurazhkovskaya et al. 2007), which are common in the polar regions (e.g. Sibeck and Korotova 1996).

In summary, while the general properties of Pc1-2 EMICWs are well established, the relative importance of sources associated with compressions, plasma plumes, or the ring current, and the significance of source modulation by Pc4-5 waves, remain unclear. Evidence for bouncing wave packets is also lacking.

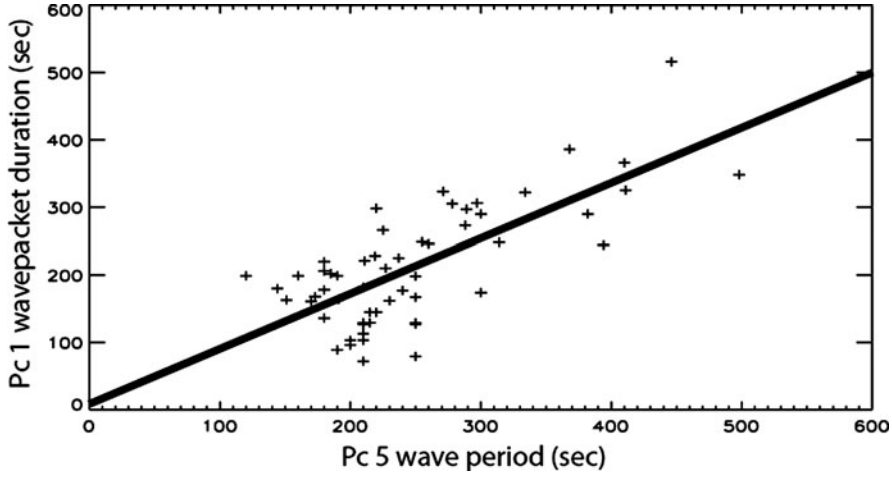

Fig. 13.8 Relationship between period of Pc1 wave packets and compressional Pc5 waves simultaneously seen at CRRES (Figure 6a from Loto'aniu et al. 2009)

13.3.2 Modeling and Simulation Studies

Recent modeling efforts have focused on clarifying the locations and conditions for EMICW generation, including the effect of heavy ion populations, and explaining the modulated appearance of wave packets. The competing generation models were reviewed by Demekhov (2007), with no clear consensus on a dominant mechanism. These are important questions since EMIC waves may control the precipitation of energetic ions (Jordanova et al. 2007) and relativistic electrons (Rodger et al. 2008). EMIC waves propagate across the Earth in the ionospheric Alfvén resonator, although the extent to which this determines the wave properties is unclear (Demekhov 2007).

Plasma density is one of the most important parameters controlling EMIC wave generation. Growth models which assume the total plasma is dominated by thermal plasma may not relate to regions where both cold plasmaspheric plasma and ring current ions are important. This situation was considered by Gamayunov and Khazanov (2008) using a global RC-EMIC simulation model referenced to plasma conditions observed during a large storm (but ignoring O^+ ions) and an analytical formulation of the Volland-Stern electric field. Their approach included wave growth, damping, propagation, refraction, reflection, and tunneling and showed that including the contribution of ring current H^+ in both the imaginary and real parts of the He^+-mode dispersion relation leads to the production of EMICWs where the suprathermal ($\leq$1 keV) ion fluxes are enhanced and the temperature anisotropy of energetic (>10 keV protons) is high. This agrees with observations by Engebretson et al. (2007) and suggests that suprathermal plasma plays a role in destabilizing the more energetic ring current and/or plasma sheet distributions to a high energy anisotropy.

Gamayunov and Khazanov (2008) also found that the results of Loto'aniu et al. (2005) are best explained by a model which assumes the EMICW source is at the equator and that waves reflect at off-equatorial latitudes at the bi-ion hybrid frequencies in conjugate hemispheres. Gamayunov et al. (2009) extended this modeling to incorporate M-I coupling including the magnetospheric electric field, ring current, plasmasphere and ionosphere. Figure 1 in their paper (not shown here) describes their approach in block diagram form. Initial simulations using this model, for the 2–4 May 1998 magnetic storm, showed that it would be necessary to extend the modeling domain to at least 72° latitude, to include a self-consistent description of the ionospheric conductance and the plasmasphere (e.g. plume structure).

In order to explain their observations that EMICW propagation is bidirectional within 11° of the magnetic equator but downward for |MLat|>11° Loto'aniu et al. (2005) suggested that EMICWs could be generated by a backward wave oscillator (BWO) in which waves generated at the equator are reflected back into this region by mirrors off the equator (not the heavy ion resonance locations), allowing feedback wave growth. This idea has been supported by quantitative modeling by Trakhtengerts and Demekhov (2007) for a threshold flux density of $\sim 10^7$ cm^{-2} s^{-1} for protons with energy $\geq$100 keV, and characteristic wave amplitude ~0.01 nT at L=6.

Further information on the role of heavy ion hybrid resonances near the equator comes from modeling by Lee et al. (2008). By solving the full wave equations for a cold plasma they found that at resonance mode conversion occurs and the fast mode wave energy is absorbed, depending on the direction of the incident waves. Waves at resonance have linear polarization but the wave amplitude and frequency depend on the plasma composition. Fraser and McPherron (1982) had earlier discussed the effect of heavy ion resonance propagation effects in EMICW spectra.

EMICWs are occasionally observed on the ground with varying dispersion characteristics. Feygin et al. (2007) showed that events with falling frequency tones are due to RH magnetosonic waves, and a combination of R- and L-mode (i.e. EMIC) waves which produce mixed frequency dispersion. The R-modes may be due to cyclotron instability with 10–100 keV proton beams moving at $v_o \geq U\|$ along the background field, where U is the thermal proton velocity in the beam. When $v_o/U\|<<1$ L-waves result. It should be noted that R-mode waves also occur on the ground due to mode conversion at the crossover frequency and tunneling at heavy ion stop bands (e.g. Rauch and Roux 1982).

The effect of heavy ion populations drifting relative to each other is to change the nonlinear dispersion relation for ICWs, leading to linear ion-acoustic instabilities and destabilizing nonlinear ion-acoustic waves (Gomberoff 2008).

The effect of Pc3-4 waves in modulating Pc1 EMICW growth rates was considered briefly in Demekhov (2007), who showed that for typical cold

plasma conditions at $L = 7$ a ± 5 nT compressional wave can vary the gain over large ranges above and below the equatorial He^+ gyrofrequency, but at lower L values much larger wave amplitudes are required.

Recently interest has also focused on whether Pc1 EMICWs are excited at plume boundaries. Jordanova et al. (2007) used a global kinetic model including a time-dependent plasmasphere to determine the EMIC growth rate with time. They found the waves were preferentially excited in regions where energetic ring current populations, plumes and steep density gradients overlap. Ray tracing calculations by Chen et al. (2009) of ICW growth in a multicomponent cold storm-time plasma incorporating a realistic plasmasphere and a plume, and an additional bi-Maxwellian hot ring current distribution, found strong wave growth near the plasmapause, in density structures within the plume, and in the low density trough.

The Usanova et al. (2008) observations of compression-related EMICW activity have been modeled by McCollough et al. (2009) using a 3-D test particle solver coupled to the time-dependent MHD fields produced by the global LFM code. This allows a range of effects including solar wind compressions to be included. They found that after a compression wave growth was expected between $L = 5$–7 in the morning sector, and near the plasmapause at most times, in agreement with observations, and that the growth rate depends not just on warm plasma temperature anisotropies but also on warm and cold plasma densities (c.f. Gamayunov and Khazanov (2008) results above).

In summary, while important progress has been made with modeling studies of EMICW generation and propagation, the following questions remain: (i) Is there a favored mechanism for Pc1 pearl formation, or a combination of mechanisms at different times? (ii) What are the implications of these new modeling approaches for the scattering of ring current ions and relativistic electrons by EMICWs?

13.4 The Ionosphere Boundary

The conducting ionosphere forms the inner boundary of the magnetospheric cavity and therefore controls not only the formation and properties of standing field line oscillations (e.g. Dungey and Southwood 1970; Hughes, 1974; Yarker and Southwood 1986; Menk et al. 1995), but also the properties of cavity modes (Kivelson and Southwood 1985). In addition, all ULF waves observed on the ground propagate through the ionosphere and are therefore affected by its properties. The best known effect is the rotation of the polarization azimuth of the downgoing wave (Nishida 1964; Hughes 1983). The fields of these propagating waves can affect the ionospheric density distribution, thereby modifying ionospheric properties. These effects can be detected with HF radars and other sounders, and may modify the total electron content along GPS signal paths.

13.4.1 Effects of the Ionosphere on ULF Waves

We consider first recent theoretical treatments and observational results regarding effects of the ionosphere on FLRs, and waves in the Pc1 range. Waters et al. (this volume) provide a more detailed treatment of the underlying principles.

MHD models now being used to investigate the effects of ionospheric conductivity on FLRs incorporate a realistic ionosphere, oblique magnetic fields, and a mixture of incident wave modes. Sciffer and Waters (2002) presented an analytic description of this form, including a reflection and wave mode conversion coefficient matrix to describe mixing and conversion between shear Alfvén and fast mode energy at the ionosphere and atmosphere. These properties were found to depend critically on the perpendicular wavenumber ky. This formulation was extended by Sciffer et al. (2004) to include an inductive shielding effect for oblique magnetic fields (and hence high to low latitudes). This effect arises from the generation of an 'inductive' rotational current by the induced part of the divergent electric field in the ionosphere, reducing the wave amplitude detected on the ground.

Using a 1-D numerical formulation Sciffer et al. (2005) found that for an oblique magnetic field the rotation of the wave polarization azimuth depends on the compressional mode characteristics and the mode conversion and reflection properties from the ionosphere. Waters and Sciffer (2008) described a 2-D MHD formulation which was used to investigate the dependence of FLR frequency on ionospheric conductivity. They found that under typical mid/low latitude summer and winter conditions the FLR frequencies

change by less than 5%. However, at auroral latitudes it is necessary to account for ionospheric feedback arising from changes in the Pedersen conductivity due to electron precipitation. Lu et al. (2007) incorporated a model of an active auroral ionosphere with a 2-D MHD model of the magnetosphere using both dipolar and stretched field geometries. They found that ionospheric feedback effects can produce strongly localized FLRs and enhanced amplitudes.

Direct observations of low-mid latitude Pc3-4wave structure with the CHAMP spacecraft and simultaneously on the ground below were described by Heilig et al. (2007) and Ndiitwani and Sutcliffe (2009). These confirm that Pc3-4 waves propagate through the magnetosphere mostly in the compressional mode and appear in the D component on the ground, coupling to discrete FLRs at the characteristic latitude, with 90° rotation in polarization of the signal on the ground.

This situation was confirmed by Pilipenko et al. (2008) using numerical modeling to calculate the relationship between Pc3 wave power above the ionosphere and on the ground. They also found that diurnal variations in the ionosphere/ground amplitude ratio do not depend strongly on ionospheric conductance, but the fast mode field is sensitive to the crustal surface conductivity.

At equatorial latitudes the nonuniform ionospheric conductivity at dawn results in strong changes in Pc3 amplitude and D component phase on the ground, although the phase of the H component is largely unchanged (Tanaka et al. 2007). It is not clear whether this results from the ionospheric effect on incident Alfvén or fast mode waves (cf. Waters et al. 2001).

New observations and modeling have confirmed the existence of quarter-mode FLRs near the dawn terminator, mostly in winter and summer in the US sector (Obana et al. 2008). These modes result from the asymmetry in ionospheric conductivity at conjugate points, and point to the need for caution in FLR-based magnetospheric density surveys. The difference in solar illumination at conjugate points also causes a strong seasonal asymmetry in plasmaspheric density that is maximum in US longitudes around $L = 2$–3 (Clilverd et al. 2007a).

In conclusion, new datasets and improvements in modeling the effect of the ionosphere are starting to provide a clear picture of the propagation of Pc3-4 signals to the ground. The question arises whether it is possible to characterize the ionospheric transfer function for incident ULF waves at all latitudes.

Consideration of ionospheric effects at Pc1 frequencies should incorporate the effect of the ionospheric Alfvén resonator (IAR). The IAR affects the spectrum of 0.1–10 Hz wave power reaching the ground (Belyaev et al. 1989; Demekhov et al. 2000) and at low latitudes is expected to be excited by lightning discharges. Properties of the IAR, including the diurnal variation, are determined mainly by the variation in Alfvén velocity at the F-layer peak (Hebden et al. 2005). Waters et al. (this issue) provide a detailed description of wave propagation in the IAR, pointing out the need to include magnetic inclination effects away from high latitudes. This changes the resonant frequency (Bösinger et al. 2002) and was described by Bösinger et al. (2009), who computed artificial power spectra of ULF fields at mid- and low-latitude ground sites. They found uneven harmonic spacing and separation in frequency of the Br and $B\varphi$ resonance components. Demekhov (2007) has outlined difficulties with the notion that the IAR determines the spectrum of Pc1 waves on the ground.

Simulations using a 3-D linear model of the propagation of kinetic Alfvén waves in the IAR in the presence of parallel and perpendicular density gradients (Lysak and Song 2008) reveal the formation of narrow-scale Alfvén waves which may be important in the auroral acceleration process. Figure 13.9 illustrates the Ex electric field component at various times after excitation. Interference between waves reflected from the ionosphere and the IAR leads to small scale structure that develops with time, and increases with increasing Pedersen conductance.

A statistical study of observations from the CHAMP spacecraft has revealed the existence of bursts of very intense kilometer-scale FACs in the auroral regions (Rother et al. 2007).

In summary, there is accumulating evidence on the formation and properties of the IAR, and while this may ultimately be important for some auroral processes, more work is required to clarify the role the IAR plays in determining the occurrence and properties of Pc1 pulsations on the ground across a range of latitudes.

13.4.2 Effects of ULF Waves on the Ionosphere

ULF wave fields drive perturbations in the ionosphere that may be detected with high frequency (HF) Doppler sounders (e.g. Menk et al. 1983; Menk 1992)

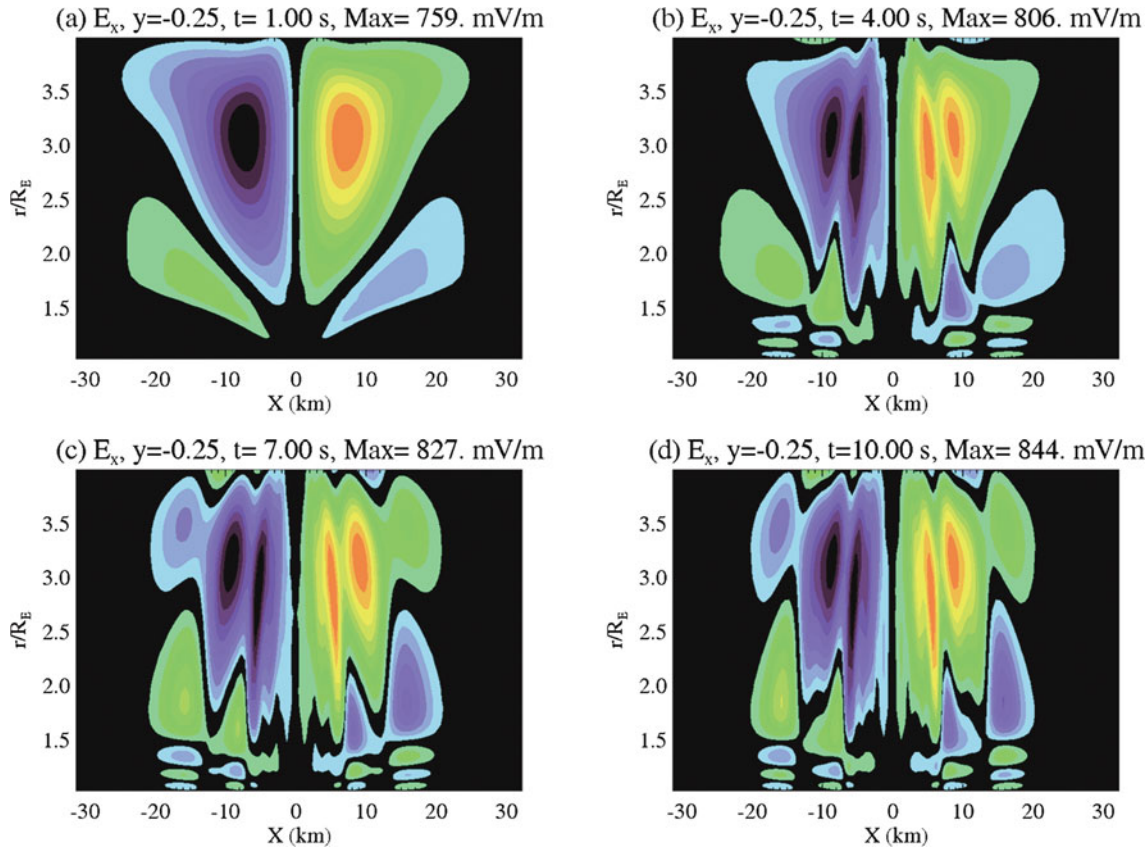

Fig. 13.9 *Ex* component of the electric field at 1, 4, 7 and 10 s after excitation by a 1 Hz 10 km wave field incident at 4 RE on a density cavity (Figure 2 from Lysak and Song 2008)

or HF radars (Ponomarenko et al. 2003) including the low latitude Arecibo radar (Ganguly and Behnke 1982). Doppler sounder measurements, in particular, have revealed the existence of a significant population of very high-*m* waves that is largely hidden from ground magnetometers (Wright et al. 1999; Wright and Yeoman 1999; Yeoman et al. 2000; Baddeley et al. 2005b). A very detailed review of new developments in HF radar science over the past decade was presented by Chisham et al. (2007).

The process by which Alfvén waves incident on and propagating through the ionosphere lead to ULF ionospheric Doppler oscillations was first described in detail by Poole et al. (1988) and Sutcliffe and Poole (1989). This was extended and generalized by Waters et al. (2007) to incorporate a mixture of downgoing wave modes and oblique magnetic field geometry, providing good agreement with observed Doppler shifts for an $m\sim150$ and $m\sim10$ event recorded by HF sounders near 66° latitude. The modeling is sensitive to the choice of wavenumber k_x and k_y and the incident wave mode mixture, but shows that the main contribution to the ionospheric Doppler shift arises from $e\times B_o$ advection motion of the ionospheric plasma driven by the ULF wave electric field.

Menk et al. (2007) reported a study of ULF Doppler oscillations in the ionosphere recorded with an array of HF sounders and ground magnetometers over $L = 1.56$–2.77. They examined the ionosphere-ground amplitude and phase relationship (see Fig. 13.10) for the perturbations as a function of frequency and latitude and compared these with the Waters et al. (2007) model predictions. As the incident wave mix changed from purely fast mode away from resonance to largely shear Alfvén mode at resonance, there was a pronounced change in the amplitude and phase of the ionospheric oscillations. In fact, at these low latitudes the ULF resonance structure was more clearly evident in the ionospheric sounder rather than the ground magnetometer signals.

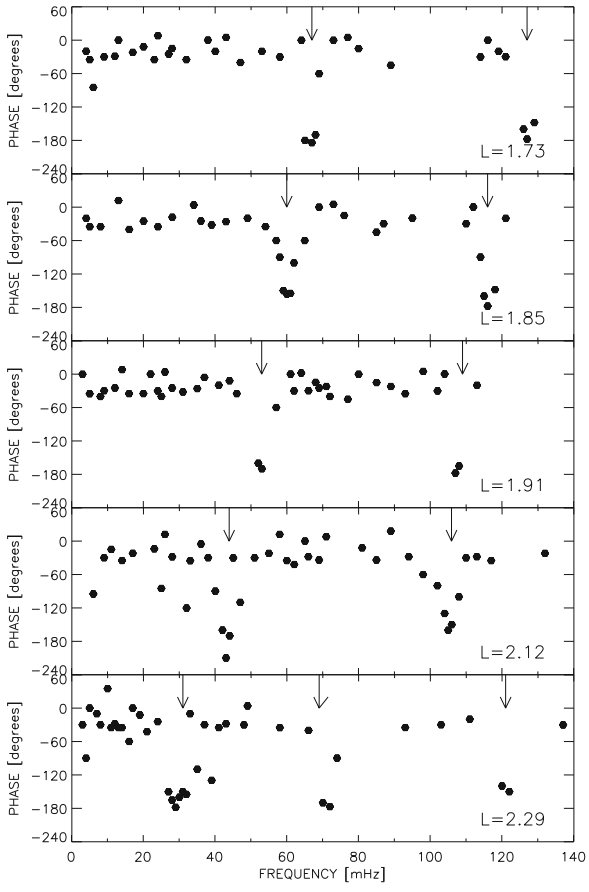

Fig. 13.10 Phase difference between ULF perturbations in the ionosphere and on the ground at low latitudes. *Arrows* indicated FLR frequencies and harmonics (Figure 2 from Menk et al. 2007)

An unusual result is the observation at $L = 1.3$ with the Arecibo radar of 1.7 mHz oscillations in ionospheric plasma frequency at two points 160 km apart in the F-region (Dyrud et al. 2008). The perturbation spectrum was qualitatively similar with GOES-10 magnetic field and WIND solar wind number density spectra, suggesting the ionospheric oscillations were caused by 'magic frequency' ULF waves propagating Earthward from the solar wind.

These results provide an interesting comparison with observations of 1.7–1.9 mHz oscillations by SuperDARN HF radars. Menk et al. (2003) showed that solar wind pressure variations in this range stimulated ULF waves and FLRs recorded by ground magnetometers, and ionospheric and ground scatter returns in high latitude HF sounder and radar signals. More recently, Mthembu et al. (2009) also reported the observation of 'magic' frequencies, in particular 1.9 mHz FLRs, in radar returns and in the upstream solar wind.

ULF waves also cause perturbations in the total electron content (TEC) of the ionosphere (Poole and Sutcliffe 1987; Karatay et al. 2010). The resultant time delays and phase shifts in HF signals propagating through the ionosphere affect GPS and radio astronomy operations (Skone et al. 2009; Waters and Cox 2009).

Mid-latitude radars can detect the ionospheric signatures of sub-auroral Pi2 pulsations associated with substorm expansion (Gjerloev et al. 2007). Comparison by them of the observed amplitude and phase relationships for a given event with the Sciffer et al. (2004) model suggests the incident wave is predominantly shear Alfvén mode wave with $m \sim 2.3$. The measured and modeled perturbations are compared in Fig. 13.11.

The inverse process, the production of ULF waves through modification of ionospheric density with modulated RF transmissions, has been demonstrated on open field lines at 1.67 mHz (Clausen et al. 2008). It is also possible in this way to artificially enhance FLRs on closed field lines, through the production of an

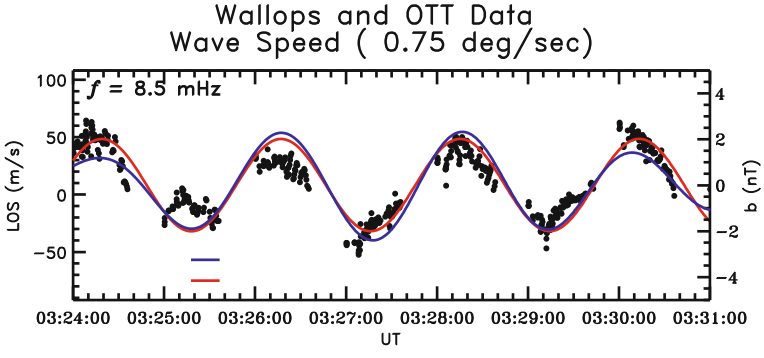

Fig. 13.11 Wallops HF radar line-of-sight drift velocities (*black dots*), ground magnetic field perturbation b_x (*blue*) and modeled ground field perturbation b_x (*red line*) for a mid-latitude Pi2 event (Figure 4 (*top*) from Gjerloev et al. 2007)

oscillating current system in the ionosphere (Badman et al. 2009). The resultant FLRs were detected by the Cluster spacecraft at ~11 R_E altitude. This is the first such report of field line 'tagging' by joint ground- and space-based techniques.

In conclusion, ULF field line signatures can be recorded in the ionosphere from low to high latitudes. In the latter case the waves may arise from solar wind pressure perturbations, or be triggered by substorms. Under appropriate assumptions of horizontal wave number and mode mix of the incident waves, relatively simple models can predict the resultant amplitude and phase profile reasonably well. Extension of these models to higher dimensions would provide more information on ULF wave properties at the ionosphere. It is clear, however, that ionospheric sounders can provide new information not available from magnetometers on ULF waves at the lower boundary of the magnetosphere-ionosphere system.

13.5 Consequences and Applications of ULF Waves

Since the Alfvén velocity depends on mass density and magnetic field strength, and since ULF waves propagate throughout the magnetosphere, they can be used as a diagnostic probe of magnetospheric density and hence structure, source region locations, and solar wind conditions (e.g. Obayashi and Jacobs 1958; Troitskaya 1961; Gul'yel'mi 1966; Troitskaya and Gul'yel'mi 1967, 1970). While much of the Earth's surface lies at low geomagnetic latitudes, the corresponding magnetic field lines map to a small fraction of the magnetospheric cavity which is difficult to study using spacecraft. Furthermore, due to charging effects it is difficult to measure the cold (< 1 eV) ion density that comprises the bulk of the inner magnetosphere population. Therefore ground-based observations are important for studying the inner magnetosphere (e.g. Menk et al. 1999, 2000). New analysis techniques including automated FLR detection algorithms facilitate such studies. At radiation belt altitudes particles can lose or gain energy via wave-particle interactions while waves are amplified or damped, and particles can be scattered into the loss cone and precipitate to low altitudes. Such interactions may have space weather consequences. It has also been suggested that some properties of ULF waves may be linked to seismic activity, and health effects.

13.5.1 Magnetospheric Remote Sensing

It has long been recognized that measurement of the eigenfrequency of magnetospheric field line resonances can provide information on the mass density threading the field line, mostly near the equatorial plane where the field-aligned Alfvén speed is a minimum (e.g. Obayashi and Jacobs 1958; Gul'yel'mi 1966; Poulter and Nielsen. 1982; Orr 1984). However, the distribution of plasma mass density along the field line alters the harmonic spacing of ULF resonances (Poulter et al. 1988; Takahashi et al. 2004) and mass loading due to heavy ions of ionospheric origin becomes important at low latitudes (Hattingh and Sutcliffe 1987; Waters et al. 1994). At high latitudes the field line geometry, and in particular the diurnal variation, plays an important role in determining the resonance frequency (Waters et al. 1995). Use of the dipole approximation introduces errors in mass density estimates for $L > \sim 3$ (Singer et al. 1981; Berube et al. 2006). The structure and location of Pc1-2 waves also provides a convenient diagnostic of high latitude topology (Menk et al. 1992). Ground based techniques for determining the FLR frequency were outlined in Menk et al. (1999).

There is growing use of ground ULF wave FLR observations to monitor magnetospheric properties such as the radial density distribution (Waters et al. 1996; Loto'aniu et al. 1999; Menk et al. 1999; Dent et al. 2003) and hence the plasmapause position (Milling et al. 2001; Menk et al. 2004; Dent et al. 2006), the presence and evolution of plasmaspheric plumes and biteouts (Abe et al. 2006; Grew et al. 2007; Takahashi et al. 2008), refilling processes (Dent et al. 2006; Obana et al. 2010), and the location of the open-closed field line boundary (Ables and Fraser 2005). Such remote sensing using ground-based observations of standing Alfvén waves is sometimes termed normal mode magnetoseismology (Chi and Russell 2005). Comparison with other techniques allows the plasma composition to be determined (Grew et al. 2007; Takahashi et al. 2008).

A statistical study of ULF field line resonance frequencies at low latitudes ($L < 2$) has demonstrated that the daily average FLR frequency, and hence

plasmas-pheric mass density, follows the 27-day variation in $F_{10.7}$ solar flux with a 1–2 day time delay (Vellante et al. 2007). This shows that at low latitudes the FLR frequency is clearly controlled by the solar EUV irradiance, and the flux tubes may be regarded as being in diffusive equilibrium with the underlying ionosphere. Vellante et al. also noted a pronounced annual variation in mass density, which probably varies with longitude as determined for electron densities using VLF whistler measurements (Clilverd et al. 1991) and is probably due to the tilt of the magnetic dipole axis from the rotation axis. The existence of quarter-mode FLRs near the dawn terminator points to the need for caution in FLR-based magnetospheric density surveys (Obana et al. 2008).

It is interesting to compare FLR-derived estimates of mass density near the equatorial plane with independent determinations of electron density, which can be used to determine the heavy ion mass loading factor (Menk et al. 1999). In particular, due to mass loading effects the electron and heavy ion density profiles may be significantly different at the plasmapause or plume boundaries, especially in the presence of an O^+ torus (Fraser et al. 2005). Sometimes the dominance of heavy ions in the plasmatrough may mask the plasmapause and plasma plume boundaries compared to electron number density or light ion data (Takahashi et al. 2008).

An intercalibration of ULF-derived mass densities, electron densities from VLF whistler measurements and IMAGE spacecraft RPI data, and IMAGE EUV He^+ density estimates, was described by Clilverd et al. (2003). Grew et al. (2007) mapped the presence of a plume and biteout and showed that during an extended disturbed interval the H^+:He^+:O^+ composition by number in the plasmasphere and plasmatrough (near $L = 2.5$) was $\sim$82:15:3, but just outside the plasmapause the O^+ concentration exceeded 50%, suggesting the presence of an oxygen torus. Takahashi et al. (2008) compared mass density measurements based on in situ E and B field measurements from CRRES, with electron number densities measured by the same spacecraft, and found that in a plasma plume H^+ was the dominant species, while O^+ accounted for $\sim$90% of the mass density.

Earlier, Berube et al. (2005) had compared the FLR-based mass density between $L = 1.7$ and $L = 3.2$ with in situ plasmaspheric electron densities determined from the IMAGE RPI, finding that heavy ion concentrations were enhanced during large storms, when a heavy ion torus is likely to form. Mass density has been found to rapidly increase over $1.6 < L < 5.1$ immediately following a very large storm onset due to rapid outflow of ionospheric O^+ (Kale et al. 2009), followed by plasmaspheric density depletion and refilling for the next few days.

A detailed study of post-storm refilling using ground-based FLR observations was reported by Obana et al. (2010). They found that refilling takes 2–3 days for $L = 2.3$ flux tubes, 3 days at $L = 2.6$, and over 4 days for $L > 3.3$, and determined the upward plasma flux (at the 1000 km level) and the daily average refilling rate. Finally, by comparison with IMAGE-EUV and VLF whistler data they estimated the O^+ plasma concentration was of order 3–7% at $L = 2.3$ and 6–13% at $L = 3.0$.

The cross-phase technique (Waters et al. 1991) is perhaps the best-known method for determining toroidal mode FLR frequencies with closely-spaced ground stations. Kale et al. (2007) showed that where the radial density gradient exceeds r^{-8} (i.e. near a steep plasmapause) the cross-phase is reversed. Such cross-phase measurements all relate to the magnetic H component between meridionally spaced stations. Menk et al. (2006) demonstrated that the D component cross-phase may also provide information on poloidal mode resonances.

These methods rely upon knowledge of the field-aligned density distribution, which is often assumed to obey a power law (e.g. Cummings et al. 1969; Berube et al. 2005; Vellante and Förster 2006). This assumption, and improvements, have been discussed by many authors (e.g. Schulz 1996; Denton and Gallagher 2000). The spacing of FLR harmonics allows the mass density at points along the field line to be determined without assuming any functional form for the density distribution (Price et al. 1999). Satellite measurements of toroidal resonance harmonics near L=7 suggest that the field-aligned density distribution is better described by a polynomial series (Takahashi et al. 2004; Takahashi and Denton 2007), revealing an equatorial density enhancement in the afternoon sector at geostationary orbit and near 4.8 R_E (Denton et al. 2009) where density varies with L like L^{-4}. However, in many situations the simple power law approach allows the radial density profile to be estimated within observational uncertainty limits (Menk et al. 2004; Vellante and Förster 2006; Maeda et al. 2008).

In addition to using the eigenfrequency of standing Alfvén field line eigenoscillations to estimate mass density, it is also possible to estimate the density distribution and hence Alfvén speed required to explain the measured travel time of MHD waves through the magnetosphere and to the ground (Matsuoka et al. 1997; Chi et al. 2001; Howard and Menk 2001, 2005; Ponomarenko et al. 2005; Chi et al. 2006). The waves essentially obey Huygens' and Fermat's principles and follow the path that minimizes the travel time and conserves the most wave energy; this path involves fast mode MHD waves propagating initially Earthward in the equatorial plane and converting to field-aligned Alfvén waves. This is a fairly common concept in geophysics (e.g. Moser 1991) and explains why Pc3 ULF pulsations appear to propagate poleward across the ground at high latitudes (Howard and Menk 2005).

In conclusion, magnetoseismology offers the ability to remotely monitor magnetospheric properties including the plasmapause location, the radial density profile, and under certain conditions the presence of plasma plumes, the field-aligned density distribution, and the plasma composition. Measurements of the field line eigenfrequency and harmonics are the most established techniques for this, although the wave travel time can also provide information on the density distribution. Further intercalibration studies are required to compare ground-based mass density estimates with in situ observations in order to understand the full utility of the technique, and the precision of composition estimates. It would also be interesting to study how mass loading and hence plasma composition varies with magnetic activity and L.

13.5.2 Energization of Magnetospheric Particles

In recent years there has been considerable interest regarding the role and efficiency of ULF waves in accelerating trapped magnetospheric particles, especially in the radiation belts (e.g. O'Brien et al. 2003; Summers et al. 2007; Shprits et al. 2008a, b). A detailed review was presented by Elkington (2006).

Many observational studies have highlighted an association between Pc3-5 ULF waves and the energization of radiation belt electrons, particularly at geosynchronous altitude (e.g. Mathie and Mann 2001; O'Brien et al. 2003). In fact, long duration elevated Pc5 wave power seems to be a strong predictor of enhancements in relativistic electron fluxes at geosynchronous orbit (O'Brien et al. 2001). Statistically there is a strong correlation between solar wind speed, Pc5 ULF wave power and MeV electron fluxes throughout the outer radiation belt, with the highest correlations late in the declining phase of the solar cycle when the radiation belts are most intense (Mann et al. 2004). There is also a clear and systematic time lag, with MeV electron fluxes at geosynchronous altitudes lagging the peak in ULF wave power by ~2 days, before peaking later at lower L shells.

Electron distribution functions in the radiation belts often peak at pitch angles perpendicular to the background field, and diffusive cross-L transport of electrons is believed to involve resonant interaction of the electron drift motion with ULF electric and magnetic field oscillations. Such processes violate the third adiabatic invariant and require the superposition of multiple stochastic interactions when averaged over a statistical ensemble incorporating different wave frequencies and phases, LT distribution, and variations in solar wind pressure (Ukhorskiy et al. 2005; Degeling et al. 2006; Elkington 2006).

Test-particle simulations have shown that perturbations in electric and magnetic fields are induced across wide regions of the magnetosphere by global magnetospheric compressions due to ULF variations in solar wind dynamic pressure and presumably also FLRs and magnetosonic waves (Ukhorskiy et al. 2006). Resonant interaction of the drift motion of electrons with these fields drives cross-L transport and radial diffusion in the inner magnetosphere, although the collective motion of outer belt electrons can exhibit large deviations from simple radial diffusion (Ukhorskiy and Sitnov 2008).

Diffusion models require the perpendicular electric and compressional magnetic diffusion coefficients to be specified in terms of ULF wave power. This means in turn that ground observations of ULF wave power need to be mapped to the equatorial plane. Analytical (e.g. Ozeke et al. 2009) and empirical/statistical (e.g. Brautigam et al. 2005) approaches may be used.

The average rate of radial diffusion is described by the diffusion coefficient and is a function of L, the wave power and mode structure. Time scales are typically of order a day (Elkington 2006). Loto'aniu et al. (2006) used ground magnetometer observations during a very large storm, when large amplitude ULF

waves and relativistic electrons were recorded deep in the slot region (L∼2–3), to calculate the in situ equatorial poloidal electric field PSD values and hence determine the radial diffusion rates. They found diffusion rates were 3–5 h at $L>4$ and 12–24 h for $L<4$, able to account for the observed increase in relativistic electrons in the slot. O'Brien et al. (2003) had earlier found during a solar cycle-long statistical survey that ULF activity is probably responsible for the main electron acceleration at geosynchronous orbit, but that VLF/ELF wave interactions were required to account for electron flux peaks at L∼4.5.

The ULF waves responsible for radial transport of trapped electrons are often believed to be toroidal mode Pc5 waves such as FLRs with low azimuthal wavenumbers and radially directed electric field perturbations (e.g. Elkington et al. 2003; Ukhorskiy and Sitnov 2008; Degeling et al. 2008). In reality the waves usually exhibit a mixture of toroidal and poloidal modes (e.g. Ukhorskiy et al. 2005; Loto'aniu et al. 2006), and although the radial electric field of the toroidal component often dominates observations, diffusion rates due to the azimuthal electric fields of the associated poloidal modes are much more important (Ukhorskiy et al. 2005; Elkington 2006). Figure 13.12 shows results of numerical test particle simulations for 1 MeV electrons, compared to theoretical expectations, for m=1 ULF waves with azimuthal and radial electric fields based on a statistical survey of wave observations from CCRES. The required stochasticity in electron motion is assumed to arise due to randomness introduced by solar wind turbulence.

There have been concerns that radial diffusion cannot account for the relativistic particle fluxes that occur during storms (e.g. Horne et al. 2005). A non-diffusive mechanism for the energization of electrons by Pc5 ULF waves has been proposed by Degeling et al. (2006, 2008). This involves adiabatic transport due to drift resonance interaction between individual packets of coherent, narrowband compressional waves and equatorially mirroring MeV electrons, leading to localized peaks in electron phase space density. The initial time-dependent compressional waves may be launched from disturbances at the magnetopause, have low azimuthal wavenumber (m∼3) in the magnetosphere, and couple to FLRs. The waves were modeled with an ideal MHD approach in a dipolar geometry and only azimuthal fields, well away

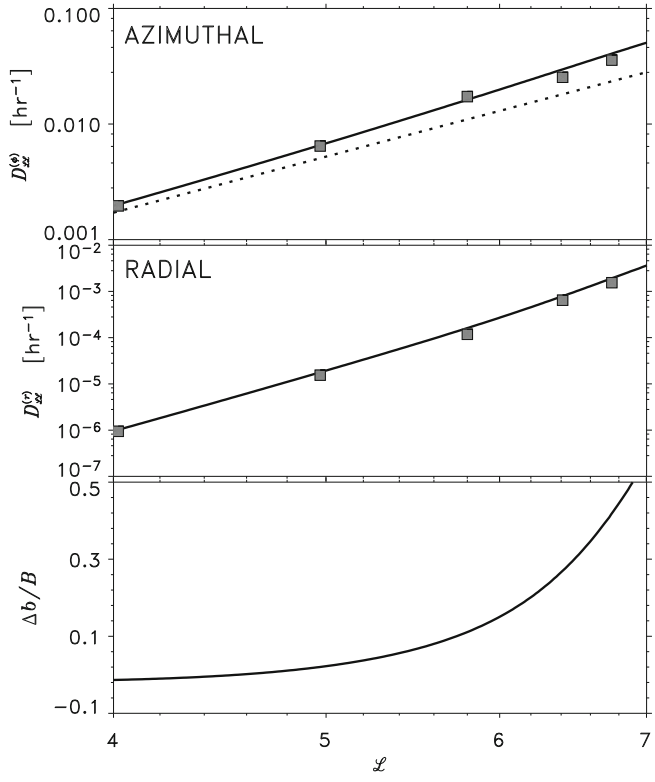

Fig. 13.12 Diffusion rates for 1 MeV equatorial electrons due to low m ULF waves. *Top*: azimuthal electric field; theoretical values shown with *solid lines*, and numerical values with *square symbols*. *Middle*: radial electric field. *Bottom*: background field asymmetry (Figure 5 from Ukhorskiy et al. 2005)

from the FLR, were considered. Because the wave phase speed and the azimuthal electron drift speed need to be similar, the drift resonance interaction region is limited to a range in L that depends on the wave amplitude.

While much attention has focused on low-m ULF waves, large amplitude internally generated high-m Pc4-5 waves also occur at storm times. Ozeke and Mann (2008) considered guided poloidal waves with mainly azimuthal electric fields and $m \geq 10$. The waves can be generated by the N=2 drift-bounce resonance interaction with energetic ring current ions (~10–15 keV H^+ or ~100–300 keV O^+). Such ion populations may occur in the inner magnetosphere at storm times when the plasmapause is at low L. The resultant waves have eastward phase propagation. In turn, eastward drifting >1 MeV radiation belt electrons may undergo drift resonance with the fundamental mode waves at $L \sim 3$–4. Note that the high-m poloidal waves could also be produced by other mechanisms, such as the Kelvin-Helmholtz instability, and are partially or largely screened from the ground due to spatial integration effects. This mechanism provides an interesting and potentially important process for particle energization at storm times.

The arrival of interplanetary shocks can stimulate high-m poloidal and toroidal waves throughout the magnetosphere, and Zong et al. (2009) used Cluster-Double Star observations to record the almost simultaneous enhancement of energetic electron fluxes in the radiation belt, probably due to drift-resonance acceleration by the waves.

Higher frequency plasma waves may accelerate radiation belt electrons through gyroresonant interactions. This includes EMIC waves (Summers et al. 2007) and fast magnetosonic waves with frequency below the lower hybrid resonance frequency but above the local proton gyrofrequency (i.e. in the range 20–60 Hz) (Horne et al. 2007). The waves are generated by ion ring distributions in the ring current at frequencies close to harmonics of the proton gyrofrequency, and interact with electrons and ions via the Doppler shifted cyclotron resonance. While it is generally believed that whistler mode chorus waves are very effective in accelerating electrons to MeV energies (e.g. Horne et al. 2005), Horne et al. (2007) suggested that magnetosonic waves may be equally important in accelerating these particles.

Recently attention has focused on the energization of auroral electrons by inertial Alfvén waves (e.g. Chaston et al. 2003; Seyler and Liu 2007). This topic is not reviewed here. Note however that the fluxes of energetic electrons and ions may be modulated by low-m standing toroidal mode Pc5 ULF waves in the outer magnetosphere, probably due to drift resonance interactions (Zong et al. 2007).

In conclusion, statistical and case studies show that ULF waves likely play a major role in the energization of relativistic particles in the radiation belts and into the slot. Questions remain concerning the relative contributions of different Pc5 wave types: radial diffusion due to broadband low-m waves, adiabatic transport due to time dependent compressional waves, and high-m waves in the ring current, as well as the role of EMIC waves.

13.5.3 Precipitation of Magnetospheric Particles

Many studies confirm that EMIC waves may cause pitch angle scattering and precipitation into the atmosphere of energetic protons (e.g. review by Yahnin and Yahnina 2007) and electrons (e.g. review by Millan and Thorne 2007).

Yahnin and Yahnina (2007) outlined observations demonstrating that localized precipitation of energetic protons is due to the scattering of particles into the loss cone by Pc1 ICWs in the equatorial plane. In the morning sector localized proton auroras may be connected with Pc1 sources associated with undulation of the plasmapause surface, while in the evening sector the waves may be generated near plasmaspheric plumes (e.g. Spasojević et al. 2004). Observations detailing the formation of an isolated subauroral proton arc (30–80 keV protons at $L \sim 4$) in the premidnight sector in association with intense Pc1 EMICWs near the plasmapause were presented by Sakaguchi et al. (2007).

There is accumulating observational evidence that EMIC waves are also responsible for relativistic electron precipitation (REP) after geomagnetic storms (e.g. Lorentzen et al. 2000; Meredith et al. 2003; Loto'aniu et al. 2006; Clilverd et al. 2007b; Blum et al. 2009). Examining an isolated proton aurora, Miyoshi et al. (2008) compared ground-based optical observations,

co-located magnetometer measurements of associated Pc1 pulsations, and data from the POES-17 satellite as it passed over the ground stations showing precipitating 10s of keV ions and MeV electrons. DMSP mapped this region to the plasmapause. Miyoshi et al. were then able to demonstrate that the pitch angle diffusion coefficients were consistent with scattering of the relativistic electrons by the EMIC waves.

Results from a new and independent method for detecting REP were presented by Rodger et al. (2008), who have established a global network of VLF receivers which monitor the absorption of artificially produced VLF signals along a range of subionospheric paths. REP results in localized VLF absorption at altitudes below ~70 km. Riometer absorption is weak or absent at these times. They detected such events near the plasmapause during small geomagnetic disturbances in association with IPDP/Pc1 EMIC activity recorded on ground based magnetometers.

There has also been considerable effort on modeling the process by which EMICWs scatter radiation belt electrons. This is usually regarded as a gyroresonance process and treated with a bounce-averaged quasi-linear diffusion approach (e.g. Summers et al. 2007). Jordanova et al. (2008) described a kinetic ring current-atmosphere interaction model (RAM) that includes radiation belt electron and ring current ion interactions with EMICWs whose excitation is incorporated self-consistently, and incorporates convective and diffusive transport and various loss processes. Using initial conditions referenced to observations and empirical models, they calculated the global precipitating electron and ion fluxes at 200 km altitude at various times during the large 21 October 2001 storm, finding that REP due to EMICWs maximized at $L \approx 4.5$ near dusk at hour 18 but with localized patches elsewhere. Outward radial diffusion was the main loss process for $L > 5$, while ion precipitation was most intense at low L shells at hour 24. Figure 13.13 summarizes their results, which compare favorably with observational studies mentioned above.

In contrast to gyroresonance scattering that violates the first invariant, Shprits (2009) pointed out that bounce resonance interaction with magnetosonic and EMIC waves, violating the second invariant, may be an important process for pitch-angle scattering of particles mirroring near the equator. It should be noted that the interaction between radiation belt electrons and EMICWs can be highly nonlinear (Albert and Bortnik 2009) and that the waves can be highly oblique (Khazanov and Gamayunov 2007).

13.5.4 New Techniques

As outlined earlier, there is growing use of ULF FLR measurements for magnetospheric remote sensing. The tedium of manually determining resonance frequencies and the existence of large ULF wave datasets has led to the development of automated detection algorithms (Berube et al. 2003; Vellante et al. 2007). An automatic algorithm to identify Pc1 wave events and

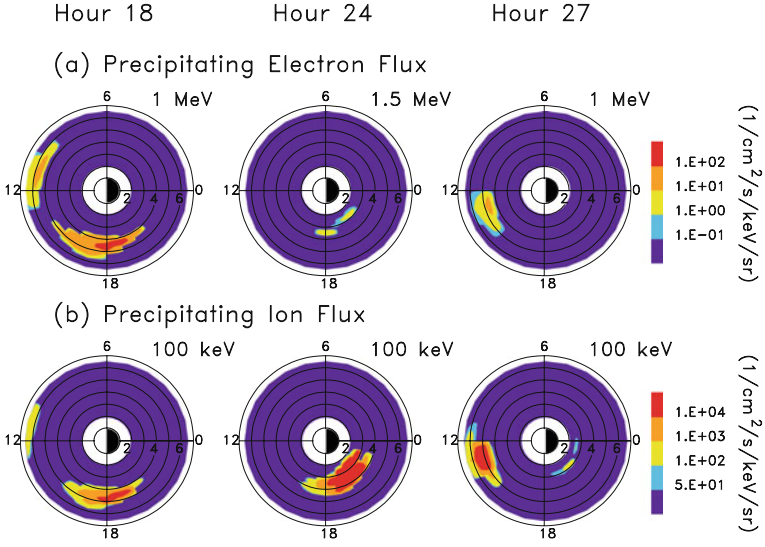

Fig. 13.13 Computed global distribution of energetic electron and ion number fluxes at selected times after 0000 UT on 21 October 2001 due to interactions with EMIC waves (Figure 6 from Jordanova et al. 2008)

simultaneously characterize their polarization properties has also been developed by Bortnik et al. (2007), who illustrated its use on 6 months of data. Their statistical analysis included the determination of cross-correlation for 12 wave parameters including wave frequency and bandwidth, azimuth angle, plasmapause location, and He^+ gyrofrequency.

The performance of FFTs to identify ULF waves in such procedures has been compared with wavelet transform (WT) techniques (Boudouridis and Zesta 2007; Heilig et al. 2007; Murphy et al. 2009), maximum entropy spectrum analysis (MESA; Ndiitwani and Sutcliffe 2009), Wigner-Ville distributions (WVD; Chi and Russell 2008), and Hilbert-Huang transforms (HHT; Kataoka et al. 2009). The FFT seems to outperform the continuous WT in automated FLR detection approaches (but the Morlet WT is better where the signal changes rapidly), while the WVD offers several advantages (especially for time-varying signals such as Pi2, Pc1 packets and phase skips in Pc3-4) including the ability to determine wave polarization properties. However, it is important to first detrend the data series and the WVD approach is more computationally intensive than the FFT or wavelet approaches. The HHT decomposes the waveform into a small number of intrinsic mode functions for which the instantaneous frequency is determined by the Hilbert transform. The method is particularly well suited for irregular signals such as Pi1, Pi2 and storm-time Pc3 packets.

The use of discrete wavelet transforms (DWTs) based on the Meyer wavelet for detecting Pi2 signals was first evaluated by Nosé et al. (1998). A detector and locator of substorm onsets based on Pi1/2 detection in this way was described by Milling et al. (2008) and Murphy et al. (2009). The first of these papers illustrated the use of the Meyer DWT to determine the onset time (resolution ~16 s) and location of Pi1 activity at substorm onset, and the subsequent expansion rate. The locations of the upward and downward field aligned currents were also determined. The second paper validated the DWT technique by comparing ULF wave onset times and locations for 5 substorms and one pseudobreakup with IMAGE-FUV observations. Figure 13.14 shows an example for a substorm initiated over the CARISMA magnetometer array.

A 'wave telescope' field line resonance detector for multipoint data was described in detail by Plaschke et al. (2008). The technique estimates the spectral energy density of the wave field across a station array,

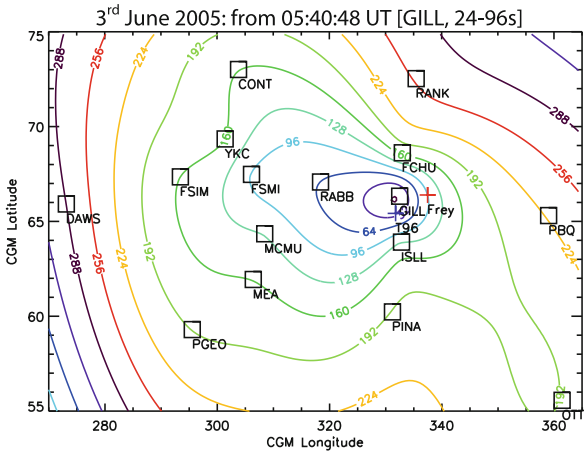

Fig. 13.14 Contours of Pi1/2-based onset times for a substorm on 3 June 2005 (Figure 6 from Murphy et al. 2009)

and is thus able to find hidden FLR phase structures because of the coherency across a large area. The use of the detector was demonstrated on 1 year of ground magnetometer data from the CARISMA array, where FLR properties such as time distribution, location, azimuthal wavenumber, see Fig. 13.15, were determined.

An important concern in magnetospheric physics is mapping ground-based observations to the magnetosphere. Ozeke et al. (2009) have shown analytically how to map magnetic field amplitudes observed on the ground, through the ionosphere, to electric field amplitudes in the equatorial plane for the guided toroidal and poloidal modes. They also compared numerical solutions with an observational example of a guided toroidal FLR, providing two simple expressions for

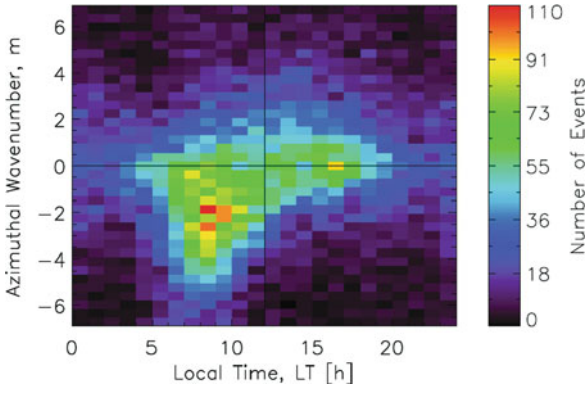

Fig. 13.15 Distribution of FLR events in 1 year of CARISMA ground data sorted by LT and azimuthal wavenumber (Figure 10 from Plaschke et al. 2008)

determining the ionospheric magnetic field and hence the equatorial electric field.

In conclusion, several important new techniques have been recently developed to facilitate the automatic detection of Pc1 ULF waves, Pi1 and Pi2 and hence substorm onsets, and FLRs, and for determining wave properties in space using ground instruments. These techniques should provide new opportunities for statistical and detailed case studies using existing and growing new datasets.

13.5.5 Other Effects

There have been reports for many years that Pc1 pulsations may be associated with seismic activity (e.g. Hayakawa et al. 2006, and associated special issue; Fraser-Smith 2008), particularly as precursors (Dovbyna 2007). Causative mechanisms are often discussed in terms of ionospheric perturbations, although there have also been many reports of no correlation between ULF/ELF/VLF phenomena, ionospheric properties and earthquakes (e.g. Rodger et al. 1996). It has also been suggested that the spectral power law across the ULF range is modified by the appearance of flicker noise before large seismic events (Smirnova and Hayakawa 2007).

Bortnik et al. (2008b) described a detailed and careful statistical study, spanning 7.5 years, of Pc1events (8913 events) and nearby earthquakes (434 M > 3.0 events within 200 km) at a low latitude site. They found a statistically significant increase, by a factor of 3–5, in the occurrence probability of daytime Pc1 pulsations ~5–15 days prior to an earthquake. Their results are summarized in Fig. 13.16. Evidence of earthquake precursors in the 0.01–0.5 Hz range has also been provided by Fraser-Smith et al. (1990) and Fraser-Smith (2008).

One of the main difficulties in this type of work is discriminating any seismic effect from the background of naturally-occurring global geomagnetic pulsations and artificial noise effects. Hattori et al. (2004a) examined for this purpose the effectiveness of a principal component analysis method, based on eigenvalue analysis of the covariance matrix of the observed signal matrix, for frequencies >10 mHz and $M > 6$ earthquakes. They also accounted for possible shaking of the sensors. Looking at 8 months data, they found earthquake-related enhancements in ULF activity first

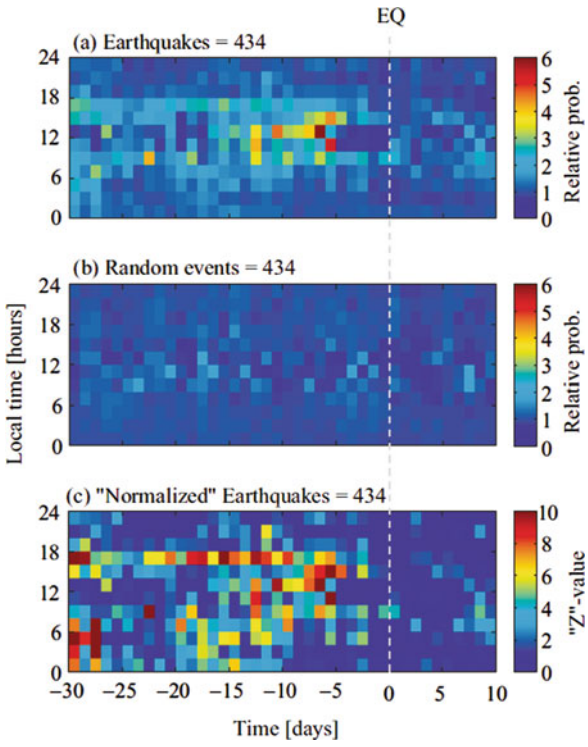

Fig. 13.16 Relative probability of Pc1 occurrence (**a**) prior to an earthquake, (**b**) with respect to a similar number of random events, and (**c**) normalized for LT. (Figure 4a–c from Bortnik et al. 2008b)

appeared about 2 weeks prior to and peaking a few days before, a large earthquake, with an average intensity of order 10^{-2} nT over the frequency range. Further extensive studies were reported in Hattori et al. (2004b, 2006). Fraser-Smith et al. (1990) reported similar effects, including 'an exceptionally high level of activity' immediately preceding an $M = 7.1$ earthquake.

There have also been recent reports that Pc1 pulsations present a potential hazard for myocardial infarction (Kleimenova et al. 2007) and other medical conditions (Matveyeva and Shchepetnov 2007). The former reports a study of nearly 86,000 instances over 3 years, suggesting that in winter, days of high myocardial incidence correspond with high Pc1 incidence.

There is much discussion in the media regarding human effects on the environment. Guglielmi and Zotov (2007) considered whether there may be a weekend effect of human origin on Pc1 wave occurrence. They examined Pc1 activity at Borok (L=2.9) over 1958–1992 and found an inherent enhancement in Pc1 occurrence of about 10% on weekends, and

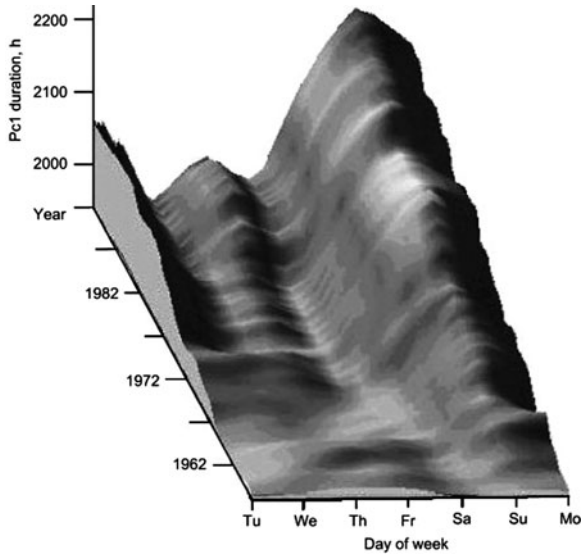

Fig. 13.17 Evolution of the weekend effect in Pc1 activity over 35 years (Figure 4 from Guglielmi and Zotov 2007)

that this value is increasing: see Fig. 13.17. In a previous 12-year study of Pc1 activity Fraser-Smith (1979) suggested that such an effect may be related to the level of power line harmonic radiation into the magnetosphere during weekends. This is an outstanding question: for example, could lower levels of artificial noise on weekends simply facilitate detection?

In conclusion, further work is required to establish whether enhanced Pc1 activity may generally precede earthquakes, and if so, the physical mechanism. The cause of the weekend effect in Pc1 activity also needs to be established.

References

Abe S, Kawano H, Goldstein J, Ohtani S, Solovyev SI, Baishev DG, Yumoto K (2006) Simultaneous identification of a plasmaspheric plume by a ground magnetometer pair and IMAGE Extreme Ultraviolet Imager. J Geophys Res. doi:10.1029/2006JA011653

Ables ST, Fraser BJ (2005) Observing the open-closed boundary using cusp-latitude magnetometers. Geophys Res Lett. doi:10.1029/2005GL022824

Albert JM, Bortnik J (2009) Nonlinear interaction of radiation belt electrons with electromagnetic ion cyclotron waves. Geophys Res Lett. doi:10.1029/2009GL038904

Allan W, Poulter EM (1984) The spatial structure of different ULF pulsation types: a review of STARE radar results. Rev Geophys 22:85–97

Allan W, Poulter EM (1992) ULF waves – their relationship to the structure of the Earth's magnetosphere. Rep Prog Phys 55:533–598

Allan W, White SP, Poulter EM (1986a) Impulse-excited hydromagnetic cavity and field-line resonances in the magnetosphere. Planet Space Sci 34:371–385

Allan W, White SP, Poulter EM (1986b) Hydromagnetic wave coupling in the magnetosphere – plasmapause effects on impulse-excited resonances. Planet Space Sci 34: 1189–1200

Altman C, Fijalkow E (1980) The horizontal propagation of Pc1 micropulsations in the ionosphere. Planet Space Sci 28:61–68

Andrews MK (1977) Magnetic pulsation behaviour in the magnetosphere inferred from whistler mode signals. Planet Space Sci 25:957–966

Archer M, Horbury TS, Lucek EA, Mazelle C, Balogh A, Dandouras I (2005) Size and shape of ULF waves in the terrestrial foreshock. J Geophys Res. doi:10.1029/2004JA010791

Arnoldy RL, Engebretson MJ, Alford JL, Erlandson RE, Anderson BJ (1996) Magnetic impulse events and associated Pc 1 bursts at dayside high latitudes. J Geophys Res. doi:10.1029/95JA03378

Arnoldy RL et al (2005) Pc 1 waves and associated unstable distributions of magnetospheric protons observed during a solar wind pressure pulse. J Geophys Res. doi:10.1029/2005JA011041

Baddeley LJ, Yeoman TK, Wright DM, Trattner KJ, Kellet BJ (2005a) On the coupling between unstable magnetospheric particle populations and resonant high *m* ULF wave signatures in the ionosphere. Ann Geophys 23: 567–577

Baddeley LJ, Yeoman TK, Wright DM (2005b) HF Doppler sounder measurements of the ionospheric signatures of small scale ULF waves. Ann Geophys 23:1807–1820

Badman SV, Wright DM, Clausen LBN, Fear RC, Robinson TR, Yeoman TK (2009) Cluster spacecraft observations of a ULF wave enhanced by Space Plasma Exploration by Active Radar (SPEAR). Ann Geophys 27:3591–3599

Belyaev PP, Polyakov SV, Rapoport VO, Trakhtengerts VY (1989) Theory of formation of the resonance spectral structure of atmospheric electromagnetic noise background in the range of short-period geomagnetic pulsations. Izvestiya vuzov-Radiofizika 32:802–810

Berube D, Moldwin MB, Weygand JM (2003) An automated method for the detection of field line resonance frequencies using ground magnetometer techniques. J Geophys Res. doi:10.1029/2002JA009737

Berube D, Moldwin MB, SF Fung, Green JL (2005) A plasmaspheric mass density model and constraints on its heavy ion concentration. J Geophys Res. doi:10.1029/2004JA010684

Berube D, Moldwin MB, Ahn M (2006) Computing magnetospheric mass density from field line resonances in a realistic magnetic field geometry. J Geophys Res. doi:10.1029/2005JA011450

Blanco-Cano X, Omidi N, Russell CT (2009) Global hybrid simulations: foreshock waves and cavitons under radial interplanetary magnetic field geometry. J Geophys Res. doi:10.1029/2008JA013406

Blum LW, MacDonald EA, Gary SP, Thomsen MF, Spence HE (2009) Ion observations from geosynchronous orbit as a proxy for ion cyclotron wave growth during storm times. J Geophys Res. doi:10.1029/2009JA014396

Bortnik J, Cutler JW, Dunson C, Bleier TE (2007) An automatic wave detection algorithm applied to Pc1 pulsations. J Geophys Res. doi:10.1029/2006JA011900

Bortnik J, Cutler JW, Dunson C, Bleier TE, McPherron RL (2008a) Characteristics of low-latitude Pc1 pulsations during geomagnetic storms. J Geophys Res. doi:10.1029/2007JA012867

Bortnik J, Cutler JW, Dunson C, Bleier TE (2008b) The possible statistical relation of Pc1 pulsations to Earthquake occurrence at low latitudes. Ann Geophys 26:2825–2836

Bösinger T, Haldoupis C, Belyaev PP, Yakunin MN, Semenova NV, Demekhov AD, Angelopolous V (2002) Spectral properties of the ionospheric Alfvén resonator observed at a low-latitude station ($L = 1.3$). J Geophys Res. doi:10.1029/2001JA005076

Bösinger T, Ermakova EN, Haldoupis C, Kotik DS (2009) Magnetic-inclination effects in the spectral resonance structure of the ionospheric Alfvén resonator. Ann Geophys 27:1313–1320

Boudouridis A, Zesta E (2007) Comparison of Fourier and wavelet techniques in the determination of geomagnetic field line resonances. J Geophys Res. doi:10.1029/2006JA011922

Brautigam DH, Ginet GP, Albert JM, Wygant JR, Rowland DE, Ling A, Bass J (2005) CRRES electric field power spectra and radial diffusion coefficients. J Geophys Res. doi:10.1029/2004JA010612

Broughton MC, Engebretson MJ, Glassmeier K-H, Narita Y, Keiling A, Fornaçon K-H, Parks GK, Remè H (2008) Ultra-low-frequency waves and associated wave vectors observed in the plasma sheet boundary layer by Cluster. J Geophys Res. doi:10.1029/2008JA013366

Chaston CC, Peticolas LM, Bonnell JW, Carlson CW, Ergun RE, McFadden JP, Strangeway RJ (2003) Width and brightness of auroral arcs driven by inertial Alfven waves. J Geophys Res. doi:10.1029/2001JA007537

Chen L, Thorne RM, Horne RB (2009) Simulation of EMIC wave excitation in a model magnetosphere including structured high-density plumes. J Geophys Res. doi:10.1029/2009JA014204

Chi PJ, Russell CT (2005) Travel-time magnetoseismology: Magnetospheric sounding by timing the tremors in space. Geophys Res Lett. doi:10.1029/2005GL023441

Chi PJ, Russell CT (2008) Use of the Wigner-Ville distribution in interpreting and identifying ULF waves in triaxial magnetic records. J Geophys Res. doi:10.1029/2007JA012469

Chi P et al (2001)Propagation of the preliminary reverse impulse of sudden commencements to low latitudes. J Geophys Res 106:18857–18864

Chi PJ, Lee DH, Russell CT (2006) Tamao travel time of sudden impulses and its relationship to ionospheric convection vortices. J Geophys Res. doi:10.1029/2005JA011578

Chisham G, Orr D, Taylor MJ, Lühr H (1990) The magnetic and optical signature of a Pg pulsation. Planet Space Sci 38:1443–1456

Chisham G et al (2007) A decade of the Super Dual Auroral Radar Network (SuperDARN): scientific achievements, new techniques and future directions. Surv Geophys. doi:10.1007/s10712-007-9017-8

Claudepierre SG, Elkington SR, Wiltberger M (2008) Solar wind driving of magnetospheric ULF waves: pulsations driven by velocity shear at the magnetopause. J Geophys Res. doi:10.1029/2007JA012890

Clausen LBN, Yeoman TK (2009) Comprehensive survey of Pc4 and Pc5 band spectral content in cluster magnetic field data. Ann Geophys 27:3237–3248

Clausen LBN, Yeoman TK, Wright DM, Robinson TR, Dhillon RS, Gane SC (2008) First results of a ULF wave injected on open field lines by Space Plasma Exploration by Active Radar (SPEAR). J Geophys Res. doi:10.1029/2007JA012617

Clausen LBN, Yeoman TK, Fear RC, Behlke R, Lucek EA, Engebretson MJ (2009) First simultaneous measurements of waves generated at the bow shock in the solar wind, the magnetosphere and on the ground. Ann Geophys 27:357–371

Clilverd MA, Smith AJ, Thomson NR (1991) The annual variation in quiet time plasmaspheric electron density, determined from whistler mode group delays. Planet Space Sci 39:1059–1067

Clilverd MA et al (2003) In situ and ground-based intercalibration measurements of plasma density at $L = 2.5$. J Geophys Res. doi:10.1029/2003JA009866

Clilverd MA, Meredith NP, Horne RB, Glauert SA, Anderson RR, Thomson NR, Menk FW, Sandel BR (2007a) Longitudinal and seasonal variations in plasmaspheric electron density: implications for electron precipitation. J Geophys Res. doi:10.1029/2007JA012416

Clilverd MA, Rodger CJ, Millan RM, Sample JG, Kokorowski M, McCarthy MP, Ulich T, Raita T, Kavanagh AJ, Spanswick E (2007b) Energetic particle precipitation into the middle atmosphere triggered by a coronal mass ejection. J Geophys Res. doi:10.1029/2007JA012395

Constantinescu OD, Glassmeier K-H, Décréau PME, Fränz M, Fornaçon K-H (2007) Low frequency wave sources in the outer magnetosphere, magnetosheath, and near Earth solar wind. Ann Geophys 25:2217–2228

Constantinescu OD et al (2009) THEMIS observations of duskside compressional Pc5 waves. J Geophys Res. doi:10.1029/2008JA013519

Cornwall JM (1965) Cyclotron instabilities and electromagnetic emissions in the ultra low frequency and very low frequency ranges. J Geophys Res 70:61–69

Criswell D (1969) Pc 1 micropulsation activity and magnetospheric amplification of 0.2 to 5.0 Hz hydromagnetic waves. J Geophys Res 74:205–224

Cummings W, O'Sullivan R, Coleman P Jr (1969) Standing Alfvén waves in the magnetosphere. J Geophys Res 74:778–793

Degeling AW, Rankin R, Kabin K, Marchard R, Mann IR (2006) The effect of ULF compressional modes and field line resonances on relativistic electron dynamics. Planet Space Sci. doi:10.1016/j.pss.2006.04.039

Degeling AW, Ozeke LG, Rankin R, Mann IR, Kabin K (2008) Drift resonant generation of peaked relativistic electron distributions by Pc5 ULF waves. J Geophys Res. doi:10.1029/2007JA012411

Degeling AW, Rankin R, Kabin K, Rae IJ, Fenrich FR (2010) Modeling ULF waves in a compressed dipole magnetic field. J Geophys Res. doi:10.1029/2010JA015410

Demekhov AG (2007) Recent progress in understanding Pc1 pearl formation. J Atmos Sol Terr Phys 69:1609–1622

Demekhov AG, Belyaev PP, Isaev SV, Manninen J, Turunen T, Kangas J (2000) Modelling the diurnal evolution of the resonance spectral structure of the atmospheric noise background in the Pc1 frequency range. J Atmos Sol Terr Phys 62:257–265

Dent ZC, Mann IR, Menk FW, Goldstein J, Wilford CR, Clilverd MA, Ozeke LG (2003) A coordinated ground-based and IMAGE satellite study of quiet-time plasmaspheric density profiles. Geophys Res Lett. doi:10.1029/2003GL016946

Dent ZC, Mann IR, Goldstein J, Menk FW, Ozeke LG (2006) Plasmaspheric depletion, refilling, and plasmapause dynamics: a coordinated ground-based and IMAGE satellite study. J Geophys Res. doi:10.1029/2005JA011046

Denton R, Gallagher D (2000) Determining the mass density along magnetic field lines from toroidal eigenfrequencies. J Geophys Res 105:27717–27725

Denton RE et al. (2009) Field line distribution of density at L=4.8 inferred from observations by CLUSTER. Ann Geophys 27:705–724

Dovbyna BV (2007) On the earthquake effects in the regime of Pc1. J Atmos Sol Terr Phys 69:1765–1769

Dungey JW, Southwood DJ (1970) Ultra low frequency waves in the magnetosphere. Space Sci Rev. doi:10.1007/BF0017551

Dyrud L, Engebretson M, Posch J, Hughes W, Fukunishi H, Arnoldy R, Newell P, Horne R (1997) Ground observations and possible source regions of two types of Pc 1-2 micropulsations at very high latitudes. J Geophys Res 102:27011–27027

Dyrud LP, Behnke R, Kepko EL, Sulzer M, Zafke S (2008) Ionospheric ULF oscillations driven from above Arecibo. Geophys Res Lett. doi:10.1029/2008GL034073

Elkington SR (2006) A review of ULF interactions with radiation belt electrons. In: Takahashi K, Chi PJ, Denton RE, Lysak RL (eds) Magnetospheric ULF waves: synthesis and new directions. American Geophysical Union, Washington, DC, pp 177–193

Elkington SR, Hudson MK, Chan AA (2003) Resonant acceleration and diffusion of outer zone electrons in an asymmetric geomagnetic field. J Geophys Res. doi:10.1029/2001JA009202

Engebretson M, Zanetti L, Potemra T, Baumjohann W, Lühr H, Acuna M (1987) Simultaneous observations of Pc3-4 pulsations in the solar wind and in the Earth's magnetosphere. J Geophys Res. doi:10.1029/JA092iA09p10053

Engebretson MJ, Posch JL, Pilipenko VA, Chugunova OM (2006) ULF waves at very high latitudes. In: Takahashi K, Chi PJ, Denton RE, Lysak RL (eds) Magnetospheric ULF waves: synthesis and new directions. American Geophysical Union, Washington, DC, pp 137–156

Engebretson MJ et al (2007) Cluster observations of Pc1-2 waves and associated ion distributions during the October and November 2003 magnetic storms. Planet Space Sci 55:829–848

Engebretson MJ et al (2008a) Pc1-2 waves and energetic particle precipitation during and after magnetic storms: superposed epoch analysis and case studies. J Geophys Res. doi:10.1029/2007JA012362

Engebretson MJ, Posch JL, Westermann AM, Otto NJ, Slavin JA, Le G, Strangeway RJ, Lessard MR (2008b) Temporal and spatial characteristics of Pc1 waves observed by ST5. J Geophys Res. doi:10.1029/2008JA013145

Engebretson MJ, Moen J, Posch JL, Lu F, Lessard MC, Kim H, Lorentzen DA (2009) Searching for ULF signatures of the cusp: observations from search coil magnetometers and auroral imagers in Svalbard. J Geophys Res. doi:10.1029/2009JA014287

Eriksson PTI, Blomberg LG, Walker ADM, Glassmeier K-H (2005) Poloidal ULF oscillations in the dayside magnetosphere: a cluster study. Ann Geophys 23:2679–2686

Eriksson PTI, Blomberg LG, Glassmeier K-H (2006a) Cluster satellite observations of mHz pulsations in the dayside magnetosphere. Adv Space Res 38:1730–1737

Eriksson PTI, Walker ADM, Stephenson JAE (2006b) A statistical correlation of Pc5 pulsations and solar wind pressure oscillations. Adv Space Res 38:1763–1771

Erikkson PTI, Blomberg LG, Schaefer S, Glassmeier K-H (2008) Sunward propagating Pc5 waves observed on the post-midnight magnetospheric flank. Ann Geophys 26:1567–1579

Erlandson RE, Anderson BJ (1996) Pc 1 waves in the ionosphere: a statistical study. J Geophys Res 101:7843–7857

Erlandson RE, Mursula K, Bösinger T (1996) Simultaneous ground-satellite observations of structured Pc 1 pulsations. J Geophys Res 101:27149–27156

Fenrich FR, Waters CL (2008) Phase coherence analysis of a field line resonance and solar wind oscillation. Geophys Res Lett. doi:10.1029/2008GL035430

Feygin FZ, Nekrasov AK, Pikkarainen T, Raita T, Prikner K (2007) Pc1 pearl waves with magnetosonic dispersion. J Atmos Sol Terr Phys 69:1644–1650

Francia P, Villante U (1997) Some evidence of ground power enhancements at frequencies of global magnetospheric modes at low latitude. Ann Geophys 15:17–23

Francia P, De Laurentis M, Vellante M, Paincatelli A (2009) ULF geomagnetic pulsations at different latitudes in Antarctica. Ann Geophys 27:3621–3629

Fraser BJ (1982) Pc1-2 observations of heavy ion effects by synchronous satellite ATS-6. Planet Space Sci 30:1229–1238

Fraser BJ (2007) ULF waves: exploring the Earth's magnetosphere. In: Duldig M (ed) Advances in geosciences, vol 14. Solar Terrestrial, World Scientific, Singapore, pp 1–32

Fraser BJ, McPherron RL (1982) Pc 1-2 magnetic pulsation spectra and heavy ion effects at synchronous orbit: ATS 6 results. J Geophys Res 87:4560–4566

Fraser BJ, Singer HJ, Hughes WJ, Wygant JR, Anderson RR, Hu YD (1996) CRRES Poynting vector observations of electromagnetic ion cyclotron waves near the plasmapause. J Geophys Res 101:15331–15343

Fraser BJ, Horwitz JL, Slavin JA, Dent ZC, Mann IR (2005) Heavy ion mass loading of the geomagnetic field near the plasmapause and ULF wave implications. Geophys Res Lett. doi:10.1029/2004GL021315

Fraser-Smith AC (1979) A weekend increase in geomagnetic activity. J Geophys Res 84:2089–2096

Fraser-Smith AC (2008) Ultralow-frequency magnetic fields preceding large earthquakes. Eos Trans AGU. doi:10.1029/2008EO230007

Fraser-Smith AC, Bernardi A, McGill PR, Ladd ME, Helliwell RA, Villard OG Jr (1990) Low-frequency magnetic field measurements near the epicenter of the Ms 7.1 Loma Prieta earthquake. Geophys Res Lett 17:1465–1468

Frey HU, Haerendel G, Mende SB, Forrester WT, Immel TJ, Østgaard N (2004) Subauroral morning proton spots (SAMPS) as a result of plasmapause-ring current interaction. J Geophys Res. doi:10.1029/2004JA010516

Fuselier SA, Gary SP, Thomsen MF, Claflin ES, Hubert B, Sandel BR, Immel T (2004) Generation of transient dayside subauroral proton precipitation. J Geophys Res. doi:10.1029/2004JA010393

Gamayunov KV, Khazanov GV (2008) Crucial role of ring current H+ in electromagnetic ion cyclotron wave dispersion relation: results from global simulations. J Geophys Res. doi:10.1029/2008JA013494

Gamayunov KV, Khazanov GV, Liemohn MW, Fok MC, Ridley AJ (2009) Self-consistent model of magnetospheric electric field, ring current, plasmasphere, and electromagnetic ion cyclotron waves: Initial results. J Geophys Res. doi:10.1029/2008JA013597

Ganguly S, Behnke R (1982) Short-period fluctuations in F region ionization observed at Arecibo. J Geophys Res 87:261–264

Gjerloev JW et al (2007) Observations of Pi2 pulsations by the Wallops HF radar in association with substorm expansion. Geophys Res Lett. doi:10.1029/2007GL030492

Gomberoff L (2008) Electrostatic instabilities triggered by finite amplitude Alfvén/ion-cyclotron waves and relative drifts among the ion components in the magnetosphere. J Geophys Res. doi:10.1029/2008JA013378

Greenstadt EW, Mellott MM, McPherron RL, Russell CT, Singer HJ, Knecht DJ (1983) Transfer of pulsation-related wave activity across the magnetopause: observations of corresponding spectra by ISEE1 and ISEE2. Geophys Res Lett 10:659–662

Greenwald RA, Walker ADM (1980) Energetics of long period resonant hydromagnetic waves. Geophys Res Lett 7:745–748

Grew RS, Menk FW, Clilverd MA, Sandel BR (2007) Mass and electron densities in the inner magnetosphere during a prolonged disturbed interval. Geophys Res Lett. doi:10.1029/2006GL028254

Guglielmi A, Zotov O (2007) The human impact on Pc1 wave activity. J Atmos Sol Terr Phys 69:1753–1758

Gul'yel'mi AV (1966) Plasma concentration at great heights according to data on toroidal fluctuations of the magnetosphere. Geomagn Aeron 6:98

Hansen HJ, Fraser BJ, Menk FW, Hu Y-D, Newell PT, Meng C-I, Morris RJ (1992) High-latitude Pc1 bursts arising in the dayside boundary layer region. J Geophys Res 97: 3993–4008

Hansen HJ, Fraser BJ, Menk FW, Erlandson RR (1995) Ground-satellite observations of Pc-1 magnetic pulsations in the plasma trough. J Geophys Res 100:7971–7985

Hasegawa H et al (2009) Kelvin-Helmholtz waves at the Earth's magnetopause: multiscale development and associated reconnection. J Geophys Res. doi:10.1029/2009JA014042

Hattingh SKF, Sutcliffe PR (1987) Pc3 pulsation eigenperiod determination at low latitudes. J Geophys Res 92:12433–12436

Hattori K, Serita A, Gotoh K, Yoshino C, Harada M, Isezaki N, Hayakawa M (2004a) ULF geomagnetic activity associated with the 2000 Izu Islands earthquake swarm. Jpn Phys Chem Earth 29:425–435

Hattori K et al (2004b) ULF geomagnetic field measurements in Japan and some recent results associated with Iwateken Nairiku Hokubu earthquakes in 1998. Phys Chem Earth 29:481–494

Hattori K, Serita A, Yoshino C, Hayakawa M, Isezaki N (2006) Singular spectral analysis and principal component analysis for signal discrimination of ULF geomagnetic data associated wth 2000 Izu Island Earthquake Swarm. Phys Chem Earth 31:281–291

Hayakawa M, Pulinets S, Parrot M, Molchanov O (2006) Recent progress in seismo-electromagnetic and related phenomena. Phys Chem Earth 31:129–131

Hebden SR, Robinson TR, Wright DM, Yeoman T, Raita T, Bösinger T (2005) A quantitative analysis of the diurnal evolution of the Ionosphere Alfvén resonator magnetic resonance features and calculation of changing IAR parameters. Ann Geophys 23:1711–1721

Heilig B, Lühr H, Rother M (2007) Comprehensive study of ULF upstream waves observed in the topside ionosphere by CHAMP and on the ground. Ann Geophys 25: 737–754

Heilig B, Lotz S, Verö J, Sutcliffe P, Reda J, Pajunpää K, Raita T (2010) Empirically modelled Pc3 activity based on solar wind parameters. Ann Geophys 28:1703–1722

Horita RE, Barfield JN, Heacock RR, Kangas J (1979) IPDP source regions and resonant proton energies. J Atmos Sol Terr Phys 41:293–309

Horne RB et al (2005) Wave acceleration of electrons in the Van Allen radiation belts. Nature. doi:10.1038/nature03939

Horne RB, Thorne RM, Glauert SA, Meredith NP, Pokhotelov D, Santolik O (2007) Electron acceleration in the Van Allen radiation belts by fast magnetosonic waves. Geophys Res Lett. doi:10.1029/2007GL030267

Howard TA, Menk FW (2001) Propagation of 10–50 mHz ULF waves with high spatial coherence at high latitudes. Geophys Res Lett 28:231–234

Howard TA, Menk FW (2005) Ground observations of high-latitude Pc3-4 ULF waves. J Geophys Res. doi:10.1029/2004JA010417

Hughes WJ (1974) The effect of the atmosphere and ionosphere on long period magnetospheric micropulsations. Planet Space Sci 22:1157–1172

Hughes WJ (1983) Hydromagnetic waves in the magnetosphere. In: Carovillano RL, Forbes JM (eds) Solar-terrestrial physics. Reidel D, Dordrecht, pp 453–477

Hughes W, McPherron R, Barfield J (1978) Geomagnetic pulsations observed simultaneously on three geostationary satellites. J Geophys Res 83:1109–1116

Jacobs JA, Watanabe T (1964) Micropulsation whistlers. J Atmos Sol Terr Phys 26:825–829

Jordanova VK, Spasojević M, Thomsen MF (2007) Modeling the electromagnetic ion cyclotron wave-induced formation of detached subauroral proton arcs. J Geophys Res. doi:10.1029/2006JA012215

Jordanova VK, Albert J, Miyoshi Y (2008) Relativistic electron precipitation by EMIC waves from self-consistent global simulations. J Geophys Res. doi:10.1029/2008JA013239

Kabin K, Rankin R, Mann IR, Degeling AW, Marchand R (2007) Polarization properties of standing shear Alfvén

waves in non-axisymmetric background magnetic fields. Ann Geophys 25:815–822
Kale ZC, Mann IR, Waters CL, Goldstein J, Menk FW, Ozeke LG (2007) Ground magnetometer observation of a cross-phase reversal at a steep plasmapause. J Geophys Res. doi:10.1029/2007JA012367
Kale ZC, Mann IR, Waters CL, Vellante M, Zhang TL, Honary F (2009) Plasmaspheric dynamics resulting from the Hallowe'en 2003 geomagnetic storm. J Geophys Res. doi:10.1029/2009JA014194
Karatay S, Arikan F, Arikan O (2010) Investigation of total electron content variability due to seismic and geomagnetic disturbances in the ionosphere. Radio Sci. doi:10.1029/2009RS004313
Kataoka R, Miyoshi Y, Morioka A (2009) Hilbert-Huang transform of geomagnetic pulsations at auroral expansion onset. J Geophys Res. doi:10.1029/2009JA014214
Keiling A, Parks GK, Wygant JR, Dombeck J, Mozer FS, Russell CT, Streltsov AV, Lotko W (2005) Some properties of Alfvén waves: observations in the tail lobes and the plasma sheet boundary layer. J Geophys Res. doi:10.1029/2004JA010907
Kepko L, Spence HE (2003) Observations of discrete, global magnetospheric oscillations directly driven by solar wind velocity variations. J Geophys Res. doi:10.1029/2002JA009676
Kessel RL (2008) Solar wind excitation of Pc5 fluctuations in the magnetosphere and on the ground. J Geophys Res. doi:10.1029/2007JA012255
Kessel RL, Mann IR, Fung SF, Milling DK, O'Connell N (2004) Correlation of Pc5 wave power inside and outside the magnetosphere during high speed streams. Ann Geophys 21:629–641
Khazanov GV, Gamayunov KV (2007) Effect of electromagnetic ion cyclotron wave normal angle distribution on relativistic electron scattering in the outer radiation belt. J Geophys Res. doi:10.1029/2007JA012282
Kim K-H, Lee DH, Takahashi K, Russell CT, Moon YJ, Yumoto K (2005) Pi2 pulsations observed from the Polar satellite outside the plasmapause. Geophys Res Lett. doi:10.1029/2005GL023872
Kivelson MG (2006) ULF waves from the ionosphere to the outer planets. In: Takahashi K, Chi PJ, Denton RE, Lysak RL (eds) Magnetospheric ULF waves: synthesis and new directions. American Geophysical Union, Washington, DC, pp 11–30
Kivelson MG, Southwood DJ (1985) Resonant ULF waves: a new interpretation. Geophys Res Lett 12:49–52
Kivelson MG, Southwood DJ (1986) Coupling of global magnetospheric MHD eigenmodes to field line resonances. Geophys Res Lett 91:4345–4351
Kleimenova NG, Kozyreva OV, Breus TK, Rapoport SI (2007) Pc1 geomagnetic pulsations as a potential hazard of the myocardial infarction. J Atmos Sol Terr Phys 69: 1759–1764
Klimushkin D (1998) Resonators for hydromagnetic waves in the magnetosphere. J Geophys Res 103:2369–2375
Korotova GI, Sibeck DG, Kondratovich V, Angelopolous V, Constantinescu OD (2009) THEMIS observations of compressional pulsations in the dawn-side magnetosphere: a case study. Ann Geophys 27:3725–3735
Kozlov DA, Leonovich AS (2008) The structure of field line resonances in a dipole magnetosphere with moving plasma. Ann Geophys 26:689–698
Krauss-Varban D (1994) Bow shock and magnetosheath simulations: wave transport and kinetic properties. In: Engebretson MJ, Takahashi K, Scholer M (eds) Solar wind sources of magnetospheric Ultra-Low Frequency waves. American Geophysical Union, Washington, DC, pp 121–134
Kurazhkovskaya NA, Klain BI, Dovbyna BV (2007) Patterns of simultaneous observations of high-latitude magnetic impulses (MIEs) and impulsive bursts in the Pc1-2 band. J Atmos Sol Terr Phys 69:1680–1689
Le G, Russell CT (1996) Solar wind control of upstream wave frequency. J Geophys Res 101:2571–2575
Lee DH, Lysak R (1999) MHD waves in a three-dimensional dipolar magnetic field: a search for Pi2 pulsations. J Geophys Res 104:28691–28699
Lee D-H, Takahashi K (2006) MHD eigenmodes in the inner magnetosphere. In: Takahashi K, Chi PJ, Denton RE, Lysak RL (eds) Magnetospheric ULF waves: synthesis and new directions. American Geophysical Union, Washington, DC, pp 73–90
Lee EA, Mann IR, Loto'aniu, TM, Dent ZC (2007)Global Pc5 pulsations observed at unusually low L during the great magnetic storm of 24 March 1991. J Geophys Res. doi:10.1029/2006JA011872
Lee D-H, Johnson JR, Kim K, Kim K-S (2008) Effects of heavy ions on ULF wave resonances near the equatorial region. J Geophys Res. doi:10.1029/2008JA013088
Liou K, Takahashi K, Newell PT, Yumoto K (2008) Polar Ultraviolet Imager observations of solar wind-driven ULF auroral pulsations. Geophys Res Lett. doi:10.1029/2008GL034953
Liu YH, Fraser BJ, Ables ST, Dunlop MW, Zhang BC, Liu RY, Zong QG (2008) Phase structure of Pc3 waves observed by Cluster and ground stations near the cusp. J Geophys Res. doi:10.1029/2007JA012754
Liu W, Sarris TE, Li X, Elkington SR, Ergun R, Angelopolous V, Bonnell J, Glassmeier KH (2009a) Electric and magnetic field observations of Pc4 and Pc5 pulsations in the inner magnetosphere: a statistical study. J Geophys Res. doi:10.1029/2009JA014243
Liu YH, Fraser BJ, Ables ST, Zhang BC, Liu RY, Dunlop MW, Waterman J (2009b) Transverse scale size of Pc3 ULF waves near the exterior cusp. J Geophys Res. doi:10.1029/2008JA013971
Lorentzen KR, McCarthy MP, Parks GK, Foat JE, Millan RM, Smith DM, Lin RP, Treilhou JP (2000) Precipitation of relativistic electrons by interaction with electromagnetic ion cyclotron waves. J Geophys Res 105:5381–5389
Loto'aniu TM, Waters CL, Fraser BJ, Samson JC (1999) Plasma mass density in the plasmatrough: comparison using ULF waves and CRRES. Geophys Res Lett 26:3277–3280
Loto'aniu TM, Fraser BJ, Waters CL (2005) The propagation of electromagnetic ion cyclotron wave energy in the magnetosphere. J Geophys Res. doi:10.1029/2004JA010816
Loto'aniu TM, Thorne RM, Fraser BJ, Summers D (2006) Estimating relativistic electron pitch angle scattering rates using properties of the electromagnetic ion cyclotron wave spectrum. J Geophys Res. doi:10.1029/2005JA011452

Loto'aniu TM, Fraser BJ, Waters CL (2009) The modulation of electromagnetic ion cyclotron waves by Pc5 ULF waves. Ann Geophys 27:121–130

Lu JY, Rankin R, Marchand R, Rae IJ, Wang W, Solomon SC, Lei J (2007) Electrodynamics of magnetosphere-ionosphere coupling and feedback on magnetospheric field line resonances. J Geophys Res. doi:10.1029/2006JA012195

Lysak RL, Song Y (2008) Propagation of kinetic Alfvén waves in the ionospheric Alfvén resonator in the presence of density cavities. Geophys Res Lett. doi:10.1029/2008GL035728

Maeda N et al (2008) Simultaneous observations of the plasma density on the same field line by the CPMN ground magnetometers and the cluster satellites. Adv Space Res. doi:10.1016/j.asr.2008.04.016

Manchester RN (1970) Propagation of hydromagnetic emissions in the ionospheric duct. Planet Space Sci 18:299–307

Mann IR, Wright AN, Mills KJ, Nakariakov VM (1999) Excitation of magnetospheric waveguide modes by magnetosheath flows. J Geophys Res 104:333–353

Mann IR, O'Brien TP, Milling DK (2004) Correlations between ULF wave power, solar wind speed, and relativistic electron flux in the magnetosphere: solar cycle dependence. J Atmos Solar-Terr Phys. doi:10.1016/j.jastp.2003.10.002

Mathie RA, Mann IR (2001) On the solar wind control of Pc5 ULF pulsation power at mid-latitudes: Implications for MeV electron acceleration in the outer radiation belt. J Geophys Res. doi:10.1029/2001JA000002

Mathie RA, Mann IR, Menk FW, Orr D (1996) Pc5 ULF pulsations associated with waveguide modes observed with the IMAGE magnetometer array. J Geophys Res 104: 7025–7036

Matsuoka H, Takahashi K, Kokubun S, Yumoto K, Yamamoto T, Solovyev SI, Vershinin EF (1997) Phase and amplitude structure of Pc 3 magnetic pulsations as determined from multipoint observations. J Geophys Res 102:2391–2403

Matveyeva ET, Shchepetnov RV (2007) Temporal characteristics and medical aspects of Pc1 geomagnetic pulsations. J Atmos Sol Terr Phys 69:1747–1752

McCollough JP, Elkington SR, Baker DN (2009) Modeling EMIC wave growth during the compression event of 29 June 2007. Geophys Res Lett. doi:10.1029/2009GL039985

Menk FW (1992) Characterization of ionospheric Doppler oscillations in the Pc3-4 and Pi2 magnetic pulsation frequency range. Planet Space Sci 40:495–507

Menk FW, Cole KD, Devlin JD (1983) Associated geomagnetic and ionospheric variations. Planet Space Sci 31:569–572

Menk FW, Fraser BJ, Hansen HJ, Newell PT, Meng C-I, Morris RJ (1992) Identification of the magnetospheric cusp and cleft using Pc1-2 ULF pulsations. J Atmos Sol Terr Phys 54:1021–1042

Menk FW, Fraser BJ, Hansen HJ, Newell PT, Meng C-I, Morris RJ (1993) Multistation observations of Pc1-2 ULF pulsations in the vicinity of the polar cusp. J Geomagnetism Geoelectricity 45:1159–1173

Menk FW, Marshall RA, Waters CL, Dunlop IS, Fraser BJ (1995) Geomagnetic pulsations in the ionosphere. Adv Space Res 16:121–129

Menk FW, Orr D, Clilverd MA, Smith AJ, Waters CL, Milling DK, Fraser BJ (1999) Monitoring spatial and temporal variations in the dayside plasmasphere using geomagnetic field line resonances. J Geophys Res. doi:10.1029/1999JA900205

Menk FW, Waters CL, Fraser BJ (2000) Field line resonances and waveguide modes at low latitudes. J Geophys Res. doi:10.1029/1999JA900268

Menk FW, Yeoman TK, Wright DM, Lester M, Honary F (2003) High-latitude observations of impulse-driven ULF pulsations in the ionosphere and on the ground. Ann Geophys 21:559–576

Menk FW, Mann IR, Smith AJ, Waters CL, Clilverd MA, Milling DK (2004) Monitoring the plasmapause using geomagnetic field line resonances. J Geophys Res. doi:10.1029/2003JA010097

Menk FW, Clilverd MA, Yearby KH, Milinevski G, Thomson NR, Rose MC (2006) ULF Doppler oscillations of $L = 2.5$ flux tubes. J Geophys Res. doi:10.1029/2005JA011192

Menk FW, Waters CL, Dunlop IS (2007) ULF Doppler oscillations in the low latitude ionosphere. Geophys Res Lett. doi:10.1029/2007GL029300

Meredith NP, Thorne RM, Horne RB, Summers D, Fraser BJ, Anderson RR (2003) Statistical analysis of relativistic electron energies for cyclotron resonance with EMIC waves observed on CRRES. J Geophys Res. doi:10.1029/2002JA009700

Mier-Jedrzejowicz WAC, Southwood DJ (1979) The east-west phase structure of mid-latitude geomagnetic pulsations in the 8–25 mHz band. Planet Space Sci 27:617–630

Millan RM, Thorne RM (2007) Review of radiation belt relativistic electron losses. J Atmos Sol Terr Phys. doi:10.1016/j.jastp.2006.06.019

Milling DK, Mann IR, Menk FW (2001) Diagnosing the plasmapause with a network of closely spaced ground-based magnetometers. Geophys Res Lett 28:115–118

Milling DK, Rae J, Mann IR, Murphy KR, Kale A, Russell CT, Angelopolous V, Mende S (2008) Ionospheric localization and expansion of long-period Pi1 pulsations at substorm onset. Geophys Res Lett. doi:10.1029/2008GL033672

Miyoshi Y, Sakaguchi K, Shiokawa K, Evans D, Albert J, Connors M, Jordanova V (2008) Precipitation of radiation belt electrons by EMIC waves, observed from ground and space. Geophys Res Lett. doi:10.1029/2008GL035727

Morley SK, Ables ST, Sciffer MD, Fraser BJ (2009) Multipoint observations of Pc1-2 waves in the afternoon sector. J Geophys Res. doi:10.1029/JA014162

Moser, T-J (1991) Shortest path calculation of seismic rays. Geophysics 56:59–67

Mthembu SH, Malinga SB, Walker ADM, Magnus L (2009) Characterization of ultra low frequency (ULF) pulsations and the investigation of their possible source. Ann Geophys 27:3287–3296

Murphy KR, Rae IJ, Mann IR, Milling DK, Watt CEJ, Ozeke L, Frey HU, Angelopoulos V, Russell CT (2009) Wavelet-based ULF wave diagnosis of substorm expansion phase onset. J Geophys Res. doi:10.1029/2008JA013548

Mursala K (2007) Satellite observations of Pc1 pearl waves: the changing paradigm. J Atmos Sol Terr Phys 69:1623–1634

Mursula K, Rasinkangas R, Bösinger T, Erlandson R, Lindqvist PA (1997) Non-bouncing Pc 1 wave bursts. J Geophys Res 102:17611–17624

Ndiitwani DC, Sutcliffe PR (2009) The structure of low-latitude Pc3 pulsations observed by CHAMP and on the ground. Ann Geophys 27:1267–1277

Ndiitwani DC, Sutcliffe PR (2010) A study of L-dependent Pc3 pulsations observed by low Earth orbiting CHAMP satellite. Ann Geophys 28:407–414

Nishida A (1964) Ionospheric screening effect and storm sudden commencement. J Geophys Res 69:1861–1874

Nosé M, Iyemori T, Takeda M, Kamei T, Milling DK, Orr D, Singer HJ, Worthington EW, Sumitomo N (1998) Automated detection of Pi2 pulsations using wavelet analysis: 1. Method and an application for substorm monitoring. Earth Planets Space 50:773–783

Obana Y, Menk FW, Sciffer MD, Waters CL (2008) Quarter-wave modes of standing Alfvén waves detected by crossphase analysis. J Geophys Res. doi:10.1029/2007JA012917

Obana Y, Menk FW, Yoshikawa I (2010) Plasma refilling rates for $L = 2.3$–3.8 flux tubes. J Geophys Res. doi:10.1029/2009JA014191

Obayashi T (1965) Hydromagnetic whistlers. J Geophys Res 70:1069–1078

Obayashi T, Jacobs JA (1958) Geomagnetic pulsations and the Earth's outer atmosphere. Geophys J R Astron Soc 1: 53–63

O′Brien T, McPherron R, Sornette D, Reeves G, Friedel R, Singer H (2001) Which magnetic storms produce relativistic electrons at geosynchronous orbit? J Geophys Res 106:15533–15544

O'Brien TP et al (2003) Energization of relativistic electrons in the presence of ULF power and MeV microbursts: Evidence for dual ULF and VLF acceleration. J Geophys Res. doi:10.1029/2002JA009784

Odera TJ (1986) Solar wind controlled pulsations: a review. Rev Geophys. doi:10.1029/RG024i001p00055

Odera TJ, Van Swol D, Russell CT, Green CA (1991) Pc 3,4 magnetic pulsations observed simultaneously in the magnetosphere and at multiple ground stations. Geophys Res Lett 18:1671–1674

Olson JV, Lee LC (1983) Pc1 wave generation by sudden impulses. Planet Space Sci 31:295–302

Orr D (1984) Magnetospheric hydromagnetic waves: their eigenperiods, amplitudes and phase variations; a tutorial introduction. J Geophys 55:76–84

Ozeke LG, Mann IR (2008) Energization of radiation belt electrons by ring current ion driven ULF waves. J Geophys Res. doi:10.1029/2007JA012468

Ozeke LG, Mann IR, Rae IJ (2009) Mapping guided Alfvén wave magnetic field amplitudes observed on the ground to equatorial electric field amplitudes in space. J Geophys Res. doi:10.1029/2008JA013041

Pahud DM, Rae IJ, Mann IR, Murphy KR, Amalraj V (2009) Ground-based Pc5 ULF wave power: solar wind speed and MLT dependence. J Atmos Sol Terr Phys 71:1082–1092. doi:10.1016/jastp.2006.12.004

Pilipenko V, Federov E, Heilig B, Engebretson MJ (2008) Structure of ULF Pc3 waves at low altitudes. J Geophys Res. doi:10.1029/2008JA013243

Plaschke F, Glassmeier K-H, Auster HU, Constantinescu OD, Magnes W, Angelopolous V, Sibeck DG, McFadden JP (2008) Statistical analysis of ground based magnetic field measurements with the field line resonance detector. Ann Geophys 26:3477–3489

Plaschke P, Glassmeier KH, Auster HU, Constantinescu OD, Magnes W, Angelopoulos V, Sibeck DG, McFadden JP (2009a) Standing Alfvén waves at the magnetopause. Geophys Res Lett. doi:10.1029/2008GL036411

Plaschke F, Glassmeier K-H, Sibeck DG, Auster HU, Constantinescu OD, Angelopolous V, Magnes W (2009b) Magnetopause surface oscillation frequencies at different solar wind conditions. Ann Geophys 27:4521–4532

Ponomarenko PV, Menk FW, Waters CL (2003) Visualization of ULF waves in SuperDARN data. Geophys Res Lett. doi:10.1029/2003GL017757

Ponomarenko PV, Menk FW, Waters CL, Sciffer MD (2005) Pc3-4 ULF waves observed by the SuperDARN TIGER radar. Ann Geophys 23:1271–1280

Poole AWV, Sutcliffe PR (1987) Mechanisms for observed total electron content pulsations at mid latitudes. J Atmos Sol Terr Phys 49:231–236

Poole AWV, Sutcliffe PR, Walker ADM (1988) The relationship between ULF geomagnetic pulsations and ionospheric Doppler oscillations: derivation of a model. J Geophys Res 93:14656–14664

Potemra TA, Lühr H, Zanetti LJ, Takahashi K, Erlandson RE, Marklund GT, Block LP, Blomberg LG, Lepping RP (1989) Multisatellite and ground-based observations of transient ULF waves. J Geophys Res 94:2543–2554

Poulter E, Nielsen E (1982) The hydromagnetic oscillation of individual shells of the geomagnetic field. J Geophys Res 87:10432–10438

Poulter EM, Allan W, Bailey GJ (1988) ULF pulsation eigenperiods within the plasmasphere. Planet Space Sci 36: 185–196

Price IA, Waters CL, Menk FW, Bailey GJ, Fraser BJ (1999) A technique to investigate plasma mass density in the topside ionosphere using ULF waves. J Geophys Res 104:12723–12732

Prikryl P, Greenwald R, Sofko G, Villain J, Ziesolleck C, Friis-Christensen E (1998) Solar wind driven pulsed magnetic reconnection at the dayside magnetopause, Pc5 compressional oscillations, and field line resonances. J Geophys Res 103:17307–17322

Pu Z, Kivelson MG (1983) Kelvin-Helmholtz instability at the magnetopause: solution for compressible plasma. J Geophys Res 88:841–852

Rae IJ, Watt CEJ, Fenrich FR, Mann IR, Ozeke LG, Kale A (2007) Energy deposition in the ionosphere through a global field line resonance. Ann Geophys 25:2529–2539

Rankin R, Kabin K, Marchand R (2006) Alfvénic field line resonances in arbitrary magnetic field topology. Adv Space Res 38:1720–1729

Rauch J, Roux A (1982) Ray tracing of ULF waves in a multicomponent magnetospheric plasma: consequences for the generation mechanism of ion cyclotron waves. J Geophys Res 87:8191–8198

Rodger C, Thomson N, Dowden R (1996) A search for ELF/VLF activity associated with earthquakes using ISIS satellite data. J Geophys Res 101:13369–13378

Rodger CJ, Raita T, Clilverd MA, Seppälä A, Dietrich S, Thomson NR, Ulich T (2008) Observations of relativistic electron precipitation from the radiation

belts driven by EMIC waves. Geophys Res Lett. doi:10.1029/2008GL034804
Rother M, Schlegel K, Lühr H (2007) CHAMP observations of intense kilometer-scale field-aligned currents, evidence for an ionospheric Alfvén resonator. Ann Geophys 25:1603–1615
Russell CT, Luhmann JG, Odera TJ, Stuart WF (1983) The rate of occurrence of dayside Pc3,4 pulsations: The *L*-value dependence of the IMF cone angle effect. Geophys Res Lett 10:663–666
Sakaguchi K, Shiokawa K, Ieda A, Miyoshi Y, Otsuka Y, Ogawa T, Connors M, Donovan EF, Rich FJ (2007) Simultaneous ground and satellite observations of an isolated proton arc at subauroral latitudes. J Geophys Res. doi:10.1029/2006JA012135
Sakurai T, Tonegawa Y, Kitagawa T, Yumoto K, Yamomoto T, Kokubun S, Mukai T, Tsuruda T (1999) Dayside magnetopause Pc3 and Pc5 ULF waves observed by the GEOTAIL satellite. Earth Planets Space 51:965–978
Samson JC, Harrold BG, Ruohoniemi JM, Greenwald RA, Walker ADM (1992) Field line resonances associated with MHD waveguides in the magnetosphere. Geophys Res Lett 25:3701–3704
Samson JC, Waters CL, Menk FW, Fraser BJ (1995) Fine structure in the spectra of low latitude field line resonances. Geophys Res Lett 22:2111–2114
Santarelli L, Lepidi S, Cafarella L (2007) Propagation of low frequency geomagnetic field fluctuations in Antarctica: comparison between two polar cap stations. Ann Geophys 25:2405–2412
Sarris TE, Loto'aniu TM, Li X, Singer HJ (2007) Observations at geosynchronous orbit of a persistent Pc5 geomagnetic pulsation and energetic electron flux modulations. Ann Geophys 25:1653–1667
Sarris TE et al (2009a)Characterization of ULF pulsations by THEMIS. Geophys Res Lett. doi:10.1029/2008GL036732
Sarris TE, Li X, Singer HJ (2009b) A long-duration narrowband Pc5 pulsation. J Geophys Res. doi:10.1029/2007JA012660
Sarris TE, Wright AN, Li X (2009c) Observations and analysis of Alfvén wave phase mixing in the Earth's magnetosphere. J Geophys Res. doi:10.1029/2008JA013606
Schäfer S, Glassmeier KH, Eriksson PTI, Pierrard V, Fornaçon KH, Blomberg LG (2007) Spatial and temporal characteristics of poloidal waves in the terrestrial plasmasphere: a CLUSTER study. Ann Geophys 25:1011–1024
Schäfer S, Glassmeier KH, Eriksson PTI, Pierrard V, Fornaçon KH, Blomberg LG (2008) Spatio-temporal structure of a poloidal Alfvén wave detected by Cluster adjacent to the dayside plasmapause. Ann Geophys 26:1805–1817
Schulz M (1996) Eigenfrequencies of geomagnetic field lines and implications for plasma density modeling. J Geophys Res 101:17385–17397
Schwartz SJ, Burgess D, Moses JJ (1996) Low frequency waves in the Earth's magnetosheath: present status. Ann Geophys 14:1134–1150
Sciffer MD, Waters CL (2002) Propagation of ULF waves through the ionosphere: Analytic solutions for oblique magnetic fields. J Geophys Res. doi:10.1029/2001JA000184
Sciffer MD, Waters CL, Menk FW (2004) Propagation of ULF waves through the ionosphere: inductive effect for oblique magnetic fields. Ann Geophys 22:1155–1169
Sciffer MD, Waters CL, Menk FW (2005) A numerical model to investigate the polarisation azimuth of ULF waves through an ionosphere with oblique magnetic fields. Ann Geophys 23:3457–3471
Seyler CE, Liu K (2007) Particle energization by oblique inertial Alfvén waves in the auroral region. J Geophys Res. doi:10.1029/2007JA012412
Shprits Y (2009) Potential waves for pitch-angle scattering of near-equatorially mirroring energetic electrons due to the violation of the second adiabatic invariant. Geophys Res Lett. doi:10.1029/2009GL038322
Shprits Y, Elkington SR, Meredith NP, Subbotin DA (2008a) Review of modelling of losses and sources of relativistic electrons in the outer radiation belt I: radial transport. J Atmos Sol Terr Phys 70:1679–1693
Shprits Y, Subbotin DA, Meredith NP, Elkington SR (2008b) Review of modelling and losses of relativistic electrons in the outer radiation belt II: local acceleration and loss. J Atmos Sol Terr Phys 70:1694–1713
Sibeck DG, Korotova GI (1996) Occurrence patterns for transient magnetic field signatures at high latitudes. J Geophys Res 101:13413–13428
Singer HJ, Southwood DJ, Walker RJ, Kivelson MG (1981) Alfven wave resonances in a realistic magnetospheric magnetic field geometry. J Geophys Res 86:4589–4596
Skone S (2009) Using GPS TEC measurements to detect geomagnetic Pc 3 pulsations. Radio Sci. doi:10.1029/2008RS004106
Smirnova NA, Hayakawa M (2007) Fractal characteristics of the ground-observed ULF emissions in relation to geomagnetic and seismic activities. J Atmos Sol Terr Phys 69:1833–1841
Spasojević M, Frey HU, Thomsen MF, Fuselier SA, Gary SP, Sandel BR, Inan US (2004) The link between a detached subauroral proton arc and a plasmaspheric plume. Geophys Res Lett. doi:10.1029/2003GL018389
Stephenson JA, Walker ADM (2002) HF radar observations of Pc5 ULF pulsations driven by the solar wind. J Geophys Res. doi:10.1029/2001GL014291
Summers D, Ni B, Meredith NP (2007) Timescales for radiation belt electron acceleration and loss due to resonant wave-particle interactions: 2. Evaluation for VLF chorus, ELF hiss, and electromagnetic ion cyclotron waves. J Geophys Res. doi:10.1029/2006JA011993
Sutcliffe P, Poole A (1989) Ionospheric Doppler and electron velocities in the presence of ULF waves. J Geophys Res 94:13505–13514
Takagi K, Hashimoto C, Hasegawa H, Fujimoto M, Tan-Dokoro R (2006) Kelvin-Helmholtz instability in a magnetotail flank-like geometry: three-dimensional MHD simulations. J Geophys Res. doi:10.1029/2006JA011631
Takahashi K, Denton RE (2007) Magnetospheric seismology using multi-harmonic toroidal waves observed at geosynchronous orbit. J Geophys Res. doi:10.1029/2006JA011709
Takahashi K, Ukhorskiy AY (2007) Solar wind control of Pc5 power at geosynchronous orbit. J Geophys Res. doi:10.1029/2007JA012483
Takahashi K, Ukhorskiy AY (2008) Timing analysis of the relationship between solar wind parameters and geosynchronous Pc5 amplitude. J Geophys Res. doi:10.1029/2008JA013327

Takahashi K, McPherron R, Terasawa T (1984) Dependence of the spectrum of Pc 3-4 pulsations on the interplanetary magnetic field. J Geophys Res 89:2770–2780

Takahashi K, Higbie P, Baker D (1985) Azimuthal propagation and frequency characteristic of compressional Pc 5 waves observed at geostationary orbit. J Geophys Res 90:1473–1485

Takahashi K, Denton RE, Anderson RR, Hughes WJ (2004) Frequencies of standing Alfvén wave harmonics and their implication for plasma mass distribution along geomagnetic field lines: statistical analysis of CRRES data. J Geophys Res. doi:10.1029/2003JA010345

Takahashi K, Liou K, Yumoto K, Kitamura K, Nosé M, Honary F (2005) Source of Pc4 pulsations observed on the nightside. J Geophys Res. doi:10.1029/2005JA011093

Takahashi K, Chi PJ, Denton RE, Lysak RL (eds) (2006) Magnetospheric ULF waves: synthesis and new directions. American Geophysical Union, Washington, DC, 359 pp

Takahashi K, Ohtani S, Denton RE, Hughes WJ, Anderson RR (2008) Ion composition in the plasma trough and plasma plume derived from a Combined Release and Radiation Effects Satellite magnetoseismic study. J Geophys Res. doi:10.1029/2008JA013248

Takahashi K, Berube D, Lee D-H, Goldstein J, Singer HJ, Honary F, Moldwin MB (2009) Possible evidence of virtual resonance in the dayside magnetosphere. J Geophys Res. doi:10.1029/2008JA013898

Tanaka Y-M, Yumoto K, Yoshikawa A, Itonaga M, Shinohara M, Takasaki S, Fraser BJ (2007) Horizontal amplitude and phase structure of low-latitude Pc 3 pulsations around the dawn terminator. J Geophys Res. doi:10.1029/2007JA012585

Tepley L, Landshoff RK (1966) Waveguide theory for ionospheric propagation of hydromagnetic emissions. J Geophys Res 71:1499–1504

Teramoto M, Nosé M, Sutcliffe PR (2008) Statistical analysis of Pi2 pulsations inside and outside the plasmasphere observed by the polar orbiting DE1 satellite. J Geophys Res. doi:10.1029/2007JA012740

Trakhtengerts VY, Demekhov AG (2007) Generation of Pc1 pulsations in the regime of backward wave oscillator. J Atmos Sol Terr Phys 69:1651–1656

Troitskaya VA (1961) Pulsation of the Earth′s electromagnetic field with periods of 1 to 15 seconds and their connection with phenomena in the high atmosphere. J Geophys Res 66:5–18

Troitskaya VA, Gul'yel'mi AV (1967) Geomagnetic micropulsations and diagnostics of the magnetosphere. Space Sci Rev 7:689–768

Troitskaya VA, Gul'yel'mi AV (1970) Hydromagnetic diagnostics of plasma in the magnetosphere. Ann Geophys 26:893

Troitskaya VA, Plyasova-Bakunina TA, Gul'yel'mi AV (1971) Connection of Pc2-4 pulsations with interplanetary magnetic field. Doklady Akad Nauk SSSR 197:1312

Turkakin H, Marchaud R, Kale ZC (2008) Mode trapping in the plasmasphere. J Geophys Res. doi:10.1029/2008JA013045

Ukhorskiy AY, Sitnov MI (2008) Radial transport in the outer radiation belt due to global magnetospheric compressions. J Atmos Sol Terr Phys. doi:10.1016/j.jastp.2008.07.018

Ukhorskiy AY, Takahashi K, Anderson BJ, Korth H (2005) Impact of toroidal ULF waves on the outer radiation belt electrons. J Geophys Res. doi:10.1029/2005JA011017

Ukhorskiy AY, Anderson BJ, Takahashi K, Tsyganenko NA (2006) Impact of ULF oscillations in solar wind dynamic pressure on the outer radiation belt electrons. Geophys Res Lett. doi:10.1029/2005GL024380

Usanova ME, Mann IR, Rae IJ, Kale ZC, Angelopolous V, Bonnell JW, Glassmeier K-H, Auster HU, Singer HJ (2008) Multipoint observations of magnetospheric compression-related EMIC waves by THEMIS and CARISMA. Geophys Res Lett. doi:10.1029/2008GL034458

Vellante M, Förster M (2006) Inference of the magnetospheric plasma mass density from field line resonances: a test using a plasmasphere model. J Geophys Res. doi:10.1029/2005JA011588

Vellante M, Förster M, Villante U, Zhang TL, Magnes W (2007) Solar activity dependence of geomagnetic field line resonance frequencies at low latitudes. J Geophys Res. doi:10.1029/2006JA011909

Viall NM, Kepko L, Spence HE (2009) Relative occurrence rates and connection of discrete frequency oscillations in the solar wind density and dayside magnetosphere. J Geophys Res. doi:10.1029/2008JA013334

Villante U (2007) Ultra low frequency waves in the magnetosphere. In: Kamide Y, Chian A (eds) Handbook of the solar-terrestrial environment. Springer, Berlin, Heidelberg, pp 397–422

Villante U, Lepidi S, Francia P, Meloni A, Palangio P (1997) Long period geomagnetic field fluctuations at Terra Nova Bay (Antarctica). Geophys Res Lett 24:1443–1446

Villante U, Francia P, Vellante M, Di Giuseppe P, Nubile A, Piersanti M (2007) Long period oscillations at discrete frequencies: a comparative analysis of ground, magnetospheric and interplanetary observations. J Geophys Res. doi:10.1029/2006JA011896

Volwerk M et al (2007) Flow burst-induced Kelvin-Helmholtz waves in the terrestrial magnetotail, Geophys Res Lett. doi:10.1029/2007GL029459

Walker ADM (1981) The Kelvin-Helmholtz instability in the low-latitude boundary layer. Planet Space Sci 29:1119–1133

Walker ADM (2000) Reflection and transmission at the boundary between two counterstreaming MHD plasmas – active boundaries or negative-energy waves? J Plasma Phys 63:203–219

Walker ADM (2005) Magnetohydrodynamic waves in geospace – the theory of ULF waves and their interaction with energetic particles in the solar-terrestrial environment. IOP Publishing, Bristol, 550 pp

Waters CL, Sciffer MD (2008) Field line resonant frequencies and ionospheric conductance: results from a 2D MHD model. J Geophys Res. doi:10.1029/2007JA012822

Waters CL, Cox SP (2009) ULF wave effects on high frequency signal propagation through the ionosphere. Ann Geophys 27:2779–2788

Waters CL, Menk FW, Fraser BJ (1991) The resonance structure of low latitude Pc3 geomagnetic pulsations. Geophys Res Lett 18:2293–2296

Waters CL, Menk FW, Fraser BJ (1994) Low latitude geomagnetic field line resonance: experiment and modeling. J Geophys Res 99:17547–17558

Waters CL, Samson JC, Donovan EF (1995) The temporal variation of the frequency of high-latitude field line resonances. J Geophys Res 100:7987–7996

Waters CL, Samson JC, Donovan EF (1996) Variation of plasmatrough density derived from magnetospheric field line resonances. J Geophys Res 101:24737–24745

Waters CL, Harrold BG, Menk FW, Samson JC, Fraser BJ (2000) Field line resonances and waveguide modes at low latitudes 2. A model. J Geophys Res 105:7763–7774

Waters CL, Sciffer MD, Fraser BJ, Brand K, Foulkes K, Menk FW, Saka O, Yumoto K (2001) The phase structure of very low latitude ULF waves across dawn. J Geophys Res 106:15599–15607

Waters CL, Takahashi K, Lee D-H, Anderson BJ (2002) Detection of ultra-low-frequency cavity modes using spacecraft data. J Geophys Res. doi:10.1029/2001JA000224

Waters CL, Menk FW, Thomsen MF, Foster C, Fenrich FR (2006) Remote sensing the magnetosphere using ground based observations of ULF waves. In: Takahashi K, Chi PJ, Denton RE, Lysak RL (eds) Magnetospheric ULF waves: synthesis and new directions. American Geophysical Union, Washington, DC, pp 319–337

Waters CL, Yeoman TK, Sciffer MD, Ponomarenko P, Wright DM (2007) Modulation of radio signals by ULF waves. Ann Geophys 25:1113–1124

Webster DJ, Fraser BJ (1985) Source regions of low-latitude Pc1 pulsations and their relationship to the plasmapause. Planet Space Sci 33:777–793

Wentworth RC (1964) Enhancement of hydromagnetic emissions after geomagnetic storms. J Geophys Res 69:2291–2298

Wild JA, Yeoman TK, Waters CL (2005) Revised time-of-flight calculations for high-latitude geomagnetic pulsations using a realistic magnetospheric magnetic field model. J Geophys Res. doi:10.1029/2004JA010964

Wright DM, Yeoman TK (1999) High-latitude HF Doppler observations of ULF waves: 2. Waves with small spatial scale sizes. Ann Geophys 17:868–876

Wright AN, Mann IR (2006) Global MHD eigenmodes of the outer magnetosphere. In: Takahashi K, Chi PJ, Denton RE, Lysak RL (eds) Magnetospheric ULF waves: synthesis and new directions. American Geophysical Union, Washington, DC, pp 51–72

Wright AN, Allan W (2008) Simulations of Alfvén waves in the geomagnetic tail and their auroral signatures. J Geophys Res. doi:10.1029/2007JA012464

Wright DM, Yeoman TK, Jones TB (1999) ULF wave occurrence statistics in a high latitude HF Doppler sounder. Ann Geophys 17:749–759

Yahnin AG, Yahnina TA (2007) Energetic proton precipitation related to ion-cyclotron waves. J Atmos Sol Terr Phys 69:1690–1706

Yahnin AG, Yahnina TA, Frey HU (2007) Subauroral proton spots visualize the Pc1 source. J Geophys Res. doi:10.1029/2007JA012501

Yarker JM, Southwood DJ (1986) The effect of non-uniform ionospheric conductivity on standing magnetospheric Alfvén waves. Planet Space Sci 34:1213–1221

Yearby KH, Clilverd MA (1996) Doppler shift pulsations on whistler mode signals from a VLF transmitter. J Atmos Sol Terr Phys 58:1489–1496

Yeoman T, Wright D, Chapman P, Stockton-Chalk A (2000) High-latitude observations of ULF waves with large azimuthal wavenumbers. J Geophys Res 105:5453–5462

Yumoto K, Saito T (1983) Relation of compressional hm waves at Goes 2 to low-latitude Pc 3 magnetic pulsations. J Geophys Res 88:10041–10052

Yumoto K, Saito T, Akasofu SI, Tsurutani B, Smith E (1985) Propagation mechanism of daytime Pc 3-4 pulsations observed at synchronous orbit and multiple ground-based stations. J Geophys Res 90:6439–6450

Ziesolleck CWS, McDiarmid DR (1994) Auroral latitude Pc5 field line resonances; quantized frequencies, spatial characteristics, and diurnal variations. J Geophys Res 99:5817–5830

Zong QG et al (2007) Ultralow frequency modulation of energetic particles in the dayside magnetosphere. Geophys Res Lett. doi:10.1029/2007GL029915

Zong QG et al (2009) Energetic electron response to ULF waves induced by interplanetary shocks in the outer radiation belt. J Geophys Res. doi:10.1029/2009JA014393

ULF Waves in the Topside Ionosphere: Satellite Observations and Modeling

14

V. Pilipenko, E. Fedorov, B. Heilig, M.J. Engebretson, P. Sutcliffe, and H. Luehr

Abstract

Low-orbiting observations at satellites with high-accuracy magnetometers onboard (Oersted, CHAMP, ST5) have provided the possibility to examine the ULF wave (Pc3, Pi2, Pc1) structure in the topside ionosphere. Pc3 waves were detected very clearly in the compressional component of the satellite magnetic data, whereas on the ground, their signature was found in the H component. The relationships between the Pc3 wave compressional magnetic component above the ionosphere and the ground response can be produced by two different mechanisms: (a) an incident Alfven wave generates an evanescent fast mode as a result of its interaction with the anisotropically conducting ionosphere; (b) transport of ULF wave energy from a distant source towards the ionosphere predominantly occurs via the fast mode. Numerical modeling and analytical estimates have been applied to the interpretation of Pc3 waves observed by CHAMP in the upper ionosphere and by ground stations at mid-latitudes. The observed ratio between the compressional component in space and the ground signal corresponds better to the scenario of direct fast mode transmission to the ground. To interpret simultaneous observations of low-latitude Pi2 pulsations at CHAMP and on the ground a simple analytical model which couples an incident compressional wave above the equatorial ionosphere with the ground response can be used. The amplitude and phase relationships between Pi2 signals in the upper ionosphere and on the ground at conjugate stations Tihany and Hermanus ($L\sim1.8$) match the theoretical predictions.

14.1 Introduction: Simultaneous Observations of ULF Waves by Low-Altitude Satellites and Ground Stations

The current knowledge of ULF wave physics is mainly based on the results of wave observations either in the near-equatorial magnetospheric domain made with geosynchronous or high-Earth orbit satellites or in the lower ionosphere with radar facilities or ground magnetometers. The region of top-side ionosphere,

V. Pilipenko (✉)
Space Research Institute, Moscow 117997, Russia
e-mail: pilipenk@augsburg.edu

W. Liu, M. Fujimoto (eds.), *The Dynamic Magnetosphere*, IAGA Special Sopron Book Series 3,
DOI 10.1007/978-94-007-0501-2_14,

above the F-layer, has remained mostly unexplored. Previously, the difficulty had been to extract the relatively small pulsation perturbation from the large background field due to the limited digitization step size of the satellite magnetometer and to the environmental noise.

Only recently, advances in precise high-rate low-noise measurements of the geomagnetic field by low Earth orbit (LEO) satellites have made it possible to detect ULF waves in the top-side ionosphere. The magnetic field measurements from CHAMP are of unprecedented accuracy and resolution, which have enabled clearly resolved observations of Pi2 and Pc3 pulsations in the ionosphere at LEO using vector magnetic field data. These observations have demonstrated that earlier opinions claiming that a comparison of ULF wave observations from a low-altitude satellite and from the ground is not very promising, because of the too-rapid movement of the satellite, must be revised.

14.1.1 Pc3 Waves

In magnetic field measurements from the low-orbiting near-polar CHAMP satellite ($h = 350$–450 km) Pc3 waves rather surprisingly were seen clearly in the magnetic field-aligned $b_{||}$ component, whereas on the ground, their signatures were found in the H component (Heilig et al. 2007a). The coherence between ground and satellite wave signatures was high over wide latitude and longitude ranges. The occurrence of a significant compressional component $b_{||}$ of the Pc3 wave structure was unexpected, because traditional notions assumed that Pc3 waves at the ground were mainly produced by field line Alfven oscillations.

Observations of Pc3 pulsations by the scalar magnetometer on the Oersted satellite ($h = 650$–$900\sim$km) also showed the dominance of the compressional component (Jadhav et al. 2001). Pc3 wave packets were almost simultaneous at Oersted and at ground magnetic stations. In nighttime events the Pc3 packets had about the same amplitude, but during the daytime Pc3 amplitudes at the satellite were larger than on the ground, especially at lower latitudes.

There have been many observations of compressional Pc3 waves in the near-equatorial regions of the magnetosphere, which were interpreted as fast mode inward transport of wave energy from the boundaries of the magnetosphere (Kim and Takahashi 1999; Takahashi et al. 1994; Yumoto and Saito 1983). The main features of the dayside compressional Pc3 activity at LEO were found to be controlled by interplanetary parameters (Heilig et al. 2007b). Wave amplitudes are controlled by the solar wind speed and the IMF cone angle, while the dominant frequency is determined first of all by the IMF strength. All these findings support the upstream origin of the compressional waves observed at LEO. However, because fast waves are expected to be reflected from regions with high Alfven velocity V_A, they are expected to be localized in the near-equatorial plane of the magnetosphere only, and they can reach the ionosphere only as an evanescent mode. Therefore, the existing theoretical view assumes that in effect only Alfven waves can reach the ionosphere. The results of the Pc3 observations by the magnetometer onboard low-altitude CHAMP satellite and along the MM100 ground array (Heilig et al. 2007a) have evidenced that this notion has to be revised.

For comparison of theoretical predictions with ground-satellite observations we introduce the ratio κ of the compressional component above the ionosphere $b_{||}$ to the ground magnetic signal $b_x^{(g)}$ (H component), namely $\kappa = b_{\|}/b_x^{(g)}$. The dependence of κ on MLT at different magnetic latitudes should elucidate the role of the ionosphere in the ULF wave structure. For that, the mean compressional wave power and the mean power of the H-component in the 20–70 mHz band were estimated for the period Jan–Apr., 2003 with wavelet transform (Heilig et al. 2007a). The global magnetic latitude-MLT dependence of the CHAMP compressional power demonstrates a near-noon (09–13 MLT) maximum at low latitudes (<15°). In addition, a nighttime maximum at low latitudes and high-latitude maxima on the day- and nightside are probably produced by the contribution to the Pc3 band by spatial structures sampled by the fast moving satellite, namely the equatorial spread F phenomenon and field-aligned currents. Figure 14.1 shows the MLT dependence of satellite and ground Pc3 wave power and satellite/ground amplitude ratio κ, estimated with the use of data from Tihany (THY, geomagnetic latitude $\Phi = 42.4°$) and CHAMP. Comparison of these plots makes it evident that Pc3 wave power both in space and on the ground decrease from noon hours to night time hours by about an order of magnitude. At

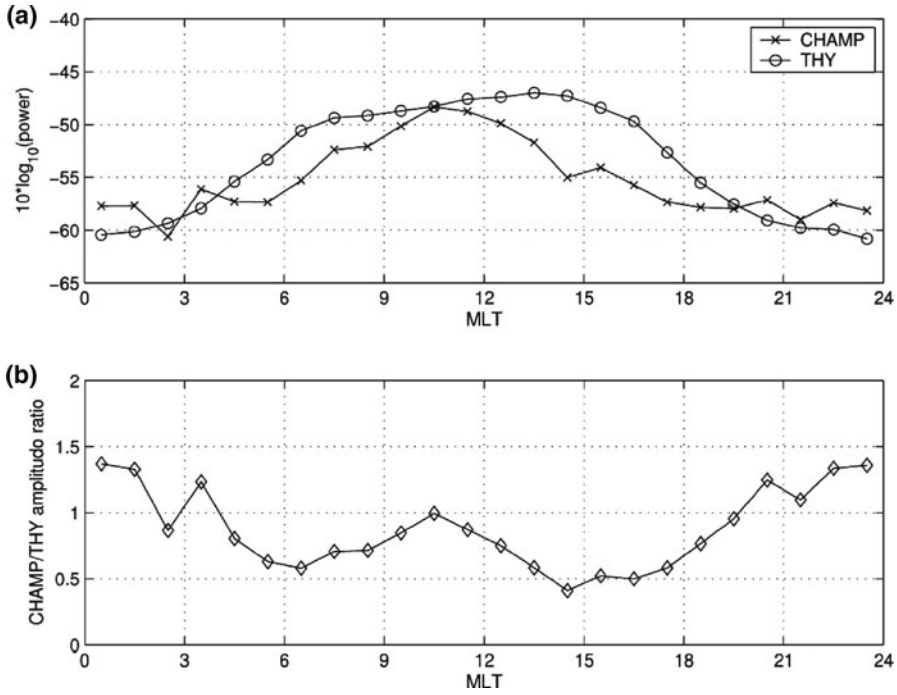

Fig. 14.1 The MLT dependence of (**a**) satellite and ground power and (**b**) the satellite/ground amplitude ratio estimated with the use of data from THY ($\Phi = 42°$) and CHAMP for the period Jan–Apr. 2003

the same time, the ratio between the Pc3 amplitudes on CHAMP and on the ground remains pretty much the same, varying in the range $\kappa = 1.0 \pm 0.5$. The same kind of dependence was found for other magnetic latitude: whereas the Pc3 power varies significantly from dayside hours to nightside hours, the ratio between the Pc3 amplitudes remains very stable at practically all MLT (Pilipenko et al. 2008). The observed ratio κ for the CHAMP-ground pair decreases slightly with latitude from ~1.0 at $\Phi = 42°$ to ~0.5 at $\Phi = 57°$.

The multi-component structure of ULF waves in the top-side ionosphere may be closely related to their propagation mechanism. That is why we suppose that the occurrence of a significant compressional component deserves thorough consideration. A model to interpret simultaneous Pc3 observations in the top-side ionosphere and on the ground was developed in (Pilipenko et al. 2008). In Section 14.2 we will give a summary of this model.

14.1.2 Pi2 Waves

Using data from CHAMP, Sutcliffe and Luehr (2003) were for the first time able to extract and clearly resolve Pi2 pulsations in vector magnetometer data at LEO. These observations showed the occurrence of a significant compressional component in Pi2 pulsations at LEO. Pi2 pulsations observed by the Orsted satellite in a low-latitude region were also nearly pure compressional/fast-mode waves (Han et al. 2004). The Pi2 compressional component mapped directly to the H-component on the ground. These observations were interpreted such that on the night side the Pi2 waves at low latitude are due to cavity fast mode wave directly incident to the ground. The idea of mid-latitude Pi2 as cavity mode oscillatory response of the inner magnetosphere to the substorm activation was firmly supported by numerous satellite observations in the nightside magnetosphere (Takahashi et al. 1995, 1999; Keiling et al. 2001).

As an example of simultaneous observations of nightside Pi2 waves at CHAMP and on the ground we show observations on April 11, 2004 when the satellite was in the northern hemisphere (Sutcliffe and Luehr 2010). The comparison of Pi2 signatures in compressional $b_{||}$, toroidal b_y, and poloidal b_x components at CHAMP and the horizontal components at the conjugate northern and southern stations Tihany (THY) and Hermanus (HER) at L~1.8 are shown in Fig. 14.2. The

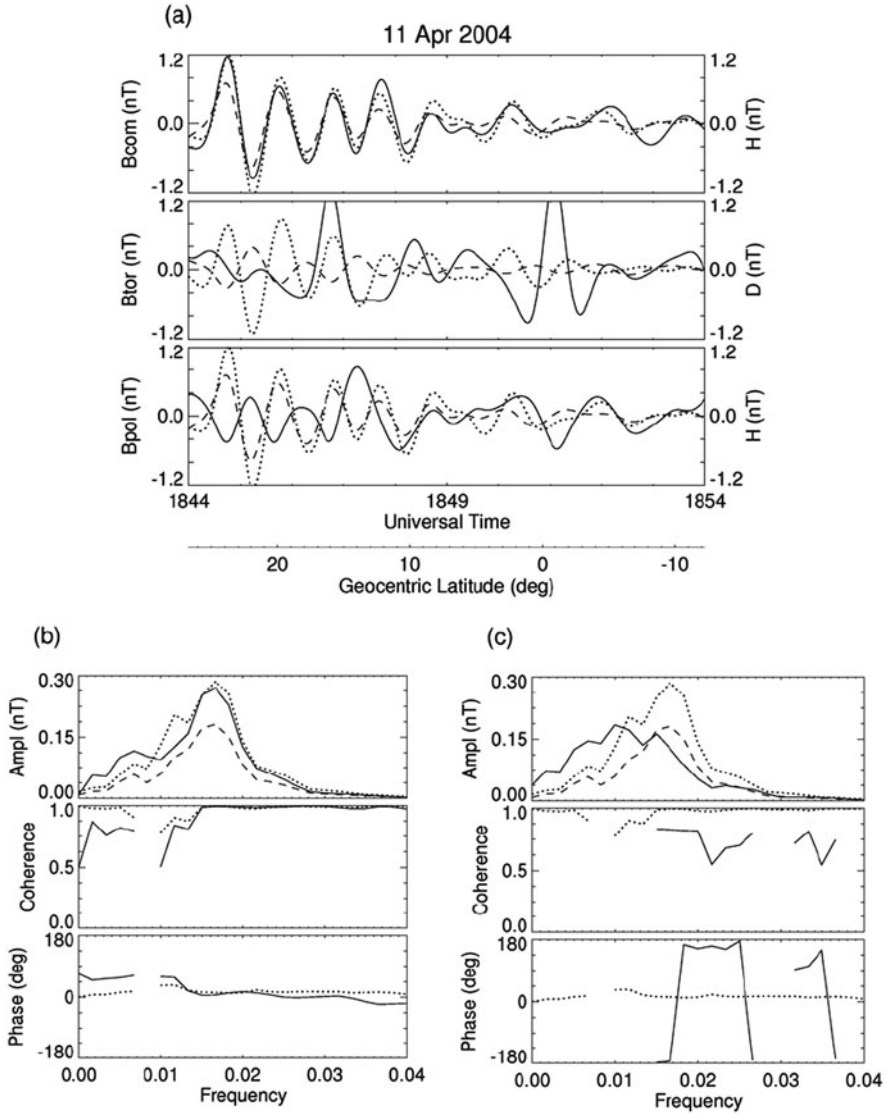

Fig. 14.2 Observations of a nightside Pi2 pulsation on April 11, 2004 when CHAMP was in the northern hemisphere. (**a**) The panels from *top* to *bottom* show the compressional, toroidal, and poloidal components at CHAMP (*solid line*) and the H and D components at conjugate stations HER (*dashed line*) and THY (*dotted line*). (**b**) and (**c**) show the spectral characteristics of the compressional and poloidal components respectively relative to the H component: the amplitude spectra for CHAMP (*solid*), HER (*dashed*), and THY (*dotted*). The *center* and *bottom panels* show the coherence and phase difference respectively for HER/CHAMP (*solid*) and HER/THY (*dotted*)

amplitude spectra for CHAMP, HER, and THY have a common peak at ∼16 mHz. The spectral power ratio at this frequency is $\kappa \sim 1.0$. The compressional component in the upper ionosphere is in phase with the H-component on the ground. The poloidal b_x component is in anti phase with the H-component at ground stations, but for events when CHAMP is in the southern hemisphere, the b_x component is in phase with the H-component.

In the Section 14.4 the model will be presented to couple the compressional component of Pi2 pulsations observed by low-orbiting satellites with the ground response.

14.1.3 Pc1 Wave Packets

Successful attempts have been made to identify high-frequency Pc1 waves on the ground and on the low-orbiting satellites MAGSAT (Iyemori and Hayashi 1989), and ST5 (Engebretson et al. 2008). A survey of ULF waves in the Pc 1 frequency range (0.2–5 Hz) recorded by the three spacecraft of the ST-5 mission in a pearls-on-a-string configuration found that regions with Pc 1 wave activity are highly localized to rather narrow L shells (<100 km). These observations showed that at least some of the Pc1 waves in the topside ionosphere could not be treated as quasi-longitudinally propagating ($k_{||} \approx k_A >> k_\perp$, where $k_A = \omega/V_A$ is the Alfven wave number) ion-cyclotron waves, as commonly assumed in theoretical modeling. A mechanism of the Pc1 wave localization and possible occurrence of the waveguides along field lines have not been resolved yet.

14.2 Relationship Between the Compressional Disturbance Above the Ionosphere and the Ground Signal: Model

The ULF wave pattern in the topside ionosphere is a complicated mixture of incident, reflected, and mutually converted waves. Therefore, interpretation of the low-altitude observations and comparison of satellite/ground measurements demands a relevant model. For low frequencies (Pc3/Pi2 pulsations) an elaboration of such a model is facilitated by the possibility to use the thin ionosphere approximation. Under such an approximation the interaction of a plane wave harmonic with the magnetosphere-ionosphere-atmosphere-ground system can be described analytically (Alperovich and Fedorov 2007). However, in the Pc1/Pi1 range the approximation of a thin ionosphere is not valid, and the full wave equations in a realistic vertically inhomogeneous ionospheric plasma must be treated. An additional complication arises, which is to be taken into account, that a part of the Pc1 wave energy can be trapped in the ionospheric cavity. This cavity can serve as a waveguide for the fast magnetosonic mode and as a resonator for the Alfven mode. The channeling of Pc1 wave energy in the ionospheric waveguide ensures the propagation of the signal to large distances along the ionosphere (Fujita and Tamao 1988). The partial trapping of the incident wave energy in the ionospheric Alfven resonator results in oscillatory frequency-dependent transmission properties of the ionosphere in the Pc1 band (Lysak 1997).

The occurrence of ULF compressional disturbance can be caused by two possible mechanisms:

- an incident Alfven wave generates an evanescent fast compressional mode upon interaction with the anisotropically conducting ionosphere (Hughes and Southwood 1976; Kivelson and Southwood 1988);
- transport of ULF wave energy from a distant source to the ionosphere occurs predominantly via the fast magnetosonic mode.

14.2.1 MHD Wave Penetration Through the Ionosphere to the Ground

The model which will be used represents the magnetosphere as a half-space filled with a cold plasma immersed in a straight magnetic field $\mathbf{B}_0$, bounded by a thin ionosphere – an anisotropically conducting layer at altitude h with height-integrated conductances Σ_P and Σ_H. The magnetospheric plasma is characterized by an Alfven velocity V_A and a wave conductance $\Sigma_A = 1/\mu_0 V_A$.

In Cartesian coordinate system the x, y and z-axes are directed southward, eastward, and upwards, respectively. The magnetic field inclination is denoted as I (>0 in the Northern and <0 in the Southern hemisphere; vertical $\mathbf{B}_0$ corresponds to $I = \pm\pi/2$, in the equatorial ionosphere $I \to 0$). In a dipole field the inclination I is related to the geomagnetic latitude Φ by the relationship $\tan I = 2 \tan \Phi$. The atmosphere and ground are assumed to be isotropic conductors with conductivities σ_a and σ_g.

The wave electric ($\mathbf{E}$) and magnetic ($\mathbf{b}$) fields can be decomposed into two modes. The magnetospheric wave fields are the sum of Alfven (A) mode, where the disturbed magnetic field $\mathbf{b}_\perp$ is perpendicular to $\mathbf{B}_0$ and divergence-free, $\nabla \cdot \mathbf{b}_\perp = 0$, whereas the longitudinal component is vanishing $b_{||} = 0$; and Fast (F) mode, where $\mathbf{b}_\perp$ is curl-free, $\nabla \times \mathbf{b}_\perp = 0$, so that the field-aligned component of the current vanishes $j_{||} = 0$.

An electromagnetic disturbance in the atmosphere and at the ground is composed of Magnetic H-mode, where the vertical component of the disturbed electric

field is absent, $E_z = 0$; and Electric E-mode, where the vertical component of the disturbed magnetic field is absent, $b_z = 0$.

The general set of Maxwell and ideal MHD equations for the electromagnetic field in the magnetospheric plasma may be decomposed into two uncoupled sets of equations for A- and F-modes. In a similar way, the decomposition into uncoupled equations for E- and H-modes takes place in the atmosphere/ground region.

We consider a harmonic incident wave $\propto \exp(-i\omega t + ikx)$ (where $k = k_x$ is the component of the horizontal wave number in the horizontal plane), and neglect the azimuthal variations $k_y = 0$. Then, the magnetospheric modes have the following properties:

The incident A-mode has an azimuthal magnetic component $b_y^{(i)}$ only, whereas $b_x^{(i)} = b_z^{(i)} = 0$; and the wave electric field with components $E_X^{(i)}$ and $E_Z^{(i)}$ lies in the meridional plane. The incident F-mode has a non-vanishing compressional component $b_{||}^{(i)}$ (therefore the $b_x^{(i)}$ and $b_z^{(i)}$ magnetic components are also non-vanishing), whereas the azimuthal component $b_y^{(i)} = 0$. Only the azimuthal electric component $E_Y^{(i)}$ does not vanish.

The boundary conditions for the electromagnetic field at the ground surface ($z = -h$) can be derived via the spectral surface impedances for E and H modes, $Z_g^{(e)}$ and $Z_g^{(h)}$, as follows (Pilipenko et al. 1998)

$$E_X^{(g)} = Z_0^{-1} Z_g^{(e)} b_y \text{ and } E_Y^{(g)} = Z_0^{-1} Z_g^{(h)} b_x$$

where $Z_0 = \sqrt{\mu_0/\varepsilon_0}$ is the impedance of free space. Usually, the wave skin-depth $\delta_g = \left(2/\omega\mu_0\sigma_g\right)^{1/2}$ in the ground is much less than the horizontal scale of the disturbance, that is $k\delta_g << 1$. In this case the electric and magnetic impedances coincide, so $Z_g = Z_g^{(e)} = Z_g^{(h)}$, and for the homogeneous semi-space the surface impedance is $Z/\omega\mu_0 = \delta_g/\sqrt{2i - \left(k\delta_g\right)^2}$.

The model is based essentially on analytical relationships extracted from the general theory of MHD wave interactions with a thin ionosphere (Alperovich and Fedorov 2007). The electromagnetic field in the magnetosphere may be presented as a combination of incident (i) and reflected (r) waves, e.g. $\mathbf{b} = \mathbf{b}^{(i)} + \mathbf{b}^{(r)}$ and $\mathbf{E} = \mathbf{E}^{(i)} + \mathbf{E}^{(r)}$. It is convenient to introduce the reflection coefficients, denoted as R_{FF}, R_{FA}, R_{AF}, and R_{AA}, for the ratio of the horizontal magnetic components $\mathbf{b}_r$ of the wave magnetic fields after and before reflection. Similarly, for the wave penetration to the ground, the transmission coefficients T_{HF}, T_{HA}, T_{EF}, and T_{EA} for the ratio of the horizontal magnetic field at the ground to the horizontal magnetic field in the ionosphere before reflection are introduced. Subscripts A or F indicate the A- or F-mode in the magnetosphere, and E and H subscripts indicate electric or magnetic mode on the ground, respectively. The reflection and transmission matrices

$$\mathbf{R} = \begin{pmatrix} R_{FF} & R_{FA} \\ R_{AF} & R_{AA} \end{pmatrix} \mathbf{T} = \begin{pmatrix} T_{HF} & T_{HA} \\ T_{EF} & T_{EA} \end{pmatrix} \tag{14.1}$$

connect magnetic components at the ionospheric level in incident $\mathbf{b}_\tau^{(i)} = b_x^{(i)}\hat{\mathbf{x}} + b_y^{(i)}\hat{\mathbf{y}}$, reflected $\mathbf{b}_\tau^{(r)} = b_x^{(r)}\hat{\mathbf{x}} + b_y^{(r)}\hat{\mathbf{y}}$, and ground $\mathbf{b}_\tau^{(g)} = b_x^{(g)}\hat{\mathbf{x}} + b_y^{(g)}\hat{\mathbf{y}}$ waves

$$\begin{pmatrix} b_x^{(r)} \\ b_y^{(r)} \end{pmatrix} = \mathbf{R} \begin{pmatrix} b_x^{(i)} \\ b_y^{(i)} \end{pmatrix} \begin{pmatrix} b_x^{(g)} \\ b_y^{(g)} \end{pmatrix} = \mathbf{T} \begin{pmatrix} b_x^{(i)} \\ b_y^{(i)} \end{pmatrix} \tag{14.2}$$

Owing to the high resistance of the atmosphere, the current density near the Earth's surface is much less than the current density of ionospheric currents. Therefore, the ratio of magnetic components of the atmospheric E-mode to the magnetic components in the ionosphere is very small: the relevant transmission coefficients $|T_{EA}| << 1$ and $|T_{EF}| << 1$. In other words, the E-mode is only very weakly excited by magnetospheric disturbances (Anisimov et al. 1993), and corresponding elements of the transmission matrix will not be considered further.

In what follows, we consider separately the mechanisms of occurrence of $b_{||}$ upon incidence of Alfven and fast waves onto the ionosphere-atmosphere-ground system.

14.2.2 Incident Alfven Waves

Upon interaction with the anisotropic ionosphere, a compressional component of the reflected evanescent mode $b_{\|A}$ can be produced by an incident Alfven wave

$$b_{||A}(z) = -R_{FA} b_y^{(i)} \exp(iI) \exp(-kz) \tag{14.3}$$

The ratio $\kappa_A(z)$ of the compressional component of an evanescent mode above the ionosphere $b_{||A}(z)$ to the ground magnetic signal $b_{xA}^{(g)}$ is

$$\kappa_A(z) = \frac{b_{||A}(z)}{b_{xA}^{(g)}} = -\exp(iI)\frac{R_{FA}}{T_{HA}}\exp(-kz) \quad (14.4)$$

Alfvenic disturbances with $f \leq 0.1$ Hz at ionospheric altitudes have small scales ($k < 10^{-2}$ km^{-1}) as compared with their field-aligned scales, $k >> k_A$. In this case for a homogeneous ground $\sigma_g = \text{const}$, (14.4) can be written as follows (Pilipenko et al. 2008)

$$\kappa_A(z) = \exp(iI)\frac{\sinh(kh)}{\exp(kz)} \times \left(1 + \frac{ik\delta_g}{\sqrt{2i - k^2\delta_g^2}}\coth(kh)\right) \quad (14.5)$$

The second term in brackets in (14.5) describes the influence of finite ground conductivity σ_g on the ULF wave structure. For a high ground conductivity and large-scale wave structure, so that $k\delta_g << 1$ and $kh << 1$, (14.5) becomes simply

$$\kappa_A = \exp(iI)\, kh* \exp(-kz)\ h* = h + (1+i)\delta_g/2 \quad (14.6)$$

Thus, the ratio κ_A between the ground magnetic signal and the compressional component above the ionosphere should not depend on the ionospheric conductance, but is determined by the ground conductivity, wave scale, and the altitude of the space monitor. The latitude (or inclination) determines the phase shift between the compressional and ground signals, but not the amplitude of their ratio.

14.2.3 Incident Fast Mode

This mechanism assumes that the wave energy is transported from a source towards the ground by a fast mode, without conversion into Alfven waves. However, the wave scale of the fast mode in the Pc3 range in the magnetosphere is expected to be very large (e.g., for $T = 30$ s, and $V_A = 10^3$km/s, $k_A \approx 2 \times 10^{-4}$ km^{-1}). Therefore, fast waves cannot reach the ionosphere directly under reasonable horizontal wave numbers, because upon their propagation toward plasma with higher V_A they encounter a non-propagation (opaque) region, where the F-mode field-aligned wave number, $k_F^2 = k_A^2 - k^2 < 0$. However, owing to its large horizontal scale, even an evanescent F-mode can convey significant wave energy towards the Earth.

The ratio of the ground magnetic signal $b_{xF}^{(g)}$ to the incident compressional wave amplitude $b_{xF}^{(i)}$ is determined (Pilipenko et al. 2008) to be

$$b_x^{(g)} = 2b_x^{(i)}/(1 - ip) \quad (14.7)$$

Here the complex parameter $p = k_0 h* Z_0 \Sigma_C$, where $k_0 = \omega/c$ is the wave number of free space, has been introduced. This parameter for an infinitely conductive ground $\sigma_g \to \infty$ becomes real: $p \to p_0 = k_0 h Z_0 \Sigma_C$. Here the Cowling-like conductivity is $\Sigma_C = \Sigma_P + \Sigma_H^2/\Sigma_P$, whereas $\tilde{\Sigma}_C = \Sigma_P + \Sigma_H^2/\left(\Sigma_P + \Sigma_A|\sin I|\right)$ is the modified Cowling conductivity with allowance for the emission of Alfven waves into the magnetosphere (Alperovich and Fedorov 2007). The parameter p controls the penetration of the fast mode through the ionosphere to the ground. The amplitude of the ground response diminishes with the increase of ionospheric conductance, as $p_0 \propto \Sigma_C$, and with frequency, as $p_0 \propto \omega$. Under nighttime conditions, when $|p| << 1$, the ionosphere becomes transparent to the fast mode, so the incident F-mode is reflected mainly from Earth's surface (e.g., for $\Sigma_C = 0.1$S, the parameter $|p| < 10^{-2}$ for $f < 0.1$ Hz). The dayside ionosphere is semi-transparent for the fast mode in Pc3 band, as $|p| \sim 1$.

The total longitudinal magnetic field (summed incident and reflected waves) of the evanescent fast mode $b_{||F} = b_{||F}^{(i)} + b_{||F}^{(r)}$ in the non-transparent region above the ionosphere, $k >> k_A$, $k_F \approx ik$, is

$$b_{||}^{(i,r)} = -q_{\pm} b_x^{(i,r)} \quad q_{\pm} = \cos I \pm (k/k_F)\sin I \quad (14.8)$$

The factor κ_F characterizing the ratio of the total compressional magnetic disturbance above the ionosphere at altitude z to the ground magnetic disturbance, induced by the fast mode, is as follows

$$\kappa_F(z) = \frac{b_{||F}(z)}{b_{xF}^{(g)}} = -\frac{q_+\exp(-ik_F z) + q_- R_{FF}\exp(ik_F z)}{T_{HF}} \quad (14.9)$$

For large-scale disturbances the relationships for the transmission and reflection coefficients are significantly simplified, namely $R_{FF} = 1$, and $T_{HF} = 2(1 - ip)^{-1}$ (Alperovich and Fedorov 2007). As a result, for low altitudes above the ionosphere, where $|k_F z| << 1$, (14.9) reduces to

$$\kappa_F(z) = -(1 - ip)(\cos I - ikz \sin I) \qquad (14.10)$$

The small linear term with respect to $|kz| << 1$ inside the second factor in (14.10) becomes significant at polar latitudes when $I \to \pm 90°$. The factor κ_F should decrease with an increase of latitude/inclination $\kappa_F \propto \cos I$.

14.3 Numerical Modeling

Here we compare the simple analytical estimates described above with the results of the more complete and exact formulas. The relationships between amplitudes of incident, reflected and transmitted modes will be presented as a dependence on the wave horizontal scale k. The key elements R_{FF} and R_{FA} of the reflection and T_{HF} and T_{HA} of the transmission matrices are given in the theory of MHD wave interaction with the thin ionosphere (Alperovich and Fedorov 2007). These complete relationships take into account the Hall effect of the Alfven wave reflection (Yoshikawa and Itonaga 1996), excitation of the ionospheric surface mode (Pilipenko et al. 2000), and the finite conductivity of the atmosphere and ground.

The results of numerical modeling of the Pc3 wave structure ($T = 30$ s) are given for the following parameters: $V_A = 800$ km/s, which gives the wave conductance $\Sigma_A \sim 800/V_A = 1$ S and Alfven wave number $k_A = 2.6 \times 10^{-4}$ km^{-1}. The ratio between the Hall and Pedersen ionospheric conductances is $\Sigma_H/\Sigma_P = 2$, and $h = 100$ km. The interval of possible wave numbers is from 10^{-6} to 10^{-1} km^{-1}, that is the interval of considered transverse scales, $\sim 1/k$, is from 10^6 to 10 km. The observations are assumed to be conducted at middle latitudes in the Northern hemisphere with inclination $I = 60°$. The ground conductivity is high, $\sigma_g = 0.1$ S/m, and corresponds to the skin-depth $\delta_g \sim 8.3$ km.

14.3.1 Dayside Ionosphere ($\Sigma_P = 10$ S)

The basic reflective properties of both modes are illustrated in Fig. 14.3. As expected for the dayside ionosphere, the Alfven wave reflection, as characterized by R_{AA} coefficient (solid line), is high (~0.9) for all scales. This value is in good agreement with the well-known approximate Alfven wave reflection coefficient for intermediate-scale waves, $k >> \mu_0 \omega \Sigma_H^2/\Sigma_P$, namely

$$R_{AA} = \frac{\Sigma_P - \Sigma_A |\sin I|}{\Sigma_P + \Sigma_A |\sin I|} \qquad (14.11)$$

The reflection of fast waves, as characterized by R_{FF} (dashed line), is also high ($|R_{FF}| \sim 1$) for large scales, $k \le 10^{-3}$km^{-1}. For this set of model parameters the factor $|p| \sim 1$, which means that fast mode will be partially reflected from the ionosphere, and partially from the Earth's surface. Excitation of a reflected Alfven wave by an incident fast wave, as characterized by R_{AF} (dashed-dotted line), is very weak (≤ 0.05). On the contrary, the excitation of a fast wave by an incident Alfven wave ($\propto R_{FA}$) grows with k until it reaches ~1.6 at $k \ge 10^{-2}$ km^{-1}.

Figure 14.4 illustrates the transmission properties of both waves. The ground magnetic response to an

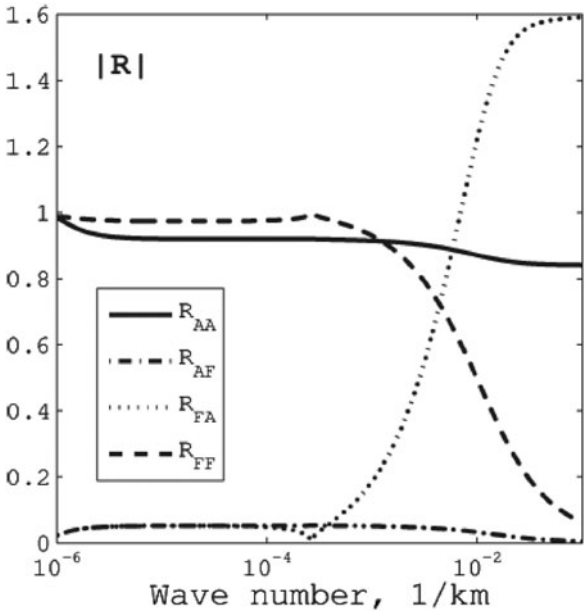

Fig. 14.3 The dependence of different reflection coefficients R on the horizontal wave number for the daytime ionosphere

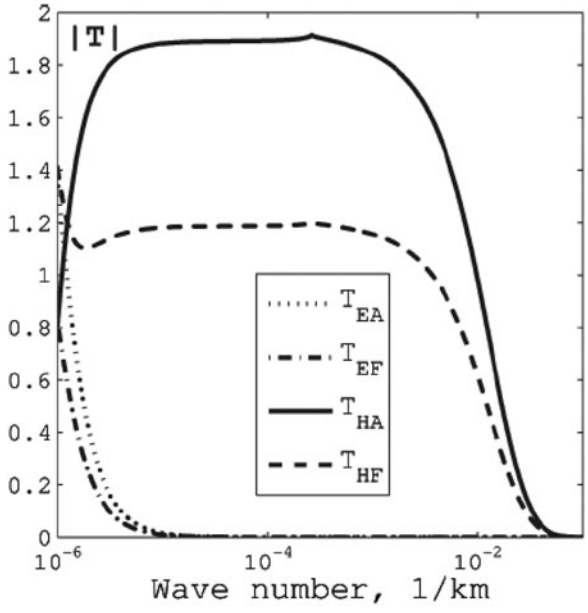

Fig. 14.4 The dependence of different transmission coefficients T on the horizontal wave number for the daytime ionosphere

incident Alfven wave is characterized by the transmission coefficient T_{HA} (solid line). The high value of $T_{HA} \leq 2$ is due to the doubling of the horizontal magnetic component near the highly conductive ground. The polarization ellipse of the H-mode is to be rotated by $\pi/2$ with respect to the polarization ellipse of the magnetospheric Alfven wave ($b_y \rightarrow b_y^{(g)}$). The dominant component on the ground is the H component $b_{xA}^{(g)}$, whereas the D-component $b_{yA}^{(g)}$ is very small, owing to the assumption $k_y \rightarrow 0$.

The rate of H-mode production in the atmosphere by an incident fast wave is characterized by the transmission coefficient T_{HF} (dashed line). In contrast to the Alfven wave, upon transmission through the ionosphere no polarization ellipse rotation of the fast mode occurs ($b_x \rightarrow b_x^{(g)}$). The excitation of the ground D-component $b_{yF}^{(g)}$ for all reasonable scales is very weak. The ionosphere screens somewhat the field of an incident magnetospheric fast wave, so the ground magnetic response even to large-scale modes, $kh << 1$, is less than just double the magnitude of the incident wave.

Thus, both fast and Alfven waves can penetrate to the ground with low attenuation, apart from small-scale structures $k > 10^{-2}\text{km}^{-1}$ that decay in the atmosphere as $\exp(-kh)$. Both modes contribute predominantly to the H component on the ground.

14.3.2 Nightside Ionosphere ($\Sigma_P = 0.2$ S)

The reflective properties of the nighttime ionosphere are illustrated in Fig. 14.5. Because of the high contrast between the ionospheric and magnetospheric wave conductances the reflection of Alfven waves from the nightside ionosphere is still high, $R_{AA} \sim 0.6$ (solid line). The excitation of an evanescent compressional mode by an incident Alfven wave, as characterized by R_{FA} (dotted line), is somewhat lower, below ~0.3, during the night time.

The nighttime ionospheric conductance exerts only a weak influence on R_{FF} (dashed line). For large-scale waves, $kh << 1$, above a highly-conductive ground $R_{FF} \sim 1$, that is the fast mode mainly reflects from the ground. In the case of small scales, $kh > 1$, the coefficient drops rapidly with k.

The transmission properties of the nightside ionosphere are illustrated in Fig. 14.6. The conversion of an incident Alfven wave into an atmospheric H-mode is slightly less efficient, $T_{HA} \sim 0.6$, than during the daytime. The nighttime ionosphere does not attenuate the incident fast mode for $kh < 1$: the magnetic field is nearly doubled near the Earth's surface, $T_{HF} \sim 2.0$ (dashed line).

For interpretation of satellite observations it is necessary to know the relation between the compressional

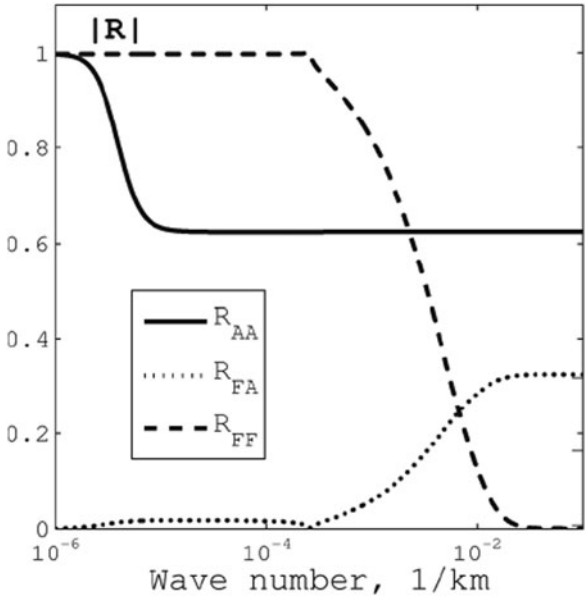

Fig. 14.5 The dependence of different reflection coefficients R on the horizontal wave number for the nighttime ionosphere

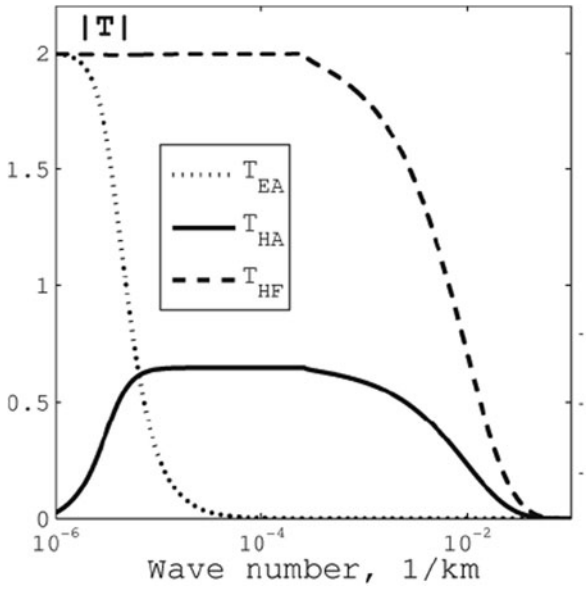

Fig. 14.6 The dependence of different transmission coefficients T on the horizontal wave number for the nighttime ionosphere

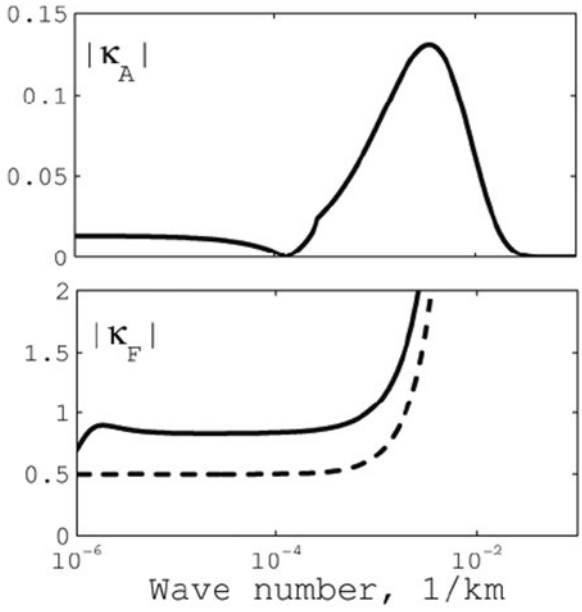

Fig. 14.7 The scale dependence of the absolute values of the factors κ_A and κ_F for Pc3 waves for dayside (*solid line*) and nightside (*dashed line*) conditions. The measurements are assumed to be made at the CHAMP altitude above the ionosphere, $z = 300$ km

$b_{||}$ and horizontal $b_x^{(g)}$ components for both mechanisms, characterized by the parameters $\kappa_A(z)$ and $\kappa_F(z)$. Figure 14.7 gives a summary of the behavior of the factors κ_A and κ_F at $z = 300$ km for the daytime (solid line) and nighttime (dashed line) ionospheres.

The compressional component produced by an incident Alfven wave becomes noticeable for wave scales in the range $k \sim 10^{-2} - 10^{-3}$ km^{-1}. In fact, the atmospheric H-mode and reflected fast mode are produced by the same ionospheric Hall current, induced by the electric field of an incident Alfven wave. As a result, the lower penetration of the magnetospheric Alfven signal to the ground and its lower efficiency of compressional mode excitation exactly compensate each other, and the ratio κ_A remains the same during nighttime as during daytime. The maximal $\kappa_A \sim 0.13$ is achieved at $k \sim (3-4) \times 10^{-3}$ km^{-1}.

The factor κ_F, characterizing the efficiency of fast mode penetration to the ground, is somewhat higher for the dayside ionosphere (∼1.0) than for the night side ionosphere (∼0.6). Comparison of the observed ratio κ (Fig. 14.1) with the modeling results (Fig. 14.7) shows a better correspondence with the scenario of direct fast mode transmission to the ground, because $\kappa \approx \kappa_F >> \kappa_A$. The observed decrease of factor κ with the latitude increase corresponds well to the model predictions. The numerical modeling has proved that simple analytical estimates are valid in a wide range of parameters with good accuracy and may be effectively used to evaluate the relationships between the MHD wave amplitudes in the top-side ionosphere and on the ground.

14.4 Model of the Compressional Mode Interaction with the Low-Latitude Ionosphere

The above theoretical model enables one to relate a compressional component detected at LEO and its ground response. However, this model cannot be directly applied to the near-equatorial region, where the magnetic field inclination $I \to 0$. At the same time, global magnetospheric disturbances (SSC, Pi2) are commonly observed at near-equatorial latitudes both on the ground and in space. They are attributed to the disturbance of the compressional (magnetosonic) large-scale mode.

Here we present a simple analytical theory, which can be applied to the description of the fast mode interaction with the near-equatorial ionosphere. The basic

formulas are adapted from Alperovich and Fedorov (2007) relating incident, reflected, and transmitted harmonic waves $\propto \exp(-i\omega t + i\mathbf{k}\cdot\mathbf{r})$ in the case of meridional propagation ($k_x = k$, $|k_y| << |k_x|$). Fast mode wave is described by the dispersion relationship $k_A^2 = k_y^2 + k_x^2$, and its field-aligned magnetic component and wave vector are

$$\begin{aligned} b_{||}^{(i,r)} &= -\left(b_x^{(i,r)}\cos I + b_z^{(i,r)}\sin I\right) \\ k_{||} &= -\left(k_x\cos I + k_z\sin I\right) \end{aligned} \tag{14.12}$$

From the equation $\nabla\cdot\mathbf{b}^{(i,r)} = 0$ it follows that $b_z^{(i,r)}/b_x^{(i,r)} = \mp k_x/k_z$, where the upper sign refers to the incident (i)-wave, while the lower sign refers to the reflected (r)-wave. In the low-frequency limit, when $k_x >> k_A$, the fast compressional mode cannot reach directly the E-layer and it reflects at some height above the ionosphere. So, in the ionosphere this mode happens to be in a non-propagating (evanescent) regime where $k_z = \left(k_A^2 - k_x^2\right)^{1/2} \approx ik_x$. Hence, the fast mode has a structure of a plane inhomogeneous wave with a circular polarization in the meridional plane: $b_z^{(i,r)}/b_x^{(i,r)} = ik_x/|k_x|$. The compressional component is $b_{||}^{(i,r)} = b_x\left[\cos I \mp k_x/i\,|k_x|\sin I\right] = b_x\exp(\pm iI)$, therefore, $|b_{||}| = |b_x|$.

We have to relate the compressional magnetic component $b_{||}$ with horizontal magnetic component at the ground $b_x^{(g)}$. Using the relation (14.8) and the expression for T_{HF} from Alperovich and Fedorov (2007) one can obtain the relationship between the incident fast wave and the ground signal

$$b_x^{(g)} = T_{HF}\frac{b_{||}^{(i)}}{q_+} \quad T_{HF} = \frac{2}{1 - ih\left(k_z + \omega\mu_0\Sigma_C\right)} \tag{14.13}$$

Near the equator, $I \to 0$, the emission of Alfven waves into the magnetosphere can be neglected, so $\tilde{\Sigma}_C \approx \Sigma_C$.

The relation for the total magnetic field can be obtained summarizing inputs from the incident and reflecting partial waves $b_{||} = b_{||}^{(i)} + b_{||}^{(r)}$. As a result, the relationship between the total compressional component $b_{||}$ and the north-south magnetic component at the ground $b_x^{(g)}$ is as follows

$$b_x^{(g)} = T_{HF}\left[(1 + R_{FF})\cos I + \frac{k}{\kappa}(1 - R_{FF})\sin I\right]^{-1} b_{||}$$

For a high ground conductivity and large-scale wave structure, so that $k\delta_g << 1$, $kh << 1$, the reflection coefficient $R_{FF} \sim 1$. Then, the above can be simplified as follows

$$\begin{aligned} \kappa_F &= \frac{b_{||}}{b_x^{(g)}} = \frac{2}{T_{HF}}\cos I \\ \frac{2}{T_{HF}} &= A_2^{-1} = 1 - ik_A h\left(\frac{\kappa}{k_A} + \frac{\tilde{\Sigma}_C}{\Sigma_A}\right) \end{aligned} \tag{14.14}$$

A relationship similar to (14.14) was derived by Itonaga (1995), namely

$$\frac{b_{||}}{b_x^{(g)}} = \frac{1}{2A_1\cos I} \quad A_1^{-1} = 1 - ik_A h\left(1 + \frac{\Sigma_C}{\Sigma_A}\right) \tag{14.15}$$

However, the relationship (14.15) was derived for the specific case only, when fast wave front coincided with a magnetic shell, i.e. $k_{||} = 0$, and for an incident compressional component $b_{||}^{(i)}$. In satellite measurements the incident and reflected components cannot be distinguished, therefore, for comparison with satellite/ground observations one should use the relationships (14.14) for the total component $b_{||}$.

The relationship (14.14) predicts that the experimentally measured ratio of total magnetic fields $b_{||}/b_g$ should be proportional to cos I, that is, it should decrease away from the dip equator. This prediction agrees with the Pi2 observations by Han et al. (2004).

In the near-equatorial region, where $\tilde{\Sigma}_C \approx \Sigma_C$, and $k_A h << 1$, the factor $A_2^{-1} = 1 + ik_A h\left[1 + \Sigma_C/\Sigma_A\right]$. During nighttime, when $\Sigma_C/\Sigma_A << 1$, the factor $A_2^{-1} \approx 1$, and during day-time, when $\Sigma_C/\Sigma_A >> 1$, the factor $A_2^{-1} \approx 1 + ik_A h\left(\Sigma_C/\Sigma_A\right) = 1 + i\omega h/V_C$, where $V_C = 1/\mu_0\Sigma_C$ is the Cowling velocity (Fedorov et al. 1999). Under typical daytime conditions $V_C \sim 20$ km/s, so in the Pi2 band ($\omega \sim 5\cdot 10^{-2}$ s^{-1}) the factor $A_2^{-1} \approx 1 + 0.25i$. Thus, the ionospheric conditions exert only weak influence on Pi2 fast mode transmission to the ground, that is $\kappa \sim 1$. The component $b_{||}$ is expected to be in phase with H-component on the ground. These theoretical predictions agree with the CHAMP/ground observations of Pi2 waves (Section 14.1).

14.5 Discussion and Conclusion

The demand for the elaboration of a reliable qualitative model of ULF transmission through the ionosphere to the ground comes not only from ULF wave studies, but from the wider space community. Such model is necessary to evaluate how adequately ground observations of ULF waves correspond to magnetospheric wave activity, which is the important driver/loss factor for ring current protons and relativistic electrons.

Observations at CHAMP of the global distribution of dayside compressional Pc3 pulsation activity and ground Pc3 waves have shown that a significant part of the magnetospheric fast mode energy can leak to the ionosphere. Assuming that the wave is elongated primarily in the East-West direction, the part of a compressional mode amplitude reaching the ionosphere can be roughly estimated as $\propto \exp(-mz_R/LR_E)$, where $z_R \sim mV_A/\omega - R_E$ is the altitude of the fast mode refection, and m is the azimuthal wave number. For typical Pc3 wave parameters $\omega = 0.2\ s^{-1}$, $V_A = 10^3$km/s, and $m = 3$, the altitude of the fast mode reflection is expected to be not very far from the ionosphere, $z_R \sim 1\ R_E$. According to this estimate, the amplitude above the ionosphere of a fast mode can be just few times less than the amplitude in the magnetosphere.

The statistics of the Pc3 time intervals considered are probably dominated by events with a larger contribution of intervals when CHAMP was away from the local Alfven resonant region. In these events a ground Pc3 signal is expected to be coherent over large distances, and resonant distortions of amplitude/phase behavior will be hardly noticeable. However, in the general situation both modes, Alfven and fast magnetosonic, are present in incident Pc3 waves. Therefore, a situation is possible in which the compressional component in the upper ionosphere is due to the fast mode, whereas the ground signal is produced mainly by the Alfven mode. This case probably corresponds to the daytime Pc3 geomagnetic pulsation events observed by CHAMP by Vellante et al. (2004) and Ndiitwani and Sutcliffe (2009). Though a close correspondence between the compressional component and the ground signals was observed, the behavior of the CHAMP azimuthal component showed specific amplitude-phase structure typical for a field line resonance and a $\pi/2$ rotation of the polarization ellipse through the ionosphere. The theoretical model for this general situation is still to be developed.

The coordinated CHAMP-ground observations of Pi2 waves are in qualitative agreement with the predictions of the theory presented in Section 14.4. Observational results and theoretical modeling have confirmed the idea of fast mode cavity mechanism of mod-latitude Pi2 oscillations.

The fast compressional waves have been found to be an inevitable element of ULF wave pattern in the top-side ionosphere, and to play a more significant role that it has been previously assumed. Because magnetic field compressions are inherently related to plasma compressions, the observations of ULF plasma oscillations in the upper ionosphere with Doppler techniques (Poole et al. 1988; Alperovich et al. 1991) or TEC monitoring techniques (Davies and Hartman 1976; Hammond et al. 2001), interpreted on the basis of the assumption of Alfven wave incidence only (Poole and Sutcliffe 1987; Poole et al. 1988; Pilipenko and Fedorov 1995), should be revisited. The model developed provides researchers with a tool to quantitatively relate ULF plasma compressions in the upper ionosphere and ground magnetic signals.

Acknowledgments This research is supported by grant 10-05-93107 from the Russian Fund for Basic Research, US National Science Foundation grants ATM-0827903 and ANT-0841033 to Augsburg College, and grants from the Hungarian Space Office (TP 153), a South African-Hungarian bilateral project funded by the Hungarian Science and Technology Foundation (OMFB-00300/2008) and DAAD (DE-HU 5/2007).

References

Alperovich LS, Fedorov EN (2007) Hydromagnetic waves in the magnetosphere and the ionosphere. Series: Astrophysics and space science library, vol 353, 2009, XXIV, 418p. ISBN: 978-1-4020-6636-8

Alperovich LS, Fedorov EN, Volgin AV, Pilipenko VA, Pokhil′ko SN (1991) Doppler sounding as a tool for the study of MHD wave structure in the ionosphere. J Atmos Sol Terr Phys 53:581–586

Anisimov SV, Kurneva NA, Pilipenko VA (1993) Input of electric mode into the field of Pc3-4 pulsations. Geomagn Aeronomy 33:35–41

Davies K, Hartman GK (1976) Short-period fluctuations in total columnar electron content. J Geophys Res 81:3431–3434

Engebretson MJ, Posch JL, Westerman AM, Otto NJ, Slavin JA, Le G, Strangeway RJ, Lessard MR (2008) Temporal and spatial characteristics of Pc1 waves observed by ST5. J Geophys Res 113:A07206. doi:10.1029/2008JA013145

Fedorov E, Pilipenko V, Surkov V, Rao DRK, Yumoto K (1999) Ionospheric propagation of magnetohydrodynamic disturbances from the equatorial electrojet. J Geophys Res 104:4329–4336

Fujita S, Tamao T (1988) Duct propagation of hydromagnetic waves in the upper ionosphere, 1. Electromagnetic field distributions in high latitudes associated with localized incidence of a shear Alfven wave. J Geophys Res 93:14665–14673

Hammond RT, Meier B, Atkins S, Davis J, Bobb L (2001) Ultralow frequency waves and total electron content fluctuations. J Appl Phys 90:2582–2590

Han DS, Iyemori T, Nose M, McCreadie H, Gao Y, Yang F, Yamashita S, Stauning P (2004) A comparative analysis of low-latitude Pi2 pulsations observed by Oersted and ground stations. J Geophys Res 109:A10209. doi:10.1029/2004JA010576

Heilig B, Luhr H, Rother M (2007a) Comprehensive study of ULF upstream waves observed in the topside ionosphere by CHAMP and on the ground. Ann Geophys 25:737–754

Heilig B, Csontos A, Pankratz L, Pajunpaa K, Kultima J, Raita T, Reda J, Vaaczyova M (2007b) Upstream wave related Pc3 pulsations observed by the MM100 meridional magnetometer array. Publ Inst Geophys Pol Acad Sci C 99: 339–346

Hughes WJ, Southwood DJ (1976) The screening of micropulsation signals by the atmosphere and ionosphere. J Geophys Res 81:3234–3240

Itonaga M (1995) Spatial structure and polarization of geomagnetic pulsations observed on the ground. J Geomagn Geoelectron 47:1023–1027

Iyemori T, Hayashi K (1989) Pc 1 micropulsations observed by Magsat in the ionospheric F region. J Geophys Res 94:93–100

Jadhav G, Rajaram M, Rajaram R (2001) Modification of daytime compressional waves by the ionosphere: first results from Oersted. Geophys Res Lett 28:103–106

Keiling A, Wygant JR, Cattel C, Kim K-H, Russell CT, Milling DK, Temerin M, Mozer FS, Kletzing CA (2001) Pi2 pulsations observed with the Polar satellite and ground stations: coupling of trapped and propagating fast mode waves to a midlatitude field line resonance. J Geophys Res 106:25891–25904

Kim KH, Takahashi K (1999) Statistical analysis of compressional Pc3-4 pulsations observed by AMPTE CCE at L = 2–3 in the dayside magnetosphere. J Geophys Res 104:4539–4558

Kivelson MG, Southwood DJ (1988) Hydromagnetic waves and the ionosphere. Geophys Res Lett 15:1271–1274

Lysak RL (1997) Propagation of Alfven waves through the ionosphere. Phys Chem Earth 22:757–766

Ndiitwani DC, Sutcliffe PR (2009) The structure of low-latitude Pc3 pulsations observed by CHAMP and on the ground. Ann Geophys 27:1267–1277

Pilipenko V, Fedorov E (1995) Modulation of total electron content in the ionosphere by geomagnetic pulsations. Geomagn Aeronomy (Eng. Translation) 34:516–519

Pilipenko V, Vellante M, Anisimov S, De Lauretis M, Fedorov E, Villante U (1998) Multi-component ground-based observation of ULF waves: goals and methods. Ann Geofisica 41:63–77

Pilipenko V, Vellante M, Fedorov E (2000) Distortion of the ULF wave spatial structure upon transmission through the ionosphere. J Geophys Res 105:21225–21236

Pilipenko V, Fedorov E, Heilig B, Engebretson MJ (2008) Structure of ULF Pc3 waves at low altitudes. J Geophys Res 113:A11208. doi:10.1029/2008JA013243

Poole AWV, Sutcliffe PR (1987) Mechanisms for observed total electron content pulsations at mid latitudes. J Atmos Sol Terr Phys 49:231–236

Poole AWV, Sutcliffe PR, Walker ADM (1988) The relationship between ULF geomagnetic pulsations and ionospheric Doppler oscillations: derivation of a model. J Geophys Res 93:14656–14664

Sutcliffe PR, Luehr H (2003) A comparison of Pi2 pulsations observed by CHAMP in low Earth orbit and on the ground at low latitudes. Geophys Res Lett 30:2105. doi:10.1029/2003GL018270

Sutcliffe PR, Luehr H (2010) A search for dayside geomagnetic Pi2 pulsations in the CHAMP low-Earth orbit data. J Geophys Res. doi:10.1029/2009JA014757

Takahashi K, Anderson BJ, Newell PT, Yamamoto T, Sato N (1994) Propagation of compressional Pc3 pulsations from space to the ground: a case study using multipoint measurements. In: Engebretson MJ, Takahashi K, Scholer M (eds) Solar wind sources of magnetospheric ULF waves. Geophysical Monograph, vol 81. AGU, Washington, DC, pp 355–363

Takahashi K, Ohtani S, Anderson BJ (1995) Statistical analysis of Pi2 pulsations observed by the AMPTE CCE spacecraft in the inner magnetosphere. J Geophys Res 100:21929–21941

Takahashi K, Anderson BJ, Yumoto K (1999) Upper atmosphere search satellite observation of a Pi2 pulsation. J Geophys Res 104:25035–25045

Vellante M, Luehr H, Zhang TL, Wesztergom V, Villante U, Lauretis MD, Piancatelli A, Rother M, Schwingenschuh K, Koren W, Magnes W (2004) Ground/satellite signatures of field line resonance: a test of theoretical predictions. J Geophys Res 109:A06 210. doi:10.1029/2004JA010392

Yoshikawa A, Itonaga M (1996) Reflection of shear Alfven waves at the ionosphere and the divergent Hall current. Geophys Res Lett 23:101–104

Yumoto K, Saito T (1983) Relation of compressional HM waves at GOES 2 to low-latitude Pc 3 magnetic pulsations. J Geophys Res 88:10041–10052

Evidence for a Multi-scale Aurora

15

Christopher C. Chaston, K. Seki, T. Sakanoi,
Kazushi Asamura, and M. Hirahara

Abstract

Auroral arc widths are observed to extend from 100s of kilometers down to several 10s of meters. The largest widths mapped outward along auroral field-lines correspond to that of plasma gradients and flow shears in the equatorial magnetosphere. The smallest widths correspond to the fundamental plasma length scales along auroral field-lines. Larger scale arcs invariably have smaller scale features imbedded within them. The physics of auroral arcs is therefore multi-scale in nature. In this brief report we review some recent results from the FAST spacecraft characterizing the *k*-spectra of Alfvénic electromagnetic fluctuations associated with electron fluxes which drive visible aurora. These results suggest a nearly scale-invariant quality to the acceleration process over much of the range of scales reported for auroral arc widths. We then present a case study using observations from the REIMEI spacecraft to qualitatively demonstrate that the broad scale-range of variations observed in electromagnetic fields is represented in the multi-scale structuring of auroral forms. Together, observations from these spacecraft suggest that auroral arc structuring is a consequence of energy transport across scales facilitated by non-linear coupling similar to that which occurs in large Reynolds number fluid flows.

15.1 Introduction

The width of a discrete auroral arc is determined by the transverse width of the region through which electrons are accelerated Earthward. On the largest scales this width is determined by the scale size of flow shears and pressure gradients in the equatorial magnetosphere/plasma sheet and boundary layers which drive field-aligned currents (Paschmann et al. 2003). These currents define the large scale morphology of the auroral oval and the turbulent motions within the source regions of these currents (Borovsky and Funsten 2003) during disturbed times is well represented in auroral displays (Angelopoulos et al. 2008). However, the size of individual auroral arcs are rarely found to scale with these features because much of the current they comprise closes through the ionosphere without driving sufficient field-aligned particle acceleration (Stenbaek-Nielsen et al. 1998; Haerendel 2007). Studies of the relationship between the field-aligned current ($J_{||}$) and the characteristic energy of accelerated electrons ($\Delta\phi$) indicate that the largest scale over which field-aligned

C.C. Chaston (✉)
Space Sciences Laboratory, University of California, Berkeley, CA 94720, USA
e-mail: ccc@ssl.berkeley.edu

W. Liu, M. Fujimoto (eds.), *The Dynamic Magnetosphere*, IAGA Special Sopron Book Series 3,
DOI 10.1007/978-94-007-0501-2_15,

potentials form that drive field-aligned particle acceleration. and hence auroral arcs, can be approximated as $L = (\Sigma_p/K)$ (Weimer et al. 1985). L is known as the M-I coupling scale-length and has values of 50–100 km at ionospheric altitudes for typical observed values for the height integrated ionospheric Pedersen conductivity (Σ_p) and field-line conductance ($K = -J_{||}/\Delta\phi$) (Lysak 1990). Conversely, the smallest theoretically possible scale over which structuring in precipitating electron fluxes can occur is the electron gyro-radius – through the auroral acceleration region this length is of the order of several meters.

There have been at least two studies which have provided statistical distributions of auroral arc widths on scales larger than 70 m. Maggs and Davis (1968) reported a histogram of arc widths in white light with an increasing number of forms observed with decreasing arc widths to 70 m – the smallest scale their camera was able to resolve. Knudsen et al. (2001) presented a histogram of arc widths observed at 577 nm which peaked at 18 ± 9 km from a camera able to resolve arc widths down to 3.4 km. The distinctly different distributions derived in these two studies suggest that two different formation mechanisms are in operation: one at the smaller scales to account for the observations of Maggs and Davis (1968) and another at larger scales to account for Knudsen et al.'s (2001) results.

Measurements from polar orbiting spacecraft such as Freja, Polar and FAST have revealed the operation of two distinct electron acceleration processes leading to the formation of discrete aurora (Paschmann et al. 2003). At first glance these two processes may go some way to account for the differing distributions reported by Knudsen et al. and Maggs and Davis. In the 'Quasi-Static' or 'inverted-V' aurora electrons are accelerated in geomagnetic field-aligned potential structures that are largely invariant over an electron transit time. These potential structures extend over transverse scales less than the M-I coupling scale length (50–100 km) and drive aurora on these scales. In the 'Alfvénic' aurora electrons are accelerated in field-aligned potential structures which vary on time-scales similar to, or shorter than, the electron transit time. The electromagnetic fields associated with these potential structures have the properties of dispersive Alfvén waves which provide field-aligned potential structures with transverse scales of the order of the $2\pi\lambda_e$ where λ_e is the electron inertial lengths. λ_e has values from 0.1 to 10 km through the auroral acceleration region. Observationally 'Alfvénic' and 'Quasi-static' aurorae are often interspersed, however in a general sense they correspond to different magnetospheric drivers with the former being time dependent and typically associated with topological boundaries (Wygant et al. 2002), such as the plasma sheet boundary layer, and the later corresponding to stable structures in the plasma sheet which drive field-aligned currents in quasi-equilibrium with the ionosphere (Haerendel 2007).

While the 'Quasi-static' and 'Alfvénic' aurora provide an appealing explanation for the disparity between Maggs and Davis and Knudsen et al.'s results, Maggs and Davis's histogram of auroral arc widths is not consistent with a histogram of current sheet widths in dispersive Alfvén waves observed from FAST (Chaston et al. 2003, 2007). In these studies it was shown that histograms of auroral arcs driven by dispersive Alfvén waves should peak at scales of $\sim$1 km with visible auroral arcs on scales less than 100 m rare. On this basis it was concluded that electron acceleration in dispersive Alfvén waves was unable to account for Maggs and Davis's distribution which increases down to 70 m. More generally, in other studies of the width of field aligned currents and electric field structures above the aurora (Peria et al. 2000; Johansson et al. 2007) peaked distributions are found between those identified by Knudsen et al. (2001) and Maggs and Davis (1968). These results therefore present some confusion in our understanding of the preferred scale size for discrete auroral arcs and indirectly in the underlying physics of auroral arc formation. This issue has remained unresolved ever since it was first discussed in detail by Borovsky et al. (1993).

Alternative approaches for characterizing the scale dependency of aurorae that may in part address this issue have been implemented which rather than a preferred scale suggest a scale-invariant nature to the auroral acceleration process. Probability distributions derived from Polar UVI camera and ground based observations of auroral 'spot' sizes and intensity show power-law dependencies (Uritsky et al. 2002; Kozelov et al. 2004). Frequency-space analysis of electric and magnetic fields from the DE-2 spacecraft reveal power-law dependencies in spectral energy densities suggestive of turbulent processes active within regions of large scale field-aligned current above auroral arcs (Golovchanskaya et al. 2006; Kozelov and Golovchanskaya 2006). Analyses of auroral vorticity as a function of scale reveal power-law dependences

derivable from the observed magnetic field scaling (Chaston et al. 2010). These results together suggest that there is perhaps no preferred width for the structuring of auroral arcs.

In this report we address the distribution of arc widths for scales less than ~60 km by combining existing statistical measurements of electric and magnetic field *k*-spectra from interferometric measurements above the aurora with auroral imagery from the REIMEI spacecraft to demonstrate that structuring in auroral forms, if not the width of discrete arcs, extends down to at least kilometer scales in visible forms and 10s meter scales in electromagnetic field fluctuations. We suggest that this structuring is part of a nearly scale-invariant spectrum of auroral forms present within broader regions of luminosity. This scaling, we purport, is indicative of the primacy of non-linear cross-scale coupling across geomagnetic field-lines in the structuring of discrete auroral forms.

15.2 Observations

Figure 15.1 shows conjunctive measurements of auroral emission in UV light and electromagnetic fields and particles from NASA's Polar and FAST spacecraft from Chaston et al. (2008). The trajectory of the FAST spacecraft mapped onto the auroral image is indicated by the blue line and the observations from FAST through the night-side auroral oval are shown in panels b through d. The latitudinal width of the night-side auroral oval shown by the yellow-red shading in panel a is ~1000 km. Within this broad region of luminosity there is considerable structure and along the FAST trajectory two regions of enhanced luminosity are observed. At the polar-cap boundary, just below 70° and over a region extending ~150 km in the North-South direction we find the brightest emissions. Then at latitudes from 65 to 55° a less intense broader region of enhanced luminosity is found. This structure is sometimes referred to as the double auroral oval (Elphinstone et al. 1995). Inspection of the FAST observations reveals that the bright feature on the polar cap boundary is co-located with rapidly varying electric (E_X – Fig. 15.1b) and magnetic fields (B_Y – Fig. 15.1b) transverse to the geomagnetic field and enhanced electron energy fluxes extending from the lowest energies measured up to a few keV (Fig. 15.1c).

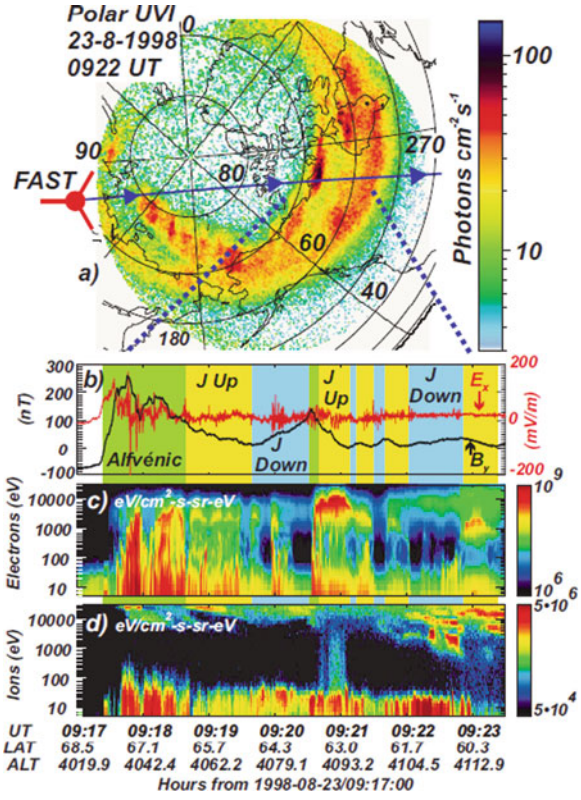

Fig. 15.1 (**a**) UV auroral image from Polar UVI instrument and FAST spacecraft trajectory. (**b**) FAST E_X (*red*) and B_Y (*black*) fields as defined in the text. (**c**) and (**d**) FAST electron and ion spectrograms (from Chaston et al. 2008)

These features are the hallmarks of the 'Alfvénic' aurora which we identify in Fig. 15.1b by the green shading. The emission at lower latitudes is also co-located with enhanced electron energy fluxes but in contrast distinct peaks are apparent at energies from a 1 to 10 keV. We also observe more slowly varying magnetic fields than found on the polar cap boundary. Under the assumption that the variation observed in B_Y is due spacecraft motion these variations correspond to spatial gradients and through Ampere's law indicate upward (negative slope) and downward (positive slope) field-aligned currents. These features are the hallmarks of the 'Quasi-static' aurora indicated by the yellow (upward current) and blue (downward current) shading. We also note that through the 'Quasi-static' regions there is a contribution from energetic electron fluxes scattered into the atmospheric loss cone through wave-particle interactions. This process forms what is known as the diffuse aurora and lies outside the scope this study.

Figure 15.2 shows spectrograms of B_Y and E_X compiled from a statistical sample of passes through the 'Alfvénic aurora' similar to (and including) that shown in Fig. 15.1. The measurements are shown in spectral energy density as a function of frequency in the spacecraft frame (f_{sp}) and also as a function of perpendicular wave number (k_x) along the spacecraft trajectory derived using interferometric techniques (Chaston et al. 2006). In general it was found that the transverse velocity (v_{sp}) of the spacecraft across the geomagnetic field was sufficiently large that the spacecraft frame frequency was approximately related to the measured transverse wave-number through spacecraft Doppler shift as $2\pi f_{sp} \approx k_X v_{sp}$. It was shown in this work, and in earlier case studies from the Freja spacecraft (Wahlund et al. 1998; Stasiewicz et al. 2000), that the relationship between E_X and B_Y obeyed the expected dispersion of inertial Alfvén waves.

Since the Alfvén speed (V_A) over the altitude range where these measurements were performed is much less than the speed of light the bulk of the energy density in these waves resides in the magnetic field fluctuations. Significantly it can be seen in Fig. 15.2 that the spectra of the magnetic field fluctuations obey power-laws in k_X with distinct transitions between the ranges in k-space where each law prevails. Importantly, the wavenumber range over which each power-law prevails extends over more than an order of magnitude. We find that transitions between power-laws occurs at wave-numbers somewhat smaller than $k_X\lambda_e \approx 1$ and at $k_X\rho_i \approx 1$ where λ_e and ρ_i are the electron inertial length and ion gyro-radii respectively derived from local electron density and ion temperatures. Ideally these measurements should be performed as an average over an Alfven wavelength along the geomagnetic field since for the larger transverse scales (smaller wavenumbers) shown in Fig. 15.2 these wavelengths can be larger than the scale of plasma parameter variation above the topside ionosphere. This is certainly the case at the wavenumber of the first spectral break-point and smaller where wavelengths along B_o can be thousands of kilometers and extend well above the altitude of the FAST spacecraft. Consequently, the location of the first breakpoint is more consistent with the inertial scale above the FAST spacecraft than the locally derived value. For observed densities over this range $\lambda_e > 1000$ m and so $k_x\lambda_e \approx 1$ occurs at wavenumbers much closer to the observed break-point than given by the local value. The scales λ_e and ρ_i are significant

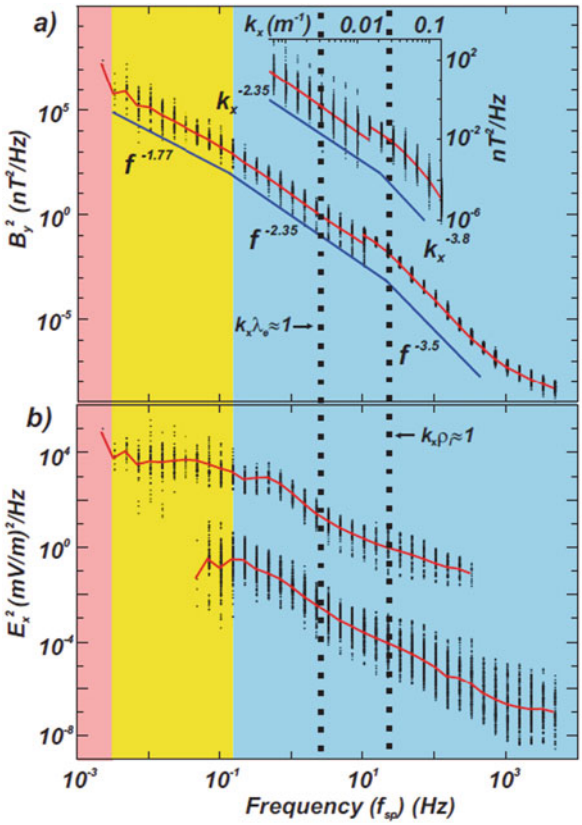

Fig. 15.2 (**a**) Average $B_Y{}^2$ (f_{sp}; k_X) spectra. (**b**) Average $E_X{}^2(f_{sp}; k_X)$ spectra for survey and burst data collection modes. The latter is down-shifted by 4 orders of magnitude. The *black bars* are composed of points representing individual measurements in each f_{sp} or k_X bin (from Chaston et al. 2008)

because they correspond to those scales where Alfvén wave dispersion is modified due to finite electron inertia and ion gyro-radii effects (Lysak and Lotko 1996a) and where Alfven waves become dissipative. In terms of the usual turbulence phenomenology, fluctuations on wavenumbers larger than these scales may comprise a dissipation range.

The two power-laws in B_y at smaller wavenumbers ($k_\perp\rho_i < 1$) shown in Fig. 15.2 are similar to those found previously by Golovchanskaya et al. (2006) under the assumption of stationarity. However we note that our trends tend to be somewhat steeper and the breakpoint separating each power-law occurs on smaller scales. This may be consequence of temporal variations in the fields quantities they measure or as a result of different scalings through the 'Alfvénic' versus 'inverted-V' aurora which were not differentiated in their analysis. Nonetheless, the power-law

dependencies we obtain are a robust result that are reproduced with every passage of the FAST spacecraft through the 'Alfvénic aurora'. Within the range of experimental error they correspond to the expected scaling for Alfvénic turbulence in a strongly magnetized plasma ($k^{-5/3}$) as described in the theory of 'critical-balance' by Goldreich-Sridhar (1995) and for kinetic Alfven waves ($k^{-7/3}$) as described by Howes et al. (2008). These results indicate that the transport of energy across scales occurs at a rate which is invariant with scale over the range where each power-law prevails. By adapting the Kolmolgorov model for fluid turbulence for these fluctuations it was shown by Chaston et al. (2008) that the rate of energy transport across scales inferred by these spectra is sufficient to power the field-aligned acceleration of electrons observed and hence the formation of the 'Alfvénic' aurora.

With this result in hand it is meaningful to consider if commensurate structuring is found in the visible aurora. Figure 15.3 shows three 5 s sequences of evolving auroral forms as observed by the REIMEI spacecraft recorded on the 7th of August 2007 looking down onto the southern auroral oval with the geomagnetic field out of the page. The spacecraft at this time is moving southward so that the features observed in consecutive frames move progressively toward the top of each image. Through active attitude control the geomagnetic foot-point of the spacecraft at 105 k km altitude is maintained within the field of view of the camera over extended intervals. This unique capability enables continuous magnetically conjugate particle and imagery measurements to be performed. When operated in 'Mode S' the REIMEI spacecraft provides imager measurements with a cadence of 0.12 s and $\sim 1 \times 1$ km pixel size covering $\sim 66 \times 66$ km of sky at 105 km altitude (Sakanoi et al. 2003). Electron distributions are provided with a cadence of 20 ms allowing features of $\sim$150 m to be resolved (Asamura et al. 2003). In Fig. 15.3 we show only every 10th image recorded. The location of the foot-point in the lower two sequences is indicated by the white rectangle and the track of the foot-point through each image is shown as the dashed line. Since the forms vary significantly over the time taken for the foot-point to move through the field of view of the camera quantitative comparison between the auroral emissions and the particle distributions can strictly only be performed at the foot-point. Since launch in August 2005 the Reimei spacecraft has recorded numerous conjugate observations of the kind shown in Fig. 15.3 and provides a excellent tool for advancing understanding of auroral acceleration and

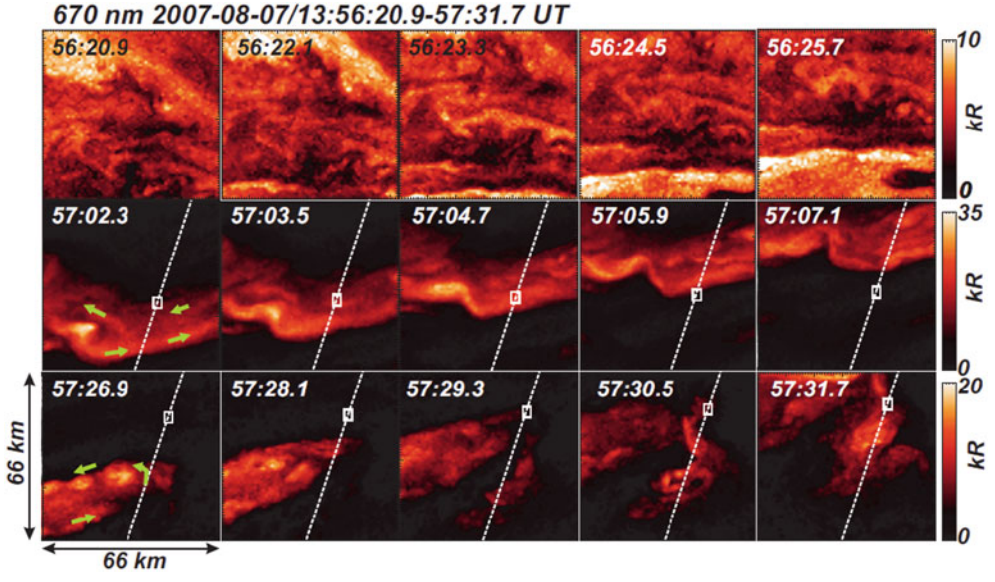

Fig. 15.3 Three sequences of evolving auroral forms observed on 7th August 2007 at 670 nm and looking down from the Reimei spacecraft in the southern hemisphere. The small white rectangle in each image shows the magnetic foot-point of the Reimei spacecraft projected onto the image plane at 105 km. The white trace is the spacecraft magnetic foot-point track through each image. Each image is separated by 1.2 s. Note that exactly conjugate data was not recorded for the first interval. Green arrows indicate the optical flow direction. South is toward the bottom of each image

the structuring of auroral forms. In what follows we qualitatively discuss the structuring observed in these images and reserve a more quantitative analysis for a future study.

Figure 15.4 shows electron energy-time spectrograms covering the time-span of the three auroral sequences shown in Fig. 15.3. The red bar on the top shows the total time-span over which imager measurements were recorded. For the first sequence of images shown in Fig. 15.3 (going left to right), the magnetic foot-point of the spacecraft was not in the field-of view of the camera but further to the south. The highly structured forms shown here correspond to these features in the electron energy-time spectrogram to the left of the red bar shown in Fig. 15.4. These include the low energy 'inverted-V' and more broadly distributed 'Alfvénic' electrons from 13:56:00 to 13:56:20 UT. Structuring in these images is apparent on scales from the scale size of the field-of view (66 km) down to the smallest scales observable (∼2 km). Motions are difficult to discern from these snapshots but the full resolution movies reveal a complicated pattern of sheared and vortical flows over a range of scales equivalent to that of the structuring in luminosity.

For the 2nd sequence of images in Fig. 15.3 the conjunctive particle measurements of Fig. 15.4 show that the bright emission is driven by electrons on the northern (or low latitude) edge of a broad inverted-V structure which extends from 13:57:00 to 13:58:15 UT – or ∼1000 km. The width of the large scale region of luminosity here normal to the main band of emission is ∼20 km. There is a large scale flow shear across this width with features on the northern side heading to the left and on the southern side to the right as shown by the green arrows. There is significant structure within this width and vortices appear, evolve, break-up and disappear over the sequence shown. These vortices exist over a range of scale sizes extending from that of the large scale shear itself, as represented by the bright feature in the lower left of the first image, down to the smallest scales resolvable from the Reimei imager.

The third sequence of images presented in Fig. 15.3 shows the evolution of a bright arc embedded within the same inverted-V as the second. Here again we have

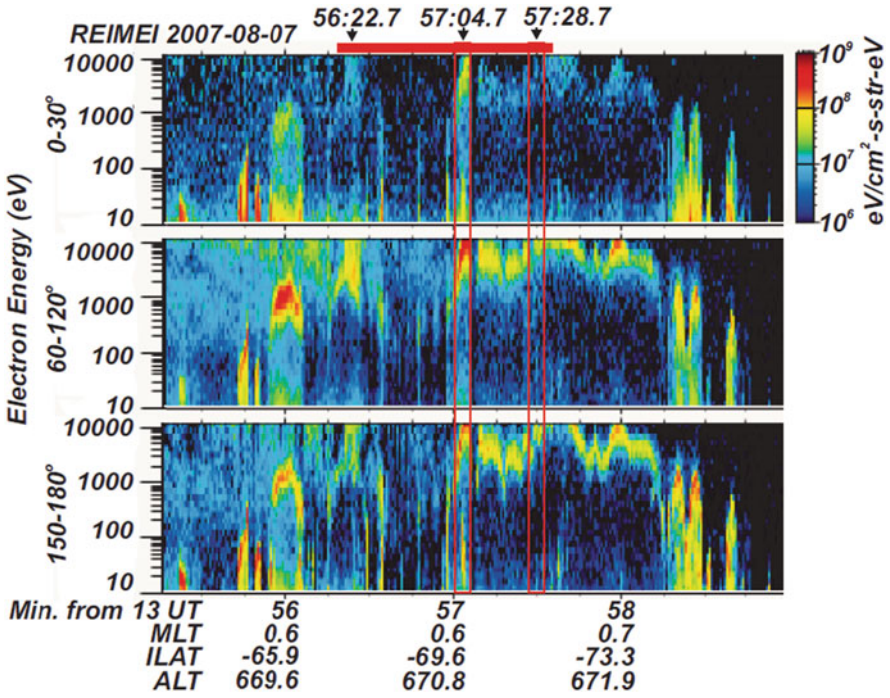

Fig. 15.4 Electron spectrograms from REIMEI measurements: the first, second and third panels show the differential energy flux of up-going electrons within 30° of B_o, electrons between 60 and 120° from B_o and down-going electrons within 30° of B_o respectively. The *red bar* shows the interval over which conjugate imager and particle measurements were recorded with the sub-intervals presented in Fig. 15.3 indicated by the *red graticles*. Note that no conjugate data was recorded for the first interval shown in Fig. 15.3

a feature with a gross-scale of ~20 km with sheared flow on this scale. However in this case the large scale flow goes through a 'hair-pin' bend, as indicated on this image, which eventually becomes unstable and breaks-up in the later snapshots. Three vortices on several kilometer scales are apparent on the northern edge in the first image in the sequence which move out of the field of view in the later snapshots. More generally however, the internal structuring within this broader-scale region of luminosity, as observed in the former two sequences, extends down to the smallest scales resolvable.

We have performed an inspection of 50 similar sequences of bright auroral forms observed from the REIMEI spacecraft through both 'Alfvénic' and 'Quasi-static' or 'inverted-V' aurora and this pattern, with some exceptions, is repeated – i.e. irrespective of the size of the larger-scale region of luminosity, the internal structuring extends to the smallest scales resolvable with no clearly preferred scale apparent. We qualify this by adding that smaller-scale regions of luminosity are generally brighter and the forms within them move more rapidly, but the same conclusion regarding the structuring applies.

15.3 Discussion and Conclusion

From the spectral results reported from FAST, and our qualitative study of the structuring of auroral forms in REIMEI imager observations, the internal structuring of bright auroral forms cannot easily be associated with a particular scale. Strictly speaking, the FAST results from Chaston et al. (2008) need to be extended to include similar measurements in the 'Quasi-static' aurora to determine if similar power-law trends as observed in the 'Alfvénic' aurora apply. However, the scale invariance observed is generally suggestive of a cascade active within the auroral acceleration region which transports energy from the larger scales, over which auroral arcs form, to smaller scales where ultimately dissipation through electron and ion acceleration occurs. These smaller scales correspond to what Hallinan and Davis (1970) have previously described as 'arc elements' embedded within broader regions of luminosity. While our study of the structuring of auroral forms is limited by the ~2 km spatial Nyquist of the Reimei camera, the observations from the study by Maggs and Davis (1968) suggests that this structuring extends below 70 m scales. If the structuring observed in electric and magnetic fields corresponds to the structuring in luminosity then the power-law spectral results from FAST show that this structuring continues down to at least 30 m which is the minimum scale resolvable from the FAST interferometric measurements shown in Fig. 15.2 when mapped to the ionosphere.

To account for the power-law k-spectra observed from FAST it seems likely that this cascade toward smaller scales is facilitated through the action of instabilities in flow shears and current sheets (Hallinan and Davis 1970; Seyler 1990; Wu and Seyler 2003) leading to non-linear coupling across scales similar to that which occurs in turbulent fluids. These processes are most obviously manifest in the internal motions within larger scale regions of luminosity which we have mentioned above. In a recent study, Chaston et al. (2010) demonstrated evidence for the action of these processes by compiling power-law vorticity k-spectra from auroral imagery. Via this means the transition from a smooth flow driven by ExB/B^2 drifts proceeds through the formation of eddies or vortices which may break-up into smaller eddies and so on. In high magnetic Reynolds number magnetized plasmas, such as that found on auroral field-lines, the current is largely advected with the flow so that these motions are faithfully represented in the motions of auroral forms. Published evidence for this process can be found in the statistical studies by Trondsen and Cogger (1998) of periodic distortions in auroral arc elements down to 100 m scales and recent extremely high resolution measurements from the ASK camera (Dahlgren et al. 2008; Dahlgren et al. 2010) which reveal secondary vortices termed 'RUFFS' forming within the larger scale vortices.

Some caveats are however implicit in this interpretation. Firstly, the observations from the Reimei images show that within regions of auroral luminosity this process is not necessarily 'space-filling'. Chaston et al. (2008) showed from a structure function analysis using FAST data that the occupancy of space by the turbulent fields varies along the spacecraft trajectory and across scales suggestive of a stretching of eddies into filamentary vortices representing intermittency. A similar trend was found by Golovchanskaya et al. (2006). In this sense the structuring observed is not strictly scale invariant. Secondly, the usual fluid-like evolution is complicated in the auroral case by the geomagnetic field (Goldreich and Sridhar 1995),

the 'stiffening' action and instability of current sheets (Chandrasekhar 1961; Wu and Seyler 2003) and coupling to the ionosphere (Lotko et al. 1987; Lysak 1990; Lysak and Song 1996b). And thirdly, because the time scale over which an auroral arc exists can be short relative to Alfvén travel times along an auroral flux-tube, this evolution may not develop into fully evolved turbulence of the kind described by Kolmolgorov or more appropriately in the context of strongly magnetized plasmas by Goldreich and Sridhar (1995). However, the salient point is that the non-linear coupling is active long enough to produce the power-law spectra from FAST and the nearly scale-invariant luminosity structuring observed from REIMEI (albeit qualitative at this stage).

So how does this interpretation of the structuring of auroral arcs fit with the studies of auroral arc widths described in the introduction? Knudsen et al.'s (2001) distribution of widths define the gross-scale of the features within which the structuring we consider occurs. Knudsen et al.'s (2001) scales correspond to those at which geomagnetic field-lines can no longer be considered equipotentials and parallel electric fields form – these may be related to the magnetosphere-ionosphere coupling scale length, to $2\pi\lambda_e$ through the auroral acceleration region or to other scale lengths which have been suggested to identify the scale over which parallel fields form on auroral field-lines (Vogt and Haerendel 1998; Pilipenko et al. 2004). However, it is the strongly sheared flows and unstable current sheets at and below these scales which evolve to form the multi-scale features we document. In this sense, the mean scale reported by Knudsen et al. (2001) provides a natural break-point for a two-scale approach for understanding the evolution of auroral forms as sometimes used in turbulence theory. This is supported by the fact that the mean arc width defined by Knudsen et al. corresponds to the scale of the spectral break-point, between the Kolmolgorov-like and $k^{-7/3}$ power-law trends shown in Fig. 15.2 when mapped to ionospheric altitudes.

In the light of these observations it seems likely that the apparent discrepancy between the distribution reported by Maggs and Davis (1968) with that reported by Knudsen et al. (2001) or by Chaston et al. (2003) may arise in defining a feature as an individual arc. If structuring in auroral luminosity extends down to the smallest scale resolvable, as we observe from REIMEI, then within the field of view of an auroral camera there will of course be more features identifiable on smaller scales than on larger scales. On average the increase in the number features resolvable will double when the scale is halved, leading to a histogram which increases exponentially with decreasing scale similar to that reported by Maggs and Davis (1968). In fact the histogram they present is what one would expect if counting structures in a turbulent fluid. Conversely, if it is required that the luminosity must go virtually to zero between features, then a fall off in the histogram below a particular scale length representing the gross-scale for auroral particle acceleration can be expected. This is what is found in the histogram reported by Knudsen et al. (2001) and in most histograms of structuring in fields quantities from spacecraft above the aurora (Chaston et al. 2003; Johansson et al. 2007). With this ambiguity in mind perhaps a more physically meaningful way to characterize the scaling of auroral features within one of Knudsen et al.'s (2001) gross-scale arcs is in the form of spectrograms of auroral luminosity as a functions of inverse scale. We have not as yet performed this analysis, since a careful consideration of the appropriate basis function is required, but such an approach could be applied to the REIMEI imager data to provide a statistical picture of how auroral luminosity varies with scale. Such a distribution would be immediately comparable to energy flux spectrograms as a function of scale taken from conjugate particle measurements onboard REIMEI and fields measurements from other polar orbiting spacecraft such as we have presented here from FAST.

Before closing it should be noted that the cross-scale coupling we emphasize in this report is but one of several processes that lead to the structuring of auroral arcs on small scales. Steep density gradients are known to exist across auroral field lines (Stasiewicz et al. 1998; Ergun et al. 1998; Chaston et al. 2006; Johansson et al. 2007). Alfvén waves propagating along these field-lines will therefore refract and 'phase mix' to produce small transverse structuring. For gradient scales represented in observations such a process has been shown to be effective in the production of small-scale structuring in Alfvén wave fields (Genot et al. 1999; Lysak and Song 2008; Allan and Wright 2000) and consequently the auroral forms they drive. Structuring in electron precipitation also provides gradients in ionospheric conductivity which are unstable to the production of small scale Alfvén waves and field-aligned currents. This leads to further structuring in electron precipitation and so on. The

consequent positive feedback leads to a cascade toward smaller scales (Lysak 1991; Streltsov and Lotko 2008) which in the non-linear case has been shown to extend down to 100m (Lysak and Song 2002). While both phase mixing and ionospheric feedback must play a role in structuring the aurora it is unclear how they can reproduce the power-law scaling observed from FAST nor the multi-scale structuring and rapid internal motions within arcs seen from REIMEI. For this reason it seems likely that much of the structuring seen in auroral forms is a consequence of the action of instabilities above and through the auroral acceleration and associated turbulent-like cross-scale coupling which can produce the power-law spectral trends and the multi-scale structuring observed.

Acknowledgements This research was supported by STEL visiting professor program, the global COE program 'Quest for Fundamental Principles in the Universe: from Particles to the Solar System and the Cosmos' of Nagoya University, NSF grant ATM-0602728 and NASA grant number NNG06GG63G.

References

Allan W, Wright A (2000) Magnetotail waveguide: fast and Alfvén waves in the plasma sheet boundary layer and lobe. J Geophys Res 105:317

Angelopoulos et al (2008) Tail reconnection triggering substorm onset. Science 1160495:10.1126

Asamura K et al (2003) Auroral particle instrument onboard the INDEX satellite. Adv Space Res 32:375–378

Borovsky JE (1993) Auroral arc thickness as predicted by various theories. J Geophys Res 98:6101–6138

Borovsky JE, Funsten HO (2003) MHD turbulence in the Earth's plasma sheet: dynamics, dissipation, and driving. J Geophys Res 108:1284. doi:10.1029/2002JA009625

Chandrasekhar S (1961) Hydrodynamic and hydromagnetic stability. Clarendon, Oxford

Chaston C, Peticolas L, Bonnell J, Carlson C, Ergun R, McFadden J, Strangeway R (2003) Width and brightness of auroral arcs driven by inertial Alfvén waves. J Geophys Res 108:1091. doi:10.1029/2001JA007537

Chaston CC, Genot V, Bonnell JW, Carlson CW, McFadden JP, Ergun RE, Strangeway RJ, Lund EJ, Hwang KJ (2006) Ionospheric erosion by Alfvén waves. J Geophys Res 111:A03206. doi:10.1029/2005JA011367

Chaston CC, Hull AJ, Bonnell JW, Carlson CW, Ergun RE, Strangeway RJ, McFadden JP (2007) Large parallel electric fields, currents, and density cavities in dispersive Alfvén waves above the aurora. J Geophys Res 112:A05215. doi:10.1029/2006JA012007

Chaston CC, Salem C, Bonnell JW, Carlson CW, Ergun RE, Strangeway RJ, McFadden JP (2008) The turbulent Alfvénic aurora. Phys Rev Lett 100:175003

Chaston CC, Seki K (2010) Small-scale auroral current sheet structuring. J Geophys Res 115:A11221. doi:10.1029/2010JA015536

Dahlgren H, Ivchenko N, Sullivan J, Lanchester BS, Marklund G, Whiter D (2008) Morphology and dynamics of aurora at fine scale: first results from the ASK instrument. Ann Geophys 26:1041–1048

Dahlgren H, Aikio A, Kaila K, Ivchenko N, Lanchester BS, Whiter DK, Marklund GT (2010) Simultaneous observations of small multi-scale structures in an auroral arc. J Atmos Sol Terr Phys 72(7–8):633–637

Elphinstone RD, Murphree JS, Hearn D, Cogger LL, Sandahl I, Newell PT, Klumpar DM, Ohtani S, Sauvaud JA, Potemra TA, Mursula K, Wright A, Shapshak M (1995) The double oval UV auroral distribution. 1. Implications for the mapping of auroral arcs. J Geophys Res 100:12093

Ergun RE, Carlson CW, McFadden JP, Mozer FS, Delory GT, Peria W, Chaston CC, Temerin M, Elphic RC, Strangeway R, Pfaff R, Cattell CA, Klumpar D, Shelley E, Petersen WK, Moebius E, Kistler L (1998) FAST satellite observations of electric field structures in the auroral zone. Geophys Res Lett 25:2025

Genot V, Louarn P, Le Queau D (1999) A study of the propagation of Alfvén waves in auroral density cavities. J Geophys Res 104:22649

Goldreich P, Sridhar S (1995) Toward a theory of interstellar turbulence, 2. Strong Alfvénic turbulence. Astrophys J 438:763

Golovchanskaya IV, Ostapenko AA, Kozelov BV (2006) Relationship between the high-latitude electric and magnetic turbulence and the Birkeland field-aligned currents. J Geophys Res 111:A12301. doi:10.1029/2006JA011835

Haerendel G (2007) Auroral arcs as sites of magnetic stress release. J Geophys Res 112:A09214. doi:10.1029/2007JA012378

Hallinan TJ, Davis TN (1970) Small-scale auroral arc distortions. Planet Space Sci 18:1735

Howes GG, Cowley SC, Dorland W, Hammett GW, Quataert E, Schekochihin AA (2008) A model of turbulence in magnetized plasmas: implications for the dissipation range in the solar wind. J Geophys Res 113:A05103. doi:10.1029/2007JA012665

Johansson T, Marklund G, Karlsson T, Lileo S, Lindqvist P-A, Nilsson H, Buchert S (2007) Scale sizes of intense auroral electric fields observed by CLUSTER. Ann Geophys 25:2413–2425

Knudsen DJ, Donovan EF, Cogger LL, Jackel B, Shaw WD (2001) Width and structure of mesoscale optical auroral arcs. Geophys Res Lett 28:705–708

Kozelov BV, Uritsky VM, Klimas AJ (2004) Power law probability distributions of multiscale auroral dynamics from ground – based TV observations. Geophys Res Lett 31:L20804. doi:10.1029/2004GL020962

Kozelov BV, Golovchanskaya IV (2006) Scaling of electric field fluctuations associated with the aurora during northward IMF. Geophys Res Lett 33:L20109. doi:10.1029/2006GL027798

Lotko W, Sonnerup B, Lysak RL (1987) Nonsteady boundary layer flow including ionospheric drag and parallel electric fields. J Geophys Res 92:8635

Lysak RL (1990) Electrodynamic coupling of the magnetosphere and the ionosphere. Space Sci Rev 52:33268

Lysak RL (1991) Feedback instability of the ionospheric resonant cavity. J Geophys Res 96:1553. doi:10.1029/90JA02154

Lysak R, Lotko W (1996a) On the kinetic dispersion relation for shear Alfvén waves. J Geophys Res 101(A3):5085–5094

Lysak RL, Song Y (1996b) Coupling of Kelvin – Helmholtz and current sheet instabilities to the ionosphere: a dynamic theory of auroral spirals. J Geophys Res 101:15411

Lysak RL, Song Y (1999) The role of Alfvén waves in the formations of parallel electric fields. In: Ohtani S, Fujii R, Hesse M, Lysak RL (eds) Magnetospheric current systems. AGU Geophysical Monograph, Washington, DC, p 147

Lysak RL, Song Y (2002) Energetics of the ionospheric feedback interaction. J Geophys Res 107:1160

Lysak RL, and Song Y (2008) Propagation of kinetic Alfvén waves in the ionospheric Alfvén resonator in the presence of density cavities, Geophys Res Lett 35:L20101. doi:10.1029/2008GL035728

Maggs JE, Davis TN (1968) Measurements of the thickness of auroral structures. Planet Space Sci 216:205–209

Paschmann G, Haaland S, Treumann R (2003) Auroral plasma physics. Kluwer, Dordrecht, p 94

Peria W, Carlson C, Ergun R, McFadden J, Bonnell J, Elphic R, Strangeway R (2000) Characteristics of field-aligned currents near the auroral acceleration region: FAST observations. In: Ohtani S et al (eds) Magnetospheric Current Systems. AGU Geophys Monogr Series, Washington, DC, Vol. 118, pp. 181–189

Pilipenko V, Fedorov E, Engebretson M, Yumoto K (2004) Energy budget of Alfvén wave interactions with the auroral acceleration region. J Geophys Res 109:A10204. doi:10.1029/2004JA010440

Sakanoi T et al (2003) Development of the multi-spectral auroral camera onboard the 238 INDEX satellite. Adv Space Res 32:379–384

Seyler CE (1990) A mathematical model of the structure and evolution of small-scale discrete auroral arcs. J Geophys Res 95:17199

Stasiewicz K, Holmgren G, Zanetti L (1998) Density depletions and current singularities observed by Freja. J Geophys Res 103:4251

Stasiewicz K et al (2000) Identification of widespread turbulence of dispersive Alfvén waves. Geophys Res Lett 27:173

Stenbaek-Nielsen HC, Hallinan TJ, Osborne DL, Kimball J, Chaston C, McFadden J, Delory G, Temerin M, Carlson CW (1998) Aircraft observations conjugate to FAST: auroral are thicknesses. Geophys Res Lett 25(12):2073–2076

Streltsov AV, Lotko W (2008) Coupling between density structures, electromagnetic waves and ionospheric feedback in the auroral zone. J Geophys Res 113:A05212. doi:10.1029/2007JA012594

Trondsen TS, Cogger LL (1998) A survey of small-scale spatially periodic distortions of auroral forms. J Geophys Res 103:9405

Uritsky VM, Klimas AJ, Vassiliadis D, Chua D, Parks G (2002) Scale-free statistics of spatiotemporal auroral emissions as depicted by POLAR UVI images: dynamic magnetosphere is an avalanching system. J Geophys Res 107:1426. doi:10.1029/2001JA000281

Vogt J, Haerendel G (1998) Reflection and transmission of Alfvén waves at the auroral acceleration region. Geophys Res Lett 25(3):277–280

Wahlund J-E, et al (1998) Broadband ELF plasma emission during auroral energization 1. Slow ion acoustic waves. J Geophys Res 103:4343

Weimer DR, Goertz CK, Gurnett DA, Maynard NC, Burch JL (1985) Auroral zone electric fields from DE 1 and DE 2 at magnetic conjunctions. J Geophys Res 90:7479–7494

Wu K, Seyler CE (2003) Instability of inertial Alfvén waves in transverse sheared flow. J Geophys Res 108:1236. doi:10.1029/2002JA009631

Wygant JR, Keiling A, Cattell CA, Lysak RL, Temerin M, Mozer FS, Kletzing CA, Scudder JD, Streltsov AV, Lotko W, Russell CT (2002) Evidence for kinetic Alfven waves and parallel electron energization at 4–6 RE altitudes in the plasma sheet boundary layer. J Geophys Res 107(A8):1201. doi:10.1029/2001JA900113

Part V
Ionospheric Driver of the Magnetosphere

Influences of the Ionosphere, Thermosphere and Magnetosphere on Ion Outflows

16

Andrew W. Yau, W.K. Peterson, and Takumi Abe

Abstract

Ion outflows from the auroral and polar cap ionosphere are highly variable in composition, energy, space and time, and constitute an important source of plasma in the magnetosphere. The variety of ion outflows fall into two categories: bulk ion flows, including the polar wind and auroral bulk ion up-flow; and suprathermal ion outflows, including ion beams, ion conics, transversely accelerated ions and upwelling ions. The bulk ion flows constitute an important source of low-energy plasma for suprathermal ion outflows above the topside ionosphere, where transverse ion acceleration results in the generation of ion conics, and parallel electric field and magnetic folding contribute to the formation of ion beams at high altitudes. Both ion outflow categories are strongly influenced by the solar EUV irradiance and solar wind energy input and the state of the magnetosphere-ionosphere-thermosphere. The acceleration of the polar wind and auroral up-flow is much larger and the ion flux of the up-flow is much lower at topside ionospheric altitudes at solar minimum than at solar maximum. Compared with H^+ and He^+, O^+ ion beams and conics exhibit a much stronger dependence on magnetic and solar activity: the active-to-quiet time and solar maximum-to-minimum ratios of the O^+ ion outflow rate being $\sim$20 and $\sim$5, respectively, compared with the ratios of 4 and 0.5 for H^+, and resulting in a factor of 10 increase in O^+/H^+ ratio at solar maximum.

16.1 Introduction

We review our current knowledge on ionospheric ion outflows and the influences of the ionosphere, thermosphere and magnetosphere on them. Our emphasis is on recent in-situ ion composition and ground-based radar observation results, particularly those that pertain to ionosphere-magnetosphere plasma redistribution.

The density and composition of the terrestrial atmosphere are believed to remain in a steady state on a geological time scale, and in a delicate balance that is influenced by electromechanical energy from the Sun via the solar wind and through the magnetosphere and the ionosphere. The discovery in Shelley et al. (1972) of energetic oxygen ions of ionospheric origin in the magnetosphere implies the existence of non-thermal processes capable of accelerating oxygen ions in the topside ionosphere to above the escape energy

A.W. Yau (✉)
Department of Physics and Astronomy, University of Calgary, Calgary, AB T2N 1N4, Canada
e-mail: yau@phys.ucalgary.ca

W. Liu, M. Fujimoto (eds.), *The Dynamic Magnetosphere*, IAGA Special Sopron Book Series 3,
DOI 10.1007/978-94-007-0501-2_16,

(∼10 eV). Extensive satellite and ground-based observations over the last four solar cycles have shown that ionospheric ion outflows are highly variable in composition, energy, space and time, and constitute an important and at times dominant source of plasma in the magnetosphere. In addition, the resulting heavy ion escape is especially dependent on solar electromagnetic and solar wind energy inputs, which are in the form of extreme ultraviolet (EUV) photons that heat and ionize the thermosphere and electromechanical energy that heats and accelerates the plasma, respectively.

The composition of the ionosphere is constrained by the temperature, composition and structure of the thermosphere, which vary with the level of solar EUV flux in a solar cycle. Figure 16.1 shows the mean, maximum and minimum solar radio flux, $F_{10.7}$, in each 27-day solar rotation in the period from 1965 to 2010 in units of solar radio flux (1 sfu $= 10^{-22}$ W m^{-2} Hz^{-1}). This period spans Solar Cycle (SC) 20 to 23, including the SC 20 maximum in 1969 and the SC 23 maximum in 2000. The $F_{10.7}$ index is used as an index of solar EUV flux, and it spans a wide range within a solar rotation near solar maximum. In other words, the level of solar EUV flux varies significantly over a solar rotation. During large solar flare events, the daily $F_{10.7}$ value occasionally exceeds 350; the daily $F_{10.7}$ values in such cases have been excluded in determining the maximum $F_{10.7}$ values in Fig. 16.1.

Figure 16.2 compares the altitude distribution of thermospheric temperature and densities at solar minimum and maximum, respectively, using the MSIS (Hedin 1987) model. It shows that at local noon at an auroral latitude (60°N, 90°W) at spring equinox, the exospheric temperature increases from ∼850 K near solar minimum ($F_{10.7} = 70$) to ∼1200 K near solar maximum ($F_{10.7} = 150$). This temperature increase results in a corresponding increase in atomic hydrogen density and escape flux in the geo-corona (above ∼2000 km), and a decrease in the density at lower altitudes. The opposite is true for the gravity-bound atomic oxygen, where the temperature increase results in a proportional increase in scale height and an increase of a factor of 2.5 and 8 in density at 300 and 500 km, respectively.

The ion-neutral chemistry in the topside ionosphere is dominated by the "accidentally resonant" charge exchange reaction between atomic hydrogen and oxygen, $H^+ + O \leftrightarrow H + O^+$, which tends to maintain the ion mixing ratio to the neutral ratio, i.e. $[O^+]/[H^+] \approx [O]/[H]$, and favors H^+ above the "crossover" altitude where the H density dominates and the charge exchange reaction results in a net H^+ production and O^+ loss. This explains the increase in the crossover altitude and the corresponding reduction in H^+ density and increase in O^+ density in the ionosphere at solar maximum. It also implies that rapid O^+ ion flow through the topside ionosphere is necessary to supply O^+ ions to higher altitudes (Moore 1980).

The composition of the ionospheric plasma is also influenced by geomagnetic activity, which increases the temperature of the thermosphere and modifies its

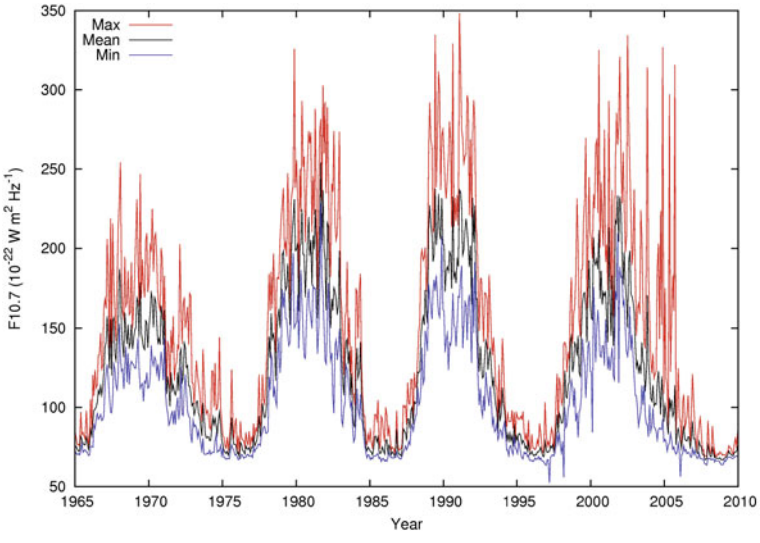

Fig. 16.1 Mean, maximum and minimum solar radio flux $F_{10.7}$ in each 27-day solar rotation from 1965 to 2005 in solar radio flux unit (1 sfu $= 10^{-22}$ W m^{-2} Hz^{-1}). Note the large variation of $F_{10.7}$ within a solar rotation near solar maximum

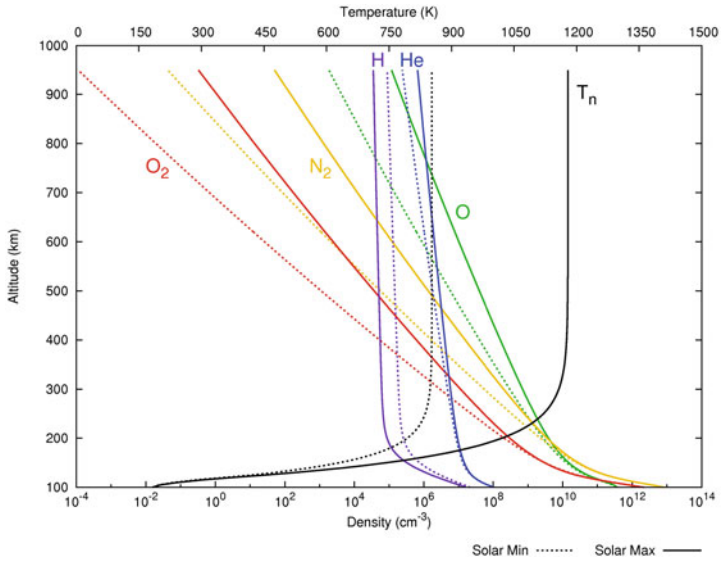

Fig. 16.2 MSIS model dayside neutral temperature and densities at auroral latitude near solar minimum ($F_{10.7} = 70$) and maximum ($F_{10.7} = 150$)

composition distribution, by heating and expanding the thermosphere on a time scale of hours or days through Joule heating and other processes. The resulting changes in thermospheric composition are largest at auroral and polar latitudes, as are changes in ionospheric composition and mass density.

At a given level of solar and geomagnetic activity, the ionosphere varies strongly with local time in density and peak altitude due to atmospheric photoionization in the day and its absence at night. At low and mid-latitudes where the flux tubes are near co-rotation with the Earth, this leads to the drainage of plasma on the night side and its refilling on the dayside. Likewise, inter-hemispheric plasma flows occur except near equinox, due to the hemispheric asymmetry in ionospheric density and height resulting from the changing inclination of the Earth's equatorial plane from the ecliptic plane, and to the enrichment in He^+ in the winter hemisphere.

During times of southward interplanetary magnetic field (IMF), the topology of horizontal circulation streamlines transitions abruptly from near co-rotation at low and mid-latitudes to a two-cell convection pattern at auroral latitudes and above. The transition latitude is dependent on the strength of the solar wind. The two-cell convection pattern usually comprises an anti-sunward and a sunward flowing region poleward and equatorward of the auroral oval, respectively (see, for example, Heppner and Maynard 1987). Thus, the auroral zone is generally the region of flow reversal and often the site of strong velocity shear, one that is sometimes co-located with the regions of field-aligned currents and acts as a source of free energy for possible plasma acceleration.

During northward IMF, the convection pattern is typically more complex, and the anti-sunward flow in the polar cap sometimes reverses in flow direction, creating regions of strong velocity shears where free energy is available for possible plasma acceleration and formation of trans-polar cap arcs. This means the auroral zone and/or the polar cap are potentially important regions of ionospheric ion acceleration and outflow depending on the IMF orientation.

At both auroral and polar cap latitudes, a plasma flux tube undergoes a circulation cycle on the order of a day or less depending on the strength of the solar wind, in which the volume of the flux tube may change by as much as a few orders of magnitude: a flux tube may be stretched from ~10 Earth radii (R_E) in length to ~ 100 R_E or greater as it convects anti-sunward in the low-latitude boundary layer, or disconnect from the conjugate hemisphere to connect itself into the solar wind during part of the cycle and then reconnect in the tail and traverse the inner magnetosphere back to its starting point.

During the stretch part of the cycle, the ionospheric plasma can expand freely into the upper reaches of the flux tube because of the negligible plasma pressure there. This results in the formation of the polar wind: an outflow of low density, supersonic flux of cold, light H^+ and He^+ (and under certain conditions heavier O^+)

ions through the polar cap and into the magnetotail lobes.

The variety of observed ion outflows in the high-latitude ionosphere may be grouped into two categories: bulk ion flows with energies up to a few eV in which all the ions acquire a bulk flow velocity, and suprathermal ion outflows in which in general a fraction of the ions are energized to much higher energies. The category of bulk ion flows includes the polar wind and auroral bulk O^+ up-flow from the topside auroral and polar-cap ionosphere. The category of suprathermal ion outflows includes ion beams, ion conics, transversely accelerated ions (TAI), and upwelling ions (UWI).

The ion outflow measurements from the different satellites were in general acquired in different phases in the 11-year solar cycle. Many ion outflow characteristics depend on specific ionospheric conditions that are modulated by the solar EUV flux, and so may exhibit significant long-term variations as well as variability on the time scale of days within a solar rotation near solar maximum. Therefore, the level of solar activity at the time of an ion outflow measurement is often an important factor, and so it is important to take into account the relative phases in the solar cycle between different measurements.

The altitude coverage and ion energy range of an ion outflow observation data set are also important. For convenience in our discussions below, we will use the term "topside ionosphere" to refer to the altitude region below 1000 km including the *F*-region, and the terms "low-", "mid-", and "high-altitude" to the regions between 1000 and 4000 km, between 4000 and 10,000 km, and above 10,000 km, respectively. As will be discussed in Sections 16.2 and 16.3, all ground-based ion outflow observations to date are confined to the topside ionosphere. Observations from most satellites are confined or primarily confined to one or two altitude regions. These include observations on DE-2 in the topside ionosphere, where the auroral bulk up-flow originates; observations on Freja and Fast and near perigee on DE-1 and Akebono at low altitude, where maximum polar wind acceleration occurs and ion conic acceleration begins; observations above perigee on Akebono and near perigee on Polar at mid altitudes, where ion beam begins to appear; and observations on Viking, DE-1 and Polar at high altitude.

16.2 Bulk Ion Flows

The discovery of the magnetotail, plasmapause, and atmospheric helium attrition in the early years of space exploration led to the postulation of the existence of the polar wind in the late sixties. In the presence of the Earth's gravitation, an ambipolar electric field ($E_{//}$) develops in the polar ionosphere, as the ion is much more massive and experiences a much larger gravitational force compared with the electron, and the spatial separation between the two produces a polarization electric field that acts to accelerate the ion in the upward magnetic field direction. An ambipolar field also develops in the presence of an anisotropic particle distribution, in order to maintain charge neutrality along the magnetic field line (Tam et al. 2007).

16.2.1 Polar Wind

In the "classical" polar wind, the ambient plasma pressure gradient and ambipolar (polarization) electric field are the only sources of acceleration for the polar wind ions, and they result in a steady-state and current-free flow of quasi-neutral plasma – electrons and light H^+ and He^+ ions – along the open geomagnetic field lines. Axford (1968) coined the term polar wind to describe the supersonic nature of the thermal outflow in analogy to the supersonic expansion of the solar wind from the solar corona into interplanetary space. Additional ion acceleration mechanisms discussed below give rise to the so-called "non-classical" polar wind.

The dominant source of polar wind H^+ ions is the accidentally resonant charge exchange reaction between O^+ and H. The source of He^+ is the photoionization of neutral helium. The polar wind ion flux is limited by the production rate of the outflowing ions and their Coulomb collision rate with other ions. For typical ionospheric densities and temperatures in the topside ionosphere and under steady-state conditions, these sources and Coulomb collision processes result in a maximum limiting H^+ flux of $\sim 3 \times 10^8$ cm^{-2} s^{-1} at 1000 km altitude at solar minimum. The H^+ limiting flux decreases to $\sim 1 \times 10^8$ cm^{-2} s^{-1} near solar maximum due to the increase in exospheric temperature and the corresponding increase in neutral oxygen density and in O–H^+ exchange at high altitude. In comparison, the limiting He^+ flux is dependent

primarily on neutral atmospheric He and N_2 densities, which affect the rate of He photo-ionization and He^+–N_2 charge-exchange, respectively; thus it varies from $\sim 1-3\times10^5$ cm^{-2} s^{-1} in solar minimum summer to $\sim 0.5-1.5\times10^7 cm^{-2}$ s^{-1} in solar maximum winter; the winter-to-summer and solar-maximum-to-minimum flux ratio is ~25 and ~2, respectively (Raitt and Schunk 1983). Therefore, the polar wind is composed primarily H^+ and a few percent of He^+.

A variety of polar wind models exist, including those based on fluid or generalized transport equations and those on collionless, collisional, or hybrid kinetic approaches; see the excellent reviews of Tam et al. (2007) and Schunk (2007). The predictions from these models were discussed and compared with observations in Yau et al. (2007).

Polar wind ion observations have been made using ion composition instruments on a number of polar-orbiting satellites, including ISIS-2, DE-1, Akebono, and Polar. Polar wind electron observations have also been made on DE-1 and Akebono. These observations spanned different phases of SC 20 to 23, and a wide range of altitudes from ~1000 km to ~50,500 km (8 R_E) altitude. The ISIS-2 and most of the DE-1 ion observations were made at low altitude (1000–4000 km) in the declining phase of the solar cycle; the DE-1 electron observations were made at mid and high altitude (7000–23,300 km). The Akebono ion observations spanned both low and mid altitudes (1000–10,000 km) and were made over a 10-year period spanning two 11-year solar cycles; most of the Akebono electron measurements were at low altitude below 3000 km. The Polar observations were made near solar minimum, and were primarily at mid altitude near its perigee (5000 km) and at high altitude near its apogee (~50,500 km) and extending down to ~22,000 km.

A composite picture of the polar wind emerges from these observations. The polar wind is regularly observed at all local times and latitudes, and is composed primarily of electrons and H^+, He^+ and O^+ ions. Its ion composition varies with the solar cycle, and is dominated in density by O^+ ions up to at least 4000 km and perhaps 6000–7000 km.

Figure 16.3 shows the averaged parallel ion velocity of each ion species observed on Akebono near solar maximum in 1990–1991 (Abe et al. 1993a) as a function of altitude on both the dayside (06–18 MLT) and the night side (18–06 MLT). The dayside and the night side profiles were qualitatively similar for all three species: the (approximately) monotonic increase in velocity with altitude, the mass dependence of the magnitude of the velocity, the largest acceleration (increase of velocity with altitude) of the H^+ velocity below 4000 km, and the starting altitude of detectable upward velocity are apparent in both cases.

On the dayside, the H^+ velocity typically reached 1 km/s near 2000 km, the He^+ and O^+ velocities near 3000 and 6000 km. For all three species, the velocity on the dayside was significantly larger than that on the night side, the H^+, He^+, and O^+ velocity at 10,000 km being about 12, 6, and 4 km/s on the dayside

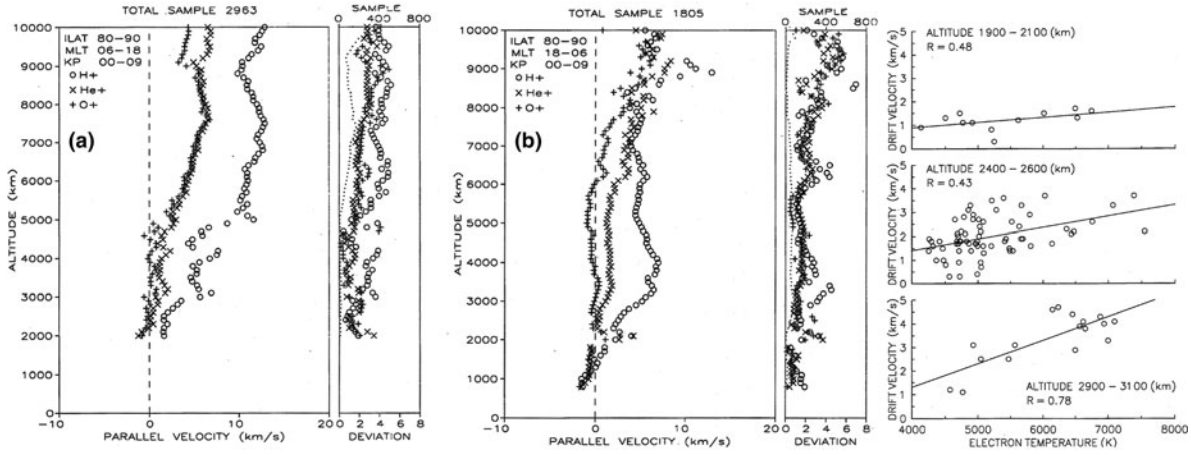

Fig. 16.3 Averaged polar wind H^+, He^+ and O^+ ion velocity above 80° invariant observed on Akebono in 1990–1991 near solar maximum on the (**a**) dayside and (**b**) night side; H^+ velocity versus electron temperature (From Abe et al. 1993a, b)

and ~7, 4, and 3 km/s on the night side, respectively. This suggests the possible increase in the amplitude of ambipolar electric field or the presence of additional ion acceleration on the dayside due to escaping atmospheric photoelectrons (Tam et al. 2007).

On the dayside, the averaged O^+ velocity began to increase near 5000 km. Its standard deviation was less than 50% of the mean above this altitude but was comparable to or greater than the mean below. This suggests that the measured velocity data samples were predominantly upward above this altitude but consisted of both upward and downward velocity samples below. On the night side, the averaged O^+ velocity started to increase from zero at 7000 km. The small negative velocity between 5000 and 6000 km probably reflects the larger number and/or velocity values of downward velocity samples compared to the upward velocity samples in this altitude region. On DE-1, the observed O^+ velocity below 4000 km was found to correlate with the IMF B_z, and was on average downward during southward IMF and upward during northward IMF (Chandler 1995).

Abe et al. (1993b) found the magnitude of ion acceleration at a given altitude to correlate strongly with the electron temperature. The right panel in Fig. 16.3 shows the scatter plot of the H^+ ion velocity versus electron temperature at 2000, 2500, and 3000 km, respectively. The velocity at each altitude increased with electron temperature. The rate of increase was smallest at the lowest altitude and largest at the highest altitude. For an increase in electron temperature from 4000 to 7000 K, the increase in velocity was ~50 percent (from 1.0 to 1.5 km/s) at 2000 km, and a factor of 3 (from 1.3 to 4 km/s) at 3000 km. The larger rate of increase at higher altitude is consistent with the cumulative increase in ion velocity due to the ambipolar electric field along the field line, and the direct relationship between the local magnitude of ion acceleration and the ambipolar electric field responsible for the acceleration, respectively.

Theoretically, the polarization electric field in the polar wind is related to the electron plasma pressure (density and temperature) as $qE = -kT_e[d\ln(n_e T_e)/dr]$, where E is the polarization electric field, n_e and T_e are the electron density and temperature, and q and k are the electron charge and the Boltzmann constant, respectively. In the case of positive electron temperature gradient (increasing electron temperature with altitude), the polarization electric field remains upward provided that the electron density decreases with altitude more rapidly, as was usually observed on Akebono up to at least 4000 km. Thus, the polar wind ions experience a continuous acceleration in velocity in the course of its upward expansion.

16.2.1.1 Magnetic and Solar Activity Dependence

Abe et al. (1993a, b) found the velocity of H^+ and He^+ to be more variable during active times ($Kp \geq 3$) than at quiet times ($Kp \leq 2$). The variability (standard deviation) of the H^+ velocity was as much as 50% of the mean during active times. However, the average velocity was only weakly dependent on Kp, and only marginally larger at active times for both species.

Likewise, the observed ion outflow rate of H^+ and O^+ was also only weakly dependent on Kp (Abe et al. 1996). At 6000–9000 km above 75° invariant, the H^+ rate decreased by a factor of 2 while the O^+ rate increased by a factor of 1.7 as Kp increased from 1 to 6, and both rates decreased with Kp for Kp above 6. The reduction in the observed rates at very high Kp may be attributed to the increased fraction of the polar wind ion population being accelerated to beyond the upper energy-limit of the thermal ion measurements.

On Akebono, Abe et al. (1996) found the outflow rate of both species to exhibit very similar IMF B_z dependence, and increased with B_z under northward IMF conditions. This increase is evidently due to the larger flux from the noon and dusk quadrants during northward IMF, and is consistent with the topside polar cap ionosphere being a stronger and more dominant source of the observed polar wind plasma in comparison with other sources such as the cleft ion fountain and auroral bulk up-flow.

Abe et al. (1996) found the MLT dependence of the polar wind ion flux to strongly resemble the corresponding dependence of the observed ion velocity. Between 6000 and 9000 km altitude above 75° invariant near solar maximum, the ion flux was largest in the noon quadrant, and smallest in the midnight quadrant. Its latitude distribution in the midnight quadrant was narrow in direct contrast to the broad distributions in the other MLT quadrants; this is consistent with the larger ambipolar electric field in the sunlit polar wind in the other quadrants.

The normalized H^+ flux (to 2000 km altitude) in the noon quadrant was in the range of

$1 - 20 \times 10^7 \text{cm}^{-2}\ \text{s}^{-1}$ and comparable to the range of flux observed on ISIS-2 at 1400 km in the declining phase of SC 20 (Hoffman and Dobson 1980). The corresponding O^+ flux was typically a factor of 1.5–2.0 smaller. The observed ion flux above 80° invariant in the polar cap was due predominantly to the polar wind. The flux below 80° invariant in the noon and dusk quadrants is believed to contain a significant contribution from the cleft ion fountain also, at least in the case of southward IMF.

Observationally, it is not always possible to definitively distinguish polar wind ions originating from the topside auroral or polar cap ionosphere from thermal-energy ions that originate from other sources, such as auroral bulk ion up-flows. This is because the various ion populations in the polar ionosphere are sometimes mixed due to horizontal plasma transport and to ion energization processes. For example, polar wind ions can be accelerated and become a part of a suprathermal ion outflow population. Under southward IMF conditions and predominantly anti-sunward convection across the polar cap, upwelling ions originating from the cusp or the cleft can appear as a "cleft ion fountain" in the polar cap, where they may be present at lower apparent temperatures than in the cleft due to velocity filtering effects (Horwitz and Lockwood 1985), and become a part of the ambipolar outflow. Auroral bulk ion up-flow is another important contributor of low-energy O^+ ions to the polar wind ion population in the polar cap.

Figure 16.4 shows the averaged H^+ and O^+ polar wind velocity at different solar flux levels ($F_{10.7}$) as a function of altitude in the sunlit (SZA < 90°) and shadow (non-sunlit; SZA > 90°) regions, respectively. In the sunlit region, the H^+ velocity increased with altitude at all altitudes for all solar flux levels, except at low solar flux ($F_{10.7} < 100$) where it remained almost constant above 4000 km. However, the velocity gradient in different altitude regions varied with solar flux. At high solar flux ($F_{10.7} > 180$), the velocity increased continuously from 1500 km to 8500 km. In comparison, at low solar flux, the velocity increase with altitude was much larger below 3600 km and much smaller above 4000 km; as a result, the averaged velocity was about 50–60% larger at 4000 km and comparable at ~7000 km. In the non-sunlit region, the velocity increased with altitude below 4000 km but did not appear to do so significantly above at both low and medium solar fluxes.

The O^+ velocity in the sunlit region remained below 1 km s^{-1} below 6500 km but increased with altitude above at high solar flux. Similar transition in the

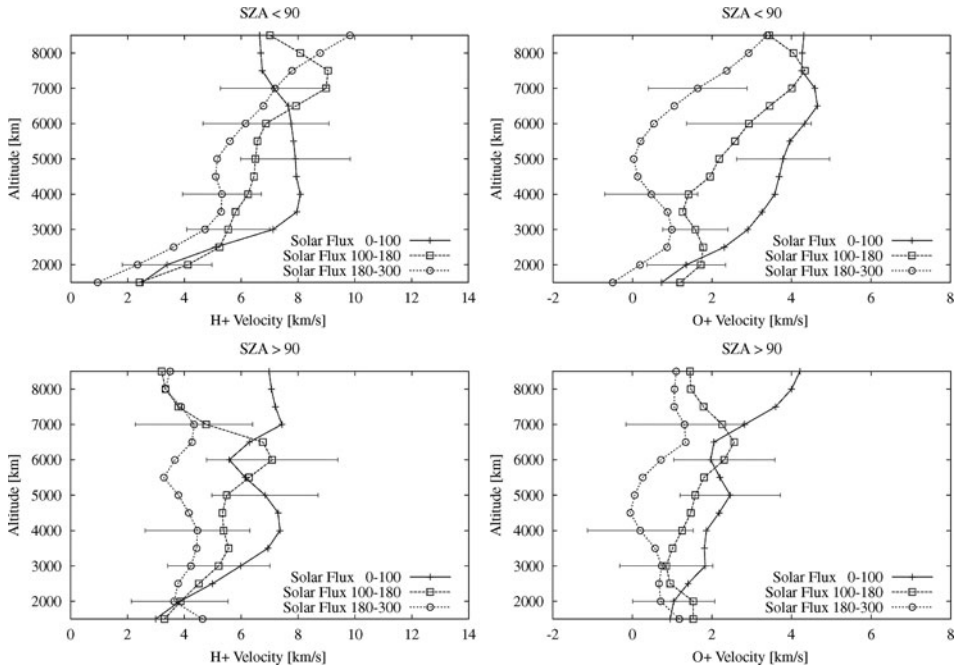

Fig. 16.4 Sunlit (*top*; SZA < 90°) and non-sunlit (*bottom*; SZA > 90°) averaged H^+ (*left*) and O^+ (*right*) velocity observed on Akebono as a function of altitude for different levels of solar radio flux ($F_{10.7}$) (From Abe et al. 2004)

velocity was observed at 4000 km at medium solar flux. At low solar flux, the velocity increased gradually with altitude from 1500 to 7000 km, reaching 4 km s^{-1} at 5000 km. In comparison, the velocity in the non-sunlit region increased with altitude more gradually. The increase was more significant as the solar flux decreased. At high solar flux, the velocity remained below 1.5 km s^{-1} at all altitudes.

In other words, the altitudinal gradients of both H^+ and O^+ velocity had very similar solar flux dependence and altitude variations, i.e. larger gradient below 5000 km and smaller gradient above 7000 km at low solar flux than at high solar flux, resulting in generally higher H^+ and O^+ velocities below 7000 and 8500 km, respectively, at low solar flux.

As the polar wind ions flow upward along open magnetic field lines to higher altitudes and undergo generally anti-sunward convection in the dayside cusp and the polar cap, they may be subject to a number of "non-classical" polar wind ion acceleration mechanisms (Yau et al. 2007), including centrifugal acceleration in the parallel direction due to strong $E \times B$ convection in regions of curved magnetic field at high altitudes above a few R_E, and continue to increase in both drift speed and temperature.

Figure 16.5 shows the occurrence distributions of H^+ and O^+ density and parallel velocity observed near Polar apogee at 50,500 km altitude near solar minimum (Su et al. 1998). The H^+ density ranged from 0.01 to 2 cm^{-3}, and averaged ~0.3 cm^{-3}. The parallel velocity ranged from 20 to 100 km s^{-1}, and averaged 45 km s^{-1}; the averaged upward number flux was 1.2×10^6 cm^{-2} s^{-1}. The O^+ density ranged from 0.001 to 0.3 cm^{-3} and averaged ~0.05 cm^{-3}. The parallel velocity ranged from 8 to 32 km s^{-1}, and averaged ~17 km s^{-1}; the averaged upward number flux was 8.3×10^4 cm^{-2} s^{-1}. The fact that O^+ was observed much less frequently and its density was an order of magnitude smaller than the H^+ density except at times of high solar wind speeds and large solar wind dynamic pressures (Elliott et al. 2001) is not unexpected, given the lower O^+/H^+ polar wind density ratio at low altitudes near solar minimum. What is perhaps surprising is the apparent lack of dependence of the O^+ density on the orientation of the IMF B_z, since at least a fraction of the O^+ observed in the high-altitude polar

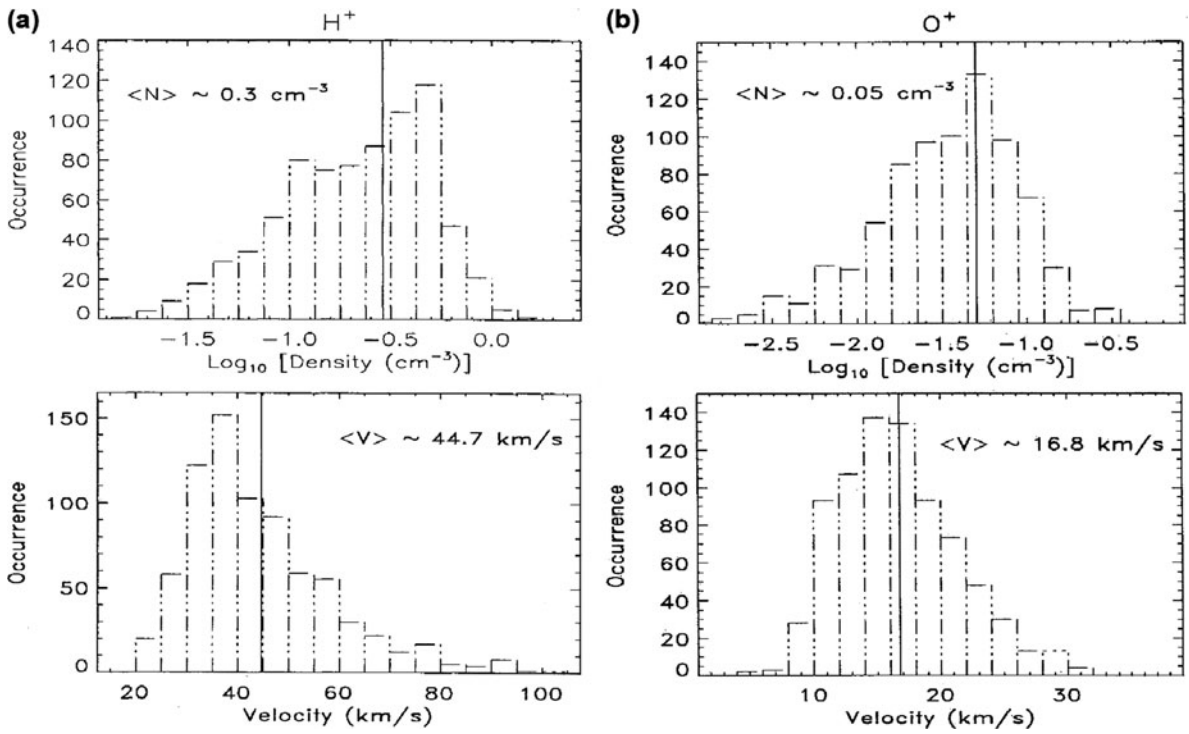

Fig. 16.5 Occurrence histograms of observed (**a**) H^+ and (**b**) O^+ polar wind density (*top*) and parallel velocity (*bottom*) on Polar at 50,500 km near solar minimum (From Su et al. 1998)

cap presumably originates from the cleft ion fountain, in which the ion trajectories depend strongly on anti-sunward convection and on IMF B_z.

The observed velocity ratio between ion species on both Akebono and Polar spans a wide range of values, and on average lies between unity and the inverse square root mass ratio of the species, e.g. $1 < v_{//}(H^+)/v_{//}(O^+) < [m(O^+)/m(H^+)]^{1/2} = 4$. This suggests that a number of processes of comparable energy gain may be contributing to the overall ion acceleration.

The temperature of polar wind ions is generally low, and was in the range of 0.05–0.35 eV between 7000 and 10,000 km on Akebono (Drakou et al. 1997). The parallel-to-perpendicular temperature ratio is less than unity (~0.52 for H^+ and ~0.55 for O^+ at 5000 km, but exceeds unity at high altitude (~1.5 for H^+ and ~2.0 for O^+ at 50,500 km) (Su et al. 1998). At Polar apogee (~50,000 km), the averaged parallel and perpendicular H^+ temperatures were ~1.7 and 1.1 eV, respectively. The corresponding O^+ temperatures were ~7.5 and 3.4 eV.

H^+, He^+ and O^+ ions in the polar wind are estimated to reach sonic speed (Mach number of 1) near 1500, 3000, and 6000 km, respectively, on average, based on the measured ion velocities in the subsonic to supersonic transition altitude region (Abe et al. 1993a) and the averaged ion temperature of 0.2 eV at 7000 km (Drakou et al. 1997), where their ion Mach number is ~1.5, 1.5, and 2.5, respectively, and increases to observed values of ~4.6 and 3.5 for H^+ and O^+, respectively, at 50,500 km on Polar (Su et al. 1998).

The electron density of the polar wind appears to transition to a slower density decrease with increasing altitude at 1000–1500 km; this is believed to be consistent with the transition of the H^+ polar wind from subsonic to supersonic speed in this altitude region. At higher altitude, the observed median electron density on DE-1 ranged from ~35 to ~1 cm^{-3} from 7000 to 23,300 km altitude (2.1 to 4.66 R_E geocentric), and followed a power law relationship with geocentric distance with an index of –3.85, i.e., $n_e \propto R^{\alpha}$; $\alpha = -3.85 \pm 0.32$ (Persoon et al. 1983). This suggests an approximately linear increase in the polar wind ion velocity with geocentric distance over this altitude range. From Figs. 16.3 and 16.5, the observed H^+ velocity to geocentric distance ratio is $\sim 2.7 \times 10^{-4}$ and $\sim 2.9 \times 10^{-4}$ s^{-1} at Akebono and Polar apogee, respectively, consistent with such a linear relationship.

The temperature of the polar wind electrons is generally higher than the ion temperature, and in the range of 0.3–0.7 eV at low altitude. The temperature of sunlit polar wind electrons is higher in the upward direction compared with that in the perpendicular and downward direction, i.e. $T_{up}/T_{\perp} \sim 1.5 - 2$, $T_{down}/T_{\perp} \sim 1$ (Yau et al. 1995). The temperature anisotropy is absent in the non-sunlit polar wind, and is attributed to the ambipolar electric field that is required to maintain quasi-neutrality along the field line in the presence of escaping atmospheric photoelectrons, and to Coulomb collisions between the electrons and the photoelectrons.

The fluxes of the different polar wind ion species have markedly different seasonal dependences in general. In the case of He^+, the flux has a winter-to-summer ratio of ~20. As noted in the Introduction, this dependence is attributed to the seasonal variations of neutral atmospheric helium and molecular nitrogen and the corresponding helium photo-ionization rate and He^+–N_2 charge-exchange rate.

The density of both H^+ and O^+ depends strongly on the solar zenith angle (SZA), and decreases by a factor of 10 and 100, respectively, at 5000 km altitude as SZA increases from 90° to 125°. The velocity of both species also decreases slowly as SZA increases above 100° (Abe et al. 2004).

A number of important questions on the polar wind remain open. The first is whether the cleft ion fountain is the sole or dominant source of O^+ polar wind in the high-altitude polar cap: observational evidence suggesting this to be the case exists, e.g. the correlation between the observed O^+ density and velocity with the location of observation from the cleft; (Su et al. 1998), but so does evidence suggesting the opposite, e.g. the lack of correlation between O^+ occurrence at Polar apogee and B_z noted above (Elliott et al. 2001). The second is whether the magnitude of the lowest-energy component of H^+ polar wind (energy-per-charge below the spacecraft potential) represents a dominant source of plasma in the magnetosphere; recent observation on Cluster (Engwall et al. 2009) suggests that "hidden" H^+ ions constitute a significant component of cold plasma in the high-altitude magnetosphere. Another question of interest is whether the polar wind flow undergoes transitions at different altitudes in different phases of the solar cycle, and whether the observed dominance of H^+ over O^+ near Polar apogee at solar minimum persists in the rest of the solar cycle.

16.2.2 Auroral Bulk Up-flow

It is generally accepted that ions in the high-latitude ionosphere obtain energy and momentum primarily through particle precipitation, heat flux, and electromagnetic field and waves from the magnetosphere, as well as from solar EUV radiation via atmospheric heating and subsequent photo-ionization and charge-exchange processes.

The occurrence of bulk thermal O^+ ion up-flow in the topside auroral ionosphere was first inferred from the scale height analysis of Alouette I sounder data near 500 km altitude (Lockwood and Titheridge 1981). Ion up-flows at velocities exceeding 1 km/s have been observed in the topside ionosphere in both the night side auroral zone and the dayside cleft on low-altitude polar-orbiting satellites, including DE-2 (Heelis et al. 1984) and Hilat; and from ground radars, including the Chatanika incoherent scatter radar at Chatanika, Alaska (Bates 1974), the European incoherent scatter radar (EISCAT) at Tromso, Norway (Wahlund and Opgenoorth 1989; Wahlund et al. 1992), and the EISCAT Svalbard radar (ESR) at Spitsbergen (McCrea et al. 2000).

The observed ion up-flow is highly variable in time and location, and generally confined to narrow latitude regions. Large upward ion flows often occur in regions of large ion convection velocities, and are dominated by O^+ and at times enhanced in molecular NO^+. A question of central importance is how the solar wind, the interplanetary magnetic field, and geomagnetic activity influence the occurrence and characteristics of ion up-flow.

Loranc et al. (1991) surveyed the occurrence of vertical ion up-flow and down-flow on the dayside (08–12 MLT) and the night side (20–24 MLT), respectively, using DE-2 ion drift data between 200 and 1000 km altitude near solar maximum. At 600–1000 km, the occurrence probability of up-flow was generally larger than that of down-flow in the auroral zone but smaller in the polar cap on both the dayside and the night side. Also, its peak spanned the convection reversal on the dayside, and was more extended in latitude and located at lower latitude on the night side. The separation between the up-flow and down-flow regions was more distinct in the topside than in the F-region (200–400 km): this suggests an association of the up-flow with the auroral zone, and the down-flow to be the return flow of the up-flow on both the dayside and the night side.

The peak occurrence probability for flows exceeding 100 m s^{-1} increased and moved equatorward with increasing Kp, from about 0.25 near 78° invariant at Kp $\leq$ 3– to about 0.35 near 70° at Kp $\geq$ 6 on the dayside; the region of peak flows also broadened. In the polar cap (>78° invariant), the occurrence probability of up-flow was several times larger during northward IMF ($B_z > 2$ nT) than during southward IMF ($B_z < -1$ nT; $\sqrt{(B_x{}^2 + B_y{}^2)} < 1$ nT). It was generally greater in the pre-noon sector than in the pre-midnight sector, and was greater in the dawn quadrant than in the dusk quadrant during active periods.

Loranc et al. (1991) attributed the observed bulk ion up-flow to upward ion expansion resulting from frictional heating and perpendicular ion temperature enhancement in regions of intensified $E \times B$ drifts, and the subsequent transient change in plasma scale height. However, Seo et al. (1997) suggested soft electron precipitation as the probable primary driver of up-flow, based on the correlation between the observed up-flow and electron temperature and the association of the largest-flux up-flow events with soft (<80 eV) precipitating electron flux in several DE-2 orbits, noting that the lowest-energy precipitating electrons are most effective in heating the topside thermal electrons.

In a follow-on study using field-aligned instead of vertical ion velocity and flux data and a larger data set consisting of ~130 DE-2 orbit passes between 300 and 1000 km altitude, Wu et al. (2000) found that in the dayside auroral region (72°–78° invariant), detectable up-flow started near 450 km altitude and accelerated with increasing altitude. Above 600 km altitude, the ion velocity ranged from 400 m s^{-1} downward to 800 m s^{-1} upward. In comparison, the range of ion velocity in the night side auroral region (63°–74° invariant) was slightly larger. In the dayside polar cap (80°–85° invariant), the flow was predominantly downward but was sometimes upward with velocities up to 800 m s^{-1}. In contrast, the flow in the night side polar cap (75°–85° invariant) was on average upward, at a velocity of 50 $\pm$ 200 m s^{-1}. The occurrence frequency of up-flow increased with altitude, reaching >70% in the dayside auroral region and 60–90% in the night side auroral and sub-auroral regions in the topside.

The averaged upward ion flux in the auroral zone increased with electron and ion temperature, to a value of $\sim 2 \times 10^9 \mathrm{cm}^{-2}\ \mathrm{s}^{-1}$ at electron temperatures above 4000 K and ion temperatures above 3500 K. In the polar cap, the ion flux changed from downward to upward at electron and ion temperatures above 3000 and 4000 K, respectively. The averaged electron temperature was higher than the ion temperature on the dayside, but was comparable to (and sometimes lower than) the ion temperature on the night side. Wu et al. (2000) attributed the higher dayside electron-to-ion temperature ratio to electron temperature enhancement driven by electron precipitation, and interpreted the temperature enhancement as a more dominant driver for up-flow on the dayside.

The observed up-flow by EISCAT was initially identified as "outflow" and classified into two types. The type-1 up-flow was associated with strong electric fields, ion temperature enhancements, anisotropic ion temperature, and very low electron densities in the F-region and below: The strong electric fields were often in regions of downward field-aligned currents adjacent to auroral arcs, and the low electron density in the E- and the low F-region was indicative of auroral precipitation being absent. The ion temperature enhancement and the perpendicular ion temperature anisotropy ($T_\perp > T_{//}$) were interpreted as frictional heating of the drifting ions through the neutral atmosphere in the presence of a strong perpendicular electric field; the increased ion temperature produces strong pressure gradients, which push the ions upward.

The type-2 up-flow was typically observed above auroral arcs, and was associated with electron temperature enhancement and sometimes also anisotropy, as well as weak to moderate electric fields. It was stronger in ion flux and occurred more frequently compared with type-1 up-flow. Wahlund et al. (1992) showed examples of type-2 outflow in which the electron temperature reached 5000–6000 K and the perpendicular electron temperature was a few hundred degrees higher than the corresponding parallel temperature above ~270 km altitude. The field-aligned ion velocity increased with altitude, to values exceeding 1 km/s at 900 km, corresponding to ion flux up to $\sim 2 \times 10^{10} \mathrm{cm}^{-2}\ \mathrm{s}^{-1}$.

The EISCAT data set was the subject of several statistical studies of ion up-flow. Keating et al. (1990) analyzed the seasonal and diurnal variations of up-flow between 200 and 500 km altitude using EISCAT data between 1985 and 1987, and found the up-flow occurrence to peak near local magnetic midnight. Foster et al. (1998) extended the study in altitude and in data period and analyzed the solar cycle variations also, using field-aligned up-flow data between 1984 and 1996 and vertical up-flow data up to 900 km altitude between 1990 and 1995.

Foster et al. (1998) showed that on average over the solar cycle, the field-aligned up-flow occurrence peaked in the pre-midnight sector, and the up-flow velocity was less than 100 m s^{-1} below 300 km altitude and increased monotonically with altitude. Roughly 50–60% of the observed up-flow events occurred during intervals of enhanced ion temperature.

Figure 16.6 shows the diurnal variations of the observed field-aligned up-flow occurrence frequency at 350, 400 and 500 km, respectively. The occurrence

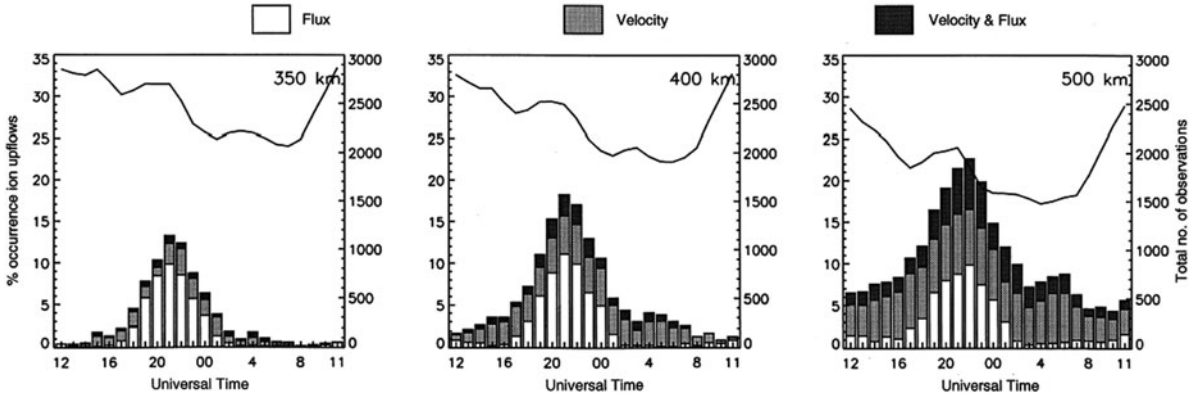

Fig. 16.6 Diurnal variations of field-aligned ion up-flow occurrence frequency observed at EISCAT Tromso from 1984 to 1996, at 350, 400 and 500 km altitude (*left* to *right*): events exceeding the flux threshold only (*white*), the velocity threshold only (*grey*), and both thresholds (*black*). Magnetic midnight is near 22 UT (From Foster et al. 1998)

frequency at 500 km reached about 23% near magnetic midnight (2200 UT at Tromso), and the up-flow velocity exceeded 100 m s^{-1} in more than half (~55%) of the observed events, including ~25% of higher-flux events in which the field-aligned ion flux exceeded 10^9 cm^{-2} s^{-1} and ~30% of lower-flux events. Since the EISCAT transmitter at Tromso is located at 69.7° N (66.2° invariant) and lies within the night side auroral oval and equatorward of the dayside oval, the observed distribution in Fig. 16.6 reflects the combined effects of both MLT and latitudinal variations of up-flow. In contrast, the EISCAT Svalbard radar (ESR) is located at 78°N (75.4° invariant), and lies within the dayside oval and poleward of the night side oval. Liu et al. (2001) compared quiet-time EISCAT (Tromso) and ESR data between 1997 and 1998 in the early rising phase of Solar Cycle 23, and found that the up-flow occurrence frequency at ESR was larger on the dayside than on the night side above 400 km, and exhibited a dawn-dusk asymmetry that increased with altitude in favor of the dawn side (04–08 MLT) over the dusk side (16–20 MLT), in contrast to EISCAT where the observed frequency was higher on the dusk side.

16.2.2.1 Magnetic and Solar Activity Dependence

Despite the considerable month-to-month variation in data sampling in their study, Foster et al. (1998) found seasonal as well as diurnal and solar cycle variations in up-flow occurrence and characteristics. Above 300 km altitude, the occurrence frequency of up-flow was greater during the winter months. Using the vertical ion velocity data at higher altitudes (500–800 km) and removing approximately the contribution of the $E \times B$ drift velocity to the vertical velocity, these authors inferred that the up-flow on the dayside started or reached an observable velocity at higher altitudes compared with the night side, and hence the dayside-to-night side occurrence frequency ratio was larger, e.g. 0.5 at 800 km compared with ~0.25 at 400 km altitude.

In comparison with the quieter phase of the solar cycle, the observed up-flow during the active phase of the cycle had a larger ion flux, a smaller ion velocity, and its occurrence frequency had a more pronounced night side maximum, i.e. larger night side-to-dayside occurrence frequency ratio. In other words, the up-flow was dominated by large ion-flux events near solar maximum and by large ion-velocity events near solar minimum, in accord with the study of Liu et al. (2001) discussed above in which the occurrence frequency of large-velocity events in the early rising phase of the solar cycle was much higher than that near solar maximum. The predominance of large flux events at solar maximum may be attributed to the higher prevailing ambient plasma density. The smaller ion velocity may be suggestive of a smaller amount of free energy being available per capita for ion acceleration and/or a larger energy loss to ion-neutral collisions.

Liu et al. (2001) investigated the geomagnetic dependence of ion up-flow using EISCAT data near solar maximum between 1988 and 1992, when disturbed-time data were more abundant. Using ion velocity as the only event selection criterion ($v_{//} >$ 100 m s^{-1}), these authors found that compared with quiet times, the up-flow occurrence frequency during disturbed times (Kp $\geq$ 4) was significantly larger at all altitudes (200–550 km) and that the increase in occurrence frequency with altitude was also stronger. The starting height of up-flow extended to lower altitude, from 350–400 km for Kp < 4 down to 200–250 km for Kp $\geq$ 4. In addition, the increase with geomagnetic activity was much more pronounced on the dawn side than on the dusk side; as a result, the occurrence frequency on the dawn side was higher than on the dusk side during disturbed times. In contrast, the quiet-time occurrence frequency was slightly lower on the dawn side than on the dusk side.

The differences in observed ion up-flow between EISCAT and ESR are consistent with the suggestion that both $E \times B$-driven ion frictional heating and precipitating soft electron-driven electron heating play an important role in ionospheric ion acceleration in the F-region and topside ionosphere. The effect of ion frictional heating is expected to increase with Kp and to be stronger on the dusk side and in the winter: this explains the higher occurrence frequency on the dusk side at EISCAT latitude, and the increase in occurrence frequency with geomagnetic activity at both ESR and EISCAT. The effect of soft electron precipitation is expected to be stronger during disturbed times, particularly in the dusk quadrant, and to play a more dominant role on the dayside where the precipitating electrons tend to be softer: this explains the higher dayside occurrence frequency at ESR compared with EISCAT at both quiet and disturbed times, and the higher frequency on the dawn side during disturbed times. It also suggests that soft electron-driven electron

heating may be more efficient than convection-driven ion heating in driving ion up-flow.

Ogawa et al. (2009) investigated the influence of geomagnetic activity, the solar wind and interplanetary magnetic field on both ion up-flow and down-flow in the F-region and topside ionosphere around the dayside cusp using ESR data in 1997 to 2006. In this study, an ion up-flow event was identified by ion velocities exceeding 100 m s^{-1} at three or more consecutive heights along a velocity versus altitude profile; the starting altitude of an ion up-flow event was defined as the lowest altitude of ion up-flow occurrence in the velocity profile.

At ESR, the starting altitude of ion up-flow on the dayside (09–15 MLT) increased with solar activity level: In periods of low solar activity ($F_{10.7} < 140$), approximately 25% of the up-flow events on the dayside started below 400 km altitude and an additional 30% between 400 and 450 km. In comparison, in period of high activity ($F_{10.7} > 140$), only about 16% and 18% of the events started below 400 km and between 400 and 450 km, respectively.

The occurrence frequency of ion up-flow at 500 km altitude peaked around geomagnetic local noon between 10 and 15 MLT, at ~11, 28 and 21% at quiet, moderately active, and disturbed periods (Kp < 2, 2 ≤ Kp < 5 and Kp ≥ 5), respectively. In comparison, the occurrence frequency of ion down-flow during quiet and moderately active periods peaked around 03–06 and 06–09 MLT at ~5 and 7%, respectively, and was less than 2–3% in the 10–15 MLT sector. During disturbed periods, the down-flow occurrence frequency peaked around 10–15 MLT and its peak value (~25%) exceeded the up-flow occurrence frequency.

Figure 16.7 shows the averaged field-aligned ion flux over only the observed ion up-flow events and over all data samples (up-, down- and non-flow events), respectively. The averaged ion flux in up-flow events reached $2 \times 10^9 \mathrm{cm}^{-2}\ \mathrm{s}^{-1}$ in the noon sector and was relatively independent of geomagnetic activity level (Kp). In comparison, the corresponding averaged flux over all data samples was upward and typically 10 to 40% of the average in up-flow events ($0.1 \times 10^9 \mathrm{cm}^{-2}\ \mathrm{s}^{-1}$ to $0.8 \times 10^9 \mathrm{cm}^{-2}\ \mathrm{s}^{-1}$) during quiet and moderately active times, but was downward and in the range of $< 0.1 \times 10^9 \mathrm{cm}^{-2}\ \mathrm{s}^{-1}$ to $0.5 \times 10^9 \mathrm{cm}^{-2}\ \mathrm{s}^{-1}$ during disturbed times.

Since ion convection in the dayside cusp and polar cap is on average anti-sunward and increases in strength with magnetic activity, the observed up-flow

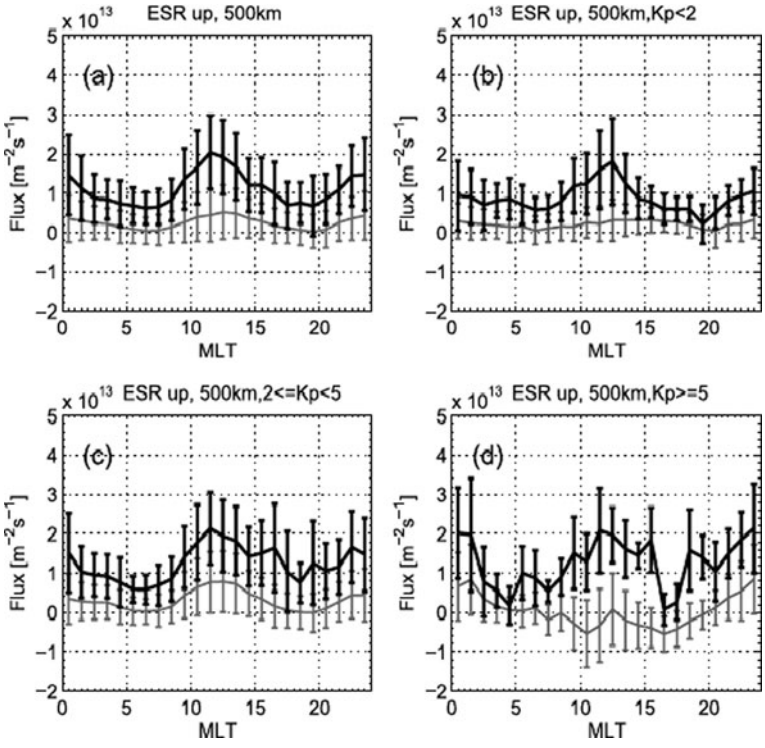

Fig. 16.7 Field-aligned ion fluxes at 500 km observed at ESR averaged over all up-flow events (*black curve*) and all data samples (all up-flow, down-flow and non-flow events; *grey curve*): (**a**) All Kp, (**b**) 0 ≤ Kp < 2, (**c**) 2 ≤ Kp < 5, and (**d**) 5 ≤ Kp. (From Ogawa et al. 2009)

occurrence frequency and ion flux in the noon sector is consistent with the ESR being in or equatorward of most of the up-flow events and observing more up-flowing than down-flowing ion flux on average. During disturbed period the region of ion up-flow was on average more equatorward and the strength of anti-sunward convection increased, resulting in ESR being poleward of more up-flow events and therefore observing more down-flow than up-flow events and more down-flowing than up-flowing ion fluxes.

Figure 16.8 shows that approximately half of the dayside ion up-flow events were accompanied by increases of both ion and electron temperatures, compared with only 10–20% of events at other local times. About 20% of the events were accompanied by electron temperature increase only, regardless of local time, and another 5–10% of noon-sector events and 20–25% of morning-sector events were accompanied by ion temperature increase, the remaining 15–40% being unaccompanied by any appreciable ion or electron heating.

As noted in the Introduction, both the ionosphere and the thermosphere are strongly affected by the level of solar activity in an 11-year solar cycle. In particular, the higher solar EUV flux near solar maximum results in a higher exospheric temperature, atmospheric scale height, neutral density and heavy-to-light ion species (O-to-H) density ratio in the thermosphere, which result in a higher rate of photo-ionization and larger plasma density in the F-region and topside ionosphere.

Ogawa et al. (2010) studied the influence of solar activity on the starting altitude of ion up-flow on the night side using data from the EISCAT Tromso UHF radar between 1984 and 2008 and the same ion up-flow event identification scheme as in their earlier (Ogawa et al. 2009) study. On average, ion up-flow was observed between 280 and 600 km altitude with an occurrence frequency of 10–15% at 21–02 MLT, compared with a frequency of ≤3% at 10–15 MLT (cf. Figure 3 in Ogawa et al. 2010). The averaged ion velocity and upward ion flux in the observed up-flow events were also higher on the night side than on the dayside, with peak values of about 150 m s^{-1} near 6 MLT and ∼ $1.5 \times 10^9 m^{-2}$ s^{-1} near 0 MLT, respectively; the averaged ion flux over all data samples was ∼3×10^8 cm^{-2} s^{-1}.

Figure 16.9 shows (a) the 12- (black) and 3-month (grey) averages of the observed occurrence frequency on the night side (19–05 MLT) between 200 and 550 km, and (b) the field-aligned ion velocity and (c) ion flux at 400 km at low ($F_{10.7} < 140$) and high ($F_{10.7} > 140$) solar flux, respectively, from 1984 to 2008. On average, the upward ion velocity in up-flow events was a factor of 2 higher at low solar flux than at high solar flux ($F_{10.7} > 140$), when the upward ion flux was a factor of 4 higher. The larger

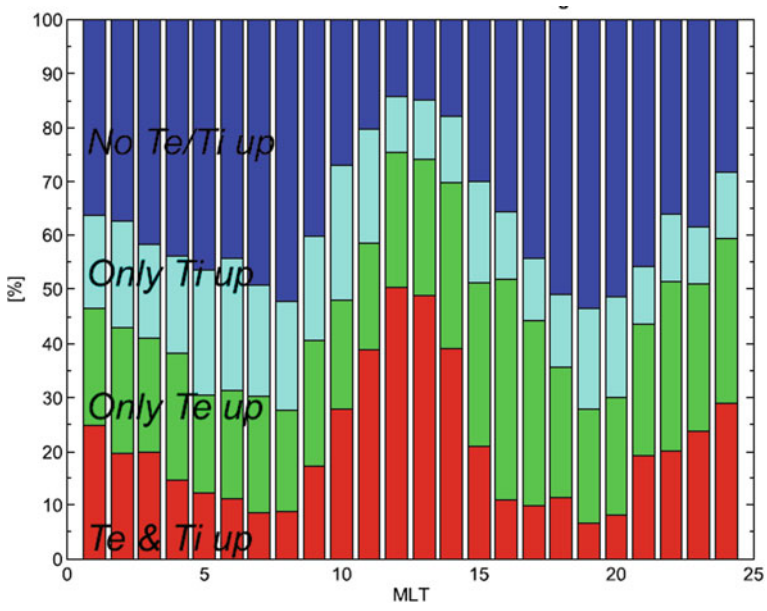

Fig. 16.8 Increase over background ion and electron temperatures associated with ion up-flow: *Top* to *bottom*: >200 K increase in neither temperature (i.e., <200 K increase in both temperatures, *blue*); in ion temperature only (*cyan*); in electron temperature only; and in both temperatures (*red*) (From Ogawa et al. 2009)

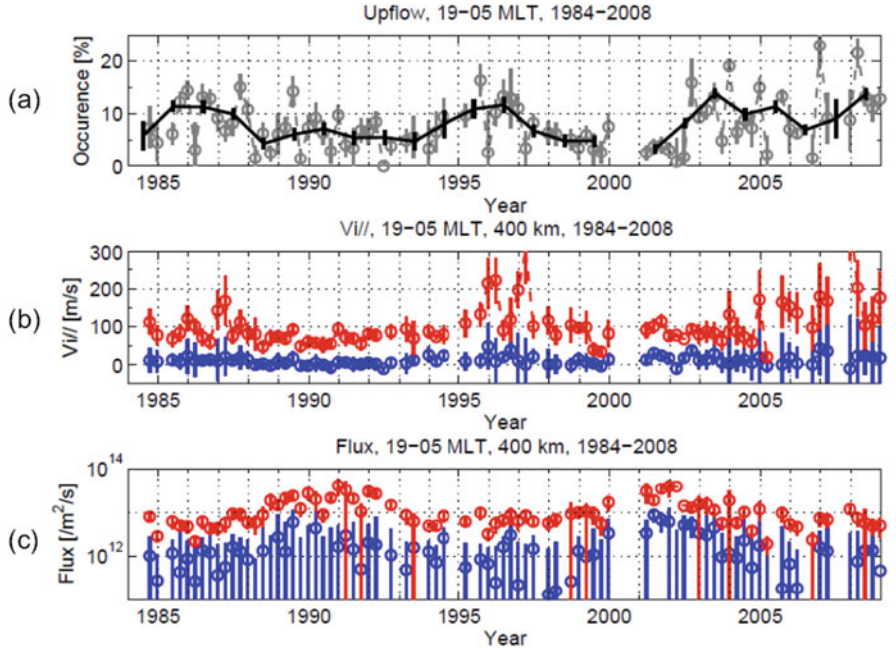

Fig. 16.9 (**a**) 12- (black) and 3-month (grey) averages of occurrence frequency of night side (19–05 MLT) ion up-flow at EISCAT starting between 200 and 550 km from 1984 to 2008; 3-month averages of (**b**) field-aligned ion velocity and (**c**) ion flux at 400 km over all up-flow events (*red*) and data samples (*blue*) (From Ogawa et al. 2010)

flux at high solar flux (i.e. near solar maximum) is attributed to the stronger solar EUV flux and resulting ionization in the F-region, and the smaller velocity to the higher ion-neutral collision frequency due to the higher exospheric temperature and neutral density in the thermosphere.

The average starting altitude of ion up-flow was found to track the measured electron density profile, and was typically 100–150 km higher than the latter. The distribution of starting altitude is quite different at low and high solar flux, respectively. At low solar flux, the distribution exhibited a broad peak starting at ~300 km and peaking near 450 km and extending to ~520 km. At high solar flux, the distribution shifted to higher altitude, starting near ~350 km and peaking more sharply near 450 km and extending to at least 540 km.

The variation of the starting height with solar activity level can be attributed to the increased atmospheric density and ion-neutral collision frequency near solar maximum. This can be seen in Fig. 16.2 above, where the neutral atomic oxygen density near solar minimum is $\sim 3 \times 10^8$ cm^{-3} at 300 km (the starting up-flow altitude at low solar flux above), and the corresponding density near solar maximum is 3.3×10^8 cm^{-3} at 450 km (the starting altitude at high solar flux). This implies that the atmospheric density and ion-neutral collision frequency at the starting up-flow altitude are comparable at solar minimum and maximum, respectively.

Approximately 61% of ion up-flow was associated with increases of both ion and electron temperatures of more than 100 K at high solar activity, and an additional 11 and 21% with ion and electron temperature increase, respectively. The corresponding percentages at low solar activity were 35, 9 and 43%, respectively. In other words, the relative occurrence of both ion and electron heating is higher at high solar activity than at low solar activity. The annual average of electron temperature increase ranged from 300–400 K at low solar activity to 500–600 K at high solar activity; the corresponding ion temperature increase was smaller and ranged from ~100–200 K to ~200 to 300 K.

Using the measured electron density and ion and electron temperature profiles, Ogawa et al. (2010) estimated the electron and ion plasma pressure gradient acceleration terms, respectively, in the momentum equation, and found the electron acceleration term to be approximately twice the ion term, and ~6 and ~1 m s^{-2} near solar minimum and maximum,

respectively; both the electron and ion terms were higher near solar minimum than near solar maximum.

As discussed in Ogawa et al. (2010), the occurrence frequency of ion up-flow at both low and high solar activity increased with Kp. The upward ion velocity and flux at 400 km altitude also increased with geomagnetic activity, the average velocity in up-flow events reaching ~100 m/s and >100 m/s at high and low solar activity, respectively, and the averaged ion flux reaching $\sim 2 \times 10^9$ and 1×10^9 cm^{-2} s^{-1}, respectively.

Ogawa et al. (2009) found the ion up-flow occurrence to increase sharply with solar wind density (above 30 cm^{-3}) and solar wind velocity (up to 700 m s^{-1}). The upward ion flux was found to increase with solar wind density and decrease with solar wind velocity. Both IMF B_y and B_z were found to affect the up-flow occurrence frequency, which increased with increasing magnitude of B_y and peaked at $B_z \sim -5$ nT: presumably the region of ion up-flow expanded and shifted longitudinally into the ESR field-of-view for increasing IMF $|B_y|$, and moved equatorward of ESR under strongly negative B_z and/or high solar wind velocity.

The apparent movement of the dayside ion up-flow region may be understood in terms of the influence of solar wind velocity and density and the IMF B_y and B_z on the shape, size and location of the up-flow region, since the location of the dayside cusp is known to move equatorward with decreasing IMF B_z or increasing solar wind dynamic pressure. The ESR results suggest that the occurrence frequency of ion up-flow is highest inside the cusp, whose latitudinal position is influenced more by the solar wind velocity than the solar wind density, while the upward ion flux is influenced by the solar wind density and not the solar wind velocity.

A significant plasma source for dayside ion up-flow during magnetic storms is storm enhanced density (SED) plasma. An ionospheric signature of the plasmaspheric drainage plume resulting from the erosion of the plasmaspheric boundary layer, SED is regularly present in the pre-midnight sub-auroral ionosphere during the early stages of magnetic storms, near the ionospheric projection of the plasma-pause and the plasmasphere boundary layer, and it appears as ionization patches and plumes of high total electron content (TEC) at the equatorward edge of the ionospheric trough near dusk.

Using 2D vertical TEC maps from ground GPS receivers, plasma density and drift velocity data from both incoherent scatter radar and DMSP, and EUV images on IMAGE, Foster et al. (2002, 2004) presented two detailed case studies of one-to-one mapping between SED plasma and plasmaspheric drainage plumes, in which the SED plume mapped into a broad, sunward-moving drainage plume from the greatly eroded plasmapause near $L = 2$ near dusk to the dayside magnetopause near noon.

Figure 16.10 shows a TEC map at 19:05 UT in the April 11, 2001 magnetic storm, and the projection of such a map at 23:00 UT to the magnetospheric equatorial plane based on the Tsyganenko (2002) magnetic field model. The TEC map reveals a strong SED plume spanning the North American continent, and its equatorial projection maps the SED plume into a broad sunward drainage plume from the plasmapause near $L = 2$ to the dayside magnetopause near noon. The peak vertical TEC exceeded 100 TEC units (TECu) for 5 h or more in a region of strong subauroral sunward convection and strong F-region sunward ion flux ($> 10^{11}$ cm^{-2} s^{-1}).

Assuming a latitude width of ~5° (500 km) and an altitude extent of ~500 km, the sunward ion flux corresponded to a total flux of $\sim 2.5 \times 10^{26}$ ions s^{-1} ions and a total transfer of $\sim 10^{30}$ ions from the plasmaspheric boundary layer to the F-region cusp.

In comparison, the flow rate of He^+ inferred from IMAGE EUV images of He^+ resonant scattering was $\sim 1.5 \times 10^{26}$ ions s^{-1}, which implies a total ion flow rate of $\sim 1.5 \times 10^{27}$ ions s^{-1}, assuming a helium abundance of 10% in the plasmasphere. Since the plasma content of the plasmaspheric boundary layer extending from $L = 3$ to $L = 4$ is $\sim 5 \times 10^{30}$ ions, assuming a mean density of 5×10^2 cm^{-3}, such a sunward drainage flux would correspond to an erosion time of ~1 hr, consistent with the observed erosion rate of the plasmapause from IMAGE EUV images (Goldstein et al. 2003).

Likewise, plasma patches in the F-region are a likely source of night side ion up-flow, because of their ability to survive the transport across the polar cap due to the long lifetime of ions in the F-region and above (a few hours). Semeter et al. (2003) presented data from the Sondrestrom incoherent scatter radar for a plasma patch near the poleward boundary of the night side auroral oval. The plasma flow was equatorward within the polar cap, and across the open and closed field line

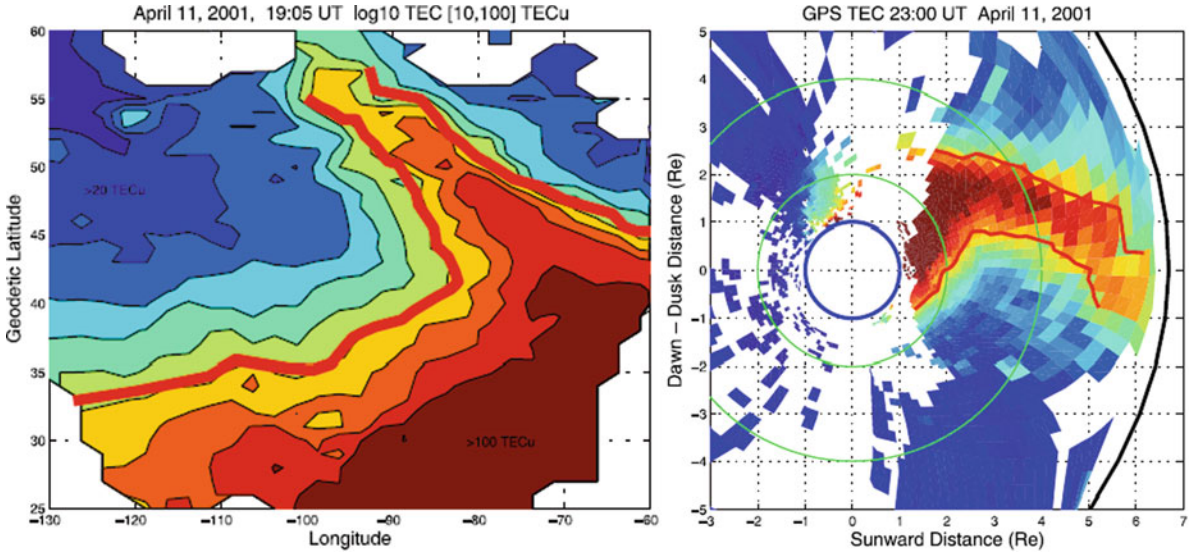

Fig. 16.10 *Left*: Total electron content (TEC) map derived from GPS observations at 19:05 UT in the April 11, 2001 magnetic storm, revealing a strong plume of storm enhanced density (SED); *Right*: Projection of TEC map into the magnetospheric equatorial plane using the Tsyganenko magnetic field model, showing a broad plasmaspheric drainage plume from the eroded plasmapause position near $L = 2$ to the dayside magnetopause near noon (From Foster et al. 2004)

boundary into the auroral zone as the result of magnetic reconnection (Robinson et al. 1985). Near the auroral precipitation boundary, the flow turned eastward in the presence of an equatorward electric field, and then westward within the oval. The ion up-flow occurred in the region of auroral precipitation, and exceeded 1 km/s in velocity at 900 km (the highest altitude of observed radar backscatter), but did not correlate with the auroral energy flux or electron or ion temperature. The connection between the observed plasma patch and the ion up-flow in the night side polar cap boundary suggests that freshly reconnected field lines at the boundary are the site of strong ion up-flows. Given the large longitudinal extent of both ion up-flow and plasma patch, and the long residency time of the latter, equatorward-drifting plasma patches at the night side polar cap boundary are believed to constitute a significant source of ion outflow at higher altitudes.

The DE-2 and the EISCAT/ESR radar observations demonstrate that both soft electron-driven electron heating and convection-driven ion heating play a significant role in auroral ion up-flow production. Frictional heating of O^+ ions enhances the ion temperature in the F-region and increases the preexisting parallel pressure gradient, and the ions respond by flowing to higher altitudes to attain a new equilibrium scale height distribution. Although the increase of the scale height is a transient feature, the up-flow can remain if new plasma is horizontally convected into the heating region. Likewise, soft precipitating electrons deposit their energy in the F-region via electron impact ionization of and collisional energy transfer with the neutrals, and thereby increase the average thermal electron energy (i.e. electron temperature) and enhance the ambipolar electric field. Another mechanism suggested is parallel electric field associated with anomalous resistivity due to ion acoustic fluctuations that are caused by a strong electron current or a relative drift of O^+ and H^+ ions (Wahlund et al. 1992). Furthermore, ion up-flows can often be related to convection velocity shears, which in a two-step process can seed plasma waves (Ganguli et al. 1994). Thus the F-region and the topside ionosphere below 1000 km supply a significant amount of upward ion flux to higher altitudes, and constitute a sufficient source of cold O^+ plasma for a multitude of ion energization processes there.

16.3 Suprathermal Ion Outflows

As noted in the Introduction, the category of suprathermal ion outflows includes ion beams, ion conics, transversely accelerated ions (TAI), and upwelling ions

(UWI). The occurrence and morphological characteristics of ion beams and conics in the different altitude regions were the subject of a number of statistical studies using S3-3, DE-1, Viking, Akebono, Freja, Fast and Polar data, including several prior to 1997 which were reviewed in details by Yau and Andre (1997; see also Moore et al. 1999a) and are summarized briefly below.

Ion beams are upflowing ions (UFI) that have a peak flux along the upward magnetic field direction. They are generally observed above 5000 km altitude but are occasionally present down to about 2000 km during active aurora. The occurrence probability of both H^+ and O^+ ion beams increases with altitude at both quiet and active times, at least up to 23,300 km (DE-1 apogee). The increase is most prominent for the lower-energy (<1 keV) ions.

In contrast, ion conics have a peak flux at an angle to the upward magnetic field direction, and are observed down to sounding rocket altitudes (1000 km or below; Yau et al. 1983), and up to several Earth radii and beyond (Hultqvist 1983; Bouhram et al. 2004). At high altitude (above ~10,000 km), the occurrence probability of low-energy conics (<1 keV) decreases with increasing altitude. The motion of an ion conic is typically non-adiabatic as it evolves along the field line.

Transversely accelerated ions (TAI) have peak pitch angles at or close to 90°, and may be regarded as a special case of ion conics. On the dayside, they are regularly present down to about 3000 km on Akebono (Whalen et al. 1991). On the night side, they were observed at 1400 km on ISIS-2 (Klumpar 1979) and below 1700 km on Freja (Andre et al. 1994) frequently, and down to ~400 km on sounding rockets (Yau et al. 1983; Arnoldy et al. 1992) during active aurora.

Upwelling ions are observed exclusively in the morning sector of the auroral oval and the lower latitudes of the polar cap, and display the effects of both parallel (upward) and perpendicular energization to energies from one to tens of eV. They are the most persistent suprathermal ion outflow feature in the cleft region, and are dominated by O^+ ions. The distinction between upwelling ions and transversely accelerated low energy ion conics is not sharp. However, compared with ion conics with the same perpendicular energy upwelling ions are more upward moving (have higher upward mean velocity). As a result of ionospheric convection, upwelling ions often appear as field-aligned ion flows at other local times in the high-altitude polar cap, where it is sometimes difficult to distinguish such "cleft ion fountain" flows from the polar wind.

Both ion beams and ion conics are a common phenomenon, with occurrence frequencies sometimes higher than 50% above 1 R_E altitude, and are dominated by H^+ and O^+ ions in the 10 eV to a few keV range; UFI of a few tens of keV energy occasionally occurs.

Distributions of UFI may evolve in different ways as they move upward. Ion conics often do not start as TAI distributions heated within a narrow altitude range and then move adiabatically up the geomagnetic field. Statistically (Miyake et al. 1993, 1996; Peterson et al. 1995), the energy of dayside ion conics increases with altitude, from ~10 eV near 2000 km to ≤100 eV near 9000 km. The cone (apex) angle of an ion conics, which is the angle between the direction of the peak flux and the upward magnetic field direction and equal to the peak pitch angle α in the southern hemisphere and $(180° - \alpha)$ in the northern hemisphere, decreases with altitude much more slowly than expected from adiabatic motion. In the so-called "restricted" ion conics, the ion distribution has a well defined cone angle. However, in the so-called "extended" or "bimodal" conics (Klumpar et al. 1984) the cone angle increases with energy and the lower energy ions have a significant flux along the field line.

16.3.1 Magnetic and Solar Activity Dependence

The occurrence probability of both H^+ and O^+ upflowing ions is fairly independent of magnetic activity (Kp index). However, the intensity distribution of O^+ UFI exhibits a marked dependence on magnetic activity that is absent in H^+. On DE-1 (Yau et al. 1984), the occurrence probability of intense ($>10^7$ $cm^{-2}s^{-1}sr^{-1}$) lower-energy (<1 keV) O^+ UFI at active times (Kp ≥ 4–) was a factor of 3 higher than at quiet times. A similar but smaller increase was also apparent in the occurrence probability of intense ($>10^6$ $cm^{-2}s^{-1}sr^{-1}$) higher-energy (>1 keV) ions. In contrast, the intensity distribution for H^+ remained fairly unchanged with Kp.

Most statistical studies of magnetic activity dependences of upflowing ions are based on the Kp index because of its availability relative to other indices, despite its well-known shortcomings as an indicator of

auroral activities. Studies of the AE or Dst dependence of ion outflow are comparatively rare, as are those on IMF and solar wind dynamic pressure dependence; notable examples are Oieroset et al. (1999), which examined the IMF B_z and AE dependences of ion outflow on Viking, and Lennartsson and Shelley (1986), which studied the AE distribution of ionospheric ion composition in the plasma sheet on ISEE-1.

The orientation of the IMF affects the ionospheric convection pattern in the polar ionosphere. Therefore, it is expected to have a direct influence on the transport of outflowing ions. Likewise, the dynamic pressure of the solar wind plays an important role in the modulation of the magnetospheric energy and momentum input, and may be expected to influence the overall ion outflow from the polar ionosphere. Indeed, the density of plasma sheet oxygen ions, which undoubtedly originate from upflowing ionospheric ions, is correlated with the solar wind energy flux (Lennartsson 1995).

The observed O^+ UFI distributions exhibit significant seasonal and long-term variations which are attributed to changes in the incident solar EUV flux on the upper atmosphere in different seasons of the year and at different phases of the 11-year solar cycle. The corresponding variations in the H^+ UFI distributions are much smaller. On DE-1, the occurrence probability of the O^+ UFI decreased by about a factor of 2 from near solar maximum in 1981 to the declining phase in 1984. The decrease in probability of the intense UFI fluxes was even larger, and about a factor of 3–4. In contrast, there was no discernible change in the H^+ occurrence probability during the same period. Throughout the period, the occurrence probability of O^+ UFI was significantly higher in the summer than in the winter, the frequency of intense events being about a factor of 2 larger.

The altitude range of perpendicular heating also appeared to vary with the season, and shifted upward during periods of increased solar radiation. The occurrence probability of O^+ TAI between 8000 and 14,000 km altitude increased by a factor of 3 near solar maximum. The O^+ conic abundance (conic to beam ratio) in the 8000–24,000 km range also increased (Yau et al. 1985a). The increase in occurrence probability, intensity, and conic abundance of O^+ UFI in periods of increased solar activity resulted in a large increase in the overall ion outflow rate.

The influence of solar EUV radiation on O^+ outflow and the energization altitude can be understood in terms of ionospheric and atmospheric scale heights. An enhanced solar EUV flux will heat both the atmosphere and the ionosophere, and increase the scale heights of their respective constituents. As noted earlier, for efficient ion heating, ions must be present at a sufficiently high altitude where the density is sufficiently low and the effect of collisions and charge-exchange is negligible. A higher solar EUV flux in the summer and near solar maximum increases the scale heights of both O^+ and O. This results in a larger increase in density at high altitude for O and O^+ than for H and H^+. Consequently, more O^+ ions occur at high altitudes where they can be heated and escape. The effect on H^+ ion acceleration is much smaller, because of the smaller increase in H^+ density and the increased effect of resonant charge exchange between H^+ and O.

In general, the characteristics of ion outflow processes depend on specific ionospheric conditions which are modulated by the solar EUV flux and the energy input from the magnetosphere. The level of solar EUV flux is highly variable over the 11-year solar cycle and within a 27-day solar rotation near solar maximum. This results in significant variability in the ion outflow rate on both substorm (∼hour) and longer (days or longer) time scales.

The composition of both thermal and energetic upflowing ions is highly variable, not only in the O^+/H^+ ratio but also in the relative abundance of ion species which are usually considered minor species. For example, the observed He^+/H^+ ratio in the polar wind varied by more than an order of magnitude in a DE-1 orbit pass near 2 R_E altitude (Nagai et al. 1984). Energetic upflowing He^+ ions are observed about half as often as either H^+ or O^+ (Collin et al. 1988). Thermal ion flux ratios in the range of 0.1–0.3 for He^+/H^+, 0.1–1.0 for N^+/O^+, and 0.1–0.5 for O^{++}/O^+ are not uncommon (Yau et al. 1991). The enhancement of N^+ relative to O^+ is largest during disturbed times, particularly in the presence of molecular upflowing ions (Yau et al. 1993).

16.3.2 Ion Energization Processes

H^+ and O^+ ions in the lower ionosphere have average ion energies of about 0.1 eV, and must be accelerated to about 1 and 10 eV, respectively, for the ions to reach escape velocity, possibly by gradual energization as the ions move upward. Andre and Yau (1997) reviewed the energization mechanisms of ion outflows.

Multiple mechanisms are believed to operate within each category of ion outflows, and a combination of categories is important for the total ion outflow. No single mechanism can explain all ion outflows. Indeed, the acceleration of ionospheric ions to suprathermal (tens to hundreds of eV) or energetic (keV or greater) ion outflows is in general a multi-step process, the first step being the acceleration of auroral ion up-flow or the polar wind, as discussed in Section 16.2.

Several wave modes can, in principle, cause transverse ion acceleration; see reviews by Lysak (1986), Andre and Chang (1993) and Andre (1997). These waves range from static structures and waves below the ion gyrofrequencies (Borovsky 1984; Hultqvist 1991), to waves at and just above the ion gyrofrequencies (Ashour-Abdalla and Okuda 1984; Chang et al. 1986), to waves above the lower hybrid frequency (Chang and Coppi 1981). We focus on the most important wave signatures in transverse ion acceleration regions below.

One common type of ion energization that has been observed to occur at all local times is associated with broadband low frequency electric wave fields, in which a fraction of the electric field spectral density near the ion gyrofrequency is due to left-hand Alfven waves or is in resonance with the ions regardless of wave mode. A fraction from about one percent to tens of percent of the observed waves is typically needed to be in resonance to account for the observed ion conical distributions (Chang et al. 1986; Retterer et al. 1987; Andre et al. 1988, 1990, Norqvist et al. 1996).

At the equatorward edge of the cusp/cleft, cool ions have been observed to drift poleward into a region of broadband low frequency waves, where the ions are energized (Andre et al. 1988, 1990; Norqvist et al. 1996; Knudsen et al. 1998). On the SCIFER sounding rocket at 1400 km in the cleft near 10 MLT (Kintner et al. 1996) the observed ion acceleration due to broadband low-frequency waves was clearly associated with a density depletion region with sharp boundaries and a scale size of tens of kilometers in the perpendicular direction. Similar ion energization was also observed in a sharply confined spatial region poleward of a premidnight auroral arc (near 23 MLT) on the AMICIST sounding rocket at 900 km (Lynch et al. 1996). Similar associations of larger regions of low plasma density and broadband low-frequency waves with ion energization were observed on Viking (Hultqvist 1991) at altitudes up to its apogee (13,500 km) and on Freja (Lundin et al. 1994; Andre 1997).

In some of the acceleration events on Freja, waves above the lower hybrid frequency were observed to be more intense than those near the oxygen or hydrogen ion gyrofrequencies, and were believed to be the major source of ion energization. In such cases, "pre-heating" of ions by waves near the ion gyrofrequencies can be important for the ions to reach sufficiently high velocities to be in resonance with the lower hybrid frequency waves, and to be energized efficiently by the latter (Andre et al. 1994). On Freja at 1700 km altitude, the observed lower hybrid frequency waves were extended over hundreds of kilometers. On sounding rockets in the topside ionosphere, the observed waves were found in thin filamentary "lower hybrid" density cavities and correlated with transverse ion energization to characteristic energies of up to ~10 eV (Kintner et al. 1992; Vago et al. 1992).

An additional energization mechanism is nonresonant "sloshing" by waves much below the ion gyrofrequency (Hultqvist 1991; Ball and Andre 1991). At these low frequencies ions will respond to the electric field essentially by a changing $E \times B$ drift. This mechanism can energize heavy ions to only a few eV in the topside ionosphere but it can do so to much higher energies at higher altitudes due to the weaker geomagnetic field there.

Andre et al. (1998) classified into four types the observed transverse ion acceleration events on Freja in which O^+ ions were accelerated to initial energies above 5–10 eV. Figure 16.11 shows that the two types that were associated with broadband low-frequency waves (Type 1 and 2) were the most common. As discussed in Andre et al. (1998), these two types of events were also associated with the highest mean O^+ energies (hundreds of eV, on the night and morning side) and ion fluxes (10^9 cm^{-2} s^{-1}, on the dayside). The other two types were much less common and their ion energies and fluxes were typically an order of magnitude lower. The Type 3 and 4 events were associated with auroral electrons and lower hybrid frequency waves or waves near half of the H^+ gyrofrequency and with precipitating H^+ or O^+ and lower hybrid frequency waves, respectively.

As noted above, some ion conics are "extended" in that their cone angle increases with energy and their low-energy component often has a significant flux along the field line. Such extended conics may be the result of ion energization over an extended altitude range in a diverging magnetic field

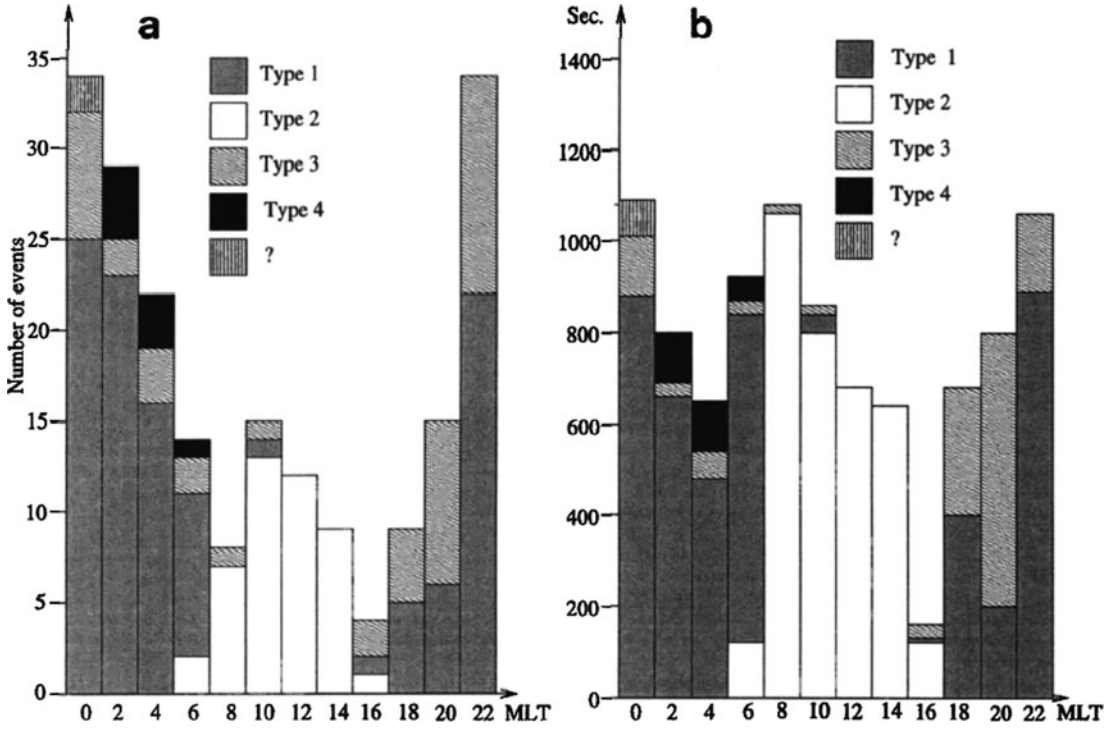

Fig. 16.11 (**a**) Number and (**b**) total duration of ion energization events observed on Freja near 1700 km in ~1300 orbit passes associated with broadband low frequency waves (Type 1 and 2); lower hybrid frequency waves and auroral electrons (Type 3); and lower hybrid frequency waves and precipitating protons or oxygen (Type 4); "?" = events not identified with any category (From Andre et al. 1998)

(Temerin 1986), upward acceleration by a parallel electric field (Klumpar et al. 1984) or velocity filtering (Horwitz 1986). The statistical studies of Peterson et al. (1992) and Miyake et al. (1996) using DE-1 and Akebono data, respectively, show that the cone angle of many conical distributions stays constant in altitude, rather than decreasing toward the upward direction as expected from adiabatic particle motion. Both the constant cone angle and the lifting of the conics can be the result of perpendicular resonant ion energization over an extended altitude region by waves at changing ion gyrofrequencies as the ions move upward.

It is clear from the foregoing that the most common and important transverse ion energization mechanism is probably resonant heating by broadband low-frequency waves at frequencies of the order of the ion gyrofrequencies. Resonant energization by waves near the lower hybrid frequency in density cavities or electromagnetic ion cyclotron waves is believed to be less important. Non-resonant energization by electric field oscillations below the ion gyrofrequencies can be important for accelerating ions to a few eV at low altitudes and to much higher energies at higher altitudes. Ion beams are caused by parallel electric fields and/or pitch-angle folding of upward moving conics, and they typically have energies from a few eV to tens of keV.

As noted earlier, it is not always possible to distinguish between different thermal ion-flow populations. Likewise, different ion outflow populations are not necessarily caused by distinctly different mechanisms. For example, upwelling ions and ion conics can be energized in the perpendicular direction by the same oscillating electric fields. An ion conic that originates at 1000 km altitude and follows adiabatic motion will have a cone angle of <10° and be identified as an ion beam at 20,000 km altitude. In general, an ion distribution can be gradually energized by different mechanisms as it flows upwards, and will be identified accordingly when observed at different altitudes.

Using Fast data in 33 storm-time orbits at 4000 km altitude through the dayside cusp and post-noon cleft (60°–80° invariant and 12–15 MLT) acquired in 1998

in the ascending phase of the solar cycle, Strangeway et al. (2000, 2005) found statistically significant correlations between the observed ion outflow flux in and poleward of the cusp and the corresponding Poynting flux, downward electron number flux, and extreme low frequency (ELF) wave amplitude, respectively. The observed ion outflow was mostly ion conics, and the correlations suggest a multi-step process wherein the enhanced Poynting flux would heat ions in the lower ionosphere, and the heated ions would form a seed population that would be energized at higher altitudes to form escaping ion conics.

Figure 16.12 shows that the averaged ion flux correlated strongly with the average DC Poynting flux, electron number flux, and ELF wave amplitude, respectively. The slope in each log-log plot indicates the power-law relationship between each parameter pair; for example, the ion flux is proportional to $S^{1.265}$, where S is the Poynting flux. The correlation was statistically significant in each case at 95% level. In contrast, the corresponding correlation with the electron energy flux (not shown) was statistically insignificant, where the slope and correlation coefficient were 0.476 and 0.203, respectively, and implies a negative correlation between the ion flux and electron energy (electron energy flux to number flux ratio) that reflects the higher efficiency of low-energy electrons in electron heating and associated ion upwelling compared with the higher-energy electrons.

The data in Fig. 16.12 included ions in the 4–300 eV range, electrons above 50 eV, and waves in the frequency range of 30 Hz to 16 kHz, including waves in the ELF frequency band of 0.3–3 kHz, higher-frequency Alfven waves, oxygen and hydrogen ion cyclotron waves, low-frequency whistler waves, and broadband ELF waves. Thus, the strong correlation between the Poynting flux and ion flux suggests the transfer of energy from the former to the latter through multiple pathways, including soft electron precipitation, ELF waves, and possibly large-scale electric field, a portion of which was included in the ELF waves.

From their regression analysis, Strangeway et al. (2005) found the relationship of $f_i = 1.022 \times 10^{9 \pm 0.341} n_{ep}{}^{2.200 \pm 0.489}$ with a correlation coefficient of 0.855, where f_i is the ion flux at 4000 km in $cm^{-2}\ s^{-1}$ and n_{ep} is the precipitating electron density in cm^{-3}; $n_{ep} = 2.34 \times 10^{-14} f_{en}{}^{3/2} f_{ee}{}^{1/2}$ and f_{en} and f_{ee} are electron number and energy flux in $cm^{-2}\ s^{-1}$ and mW m^{-2}, respectively, at 4000 km. In comparison, $f_i = 2.142 \times 10^{7 \pm 0.242} S^{1.265 \pm 0.445}$ with a correlation coefficient of 0.721, where S is the Poynting flux in mW m^{-2}. Note that the Poynting flux and precipitating electron density are not independent of each other, since Alfven waves may enhance soft electron precipitation on both the dayside (Keiling et al. 2003) and the night side (Wygant et al. 2000). As noted in Strangeway et al. (2005), the application of these relationships needs to take into consideration factors such as ion composition, characteristic ion energy, and solar cycle, seasonal, and MLT dependences.

Zheng et al. (2005) performed a similar study using data from the Thermal Ion Dynamic Experiment (TIDE) instrument in 37 mostly dayside ion outflow events near Polar perigee in 2000 near the solar maximum. The averaged ion outflow flux in the TIDE energy range (0.3–400 eV) in each event was correlated in log-log scale with the corresponding Poynting flux, precipitating electron density, and electron energy

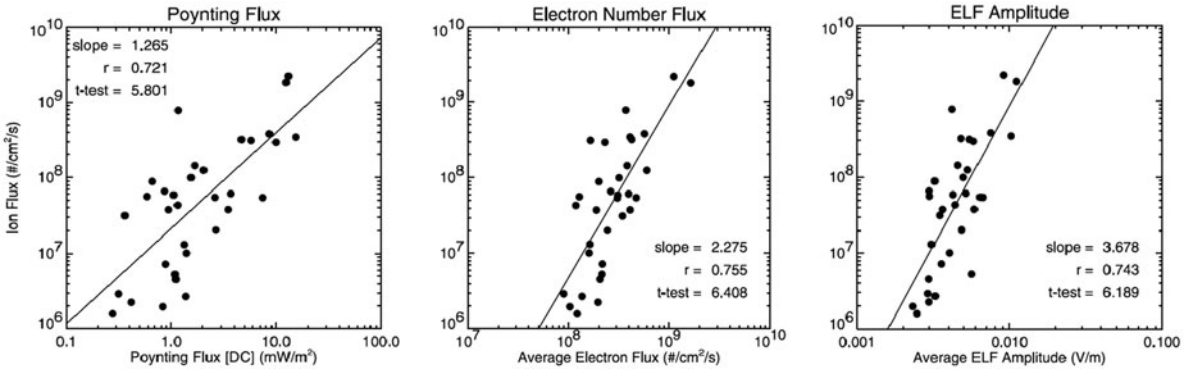

Fig. 16.12 Correlations between averaged ion flux and DC Poynting flux (*left*), electron number flux (*middle*) and ELF amplitude (*right*) on Fast (From Strangeway et al. 2005)

flux and temperature, respectively. The ion outflow flux was found to correlate best with the Poynting flux, which was associated with low-frequency (<1/6 Hz) Alfven waves and/or field-aligned currents: the correlation coefficient was 0.724 and the slope was 0.535. In comparison, the correlation with electron density was weaker, the corresponding correlation coefficient and slope being 0.551 and 0.484, respectively.

No correlation was found with the electron energy flux and electron temperature, the correlation coefficient being <0.1 in both cases. The lack of correlation with the electron energy flux is not surprising, given the result in Fast above and the fact that the measured electron energy flux included a significant component of energetic (>keV) magnetospheric electrons, which unlike soft (<1 keV) electrons are expected to deposit their energy below the F-region and the starting altitude region of ion up-flow. As discussed in Section 16.2, enhanced electron temperature gives rise to increased ambipolar electric field and thereby enhances ion up-flow in the topside ionosphere. The lack of correlation with electron temperature suggests that enhanced electron temperature may have a negligible effect on ion conic generation above the topside ionosphere, and is in itself not sufficient for ion conic production despite the fact that it can play an important role in the generation of the cold plasma source for ion conics and the resulting ion outflow.

Peterson et al. (2006) investigated the effects of solar illumination on the flux and characteristic energy of ion outflow using data from the Toroidal Ion Mass Spectrograph (TIMAS) instrument on Polar at 5000–7000 km altitude in 1996–1998 near solar minimum. The measured angular distribution of energetic (0.015–33 keV) ions in each 12-s interval was separated into three broad energy bands, to identify the possible presence of a pitch-angle peak above an energy-dependent noise threshold in each energy band, in which the ion flux exceeded 10^6 ions/cm^2 s sr and the pitch-angle width was <45° (FWHM). Since the data were acquired in the southern hemisphere, a distribution with a pitch angle peak in the range of 0°–30°, 30°–75°, or 0°–75° was classified as an ion beam, ion conic, and upflowing ion (UFI), respectively. In other words, an upflowing ion was defined as either an ion beam or a conic. For simplicity, we refer to such outflow distributions as "distinct" outflows below, to distinguish them from "non-distinct" outflow distributions that do not meet the above criteria but nevertheless carry a net upward ion flux.

Peterson et al. (2006) identified an anti-correlation in the dependence of beam and conic fluxes on solar illumination, which was attributed to variations in the altitude at which auroral acceleration processes occur. They concluded that the cusp is an important but not a dominant source of ionospheric plasma for the magnetosphere, and that significantly different plasma energization and/or transport mechanisms are dominant in the cusp and the midnight sectors. Moreover, variations in the solar EUV and geomagnetic energy inputs into the ionosphere, rather than the longer time-scale seasonal and annual variations in solar illumination, determine the global rates of H^+ and O^+ outflow.

The observed O^+ upflowing ions had a much higher conic-to-beam ratio compared with H^+ and He^+: the beams were found to constitute 37, 25 and 38% of the observed H^+, O^+ and He^+ upflowing ions, respectively, and the conics 31, 58 and 18%. The MLT distribution of the observed O^+ ions was also different from the corresponding H^+ and He^+ distributions: the largest fraction of outflowing H^+ and He^+ (34 and 40%, respectively) was observed in the midnight quadrant, but the largest fraction of outflowing O^+ was in the noon quadrant (37%, compared with 32% in the midnight quadrant), where the characteristic energy of both H^+ and O^+ conics was the lowest (<100 eV).

Figure 16.13 shows the averaged net ion outflow rates and characteristic energies for each ion species as a function of the SZA for beams, conics, and upflowing ions (beams and conics combined), and all (distinct and non-distinct) outflows. Detailed analysis of the Polar data in each MLT quadrant shows that the increase in the flux of H^+ and O^+ ion beams with decreasing solar illumination was accompanied by a decrease in the rate of the conics except in the midnight quadrant, where the characteristic energies of beams and conics have different behaviors between H^+ and O^+: the O^+ beam and conic and the H^+ beam energies increased but the H^+ conic energy decreased with decreasing solar illumination. The variations in characteristic energies with the SZA in the other three quadrants were more complex, but in general, the conic energies were significantly smaller than the beam energies. The increase in conic-to-beam flux ratio with increasing solar illumination implies that sunlight favors conics while darkness favors beams.

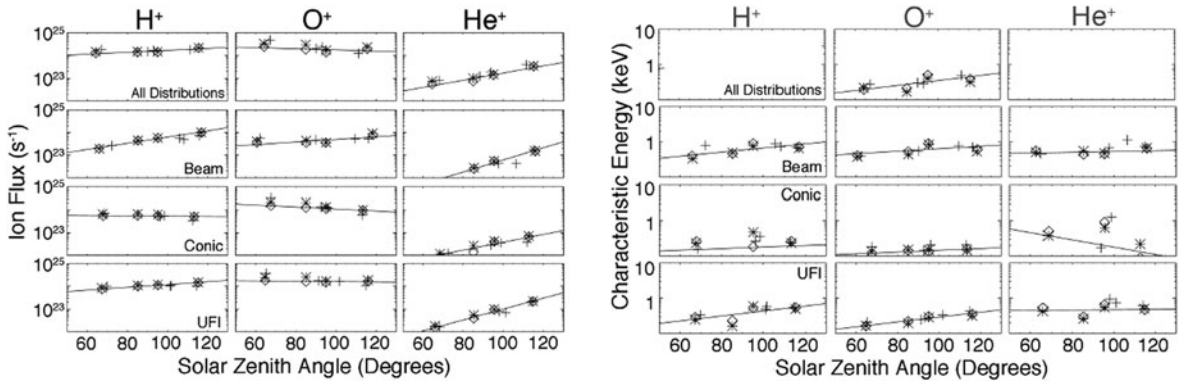

Fig. 16.13 Average net hemispheric ion outflow rate and characteristic energy of H^+, O^+, He^+ (from *left* to *right*) observed by TIMAS on Polar, including all (distinct and non-distinct) outflow distributions and only beams, conics, and upflowing ions (UFI), respectively (from *top* to *bottom*), as a function of averaged SZA at the magnetic footprint of the Polar satellite. *Diamond*: quiet-time (Dst > -50 nT) data; asterisk (*): full data set; plus (+): seasonal data within ±30 days of solstice or equinox; *straight line*: fits to quiet-time data. (From Peterson et al. 2006)

Figure 16.13 demonstrates the influence of solar energy input on the different types of ion outflow and energization process on a shorter than seasonal time scale and the differences in this influence between the dayside and night side. Peterson et al. (2006) showed that in the midnight quadrant, the net outflow rates of all ion species and outflow classifications increased with decreasing solar illumination. In the other quadrants, the rates of all ion beams increased but the rates of both H^+ and O^+ conics decreased with decreasing illumination, with the decrease in the rate of conics slightly dominating over the increase in the rate of beams in the noon quadrant. This suggests an increase in the supply of ions for H^+ and O^+ ion conic generation from the topside ionosphere and/or the efficiency of ion conic acceleration with increasing illumination. In comparison, the dependence of the He^+ conic outflow rate on solar illumination is more ambiguous, possibly due to the offsetting effects between the dependences of different controlling factors of He^+ production and acceleration.

Increasing solar illumination enhances the ionization density and conductivity in the topside ionosphere and the resulting supply of ions to higher altitudes, and raises the average altitude of the acceleration. It also reduces the overall strength of the field-aligned potential drop and the resulting intensity of auroral acceleration processes responsible for ion beam generation (Newell et al. 1996; Collin et al. 1998). Thus, variation in the solar EUV and geomagnetic energy inputs into the ionosphere, rather than heating and cooling of the ionosphere on a seasonal time scale, primarily determines the global H^+ and O^+ outflow rates.

Figure 16.13 underscores the importance of solar illumination in the energization and transport of thermal O^+ ions, and confirms the preference for dayside energization of O^+ observed on Akebono (Abe et al. 2004), which was attributed to the enhancement in ambipolar electric field due to escaping atmospheric photoelectrons. On Fast, Andersson et al. (2005) observed an increase in upward O^+ ion flux from 1500 to 4200 km, as the thermal O^+ ions were being energized into the detector energy range of 3 eV to 12 keV. Also, the altitude dependence of the characteristic energy was distinctly different in the four MLT quadrants; this implies that the dominant physical process and/or transport are different in the four quadrants.

Peterson et al. (2008) recast the observed ion outflow flux and energy distributions near Polar perigee in dynamic boundary-related coordinates, in which the polar cap and equatorward auroral boundaries in a polar cap crossing were identified using in-situ energetic electron and ion data, and the ion beams, conics and upflowing ions (distinct outflows) observed in each crossing were distributed into 10 dynamic boundary-related latitude bins and 2-h MLT bins.

Table 16.1 shows the net hemispheric flux of the observed upflowing ions in each MLT quadrant in the auroral zone and in the polar cap, respectively. For all three ion species (H^+, O^+ and He^+), only a very small fraction (~2–3%) of the observed energetic UFI was

Table 16.1 Net hemispheric UFI flux, flux percentage and characteristic energy at 5000–7000 km[a]

Quadrant	H^+				O^+				He^+			
	Noon	Dusk	Night	Dawn	Noon	Dusk	Night	Dawn	Noon	Dusk	Night	Dawn
F(PC)	0.005	0.004	0.01	0.01	0.01	0.003	0.006	0.03	0.000	0.001	0.002	0.001
F(AZ)	0.41	0.15	0.52	0.22	0.66	0.18	0.46	0.36	0.03	0.009	0.07	0.02
F(PC + AZ)	0.42	0.16	0.53	0.23	0.67	0.18	0.46	0.4	0.03	0.01	0.07	0.03
%(PC)	*1.2*	*2.5*	*1.9*	*4.3*	*1.5*	*1.7*	*1.3*	*7.5*	*1.0*	*10.0*	*2.9*	*2.0*
E(PC)	0.3 (0.001)				0.19 (0.008)				0.7 (0.008)			
E(AZ)	0.20	0.31	0.88	0.30	0.12	0.41	0.59	0.18	0.24	0.60	0.85	0.36
	0.56 (0.03)				0.30 (0.1)				0.7 (0.11)			

[a] Flux (F) in 10^{24} ions s^{-1}, characteristic energy (E) in keV; value in parenthesis is estimate including thermal ion flux below 15 eV (see text); PC = polar cap, AZ = auroral zone

in the polar cap. However, their presence confirms that not only are energetic ions being transported by prevailing convection electric fields to the high-altitude polar cap, but they are also produced by ion acceleration events in the polar cap ionosphere. In the auroral zone, the flux in the midnight quadrant dominated, and consisted of ~50% of the total H^+ and He^+ flux and ~30% of the O^+ flux, compared with ~37% of O^+ flux in the noon quadrant where most of the flux was on cusp field lines (see e.g. Zheng et al. 2005).

Note that the flux averages in Table 16.1 exclude both the non-distinct outflows in polar cap crossings with identifiable dynamic boundaries and all data samples in crossings without identifiable dynamic boundaries. As discussed in Peterson et al. (2008), including all data samples (of both distinct and non-distinct outflows as well as non outflows) in an analysis based on static (invariant) coordinates increases the average H^+, O^+ and He^+ flux by ~15, 40 and 30%, respectively, but does not materially alter the MLT or latitude distribution.

Table 16.1 also shows the characteristic energies of the observed energetic upflowing ions in the polar cap and each MLT quadrant in the auroral zone. The energies were derived from the UFI number to energy flux ratio. For comparison, the estimated energy values including the contributions from thermal ion flux below 15 eV are given in the parentheses. Table 16.1 suggests that the relative energization and acceleration of O^+ in the noon quadrant are significantly different from those in the other MLT quadrants, and that a larger fraction of O^+ is energized above 15 eV compared with H^+ at Polar perigee. This would imply that auroral and cusp energization processes acting below have significant mass dependencies, and that O^+ ions follow activity-dependent transport paths from the ionosphere to the plasma sheet and the ring current.

A number of factors complicate the direct interpretation of the observed ion energy flux to number flux ratio as characteristic energy, including complications arising from net downward flux regions, significant fluxes below the measurement energy threshold, and corrections for the trapped ion component, respectively. Nevertheless, taking approximate account of the portion of ion flux below 15 eV with sufficient energy to reach the plasma sheet without further energization, Peterson et al. (2008) inferred the characteristic energy of H^+ and O^+ ion outflows to be between 30 and 300 eV and about 100 eV, respectively, in the cusp, and between 30 and 1200 eV and between 150 and 160 eV in the midnight quadrant.

Figure 16.14 shows the net ion outflow rates of both H^+ and O^+, obtained by integrating the DE-1 ion flux measurements over all magnetic local times and all invariant latitudes above 56°, as a function of the magnetic Kp index for three $F_{10.7}$ ranges (Yau et al. 1985b, 1988). The O^+ rate increased exponentially with Kp, by a factor of 20 from Kp = 0 to 6, and exceeded 3×10^{26} ions s^{-1} at times of high solar and magnetic activity. The rate at low solar activity was about a factor of 5 smaller than that at high activity. In contrast, the H^+ rate in the three $F_{10.7}$ ranges was very similar. In all three $F_{10.7}$ ranges, the dependence of the O^+ rate on Kp was similar. In comparison, the H^+ rate increased with Kp more moderately, by a factor of 4 from Kp = 0 to 6.

Figure 16.15 compares the observed low-energy ion outflow rates observed on Akebono below 9000 km near solar minimum with the corresponding

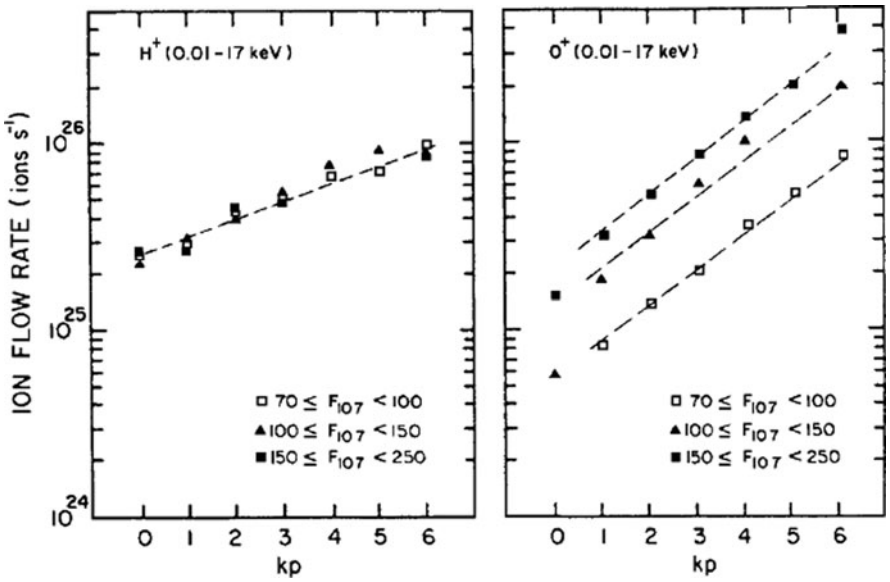

Fig. 16.14 H^+ and O^+ ion outflow rates at 0.01–17 keV observed at 16,000–24,000 km on DE-1, integrated over all MLT above 56° invariant in both hemispheres as a function of Kp, for different ranges of $F_{10.7}$ (From Yau et al. 1988)

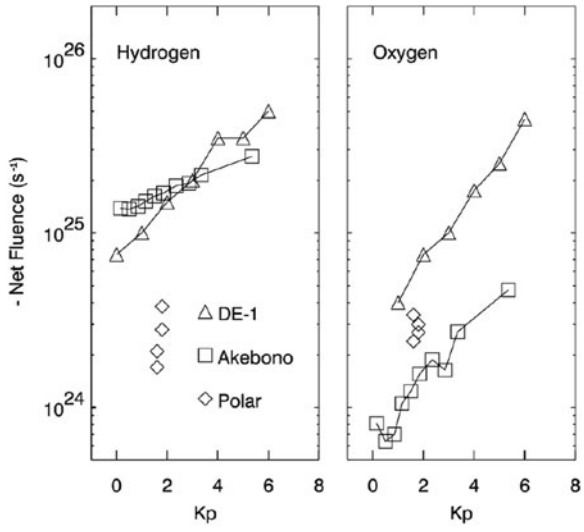

Fig. 16.15 H^+ and O^+ ion outflow rates near solar minimum as a function of Kp. □: low-energy rate on Akebono below 9000 km; △: suprathermal energy rate on DE-1 above 16,000 km; ◇: suprathermal energy rate on POLAR below 9000 km (From Cully et al. 2003)

suprathermal energy rates on Polar at the same altitudes (15 eV–16 keV) and on DE-1 above 16,000 km (10 eV–16 keV), respectively. In the case of H^+, the low-energy rate on Akebono was comparable with the suprathermal energy rate on DE-1 and a factor of 4–10 higher than the suprathermal energy rate on Polar. This indicates that significant acceleration of H^+ occurs above 9000 km in the high-latitude ionosphere. In contrast, in the case of O^+, the low-energy outflow rate below 9000 km is below the corresponding suprathermal rate above this altitude, which is in turn below the corresponding suprathermal rate above 16,000 km. This means that a significant fraction of the O^+ ions is accelerated below 9,000 km, and that the acceleration continues between 9,000 and 16,000 km.

In other words, a significant fraction of low-energy ions at low altitudes in the high-latitude ionosphere, including polar wind ions and auroral ion up-flows, is accelerated to suprathermal energies at higher altitudes, where the ions "lose their identities" as thermal-energy ions. Thus, it is important to consider both thermal ion flow (Section 16.2) and suprathermal ion

outflow (this section) in the high-latitude ionosphere as an integrated entity.

The dayside polar ionosphere is believed to respond instantaneously to the changing solar wind, while the night side polar ionosphere is expected to respond more to the release of stored energy from the magnetotail (Baker et al. 1997). Since the solar wind density and pressure and the IMF control the detailed distributions of particle precipitation and electric field in the polar ionosphere, they are expected to drive the ionospheric convection pattern and modulate the amount of free energy available for ionospheric ion acceleration, and thereby influence the overall characteristics of ion up-flows and outflows, particularly on the dayside.

As noted earlier in this section, the majority of statistical studies on the magnetic activity dependences of ion outflow were based on the Kp index. Studies based on AE, Dst, IMF or solar wind plasma pressure are rarer. On DE-1, a good correlation was found between the occurrence frequency of upwelling ions and the solar wind dynamic pressure (Giles et al. 1994), but no significant correlation was found between the IMF B_z and the upwelling ion flux (Pollock et al. 1990). On Viking, Oieroset et al. (1999) also found no clear correlation between the observed upward flux of energetic ions and IMF B_y.

On Akebono, Cully et al. (2003) found the observed (1–20 eV) H^+ and O^+ ion outflow rates to exhibit a strong correlation with the solar wind kinetic pressure, density, and electric field, and the variability in the IMF in the preceding hour; the observed rates also anti-correlated with the solar wind velocity. However, no clear correlation was found between the ion outflow rates and the IMF clock angle (i.e. orientation; B_z/B_y). On the other hand, the dayside ion conics were observed more frequently when IMF B_y was large (Miyake et al. 2000).

On Polar, Elliott et al. (2001) found a good correlation between thermal-energy (a few eV) ion flux and solar wind kinetic pressure, but no clear correlation between the ion flux and IMF B_y. Lennartsson et al. (2004) found the occurrence of energetic ($\leq$33 keV) ion outflow to be correlated with the solar wind, and the O^+ outflow rate to increase by a factor of 2.5–3 during periods of negative B_z (<–3 nT) compared with those of positive B_z (>3 nT). In addition, Moore et al. (1999b) found a clear correlation between suprathermal (tens of eV) O^+ flux and the variability (standard deviation in the preceding hour) of solar wind kinetic pressure.

It is clear that the solar wind and the IMF exert a direct influence on both the thermal and the suprathermal components of the ion outflow. In particular, the solar wind kinetic pressure affects strongly the overall magnitude of the outflow, as does the north-south component of the IMF in some cases. However, a coherent picture of the influence of the IMF does not yet exist due to the paucity of available observations.

16.4 Summary and Conclusion

Extensive satellite and ground-based observations over the last four solar cycles have shown that ionospheric ion outflows are highly variable in composition, energy, space and time, and constitute an important and at times dominant source of plasma in the magnetosphere. The composition of the ionosphere is constrained by the temperature and composition of the thermosphere at different levels of solar EUV flux in a solar cycle, and is influenced by geomagnetic activity, which increases the temperature of the thermosphere and modifies its composition distribution at auroral and polar cap latitudes.

The auroral zone is generally the region of ionospheric ion convection reversal and a region of field-aligned currents and free energy sources for possible ionospheric ion acceleration and outflow, as is the polar cap during northward IMF conditions.

The variety of ion outflows may be grouped into two categories: bulk ion flows, including the polar wind and auroral bulk ion up-flow; and suprathermal ion outflows, including ion beams, ion conics, transversely accelerated ions and upwelling ions.

The polar wind is composed primarily of electrons and H^+, He^+ and O^+ ions, and is driven by ambient plasma pressure gradient and ambipolar electric field along open magnetic field lines in the polar ionosphere at low altitude, and additional mechanisms including centrifugal acceleration at high altitude. Its acceleration (increase in velocity with altitude) is largest below 4000 km (Fig. 16.3), and depends strongly on solar activity level: the velocity increase at solar minimum (low solar EUV flux) is much larger below 3600 km and much smaller above 4000 km than at solar maximum (Fig. 16.4). Its velocity is larger on the dayside than on the night side and correlated with the electron

temperature, and increases approximately linearly with geocentric distance, at least between 1 and 9 R_E altitude, reaching H^+ and O^+ velocities of ~12 and 4 km/s at 10,000 km and 45 and 17 km/s at 50,000 km, respectively (Figs. 16.3 and 16.5). During magnetically active times, its variability in velocity is as much as 50% of the mean velocity, and its H^+ and O^+ ion outflow rates are higher.

Auroral bulk ion up-flow is highly variable and generally confined to narrow latitude regions of enhanced ion and/or electron temperatures in the dayside cusp/cleft and the night side auroral region (Fig. 16.8). It is dominated by O^+ ions, and is driven by soft electron precipitation and convection-driven Joule heating. It carries upward ion flux up to $\sim 2 \times 10^9$ $cm^{-2}s^{-1}$ and its velocity sometimes exceeds 1 km/s below 1000 km in the topside ionosphere (Fig. 16.7). On average, its velocity is a factor of 2 higher and its flux a factor of 4 lower at solar minimum than at solar maximum (Fig. 16.9); this results in a higher observed occurrence probability of up-flow based on ion velocity measurements near solar minimum. Its averaged starting altitude shifts from ~300 km near solar minimum to ~350 km near solar maximum. The observed solar-activity dependence of its occurrence and characteristics is attributed to the stronger EUV flux at solar maximum and the resulting higher ionization and ion-neutral collision frequency in the F-region. Both its velocity and upward ion flux increase with geomagnetic activity (Kp); storm-enhanced density (SED) plumes and F-region plasma patches are sources of strong ion up-flows on the storm-time dayside and the substorm-time night side, respectively (Fig. 16.10). The shape, size and location of the dayside ion upflow region appear to be influenced by the solar wind velocity and density and the IMF B_y and B_z.

Both ion beams and conics are a common phenomenon, with occurrence frequencies sometimes higher than 50% above 1 R_E altitude, and are dominated by H^+ and O^+ ions in the 10 eV to a few keV range. Ion beams are generally observed above 5000 km altitude, and increase in occurrence probability with altitude. Ion conics are observed down to 1000 km on the night side and ~3000 km on the dayside, and up to several R_E altitude and beyond at decreasing occurrence probability with altitude above ~10,000 km.

The two most important mechanisms for transversely accelerated ions are resonant energization by broadband low-frequency waves in the ion gyrofrequency range and waves near the lower hybrid frequency, respectively (Fig. 16.11). Transverse ion acceleration occurs down to ~500 km during active night side aurora, and to ~3000 km regularly on the dayside cleft, where the resulting upwelling ions have a higher upward mean velocity.

The flux of ion conics correlates strongly with the downward Poynting and soft electron number flux and ELF wave amplitude (Fig. 16.12). The correlation is indicative of a multi-step energization involving ion heating in the lower ionosphere and subsequent ion conic formation at higher altitudes. At ~ 1 R_E altitude, upflowing ions have characteristic energies on the order of 100 eV in the cusp and higher energies on the night side.

Compared with H^+ and He^+, O^+ upflowing ions have a higher conic-to-beam and noon-to-midnight ion flux ratio, and exhibit much stronger dependence on magnetic and solar activity. The occurrence probability of intense O^+ upflowing ions is a factor of 3 higher at active times compared with quiet times, and a factor of 3–4 higher at solar maximum compared with the declining phase of the solar cycle. The O^+ ion outflow rate increases exponentially with Kp by a factor of 20 from Kp = 0 to 6, and exceeds 3×10^{26} ions s^{-1} at times of high solar and magnetic activity; in comparison, the H^+ rate increases by a factor of 4. The O^+ ion outflow rate increases by a factor of ~5 from solar minimum to solar maximum, while the H^+ rate decreases by a factor of ~2, resulting in an order-of-magnitude increase in the O^+/H^+ composition ratio from solar minimum to maximum (Fig. 16.14).

A few percent of observed energetic upflowing ions is in the polar cap; this is indicative of ion acceleration in the polar cap ionosphere. In the auroral zone, the cusp is an important but not a dominant source of energetic ionospheric plasma for the magnetosphere – the midnight quadrant is. The net outflow rate and conic-to-beam-ratio of both H^+ and O^+ upflowing ions increase with solar illumination: this suggests that sunlight favors conics while darkness favors beams (Fig. 16.13).

Both the polar wind and ion up-flow constitute an important source of low-energy ("cold") plasma for suprathermal ion outflows above the topside ionosphere, where the transverse ion acceleration plays an important role in the generation of ion conics, and both parallel electric field and magnetic folding

contribute to the formation of ion beams at high altitudes (Fig. 16.15).

As discussed earlier, it is not always possible to distinguish between the contributions from the polar wind and other low-energy ions such as the cleft ion foundation in the high-altitude polar cap. The observed velocity ratio between H^+, O^+ and He^+ provides interesting insight into this point. At Polar apogee, Su et al. (1998) found that $v_{//}(H^+) : v_{//}(He^+) : v_{//}(O^+) \sim 2.6 : 1.5 : 1 \sim 1 : 0.57 : 0.38$. In comparison, the expected ratio is 4 : 2 : 1 in the case of equal energy gain due to ambipolar electric field, and 1:1:1 in the case of velocity filtering from a single distant source such as the cleft ion fountain. The fact that the observed ratio lies between these two cases and spans a wide range of values suggests that a number of processes and factors of comparable energy gain probably contribute to the overall ion acceleration observed in the high-altitude polar cap, including ambipolar electric field, velocity filtering associated with the cleft ion fountain, gravitational force, and centrifugal acceleration at high altitude due to strong convection electric field in a region of large-curvature or rapidly changing magnetic field.

It is clear that the characteristics and dynamics of ion outflow are strongly influenced by the state of the solar electromagnetic energy input and the conditions of the magnetosphere-ionosphere-thermosphere system. It is also clear that ion outflow directly affects the structure and dynamics of the magnetosphere-ionosphere-thermosphere system. However, a detailed review of these effects is beyond our scope.

Acknowledgments We gratefully acknowledge the funding support for this research from the Canadian Space Agency (CSA) and the Natural Science and Engineering Research Council of Canada (NSERC) Industrial Research Chair Program. We would also like to thank the NASA Heliophysics Program for support.

References

Abe T, Whalen BA, Yau AW, Horita RE, Watanabe S, Sagawa E (1993a) EXOS-D (Akebono) SMS observations of the polar wind. J Geophys Res 98:11191–11203

Abe T, Whalen BA, Yau AW, Watanabe S, Sagawa E, Oyama KI (1993b) Altitude profile of the polar wind velocity and its relationship to ionospheric conditions. Geophys Res Lett 20:2825–2828

Abe T, Watanabe S, Whalen BA, Yau AW, Sagawa E (1996) Observations of polar wind and thermal ion outflow by Akebono/SMS. J Geomagnetism Geoelectricity 48:319–325

Abe T, Yau AW, Watanabe S, Yamada M, Sagawa E (2004) Long-term variation of the polar wind velocity and its implication for the ion acceleration process: Akebono suprathermal ion mass spectrometer observations. J Geophys Res 109. doi: A09305, 2003JA010223

Andersson L, Peterson WK, McBryde KM (2005) Estimates of the suprathermal O^+ outflow characteristics and relative location in the auroral oval. Geophys Res Lett 32:L09104. doi: 10.1029/2004GL021434

Andre M (1997) Waves and wave-particle interactions in the auroral region. J Atmos Sol Terr Phys 59(14):1687

Andre M, Chang T (1993) Ion heating perpendicular to the magnetic field. In: Andre M, Chang T (eds) Physics of space plasmas, SPI conference proceedings and reprint series, vol 15. Scientific Publishers, Cambridge, MA, pp 35–71

Andre M, Yau A (1997) Theories and observations of ion energization and outflow in the high latitude magnetosphere. Space Sci Rev 80(1–2):27–48

Andre M, Koskinen H, Matson H, Erlandson R (1988) Local transverse ion energization in and near the polar cusp. Geophys Res Lett 15:107–110

Andre M, Crew GB, Peterson WK, Persoon AM, Pollock CJ, Engebretson MJ (1990) Ion heating by broadband low-frequency waves in the cusp/cleft. J Geophys Res 95:20809–20823

Andre M, Norqvist P, Vaivads A, Eliasson L, Norberg O, Eriksson AI, Holback B (1994) Transverse ion energization and wave emissions observed by the Freja satellite. Geophys Res Lett 21:1915–1918

Andre M, Norqvist P, Andersen L, Eliasson L, Eriksson AI, Blomberg L, Erlandson RE, Waldemark J (1998) Ion energization mechanisms at 1700 kilometer in the auroral region. J Geophys Res 103:4199–4222

Arnoldy RL, Lynch KA, Kintner PM, Vago J, Chesney S, Moore TE, Pollock CJ (1992) Bursts of transverse ion acceleration at rocket altitudes. Geophys Res Lett 19:413–416

Ashour-Abdalla M, Okuda H (1984) Turbulent heating of heavy ions on auroral field lines. J Geophys Res 89:2235–2238

Axford WI (1968) The polar wind and the terrestrial helium budget. J Geophys Res 73:6855–6859

Baker DN, Pulkkinen TI, Hesse M, McPherron RL (1997) A quantitative assessment of energy storage and release in the Earth's magnetotail. J Geophys Res 102:7159–7168

Ball L, Andre M (1991) Heating of H^+ ions in the cusp/cleft: double-cyclotron absorption versus cyclotron resonance. J Geophys Res 96:1429–1437

Bates HF (1974) Atmospheric expansion from Joule heating. Planet. Space Sci 22:925–937

Borovsky JE (1984) The production of ion conics by oblique double layers. J Geophys Res 89:2251–2266

Bouhram M, Klecker B, Miyake W, Reme H, Sauvaud JA, Malingre M, Kistler L, Blagau A (2004) On the altitude dependence of transversely heated O^+ distributions in the cusp/cleft. Ann Geophys 22(380):1787–1798

Chandler MO (1995) Observations of downward moving O^+ in the polar topside ionosphere. J Geophys Res 100 (A4):5795–5800

Chang T, Coppi B (1981) Lower hybrid acceleration and ion evolution in the suprauroral region. Geophys Res Lett 8:1253–1256

Chang T, Crew GB, Hershkowitz N, Jasperse JR, Retterer JM, Winningham JD (1986) Transverse acceleration of oxygen ions by electromagnetic ion cyclotron resonance with broad band left-hand polarized waves. Geophys Res Lett 13:636–639

Collin HL, Peterson WK, Drake JF, Yau AW (1988) The helium components of energetic terrestrial ion upflows: their occurrence, morphology, and intensity. J Geophys Res 93:7558–7564

Collin HL, Peterson WK, Lennartsson OW, Drake JF (1998) The seasonal variation of auroral ion beams. Geophys Res Lett 25:4071–4074

Cully CM, Donovan EF, Yau AW, Arkos GG (2003) Akebono/Suprathermal mass spectrometer observations of low energy ion outflow: dependence on magnetic activity and solar wind conditions. J Geophys Res 108(A2):1093. doi: 10.1029/2001JA009200

Drakou E, Yau AW, Abe T (1997) Ion temperature measurements from the Akebono suprathermal mass spectrometer: application to the polar wind. J Geophys Res 102:17523–17539

Elliott HA, Comfort RH, Craven PD, Chandler MO, Moore TE (2001) Solar wind influence on the oxygen content of ion outflow in the high-altitude polar cap during solar minimum conditions. J Geophys Res 106:6067–6084

Engwall E, Eriksson AI, Cully CM, Andre M, Torbert R, Vaith H (2009) Earth's ionospheric outflow dominated by hidden cold plasma. Nat Geosci. doi: 10.1038/NGEO387

Foster C, Lester M, Davies JA (1998) A statistical study of diurnal, seasonal and solar cycle variations of F-region and topside auroral upflows observed by EISCAT between 1984 and 1996. Ann Geophys 16:1144–1158

Foster JC, Coster AJ, Erickson PJ, Goldstein J, Rich FJ (2002) Ionospheric signatures of plasmaspheric tails. Geophys Res Lett 29:1623. doi:10.1029/2002GL015067

Foster JC, Coster AJ, Erickson PJ, Rich FJ, Sandel BR (2004) Stormtime observations of the flux of plasmaspheric ions to the dayside cusp/magnetopause. Geophys Res Lett 31:L08809. doi:10.1029/2004GL020082

Ganguli G, Keskinen MJ, Romero H, Heelis R, Moore T, Pollock C (1994) Coupling of microprocesses and macroprocesses due to velocity shear: an application to the low-altitude ionosphere. J Geophys Res 99(A5):8873

Giles BL, Chappell CR, Moore TE, Comfort CR, Waite JH Jr (1994) Statistical survey of pitch angle distributions in core (0–50 eV) ions from Dynamics Explorer 1: outflow in the auroral zone, polar cap, and cusp. J Geophys Res 99:17483

Goldstein J, Sandel BR, Forrester WT, Reiff PH (2003) IMF-driven plasmasphere erosion of 10 July 2000. Geophys Res Lett 30:1146. doi:10.1029/2002GL016478

Hedin AE (1987) MSIS-86 thermospheric model. J Geophys Res 92:4649–4662

Heelis RA, Winningham JD, Suguira M, Maynard NC (1984) Particle acceleration parallel and perpendicular to the magnetic field observed by DE-2. J Geophys Res 89: 3893–3902

Heppner JP, Maynard NC (1987) Empirical high-latitude electric field models. J Geophys Res 92(A5):4467–4489

Hoffman JH, Dodson WH (1980) Light ion concentrations and fluxes in the polar regions during magnetically quiet times. J Geophys Res 85:626–632

Horwitz JL (1986) The tail lobe ion spectrometer. J Geophys Res 91:5689–5699

Horwitz JL, Lockwood M (1985) The cleft ion fountain: a two-dimensional kinetic model. J Geophys Res 90:9749

Hultqvist B (1983) On the origin of the hot ions in the disturbed dayside magnetosphere. Planet. Space Sci 31:173–184

Hultqvist B (1991) Extraction of ionospheric plasma by magnetospheric processes. J Atmos Sol Terr Phys 53:3–15

Keating JG, Mulligan J, Doyle DB, Winser KJ, Lockwood M (1990) A statistical study of large field-aligned flows of thermal ions at high-latitudes. Planet Space Sci 38:1187–1201

Keiling A, Wygant JR, Cattell CA, Mozer FS, Russell CT (2003) The global morphology of wave Poynting flux: powering the aurora. Science 299:383–386

Kintner PM, Vago J, Chesney S, Arnoldy RL, Lynch KA, Pollock CJ, Moore TE (1992) Localized lower hybrid acceleration of ionospheric plasma. Phys Rev Lett 68:2448

Kintner PM, Bonnell J, Arnoldy R, Lynch K, Pollock C, Moore T (1996) SCIFER – Ion acceleration and plasma waves. Geophys Res Lett 23:1873–1876

Klumpar DM (1979) Transversely accelerated ions: an ionospheric source of hot magnetospheric ions. J Geophys Res 84:4229

Klumpar DM, Peterson WK, Shelley EG (1984) Direct evidence for two-stage (bimodal) acceleration of ionospheric ions. J Geophys Res 89:10779–10787

Knudsen DJ, Clemmons JH, Wahlund JE (1998) Correlation between core ion energization, suprathermal electron bursts, and broad-band ELF plasma waves. J Geophys Res 103:4171–4178

Lennartsson OW (1995) Statistical investigation of IMF B_z effects on energetic (0.1–16 keV) magnetospheric O^+ ions. J Geophys Res 100:23261–23635

Lennartsson OW, Shelley EG (1986) Survey of 0.1-16 keV/e plasma sheet ion composition. J Geophys Res 91:3061–3076

Lennartsson OW, Collin HL, Peterson WK (2004) Solar wind control of Earth's H^+ and O^+ outflow rates in the 15-eV to 33-keV energy range. J Geophys Res 109:A12212. doi:10.1029/2004JA010690

Liu HX, Ma SY, Schlegel K (2001) Diurnal, seasonal, and geomagnetic variations of large field-aligned ion upflows in the high-latitude ionospheric F-region. J Geophys Res 106:24651–24661

Lockwood M, Titheridge JE (1981) Ionospheric origin of magnetospheric O^+ ions. Geophys Res Lett 8:381–384

Loranc M, Hanson WB, Heelis RA, St-Maurice JP (1991) A morphological study of vertical ionospheric flows in the high-latitude F region. J Geophys Res 96:3627–3646

Lundin R, Haerendel G, Boehm M, Holback B (1994) Large-scale auroral plasma density cavities observed by Freja. Geophys Res Lett 21:1903

Lynch KA, Arnoldy RL, Kintner PM, Bonnell J (1996) The AMICIST auroral sounding rocket: a comparison of transverse ion acceleration mechanisms. Geophys Res Lett 23:3293–3296

Lysak RL (1986) Ion acceleration by wave-particle interaction. In: Chang T (ed) Ion acceleration in the magnetosphere and ionosphere. Geophysical monograph, vol 38. American Geophysical Union, Washington, DC, pp 261–270

McCrea IW, Lockwood M, Moen J, Pitout F, Eglitis P, Aylward AD, Cerisier JC, Thorolfssen A, Milan SE (2000) ESR and EISCAT observations of the response of the cusp and cleft to IMF orientation changes. Ann Geophys 18:1009–1026. doi: 10.1007/s00585-000-1009-7

Miyake W, Mukai T, Kaya N (1993) On the evolution of ion conics along the field line from EXOS-D observations. J Geophys Res 98:11127–11134

Miyake W, Mukai T, Kaya N (1996) On the origins of the upward shift of elevated (bi-modal) ion conics in velocity space. J Geophys Res 101:26961–26969

Miyake W, Mukai T, Kaya N (2000) Interplanetary magnetic field control of dayside ion conics. J Geophys Res 105:23,339–23,344. doi: 10.1029/2000JA900082

Moore TE (1980) Modulation of terrestrial escape flux composition (by low-altitude acceleration and charge exchange chemistry). J Geophys Res 85:2011–2016

Moore TE, Lundin R, Alcayde D, Andre A, Ganguli SB, Temerin M, Yau AW (1999a) Source processes in the high-latitude ionosphere. Space Sci Rev 88:7–84

Moore TE, Peterson WK, Russell CT, Chandler MO, Collier MR, Collin HL, Craven PD, Fitzenreiter R, Giles BL, Pollock CJ (1999b) Ionospheric mass ejection in response to a CME. Geophys Res Lett 26:2339–2342

Nagai T, Waite JH Jr., Green JL, Chappell CR (1984) First measurements of supersonic polar wind in the polar magnetosphere. Geophys Res Lett 11:669–672

Newell PT, Meng CI, Lyons KM (1996) Suppression of discrete aurora by sunlight. Nature 381:766

Norqvist P, Andre M Eliasson L, Erikson AI, Blomberg L, Luhr H, Clemmons JH (1996) Ion cyclotron heating in the dayside magnetosphere. J Geophys Res 101:13179

Ogawa Y, Buchert SC, Fujii R, Nozawa S, van Eyken AP (2009) Characteristics of ion upflow and downflow observed with the European Incoherent Scatter Svalbard radar. J Geophys Res 114:A05305. doi:10.1029/2008JA013817

Ogawa Y, Buchert SC, Sakurai A, Nozawa S, Fujii R (2010) Solar cycle dependence of ion upflow in the polar ionosphere observed with the EISCAT Tromso UHF radar. J Geophys Res 115:A07310. doi:10.1029/2009JA014766

Oieroset M, Yamauchi M, Liszka L, Hultqvist B (1999) Energetic ion outflow from the dayside ionosphere: categorization, classification, and statistical study. J Geophys Res 104:24915–24927

Persoon AM, Gurnett DA, Shawhan SD (1983) Polar cap electron densities from DE-1 plasma wave observations. J Geophys Res 88:10123–10136

Peterson WK, Collin HL, Doherty MF, Bjorklund CM (1992) O^+ and H^+ restricted and extended (bi-modal) ion conics distributions. Geophys Res Lett 14:1439–1442

Peterson WK, Collin HL, Doherty MF, Bjorklund CM (1995) Extended (bi-modal) ion conics at high altitudes. In: Ashour-Abdalla M, Chang T, Duesenbery P (eds) Space plasmas: coupling between small and medium scale processes. geophysical monograph, vol. 86. American Geophysical Union, Washington, DC, p 105

Peterson WK, Collin HL, Lennartsson OW, Yau AW (2006) Quiet time solar illumination effects on the fluxes and characteristic energies of ionospheric outflow. J Geophys Res 111:A11S05. doi:10.1029/2005JA011596

Peterson WK, Andersson L, Callahan BC, Collin HL, Scudder JD, Yau AW (2008) Solar-minimum quiet time ion energization and outflow in dynamic boundary related coordinates. J Geophys Res 113:A07222. doi: 10.1029/2008JA013059

Pollock CJ, Chandler MO, Moore TE, Waite JH Jr, Chappell CR, Gurnett DA (1990) A survey of upwelling ion event characteristics. J Geophys Res 95:18969–18980

Raitt WJ, Schunk RW (1983) Composition and characteristics of the polar wind. In: Johnson RG (eds) Energetic ion composition in the earth's magnetosphere. Terra Scientific Publishing, Tokyo, pp 99–141

Retterer JM, Chang T, Crew GB, Jasperse JR, Winningham JD (1987) Monte Carlo modeling of ionospheric oxygen acceleration by cyclotron resonance with broadband electromagnetic turbulence. Phys Rev Lett 59:148–151

Robinson RM, Tsunoda RT, Vickery JF, Guerin L (1985) Sources of F-region ionization mechanisms in the nightside auroral zone. J Geophys Res 90:7533–7546

Schunk RW (2007) Time-dependent simulations of the global polar wind. J Atmos Sol Terr Phys 69:2028–2047

Semeter J, Heinselman CJ, Thayer JP, Doe RA (2003) Ion upflow enhanced by drifting F-region plasma structure along the nightside polar cap boundary. Geophys Res Lett 30:2139. doi:10.1029/2003GL017747

Seo Y, Caton R, Horwitz JL (1997) Statistical relationship between high-latitude ionospheric F-region/topside upflows and their drivers: DE-2 observations. J Geophys Res 102(A4):7493–7500

Shelley EG, Johnson RG, Sharp RD (1972) Satellite observations of energetic heavy ions during a geomagnetic storm. J Geophys Res 77:6104–6110

Strangeway RJ, Russell CT, Carlson CW, McFadden JP, Ergun RE, Temerin M, Klumpar DM, Peterson WK, Moore TE (2000) Cusp field-aligned currents and ion outflows. J Geophys Res 105:21,129–21,142

Strangeway RJ, Ergun RE, Su YJ, Carlson CW, Elphic RC (2005) Factors controlling ionospheric outflows as observed at intermediate altitudes. J Geophys Res 110:A03221. doi:10.1029/ 2004JA010829

Su YJ, Horwitz JL, Moore TE, Giles BL, Chandler MO, Craven PD, Hirahara M, Pollock CJ (1998) Polar wind survey with the thermal ion dynamics experiment/plasma source instrument suite aboard polar. J Geophys Res 103:29305–29337

Tam SWY, Chang T, Pierrard V (2007) Kinetic modeling of the polar wind. J Atmos Sol Terr Phys 69:1984–2027

Temerin M, Roth I (1986) Ion heating by waves with frequencies below the ion gyrofrequency. Geophys Res Lett 13:1109–1112

Tsyganenko NA (2002) A model of the near magnetosphere with a dawn-dusk asymmetry: 1 Mathematical structure. J Geophys Res 107:1179. doi:10.1029/2001JA000219

Vago JL, Kintner PM, Chesney SW, Arnoldy RL, Lynch KA, Moore TE, Pollock CJ (1992) Transverse ion acceleration by localized lower hybrid waves in the topside auroral ionosphere. J Geophys Res 97:16935–16957

Wahlund JE, Opgenoorth HJ (1989) EISCAT observations of strong ion outflows from the F-region ionosphere during auroral activity – preliminary results. Geophys Res Lett 16:727–730

Wahlund JE, Opgenoorth HJ, Haggstrom I, Winser KJ, Jones GOL (1992) EISCAT observations of topside ionospheric ion

outflows during auroral activity: revisited. J Geophys Res 97:3019–3037

Whalen BA, Watanabe S, Yau AW (1991) Thermal and suprathermal ion observations in the low altitude transverse ion energization region. Geophys Res Lett 18:725–728

Wu XY, Horwitz JL, Seo Y (2000) Statistical analysis of F region and topside ionospheric ion field-aligned flows at high latitudes. J Geophys Res 105:2477–2494

Wygant J, Keiling A, Cattell CA et al (2000) Polar spacecraft based comparisons of intense electric fields and Poynting flux near and within the plasma sheet-tail lobe boundary to UVI images: an energy source for the aurora. J Geophys Res 105:18675–18692

Yau AW, Andre M (1997) Sources of Ion Outflow in the High Latitude Ionosphere. Space Sci Rev 80(1–2):1–26

Yau AW, Whalen BA, McNamara AG, Kellogg PG, Bernstein W (1983) Particle and wave observations of low-altitude ionospheric ion acceleration events. J Geophys Res 88:341–355

Yau AW, Whalen BA, Peterson WK, Shelley EG (1984) Distribution of upflowing ionospheric ions in the high-altitude polar cap and auroral ionosphere. J Geophys Res 89:5507–5522

Yau AW, Beckwith BH, Peterson WK, Shelley EG (1985a) Long-term (solar-cycle) and seasonal variations of upflowing ionospheric ion events at DE-1 altitudes. J Geophys Res 90:6395–6407

Yau AW, Shelley EG, Peterson WK, Lenchyshyn L (1985b) Energetic auroral and polar ion outflow at DE-1 altitudes: magnitude, composition, magnetic activity dependence and long-term variations. J Geophys Res 90:8417–8432

Yau AW, Peterson WK, Shelley EG (1988) Quantitative parametrization of energetic ionospheric ion outflow. In: Moore TE, Waite JH Jr (eds) Modeling magnetospheric plasma. Geophysical monograph, vol 44. American Geophysical Union, Washington, DC, pp 211–217

Yau AW, Whalen BA, Sagawa E (1991) Minor ion composition in the polar ionosphere. Geophys Res Lett 18:345–348

Yau AW, Whalen BA, Goodenough C, Sagawa E, Mukai T (1993) EXOSD (Akebono) observations of molecular NO^+ and $N_2{}^+$ upflowing ions in the high-altitude auroral ionosphere. J Geophys Res 98:11205–11224

Yau AW, Whalen BA, Abe T, Mukai T, Oyama KI, Chang T (1995) Akebono observations of electron temperature anisotropy in the polar wind. J Geophys Res 100: 17451–17463

Yau AW, Abe T, Peterson WK (2007) The polar wind: recent observations. J Atmos Sol Terr Phys 69:1936–1983

Zheng Y, Moore TE, Mozer FS, Russell CT, Strangeway RJ (2005) Polar study of ionospheric ion outflow versus energy input. J Geophys Res 110:A07210. doi:10.1029/2004JA010995

Heavy Ion Energization, Transport, and Loss in the Earth's Magnetosphere

17

Hans Nilsson

Abstract

The magnetic field of the Earth acts like a shield against the solar wind, leading to a magnetopause position many planetary radii away from the planet, in contrast to the situation at non- or weakly magnetized planets such as Mars and Venus. Despite this there is significant ion outflow from the cusp and polar cap regions of the Earth's ionosphere. Effective interaction regions form, in particular in the ionospheric projection of the cusp, where ionospheric plasma flows up along the field-lines in response to magnetospheric energy input. Strong wave particle interaction at altitudes above the ionosphere further accelerates the particles so that gravity is overcome. For the particles to enter a direct escape path they must be accelerated along open magnetic field lines so that they cross the magnetopause or reach a distance beyond the return flow region in the tail. Else the Earth's magnetic field will guide the transport of the particles back towards the Earth. This return flow may also be either lost to space or returned to the atmosphere. Throughout this transport chain the heating and acceleration experienced by the particles will have an influence on the final fate of the particles, as well as determine which populations can be measured by particle instruments. We will present quantitative estimates of centrifugal acceleration and perpendicular heating along the escape path from the cusp, through the high altitude polar cap/mantle. Finally we will compare this with the situation at the unmagnetized planets Mars and Venus and discuss to what extent a magnetic field protects an atmosphere from loss through solar wind interaction.

17.1 Introduction

The upper atmospheres of the terrestrial planets are all affected by the solar wind. In the case of the unmagnetized planets Mars and Venus the interaction is rather direct, with a pressure balance forming between the ionized part of the atmosphere, the ionosphere, and the shocked solar wind (e.g. Luhmann 1990; Dubinin et al. 2008; Nilsson et al. 2009). At Earth the geomagnetic field creates an obstacle to the solar wind flow, deflecting the flow around the planet at about 10 planetary radii distance where a magnetopause is formed (e.g. Cowley 1995). The magnetopause separates the two plasma regimes of the shocked solar wind, termed the magnetosheath, and the

H. Nilsson (✉)
Swedish Institute of Space Physics, Kiruna, Sweden
e-mail: hans.nilsson@irf.se

W. Liu, M. Fujimoto (eds.), *The Dynamic Magnetosphere*, IAGA Special Sopron Book Series 3,
DOI 10.1007/978-94-007-0501-2_17,

magnetosphere. This separation is not perfect, and a significant amount of mass and energy transfer takes place across it. Most of this energy transfer is concentrated to the regions where the dipole magnetic field of the Earth is weak, the cusp. The strength and morphology of the cusp is modified by the solar wind dynamic pressure and the interplanetary magnetic field (IMF). One important mechanism to make energy and mass transfer possible is the process of reconnection (e.g. Lockwood et al. 1989). Reconnection opens up magnetic field lines of terrestrial origin, connecting them to the magnetosheath. Plasma from the magnetosheath and associated waves and electric fields can efficiently propagate along these field lines. Energy from the solar wind is also transferred into magnetic energy, forming a magnetotail extending in the anti-sunward direction from the planet (for a recent example see Rosenqvist et al. 2008). Such energy is quasi-periodically released in magnetic substorms, which mainly affects the nightside of the Earth's magnetosphere. The energy release processes involve the closure of previously open magnetic field lines through reconnection in the tail. The dayside is much more directly affected by the influx of solar wind origin magnetosheath ions onto the field-lines of the Earth's polar caps. The polar cap field lines are the ones which are connected to the magnetosheath and solar wind, thus known as open field-lines. The most recently opened field-lines are known as the magnetospheric cusps (one in each hemisphere). In these regions the solar wind plasma and motional electric field can most directly interact with the Earth's ionosphere. The connection between the magnetic field-lines of the Earth and interplanetary space does not only facilitate energy input into the magnetosphere and subsequently the atmosphere. It also facilitates the escape of sufficiently energized ionospheric origin ions, both by allowing the transfer of energy from the solar wind and by providing an effective escape path from the magnetosphere and into the magnetosheath and subsequently the solar wind. The outflow from the polar cusp regions along open magnetic field lines is thus the outflow most likely to lead to atmospheric loss. It also turns out that the outflow emanating from the ionospheric projection of the cusp is where most of the energetic ion outflow is observed (Lockwood et al. 1985; Øieroset et al. 2000; Bouhram et al. 2004). This is therefore the region which is most interesting to compare to the solar wind interaction with unmagnetized planets.

The terrestrial magnetic field does not completely shield the atmosphere from the solar wind. It rather channels the interaction into the spatially limited regions of the polar caps, and in particular the ionospheric projection of the magnetospheric cusp. The magnetic field also plays another important role in atmospheric escape, that of keeping ions escaping from the atmosphere bound within the Earth's magnetosphere. If ions flowing up from the polar cap are to escape they must not only overcome gravity, they must also overcome the restoring force of the magnetic field of the Earth. Even if a particle is on an open field line when it starts its journey along a field-line, the field line may close through magnetotail reconnection before the ion escapes into interplanetary space. In such a case the magnetotail flow will bring the ions back towards the Earth. Ions flowing along closed magnetic field lines (i.e. not connected to the solar wind) will either return to the atmosphere in the opposite hemisphere or be magnetically trapped within the magnetosphere. Trapped ions can also be lost to interplanetary space, either by being brought to the magnetopause by magnetospheric convection, or through charge exchange reactions. The rest is returned to the atmosphere either as ion precipitation or energetic neutral atom precipitation. This constitutes the return flux of the global magnetospheric ion circulation.

In order to understand ion escape from a magnetized planet we must understand the initial ionospheric upflow and energization necessary to overcome gravity as well as the subsequent energization necessary to escape the magnetosphere. For a full picture we need also to understand the return flow in the tail and the eventual fate of these returning ions, loss to the atmosphere or to interplanetary space. In this chapter we will look at some of the most recent work on cusp origin ion outflow and the subsequent acceleration mechanisms affecting the outflowing ions, all mainly based on ion data from the Cluster mission (Escoubet et al. 2001). We will briefly review the need for future work on the ion return flow and finally put the atmospheric escape from a magnetized planet into the context of the most recent results from the unmagnetized planets Mars and Venus. Does a magnetic field really protect an atmosphere from losses caused by the solar wind interaction?

17.2 Ionospheric Upflow in the Cusp

The ionospheric projection of the magnetospheric cusp is subject to energy inflow in the form of ion and electron precipitation as well as DC electric fields and waves (Yordanova et al. 2007). The soft electron precipitation (of the order of 100 eV energy) mainly affects the ionospheric *F*-region, causing strong electron heating which can be directly observed by incoherent scatter radar (Nilsson et al. 1994, 1996; Ogawa et al. 2003). Such electron heating will lead to an enhanced polarization electric field and subsequent enhanced ion outflow (Moore et al. 1999). The DC electric field in the cusp area can lead to significant Joule heating in the ionosphere (Schunk et al. 1975). This in turn can to some extent be affected by conductance changes due to the cusp proton precipitation (Nilsson et al. 1998). Both experimental data, e.g. Ogawa et al. (2003), Strangeway et al. (2005) and simulations, e.g. Blelly et al. (1996), Vontrat-Reberac et al. (2001), points towards the importance of the electron precipitation in producing large ionospheric upflows in the cusp ionosphere. The up-flow region is then mainly determined by the cusp precipitation region. Geophysical conditions can further enhance this upflow, for example the Storm Enhanced Density (SED) associated with magnetic storms has a significant effect on the outflow by providing an enhanced ionospheric source region, e.g. Zeng and Horwitz (2008). Such SED enhancements also give rise to enhanced outflow in the nightside (e.g. Yuan et al. 2008), which may then resemble the cusp outflow in intensity, but because of the magnetospheric convection is likely to have a different fate from the cusp origin upflow.

The cusp precipitation is very dynamic and intermittent, to the extent that ground-based observations lead to the suggestion that the entire cusp is pulsed (Lockwood et al. 1993), built up by consecutive pulses of transient reconnection, flux transfer events (FTE). Whereas this remains a controversial subject, recent measurements have shown a one-to-one relationship between transient poleward moving auroral forms and ionospheric up-flows in the cusp (Moen et al. 2004). The poleward moving auroral forms have a similar temporal distribution as flux transfer events (Elphic et al. 1990), and are believed to be the ionospheric signature of a magnetospheric flux transfer event.

The cusp origin outflow continues into the high altitude mantle region, the region tailward of the cusp where magnetosheath origin protons are also flowing outward after having been reflected by the magnetic field of the Earth. The Cluster spacecraft spend several consecutive hours in the ion outflow region when passing through the high altitude mantle, and can therefore study transients on flux transfer event time scales of about 8 min. Nilsson et al. (2008a) could show, using Cluster data from the high altitude mantle, that transients in the number flux of O^+ ions occurred with a typical time interval of 5–10 min, fully consistent with the FTE time scale. The transients were not associated with heating, indicating that the suddenly enhanced number flux of O^+ was not due to cold ions being energized and thus brought into the ion spectrometer measurement range. For studies of heavy ion fluxes the high altitude mantle has the advantage that convection is usually high enough to bring all particles into the measurement range of a typical ion spetrometer, something we will discuss in Section 17.3.3. Thus the modulation of the high altitude magnetospheric heavy ion fluxes is caused by modulation at the source. Because the recurrence of the transients in the ionospheric upflow and in the high altitude outflow are so similar it was concluded that the ionospheric upflow was the limiting factor. This is by no means an obvious result. The ionospheric upflow within the altitude range of incoherent scatter radars (i.e. up to about 1000 km altitude) reaches about 1 km/s, well below escape velocity. Without successive acceleration at higher altitudes the ions would simply fall back into the ionosphere again. The results of Nilsson et al. (2008a) suggest that such further acceleration is common enough and it is the initial ionospheric upflow which modulates the higher altitude outflow.

The ionosphere at altitudes accessible to incoherent scatter radars (<1000 km) is essentially dominated by O^+ ions, and at lower altitudes heavier molecular ions. There is also an important escape of light ions, mainly protons, from the topside ionosphere of the polar cap. This outflow is termed the polar wind, in analogy with the solar wind (Axford 1968; Banks and Holzer 1968). It is difficult to study this outflow using ion spectrometers in the cusp region, as the ionospheric outflow of protons is likely to drown in the intense flux of protons of solar wind origin. Initially the polar wind has much lower energy than the solar wind origin protons, making it possible to distinguish the two populations

if the low energy population can be measured at all. The polar wind has been observed at several altitudes (Hoffman and Dodson 1980; Nagai et al. 1984; Cully et al. 2003a; Moore et al. 1997). Models predict that this outflow continues into the magnetotail lobes where it is either fed to the plasma sheet or escape (Chappell et al. 2000; Cully et al. 2003b). Just as for the heavier ions, the further acceleration along the flight path decides the ultimate fate of the ions.

17.3 Magnetospheric Acceleration of Outflowing Ions

In the previous section we discussed that upflowing ions seen by incoherent scatter radars are still gravitationally bound. In order to become outflowing ions further acceleration is needed. This acceleration can take the form of perpendicular heating with subsequent outflow due to the action of the mirror force, or through direct field-aligned acceleration due to field-aligned electric fields or the centrifugal acceleration mechanism. The perpendicular heating is particularly interesting as it highlights the ambiguous role of the magnetic field in protecting an atmosphere. Indeed the magnetic field will shield large parts of the atmosphere from the direct influence of the solar wind. On the other hand ions heated transverse to the magnetic field-line will, due to the mirror force, turn this into a field-aligned outflow. The magnetic field in the polar cap in essence expels heated plasma. If there is enough acceleration, this will lead to escape. The direct field-aligned acceleration in the cusp/mantle region seems to be mainly in the form of centrifugal acceleration (Nilsson et al. 2008b). At times field-aligned acceleration that appears to be due to field-aligned electric fields (just as in the main auroral oval) is seen in the cusp and mantle region, e.g. Maggiolo et al. (2006). In this text we will only pay attention to the centrifugal acceleration of these two field-aligned outflow mechanisms.

17.3.1 Centrifugal Acceleration

The centrifugal acceleration mechanism was first discussed for cusp ion outflow by Cladis (1986). This type of acceleration occurs when there is a change of direction of the magnetic field and a finite convection electric field. The energy for the acceleration is provided by the convection electric field. A simple picture can be obtained by considering the curved path of the $E \times B$ drift in a geometry where the magnetic field curvature changes along the drift path of the ions. The centrifugal acceleration associated with the curvature of the drift corresponds to the centrifugal acceleration of the ions due to a change of the magnetic field direction when moving transverse to the magnetic field. There is a corresponding acceleration due to a change of the magnetic field-line direction when moving in the parallel direction, and finally a term due to temporal changes of the magnetic field direction (Northrop 1963).

In order to properly estimate the centrifugal acceleration one must be able to determine the 3-dimensional gradient of the magnetic field vector, which can be done with the Cluster four-spacecraft constellation, as well as the $E \times B$ drift and the parallel velocity of the outflowing particles. This has been done for the high altitude mantle by Nilsson et al. (2008b) and for the magnetotail lobes by Nilsson et al. (2010). In the latter paper the drift velocities (parallel and perpendicular) did not come from particle data, but instead from the electric field and wave instrument in combination with the electron drift instrument, see Engwall et al. (2009a), Nilsson et al. (2010) for details. These ion fluxes in the magnetotail lobes are normally hidden from ion spectrometers such as the Cluster CIS instrument (Rème et al. 2001) due to the energy threshold of the instrument and the typical spacecraft charge of a sunlit spacecraft in a tenuous plasma. We will discuss the role of hidden populations further in Section 17.3.3. The total centrifugal acceleration experienced by a particle along a given flight path will depend on its initial parallel velocity. We show in Fig. 17.1 (reproduced from Nilsson et al. 2010) the average observed parallel velocity for different altitudes in the mantle (black circles with error bars) and the same for observed proton flows in the lobes (red circles with error bars). Filled black lines show the parallel velocity of a test particle experiencing the average observed centrifugal acceleration (calculated for the same intervals as the observed parallel velocities) along the two paths, for a number of different initial velocities. See Nilsson et al. (2010) for details. The centrifugal acceleration is much stronger for the high altitude cusp/mantle ion paths than for the lobes. In both cases we expect heavy ions to reach energies

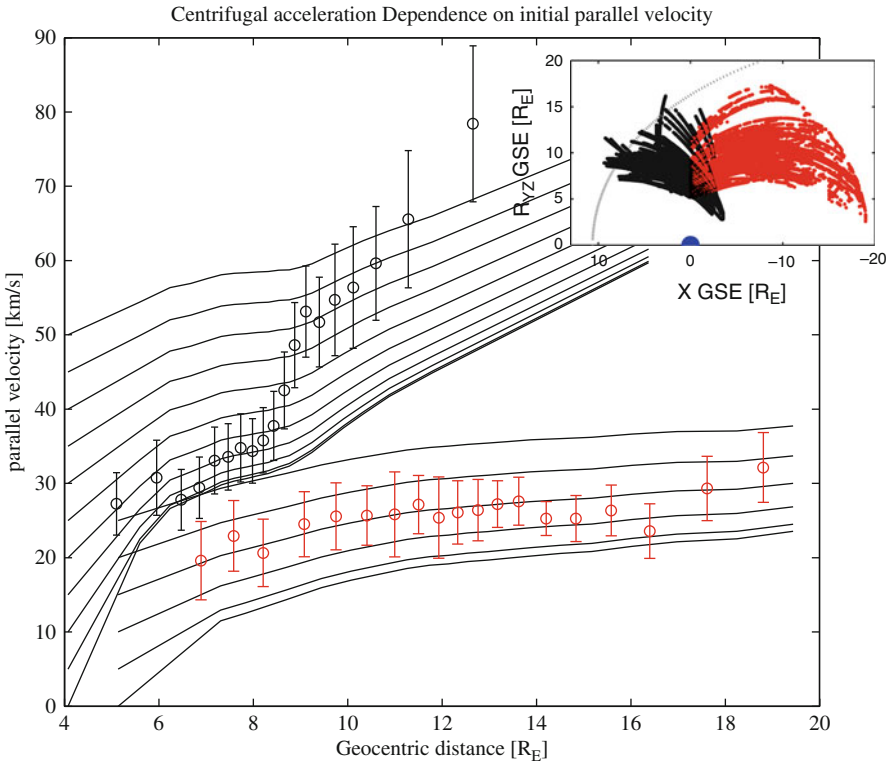

Fig. 17.1 Average O^+ mantle (*black*) and H^+ lobe (*red*) parallel velocity ([km s^{-1}] with error bars indicating a 95% confidence interval. *Solid black lines* indicate the parallel velocity resulting from the average observed centrifugal acceleration for test particles with different initial velocities at the leftmost boundary of the plot. The inserted figure in the *upper right* shows the location where the data was taken for the two data sets (*black cusp/mantle, red lobes*), in X–R $\left(\mathrm{R} = \sqrt{\mathrm{Y}^2 + \mathrm{Z}^2}\right)$ coordinates, with the Earth as a blue ball and a model magnetopause indicated with a dotted gray line

observable by ion spectrometers, indicating that there should most of the time not be any populations of heavy ions which cannot be observed by ion spectrometers. Furthermore we can see that there seems to be a region of strong acceleration other than centrifugal acceleration affecting ions along the mantle flight path at geocentric distances above 8R_E. This is consistent with significant perpendicular heating and subsequent enhanced parallel velocity discussed in Section 17.3.2. However the parallel velocity below 8 R_E is about 30 km/s, less than the 30–100 km/s for this altitude region reported by Bouhram et al. (2004). This indicates that we are to some extent seeing an artefact of the orbit geometry. The lower altitudes are sampled in the poleward part of the cusp, where only slower ions are seen due to velocity dispersion. The higher altitude region is not affected by this velocity dispersion effect (Section 17.3.2). The perpendicular temperature starts to increase from about 8 R_E geocentric distance, from about 100 eV up to more than 1 keV above 10 R_E (not shown, see also Section 17.3.2). The regions where the two data sets were obtained is shown in a small figure inserted in the upper right part of Fig. 17.1, where black dots indicates the cusp/mantle and red dots the lobes.

17.3.2 Transverse Heating of Outflowing Ions

Studies using the Freja satellite show that efficient ion heating, sufficient to overcome gravity, is common at about 1700 km altitude or below (Norqvist et al. 1998), and for example Andre et al. (1990) have shown that ion heating continues up to altitudes of a few R_E. The most complete survey of the altitude dependence of transverse ion heating was done by Bouhram et al. (2004), who combined data from Akebono, Interball-2 and Cluster to obtain the evolution of cusp transverse heating of heavy outflowing

ions at altitudes up to about 5.5 R_E. Barghouthi (2008) has recently summarized several current models of ion heating of heavy ions in the cusp/mantle region. In all cases it is found that only a small fraction of the observed wave amplitudes is needed in order to reproduce observed transverse ion heating through ion cyclotron resonance, typically of the order of a few percent. The waves associated with ion heating are typically broadband waves, so not all of the wave intensity is likely to be effective in the ion heating process. Therefore the mechanism involved in ion heating up to altitudes of about 5.5 R_E is partially understood, though the wave modes involved and their generation remain to be fully determined. Though heating is most efficient at around the cyclotron frequency, there are also a number of other mechanisms which may be efficient over a broader frequency range, either through stochastic motion of the gyro center (Chaston et al. 2004) or through the ponderomotive force resulting from wave particle interaction (Guglielmi and Lundin 2001; Lundin and Guglielmi 2006). Even if we do not know the precise heating mechanism it seems quite clear that there is an ample source for the heating available in the rich wave activity in the ion outflow region. As to the ultimate source of this energy, it is believed to be the solar wind. The solar wind origin ions streaming down the field-lines of the cusp is a source of wave activity at the local gyro-frequency (Nykyri et al. 2006; Sundkvist et al. 2005). For a general theory of ion outflow from a magnetized planet we must understand what is limiting this process of energy transfer from inflowing particles to escaping particles.

Recent Cluster work indicates that things are different at higher altitudes, at geocentric distances of about 8 R_E and above. Significant transverse heating is observed in this altitude region of the mantle (Nilsson et al. 2006). In a recent case study (Waara et al. 2010) studied a prolonged event of strong heating with perpendicular temperatures up to 8 keV and a perpendicular to parallel temperature ratio of more than 2, suggesting relatively local heating. It was found that even using 100% of the observed wave amplitude around the O^+ gyro frequency it was not possible to explain the heating using a simple ion cyclotron resonance model (Chang et al. 1986). Allowing for long periods (altitude intervals) of heating led to much higher parallel velocities (due to the mirror force) than observed. The heating of heavy ions appeared much more effective than the heating of protons, consistent with the statistical results of Nilsson et al. (2006) based on 3 year (2001–2003) of Cluster data from the spring period (January to May) when the Cluster orbits cover the high altitude mantle region. The studies of Nilsson et al. (2006) and Waara et al. (2010) together indicate that strong and effective transverse heating of ions occur in the altitude interval above about 8 R_E. This can then explain the strong increase in parallel velocity in the altitude region between 8 and 10 R_E seen in Fig. 17.1, which results from transverse heating in combination with the mirror force. The mechanism behind the heating remains to be explained. The precise altitude region of effective heating may be an artefact of the Cluster orbit, but not the presence of such a region.

In order to fully model and understand the acceleration and final atmospheric escape from magnetized planets we must understand what is limiting the transverse heating at different altitudes. Empirically, the heating in the high altitude polar cap of Earth is quite well characterized in the study of Nilsson et al. (2006). The study period corresponds to solar maximum conditions and the beginning of the declining phase. We summarize some of their result in a new form in Fig. 17.2. The upper panel shows the average flux and the lower panel the average perpendicular temperature, both as function of the parallel bulk velocity and for geocentric distances above 10 R_E. As can be seen the average flux has only a weak dependence on the parallel velocity, and is increasing with increasing velocity. This indicates that the observed parallel velocity results from a bulk parallel acceleration rather than a velocity filter effect (i.e. where ions from a limited source region are spread out along a field-line according to their parallel velocities, described for the cusp/mantle outflow in Nilsson et al. 2004). In the latter case we would expect high velocities to correspond to the tail of a velocity dispersed ion distribution, which should have significantly lower fluxes for higher velocities. The higher velocities typically correspond to higher perpendicular temperatures as well (bottom panel). This points to a continuous perpendicular heating. The perpendicular energy will in due time be turned into parallel energy by the mirror force. The average outflow velocity is 70 km s^{-1} (400 eV) for altitudes above 10 R_E, and the average perpendicular temperature is 1.2 keV.

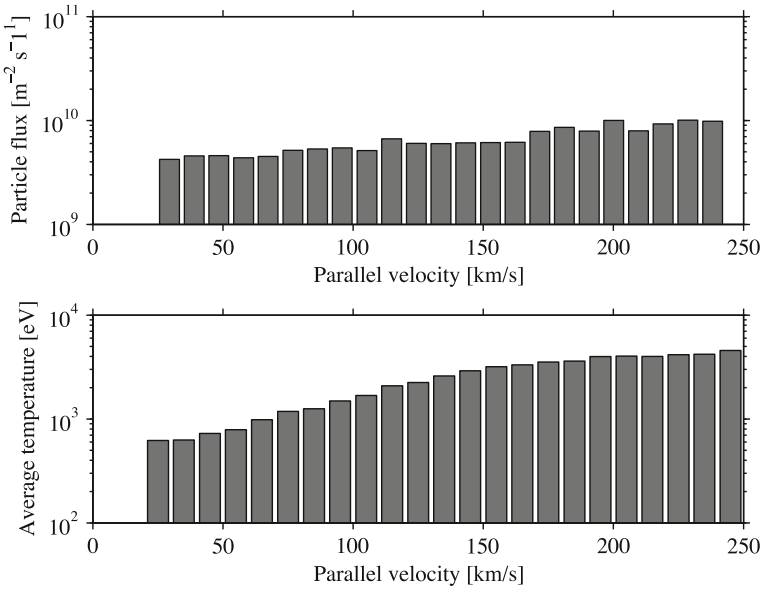

Fig. 17.2 Average O^+ particle flux ([$m^{-2}s^{-1}$] *upper panel*) and perpendicular temperature ([eV] *lower panel*) as function of bulk parallel velocity [km/s]

17.3.3 Hidden Ion Populations

Energetic ion populations in the magnetosphere are typically studied with ion spectrometers. In particular for mass resolved measurements it is necessary to use direct measurements of the particles. This can present a problem for measurements of low energy particles, as most instruments have a minimum energy threshold of typically 1–10 eV, and because of the spacecraft potential which may subtract more than 10 eV from the ions before they can reach the detector. The latter can be overcome by active control of the spacecraft potential, which has for example been done by Moore et al. (1997). Another way of overcoming the low energy problem is to determine the density using Langmuir probes or wave instruments which can record waves whose frequency is a function of the local plasma density (Trotignon et al. 2001). The perpendicular flow can be inferred from other drift estimates like DC electric and magnetic fields or instruments like the electron drift instrument on Cluster (Paschmann et al. 2001).

Engwall et al. (2009b) used a method where the wake electric field created by a streaming cold plasma could be used to calculate the velocity, which together with density estimates could provide the flux of a hidden ion population in the magnetotail lobes. They found a total flux of 10^{26} s^{-1} in the lobes. Nilsson et al. (2010) calculated the centrifugal acceleration in the lobes for this data set (see Section 17.3.1), and found that if part of the outflowing population was heavy ions those ions should have been accelerated to energies observable by ion spectrometers. The wake field method cannot give the composition of the plasma, but the result indicates that most of the lobe outflow is protons, not heavy ions.

Peterson et al. (2008) recently summarized the observations of ion outflow at lower altitudes than the lobes, both estimated thermal fluxes and the more energetic ions observable by typical ion spectrometers. For protons the highest fluxes, of the order of 10^{26} s^{-1} were reported for instruments measuring thermal ions rather than energetic ions, both at 5000 and 50000 km, e.g. using the TIDE instrument on Polar (Su et al. 1998; Huddleston et al. 2005). The corresponding O^+ fluxes were in the range 10^{24}–10^{25} s^{-1} with similar figures for cold ions and ions above 15 eV.

The high altitude Cluster measurements used in Nilsson et al. (2006) are not particularly well suited for determinations of the total outflow, as the area of the outflow becomes progressively more uncertain the higher the altitude. However the data set has an important advantage which has not been used before: magnetospheric convection is frequently high enough to bring also cold ions into the Cluster ion spectrometer measurement range. We have therefore investigated the possible presence of a hidden O^+ ion population in the high altitude cusp/mantle by comparing a total outflow estimate for two data sets, the same data used in Nilsson et al. (2006), and a sub-set of that data where we only use data with magnetospheric

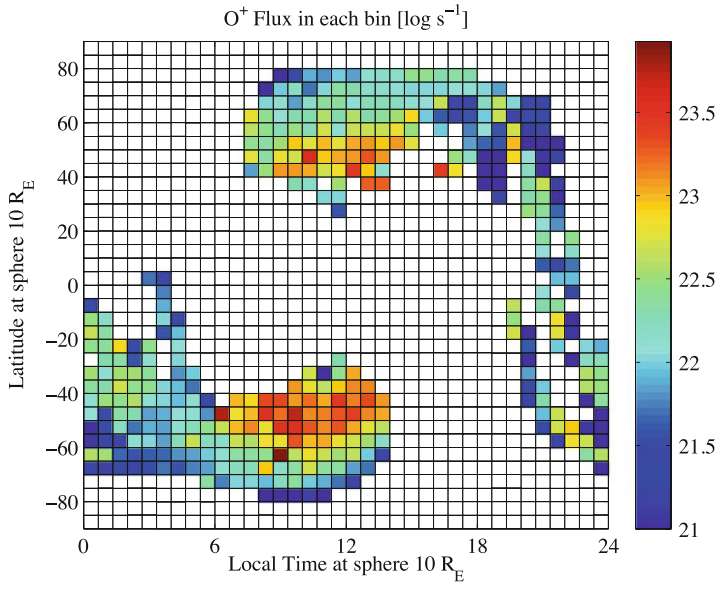

Fig. 17.3 Average O^+ particle flux ([$\log_{10} s^{-1}$]) in each bin on a sphere at 10 R_E. Cluster measurements in the high altitude polar cap were mapped to the sphere using the Tsyganenko T89c magnetic field model

convection higher than 22 km s^{-1}, i.e. bulk drift energy above 40 eV for O^+. The total outflow was estimated by mapping the observations to a reference altitude of 10 R_E (close to the median of the data set), adjusting the flux density according to the difference in magnetic field density of the magnetic field model. Mapping was done using the Tsyganenko T89c model (Tsyganenko 1989), using *Kp* index as input. If there is typically a hidden ion population in a significant fraction of the data we should get a higher average flux when using only data where we can be certain to measure also such a population. There was no significant difference between the two data sets. The result for the case with no demand on the perpendicular bulk velocity is shown in Fig. 17.3. The significant outflow occurs in a restricted local time/latitude range corresponding to the cusp/mantle, and can be seen extending into the corresponding night-time region for the cases when the observations where made anti-sunward of the pole. The total outflow in both our cases is $2 \cdot 10^{25}$ s^{-1}, well in line with the studies summarized in Peterson et al. (2008). This average outflow is for the 2/3 of the appropriate Cluster orbits when significant ion beams were observed. The 1/3 of the orbits not used in the Nilsson et al. (2006) study because of lack of significant O^+ fluxes corresponds mainly to northward IMF (not shown). Given the uncertainty in the area estimate we still find that 10^{25} s^{-1} is an appropriate order of magnitude estimate for the high altitude polar cap O^+ outflow. Our conclusion is that there is in general no hidden O^+ population for the high altitude polar cap ion outflow. This is also in line with the significant centrifugal acceleration in the high altitude cusp/mantle region. This general result does of course not rule out significant cold O^+ populations during certain time intervals.

17.4 Fate of the Outflowing Ions

We have seen that the high altitude mantle cusp O^+ outflow is significantly accelerated, by both centrifugal acceleration and efficient transverse heating (e.g. Nilsson et al. 2006). What will be the fate of these outflowing ions? The ions have been seen in the distant tail as reported by Seki et al. (1998), where cold oxygen beams (COB) where seen, streaming at nearly the same velocity as solar wind origin protons. Cold here denotes a temperature well below the bulk drift of the ions, so that populations with different mass but same drift can be easily separated in energy space. Seki et al. (1998) discussed the origin of the COB, and noted that the cusp ion outflow would be a viable source if there was a further energization of about 3 keV energy, as compared to the low altitude (1.2–3 R_E) cusp outflow with energies of up to about 30 eV (Lockwood et al. 1985). The results presented here, and in Nilsson et al. (2006, 2008b; Arvelius et al. 2005), using high altitude (8–12 R_E) cusp/mantle data, show that the cusp/mantle indeed is a likely source of the COB. However, the fate

of the COB is not entirely clear, as the total flux appear to decrease with tail distance (Seki et al. 2001). This can be interpreted as due to loss through the magnetopause or loss through transport into the plasma sheet and subsequent transport back towards the Earth. Seki et al. (2001) argued that the latter was the most likely case, and that most of the outflowing O^+ was actually returned to Earth. However it was argued in Seki et al. (2001) that 90% of the initial outflow has energy below 1 keV. The more recent Cluster results show that in the high altitude mantle we see acceleration to about 1–2 keV on average. The more energy provided to the outflowing ions, the more likely the escape. Furthermore the actual return flow has not yet been observed. Therefore a next step in the O^+ outflow studies will be to study the ion fluxes in the tail and plasma sheet as well as in the vicinity of the tail magnetopause. The Cluster spacecraft are suitable for this.

Another approach is to trace model particles in an average magnetic and electric field model of the magnetosphere. This has been done for O^+ by Ebihara et al. (2006). They found that using an initial ion distribution based on empirical results from Akebono, most outflowing ions ended up in the ring current, not at the magnetopause, though the cusp/mantle was a minor contributor to this near-Earth ion circulation. They also found that escape to the magnetopause was dominant for quiet conditions, i.e. when magnetospheric convection is less effective in providing a return flow in the tail. The outflow from the cusp mantle region was mostly to the magnetopause and distant tail (i.e. lost from the magnetosphere) for particle velocities in excess of about 20 km/s at 1 R_E. The Cluster results show parallel velocities of about 70 km/s and transverse temperatures of about 1 keV at 10 R_E which seems likely to lead to magnetospheric escape according to these simulations, as the further velocity increase between 1 and 10 R_E in the model was much smaller then 50 km/s. New simulations based on the Cluster measurements would be desirable to confirm this. In the simulation of Ebihara et al. (2006) most of the return flow is lost at the magnetopause eventually, not returned to the atmosphere. This is in part due to the static electric and magnetic fields used. In reality part of the plasma will be returned to the atmosphere through pitch-angle diffusion and subsequent precipitation. Another way of addressing the problem of the return flow is to back-trace populations observed in the inner magnetosphere. This has for example been done for protons by Ebihara et al. (2001), Yamauchi and Lundin (2006) and Yamauchi et al. (2006, 2009). These results indicate that the source is sometimes a cold population in the plasma sheet, which then is likely to be a part of the cold ion outflow in the lobes reported by Engwall et al. (2009b). At other times the source was a more energetic population emanating from the auroral or sub-auroral region. In no case was the cusp/mantle a viable source region.

Conclusions

Due to the shielding effect of its magnetic field, relatively direct solar wind–atmosphere interaction at Earth is restricted to the ionospheric projection of the polar cusps. The total O^+ outflow is regulated by initial transient upflow in the ionosphere, followed by transverse heating. Due to the mirror force the heated plasma is expelled by the magnetic field. Further acceleration is provided by the centrifugal acceleration which can explain much of the velocity increase from about 5 R_E up to about 8 R_E geocentric distance. Above about 8 R_E and up to about 10 R_E, in the part of the mantle sampled by Cluster, effective transverse heating once again plays a major role in accelerating the outflowing plasma. Both perpendicular bulk drift and the expected centrifugal acceleration are strong enough to make also cold heavy ion populations measurable by ion spectrometers. High altitude polar cap measurements such as those made with Cluster thus provides a complete picture of the outflow, at least on the low energy side. Our estimate indicates that the total cusp/ polar cap outflow of O^+ is of the order of 10^{25} s^{-1} for the high solar activity case. The high altitude heating and centrifugal acceleration provides an average parallel velocity of 70 km/s and an average perpendicular temperature of 1.2 keV for geocentric distances above 10 R_E in the cusp/mantle region. According to simulations (Ebihara et al. 2006) this seems enough to allow the heavy ions to escape the magnetosphere and be lost from the Earth. For H^+ at Earth there is a significant escape through the lobes, amounting to about 10^{26} s^{-1} (Engwall et al. 2009b). Back-tracing of particles from the inner magnetosphere indicates that part of the proton fluxes in the lobes are returning to Earth, though the percentage is still highly uncertain.

This can be compared with heavy ion escape rates from Mars which have been estimated to between $5 \cdot 10^{24}$ s^{-1} (Verigin et al. 1991) up to $3 \cdot 10^{25}$ s^{-1} (Lundin et al. 1989) for the high solar activity case based on Phobos measurements, and between $3 \cdot 10^{23}$ s^{-1} (Barabash et al. 2007) and $3 \cdot 10^{24}$ s^{-1} (Lundin et al. 2008) for low solar activity based on Mars Express measurements. The latter study was based on a more limited data set but with better coverage in energy. The Mars estimates includes O^+ and O_2^+ in about equal amounts as well as a fraction of CO_2^+. For Venus the escape estimates are of the order of 10^{25} s^{-1} for O^+ and 10^{26} s^{-1} for H^+ (Lammer et al. 2006 and references therein). The Venus figures are expected to be updated soon using Venus Express data, but it still seems clear that the order of magnitude of the loss is similar at all the three planets. One may note here that differences in planetary atmospheric densities are not important in themselves, this will mainly affect the precise altitude where the ionosphere will form. Atmospheric and ionospheric scale height is likely to matter as well as the gravity of the planet, where Mars has a significantly lower gravity than Earth and Venus. The distance to the sun will affect both solar wind intensity and the ionospheric production rate due to solar EUV. Solar wind and EUV intensity at Venus is about twice that at Earth, and that at Mars about half. This variance is less than the variance through the solar cycle, and does not really affect our conclusion that the loss rates are similar.

One uncertainty is then the return flow at Earth, which Seki et al. (2001) estimated to bring the direct loss down by about an order of magnitude. We have shown that it is at least plausible that most of the cusp/mantle outflow is directly lost, and that centrifugal acceleration and transverse heating due to wave particle acceleration at high altitude are two important mechanisms providing the acceleration necessary for escape. Modeling of the fate of the return flow (Ebihara et al. 2006) also indicates that most of the return flow is actually lost as well. This latter study was however conducted using a static electric and magnetic field, so in reality loss through precipitation may return a significant part of the ion return flow to the atmosphere. Our conclusion is that the direct outflow from the polar caps of the magnetized planet Earth is similar to the loss from the unmagnetized planets Mars and Venus. The magnetic field shields part of the atmosphere, but the area of interaction, the magnetopause, is much larger. Energy and mass from the interaction region is channelled down to the ionospheric cusp where efficient interaction takes place. If the magnetic field plays a role in protecting the atmosphere of Earth it is by keeping escaping plasma within the magnetosphere and bringing it back to the planet. To fully assess if this is the case we need proper assessments of the tail heavy ion return flow at a distance corresponding to tail return flow, i.e. further out than the auroral oval nightside heavy ion source (which we have omitted in our discussion). To complete the picture we would also need an experimental assessment of the return of heavy ions to the atmosphere through ion and energetic neutral atom precipitation. Finally, for a general theory on ion outflow we must understand what is limiting the energy transfer to the outflowing ions in the cusp/mantle heating regions, both at low and high altitude.

References

André M, Crew GB, Peterson WK, Persoon AM, Pollock CJ (1990) Ion heating by broadband low-frequency waves in the cusp/cleft. J Geophys Res 95:20809–20823. doi:10.1029/JA095iA12p20809

Arvelius S, Yamauchi M, Nilsson H, Lundin R, Hobara Y, Rème H, Bavassano-Cattaneo MB, Paschmann G, Korth A, Kistler L, Parks GK (2005) Statistics of high-altitude and high-latitude ion outflows observed by Cluster/CIS. Ann Geophys 23:1909–1916

Axford WI (1968) The polar wind and the terrestrial helium budget. J Geophys Res 73:6855–6859. doi:10.1029/JA073i021p06855

Banks PM, Holzer TE (1968) The polar wind. J Geophys Res 73:6846–6854. doi:10.1029/JA073i021p06846

Barabash S, Fedorov A, Lundin R, Sauvaud JA (2007) Martian atmospheric erosion rates. Science 315:501–503

Barghouthi IA (2008) A Monte Carlo study for ion outflows at high altitude and high latitude: Barghouthi model. J Geophys Res (Space Phys) 113:8209–+. doi:10.1029/2008JA013274

Blelly PL, Robineau A, Alcaydé D (1996) Numerical modelling of intermittent ion outflow events above EISCAT. J Atmos Sol Terr Phys 58:273–285

Bouhram M, Klecker B, Miyake W, Rème H, Sauvaud JA, Malingre M, Kistler L, Blăgău A (2004) On the altitude dependence of transversely heated distributions in the cusp/cleft. Ann Geophys 22:1787–1798

Chang T, Crew GB, Hershkowitz N, Jasperse JR, Retterer JM (1986) Transverse acceleration of oxygen ions by electromagnetic ion cyclotron resonance with broad band

left-hand polarized waves. Geophys Res Lett 13:636–639. doi 10.1029/GL013i007p00636

Chappell CR, Giles BL, Moore TE, Delcourt DC, Craven PD, Chandler MO (2000) The adequacy of the ionospheric source in supplying magnetospheric plasma. J Atmos Sol Terr Phys 62:421–436. doi:10.1016/S1364-6826(00)00021-3

Chaston CC, Bonnell JW, Carlson CW, McFadden JP, Ergun RE, Strangeway RJ, Lund EJ (2004) Auroral ion acceleration in dispersive Alfvén waves. J Geophys Res 109(A04205). doi:10.1029/2003JA010053

Cladis JB (1986) Parallel acceleration and transport of ions from polar ionosphere to plasmasheet. J Geophys Res 13:893–896

Cowley SWH (1995) Theoretical perspectives of the magnetopause: a tutorial review. In: Song P, Sonnerup BUO, Thomsen MF (eds) Physics of the magnetopause, vol 90. The American Geophysical Union, Washington, DC, pp 29–43

Cully CM, Donovan EF, Yau AW, Arkos GG (2003a) Akebono/Suprathermal mass spectrometer observations of low-energy ion outflow: Dependence on magnetic activity and solar wind conditions. J Geophys Res (Space Phys) 108:1093–+. doi:10.1029/2001JA009200

Cully CM, Donovan EF, Yau AW, Opgenoorth HJ (2003b) Supply of thermal ionospheric ions to the central plasma sheet. J Geophys Res (Space Phys) 108:1092–+. doi:10.1029/2002JA009457

Dubinin E, Modolo R, Fraenz M, Woch J, Duru F, Akalin F, Gurnett D, Lundin R, Barabash S, Plaut JJ, Picardi G (2008) Structure and dynamics of the solar wind/ionosphere interface on Mars: MEX-ASPERA-3 and MEX-MARSIS observations. Geophys Res Lett 35. doi:10.1029/2008GL033730

Ebihara Y, Yamauchi M, Nilsson H, Lundin R, Ejiri M (2001) Wedge-like dispersion of sub-keV ions in the dayside magnetosphere: Particle simulation and viking observation. J Geophys Res 106:29571–29584. doi 10.1029/2000JA000227

Ebihara Y, Yamada M, Watanabe S, Ejiri M (2006) Fate of upflowing suprathermal oxygen ions that originate in the polar ionosphere. J Geophys Res 111(A04219). doi:10.1029/2005JA011403

Elphic RC, Lockwood M, Cowley SWH, Sandholt PE (1990) Flux transfer events at the magnetopause and in the ionosphere. Geophys Res Lett 17(12):2241–2344

Engwall E, Eriksson AI, Cully CM, André M, Puhl-Quinn PA, Vaith H, Torbert R (2009a) Statistics of the cold hidden component of ionospheric outflow determined from 5 to 19 in the Earth's magnetotail. Ann Geophys 27:3185–3201

Engwall E, Eriksson AI, Cully CM, André M, Torbert R, Vaith H (2009b) Earth's ionospheric outflow dominated by hidden cold plasma. Nat Geosci 2:24–27

Escoubet CP, Fehringer M, Goldstein M (2001) Introduction The cluster mission. Ann Geophys 19:1197–1200

Guglielmi A, Lundin R (2001) Ponderomotive upward acceleration of ions by ion cyclotron and Alfvén waves over the polar regions. J Geophys Res 106:13219–13236

Hoffman JH, Dodson WH (1980) Light ion concentrations and fluxes in the polar regions during magnetically quiet times. J Geophys Res 85:626–632. doi:10.1029/JA085iA02p00626

Huddleston MM, Chappell CR, Delcourt DC, Moore TE, Giles BL, Chandler MO (2005) An examination of the process and magnitude of ionospheric plasma supply to the magnetosphere. J Geophys Res (Space Phys) 110:12202–+. doi:10.1029/2004JA010401

Lammer H, Lichtenegger HIM, Biernat HK, Erkaev NV, Arshukova IL, Kolb C, Gunell H, Lukyanov A, Holmström M, Barabash S, Zhang TL, Baumjohann W (2006) Loss of hydrogen and oxygen from the upper atmosphere of Venus. Planet Space Sci. 54:1445–1456. doi:10.1016/j.pss.2006.04.022

Lockwood M, Waite JH Jr, Moore TE, Chappell CR, Johnson JFE (1985) A new source of suprathermal ions near the dayside polar cap boundary. J Geophys Res 90:4099–4116

Lockwood M, Sandholt PE, Cowley SWH, Oguti T (1989) Interplanetary magnetic field control of dayside auroral activity and the transfer of momentum across the dayside magnetopause. Planet Space Sci 37:1347–1365

Lockwood M, Denig WF, Farmer AD, Davda VN, Cowley SWH, Lühr H (1993) Ionospheric signatures of pulsed reconnection at the Earth's magnetopause. Nature 361:424–428

Luhmann JG (1990) The solar wind interaction with unmagnetized planets – A tutorial. Geophysical monograph series, vol 58. American Geophysical Union, Washington, DC, pp 401–411

Lundin R, Guglielmi A (2006) Ponderomotive Forces in Cosmos. Space Sci Rev 127:1–116. doi:10.1007/s11214-006-8314-8

Lundin R, Zakharov A, Pellinen R, Hultqvist B, Borg H, Dubinin E, Barabash S, Pissarenko N, Koskinen H, Liede I (1989) First results of the ionospheric plasma escape from Mars. Nature 341:609–612

Lundin R, Barabash S, Holmström M, Nilsson H, Yamauchi M, Fraenz M, Dubinin EM (2008) A comet-like escape of ionospheric plasma from Mars. Geophys Res Lett 35. doi:10.1029/2008GL034811

Maggiolo R, Sauvaud JA, Fontaine D, Teste A, Grigorenko E, Balogh A, Fazakarley A, Paschmann G, Rème H (2006) A multi-satellite study of accelerated ionospheric ion beams above the polar cap. Ann Geophys 24:1665–1684

Moen J, Oksavik K, Carlson HC (2004) On the relationship between ion upflow events and cusp auroral transients. Geophys Res Lett 31(L11808). doi:10.1029/2004GL020129

Moore TE, Chappell CR, Chandler MO, Craven PD, Giles BL, Pollock CJ, Burch JL, Young DT, Waite JH Jr, Nordholt JE, Thomsen MF, McComas DJ, Berthelier JJ, Williamson WS, Robson R, Mozer FS (1997) High-altitude observations of the polar wind. Science 277:349–351. doi 10.1126/science.277.5324.349

Moore TE, Lundin R, Alcayde D, André M, Ganguli SB, Temerin M, Yau A (1999) Source processes in the high-altitude ionosphere. Space Sci Rev 88:7–84

Nagai T, Waite JH Jr, Green JL, Chappell CR, Olsen RC, Comfort RH (1984) First measurements of supersonic polar wind in the polar magnetosphere. Geophys Res Lett 11:669–672. doi 10.1029/GL011i007p00669

Nilsson H, Kirkwood S, Eliasson L, Norberg O, Clemmons J, Boehm M (1994) The ionospheric signature of the cusp: A case study using Freja and the Sondrestrom radar. Geophys Res Lett 21:1923–1926

Nilsson H, Yamauchi M, Eliasson L, Norberg O, Clemmons J (1996) The ionospheric signature of the cusp as seen by incoherent scatter radar. J Geophys Res 101:10947–10963

Nilsson H, Kirkwood S, Moretto T (1998) Incoherent scatter radar observations of the cusp acceleration region and cusp field–aligned currents. Geophys J Res 103:26721–26730

Nilsson H, Joko S, Lundin R, Rème H, Sauvaud JA, Dandouras I, Balogh A, Carr C, Kistler LM, Klecker B, Carlson CW, Bavassano-Cattaneo MB, Korth A (2004) The structure of high altitude energization and outflow: a case study. Ann Geophys 22:2497–2506

Nilsson H, Waara M, Arvelius S, Marghitu O, Bouhram M, Hobara Y, Yamauchi M, Lundin R, Rème H, Sauvaud JA, Dandouras I, Balogh A, Kistler LM, Klecker B, Carlson CW, Bavassano-Cattaneo MB, Korth A (2006) Characteristics of high altitude oxygen ion energization and outflow as observed by cluster; a statistical study. Ann Geophys 24:1099–1112

Nilsson H, Waara M, Marghitu O, Yamauchi M, Lundin R, Rème H, Sauvaud JA, Dandouras I, Lucek E, Kistler LM, Klecker B, Carlson CW, Bavassano-Cattaneo MB, Korth A (2008a) Transients in oxygen outflow above the polar cap as observed by the Cluster spacecraft. Ann Geophys 26:3365–3373

Nilsson H, Waara M, Marghitu O, Yamauchi M, Lundin R, Rème H, Sauvaud JA, Dandouras I, Lucek E, Kistler LM, Klecker B, Carlson CW, Bavassano-Cattaneo MB, Korth A (2008b) An assessment of the role of the centrifugal acceleration mechanism in high altitude polar cap oxygen ion outflow. Ann Geophys 26:145–157

Nilsson H, Carlsson E, Brain D, Yamauchi M, Holmström M, Barabash S, Lundin R, Futaana Y (2010) Ion escape from mars as a function of solar wind conditions: A statistical study. Icarus 206:40–49. doi:10.1016/j.icarus.2009.03.006

Nilsson H, Engwall E, Eriksson A, Puhl-Quinn PA, Arvelius S (2010) Centrifugal acceleration in the magnetotail lobes. Ann Geophys 28:569–576

Norqvist P, André M, Tryland M (1998) A statistical study of ion energization mechanisms in the auroral region. J Geophys Res 103:23459–23474

Northrop TG (1963) The adiabatic motion of charged particles. Interscience, New York, NY

Nykyri K, Grison B, Cargill PJ, Lavraud B, Lucek E, Dandouras I, Balogh A, Cornilleau-Wehrlin N, Rème H (2006) Origin of the turbulent spectra in the high-altitude cusp: Cluster spacecraft observations. Ann Geophys 24:1057–1075

Ogawa Y, Fujii R, Buchert SC, Nozawa S, Ohtani S (2003) Simultaneous EISCAT Svalbard radar and DMSP observations of ion upflow in the dayside polar ionosphere. J Geophys Res 108(1101). doi:10.1029/2002JA009590

Øieroset M, Yamauchi M, Liszka L, Christon SP (2000) Energetic ion outflow from the dayside ionosphere and its relationship to the interplanetary magnetic field and substorm activity. J Atmos Sol Terr Phys 62:485–493. doi 10.1016/S1364-6826(00)00016-X

Paschmann G, Quinn JM, Torbert RB, Vaith H, McIlwain CE, Haerendel G, Bauer OH, Bauer T, Baumjohann W, Fillius W, Förster M, Frey S, Georgescu E, Kerr SS, Kletzing CA, Matsui H, Puhl-Quinn P, Whipple EC (2001) The Electron Drift Instrument on Cluster: overview of first results. Ann Geophys 19:1273–1288

Peterson WK, Andersson L, Callahan BC, Collin HL, Scudder JD, Yau AW (2008) Solar-minimum quiet time ion energization and outflow in dynamic boundary related coordinates. J Geophys Res (Space Phys) 113:7222–+. doi 10.1029/2008JA013059

Rème H, Aoustin C, Bosqued JM, Dandouras I, Lavraud B, Sauvaud JA, Barthe A, Bouyssou J, Camus T, Coeur-Joly O, Cros A, Cuvilo J, Ducay F, Garbarowitz Y, Medale JL, Penou E, Perrier H, Romefort D, Rouzaud J, Vallat C, Alcaydé D, Jacquey C, Mazelle C, d'Uston C, Möbius E, Kistler LM, Crocker K, Granoff M, Mouikis C, Popecki M, Vosbury M, Klecker B, Hovestadt D, Kucharek H, Kuenneth E, Paschmann G, Scholer M, Sckopke N, Seidenschwang E, Carlson CW, Curtis DW, Ingraham C, Lin RP, McFadden JP, Parks GK, Phan T, Formisano V, Amata E, Bavassano-Cattaneo MB, Baldetti P, Bruno R, Chionchio G, Lellis AD, Marcucci MF, Pallocchia G, Korth A, Daly PW, Graeve B, Rosenbauer H, Vasyliunas V, McCarthy M, Wilber M, Eliasson L, Lundin R, Olsen S, Shelley EG, Fuselier S, Ghielmetti AG, Lennartsson W, Escoubet CP, Balsiger H, Friedel R, Cao JB, Kovrazhkin RA, Papamastorakis I, Pellat R, Scudder J, Sonnerup B (2001) First multispacecraft ion measurements in and near the Earth's magnetosphere with the identical Cluster ion spectrometry (CIS) experiment. Ann Geophys 19:1303–1354

Rosenqvist L, Opgenoorth HJ, Rastaetter L, Vaivads A, Dandouras I, Buchert S (2008) Comparison of local energy conversion estimates from Cluster with global MHD simulations. Geophys Res Lett 35:21104–+. doi 10.1029/2008GL035854

Schunk RW, Raitt WJ, Banks PM (1975) Effect of electric fields on the daytime high-latitude e and f regions. J Geophys Res 80:3121–3130

Seki K, Hirahara M, Terasawa T, Mukai T, Saito Y, Machida S, Yamamoto T, Kokubun S (1998) Statistical properties and possible supply mechanisms of tailward cold beams in the lobe/mantle regions. Geophys J Res 103:4477– 4489

Seki K, Elphic RC, Hirahara M, Terasawa T, Mukai T (2001) On atmospheric loss of oxygen ions from Earth through magnetospheric processes. Science 291:1939–1941

Strangeway R, Ergun RE, Su YJ, Carlson CW, Elphic RC (2005) Factors controlling ionospheric outflows as observed at intermediate altitudes. J Geophys Res 110(A3). doi:10.1029/2004JA010829

Su YJ, Horwitz JL, Moore TE, Giles BL, Chandler MO, Craven PD, Hirahara M, Pollock CJ (1998) Polar wind survey with the Thermal Ion Dynamics Experiment/Plasma Source Instrument suite aboard POLAR. J Geophys Res 103:29305–29338. doi 10.1029/98JA02662

Sundkvist D, Vaivads A, André M, Wahlund J, Hobara Y, Joko S, Krasnoselskikh VV, Bogdanova YV, Buchert SC, Cornilleau-Wehrlin N, Fazakerley A, Hall J, Rème H, Stenberg G (2005) Multi-spacecraft determination of wave characteristics near the proton gyrofrequency in high-altitude cusp. Ann Geophys 23:983–995

Trotignon JG, Décréau PME, Rauch JL, Randriamboarison O, Krasnoselskikh V, Canu P, Alleyne H, Yearby K, Le Guirriec E, Séran HC, Sené FX, Martin P, Lévêque M, Fergeau P (2001) How to determine the thermal electron density and the magnetic field strength from the Cluster/Whisper observations around the Earth. Ann Geophys 19: 1711–1720

Tsyganenko NA (1989) A magnetospheric model with a warped tail current. Planet Space Sci 37:5–20

Verigin MI, Shutte NM, Galeev AA, Gringauz KI, Kotova GA, Remizov AP, Rosenbauer H, Hemmerich P, Livi S, Richter AK, Apathy I, Szego K, Riedler W, Schwingenschuh K, Steller M, Yeroshenko YG (1991) Ions of planetary origin

in the martian magnetosphere (phobos 2/taus experiment). Planet Space Sci 39:131–137

Vontrat-Reberac A, Fontaine D, Blelly P, Galand M (2001) Theoretical predictions of the effect of cusp and dayside precipitation on the polar ionosphere. J Geophys Res 106:28857–28866. doi 10.1029/2001JA900131

Waara M, Nilsson H, Stenberg G, André M, Réme H (2010) Oxygen ion energization observed at high altitudes. Ann Geophys 28:907–916

Yamauchi M, Lundin R (2006) Sub-keV ring current ions as the tracer of substorm injection. Ann Geophys 24:355–366

Yamauchi M, Brandt PC, Ebihara Y, Dandouras I, Nilsson H, Lundin R, Rème H, Vallat C, Lindqvist P, Balogh A, Daly PW (2006) Source location of the wedge-like dispersed ring current in the morning sector during a substorm. J Geophys Res (Space Phys) 111:11–+. doi :10.1029/2006JA011621

Yamauchi M, Ebihara Y, Dandouras I, Rème H (2009) Dual source populations of substorm-associated ring current ions. Ann Geophys 27:1431–1438

Yordanova E, Sundkvist D, Buchert SC, André M, Ogawa Y, Morooka M, Margithu O, Amm O, Fazakerley AN, Réme H (2007) Energy input from the exterior cusp into the ionosphere: Correlated ground-based and satellite observations. Geophys Res Lett 34:4102–+. doi 10.1029/2006GL028617

Yuan Z, Deng X, Wang J (2008) DMSP/GPS observations of intense ion upflow in the midnight polar ionosphere associated with the SED plume during a super geomagnetic storm. Geophys Res Lett 35:19110–+. doi 10.1029/2008GL035462

Zeng W, Horwitz JL (2008) Storm enhanced densities (SED) as possible sources for Cleft Ion Fountain dayside ionospheric outflows. Geophys Res Lett 35:4103–+. doi 10.1029/2007GL032511

Data Assimilation Models: A 'New' Tool for Ionospheric Science and Applications

18

Ludger Scherliess, Donald C. Thompson, and Robert W. Schunk

Abstract

The Earth's space environment is a complex and dynamic system that exhibits weather features at all times. As shown by meteorologists and oceanographers, a powerful way of modeling dynamic systems is with the use of data assimilation models. Recently, two data assimilation models for the ionosphere have been developed at Utah State University that provide global and regional specifications of the 3-dimensional (3-D) ionospheric plasma densities. The two models are based on approximations to the full Kalman filter in order to reduce the enormous computational requirements associated with it. The first model uses a physics-based ionosphere model to provide the background plasma density field but uses a simpler statistical Gauss-Markov process to replace the physical model in the Kalman filter. The second model is an ensemble Kalman filter model, which uses a physics-based model for the ionosphere-plasmasphere system. The latter model covers the ionosphere-plasmasphere system from 90 to 30,000 km altitude and includes 6 ion species. An important strength of this model is that in addition to the 3-D plasma density distribution it also self-consistently determines the corresponding ionospheric drivers, including the thermospheric neutral winds and the low-latitude electric fields. Both models can assimilate a variety of space- and ground-based data types. Some of the data that can be assimilated include total electron content (TEC) from hundreds of ground-based GPS receivers, in situ electron densities (N_e) and ultraviolet (UV) emissions from several DMSP satellites, bottomside N_e profiles from tens of ionosondes, and limb TEC data from occultation satellites. The applied data assimilation techniques, although here used to specify ionospheric parameters, should also be beneficial to the study of other regions of the space environment.

18.1 Introduction

The ionosphere, like other regions of the space environment, is a complex and dynamic system that exhibits weather features at all latitudes and longitudes. At middle latitudes, for example, storm-enhanced plasma densities (SEDs) are frequently

L. Scherliess (✉)
Center for Atmospheric and Space Sciences, Utah State University, Logan, UT, USA
e-mail: ludger.scherliess@usu.edu

W. Liu, M. Fujimoto (eds.), *The Dynamic Magnetosphere*, IAGA Special Sopron Book Series 3,
DOI 10.1007/978-94-007-0501-2_18,

observed during periods of enhanced geomagnetic activity. These bands of largely increased density structures, often extending from Florida over the Great Lakes region into central Canada, are believed to be caused by storm-time electric fields that transport plasma from low to middle latitudes (Foster et al. 2002). At low latitudes ionospheric weather phenomena are often related to variations in the $\mathbf{E}\times\mathbf{B}$ plasma drift, which during the daytime lifts ionization upward near the dip equator and in concert with the parallel motion down the field lines creates the equatorial ionization anomaly. The largest densities and TEC values occur in the ionization anomaly peaks with typical day-to-day variations (ionospheric weather) of the order of 40% (Scherliess et al. 2008). Furthermore, during nighttime the low latitude ionosphere often exhibits plasma instabilities and bubbles that largely vary in occurrence and strength from one night to the next. The largest variability, however, is probably found at high latitudes where convection electric fields originating from the magnetosphere and particle precipitation can dramatically change the plasma distribution in a matter of minutes. It is believed that the ionospheric weather (variability) at low-, mid-, and high-latitudes is caused by variations in the external forces that originate from the thermosphere, the magnetosphere, and the lower atmosphere (Schunk and Nagy 2000).

Ionospheric weather and its associated structures, gradients and variability has large impacts on a variety of technological systems and can strongly affect navigation, communication, and radar operations. Over the past decades numerous analytical, parameterized, and global physics-based models have been developed in an effort to better understand and specify ionospheric weather. In addition, coupled models that combine different spatial domains have been developed and a review of recent model developments is given by Schunk et al. (2002). Although physics-based models of the ionosphere reproduce many of the observed climatological features, these models generally fail to specify ionospheric weather. This lack of reliable specifications is largely attributed to a lack of reliable specifications of the ionospheric drivers, which include the thermospheric composition and winds, the equatorial and high-latitude electric fields and the high-latitude particle precipitation. Currently, the most promising models for ionospheric weather specification are data assimilation models that combine physics-based models of the ionosphere with observations. Such models have become a dominant tool over the past decades in meteorology and oceanography for specifications and forecasts and more recently have also been used for the space environment. In particular, over the past several years data assimilation models were developed for the Earth's ionosphere (e.g., Scherliess et al. 2004, 2006, 2009; Pi et al. 2003; Mandrake et al. 2005; Bust et al. 2004; Mitchell and Spencer 2003) and the first ionospheric data assimilation model is now operational at the Air Force Weather Agency (AFWA). Data assimilation techniques have also recently been used to study the thermosphere (Minter et al. 2004; Codrescu et al. 2004), the radiation belts (Koller et al. 2007), and the solar corona (Brun 2007).

For the space environment, data assimilation techniques are currently becoming one of the foremost tools for integrating observations from different sources and producing a coherent picture of the space system dynamics, chemistry, and thermodynamics. In general, observations from only one observational platform only offer incomplete information about the phenomena under study. Combining observations from different observation systems, in a manner that is consistent with a physics-based model representation of the dynamical and chemical relationships that describe the system, is a powerful means of extracting the full information content of the observations. For the ionosphere, numerical models that solve the continuity, momentum, and energy equations constitute an ideal framework for a systematic integration (assimilation) of data from multiple sources. Data assimilation techniques optimally combine the diverse and incomplete observations with a short term forecast from the numerical model to produce the best estimate of the variables given by the model. The numerical model serves to maintain the dynamical, physical, and chemical consistency between the time-dependent fields. In this context, data assimilation is the optimal method to directly compare predictions obtained from the numerical model with satellite and ground based observations at corresponding locations and times, and in turn, correct the model trajectory and determine unknown external driving forces and model parameters. Data assimilation is, however, also "a systematic, structured, and open-ended learning process" (National Research Council 1991). By continually comparing the numerical model with observations, the data assimilation scheme quantifies the mismatch between the observations and the model forecasts,

and provides clues for further model improvements. This interactive linkage between the model and data is one of the most important benefits of data assimilation.

At Utah State University, we have developed two physics-based Kalman-filter data assimilation models for the near-Earth space environment. The two models are the Gauss-Markov Kalman Filter Model (GAIM-GM) and the Full Physics-Based Kalman Filter Model (GAIM-FP) (Schunk et al. 2004, 2005; Scherliess et al. 2004, 2006; McDonald et al. 2006; Thompson et al. 2006, 2009; Sojka et al. 2007; Jee et al. 2007, 2008). Both models are part of the Global Assimilation of Ionospheric Measurements (GAIM) project. Our Gauss-Markov Kalman filter model is a simpler model that can be run on 1 CPU and provides the global electron density distribution. Recently, the accuracy of this model for global and regional ionospheric specifications has been shown by Scherliess et al. (2006), Thompson et al. (2006), Sojka et al. (2007), and independently by Decker and McNamara (2007), McNamara et al. (2007, 2008, 2010), and McDonald et al. (2006). These studies have concluded that our Gauss-Markov Kalman filter model is well suited to accurately capture the electron density distribution and its variations in the global ionosphere. Our Full Physics-Based Kalman filter model is a sophisticated data assimilation model that is run on multiple CPUs. This model uses a physics-based ionosphere-plasmasphere model and an ensemble Kalman filter as a basis for assimilating a diverse set of measurements. The model provides specifications of the 3-dimensional electron and ion (NO^+, O_2^+, N_2^+, O^+, H^+, He^+) density distributions from 90 km to geosynchronous altitude (30,000 km). In addition, the model provides the self-consistent global distributions of the ionospheric drivers (electric field, neutral wind, and composition). Some of the data that we have already assimilated in our data assimilation models include in situ electron density and ultra-violet measurements from DMSP satellites, bottomside electron density profiles from ionosondes, GPS-TEC data from a network of up to 1000 ground stations, and radio occultation data from the CHAMP, SAC-C, IOX, and COSMIC satellites.

In the following sections we will first give a general overview of data assimilation techniques with a special emphasize on the Kalman filter and then describe our two ionospheric data assimilation models.

18.2 Overview of Data Assimilation

Data Assimilation techniques have long been used in many areas of science and engineering and are generally based on estimation and control theory (Gelb 1974; Maybeck 1979). Over the past decades, these techniques have become a dominant tool for specifications and forecasts in meteorology and oceanography and more recently data assimilation techniques have also been used in space physics. For meteorologists the problem addressed by data assimilation is weather specification and forecast for a complex systems that tends to become chaotic. In this case, data assimilation is not understood as data fusion or data interpolation, but instead, the large data sets are used to constrain the model trajectory at each time step in order to provide for a model forecast (Daley 1991). For the ionosphere, which is strongly driven by external forces originating from the magnetosphere, the thermosphere, and the lower atmosphere, data assimilation techniques are not only being used to constrain the model trajectory but are also becoming increasingly more important to specify the global distribution of the self-consistent external driving forces, including the neutral wind, the neutral composition, and the electric field (Pi et al. 2003; Datta-Barua et al. 2009; Scherliess et al. 2009).

Historically, the available data sets from in situ satellites and ground-based facilities have not been sufficient to sustain a data assimilation model for the ionosphere. Over the past decade, however, with the addition of UV measurements from DMSP satellites, GPS measurements from occultation satellites, and the widespread networks of ground-based GPS receivers, data assimilation models have become feasible. Yet, even with these new data sets only a limited number of observations are available to determine the state of the ionosphere at each instant in time. Furthermore, the observations generally come from many different data sources and are often inhomogeneously distributed in space. In addition, observations from different instruments typically have different error characteristics and different availability and cadence. Therefore, it comes at no surprise that additional information is needed to create a detailed and coherent picture of the ionosphere. In data assimilation models this additional information is obtained from the numerical model, which in our case is a physics-based model

of the ionosphere. With this, observations distributed in time can be used to construct a consistent picture that agrees with the data and the physical laws embedded in the model. The information of previous observations is preserved in the assimilation process, and consequently, data assimilation is not just a question of fitting new data. Since the model needs to preserve and evolve all the information acquired from the past observations, it is important that the model not only has a sufficiently high resolution but also that it incorporates all of the important physical processes.

Typically, data assimilation proceeds sequentially through time. At any instance, the numerical model organizes the information obtained from previous observations and then propagates this information forward in time to provide a short-term forecast. New observations, as they become available, are compared to the model forecast and used to correct the model state, to obtain an optimal estimate (in a statistical sense) of the state that is consistent with the observational data and all the previous information. This correction can include modifications of the state's initial conditions and estimations of uncertain internal model parameters and external driving forces. In this scheme the model organizes the information embedded in the observational data and interpolates and extrapolates the information into data-void regions in time and space. The data, on the other hand, keep the model trajectory "on the road".

Figure 18.1 shows a flow chart of a data assimilation procedure (after Robinson and Lermusiaux 2000). The goal is an estimation of the state variables, which for the ionosphere can include the plasma densities, temperatures, and velocities. Internal model parameters, such as collision coefficients and chemical production and loss rates as well as external driving forces, may also be estimated. Since the observational data may be incomplete, inaccurate, or biased, a crucial initial step after data acquisition is the quality control of the available data. In this step, obviously wrong observations are rejected and appropriate data errors are assigned. These errors can consist of two parts: An instrumental error associated with the data taking, e.g., the observational error, and an error associated with the representativeness of the observation. The latter, for example, accounts for errors arising from subgrid structures observed in the data but not modeled by the assimilation model (e.g., Daley 1991). In the next

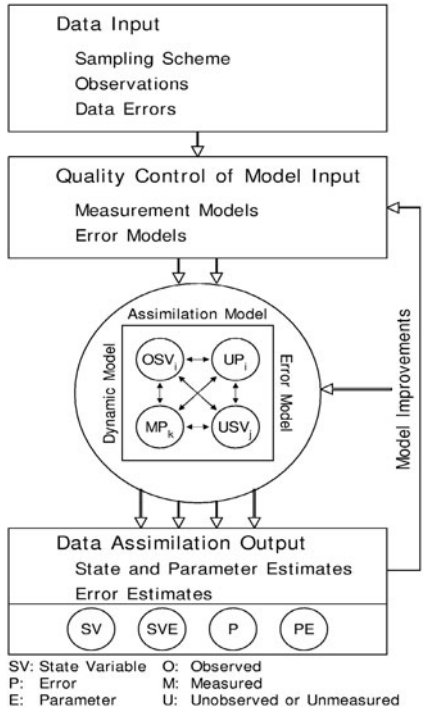

Fig. 18.1 Data assimilation flow chart: The observational data are linked to the state variables via the measurement models. Error estimates and error control play a critical role in the data assimilation scheme. The observational data and the model forecast are combined in the data assimilation models with weights that are inversely proportional to their relative errors (after Robinson and Lermusiaux 2000)

step the remaining quality-controlled observations are assimilated to create a global map of the state variables, and possibly estimates of internal parameters and external driving forces. Starting from these values the physical/numerical model evolves the system in time and provides the background model for the next assimilation run.

Generally, the estimation of the state of the system is constructed from weighted combinations of the observational data and the model forecast. The weights in this scheme are determined from the errors in the observational data and the errors in the numerical forecast. In the concept of data assimilation, error estimates are of critical importance and most advanced data assimilation methods are based on a statistical foundation that includes both model and data errors. The observations, as mentioned above, have errors associated with instrumental noise and the representativeness. The numerical model, on the other hand, is also imperfect, with errors arising from missing

physics, approximations of certain physical processes, uncertainties in model parameters, and a space and time discretizations of the model domain.

However, the use of errors in the assimilation scheme also creates its biggest challenge. To obtain reliable estimates and predictions of the Earth's upper atmosphere, millions of numbers are needed to represent the state. The estimation of all their likely errors, their interrelationships, and their evolution is extremely difficult, if not impossible. In order to overcome some of these difficulties, several approximation schemes have been developed. In the following section we will first give a brief introduction to one of the main data assimilation techniques, namely the Kalman filter, and then describe two approximations to the full Kalman filter that we have used in our GAIM data assimilation models. Examples of ionospheric specifications obtained from these two models will also be shown.

18.3 The Kalman Filter

The Kalman filter is a well-documented (e.g., Gelb 1974; Howe et al. 1998) technique that can be derived as a recursive algorithm that minimizes the error (i.e., finding the best estimate of the state) at a time t based on all information prior to this time. The filter combines the observational data with the information obtained from the numerical model and their corresponding statistical description of uncertainties. Formally, the filter performs a recursive least-squares inversion of the observations (e.g., slant TEC) for the model variables (e.g., N_e) using a dynamical model as a constraint. In practice, a weighted average of the model estimate and of the data is performed, using the relative accuracy of the two as the weights. As a result, an improved estimate of the model variables is obtained, where the improvement is in a statistical sense, i.e., it has the least expected error given the observations and the model, along with their error statistics. In this approach, the specification of the error covariances for both the model and the observations is of crucial importance. The model dynamics is described by a first-principles physics-based model, which provides the temporal evolution of both the state vector and the model error covariance matrix. Along with the best estimate of the state, the Kalman filter also generates a theoretical estimate of the analysis error. Since the Kalman filter is dynamic, the model evolves in time and learns what model components are producing the best estimates for any time of day and sets the weights accordingly.

Table 18.1 Kalman filter equations (adapted from Howe et al. 1998)

Equation	Equation	Comments
(K1)	$\mathbf{x}^f = \mathbf{M}\mathbf{x} + \boldsymbol{\eta}$	Model-state forecast
(K2)	$\mathbf{P}^f = \mathbf{M}\mathbf{P}\mathbf{M}^T + \mathbf{Q}$	Model-state forecast error
(K3)	$\mathbf{y}^O = \mathbf{H}\mathbf{x} + \boldsymbol{\varepsilon}$	Measurement equation
(K4)	$\mathbf{K} = \mathbf{P}^f\mathbf{H}^T(\mathbf{H}\mathbf{P}^f\mathbf{H}^T + \mathbf{R})^{-1}$	Kalman gain
(K5)	$\mathbf{x}^a = \mathbf{x}^f + \mathbf{K}(\mathbf{y}^o - \mathbf{H}\mathbf{x}^f)$	Model-state analysis
(K6)	$\mathbf{P}^a = (\mathbf{I} - \mathbf{K}\mathbf{H})\mathbf{P}^f$	Model-state analysis error

Table 18.1 summarizes the Kalman filter equations using the conventional notation of Ide et al. (1997). The details of these equations have been described by Howe et al. (1998) and by Scherliess et al. (2004) but will be repeated here for completeness.

Using equation (K1), a forecast of the state vector **x** is made by linearly relating the state vector at a time t+1 to the state at the previous time step t through the transition matrix **M**, where η represents the error generated by the operator (model error). This error, as well as the observation error ε is assumed to be white and have respective covariance matrices **Q** and **R**. In general, the transition model comes from the numerical integration of a system of coupled partial differential equations, which is in our case performed by the ionosphere model. In the case of a non-linear dynamical model a linearization of the model evolution at time *t* is performed to obtain the transition matrix **M**. Similar to the forecast of the state vector, a forecast of the model error covariance matrix $\mathbf{P}^f$ (K2) is performed, which depends on the previous error and the transition model error covariance **Q**.

Observations enter the Kalman filter through equation (K3), which linearly relates the measurements $\mathbf{y}^o$ to the state vector through the measurement matrix **H**. The observational database can contain line-of-sight (column integrated) optical emissions, digisonde measurements of the bottomside electron density profile, in situ measurements of electron densities form multiple satellites, hundreds of slant-path total electron content (TEC) measurements from radio beacons and/or GPS satellites, and thousands of occultation

measurements. In the case of a nonlinear relationship between the observations and the electron density (e.g., column integrated optical emissions), linearization and iteration is typically performed.

The Kalman gain **K** (K4), which gives the optimum combination of the model state and the data given their respective error covariances, combines the model state forecast $\mathbf{x}^{\mathbf{f}}$ with the data to obtain the new model state estimate, the so-called analysis (K5). The model error covariance matrix (K6) is then reduced by the amount related to the new information entered in the system through the data. Equations (K2) and (K6) together describe the evolution of the error covariance matrix and form the so-called Riccati equations. At this point, a new forecast (K1 and K2) is performed and the assimilation is repeated.

18.3.1 Approximate Kalman Filter

Although in theory it is straightforward to apply the Kalman filter to ionospheric data assimilation, difficulties arise when implementing the system due to the enormous computational requirements, both in storage and CPU time, associated with the propagation of the model error covariance matrix (K2) (for a full discussion of this problem see Fukumori and Malanotte-Rizzoli (1995)). As a practical method, we have developed two data assimilation models that use different approximations to the full Kalman filter model. In the first model, which is our Gauss-Markov Kalman Filter model (GAIM-GM) we have replaced the dynamical model that appear in equations K1 and K2 with a simpler statistical model. In the second model, which is our Full-Physics-Based Kalman Filter model (GAIM-FP), we have used an ensemble Kalman filter technique. Both approximations lead to a dramatic reduction in the computational requirements. Formally, the two approximations could lead to suboptimal estimations, but the uncertainty associated with the observation and model errors may lead to statistically indistinguishable differences between the truly optimal and suboptimal estimates (Cane et al. 1996). The strength of these approximations, however, lies in the otherwise not-possible use of the Kalman filter framework to objectively evaluate the model state error covariances. These errors are typically anisotropic and inhomogeneous and are difficult to specify. In the following the two models are briefly discussed and examples obtained from the two models are shown.

18.3.2 Gauss-Markov Kalman Filter Model

The GAIM Gauss-Markov Kalman Filter model (GAIM-GM) (Scherliess et al. 2006) is a relatively simple model that uses the ionospheric plasma densities obtained from the physics-based Ionospheric Forecast Model (IFM) (Schunk et al. 1997) as a background density field on which perturbations are superimposed. To reduce the computational requirements, these perturbations and the associated errors evolve over time with a statistical model (Gauss-Markov process) and not rigorously with the physical model. The background ionospheric densities, however, evolve with the full physical model. As a result, the Gauss-Markov Kalman filter can be executed on a single CPU workstation.

In this scheme the total electron density at each grid point is expressed as:

$$N = N_{IFM} + N_{pert} \tag{18.1}$$

where N_{IFM} is the electron density obtained from the IFM and N_{pert} is a perturbation density determined by the Kalman filter. The perturbation densities N_{pert} are expressed in a geographic frame and evolve over one assimilation time step (15 min) via:

$$N^{f}_{pert} = \mathbf{M} N_{pert} \tag{18.2}$$

The transition matrix **M** is a product of a translation matrix $\mathbf{M}_1$ and a diagonal matrix $\mathbf{M}_2$. The matrix $\mathbf{M}_1$ convects the perturbation density field at each time step in a magnetic sun-synchronous frame and the diagonal matrix $\mathbf{M}_2$ relaxes the perturbations to a zero value in the absence of data. In more detail, the diagonal matrix is composed of diagonal elements equal to $exp(-\Delta t/\boldsymbol{\tau})$, where Δt is the assimilation time step and τ is a relaxation time. In the current version of the model the value of τ is set globally to $\tau = 5$ h, but can in future versions be spatially and temporally adjusted to better represent the changing geophysical conditions. Currently, the model assimilates phase-leveled GPS slant TEC observations from several hundred ground sites located between $\pm 60°$ geographic latitude, bottomside N_e profiles from

ionosondes, nighttime 1356 Å UV-radiances from the Special Sensor Ultraviolet Spectrographic Imager (SSUSI) aboard the DMSP satellites as well as in situ electron densities from DMSP satellites. In the near future, the Gauss-Markov model will also assimilate GPS occultation data from the C/NOFS and from the six COSMIC satellites. More details regarding the Gauss-Markov model can be found in Scherliess et al. (2006).

Figure 18.2 shows an example of the Gauss-Markov model output that demonstrates the 3-dimensional character of the model. Slant TEC data from more than 300 ground-based GPS receivers and bottomside electron density profiles from about 20 ionosondes were assimilated in 15-min intervals over a 30-day period in April of 2007. The results correspond to a snapshot at 2000 UT on April 11, 2007. In the top left panel, the global distribution of vertical TEC is shown, which is obtained by integrating through the 3-dimensional electron density distribution from 90 to 1400 km altitude. The bottom left panel shows the peak electron density in the F-region (NmF2) and the right panels show the electron density variations at selected altitudes. Clearly seen in Fig. 18.2 are the equatorial anomaly peaks on both sides of the magnetic equator. Also note the asymmetry in the altitude distribution of the anomalies (right panels), with the southern anomaly being located at a lower altitude than the northern anomaly. This asymmetry is most likely related to an interhemispheric neutral wind pushing the plasma down the field line in the southern hemisphere and up the field line in the northern hemisphere. A detailed discussion of the accuracy of the Gauss-Markov model for global and regional ionospheric specifications is given by Scherliess et al. (2006), Thompson et al. (2006), Sojka et al. (2007), Decker and McNamara (2007), McNamara et al. (2007, 2008), and McDonald et al. (2006). These studies have concluded that the Gauss-Markov model is well suited to accurately capture the electron density distribution and its variations in the global ionosphere.

In order to assess the improvements in the fidelity of the results of our data assimilation model, measurements form 11 Australian ionosonde stations were compared with results from the International Reference Ionosphere (IRI) and the Gauss Markov data assimilation model (Sojka et al. 2007). The study period spanned the 31 days from 20 March through 19 April 2004. In order to quantitatively describe the improvements of using the data assimilation model a skill score was developed for the day-to-day weather by defining the IRI as the reference model. This skill score is based on first determining the GAIM and IRI scores against the observed weather. The scores are the root mean square error (RMSE) for each model given by

$$Score_{Model} = \frac{1}{N}\sqrt{\Sigma\left(N_mF_2{}^{obs} - N_mF_2{}^{Model}\right)^2} \tag{18.3}$$

where *Model* is the IRI or the data assimilation model, respectively. The individual scores were then

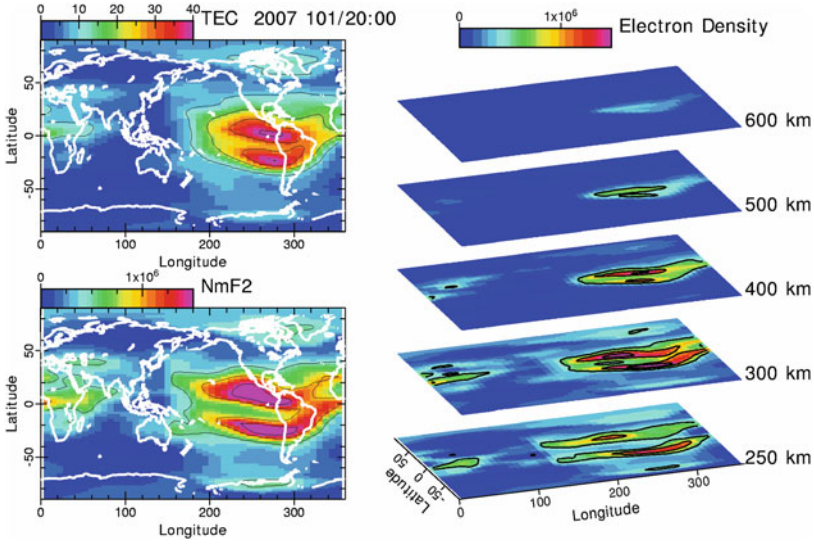

Fig. 18.2 Example of the output obtained from the Gauss-Markov Kalman filter Model for 2000 UT on April 11, 2007. Shown is (*top left*) a global distribution of the vertical TEC obtained by integrating through the three-dimensional model output from 90 to 1400 km, (*bottom left*) the peak electron density in the F-region (NmF2), and (*right*) the electron density variation at five selected altitudes

combined to generate the GAIM skill scores using the IRI score as the reference model,

$$GAIM_{Skill} = \left(1.0 - \frac{Score_{GAIM}}{Score_{IRI}}\right) \times 100 \qquad (18.4)$$

These skill scores are expressed as percentages and are bounded when the data assimilation model exactly matches the observation. A value of zero implies that the model is equivalent to the IRI, while a negative value indicates that IRI is better in reproducing the observations. Figure 18.3 shows the skill scores for all 11 stations versus solar local time. The figure shows that the data assimilation model is on the average 39% more capable to capture weather variability. However, Fig. 18.3 also indicates that the current version of the data assimilation model has difficulty around sunrise, when the model performance can be poorer than IRI. In order to compare the improvements with those of a stand-alone physics-based model, a skill score was also determined for the Ionospheric Forecast Model (IFM), which was found to be a 10% improvement with respect to IRI (for more details see Sojka et al. 2007). These results clearly indicate the strength of a data assimilation model to capture ionospheric variability.

18.3.3 Full Physics-Based Ensemble Kalman Filter

The Full Physics-Based Kalman filter model is the second of our ionospheric data assimilation models and is currently still under development at USU. The model covers the low and mid-latitudes and provides specifications of the 3-dimensional electron and ion (NO^+, O_2^+, N_2^+, O^+, H^+, He^+) density distributions from 90 km to geosynchronous altitude (30,000 km). The model excludes, in its current version, geomagnetic latitudes poleward of $\approx \pm 60°$ geomagnetic latitude due to the vastly different physical processes that govern the high-latitude regions, e.g. convection electric fields, particle precipitation, etc.

The Full Physics-Based model is significantly more sophisticated than our Gauss-Markov model and uses an Ensemble Kalman filter (EnKF) technique to rigorously evolve the three-dimensional electron density field and its associated errors in time (Scherliess et al. 2009). Over the past decade, the EnKF technique has been successfully employed in meteorological and oceanographic data assimilation (Evensen 2003) and is now being widely used as a sequential data assimilation method primarily due to its ease of implementation, resulting from replacing the covariance evolution in the traditional Kalman filter (Equation K2 in Table 18.1) by an approximate Monte Carlo ensemble sampling (Li and Xiu 2008). Specifically, by integrating an ensemble of model states forward in time, it is possible, using standard statistical techniques, to calculate the mean state and the error covariances needed at the analysis time. Therefore, as a practical method, an ensemble Kalman filter can be used to calculate the state error covariance matrix (Evensen 2003). This approximation leads to a dramatic reduction in the computational requirements associated with equation K2 and also eliminates the time-consuming numerical linearization of the model.

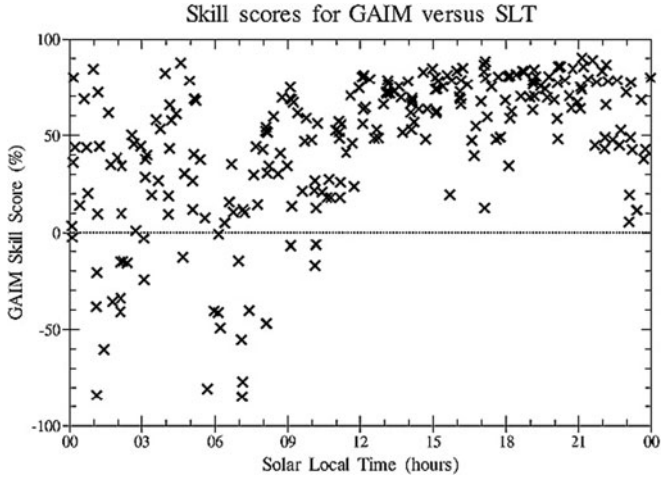

Fig. 18.3 Hourly skill scores for the GAIM Gauss Markov model for 11 ionosonde stations located in Australia. The skill scores are shown versus solar local time (after Sojka et al. 2007)

Instead, the full nonlinear physical model can be used. A detailed discussion and an overview of the EnKF technique is given by Evensen (2009).

For our Full Physics-Based Ensemble Kalman Filter model, we use the physics-based numerical Ionosphere-Plasmasphere Model (IPM) (Schunk et al. 2004, 2005; Scherliess et al. 2004, 2009) to integrate the state (e.g. electron and ion densities) forward in time and to evaluate the state error covariances. The use of the model explicitly incorporates the ionospheric production, loss, and transport processes directly into the data assimilation scheme. The ensemble consists of about 30 IPM model runs, which are launched at each assimilation time step in order to calculate the covariances. In our case, tests with different numbers of ensemble members indicate that about 30 model runs are needed. The number of ensemble members is, however, fully flexible and can easily be adjusted.

It is important to note that the estimation of the ionospheric drivers is an integral part of our ensemble Kalman filter and is achieved by using the internal physics-based model sensitivities to the various driving forces. In this procedure, the ionospheric data are used to adjust the plasma densities and its drivers so that a consistency between the observations (within their errors) and the physical model is achieved. In the next step, the drivers are fed back into the model, which subsequently leads to a self-consistent solution of the ionospheric densities and their driving forces (electric field, neutral wind and composition).

The use of the physics-based model as an integral part of the data assimilation process should provide a much more realistic evolution of the plasma density distribution and the state error covariance. The determination and subsequent feedback of the drivers into the data assimilation model should provide a much improved altitude structure of the low- and mid-latitude plasma distribution. In particular the height of the F2 region (hmF2) should be improved when compared to the Gauss-Markov Kalman filter model. This latter model lacks this driver estimation and feedback.

Figure 18.4 shows an example of the driver estimation obtained from the Full Physics-Based Kalman filter model. Shown is the meridional neutral wind obtained from the filter for March 31, 2007. The wind velocities correspond to a daily averaged pattern obtained by zonaly averaging the wind velocities in a local time/geographic latitude reference frame. Figure 18.4 shows that the meridional wind is equatorward during the night and poleward during the day, in agreement with empirical representations of the wind velocity (Hedin et al. 1991).

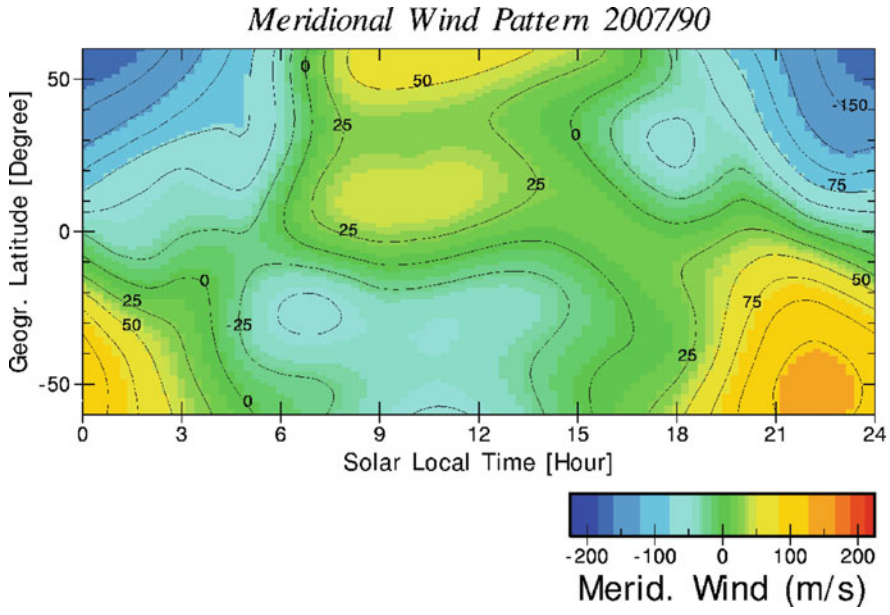

Fig. 18.4 Example of the longitudinally averaged meridional wind field obtained from the Full Physics-Based Ensemble Kalman filter model for March 31, 2007. Positive wind velocities denote a northward wind

18.4 Summary and Conclusions

Over the past several years, data assimilation models have become a dominant tool to integrate space- and ground-based observations into physics-based models of the space environment. At USU we have developed two data assimilation models for the ionosphere that use approximations to the full Kalman filter technique. The first model uses a statistical model (Gauss Markov process) to evolve the state and covariances in the Kalman filter, whereas the second model employs an ensemble Kalman filter technique. Both approximations lead to a dramatic reduction in the computational requirements and allow for the use of the Kalman filter framework to objectively evaluate the model state error covariances. The presented approximation to the full Kalman filter are well established for the ionosphere but will also be applicable for other areas of the space environment. It is expected that over the next few years these techniques will become increasingly more important for many areas of space science and applications.

Acknowledgments This research was supported by Office of Naval Research grant N00014-09-1-0292 to Utah State University.

References

Brun AS (2007) Towards using modern data assimilation and weather forecasting methods in solar physics. Astron Nachr 328, No. 3/4, 329–338. doi:10.1002/asna.200610739329

Bust GS, Garner TW, Gaussiran TL (2004) Ionospheric data assimilation three-dimensional (IDA3D): a global, multisensor, electron density specification algorithm. J Geophys Res 109:A11312. doi:10.1029/2003JA010234

Cane MA, Kaplan A, Miller RN, Tang B, Hackert EC, Busalacchi AJ (1996) Mapping tropical Pacific sea level: data assimilation via a reduced state space Kalman filter. J Geophys Res 101:22,599–22,617

Codrescu MV, Fuller-Rowell TJ, Minter CF (2004) An ensemble-type Kalman filter for neutral thermospheric composition during geomagnetic storms. Space Weather 2:S11003. doi:10.1029/2004SW000088

Daley R (1991) Atmospheric data analysis. Cambridge University Press, Cambridge, UK

Datta-Barua S, Bust GS, Crowley G, Curtis N (2009) Neutral wind estimation from 4-D ionospheric electron density images. J Geophys Res 114:A06317. doi:10.1029/2008JA014004

Decker DT, McNamara LF (2007) Validation of ionospheric weather predicted by Global Assimilation of Ionospheric Measurements (GAIM) models. Radio Sci 42:RS4017. doi:10.1029/2007RS003632

Evensen G (2003) The ensemble Kalman filter: theoretical formulation and practical implementation. Ocean Dynamics 53:343–367

Evensen, G (2009) Data assimilation: the ensemble Kalman filter, 2nd edn. Springer, Berlin

Foster JC, Erickson PJ, Coster AJ, Goldstein J, Rich FJ (2002) Ionospheric signatures of plasmaspheric tails. Geophys Res Lett 29(13). doi:10.1029/2002GL015067

Fukumori I, Malanotte-Rizzoli P (1995) An approximate Kalman filter for ocean data assimilation: an example with an idealized Gulf Stream model. J Geophys Res 100:6777–6793

Gelb A (1974) Applied optimal estimation. MIT Press, Cambridge

Hedin A et al (1991) Revised global model of thermosphere winds using satellite and ground-based observations. J Geophys Res 96(A5):7657–7688

Howe BM, Runciman K, Secan JA (1998) Tomography of the ionosphere: four-dimensional simulations. Radio Sci 33:109–128

Ide K, Bennett AF, Courtier P, Ghil M, Lorenc AC (1997) Unified notation for data assimilation: operational, sequential and variational. J Meteorol Soc Jpn 75(1B):181–189

Jee G, Burns AG, Wang W, Solomon SC, Schunk RW, Scherliess L, Thompson DC, Sojka JJ, Zhu L (2007) Duration of ionospheric data assimilation initialization of a coupled thermosphere-ionosphere model. Space Weather J 5:S01004. doi:10.1029/2006SW000250

Jee G, Burns AG, Wang W, Solomon SC, Schunk RW, Scherliess L, Thompson DC, Sojka JJ, Zhu L (2008) Continual initialization of the TING model with GAIM electron densities: ionospheric effects on the thermosphere. J Geophys Res 113:A03305. doi:10.1029/2007JA012580.

Koller J, Chen Y, Reeves GD, Friedel RHW, Cayton TE, Vrugt JA (2007) Identifying the radiation belt source region by data assimilation. J Geophys Res 112:A06244. doi:10.1029/2006JA012196

Li J, Xiu D (2008) On numerical properties of the ensemble Kalman filter for data assimilation. Comput Methods Appl Mech Eng 197. doi:10.1016/j.cma.2008.03.022

Mandrake L, Wilson B, Wang C, Hajj G, Mannucci A, Pi X (2005) A performance evaluation of the operational Jet Propulsion Laboratory/University of Southern California Global Assimilation Ionospheric Model (JPL/USC GAIM). J Geophys Res 110:A12306. doi:10.1029/2005JA011170

Maybeck P (1979). Stochastic models, estimation, and control – vol 1. Academic, New York, NY

McDonald SE, Basu S, Basu S, Groves KM, Valladares CE, Scherliess L, Thompson D, Schunk RW, Sojka JJ, Zhu L (2006) Extreme longitudinal variability of plasma structuring in the equatorial ionosphere on a magnetically quiet equinoctial day. Radio Sci 41:RS6S24. doi:10.1029/2005RS003366

McNamara LF, Decker DT, Welsh JA, Cole DG (2007) Validation of the Utah State University Global Assimilation of Ionospheric Measurements (GAIM) model predictions of the maximum usable frequency for a 3000 km circuit. Radio Sci 42:RS3015. doi:10.1029/2006RS003589

McNamara LF, Baker CR, Decker DT (2008) Accuracy of USU-GAIM specifications of foF2 and M(3000)F2 for a

worldwide distribution of ionosonde locations. Radio Sci 43:RS1011. doi:10.1029/2007RS003754

McNamara LF, Retterer JM, Baker CR, Bishop GJ, Cooke DL, Roth CJ, Welsh JA (2010) Longitudinal structure in the CHAMP electron densities and their implications for global ionospheric modeling. Radio Sci 45:RS2001. doi:10.1029/2009RS004251

Minter CF, Fuller-Rowell TJ, Codrescu MV (2004) Estimating the state of the thermospheric composition using Kalman filtering. Space Weather 2:S04002. doi:10.1029/2003SW000006

Mitchell CN, Spencer PSJ (2003) A three dimensional time dependent algorithm for ionospheric imaging using GPS signals. Ann Geophys 46:687–696

National Research Council (1991) Four-dimensional model assimilation of data: a strategy for the earth system sciences. National Academy Press, Washington, DC

Pi X, Wang C, Hajj GA, Rosen G, Wilson DB, Bailey JG (2003) Estimation of E×B drift using a global assimilative ionospheric model: an observation system simulation experiment. J Geophys Res 108:A2. doi:10.1029/2001JA009235

Robinson A, Lermusiaux PFJ (2000) Overview of data assimilation. Harvard reports in physical/interdisciplinary ocean science no 62

Scherliess L, Schunk RW, Sojka JJ, Thompson D (2004) Development of a physics-based reduced state Kalman filter for the ionosphere. Radio Sci 39:RS1S04. doi:10.1029/2002RS002797

Scherliess L, Schunk RW, Sojka JJ, Thompson DC, Zhu L (2006) The USU GAIM Gauss-Markov Kalman Filter model of the ionosphere: model description and validation. J Geophys Res 111:A11315. doi:10.1029/2006JA011712

Scherlies L, Thompson D, Schunk RW (2008) Longitudinal variability of low-latitude total electron content: tidal influences. J Geophys Res 113:A01311. doi:10.1029/2007JA012480

Scherliess L, Thompson CD, Schunk WR (2009) Ionospheric dynamics and drivers obtained from a physics-based data assimilation model. Radio Sci 44:RS0A32. doi:10.1029/2008RS004068

Schunk RW, Nagy FA (2000) Ionospheres. Cambridge University Press, Cambridge, UK

Schunk RW, Scherliess L, Sojka JJ (2002) Ionospheric specification and forecast modeling. J Spacecraft Rockets 39: 314

Schunk RW, Scherliess L, Sojka JJ, Thompson D (2004) Global assimilation of ionospheric measurements (GAIM). Radio Sci 39:RS1S02. doi:10.1029/2002RS002794

Schunk RW, Scherliess L, Sojka JJ, Thompson D, Zhu L (2005) Ionospheric weather forecasting on the horizon. Space Weather 3:S08007. doi:10.1029/2004SW000138

Schunk RW, Sojka JJ, Eccles JV, Thompson DC (1997) Expanded capabilities for the ionospheric forecast model, AFRL Rep. AFRL-VS-HA-TR-98-0001. Air Force Res Lab, Hanscom Air Force Base, Mass

Sojka JJ, Thompson DC, Scherliess L, Schunk RW, Harris TJ (2007) Assessing models for ionospheric weather specification over Australia during the 2004 CAWSES Campaign. J Geophys Res 112:A09306. doi:10.1029/2006JA012048

Thompson DC, Scherliess L, Sojka JJ, Schunk RW (2006) The Utah state university Gauss-Markov Kalman filter of the ionosphere: the effects of Slant TEC and electron density profile data on model fidelity. J Atmos Sol Terr Phys. doi:10.1016/j.jastp.2005.10.011

Thompson DC, Scherliess L, Sojka JJ, Schunk WR (2009) Plasmasphere and upper ionosphere contributions and corrections during the assimilation of GPS slant TEC. Radio Sci 44:RS0A02. doi:10.1029/2008RS004016

Part VI
Extraterrestrial Magnetospheres

Large-Scale Structure in the Magnetospheres of Jupiter and Saturn

19

Christopher S. Arridge

Abstract

The magnetospheres surrounding Jupiter and Saturn are unique in the solar system because of their important internal plasma sources, rapid planetary rotation and strong magnetosphere-ionosphere coupling, the prevailing solar wind conditions, and the complex multi-phase and multi-species nature of their magnetospheric plasma and neutral environments. In this chapter the large-scale structure of the jovian and saturnian magnetospheres will be reviewed. The physical origins of this structure will be examined and we discuss dynamical and periodic modulations within each system and their responses to internal and external perturbations.

19.1 Introduction

The rapidly rotating magnetospheres surrounding Jupiter and Saturn are important natural laboratories for the study of space plasma physics. Their significance stems from the presence of heavy ion plasma sources within the magnetosphere, the multi-phase and multi-species nature of the magnetospheric plasma and neutral environment, and the rapid rotation of these planets which, via magnetosphere-ionosphere coupling processes, is at least partially imposed onto much of the magnetosphere. As a consequence of this latter fact, pseudo (inertial) forces become important in magnetospheric equilibria and dynamics. The sidereal rotation period of Jupiter is relatively well constrained at 9.92425 h (Weiss 2004) based on periodicities in radio emissions from Jupiter's auroral regions, whereas the rotation period of Saturn (determined from the same method) is poorly known. The corresponding period at Saturn has been found vary from 10h39m22s in the Voyager epoch (Carr et al. 1981) to >10h48m in the Cassini epoch (Kurth et al. 2008, and references therein). This large long-term drift in period strongly suggests that it does not represent Saturn's rotation period and so this drifting period is now commonly referred to as the "magnetospheric period".

At the time of writing the jovian magnetosphere has been studied in situ by eight spacecraft and is the most studied magnetosphere beyond Earth. In contrast the saturnian magnetosphere has been studied by four spacecraft, most recently the Cassini orbiter. Prior to the arrival of Cassini at Saturn it was thought that the saturnian magnetosphere was "Earth-like" or intermediate between Jupiter and Earth in terms of its structure and dynamics. Recent Cassini studies of the saturnian environment have shown that the jovian and saturnian magnetospheres have many common

C.S. Arridge (✉)
Mullard Space Science Laboratory, Department of Space and Climate Physics, University College London, Dorking, Surrey RH5 6NT, UK; The Centre for Planetary Sciences at UCL/Birkbeck, London WC1E 6BT, UK
e-mail: csa@mssl.ucl.ac.uk

W. Liu, M. Fujimoto (eds.), *The Dynamic Magnetosphere*, IAGA Special Sopron Book Series 3,
DOI 10.1007/978-94-007-0501-2_19,

elements and are surprisingly similar in many ways. However, there are important differences, such as in the ratio of plasma to neutrals, the generation of main auroral emissions, and the effects of the solar-wind interaction and mass-loading on reconnection and "substorm-like" behaviour. Cassini studies have also produced new lessons for studies of the jovian magnetosphere, for example in the nature of neutral-plasma interactions, magnetodisc equilibria, the generation of magnetospheric periodicities, and auroral morphology and dynamics.

Modelling of Saturn's internal magnetic field has consistently revealed a highly symmetric internal field and a priori one might expect Saturn's magnetosphere to be highly azimuthally symmetric (apart from the obvious local time asymmetries imposed by the solar wind). The first hints of the presence of large-scale periodicities in Saturn's magnetosphere were provided by observations of kilometric radio emissions (known as Saturn Kilometric Radiation or SKR) which were found to be modulated at a period close to the atmospheric rotation period. Hence, the period of SKR was rapidly adopted as the rotation period of Saturn's deep interior by analogy with similar radio emissions at Jupiter (see Kurth et al. (2009) for a recent review). Subsequently this modulation was shown to drift in period by around 1% both on long and short time scales. Since such large changes in Saturn's angular momentum cannot occur on such short time scales, this shows that these radio emissions cannot be strongly linked with the rotation of Saturn's deep interior. Observations since the Pioneer-era have shown evidence for other periodic phenomena in Saturn's magnetosphere, which have the same period as SKR, such as: motion of the auroral oval (Nichols et al. 2008), magnetic fields (e.g., Espinosa et al. 2003; Southwood and Kivelson 2007; Andrews et al. 2008; Provan et al. 2009), energetic particles (e.g., Carbary et al. 2007), plasma (e.g., Gurnett et al. 2007; Arridge et al. 2008a; Burch et al. 2009), energetic neutral atoms (ENAs) (Carbary et al. 2008a), and the location of the magnetopause (e.g., Clarke et al. 2010a) and bow shock (Clarke et al. 2010b). To add further intrigue, Gurnett et al. (2009) have recently presented evidence showing that the modulation of SKR emissions from the northern hemisphere has a different period to that of the southern hemisphere. Whilst spin-periodic signatures are relatively well-understood at Jupiter there are other periodicities that are not well understood, such as System IV periodicities in the Io plasma torus (Sandal and Dessler 1988).

In this chapter the large-scale structure of the jovian and saturnian magnetospheres will be discussed. In Section 19.2 the main features of giant rapidly rotating magnetospheres are described and issues relating to their global configuration and equilibrium are discussed. The perturbation of this configuration and equilibrium by periodic modulations in the magnetosphere will also be described in Section 19.2. In Section 19.3 some selected aspects of large-scale magnetospheric dynamics will described. Some open questions and prospects for future missions are discussed in the summary.

19.2 Global Configuration and Equilibria

Figure 19.1 contains an illustration of the general large-scale structures in the magnetospheres of Jupiter and Saturn. Within the inner magnetosphere the magnetic field is dominated by the internal magnetic field of the planet which at Jupiter (Saturn) is inclined by around 9.6° (0.1°) to the rotation axis (e.g., Russell and Dougherty 2009). Sputtering, jets, volcanism and exospheric/atmospheric loss processes produce neutral torii around natural satellites which are ionised by charge-exchange and photoionisation processes to produce plasma torii. At Jupiter, the main plasma/neutral torus is due to Io whereas at Saturn a group of icy satellites including Enceladus, Dione and Tethys produce a large dusty neutral torus called the E-ring which is ionised to produce the E-ring plasma torus. Thus mass-loading in Saturn's magnetosphere is rather more radially distributed compared to Jupiter where most of the mass-loading occurs in a limited region. This is not the only difference between these two systems.

Figure 19.2 schematically illustrates the flow of mass and energy in the neutral/plasma torii at Jupiter and Saturn, based on results from a physical chemistry model (Delamere et al. 2007). These models show that at Jupiter (Saturn) 49% (95%) of the torus ions are last as fast neutrals. At Jupiter ions are mainly produced via electron impact ionisation of the neutral gas from both thermal and hot electrons. Thermal electrons in the torus are heated via Coulomb collisions with the pickup ions and achieve a temperature of 4.8–6.8 eV which means that they can

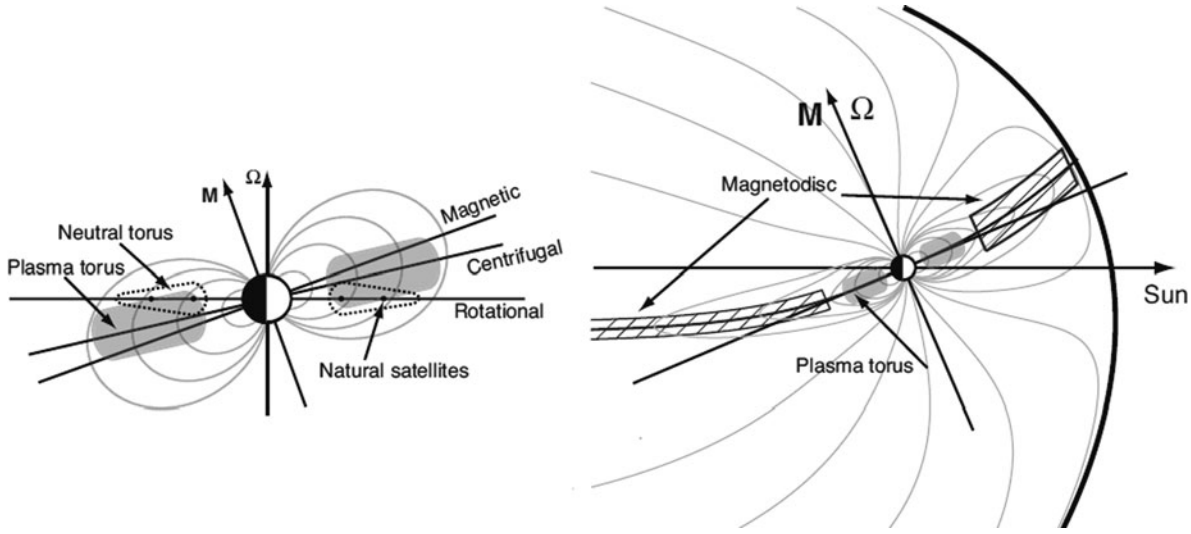

Fig. 19.1 Simplified schematic of the giant magnetospheres of Jupiter and Saturn showing the main structural elements with a zoom-in of the inner magnetosphere (*left*) showing plasma and neutral torii. The inner magnetosphere is shown for the fully general case where there is a tilt between the dipole and spin axes but this tilt is absent at Saturn so the natural satellites and plasma and neutral torii collapse together into the same plane (magnetic dipole and rotational equators). For simplicity, the large-scale magnetospheric view is shown for the case of no tilt between the magnetic dipole and spin axes, or can be thought of as for a particular orientation of dipole where it is in/out of the plane of the diagram

produce additional ionisation through electron impact ionisation. However, at Saturn the ion pickup energy is four times smaller due to the smaller plasma velocity near Enceladus which results in lower thermal electron temperatures (1.3 eV). These thermal electrons are too cool to produce significant additional ionisation resulting in a neutral-dominated system. Electron-ion coupling resulting in ion excitation at Jupiter drives strong UV emissions and is the dominant energy sink for the system, whereas at Saturn charge-exchange results in the production of fast-neutrals which are the dominant energy and mass sink for the system.

The mass introduced into the magnetosphere cannot build up indefinitely and small-scale plasma transport processes move this plasma radially outwards into the magnetosphere. These processes have been modelled in global MHD simulations of the magnetosphere (e.g., Kidder et al. 2009) and also using the Rice Convection Model (e.g., Wu 2009). This mass-loading process and the outward transport of plasma both act to slow the azimuthal flow of plasma around the planet, a process which is countered by the transport of angular momentum, via field-aligned currents, from the upper atmospheres of Jupiter and Saturn into the equatorial plasma sheet. This extraction of energy from the planets is the engine that powers the jovian magnetosphere and which also plays a strong role in the saturnian magnetosphere.

It is commonly thought that the jovian magnetosphere is more heavily mass-loaded and severely stressed than the saturnian magnetosphere. However, relative to field strength Vasyliūnas (2008) has argued that Saturn's magnetosphere is more heavily mass-loaded than Jupiter's and one can also show that the ring current is also stronger than Jupiter's (Achilleos et al. 2010). This latter point is also revealed in the geometry of the magnetospheric magnetic field, where the geometry of Saturn's magnetic field deviates significantly from a dipole at a smaller radial distance than at Jupiter ($\sim 16\ R_S$ vs $\sim 20\ R_J$, or 0.96×10^6 km vs 1.4×10^6 km where $1\ R_S = 60268$ and $1\ R_J = 71492$ km), as measured for example by the angle between the lobe field and the equatorial plane (e.g. Arridge et al. 2008c).

19.2.1 Ring Current and Magnetodisc Morphology

In common with the terrestrial magnetosphere, trapped particles within the jovian and saturnian magnetospheres are subject to mechanical stresses which

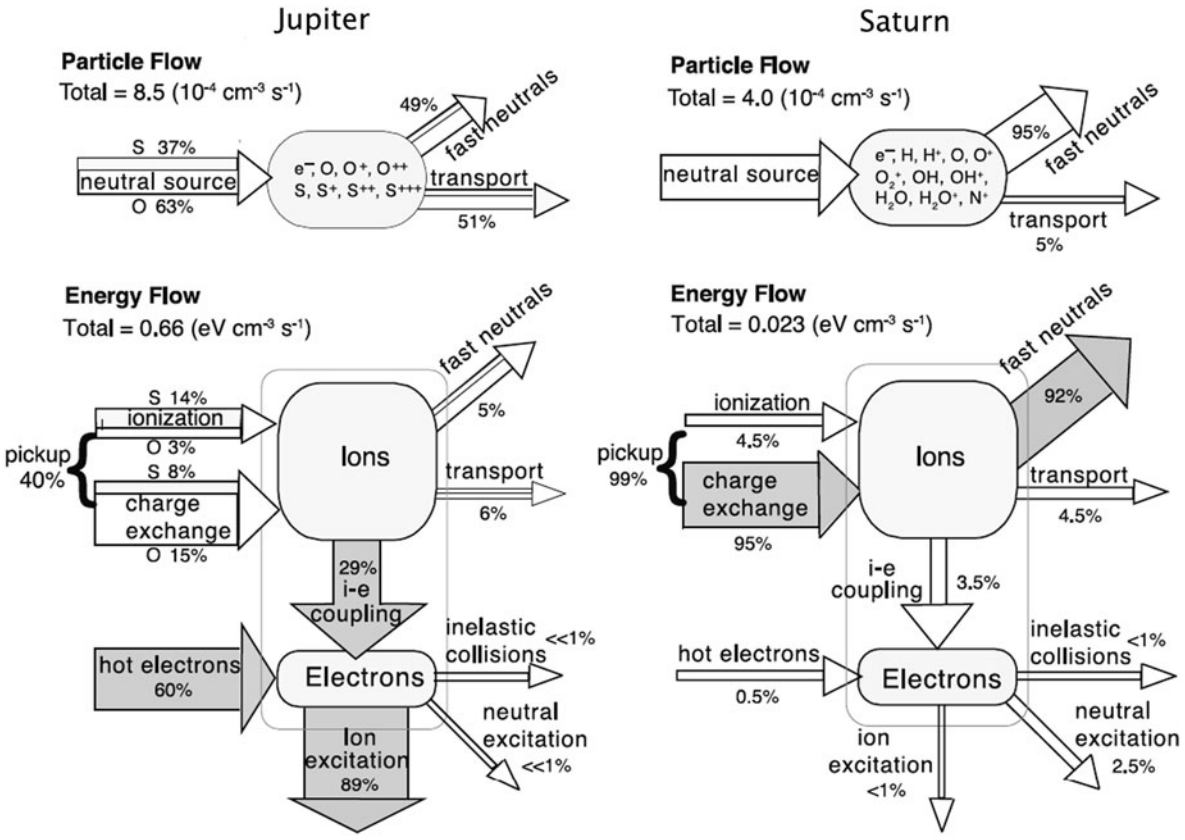

Fig. 19.2 Illustration of mass and energy flow in a (*left*) sulphur/oxygen-based jovian and oxygen-based saturnian neutral/plasma cloud model from Delamere et al. (2007). The model results show that at Jupiter UV emissions (ion excitation) are primarily driven by energy from ion pickup and hot electrons, whereas at Saturn the energy from ion pickup mainly goes into fast neutrals as the electrons are not sufficiently heated by the lower ion pickup energy at Saturn

generate currents in order to maintain stress balance. These ring currents circulate azimuthally in the magnetosphere and act to depress the field strength near the planet and stretch and inflate the field further out. In contrast with the terrestrial magnetosphere, inertial (centrifugal) forces are an important source of stress and add to pressure gradients and pressure anisotropy in generating the ring current. In the terrestrial magnetosphere the ring current does not exert a significant stretching effect on the field but at Jupiter and Saturn the "ring current" can circulate azimuthally around the planet out to large distances. The field perturbation introduced by this extended current system deforms the field to such an extent that a thin disc-like current and plasma sheet forms beyond distances of 16 R_S (20 R_J) at Saturn (Jupiter). This is known as the magnetodisc (represented by the hatched structure in Fig. 19.1) and is an important structure in regulating mass and energy transport within rapidly rotating magnetospheres. On physical grounds one cannot distinguish between the azimuthal currents flowing in this magnetodisc and in the quasi-dipolar region inside 16 R_S or 20 R_J, but despite this many authors restrict the use of the term "ring current" to the azimuthal currents flowing within the quasi-dipolar region (this is the definition employed in this chapter), yet other authors use the term to refer to the pressure anisotropy- and gradient-driven component of the ring current (in analogy with the terrestrial magnetosphere). Magnetospheric currents, including this magnetodisc structure, have been studied from the results of global MHD simulations of both the jovian and saturnian magnetospheres (e.g., Miyoshi and Kusano 1997; Walker and Ogino 2003; Moriguchi et al. 2008; Kidder et al. 2009).

This severe stretching effect on the jovian field and the consequences for Jupiter's magnetospheric plasma

were first identified in Pioneer 10 data (e.g., Smith et al. 1974) and have been studied in some detail (e.g., Goertz 1979; Achilleos et al. 2010 and references therein; Khurana 2001). Although Saturn's magnetosphere appeared to have all the necessary ingredients for a magnetodisc, the flybys of Pioneer 11, and Voyagers 1 and 2 suggested the presence of a more quasi-dipolar magnetosphere reminiscent of the terrestrial magnetosphere. However, Smith et al. (1980) commented that observations of stretched field lines on the dawn flank may be associated with a magnetodisc-type configuration at Saturn, whilst the dayside may have been in a state of magnetospheric compression resulting in a more dipolar dayside. Arridge et al. (2007) studied similar stretched fields on the dawn flank using Cassini data and used a stress balance argument to propose that the stretched field and associated current sheet was evidence of Saturn's magnetodisc. Subsequently, Arridge et al. (2008c) surveyed Cassini magnetometer data inside the magnetosphere from midnight, dawn and pre-noon and showed that stretched current-sheet-like fields could be found at all these local times, hence demonstrating that a magnetodisc configuration could often be seen in Saturn's magnetosphere. They went on to show that the dayside Cassini passes where the magnetodisc was not present were under compressed magnetospheric conditions. This argument also holds for the dayside passes of Pioneer 11 and Voyagers 1 and 2. Such a suppression effect has also been found in MHD models of the jovian magnetosphere (Miyoshi and Kusano 1997; Walker and Ogino 2003).

Periodicities in the quasi-dipolar part of Saturn's magnetosphere, referred to as the "core" or "camshaft region", have been observed since the Pioneer and Voyager flybys (Espinosa et al. 2003) and have been shown to be consistent with a quasi-uniform field rotating in the equatorial plane at the SKR period (e.g., Southwood and Kivelson 2007; Andrews et al. 2008) with an associated north-south perturbation field (Andrews et al. 2008). The form of the north-south perturbation field has led some authors to associate this perturbation with a rotating partial ring current (e.g., Khurana et al. 2009; Provan et al. 2009) and the rotating uniform field with a corotating convection pattern (Gurnett et al. 2007) and patterns of field-aligned currents (Southwood and Kivelson 2007). ENA images of the energetic ion component of Saturn's ring current show a periodic modulation in the ring current region consistent with the idea of a partial ring current (Krimigis et al. 2007). The presence of a periodic density asymmetry in the core region between 3 and 5 R_S (Gurnett et al. 2007) supports the corotating convection model but the symmetry of the core region magnetic field perturbations and their implications for plasma flows does not (Southwood and Kivelson 2007).

19.2.2 Stress Balance in the Ring Current and Magnetodisc

Determining the exact contributors to stress balance within the current/plasma sheets in the magnetosphere is a difficult and non-trivial task. Early studies of stress balance in the ring currents and magnetodiscs of Jupiter and Saturn using Voyager fields and particles measurements suggested that pressure gradients and centrifugal forces were important within 14 R_S at Saturn but with centrifugal forces becoming dominant beyond this distance (McNutt 1984; Mauk et al. 1985). At Jupiter it was first suspected that centrifugal forces would be dominant throughout the magnetosphere due to the intense mass-loading from Io and rapid rotation of the magnetosphere (e.g., Smith et al. 1974). However, the most recent analyses showed that pressure gradients and anisotropies were the dominant mechanical stresses in the ring current and magnetodisc (Mauk and Krimigis 1987; Paranicas et al. 1991).

Using Cassini data at Saturn, Arridge et al. (2007) investigated the stress balance within the dawn magnetodisc and concluded that beyond a distance of 25 R_S centrifugal forces were dominant, but at around 20 R_S pressure gradients and centrifugal forces were equal contributors. Sergis et al. (2010) and Kellett et al. (2010) have investigated stress balance in the ring current region using Cassini data using statistical techniques and case-studies, respectively. These authors concluded that the centrifugal component dominated inside of around 7 R_S, despite being partially cancelled by a significant pressure anisotropy in the thermal plasma, and that pressure gradients in thermal and hot ions dominated between 7 and 15 R_S (the radial limit of these studies). Overall, the observational work to date suggests an inner core of centrifugally dominated ring current, surrounded by a pressure-dominated ring current out to at least 20 R_S, beyond which the field is distorted into the magnetodisc and the mechanical

stresses are dominated by the centrifugal force. There appears to be a transition region at the outer edge of the ring current/inner edge of the magnetodisc where the stress balance changes.

Stress balance has also been examined theoretically using a range of models. Global simulations of the magnetosphere have been used to examine the stress balance in the magnetosphere with an emphasis on how this response to changes in solar wind conditions (e.g., Miyoshi and Kusano 2001; Walker et al. 2001; Kidder et al. 2009). A particularly elegant approach is to use Euler potentials (Achilleos et al. 2010, and references therein) and such models have been used to address jovian and saturnian stress balance. These models require empirically determined input conditions for the cold and hot plasma populations, and the azimuthal plasma velocity. The method involves self-consistently searching for an equilibrium magnetic configuration which balances the mechanical stresses. Generally the results of these models are in agreement with observations. Figure 19.3 shows the two-dimensional distribution of azimuthal volume current due to centrifugal stress and pressure gradients, and the relative contributions of each, as calculated using the model of Achilleos et al. (2010). One can see that the currents are rather more distributed at Saturn compared to Jupiter and that the currents are generally weaker at Saturn. At Jupiter, peaks in hot plasma pressure and centrifugal current are spatially separated whereas at Saturn they spatially overlap. Recent work has shown that more or less extended pressure gradient-dominated regions can be obtained for more or less disturbed states (N. Achilleos, private communication 2009). Magnetodisc suppression under compressed magnetospheric conditions is also found in the model.

19.2.3 Symmetry Breaking: Effects of Dipole Tilt, Season and Periodicities

The solar-wind suppression of the dayside magnetodisc is an example of solar wind forcing on the dayside magnetosphere. Arridge et al. (2008b) identified a second solar wind forcing effect on Saturn's magnetosphere and magnetodisc: a northward warping

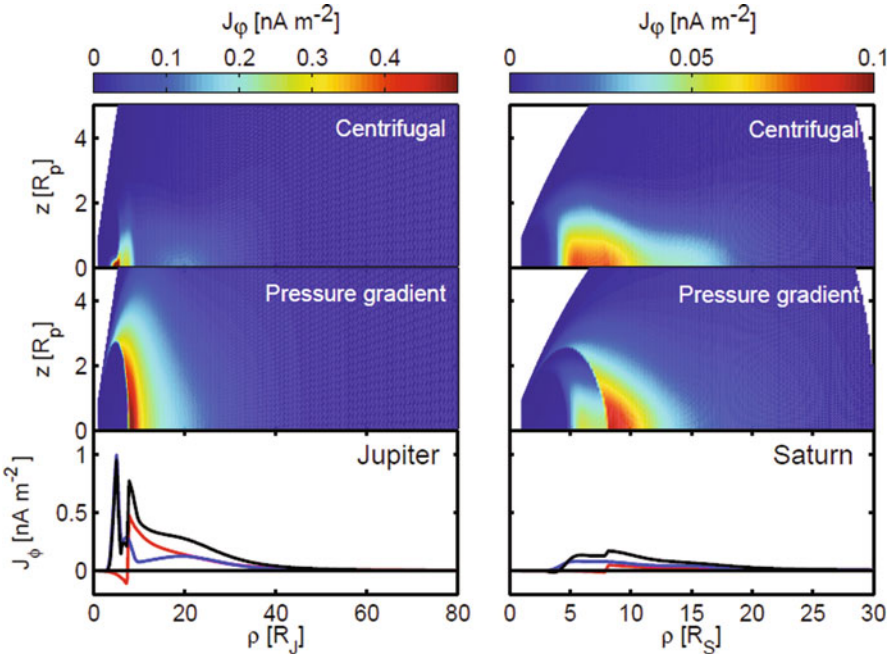

Fig. 19.3 Azimuthal volume current densities as calculated from the model of Achilleos et al. (2010) for Jupiter (*left*) and Saturn (*right*). The coloured panels show the distribution of current in the (ρ,z) plane where z is the perpendicular distance from the plane of the current sheet and ρ is the (cylindrical) radial distance in that plane. Note the different current density colour scales between Jupiter and Saturn. The bottom panels show the equatorial volume current density from centrifugal forces (*blue*), hot plasma pressure gradients (*red*) and the total current density (*black*)

during southern hemisphere summer. Beyond a cylindrical radial distance of ≈15 R_S the magnetodisc was found to be displaced out of the rotational equator at all local times sampled by Cassini, thus the magnetodisc was bent into a bowl-type shape by the action of the solar wind. ENA images of the plasma sheet taken from the dawn flank confirm this warping on the nightside but show the plasma sheet lying closer to the equator on the dayside (Carbary et al. 2008b). This discrepancy between the magnetometer observations and the ENA images is possibly due to the smaller standoff distance of the magnetopause when the ENA images were taken, indicating an effect of upstream conditions. This distortion is also found in global MHD simulations of the saturnian magnetosphere (e.g., Hansen et al. 2005; Kidder et al. 2009) and in the latter study the authors showed that the IMF can also play a role in moving the plasma sheet down towards the equator which may help in further understanding the dayside discrepancy between the results of Arridge et al. (2008b) and Carbary et al. (2008b).

This is an example of a seasonal solar wind effect due to the inclination of the solar wind flow to Saturn's rotational equator. When Cassini arrived at Saturn the tilt between the rotational equator and the solar wind flow (termed the magnetospheric tilt) was around –25° indicating that the solar wind was blowing from a southerly direction "underneath" the magnetodisc thus lifting it northward. During northern hemisphere summer this effect is expected to reverse where the magnetodisc is displaced southward as the solar wind blows from a northerly direction. This is an example of magnetospheric symmetry breaking and a similar solar-wind driven mechanism is also found at Earth and Jupiter, although the dayside warping effect has not yet been found at these planets. In the jovian magnetosphere the dipole and spin axes are inclined by 9.6° so there is a component of the centrifugal force which acts to push plasma from the magnetic dipole equator towards the rotational equator. In reality the forces on the plasma are not sufficient to push the plasma into the rotational equator and the plasma instead lies in a plane ≈1/3 of the way to the rotational equator from the magnetic equator. This location is referred to as the centrifugal equator (Hill et al. 1974). This displacement is readily observed in the Io plasma torus (e.g., Bagenal 1994) but was more controversial in the jovian middle and outer magnetosphere until Khurana (1992) demonstrated that the observed displacement of the current sheet from the dipole magnetic equator was more consistent with a solar wind-driven distortion than the centrifugal mechanism. Figure 19.1 illustrates both of these distortions.

Periodic motions of the plasma sheet have been observed in both the jovian and saturnian magnetospheres. Such periodicities at Jupiter are well understood in terms of the tilt between the jovian spin and dipole axes (e.g., Khurana et al. 1992) but there is a lack of consensus on their origin at Saturn (e.g., Carbary et al. 2007; Arridge et al. 2008a; Khurana et al. 2009; Arridge et al., Periodic motion of Saturn's nightside plasma sheet, submitted manuscript; Morooka et al. 2009). In modelling carried out by Arridge et al. (submitted) this periodic behaviour was accurately modelled by a plasma sheet geometry that consisted of a warped and flapping plasma sheet with a constant plasma sheet thickness. ENA observations from the dawn magnetospheric flank support such a flapping paradigm where they have revealed a clear periodic tilting of the plasma sheet (Carbary et al. 2008a). Several authors have developed theories which explain how such plasma sheet periodicities can arise and how they are linked with periodicities in the core region (e.g., Carbary et al. 2007, Khurana et al. 2009; Southwood and Kivelson 2007; Provan et al. 2009). In complementary work, Morooka et al. (2009) found that they were unable to reproduce density periodicities using a flapping model and instead favoured a model which combined flapping with a longitudinal density asymmetry in the plasma sheet. The reconciliation of such results may lie in correctly modelling the transition from compressional fluctuations in Saturn's lobe (Krupp et al. 2005) to tangential (flapping) motions near the plasma sheet (Arridge et al. submitted).

19.2.4 Magnetospheric Lobes

The lobes of Earth's magnetotail are sites of magnetic flux and energy storage where open magnetic flux accumulates following reconnection at the dayside magnetopause. However, the presence of large extended open flux regions in outer planet magnetospheres, that respond dynamically to the solar wind is the topic of some controversy, particularly relating to the extent of the solar wind influence in the jovian magnetosphere (e.g., McComas and Bagenal

2007; Cowley et al. 2008a; McComas and Bagenal 2008). There is good evidence from IR H_3^+ auroral observations for the existence of an open polar cap at Jupiter (e.g., Stallard et al. 2003) and whilst there is observational evidence for dayside reconnection at both Jupiter and Saturn (see Section 19.3.3), the mechanisms for closing this open flux and the magnetospheric consequences of such processes have yet to be firmly established. One interesting consequence of rapid planetary rotation on a significant open polar cap and associated tail lobes is a twisting of the field in the lobes. Because the lobe field lines are anchored in the polar cap ionosphere, as the planet rotates the lobe field will be twisted up. This process was first proposed by Isbell and co-workers and its consequences were explored quantitatively by Milan et al. (2005, and references therein). However, observational evidence for this effect has yet to be presented.

19.3 Dynamics

A thorough understanding of magnetospheric equilibria can naturally lead to a good understanding of how the system becomes unstable, leading to magnetospheric dynamics. Whilst dynamics of the jovian and saturnian magnetosphere are large subjects (see Mitchell et al. (2009a) and Krupp et al. (2004) for recent reviews) some discussion of key topics on the large scale dynamics of the magnetosphere is important. Below we discuss the effect of magnetospheric compressions, mass-loading variability and magnetic reconnection on the large-scale structure of the magnetosphere.

19.3.1 Large-Scale Magnetospheric Response to Compression

The magnetopause standoff distance R_0 is typically $\backsim 23\ R_S$ (1.4×10^6 km) at Saturn (Achilleos et al. 2008), with a range between ~16 and 30 R_S, and 60 R_J (4.3×10^6 km) at Jupiter (Huddleston et al. 1998) with a range between ~50 and 90 R_J. The response of the standoff distance to changes in solar wind dynamic pressure is a useful diagnostic of stress balance inside the magnetosphere. This response is often characterised by a power-law: $R_0 \propto {P_{SW}}^{1/\alpha}$ where $\alpha = 6$ is the canonical value for a vacuum magnetic dipole inside the magnetopause. Larger values of α indicate a "stiff" magnetosphere which is relatively insensitive to changes in dynamic pressure and smaller values of α indicate a highly compressible magnetosphere. Observational studies of the terrestrial magnetopause have confirmed this relationship (e.g., Shue et al. 1997) but studies of the jovian magnetopause showed a different relationship with $\alpha \approx 4$ (Slavin et al. 1985; Huddleston et al. 1998). This is corroborated by the large range in observed standoff distances of the jovian magnetopause compared to the range of solar wind dynamic pressures (e.g., Smith et al. 1974). Although initial Pioneer/Voyager studies of the saturnian magnetopause indicated that the magnetosphere was as stiff as the terrestrial magnetosphere (e.g. Slavin et al. 1985), subsequent Cassini studies have demonstrated a more compressible magnetosphere, approaching the compressibility of the jovian magnetosphere with $\alpha \approx 5$ (Arridge et al. 2006; Kanani et al. 2010). These observational results are supported by global MHD modelling results (Hansen et al. 2005).

Although attributed to the effects of hot plasma pressure and centrifugal forces (e.g., Huddleston et al. 1998) the exact physical origin of $\alpha < 6$ in the magnetospheres of Jupiter and Saturn was quantitatively investigated by Bunce et al. (2007) in a study of the response of Saturn's ring current to changes in solar wind dynamic pressure and magnetopause standoff distance. They examined how inertia and gradient drift currents varied with changing magnetopause standoff distance and showed that gradient drift currents were relatively insensitive to changes in standoff distance, but inertia currents (i.e., centrifugal stresses) increased strongly with standoff distance. Hence, changes in solar wind dynamic pressure strongly affect centrifugal stresses inside the magnetosphere producing a more compressible magnetosphere. However, it remains to be established how important centrifugal stress needs to be in the ring current for this effect to operate.

The aurora provides a direct view into the dynamical state of the magnetosphere and are visible in both the UV and IR with UV brightnesses of up to 10 MR at Jupiter (Clarke et al. 2004) and 15 kR at Saturn (Kurth et al. 2009). The response of the aurora to magnetospheric compression aids in understanding

the origin of the auroral current systems and precipitation responsible for the auroral emissions, and in understanding the dynamical response of the system to compression. The association of Jupiter's main auroral emission with field-aligned corotation-enforcement currents (Hill 2001; Southwood and Kivelson 2001; Cowley and Bunce 2001) is now well-established and Fig. 19.4 illustrates the Birkeland and radial currents responsible for corotation enforcement. Current is drawn out of the ionosphere (corresponding to downward electron precipitation, thus driving auroral emissions) and flows radially through the equatorial plasma sheet, providing a $\mathbf{j} \times \mathbf{B}$ force which tries to accelerate the plasma back up to corotation. The dynamical response of this system to variations in solar wind dynamic pressure has also been investigated. Under situations of magnetospheric compression the system will contract and conservation of angular momentum will act to spin up the equatorial plasma (e.g., Hanlon et al. 2004), thus requiring less corotation enforcement, and the main auroral emissions should weaken due to the weaker field-aligned currents (e.g., Southwood and Kivelson 2001). The opposite should occur during magnetospheric expansion. More recent work indicates that larger solar wind compressions can be associated with a transient brightening in the main emission as plasma supercorotates in the outer magnetosphere, thus requiring field-aligned coupling to slow the plasma down (Cowley et al. 2007). At Saturn these field-aligned coupling currents are too weak to explain the intensity of the observed auroral emissions (e.g., Cowley et al. 2008b and references therein). Instead it has been theoretically and observationally argued that Saturn's main emission is related to velocity shear at the open/closed field line boundary (Bunce et al. 2008; Cowley et al. 2008b) and so the auroral emission should brighten during magnetospheric compression.

The response of global magnetospheric field-aligned current systems to changes in upstream conditions have also been investigated using global MHD simulations (e.g., Fukazawa et al. 2005, 2006; Walker et al. 2001; Walker and Ogino 2003; Moriguchi et al. 2008). In a number of studies the resulting precipitating electron energy fluxes in upward current regions have been converted into a UV brightness and found to be compatible with UV auroral observations.

The observational response of the jovian and saturnian auroral main emission to changes in solar wind dynamic pressure has been investigated in a number of studies, but most recently by Clarke et al. (2009, and references therein). In this comprehensive study both the saturnian and jovian main auroral ovals were found to brighten at the arrival of solar wind forward shocks supporting theoretical discussions (Cowley et al. 2007, 2008b). In addition substantial periods of activity were observed in the jovian auroral emissions that appeared to be unrelated to solar wind activity, indicating internally-driven dynamics.

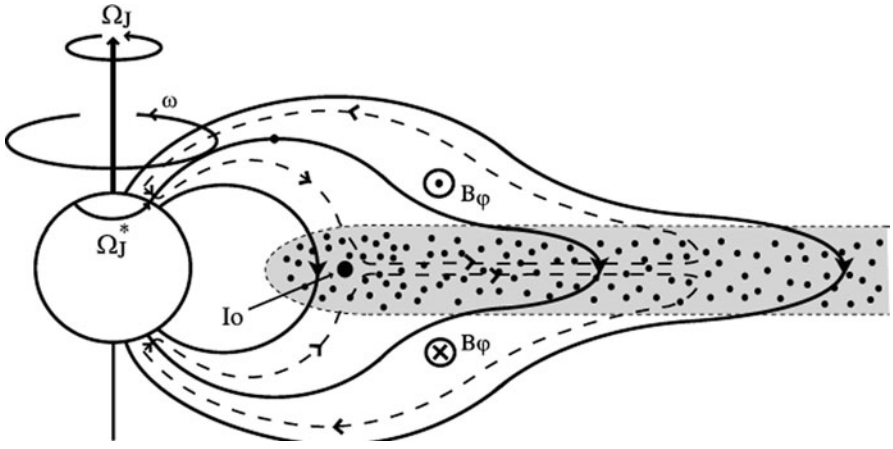

Fig. 19.4 Illustration of corotation enforcement currents at Jupiter from Cowley and Bunce (2001). Current is drawn out of the ionosphere along field-lines into the plasma sheet and flows radially through the plasma sheet before returning to higher latitudes via another field-aligned current at greater distances from the planet. The radial current in the equatorial plane gives rise to azimuthal magnetic fields

19.3.2 Mass-Loading Variability

The neutral source rate from Io is widely assumed to be around 10^3 kg s^{-1} and most of these neutrals are ionised, although around 50% of this plasma is lost from the system as neutrals via charge exchange (Delamere et al. 2007). The saturnian neutral source rate is a less well-known quantity but is typically taken to be $\approx$300 kg s^{-1}. Although not all of these neutrals are ionised, and many are lost from the system via charge-exchange, the plasma source rate has been found to be$\approx$ 10–100 kg s^{-1} but values vary depending on the dataset, analysis technique, and assumptions used (see for example Gombosi et al. 2009 and Khurana et al. 2007). In global MHD simulations the mass-loading rate can often be set as a free parameter and Hansen et al. (2005) used this flexibility to estimate a neutral source rate of $\approx$300 kg s^{-1} (corresponding to a source rate of 10^{28} neutrals s^{-1}).

The variability of neutral production at Io and Enceladus, through variability in Io volcanism (e.g., Spencer and Schneider 1996) or Enceladus plume activity (e.g., Saur et al. 2008), and the subsequent mass-loading of magnetic field lines provides a mechanism for internally driven dynamics. Such internally driven dynamics, including possible periodic effects may for example drive variability in the location of the magnetopause (e.g., Arridge et al. 2006; Achilleos et al. 2008), plasma sheet motions (e.g., Waldrop et al. 2005; Arridge et al. 2007), auroral activity (e.g., Clarke et al. 2009), variable intensity of ring and magnetodisc current sheets (e.g., Russell et al. 1999; Leisner et al. 2007; Arridge et al. 2008c) and the release of plasmoids (e.g., Jackman et al. 2007). The dynamical effects of such impulsive mass-loading have not received much attention in the literature and deserve further study, however the large inertia of the jovian and saturnian neutral atmospheres may exert a flywheel effect on the magnetosphere, smoothing out the effects of rapid variations in mass-loading (e.g., Pontius 1995).

19.3.3 Magnetic Reconnection and Plasmoid Release

Direct evidence for dayside reconnection has been provided via in-situ observations at the magnetopauses of Jupiter (Huddleston et al. 1997) and Saturn (McAndrews et al. 2008). At both Jupiter and Saturn, significant fields normal to the magnetopause were detected by the Voyager spacecraft (Huddleston et al. 1997) thus suggesting the presence of dayside reconnection. At Saturn observations of plasma acceleration at the magnetopause have also been presented (McAndrews et al. 2008). In the Saturn's geometric mid-altitude cusp evidence for both dayside and lobe reconnection has been found in the form of energy-latitude and energy-pitch angle ion dispersions (Arridge et al. Cassini observations of Saturn's southern polar cusp, in preparation). The location and morphology of dayside reconnection at Saturn and the resulting global convection pattern has been discussed by Fukazawa et al. (2007a, b) from global MHD simulations.

Dayside reconnection and the subsequent convection of open field lines into the magnetotail is the mechanism by which open magnetic flux is added to the magnetotail, which eventually must be closed by magnetic reconnection in the magnetotail. The time dependence of the open flux content of the magnetosphere has been estimated using upstream spacecraft data at both Saturn (e.g., Jackman et al. 2004; Badman et al. 2005) and Jupiter (Nichols et al. 2006). In these studies a transfer function, which is dependent on the IMF and the solar wind velocity, is used to infer the reconnection rate due to dayside reconnection. The results of these studies suggest peak reconnection rates of 10^5 Wb s^{-1} (100 kV) and 10^6 Wb s^{-1} (1000 kV) at Saturn and Jupiter respectively, compared with 3.5×10^{10} (Nichols et al. 2006) and 4×10^{11} Wb (Jackman et al. 2004) for the total open flux content of each magnetosphere. Although these estimates have been criticised due to their assumption that the reconnection process is as efficient as at Earth.

Plasmoids are structures containing closed loops of magnetic flux which provide a mechanism for closing this open lobe flux and also removing plasma from a magnetosphere, whilst conserving magnetic flux, and play an important role in the "magnetospheric substorm" process in the terrestrial magnetosphere. Plasmoids have also been detected in the jovian (e.g., Russell et al. 1998; Kronberg et al. 2005) and saturnian (e.g., Jackman et al. 2007, 2008; Hill et al. 2008) magnetotails. The release of plasmoids can be attributed to the storage of open magnetic flux in the magnetotail lobes or to the storage and release of plasma in the plasma sheet. Observations from the terrestrial and

jovian magnetospheres indicate that tail reconnection proceeds periodically (e.g., Freeman and Morley 2004; Kronberg et al. 2005) and which has been interpreted as the result of the timescales for open flux accumulation (e.g., Freeman and Morley 2004) at Earth and internal mass accumulation at Jupiter (Kronberg et al. 2007). Both cases have been discussed in relation to Saturn (e.g., Jackman et al. 2007; Russell et al. 2008) and evidence for open flux accumulation and release have been presented by Bunce et al. (2005) and Jackman et al. (2010). Figure 19.5 illustrates the centrifugally-driven release of plasmoids in the jovian tail (the "Vasyliūnas" cycle) producing a so-called planetary wind (and the implied X-line across the jovian tail). The ejection of plasmoids has been found in global MHD simulations (e.g. Fukazawa et al. 2005, 2006; Moriguchi et al. 2008; Fukazawa et al. 2007b) and periodic plasmoid release has been observed in simulations of the jovian (e.g. Fukazawa et al. 2005) and saturnian (Zieger et al. 2010) magnetospheres and where the repetition period appears to be dependent on upstream solar wind conditions.

Russell et al. (2008) have argued that Saturn's largest moon Titan exerts some control on the release of plasmoids. Out of the six plasmoids observed at the time of publication, four of these occurred when Titan was within one Saturn rotation period of local midnight. Russell et al. (2008) argued that enhanced mass-loading from Titan in the midnight sector could provide additional centrifugal stress to trigger magnetic reconnection. In support of this argument, Menietti et al. (2007) have shown that SKR emissions are strongest when Titan is close to local midnight. It remains to be seen if this correlation survives as more plasmoids are discovered.

An alternative view of plasma sheet flapping in Saturn's outer magnetosphere was advanced by Burch et al. (2008) who also studied plasma periodicities in the outer magnetosphere. They instead interpreted these as the periodic passage of plasmoids, using observations of northward magnetic fields on the trailing edge of each pulse of plasma as evidence of the plasmoid. Jackman et al. (2009) have emphasised the clear difference between the periodic plasma and magnetic field signatures in the magnetotail, and unambiguously detected plasmoids. They went on to show that the northward field signatures described by Burch et al. (2008) can naturally arise in a wavy (flapping) magnetodisc model, where both radial and azimuthal currents flow, due to the periodically changing orientation of the current sheet with respect to the coordinate system used to study the data. Figure 19.6 shows an illustration of how such flapping motions can lead to apparent northward field signatures in magnetic field data and such an idea was first advanced to explain such signatures at Earth (see Jackman et al. 2009, and references therein). However, evidence from ENA imaging (Mitchell et al. 2009b) does support the idea of recurrent energisation of plasma in the midnight-dawn sector. These energisations are highly

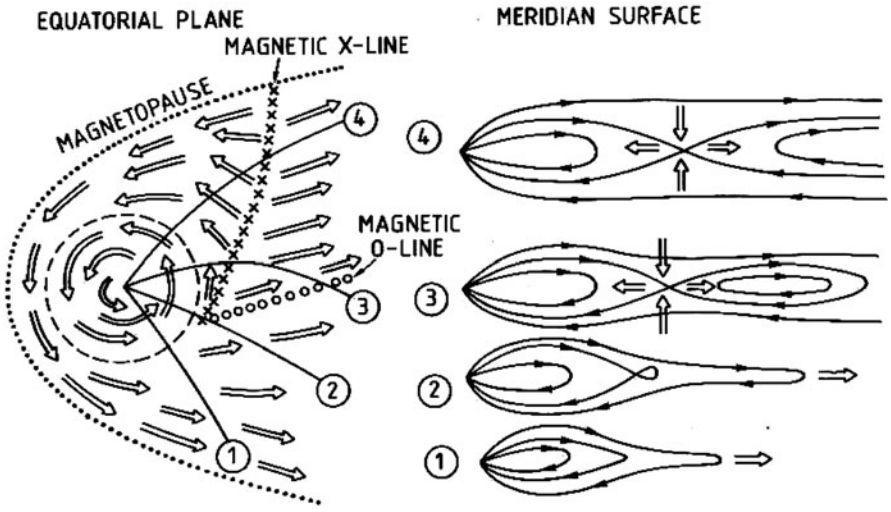

Fig. 19.5 Illustration of centrifugally-driven plasmoid release in the jovian magnetosphere taken from Vasyliūnas (1983)

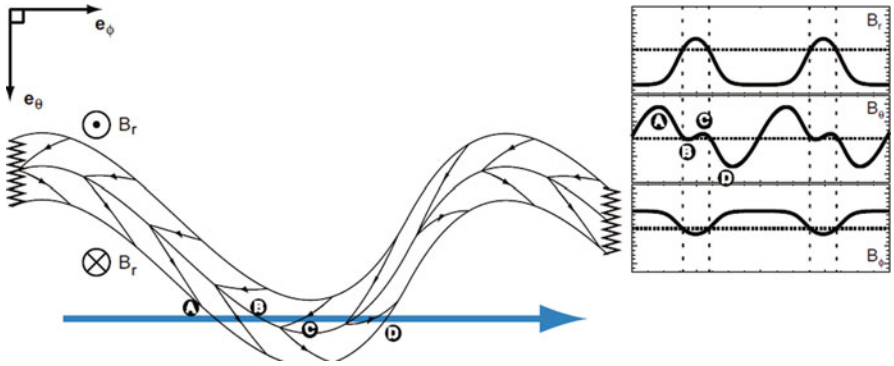

Fig. 19.6 Illustration of a flapping plasma sheet showing how such oscillations can lead to apparent northward fields (opposite to the planetary dipole). The spacecraft follows the arrowed trajectory through the current sheet and the expected magnetic field profile is illustrated. Note the reversals in B_r and B_φ that are to be expected when the spacecraft crosses the centre of the current sheet where both radial and azimuthal currents flow

organised by SKR suggesting a preferential longitude or range of longitudes in the rotational magnetosphere-ionosphere system which favours the growth of an instability that accelerates energetic particles when such an "active sector" reaches the midnight local time sector. However, this study does not tell us about the nature of this instability or the origin of the particular local-time and longitudinal sectors. The presence of such active sectors is highly reminiscent of early work on Jupiter which studied unexpected phase shifts in the arrival of current sheet crossings (Vasyliūnas and Dessler 1981).

19.4 Summary and Outlook

The jovian and saturnian magnetospheres share remarkable similarities in their structure, equilibria and dynamics, despite their different sizes, mass-loading rates, field strengths and neutral/plasma ratios. The similarities between System IV (e.g., Sandal and Dessler 1988) periodicities at Jupiter and the drifting period modulations at Saturn are quite striking and suggest that the periodicities that have been studied at Saturn thus far are essentially "System IV" in origin with the equivalent System III period (connected to the rotation of Saturn's deep interior) remaining unmeasured (Russell and Dougherty 2009). The recent observation of dual SKR periods (Gurnett et al. 2009) have led some to propose that one period is that of Saturn's deep interior (i.e., System III), and the other is essentially the thermospheric period (i.e., System IV) (Crary and Hill, Dual periodicities in the magnetospheres of Jupiter and Saturn, presented at the AGU Fall Meeting, 2009). Models of magnetospheric periodicities at Saturn which invoke the presence of persistent partial ring currents are a popular focus of current research (e.g., Provan et al. 2009; Khurana et al. 2009; Brandt et al. 2010) and have many attractive features in being able to explain a number of periodic phenomena with a single conceptual model. Some of these models require recurrent partial ring current energisation (e.g., Khurana et al. 2009) in order to maintain the ring current asymmetry. They invoke mechanisms whereby the ring current asymmetry produces magnetotail asymmetries that make it more likely for instabilities of the type discussed by Mitchell et al. (2009b) to inject energetic particles into the asymmetric part of the ring current, thus maintaining the phase of the system. The stability of the phases of SKR (Kurth et al. 2008) and magnetic fields in the core region (Andrews et al. 2008) suggests a tightly controlled system and in these models it is not clear how stable the system would be to external (such as variations in solar wind dynamic pressure) and internal (such as the variability in mass-loading in the E-ring torus) dynamics. It is interesting to note that such a partial ring current and associated Birkeland current system, and corotating convection cycles (e.g., Gurnett et al. 2007) were once of considerable interest at Jupiter (Dessler 1980).

The acceleration of plasma in the magnetospheres of Saturn and Jupiter has been a poorly understood process for over 30 years and is a leading open question with broader ramifications for understanding particle acceleration in the Universe. Instabilities and particle

acceleration processes may also play a role in maintaining periodic modulations in the magnetosphere of Saturn. Other open questions include (1) how are periodicities generated and maintained in the saturnian magnetosphere, (2) how is plasma transported through magnetodisc regions with stretched fields and high beta plasma sheets, (3) how does the solar wind influence the magnetosphere, (4) what is the reconnection efficiency at the magnetopause of the outer planets, and (5) in the presence of stretched distorted field lines in the outer magnetospheres of Jupiter and Saturn where are the dominant reconnection sites?

The outlook for future Jupiter and Saturn missions is bright. The Juno mission to Jupiter, scheduled for launch in August 2011 will explore the high-latitude regions of Jupiter's magnetosphere and will provide the best understanding yet on Jupiter's internal structure and internal magnetic field. The Europa Jupiter System Mission is a two/three-spacecraft mission currently undergoing a selection process by the European Space Agency and NASA with a proposed launch date of 2020 and has the potential to provide a unique insight into the dynamics of the jovian system. These future missions and support for the ongoing Cassini mission will make important contributions to the open science questions outlined above.

Acknowledgements CSA was funded by an STFC postdoctoral fellowship under grant ST/G007462/1 and the STFC rolling grant to MSSL/UCL. CSA thanks Nick Achilleos, Fran Bagenal, Stan Cowley, Michele Dougherty, Caitríona Jackman, Margy Kivelson, Krishan Khurana, Chris Russell, Beth Semikin, David Southwood, and the Cassini CAPS, MAG, MIMI and RPWS teams for insightful discussions and comments on the manuscript, and both reviewers for useful comments.

References

Achilleos N, Arridge CS, Bertucci C, Jackman CM, Dougherty MK, Khurana KK, Russell CT, Crary FJ, Young DT (2008) Large-scale dynamics of Saturn's magnetopause: observations by Cassini. J Geophys Res 113:A11209. doi:10.1029/2008JA013265

Achilleos N, Guio P, Arridge CS (2010) A model of force balance in Saturn's magnetodisc. MNRAS 401(4):2349–2371. doi:10.1111/j.1365-2966.2009.15865.x

Andrews DJ, Bunce EJ, Cowley SWH, Dougherty MK, Provan G, Southwood DJ (2008) Planetary period oscillations in Saturn's magnetosphere: phase relation of equatorial magnetic field oscillations and Saturn kilometric radiation modulation. J Geophys Res 113:A09205. doi:10.1029/2007JA012937

Arridge CS, Achilleos N, Bertucci CL, Dougherty MK, Khurana KK, Russell CT (2006) Modeling the size and shape of saturn's magnetopause with variable dynamic pressure. J Geophys Res 111(A11):A11227. doi:10.1029/2005JA011574

Arridge CS, Russell CT, Khurana KK, Achilleos N, André N, Rymer AM, Dougherty MK (2007) The mass of Saturn's magnetodisc: Cassini observations. Geophys Res Lett 34(9):L09108. doi:10.1029/2006GL028921

Arridge CS, André N, Achilleos N, Khurana KK, Bertucci CL, Gilbert LK, Lewis GR, Coates AJ, Dougherty MK (2008a) Thermal electron periodicities at 20 RS in Saturn's magnetosphere. Geophys Res Lett 35:L15107. doi:10.1029/2008GL034132

Arridge CS, Khurana KK, Russell CT, Southwood DJ, Achilleos N, Dougherty MK, Coates AJ, Leinweber HK (2008b) Warping of Saturn's magnetospheric and magnetotail current sheets. J Geophys Res 113:A08217. doi:10.1029/2007JA012963

Arridge CS, Russell CT, Khurana KK, Achilleos N, Cowley SWH, Dougherty MK, Bunce EJ: (2008c) Saturn's magnetodisc current sheet. J Geophys Res 113:A04214. doi:10.1029/2007JA012540

Badman SV, Bunce EJ, Clarke JT, Cowley SWH, Gérard J-C, Grodent D, Milan SE (2005) Open flux estimates in Saturn's magnetosphere during the January 2004 Cassini-HST campaign, and implications for reconnection rates. J Geophys Res 110:A11216. doi:10.1029/2005JA011240

Bagenal F (1994) Empirical model of the Io plasma torus: voyager measurements. J Geophys Res 99(A6):11043–11062

Brandt PC, Khurana KK, Mitchell DG, Sergis N, Dialynas K, Carbary JF, Roelof EC, Paranicas CP, Krimigis SM, Mauk BH (2010) Saturn's periodic magnetic field perturbations caused by a rotating partial ring current. Geophys Res Lett 37:L22103. doi:10.1029/2010GL045285

Bunce EJ, Cowley SWH, Wright DM, Coates AJ, Dougherty MK, Krupp N, Kurth WS, Rymer A (2005) In-situ observations of a solar wind compression-induced hot plasma injection in Saturn's tail. Geophys Res Lett 32:L20S04. doi:10.1029/2005GL022888

Bunce EJ, Cowley SWH, Alexeev II, Arridge CS, Dougherty MK, Nichols JD, Russell CT (2007) Cassini observations of the variation of Saturn's ring current parameters with system size. J Geophys Res 112:A10202. doi:10.1029/2007JA012275

Bunce EJ, Arridge CS, Clarke JT, Coates AJ, Cowley SWH, Dougherty MK, Gérard J-C, Grodent D, Hansen KC, Nichols JD, Southwood DJ, Talboys DL (2008a) Origin of Saturn's aurora: simultaneous observations by Cassini and the Hubble Space Telescope. J Geophys Res 113:A09209. doi:10.1029/2008JA013257

Burch JL, Goldstein J, Mokashi P, Lewis WS, Paty C, Young DT, Coates AJ, Dougherty MK, André N (2008) On the cause of Saturn's plasma periodicity. Geophys Res Lett 35:L14105. doi:10.1029/2008GL034951

Burch JL, DeJong AD, Goldstein J, Young DT (2009) Periodicity in Saturn's magnetosphere: plasma cam. Geophys Res Lett 36:L14203. doi:10.1029/2009GL039043

Carbary JF, Mitchell DG, Krimigis SM, Hamilton DC, Krupp N (2007) Spin-period effects in magnetospheres with no axial tilt. Geophys Res Lett 34:L18107. doi:10.1029/2007GL030483

Carbary JF, Mitchell DG, Brandt P, Roelof EC, Krimigis SM (2008a) Periodic tilting of Saturn's plasma sheet. Geophys Res Lett 35:L24101. doi:10.1029/2008GL036339

Carbary JF, Mitchell DG, Paranicas C, Roelof EC, Krimigis SM (2008b) Direct observation of warping in the plasma sheet of Saturn. Geophys Res Lett 35:L24201. doi:10.1029/2008GL035970

Carr TD, Schauble JJ, Schauble CC (1981) Pre-encounter distributions of Saturn's low frequency radio emission. Nature 292:745–747

Clarke JT, Grodent D, Cowley SWH, Bunce EJ, Zarka P, Connerney JEP, Satoh T (2004) Jupiter's aurora. In: Bagenal F, Dowling TE, McKinnon WB (eds) Jupiter: the planet, satellites and magnetosphere. Cambridge University Press, Cambridge, pp 639–670

Clarke JT, Nichols JD, Gérard J-C, Grodent D, Hansen KC, Kurth W, Gladstone GR, Duval J, Wannawichian S, Bunce E, Cowley SWH, Crary F, Dougherty M, Lamy L, Mitchell D, Pryor W, Retherford K, Stallard T, Zieger B, Zarka P, Cecconi B (2009) Response of Jupiter's and Saturn's auroral activity to the solar wind. J Geophys Res 114:A05210. doi:10.1029/2008JA013694

Clarke KE, Andrews DJ, Arridge CS, Coates AJ, Cowley SWH, Dougherty MK (2010a) Magnetopause oscillations near the planetary period at Saturn: occurrence, phase and amplitude. J Geophys Res 115:A08209. doi:10.1029/2009JA014745

Clarke KE, Andrews DJ, Coates AJ, Cowley SWH, Masters A (2010b) Magnetospheric period oscillations of Saturn's bow shock. J Geophys Res 115:A05202. doi:10.1029/2009JA015164

Cowley SWH, Bunce EJ (2001) Origin of the main auroral oval in Jupiter's coupled magnetosphere-ionosphere system. Planet Space Sci 49:1067–1088. doi:10.1016/S0032-0633(00)00167-7

Cowley SWH, Nichols JD, Andrews DJ (2007) Modulation of Jupiter's plasma flow, polar currents, and auroral precipitation by solar wind-induced compressions and expansions of the magnetosphere: a simple theoretical model. Ann Geophys 25:1433–1463

Cowley SWH, Badman SV, Imber SM, Milan SE (2008a) Comment on ''Jupiter: A fundamentally different magnetospheric interaction with the solar wind'' by D. J. McComas and F. Bagenal. Geophys Res Lett 35:L10101. doi:10.1029/2007GL032645

Cowley SWH, Arridge CS, Bunce EJ, Clarke JT, Coates AJ, Dougherty MK, Gérard J-C, Grodent D, Nichols JD, Talboys DL (2008b) Auroral current systems in Saturn's magnetosphere: comparison of theoretical models with Cassini and HST observations. Ann Geophys 26(9):2613–2630

Delamere PA, Bagenal F, Dols V, Ray LC (2007) Saturn's neutral torus versus Jupiter's plasma torus. Geophys Res Lett 34:L09105. doi:10.1029/2007GL029437

Dessler AJ (1980) Corotating Birkeland currents in Jupiter's magnetosphere – an Io plasma-torus source. Planet Space Sci 28:781–788

Espinosa SA, Southwood DJ, Dougherty MK (2003) Reanalysis of Saturn's magnetospheric field data view of spin-periodic perturbations. J Geophys Res 108(A2):1085. doi:10.1029/2001JA005083

Freeman MP, Morley SK (2004) A minimal substorm model that explains the observed statistical distribution of times between substorms. Geophys Res Lett 31:L12807. doi:10.1029/2004GL019989

Fukazawa K, Ogino T, Walker RJ (2005) Dynamics of the jovian magnetosphere for northward interplanetary magnetic field (IMF). Geophys Res Lett 32:L03202. doi:10.1029/2004GL021392

Fukazawa K, Ogino T, Walker RJ (2006) Configuration and dynamics of the jovian magnetosphere. J Geophys Res 111:A10207. doi:10.1029/2006JA011874

Fukazawa K, Ogino T, Ogi S-I, Walker RJ (2007a) Magnetospheric convection at Saturn as a function of IMF B_z. Geophys Res Lett 34:L01105. doi:10.1029/2006GL028373

Fukazawa K, Ogino T, Walker RJ (2007b) Vortex-associated reconnection for northward IMF in the kronian magnetosphere. Geophys Res Lett 34:L23201. doi:10.1029/2007GL031784

Goertz CK (1979) The jovian magnetodisk. Space Sci Rev 23:319–343

Gombosi TI, Armstrong TP, Arridge CS, Khurana KK, Krimigis SM, Krupp N, Persoon AM, Thomsen MF (2009) Saturn's magnetospheric configuration. In: Dougherty MK, Esposito LW, Krimigis SM (eds) Saturn from Cassini-Huygens. pp 203–255. doi:10.1007/978-1-4020-9217-6_9 Springer

Gurnett DA, Persoon AM, Kurth WS, Groene JB, Averkamp TF, Dougherty MK, Southwood DJ (2007) The variable rotation period of the inner region of Saturn's plasma disk. Science 316:442. doi:10.1126/science.1138562

Gurnett DA, Lecacheux A, Kurth WS, Persoon AM, Groene JB, Lamy L, Zarka P, Carbary JF (2009) Discovery of a north-south asymmetry in Saturn's radio rotation period. Geophys Res Lett 36:L16102. doi:10.1029/2009GL039621

Hanlon PG, Dougherty MK, Krupp N, Hansen KC, Crary FJ, Young DT, Tóth G (2004) Dual spacecraft observations of a compression event within the jovian magnetosphere: signatures of externally triggered supercorotation? J Geophys Res 109:A09S09. doi:10.1029/2003JA010116

Hansen KC, Ridley AJ, Hospodarsky GB, Achilleos N, Dougherty MK, Gombosi TI, Tóth G (2005) Global MHD simulations of Saturn's magnetosphere at the time of Cassini approach. Geophys Res Lett 32:L20S06. doi:10.1029/2005GL022835

Hill TW (2001) The Jovian auroral oval. J Geophys Res 106(A5):8101–8107

Hill TW, Dessler AJ, Michel FC (1974) Configuration of the Jovian magnetosphere. Geophys Res Lett 1(1):3–6

Hill TW, Thomsen MF, Henderson MG, Tokar RL, Coates AJ, McAndrews HJ, Lewis GR, Mitchell DG, Jackman CM, Russell CT, Dougherty MK, Crary FJ, Youn DT (2008) Plasmoids in Saturn's magnetotail. J Geophys Res 113:A01214. doi:10.1029/2007JA012626

Huddleston DE, Russell CT, Le G, Szabo A (1997) Magnetopause structure and the role of reconnection at the outer planets. J Geophys Res 102(A11):24289–24302

Huddleston DE, Russell CT, Kivelson MG, Khurana KK, Bennett L (1998) Location and shape of the jovian magnetopause and bow shock. J Geophys Res 103(E9):20075–20082. doi:10.1029/98JE00394

Jackman CM, Achilleos N, Bunce EJ, Cowley SWH, Dougherty MK, Jones GH, Milan SE, Smith EJ (2004) Interplanetary magnetic field at ~9 AU during the declining phase of the

solar cycle and its implications for Saturn's magnetospheric dynamics. J Geophys Res 109(1):A11203

Jackman CM, Russell CT, Southwood DJ, Arridge CS, Achilleos N, Dougherty MK (2007) Strong rapid dipolarizations in Saturn's magnetotail: in situ evidence of reconnection. Geophys Res Lett 34:L11203. doi:10.1029/2007GL029764

Jackman CM, Arridge CS, Krupp N, Bunce EJ, Mitchell DG, McAndrews HJ, Dougherty MK, Russell CT, Achilleos N, Jones GH, Coates AJ (2008) A multi-instrument view of tail reconnection at Saturn. J Geophys Res 113:A11213. doi:10.1029/2008JA013592

Jackman CM, Arridge CS, McAndrews HJ, Henderson MG, Wilson RJ (2009) Northward field excursions in Saturn's magnetotail and their relationship to magnetospheric periodicities. Geophys Res Lett 36(16):L16101. doi:10.1029/2009GL039149

Jackman CM, Arridge CS, Slavin JA, Milan SE, Lamy L, Dougherty MK, Coates AJ (2010) In situ observations of the effect of a solar wind compression on Saturn's magnetotail. J Geophys Res 115:A10240. doi:10.1029/2010JA015312

Kanani SJ, Arridge CS, Jones GH, Fazakerley AN, McAndrews HJ, Sergis N, Krimigis SM, Dougherty MK, Coates AJ, Young DT, Hansen KC, Krupp N (2010) A new form of Saturn's magnetopause using a dynamic pressure balance model, based on in-situ, multi-instrument Cassini measurements. J Geophys Res 115:A06207. doi:10.1029/2009JA014262

Kellett S, Arridge CS, Bunce EJ, Coates AJ, Cowley SWH, Dougherty MK, Persoon AM, Sergis N, Wilson RJ (2010) Nature of the ring current in Saturn's dayside magnetosphere. J Geophys Res 115:A08201. doi:10.1029/2009JA015146

Khurana KK (1992) A generalized hinged-magnetodisc model of Jupiter's nightside current sheet. J Geophys Res 97:6269–6276

Khurana KK (2001) Influence of solar wind of Jupiter's magnetosphere deduced from currents in the equatorial plane. J Geophys Res 106(A11):25999–26016

Khurana KK, Dougherty MK, Russell CT, Leisner JS (2007) Mass loading of Saturn's magnetosphere near Enceladus. J Geophys Res 112:A08203. doi:10.1029/2006JA012110

Khurana KK, Mitchell DG, Arridge CS, Dougherty MK, Russell CT, Paranicas C, Krupp N, Coates AJ (2009) Sources of rotational signals in Saturn's magnetosphere. J Geophys Res 114:A02211. doi:10.1029/2008JA013312

Kidder A, Winglee RM, Harnett EM (2009) Regulation of the centrifugal interchange cycle in Saturn's inner magnetosphere. J Geophys Res 114:A02205. doi:10.1029/2008JA013100

Krimigis SM, Sergis N, Mitchell DG, Hamilton DC, Krupp N (2007) A dynamic rotating ring current around Saturn. Nature 450(7172):1050–1053. doi:10.1038/nature06425

Kronberg EA, Woch J, Krupp N, Lagg A, Khurana KK, Glassmeier K-H (2005) Mass release at Jupiter: substorm-like processes in the jovian magnetotail. J Geophys Res 110:A03211. doi:10.1029/2004JA010777

Kronberg EA, Glassmeier K-H, Woch J, Krupp N, Lagg A, Dougherty MK (2007) A possible intrinsic mechanism for the quasi-periodic dynamics of the jovian magnetosphere. J Geophys Res 112:A05203. doi:10.1029/2006JA011994

Krupp N, Vasyliūnas VM, Woch J, Lagg A, Khurana KK, Kivelson MG, Mauk BH, Roelof EC, Williams DJ, Krimigis SM, Kurth WS, Frank LA, Paterson WR (2004) Dynamics of the Jovian Magnetosphere. In: Bagenal F, Dowling TE, McKinnon WB (eds) Jupiter. The planet, satellites and magnetosphere. Cambridge University Press, Cambridge, pp 617–638

Krupp N et al (2005) The saturnian plasma sheet as revealed by energetic particle measurements. Geophys Res Lett 32:L20S03. doi:10.1029/2005GL022829

Kurth WS, Averkamp TF, Gurnett DA, Groene JB, Lecacheux A (2008) An update to a Saturnian longitude system based on kilometric radio emissions. J Geophys Res 113:A05222. doi:10.1029/2007JA012861

Kurth WS, Bunce EJ, Clarke JT, Crary FJ, Groden DC, Ingersoll AP, Dyudina UA, Lamy L, Mitchell DG, Persoon AM, Pryor WR, Saur J, Stallard T (2009) Auroral processes. In: Dougherty MK, Esposito LW, Krimigis SM (eds) Saturn from Cassini-Huygens. Springer, Berlin, pp 333–374. doi:10.1007/978-1-4020-9217-6_12

Leisner JS, Russell CT, Khurana KK, Dougherty MK (2007) Measuring the stress state of the Saturnian magnetosphere. Geophys Res Lett 34:L12103. doi:10.1029/2007GL029315

Mauk BH, Krimigis SM (1987) Radial force balance within Jupiter's dayside magnetosphere. J Geophys Res 92(A9):9931–9941

Mauk BH, Krimigis SM, Lepping RP (1985) Particle and field stress balance within a planetary magnetosphere. J Geophys Res 90(A9):8253–8264

McAndrews HJ, Owen C, Thomsen MF, Lavraud B, Coates AJ, Dougherty MK, Young DT (2008) Evidence for reconnection at Saturn's magnetopause. J Geophys Res 113:A04210. doi:10.1029/2007JA012581

McComas DJ, Bagenal F (2007) Jupiter: a fundamentally different magnetospheric interaction with the solar wind. Geophys Res Lett 34:L20106. doi:10.1029/2007GL031078

McComas DJ, Bagenal F (2008) Reply to comment by S. W. H. Cowley et al. on 'Jupiter: A fundamentally different magnetospheric interaction with the solar wind'. Geophys Res Lett 35:L10103. doi:10.1029/2008GL034351

McNutt RL (1984) Force balance in outer planet magnetosphere. In: Belcher J, Bridge H, Change T, Coppi B, Jasperse J (eds) Physics of space plasmas. Proceedings of the 1982–1984 MIT symposia, number 5 in SPI conference proceedings and reprint series. Scientific Publishers, Cambridge, MA, pp 179–210

Menietti JD, Groene JB, Averkamp TF, Hospodarsky GG, Kurth WS, Gurnett DA, Zarka P (2007) Influence of saturnian moons on Saturn kilometric radiation. J Geophys Res 112:A08211. doi:10.1029/2007JA012331

Milan SE, Bunce EJ, Cowley SWH, Jackman CM (2005) Implications of rapid planetary rotation for the Dungey magnetotail of Saturn. J Geophys Res 110:A03209. doi:10.1029/2004JA010716

Mitchell DG, Carbary JF, Cowley SWH, Hill TW, Zarka P (2009a) The dynamics of saturn's magnetosphere. In: Dougherty MK, Esposito LW, Krimigis SM (eds) Saturn from Cassini-Huygens. Springer, Berlin, pp 257–280. doi:10.1007/978-1-4020-9217-6_10

Mitchell DG, Krimigis SM, Paranicas C, Brandt PC, Carbary JF, Roelof EC, Kurth WS, Gurnett DA, Clarke JT, Nichols JD, Gérard J-C, Grodent DC, Dougherty MK, Pryor WR (2009b) Recurrent energization of plasma in the midnight-to-dawn

quadrant of Saturn's magnetosphere, and its relationship to auroral UV and radio emissions. Planet Space Sci 57(14–15):1732–1742. doi:10.1016/j.pss.2009.04.002

Miyoshi T, Kusano K (1997) MHD simulation of a rapidly rotating magnetosphere interacting with the external plasma flow. Geophys Res Lett 24(21):2627–2630. doi:10.1029/97GL52739

Miyoshi T, Kusano K (2001) A global MHD simulation of the jovian magnetosphere interacting with/without the interplanetary magnetic field. J Geophys Res 106(A6):10723–10742

Moriguchi T, Nakamizo A, Tanaka T, Obara T, Shimazu H (2008) Current systems in the jovian magnetosphere. J Geophys Res 113:A05204. doi:10.1029/2007JA012751

Morooka MW, Modolo R, Wahlund J-E, André M, Eriksson AI, Persoon AM, Gurnett DA, Kurth WS, Coates AJ, Lewis GR, Khurana KK, Dougherty M (2009) The electron density of Saturn's magnetosphere. Ann Geophys 27:2971–2991

Nichols JD, Cowley SWH, McComas DJ (2006) Magnetopause reconnection rate estimates for Jupiter's magnetosphere based on interplanetary measurements at ∼5AU. Ann Geophys 24(1):393–406

Nichols JD, Clarke JT, Cowley SWH, Duval J, Farmer AJ, Gérard JC, Grodent D, Wannawichian S (2008) Oscillation of Saturn's southern auroral oval. J Geophys Res 113:A11205. doi:10.1029/2008JA013444

Paranicas CP, Mauk BH, Krimigis SM (1991) Pressure anisotropy and radial stress balance in the jovian neutral sheet. J Geophys Res 96(A12):21135–21140

Pontius DH (1995) Implications of variable mass loading in the Io torus: the jovian flywheel. J Geophys Res 100(A10):19531–19539

Provan G, Andrews DJ, Arridge CS, Coates AJ, Cowley SWH, Milan SE, Dougherty MK, Wright DM (2009) Polarization and phase of planetary period oscillations on high latitude field lines in Saturn's magnetosphere. J Geophys Res 114:A02225. doi:10.1029/2008JA013782

Russell CT, Khurana KK, Huddleston DE, Kivelson MG (1998) Localized reconnection in the near jovian magnetotail. Science 280:1061

Russell CT, Huddleston DE, Khurana KK, Kivelson MG (1999) Observations at the inner edge of the jovian current sheet: evidence for a dynamic magnetosphere. Planet Space Sci 47:521–527

Russell CT, Jackman CM, Wei HY, Bertucci C, Dougherty MK (2008) Titan's influence of saturnian subsstorm occurrence. Geophys Res Lett 35:L12105. doi:10.1029/2008GL034080

Russell CT, Dougherty MK (2009) Magnetic fields of the outer planets. Space Sci Rev doi:10.1007/s11214-009-9621-7

Sandal BR, Dessler AJ (1988) Dual periodicity of the jovian magnetosphere. J Geophys Res 93:5487–5504

Saur J, Schilling N, Neubauer FM, Strobel DF, Simon S, Dougherty MK, Russell CT, Pappalardo RT (2008) Evidence for temporal variability of Enceladus' gas jets: modeling of Cassini observations. Geophys Res Lett 35:L20105. doi:10.1029/2008GL035811

Sergis N, Krimigis SM, Roelof EC, Arridge CS, Rymer AM, Mitchell DG, Hamilton DC, Krupp N, Thomsen MF, Dougherty MK, Coates AJ, Young DT(2010) Particle pressure, inertial force, and ring current density profiles in the magnetosphere of Saturn, based on Cassini measurements. Geophys Res Lett 37:L02102. doi:10.1029/2009GL041920

Shue J-H, Chao JK, Fu HC, Russell CT, Song P, Khurana KK, Singer HJ (1997) A new functional form to study the solar wind control of the magnetopause size and shape. J Geophys Res 102(A5):9497–9512

Slavin JA, Smith EJ, Spreiter JR, Stahara SS (1985) Solar wind flow about the outer planets – Gas dynamic modelling of the Jupiter and Saturn bow shocks. J Geophys Res 90:6275–6286

Smith EJ, Davis L Jr, Jones DE, Coleman PJ Jr, Colburn DS, Dyal P, Sonett CP, Frandsen AMA (1974) The planetary magnetic field and magnetosphere of Jupiter: Pioneer 10. J Geophys Res 79:3501–3513. doi:10.1029/JA079i025p03501

Smith EJ, Davis L Jr, Jones DE, Coleman PJ, Colburn DS, Dyal P, Sonett CP (1980) Saturn's magnetosphere and its interaction with the solar wind. J Geophys Res 85(A11):5655–5674

Southwood DJ, Kivelson MG (2001) A new perspective concerning the influence of the solar wind on Jupiter. J Geophys Res 106:6123

Southwood DJ, Kivelson MG (2007) Saturnian magnetospheric dynamics: elucidation of a camshaft model. J Geophys Res 112:A12222. doi:10.1029/2007JA012254

Spencer JR, Schneider NM (1996) Io on the eve of the Galileo mission. Annu Rev Earth Planet Sci 24:125–190

Stallard TS, Miller S, Cowley SWH, Bunce EJ (2003) Jupiter's polar ionospheric flows: measured intensity and velocity variations poleward of the main auroral oval. Geophys Res Lett 30(5):1221. doi:10.1029/2002GL016031

Vasyliūnas VM (1983) Plasma distribution and flow. In: Dessler AJ (ed) Physics of the jovian magnetosphere. Cambridge University Press, Cambridge, pp 395–453

Vasyliūnas VM (2008) Comparing Jupiter and Saturn: dimensionless input rates from plasma sources within the magnetosphere. Ann Geophys 26:1341–1343

Vasyliūnas VM, Dessler AJ (1981) The magnetic-anomaly model of the jovian magnetosphere: A post-Voyager assessment. J Geophys Res 86:8435–8446

Waldrop LS, Fritz TA, Kivelson MG, Khurana K, Krupp N, Lagg A (2005) Jovian plasma sheet morphology: particle and field observations by the Galileo spacecraft. Planet Space Sci 53:681–692

Walker RJ, Ogino T (2003) A simulation study of currents in the Jovian magnetosphere. Planet Space Sci 51:295–307

Walker RJ, Ogino T, Kivelson MG (2001) Magnetohydrodynamic simulations of the effects of the solar wind on the jovian magnetosphere. Planet Space Sci 49:237–245

Weiss JW (2004) Appendix 2: planetary parameters. In: Bagenal F, Dowling TE, McKinnon WB (eds) Jupiter: the planet, satellites and magnetosphere. Cambridge University Press, Cambridge, pp 699–706

Wu H (2009) Rice convection model simulations of the centrifugal interchange instability in the magnetospheres of Jupiter and Saturn, PhD thesis, Rice University, ISBN: 9781109218008

Zieger B, Hansen KC, Gombosi TI, De Zeeuw DL (2010) Periodic plasma escape from the mass-loaded kronian magnetosphere. J Geophys Res 115:A08208. doi:10.1029/2009JA014951

Lunar Plasma Environment

20

Yoshifumi Saito, Masaki N. Nishino, Shoichiro Yokota, Takaaki Tanaka, Tadateru Yamamoto, Kazushi Asamura, Hideo Tsunakawa, Hidetoshi Shibuya, Hisayoshi Shimizu, Futoshi Takahashi, and Masaki Matsushima

Abstract

The Moon has no global intrinsic magnetic field and thick atmosphere. These properties of the Moon significantly affect the interaction between the solar wind and the Moon. Recent in-situ measurements of low energy ions around the Moon by Kaguya (SELENE) have revealed dynamic aspect of the lunar plasma environment. Besides the solar wind, there exist four clearly distinguishable ion populations on the dayside of the Moon: (1) solar wind protons backscattered at the lunar surface, (2) solar wind protons reflected by magnetic anomalies on the lunar surface, (3) reflected/backscattered protons picked-up by the solar wind, 4) ions originating from the lunar surface/lunar exosphere. In the lunar wake region, two types of ion entry into the lunar wake (Type-I entry and Type-II entry) are observed. The newly obtained knowledge about the lunar plasma environment by Kaguya can be applied to the understanding of the plasma environment around non-magnetized solar system objects.

20.1 Introduction

The interaction between the solar wind and an object in the solar system varies according to the object's properties, such as the existence of a global intrinsic magnetic field and/or thick atmosphere. The Moon's case is characterized by the absence of both properties. Although the Moon is the celestial object nearest Earth, understanding of its plasma environment, including its interaction with the solar wind, was insufficient. One of the major reasons was that we had only significantly limited information about the low energy ions around the Moon due to the lack of in-situ observations. The lunar plasma environment was monitored by the lunar orbiters and landers in the 1960s and 1970s (Anderson et al. 1972; Clay et al. 1972; Colburn et al. 1967; Hills et al. 1972; Howe et al. 1974; Lyon et al. 1967; Neugebauer et al. 1972). After the 1990s, three-dimensional low energy electron measurements by Lunar Prospector revealed the lunar plasma environment, including plasma interactions with crustal magnetic fields, surface charging, and wake structure (Halekas et al. 2001, 2002, 2005, 2008, 2009a, b; Lin et al. 1998). The Wind spacecraft during its Moon fly-by showed features of the lunar wake (Ogilvie et al. 1996). Remote detection of lunar

Y. Saito (✉)
Institute of Space and Astronautical Science, Japan Aerospace Exploration Agency, Sagamihara, Kanagawa, Japan
e-mail: saito@stp.isas.jaxa.jp

W. Liu, M. Fujimoto (eds.), *The Dynamic Magnetosphere*, IAGA Special Sopron Book Series 3,
DOI 10.1007/978-94-007-0501-2_20, © Springer Science+Business Media B.V. 2011

ions by AMPTE/IRM (Hilchenbach et al. 1993), Wind (Mall et al. 1998), and Nozomi (Futaana et al. 2003), lunar electrons by Nozomi (Futaana et al. 2001), and of ULF waves generated by electron beams around the lunar wake by Geotail (Nakagawa et al. 2003) were also reported.

MAP-PACE (MAgnetic field and Plasma experiment – Plasma energy Angle and Composition Experiment) on Kaguya was developed in order to make comprehensive three-dimensional plasma measurements around the Moon (Saito et al. 2007, 2008a). Especially, low energy ion measurements on a lunar orbit were realized more than 30 years after the Apollo period. Kaguya was successfully launched on 14 September 2007 by the H2A launch vehicle from Tanegashima Space Center in Japan. Kaguya was inserted into a circular lunar polar orbit of 100 km altitude and continued observations for nearly 1.5 years until it hit the Moon on 10 June 2009. During the last 5 months, the orbit was lowered to ~50 km altitude between January 2009 and April 2009 and some orbits had an even lower perilune altitude of ~10 km after April 2009. MAP-PACE consists of 4 sensors: ESA (Electron Spectrum Analyzer)-S1, ESA-S2, IMA (Ion Mass Analyzer), and IEA (Ion Energy Analyzer). ESA-S1 and S2 measured the distribution function of low energy electrons in the energy range of 6 eV–9 keV and 9 eV–16 keV, respectively. IMA and IEA measured the distribution function of low energy ions in the energy range of 7 eV/q–28 keV/q and 7 eV/q–29 keV/q. IMA is an LEF-TOF (Linear Electric Field –Time Of Flight) energy mass spectrometer capable of identifying ion species with mass up to ~60 atomic mass units (Yokota et al. 2005). Since Kaguya is a three-axis stabilized spacecraft that keeps one of its spacecraft panels (+Z panel) facing the Moon, a pair of sensors (ESA-S1 and ESA-S2 for electrons and IMA and IEA for ions), having hemispherical fields of view in opposite directions to each other, are necessary for obtaining three-dimensional particle distribution functions as shown in Fig. 20.1.

Following the launch of Kaguya, two Asian Moon orbiters Chinese Chang'E-1 and Indian Chandrayaan-1 were launched on October 24, 2007 and October 22, 2008, respectively. Solar Wind Ion Detector (SWID) on Chang'E-1 and Solar Wind Ion Monitor (SWIM) on Chandrayaan-1 (Wieser et al. 2009) also observed low energy ions around the Moon.

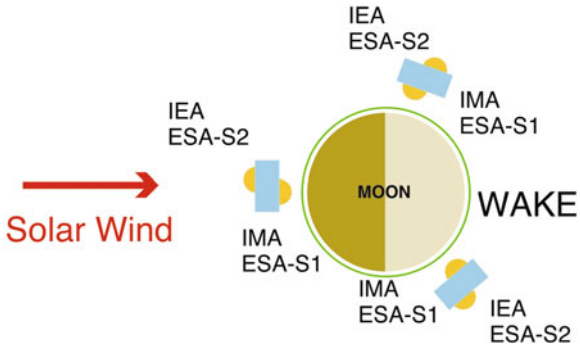

Fig. 20.1 Field of view of the PACE sensors. Since ESA-S1 and IMA were installed on the spacecraft panel facing the Moon surface, ESA-S1 and IMA mostly measured electrons and ions propagating away from the Moon. On the other hand, ESA-S2 and IEA which were installed on the opposite spacecraft panel mostly measured electrons and ions going towards the Moon. Note that solar wind ions were detected by IEA or IMA depending on the position of the spacecraft. While IEA measured solar wind ions on the dayside, IMA measured solar wind ions near the day-night terminator line

20.2 Ion Populations Around the Moon

20.2.1 Ion Populations on the Dayside of the Moon

Figure 20.2a summarizes the newly observed low energy ion populations on the dayside of the Moon at 100 km altitude. The newly observed ion populations comprise the four following components: (1) solar wind protons backscattered at the lunar surface, (2) solar wind protons reflected by magnetic anomalies on the lunar surface, (3) reflected/backscattered protons picked-up by the solar wind, and (4) ions originating from the lunar surface/lunar exosphere. In the following sections, we will describe these four populations in detail.

20.2.1.1 Solar Wind Proton Scattering at the Lunar Surface

Saito et al. (2008a) found that about 0.1 to 1% of the incident solar wind ions were backscattered instead of being perfectly absorbed by the lunar surface. As indicated in Fig. 20.2a and b, the backscattered ions had lower energy than the incident solar wind ions since part of the energy was lost when solar wind ions collided with the Moon. Although the solar wind consists of alpha particles as a second major component, it was found that the backscattered ions consisted of almost

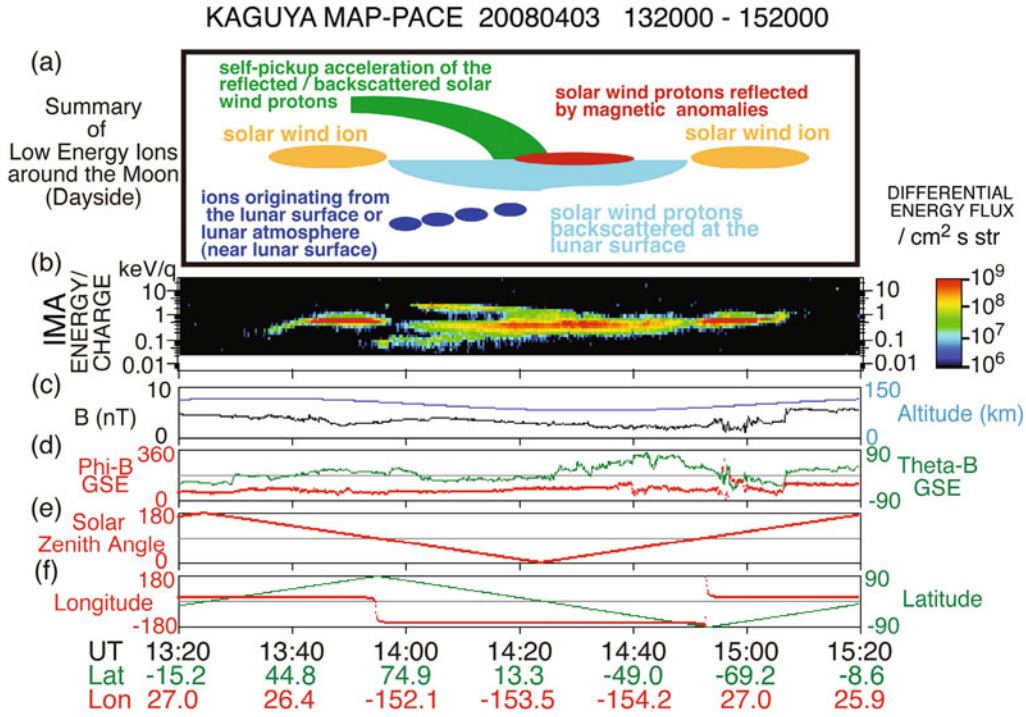

Fig. 20.2 Panel (**a**) shows a summary of low-energy ion population on the dayside of the Moon. Panel (**b**) is an omni-directional E-t spectrogram from IMA. The vertical scale is the energy of ions while the horizontal axis is time. The color of each bin depicts the ion differential energy flux in each energy bin at the time of observations. All the populations shown in Panel (**a**) can be found in Panel (**b**). Panels (**c**) and (**d**) are altitude of Kaguya, magnetic field intensity and direction in the Geocentric Solar Ecliptic (GSE) polar coordinate system observed by MAP-LMAG (Shimizu et al. 2008; Takahashi et al. 2009). Panels (**e**) and (**f**) show the solar zenith angle and latitudinal/longitudinal position of Kaguya in the Mean Earth/Polar Axis (ME) coordinate system

no alpha particles. While the maximum energy of these ions was constant at slightly lower than the solar wind proton energy, the width of the energy distribution varied gradually, so that the minimum energy was larger at high latitudes than at the equator. It indicates that the energy loss is large when the solar wind impacts the Moon vertically, while the energy loss is small when the solar wind impacts the Moon tangentially.

20.2.1.2 Solar Wind Proton Reflection by Magnetic Anomalies on the Lunar Surface

When Kaguya flew over magnetic anomalies, solar wind ions reflected by magnetic anomalies were observed. As indicated in Fig. 20.2a and b, these magnetically reflected ions had nearly the same energy as the incident solar wind ions. The flux of the magnetically reflected solar wind ions was much higher than the backscattered solar wind ions and was more than 10% of the incident solar wind ions. When magnetically reflected ions were observed, the electrons measured simultaneously were often heated and the incident solar wind ions were sometimes slightly decelerated.

20.2.1.3 Self-Pickup Acceleration of the Reflected/Scattered Solar Wind Protons

The third characteristic ion population found by the MAP-PACE ion sensors is solar wind ions that are backscattered or magnetically reflected and then accelerated. Since there exists a solar wind convection electric field seen from the rest frame of the Moon, the backscattered and magnetically reflected solar wind ions are accelerated by the electric field (see Fig. 20.2a and b). Saito et al. (2008b) showed the acceleration of backscattered solar wind protons for the first time and they named the acceleration as "self-pickup acceleration". This acceleration process should be common to backscattered solar wind ions

and magnetically reflected solar wind ions. Since the backscattered/magnetically reflected solar wind ions have initial velocities that are lower than or equal to the incident solar wind ions, the maximum possible acceleration is three times the solar wind velocity, which is different from the pickup acceleration of the ionized neutral particles that have been observed around comets where the maximum acceleration is twice the solar wind velocity (Coates 2004; Mukai et al. 1986).

20.2.1.4 Ions Originating from the Moon Surface/Lunar Exosphere

In the Solar Wind

Yokota et al. (2009) reported the first in situ detection of alkali ions originating from the Moon surface/exosphere. The ions generated on the lunar surface by solar wind sputtering, solar photon stimulated desorption, or micro-meteorite vaporization are accelerated by the solar wind convection electric field and detected by IMA. As indicated in Fig. 20.2, these ions have the characteristic that the energy is lowest in polar regions (high latitude region) and their energy gradually increased as the spacecraft moved from the polar region to equator region. The ions were observed in only one of the hemispheres. The source region of these ions was the dayside lunar surface or lunar exosphere. The ions generated were accelerated by the solar wind convection electric field. Since the acceleration distance was longer for the ions detected in the equatorial region than the ions detected in the polar region, the observed energy of the ions was higher in the equatorial region than in the polar region. The ions were not observed in one of the hemispheres because the direction of the solar wind convection electric field was toward the lunar surface in that hemisphere. Figure 20.3 shows an example of the mass profile of these ions. We can find peaks for the heavy ions including C^+, O^+, Na^+, K^+ and Ar^+.

In the Earth's Magnetosphere (Lobe)

In addition to the observation of ions originating from the Moon surface/exosphere in the solar wind, IMA also found ions originating from the Moon surface/exosphere in the Earth's magnetosphere (Tanaka et al. 2009). Figure 20.4 shows an example of these ions (indicated by white arrows). These ions were observed when the Moon was in the magnetospheric lobe, on the dayside of the Moon. The mass profile of these ions show peaks for the heavy ions including C^+, O^+, Na^+, K^+, and Ar^+ similarly to the ions originating from the Moon surface/exosphere observed in the solar wind. It was quite surprising that ions were generated in the lobe where no intense ion flux impacting the lunar surface such as the solar wind ion flux or plasma sheet ion flux existed. It clearly indicates that lunar alkali ions can be generated by mechanisms

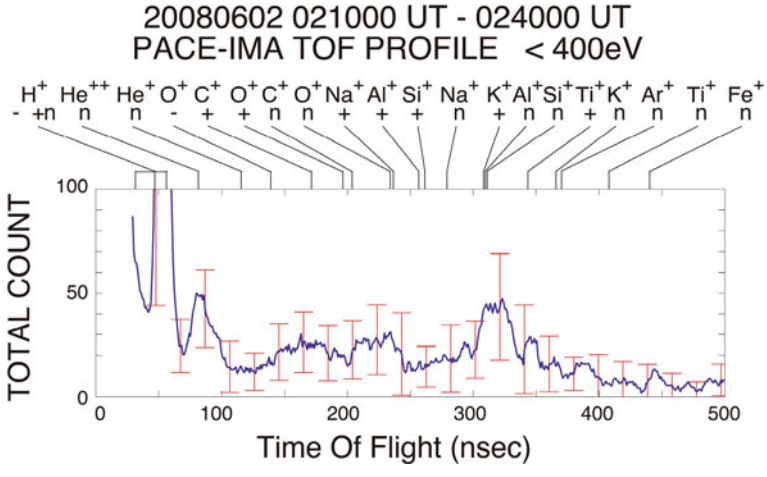

Fig. 20.3 Mass profile of the ions originating from the Moon surface/exosphere. The data below 400 eV/q obtained between 02:10:00UT and 02:40:00UT on 2 June 2008 are added up. The blue line shows 10.7nsec (11 data) running averaged TOF data with statistical error bars (red lines) at 68% confidence level. The TOF of ions determined by laboratory calibration and/or numerical simulation are also shown. The letters "-", "+", and "n" below the ion species indicate the charge state of incident ions, negative, positive or neutral, respectively, after exiting the carbon foil. Although the TOF varies slightly with energy, the indicated TOF is for ions with energy of 100 eV/q

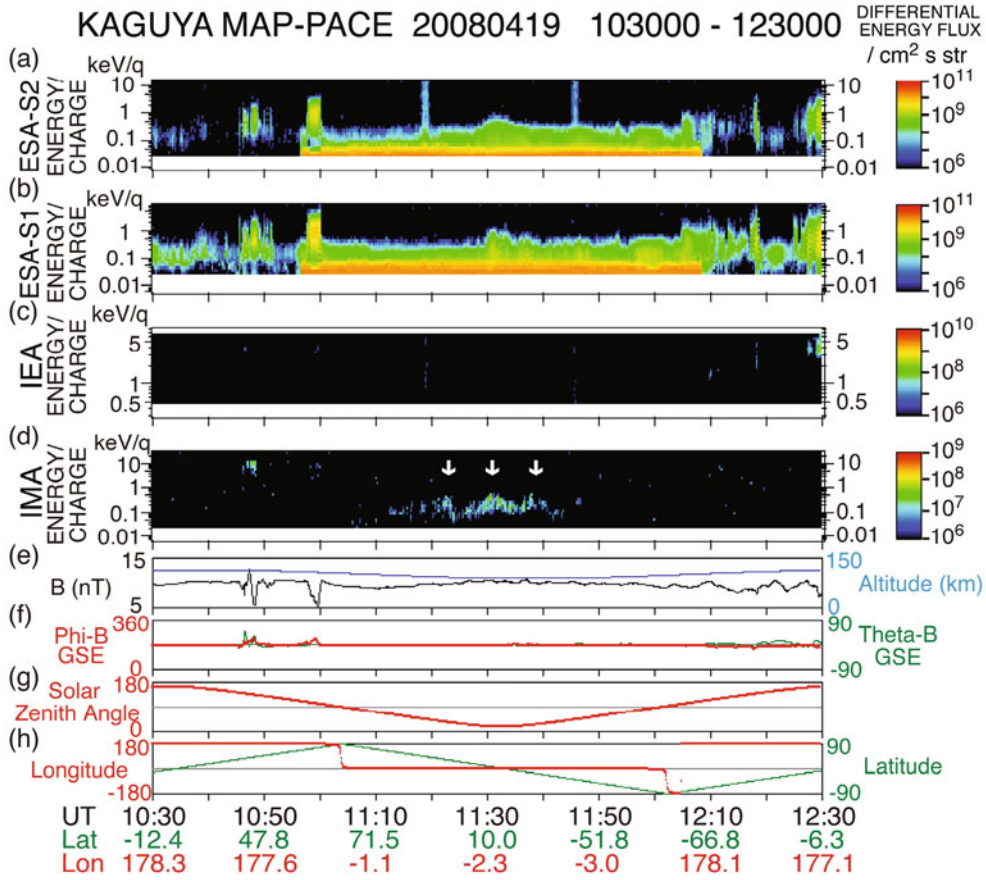

Fig. 20.4 Ions originating from the Moon surface/exosphere observed in the Earth's magnetosphere (lobe) (indicated by *white arrows*) observed on 19 April, 2008. Panels (**a**)–(**d**) are omni-directional E-t spectrograms from the PACE sensors. Panels (**e**)–(**f**) show altitude of Kaguya, magnetic field intensity and direction in GSE coordinates. Panels (**g**)–(**h**) show solar zenith angle and latitudinal/longitudinal position of Kaguya in ME coordinates

other than solar wind ion sputtering, for example, photon stimulated desorption. It was also surprising that the ions originating from the Moon surface/exosphere were accelerated to Kaguya in the lobe region where the convection electric field should be much weaker than in the solar wind. These ions were possibly accelerated by the potential difference between the lunar surface and Kaguya.

20.2.2 Ion Populations on the Night Side of the Moon

20.2.2.1 Solar Wind Type I Entry into the Lunar Wake

Type-I entry is a phenomenon of solar wind proton entry due to its thermal motion and ambipolar electric field around the wake boundary, and it depends on the direction of the Interplanetary Magnetic Field (IMF) (Nishino et al. 2009a). A typical type-I entry event was observed on April 3, 2008. On this day the Moon was located at $(X, Y, Z) = (48, -34, 1)\ R_E$ in GSE, being exposed to the solar wind flow upstream of the Earth's bow shock. The Kaguya spacecraft flew near the noon-midnight meridian plane, orbiting from south to north through the tenuous wake on the night side, and then went southward on the dayside. Kaguya observed solar wind flows near both poles around 12:55 UT and 13:50 UT (Fig. 20.5a). Between 12:56 and 13:12 UT a gradual increase in proton energy from ~0.5 keV to ~0.9 keV was observed around the southern wake boundary. The spacecraft passed the boundary between sunlit and shaded regions at 72°S (Solar Zenith Angle (SZA) ~108°) at 13:01 UT and the spacecraft location

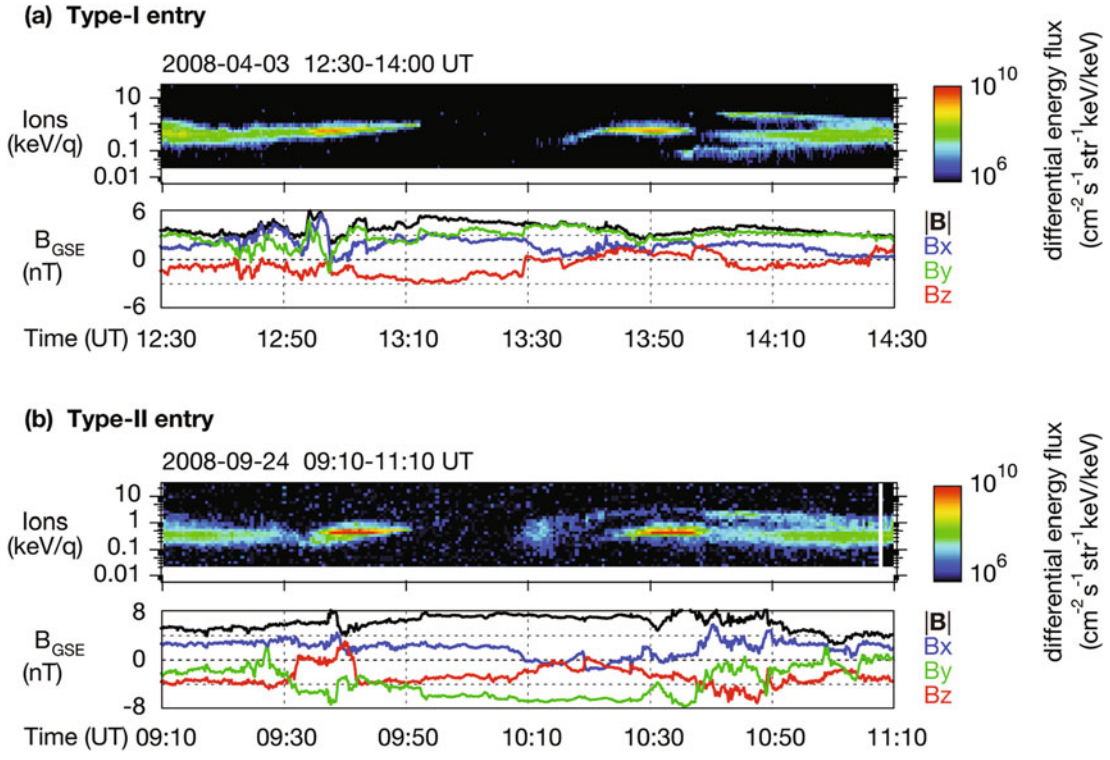

Fig. 20.5 Typical events of type-I and type-II entry. (**a**) Energy-time spectrum from IMA and magnetic field data in GSE coordinates between 12:30 and 14:30 UT on April 3, 2008, and (**b**) data for 09:10–11:10 UT on September 24, 2008 are presented

at 13:12 UT was at 38°S (SZA ∼142°), which means that the solar wind protons intruded deep into the wake. After Kaguya stayed in the almost vacuum region in the deep wake, it began to detect protons whose energy was as low as ∼0.2 keV around 13:35 UT when the spacecraft was located at lat.∼ 32°N (SZA ∼148°). The energy of protons gradually increased to the level of the original solar wind flow until 13:45 UT. These observations show that the solar wind protons gain (lose) kinetic energy in the southern (northern) hemisphere around the wake boundary as they intrude deep into the wake.

In this event, the IMF was dominated by positive B_Y that is the controlling factor of the phenomenon. During other intervals, similar energy gain/loss features were observed and their location was dependent on the IMF; when the IMF B_Y is positive (negative), the energy gain is found in the southern (northern) hemisphere. The energy gain/loss of the protons is due to acceleration/deceleration by the ambipolar (inward) electric field around the wake boundary, which generally occurs when the non-radial component of the IMF is dominant.

20.2.2.2 Solar Wind Type II Entry into the Lunar Wake

Type-II entry is related to proton scattering/reflection on the lunar dayside. A portion of self-pickup protons can come into the deepest wake due to their large gyro radius (Nishino et al. 2009b). This mechanism also strongly depends on the IMF direction. On 24 September 2008 the Moon was located at (X, Y, Z) = (28, −51, 1) R_E in GSE, interacting with the solar wind flow upstream of the Earth's bow shock. The solar wind speed observed by the Wind spacecraft was ∼300 km/s (∼0.47 keV for protons), and the IMF whose strength was about 5 nT was dominated by the negative B_Y component. On this day the Kaguya spacecraft flew near the noon-midnight meridian plane, orbiting from south to north on the dayside and going through the tenuous wake on the night side. We examine proton signatures observed by Kaguya between 09:10 and 11:10 UT. Before 09:38 UT the protons scattered at the lunar dayside surface (Saito et al. 2008b) were detected by IMA (Fig. 20.5b). The spacecraft passed above the North Pole at 09:37 UT and crossed the terminator at 09:44 UT. Between

09:36 and 09:51 UT Kaguya observed solar wind proton entry near the North Pole, which is categorized into the type-I entry. After Kaguya passed through the almost vacuum region in the northern hemisphere, it began to detect protons around 10:08 UT in the deepest wake (SZA 168°) solar wind protons that are not anticipated to access via the type-I entry. These protons were indeed reflected on the dayside and came into the deepest wake (see the original paper for the details, Nishino et al. 2009b). The proton flux in the deep wake was the largest around 10:12 UT, and its energy ranged broadly between 0.1 and 1 keV. Between 10:20 and 10:40 UT the proton energy was higher than the original solar wind energy, and peaked at ∼3 keV around 10:34–10:38 UT near the South Pole. The increase in energy (factor ∼6) over the solar wind is consistent with the previous observations of self-pickup protons (Saito et al. 2008b).

When the protons were observed in the deep wake, the magnetic field was dominated by the B_Y component (Fig. 20.5b). The averaged magnetic field between 10:08 and 10:30 UT was (–0.3, –6.7, –1.4) nT, which means that both ends of the magnetic field at the Kaguya locations would be connected to the solar wind. Besides this event, similar proton entry into the deepest wake was at times observed under the non-radially directed IMF condition. The type-II entry is an important mechanism that forms proton-governed region in the wake region.

Conclusion

One of the scientific instruments on Kaguya, MAP-PACE, has completed its ∼1.5 years of observation of low energy charged particles around the Moon from a ∼100 km altitude (and below) polar orbit. The newly observed data showed characteristic ion populations on the dayside of the Moon. The MAP-PACE sensors also found new low energy ion/electron populations in the lunar wake region. By analyzing the data obtained in more detail, it is expected that many unresolved problems concerning the lunar plasma environment will be elucidated in the near future.

Acknowledgments The authors wish to express their sincere thanks to all the team members of MAP for their great support in processing and analyzing the MAP data. The authors also wish to express their grateful thanks to all system members of the Kaguya project. Kaguya-MAP-PACE sensors were manufactured by Mitaka Kohki Co. Ltd., Meisei Elec. Co., Hamamatsu Photonics K.K., and Kyocera Co.

References

Anderson KA, Chase LM, Lin RP, McCoy JE, McGuire, RE (1972) Solar-wind and interplanetary electron measurements on the Apollo 15 subsatellite, J Geophys Res 77:4611

Clay DR, Goldstein BE, Neugebauer M, Snyder CW (1972) Solar-wind spectrometer experiment, Apollo 15 Preliminary Science Report, NASA Spec Publ 289:10-1

Coates AJ (2004) Ion pickup at comets, Adv Space Res 33:1977

Colburn DS, Currie RG, Mihalov JD, Sonett CP (1967) Diamagnetic solar-wind cavity discovered behind Moon, Science 158:1040

Futaana Y, Machida S, Saito Y, Matsuoka A, Hayakawa H (2001) Counterstreaming electrons in the near vicinity of the Moon observed by plasma instruments on board NOZOMI, J Geophys Res 106:18729

Futaana Y, Machida S, Saito Y, Matsuoka A, Hayakawa H (2003) Moon-related nonthermal ions observed by Nozomi: Species, sources, and generation mechanisms, J Geophys Res 108(A1):1025. doi:10.1029/2002JA009366

Halekas JS, Mitchell DL, Lin RP, Frey S, Hood LL, Acuna MH, Binder AB (2001) Mapping of crustal magnetic anomalies on the lunar near side by the Lunar Prospector electron reflectometer, J Geophys Res 106:27841

Halekas JS, Mitchell DL, Lin RP, Hood LL, Acuna MH, Binder AB (2002) Evidence for negative charging of the lunar surface in shadow, Geophys Res Lett 29(10):1435. doi:10.1029/2001GL014428

Halekas JS, Bale SD, Mitchell DL, Lin RP (2005) Electrons and magnetic fields in the lunar plasma wake, J Geophys Res 110:A07222. doi:10.1029/2004JA010991

Halekas JS, Delory GT, Lin RP, Stubbs TJ, Farrell WM (2008) Lunar Prospector observations of the electrostatic potential of the lunar surface and its response to incident currents, J Geophys Res 113:A09102. doi:10.1029/2008JA013194

Halekas JS, Delory GT, Lin RP, Stubbs TJ, Farrell WM (2009a) Lunar Prospector measurements of secondary electron emission from lunar regolith, Planet Space Sci 57:78. doi:10.1016/j.pss.2008.11.09

Halekas JS, Delory GT, Lin RP, Stubbs TJ, Farrell WM (2009b) Lunar surface charging during solar energetic particle events: Measurement and prediction, J Geophys Res 114:A05110. doi:10.1029/2009JA014113

Hilchenbach M, Hovstadt D, Klecker B, Möbius E (1993) Observation of energetic lunar pick-up ions near earth, Adv Space Res 13:321

Hills HK, Meister JC, Vondrak RR, Freeman JW Jr (1972) Suprathermal ion detector experiment, Apollo 15 Preliminary Science Report, NASA Spec Publ 289:12-1

Howe HC, Lin RP, McGuire RE, Anderson KA (1974) Energetic Electron Scattering from the Lunar Remanent Magnetic Field, Geophys Res Lett 1:101

Lin RP, Mitchell DL, Curtis DW, Anderson KA, Carlson CW, McFadden J, Acuna MH, Hood LL, Binder A (1998) Lunar

surface magnetic fields and their interaction with the solar wind: results from Lunar Prospector, Science 281:1480

Lyon EF, Bridge HS, Binsack JH (1967) Explorer 35 plasma measurements in the vicinity of the Moon, J Geophys Res 72:6113

Mall U, Kirsch E, Cierpka K, Wilken B, Söding A, Neubauer F, Gloeckler G, Galvin A (1998) Direct observation of lunar pick-up ions near the Moon, Geophys Res Lett 25:3799

Mukai T, Miyake W, Terasawa T, Kitayama M, Hirao K (1986) Plasma observation by Suisei of solar wind interaction with comet Halley, Nature 321:299

Nakagawa T, Takahashi Y, Iizima M (2003) Geotail observation of upstream ULF waves associated with lunar wake, Earth Planets Space 55:569

Neugebauer M, Snyder CW, Clay DR, Goldstein BE (1972) Solar wind observations on the lunar surface with the Apollo-12 ALSEP, Planet Space Sci 20:1577

Nishino MN, Maezawa K, Fujimoto M, Saito Y, Yokota S, Asamura K, Tanaka T, Tsunakawa H, Matsushima M, Takahashi F, Terasawa T, Shibuya H, Shimizu H (2009a) Pairwise energy gain-loss feature of solar wind protons in the near-Moon wake, Geophys Res Lett 36:L12108. doi:10.1029/2009GL039049

Nishino MN, Fujimoto M, Maezawa K, Saito Y, Yokota S, Asamura K, Tanaka T, Tsunakawa H, Matsushima M, Takahashi F, Terasawa T, Shibuya H, Shimizu H (2009b) Solar-wind proton access deep into the near-Moon wake, Geophys Res Lett 36:L16103. doi:10.1029/2009GL039444

Ogilvie KW, Steinberg JT, Fitzenreiter RJ, Owen CJ, Lazarus AJ, Farrell WJ, Torbert RB (1996) Observations of the lunar plasma wake from the WIND spacecraft on December 27, 1994, Geophys Res Lett 23:1255

Saito Y, Yokota S, Asamura K, Tanaka T, Mukai T (2007) Low Energy Charged Particle Measurement by Japanese Lunar Orbiter SELENE, Advances in Geosciences, Volume 7, Adv Geosci 7:33

Saito Y, Yokota S, Asamura K, Tanaka T, Akiba R, Fujimoto M, Hasegawa H, Hayakawa H, Hirahara M, Hoshino M, Machida S, Mukai T, Nagai T, Nagatsuma T, Nakamura M, Oyama K, Sagawa E, Sasaki S, Seki K, Terasawa T (2008a) Low energy charged particle measurement by MAP-PACE onboard SELENE, Earth Planets Space 60:375

Saito Y, Yokota S, Tanaka T, Asamura K, Nishino MN, Fujimoto M, Tsunakawa H, Shibuya H, Matsushima M, Shimizu H, Takahashi F, Mukai T, Terasawa T (2008b) Solar wind proton reflection at the lunar surface: Low energy ion measurement by MAP-PACE onboard SELENE (KAGUYA), Geophys Res Lett 35:L24205. doi:10.1029/2008GL036077

Shimizu H, Takahashi F, Horii N, Matsuoka A, Matsushima M, Shibuya H, Tsunakawa H (2008) Ground calibration of the high- sensitivity SELENE lunar magnetometer LMAG, Earth Planets Space 60:353

Takahashi F, Shimizu H, Matsushima M, Shibuya H, A, Matsuoka, Nakazawa S, Iijima Y, Otake H, Tsunakawa H (2009) In-orbit calibration of the lunar magnetometer onboard SELENE (KAGUYA), Earth Planets Space 61:1269

Tanaka T, Saito Y, Yokota S, Asamura K, Nishino MN, Tsunakawa H, Shibuya H, Matsushima M, Shimizu H, Takahashi F, Fujimoto M, Mukai T, Terasawa T (2009) First in situ observation of the Moon-originating ions in the Earth's Magnetosphere by MAP-PACE on SELENE (KAGUYA), Geophys Res Lett 36:L22106. doi:10.1029/2009GL040682

Wieser M, Barabash S, Futaana Y, Holmström M, Bhardwaj A, Sridharan R, Dhanya MB, Wurz P, Schaufelberger A, Asamura K (2010) First observation of a mini-magnetosphere above a lunar magnetic anomaly using energetic neutral atoms. Geophys Res Lett 37:L05103

Yokota S, Saito Y, Asamura K, Mukai T (2005) Development of an ion energy mass spectrometer for application on board three-axis stabilized spacecraft, Rev Sci Instrum 76:014501-1

Yokota S, Saito Y, Asamura K, Tanaka T, Nishino MN, Tsunakawa H, Shibuya H, Matsushima M, Shimizu H, Takahashi F, Fujimoto M, Mukai T, Terasawa T (2009) First direct detection of ions originating from the Moon by MAP-PACE IMA onboard SELENE (KAGUYA), Geophys Res Lett 36:L11201. doi:10.1029/2009GL038185

Index

W. Liu, M. Fujimoto (eds.), *The Dynamic Magnetosphere*, IAGA Special Sopron Book Series 3,
DOI 10.1007/978-94-007-0501-2, © Springer Science+Business Media B.V. 2011